30/10-15-91 95 (2)

LBL-29700
UC-403

Annual Report 1990

Earth Sciences Division

DISCLAIMER

This document was prepared as an account of work sponsored by the United States Government. Neither the United States Government nor any agency thereof, nor The Regents of the University of California, nor any of their employees, makes any warranty, express or implied, or assumes any legal liability or responsibility for the accuracy, completeness, or usefulness of any information, apparatus, product, or process disclosed, or represents that its use would not infringe privately owned rights. Reference herein to any specific commercial product, process, or service by its trade name, trademark, manufacturer, or otherwise, does not necessarily constitute or imply its endorsement, recommendation, or favoring by the United States Government or any agency thereof, or The Regents of the University of California. The views and opinions of authors expressed herein do not necessarily state or reflect those of the United States Government or any agency thereof or The Regents of the University of California and shall not be used for advertising or product endorsement purposes.

This report has been reproduced directly from the best available copy.

Available to DOE and DOE Contractors
from the Office of Scientific and Technical Information
P.O. Box 62, Oak Ridge, TN 37831
Prices available from (615) 576-8401, FTS 626-8401

Available to the public from the
National Technical Information Service
U.S. Department of Commerce
5285 Port Royal Road, Springfield, VA 22161

Lawrence Berkeley Laboratory is an equal opportunity employer.

EARTH SCIENCES DIVISION ANNUAL REPORT 1990

Lawrence Berkeley Laboratory
University of California
Berkeley, California 94720

June 1991

Prepared for the U.S. Department of Energy under Contract No. DE-AC03-76SF00098

MASTER

DISTRIBUTION OF THIS DOCUMENT IS UNLIMITED

ACKNOWLEDGMENTS

This work was supported through U.S. Department of Energy Contract No. DE-AC03-76SF00098 by (1) the DOE Director, Office of Energy Research, (i) Office of Basic Energy Sciences and (ii) Office of Health and Environmental Research, and (iii) Office of Field Operations Management; (2) the DOE Director, Office of Civilian Radioactive Waste Management, Office of Facilities Siting and Development; (3) the DOE Assistant Secretary for Conservation and Renewable Energy, Geothermal Division; (4) the DOE Assistant Secretary for Fossil Energy, Office of Oil, Gas, and Shale Technologies; (5) the DOE Director, Office of Environmental Restoration and Waste Management, Office of Environmental Restoration; (6) U.S. Government Offices in (i) Agency for International Development, (ii) Bureau of Reclamation, (iii) Environmental Protection Agency, (iv) Geological Survey, and (v) National Science Foundation through various Universities; (7) the State of California, (i) Department of Health Services, (ii) State Lands Commission, and (iii) University of California; (8) the Gas Research Institute; and (9) the Electric Power Research Institute; and through national and international grants from commercial and public institutions.

LBL--29700

DE92 000647

CONTENTS

INTRODUCTION

Scientists and engineers of the Earth Sciences Division, following the mission of a multipurpose National Laboratory, conduct research on a wide variety of topics relevant to the nation's energy development programs. This report summarizes the activities for 1990. The Earth Sciences Division has developed unique expertise in several research areas. This expertise is due in part to the special resources and facilities available to researchers at the Lawrence Berkeley Laboratory and in part to the Laboratory's commitment to technical and scientific excellence. In addition to the permanent Laboratory staff, University faculty members, postdoctoral fellows, students, and visiting scientists participate in many investigations. Each year, several Ph.D. and Master's theses are founded in research within the Division. Interlaboratory cooperation within the U.S. Department of Energy system and collaboration with other research institutions provide access to unmatched intellectual and technological resources for the study of complex problems.

Much of the Division's research deals with the physical and chemical properties and processes in the earth's crust, from the partially saturated, low-temperature near-surface environment to the high-temperature environments characteristic of regions where magmatic-hydrothermal processes are active. Strengths in laboratory and field instrumentation, numerical modeling, and in situ measurement allow study of the transport of mass and heat through geologic media—studies that now include the appropriate chemical reactions and the hydraulic-mechanical complexities of fractured rock systems. Related and parallel laboratory and field investigations address the effects of temperature, pressure, stresses, pore fluids, and fractures on the elastic and electrical properties of rock masses. These studies are concerned with rock behavior in the brittle and ductile crustal regimes, and they drive the development of improved geomechanical and geophysical tools and techniques for mapping and characterizing heterogeneity in the subsurface. Recent initiatives in special areas of research have been generated in response to needs perceived by Congress, by DOE, by industry, or by the scientific community at large. Of particular note are three major Division efforts addressing problems in the discovery and recovery of petroleum, the application of isotope geochemistry to the study of geodynamic processes and earth history, and the development of borehole methods for high-resolution imaging of the subsurface using seismic and electromagnetic waves. In 1989 a major DOE-wide effort was launched in the areas of Environmental Restoration and Waste Management. Many of the methods previously developed for and applied to deeper regions of the earth will in the coming years be turned toward process definition and characterization of the very shallow subsurface, where man-induced contaminants now intrude and where remedial action is required.

This Annual Report presents summaries of selected representative research activities grouped according to the principal disciplines of the Earth Sciences Division: Reservoir Engineering and Hydrogeology, Geology and Geochemistry, and Geophysics and Geomechanics. We are proud to be able to bring you this report, which we hope will convey not only a description of the Division's scientific activities but also a sense of the enthusiasm and excitement present today in the Earth Sciences.

RESERVOIR ENGINEERING AND HYDROGEOLOGY

The scientists and engineers of the Reservoir Engineering and Hydrogeology group are primarily concerned with the fundamental problem of the movement of mass and energy through porous or fractured-porous geologic formations. Several approaches—including modeling studies, laboratory measurements, and field experimentation—are used to unravel the complex physics that controls such systems.

The group has contributed significantly to the understanding of fluid flow and tracer transport through single fractures and fracture networks in rocks. There is substantial activity in the area of multiphase and multicomponent nonisothermal flow through fractured porous media. A major modeling effort is being used to address the rather difficult problem of coupled effects relating thermal transfer, fluid flow, and mechanical stress changes in rocks. Another area of the group's diverse research program involves the development and field application of quantitative techniques for monitoring and predicting the movement of organic liquids and inorganic solutes in the subsurface.

Results of these different studies have found application in geothermal reservoir engineering, nuclear waste geologic disposal, and environmental evaluation and remediation projects. Other projects in which the group is active include thermal energy storage in unsaturated soils and advanced borehole testing techniques.

Reservoir Analysis of the Palinpinon Geothermal Field, Negros Oriental, Philippines

A. E. Amistoso, B. G. Aquino,* Z. P. Aunzo,* O. T. Jordan,* F. X. M. Sta. Ana,* G. S. Bodvarsson, and C. Doughty*

Over the last decade the United Nations Development Program (UNDP) has supported the Philippine National Oil Company (PNOC) in the development of geothermal resources in the Philippines. Two major objectives of this program have been (1) to train PNOC engineers and scientists and (2) to help develop a reservoir management program for the three major PNOC projects in Palinpinon, Bacman, and Tongonan.

In 1987 PNOC and Lawrence Berkeley Laboratory (LBL) started an informal cooperative project on the reservoir evaluation of Palinpinon under the auspices of UNDP. PNOC reservoir engineers have been trained to use LBL's computer codes for reservoir evaluation, and PNOC has obtained the results of the simulation studies for predicting the long-term response of the reservoir to exploitation. LBL has obtained high-quality data from PNOC geothermal fields that allow state-of-the-art reservoir evaluation techniques to be tested. The field data also offer insight into complex reservoir processes and help suggest new research problems that need to be addressed. Of special interest are reinjection data showing chemical and thermal breakthrough at producing wells. The primary activities of this cooperative project are

1. To conduct a numerical modeling and simulation study of the Palinpinon field.
2. To evaluate the size of the power plant that can be sustained by the Palinpinon I and II fields, given the current and predicted future responses of the existing production and injection wells to the exploitation of Palinpinon I, over a given plant amortization period.
3. To analyze injection data in terms of chemical and thermal breakthrough. The correlation between chemical and thermal fronts is of great interest to geothermal developers worldwide.
4. To recommend appropriate development strategies for Palinpinon II and reservoir management operating policies for Palinpinon I, such as the location and number of necessary make-up wells.

*Philippine National Oil Company, Geothermal Division—Energy Companies Bldg., PNPC Complex, Merritt Rd. Ft. Bonifacio, Makabi, Metro-Manila, Philippines

THE PALINPINON FIELD

The Palinpinon field is situated roughly 15 km west of the coastal city of Dumaguete on Negros Island in the Philippines. This field is divided into three sectors (Figure 1). In the eastern half is the Puhagan sector, where the first large plant, Palinpinon I, was constructed by the National Power Corporation. This plant has a generating capacity of 112.5 MWe and began its commercial operation in May 1983. Steam is produced from 20 production wells located in the southern part of Puhagan, and the separated waste liquid is reinjected into 10 reinjection wells located in the northern part of Puhagan. The well utilization and the number of wells on line at a given time depend upon the existing load demand, as well as established priorities determined from current field management operating philosophies.

The western half of the Palinpinon field encompasses the Nasuji and Sogongon sectors and has been allotted for the proposed development of the Palinpinon II geothermal field. Step-out exploration and delineation drilling started in 1980 and were followed by production drilling, which continued through 1983. At that time further development was suspended because of a decline in the expected industrial load brought on by a reduction of copper prices and the ensuing shutdown of mines located on the island and in its neighboring provinces. Results from the Nasuji and Sogongon wells were utilized in the preparation of a series of resource assessment reports (KRTA, 1982; PNOC-EDC/KRTA, 1983; and Urbino et al., 1988). The first report concludes that the production of electric power from Palinpinon II is both technically and economically feasible; the second concludes that there is a reasonable basis for proceeding with development of an additional 75-MWe power plant.

Figure 1 shows that reservoir temperatures at Palinpinon range from 250°C to over 300°C, with the main up-flow area being south of Puhagan and east of Nasuji. Pressures are nearly hydrostatic for the prevailing temperature at about 8 MPa/km (Urbino et al., 1988). The reservoir rocks are primarily fractured andesites, with transmissivity in the range of 1–10 Dm (Torrejos and Aquino, 1985; Amistoso et al., 1990). The well production rates vary from 10–240 kg/s, depending upon the near-well permeability and the enthalpy of the discharge, with an average power output of 6–7 MWe. The pre-exploitation average field enthalpy was about 1240 kJ/kg, which corresponds to liquid water at 280°C. The average field

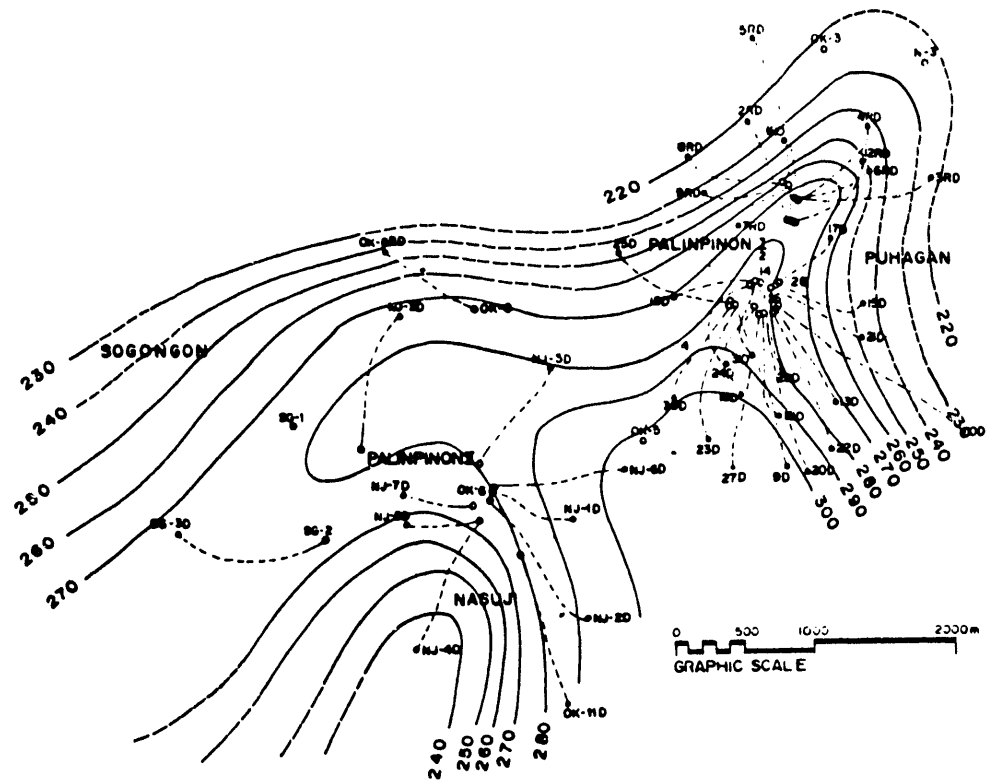

Figure 1. Map of the Palinpinon geothermal field. Contours show the distribution of temperature (°C) at 1000 m below mean sea level (after Urbino et al., 1988). [XBL 913-457]

enthalpy has increased from that value to about 1450 kJ/kg as a result of exploitation.

RESERVOIR STUDIES

The project was performed in three stages:

1. A two-dimensional well-by-well model of the Palinpinon geothermal reservoir was developed to determine the general distribution of the reservoir properties (e.g., rock matrix porosity, permeabilities, etc.) and to simulate the reservoir response to exploitation during the first 6 years of operation of the 112.5-MWe Palinpinon I geothermal power station in Puhagan.
2. The reservoir properties determined in the two-dimensional modeling study were used as initial input data for a larger more complex three-dimensional, three-layer model. The model was first calibrated against the pre-exploitation thermodynamic state of the reservoir and was then further refined by matching the exploitation history of the field during the first 6 years of production of the Palinpinon I plant in Puhagan. Various production scenarios were developed and evaluated to determine the likely response of the reservoir to future exploitation.
3. A smaller three-dimensional model of just the Puhagan section was developed from the large model and used to study the transient geochemical (chloride) and thermal responses to production and injection. This provided useful information on preferred flow channels within the reservoir.

These model studies were performed with the numerical model MULKOM (Pruess, 1983), using the grid generator CMESH (developed by Peter Fuller of LBL). Previous model studies of Palinpinon include work by Amistoso (1988) and Sta. Ana and O'Sullivan (1988).

RESULTS

The three-dimensional models were calibrated against the pre-exploitation temperature and pressure distributions, the observed pressure decline, and changes in enthalpy and chloride content of the produced fluids. The mass flow rates of the wells were prescribed, because their irregular on-off schedule prohibited the use of a productivity model to match the rates. The observed pressure decline was matched by adjusting the permeability distribution; one example match is given in Figure 2. For most of the wells the model matched the pressure decline reasonably well, although in some cases uncertainties in the data did not

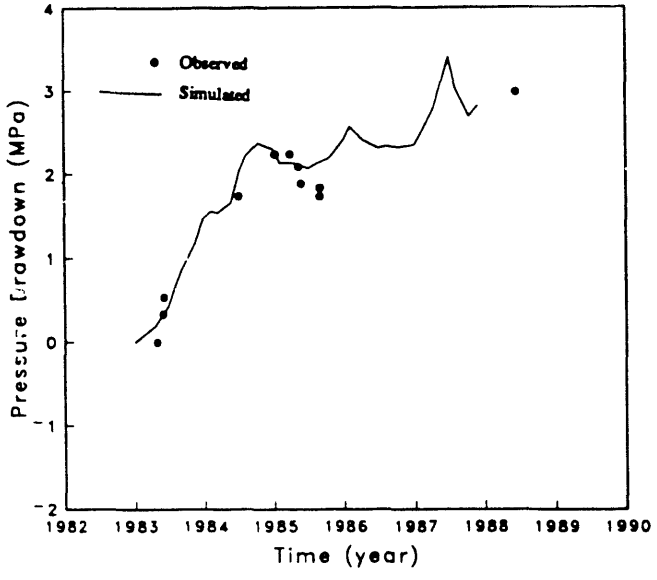

Figure 2. Observed and calculated pressure decline with time for well PN-24D. [XBL 913-458]

allow for rigorous matching. The initial estimate of the permeability distribution was obtained from the two-dimensional areal model and from the natural state modeling of the observed pressure and temperature distributions. The results of the modeling yielded an average reservoir transmissivity of about 10–20 Dm, with strong anisotropy due to the extensive fault systems and the stratigraphy. The reservoir porosity was used as an adjustable parameter to match the reservoir enthalpy, although for many of the wells the depth of the major feedzone determined the enthalpy rise. The reason for this is that a two-phase zone with high steam saturation develops in the shallow part of the reservoir in response to exploitation. Other constraining information on the porosity distribution were the changes in the chloride concentrations at producing wells (Harper and Jordan, 1985). In general, the reservoir porosity was estimated to range from 1 to 8% in the different reservoir regions. This range of values is in agreement with core porosity measurements performed by Bromley (1982) and DeLeon (1984).

Although the large-scale three-dimensional model of Puhagan is basically a porous medium model, it contains a double porosity submodel in the area where reinjection effects are strong. The incorporation of a fracture model was necessary to match some of the chloride changes at producing wells due to returns of injected water and, especially, to match the subsequent temperature decline. Because of the high heat capacity of gridblocks in porous medium models, one cannot adequately simulate breakthrough of the injected water and the resulting temperature decline. In the double porosity model the fracture porosity was used as an adjustable parameter to match the chloride changes, and the fracture spacing—or equivalently, the fracture/matrix block surface area—was used to match the thermal front movement. Figures 3 and 4 show examples of the matches obtained for the chloride changes and the temperature decline for well PN-19D, respectively. The three-dimensional model matches the chloride changes very well for almost all of the wells, and the temperature matches are also reasonable. In general, the results obtained suggest a heavily fractured rock near the area of injection but a larger fracture spacing close to the producers. The large-scale three dimensional model was used for predicting the reservoir response to various production scenarios.

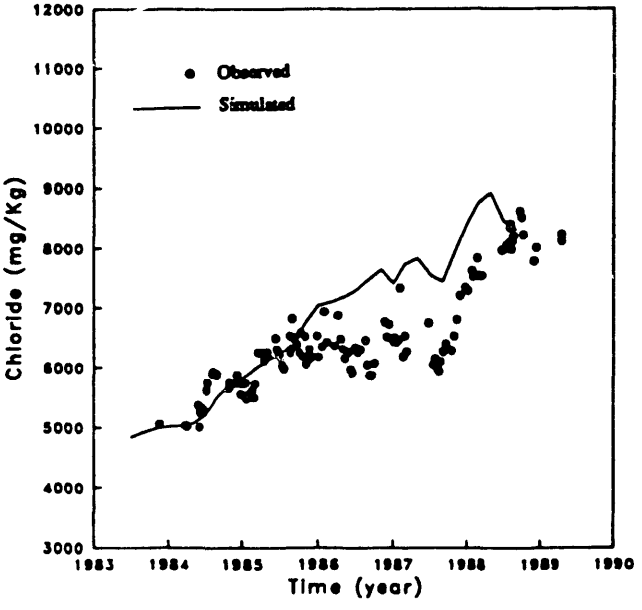

Figure 3. Observed and calculated concentration of chloride versus time for well PN-19D. [XBL 913-459]

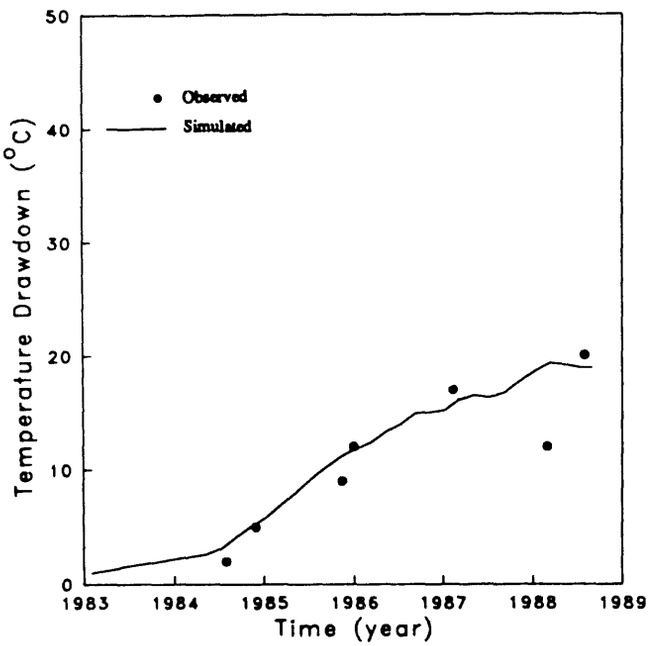

Figure 4. Temperature trend versus time (fracture medium model) for well PN-19D. [XBL 913-460]

ACKNOWLEDGEMENT

The authors express their appreciation to V. Stefansson of the United Nations for playing a major role in developing the cooperative agreement between PNOC and LBL.

REFERENCES

Amistoso, A.E., 1988. Palinpinon I/II simple lumped parameter modeling and its implications on the development strategy for Palinpinon II. PNOC-EDC Internal Report.

Amistoso, A.E., Aquino, B.G., Aunzo, Z.P., Jordan, O.T., Sta. Ana, F.X.M., Bodvarsson, G.S., and Doughty, C., 1990. Reservoir analysis and numerical modelling of the Palinpinon geothermal field, Negros Oriental, Philippines. UN-DTCD Project PHI/86/006 PNOC-ECD Final Report, 2 volumes.

Bromley, C.J., 1982. Notes on the porosity measurements of different rock types in the Southern Negros Geothermal Project. PNOC-EDC Internal Memo, p. 1–4.

DeLeon, M.M., 1984. Porosity calculations of some core rocks from Southern Negros geothermal field. PNOC-EDC Internal Report, p. 1–6.

Harper, R.T. and Jordan, O.T., 1985. Geochemical changes in response to production and reinjection for Palinpinon I geothermal field, Negros Oriental, Philippines. Proceedings, 7th New Zealand Geothermal Workshop, p. 40–43.

KRTA, 1982. Southern Negros Geothermal Project. Palinpinon II Development Feasibility Report, Vol. I, KRTA Limited, Auckland, New Zealand.

PNOC-EDC/KRTA, 1983. Resource assessment, Palinpinon geothermal field, Southern Negros, Philippines. PNOC-EDC Internal Report.

Pruess, K., 1983. Development of the general purpose simulator MULKOM. Earth Sciences Division Annual Report 1982. Lawrence Berkeley Laboratory Report LBL-15500, p. 133–134.

Sta. Ana, F.X.M., and O'Sullivan, M.J., 1988. Computer modelling of the Southern Negros geothermal field, Philippines. Proceedings, 10th New Zealand Geothermal Workshop, p. 100–102.

Torrejos, A.T., and Aquino, B.G., 1985. Preliminary interpretations of the results of the pressure monitoring and interference tests at Southern Negros geothermal field. PNOC-EDC Internal Report.

Urbino, M.E.G., Amistoso, A.E., and Aquino, B.G., 1988. Preliminary assessment of the Palinpinon field, Southern Negros, Philippines. PNOC-EDC Internal Report.

Overview of Kesterson Reservoir Selenium Remediation Project

S. M. Benson, T. K. Tokunaga, P. Zawislanski, A. W. Yee, R. Solbau, J. S. Daggett, J. M. Oldfather, and D. S. Lipton

From 1985 to the present scientists in Lawrence Berkeley Laboratory's Earth Sciences Division have studied the behavior of selenium in various habitats and environments at Kesterson Reservoir, Merced County, California (Figure 1). Investigations have been directed toward evaluating the efficacy of several remedial alternatives, from innovative techniques relying on the complex geochemical behavior in aquatic environments to conventional excavation schemes. Ultimately, results of these studies supported two cost-effective remedial measures; deliveries of drainage water were terminated in 1986, and 1 million cubic yards of soil were imported in 1988 to fill the low-lying areas of the former Kesterson Reservoir. To date, these two actions appear to have eliminated the aquatic habitat that caused waterfowl death and deformity at Kesterson from the early 1980s to 1987. As expected from scientific investigations carried out at Kesterson, biological, surface water, and groundwater monitoring data collected by the USBR indicate that Kesterson is now a much safer environment than in past years when drainage water containing 300 µg/L of selenium was delivered to the Reservoir.

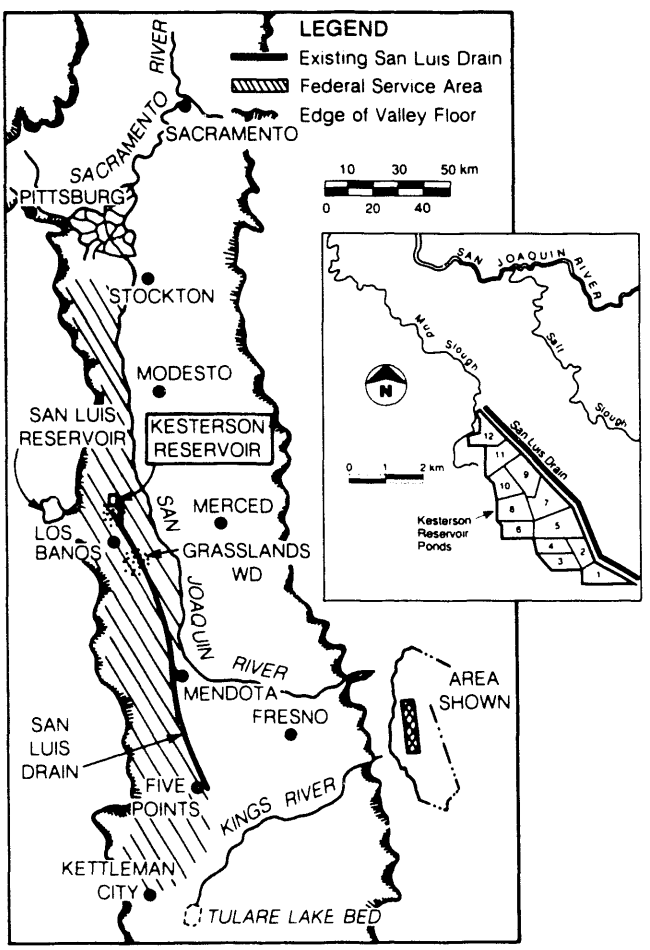

Figure 1. Location map of Kesterson Reservoir, Merced County, California. [XBL 859-10731B]

However, the continued presence of a large inventory of selenium within the upper portions of unfilled areas of Kesterson Reservoir and immediately below the fill material requires that a continued awareness of the status of this inventory be maintained. Of particular concern from the perspective of potential future exposures to selenium are (1) the distribution of soil selenium among fractions of differing availability, (2) transformations of the presently large insoluble fraction of this selenium inventory into more mobile and bioavailable soluble forms, (3) movement of this soluble selenium inventory up and down the soil profile, (4) mixing of selenium into rainwater pools, (5) leaching of selenium into the shallow water table, and (6) uptake of selenium through the food chain. Consequently, our investigations are now directed to monitoring and predicting the fate of the selenium inventory residing in the surface soils at Kesterson. Of particular concern is the likelihood of surface ponding during particularly wet years, when surface pools might contain levels of selenium in excess of "safe" concentrations of 2 to 5 µg/L. These issues are being addressed in a number of ways through our research programs, ranging from long-term monitoring of selenium concentrations in the vadose zone to field trials of selenium dissipation through microbial volatilization. Field experimentation and monitoring activities are supported by laboratory investigations of these same processes under more-controlled conditions.

Major topics of these investigations include the following:

1. Chemical evolution of the inventory of selenium residing in Kesterson soils, including physical redistribution within the soil profile, biological and geochemical transformation from immobile to mobile forms, and transformation to volatile forms.
2. Transport of selenium from soils to surface water pools formed by ponding of rainwater on Kesterson soils.
3. Processes and rates of processes leading to dissipation of the surficial inventory of selenium through microbial volatilization.

4. Feasibility of land disposal of seleniferous San Luis Drain sediments, including evaluation of potential application rates, transport to groundwater, and biological uptake in grasses and shrubs.
5. Reservoir-wide assessment of total selenium concentration and the fraction of this inventory that is soluble.

The current status of these investigations and implications for management of the former Kesterson Reservoir are summarized below.

Four years' of data are now available for assessing trends in selenium and salt concentrations in a *Distichlis*- and *Cressa*-vegetated region of Pond 11 (see Figure 1 for the location of Pond 11). Shortly after the Reservoir was dried out, rapid increases in salt and selenium concentrations were observed in the vadose zone. Over the past year this trend either slowed or leveled off. Overall, about 6% of the initially insoluble inventory was solubilized over the past 3 years, increasing the soluble fraction to about 15% of the total selenium inventory. In the same period, dissolved salt concentrations increased by about 50%, largely due to plant uptake of soil moisture. Increases in dissolved salt concentrations have slowed because plant growth has been less vigorous. Years of higher than average rainfall are expected to periodically reverse these trends, giving rise to increases in selenium and salt concentrations. The net trends resulting from a sequence of wet and dry years, as can be expected in the Central Valley, remain uncertain.

Continued monitoring of two test plots, one in Pond 8 and one in Pond 9 (see Figure 1 for pond locations), show that large increases in dissolved selenium and salt concentrations are associated with revegetation of playa areas within the Reservoir. These trends appear to be associated with drying of the soil profile due to uptake of moisture by plants and consequent oxidation of the soil environment. The magnitudes of salt and selenium increases in these environments are similar to those observed in the Pond 11 test plot described above. Future trends in recently revegetated areas are expected to slow down as a stable soil-moisture regime is established.

Soil selenium concentrations in the top 0.15 m are strongly influenced by rainfall infiltration. Selenate, in particular, is readily leached downward in the soil profile by winter rains, and this will tend to decrease the inventory of soluble selenium that is available for dissolution in rainwater pools that form at Kesterson.

Soil selenium concentrations in the fill areas are increasing as a result of evaporative and transpirative flux of soil moisture from the water table toward the root zone and soil surface (molecular diffusion will also tend to increase soil selenium concentrations in the fill material). At two monitoring sites, one in Pond 5 and one in Pond 7 (Figure 1), dissolved selenium concentrations within the root zone of *Kochia scoparia*, the dominant plant in the filled areas, are now nearly the same as in the unfilled areas (e.g., thousands of µg/L). A Reservoir-wide sampling of filled areas (18 sample sites) indicates that these elevated levels of soluble selenium have not yet reached the surface of the dirt fill.

Selective extraction procedures have been developed and applied in an effort to determine the dominant forms of selenium in Kesterson soils. These experiments indicate that within surface soils, the dominant forms of selenium are extracted with a solution commonly believed to dissolve soil-organic matter. The precise forms of selenium associated with this pool have not been resolved, but likely forms include elemental selenium, organic forms of selenium, and adsorbed selenite. The strong association between selenium and soil organic matter is consistent with the processes that lead to accumulation of selenium in the organic-rich marsh-bottom sediments present when Kesterson was in operation. It also suggests that the evolution and fate of selenium in Kesterson soils is closely coupled to cycling of soil organic matter. Implications of this association are being pursued in a set of laboratory experiments.

From a Reservoir-wide synoptic sampling of selenium concentrations in the top 0.15 m of soil, the following information has been obtained. Representative mean values (and ±95% confidence intervals) for the total selenium values are <2, 2.8 (±3.8), and 9.3 (±11.8) mg/kg of soil, in the fill, grassland, and open areas, respectively. Representative mean values for the water-extractable total selenium values are 0.04 (±0.14), 0.15 (±0.15), and 0.33 (±1.0) mg/kg of soil, in the fill, grassland, and open areas, respectively. Selenium concentrations within any "habitat" range over an order of magnitude, making conclusions on appropriate management action by habitat type unreliable. The fraction of the total selenium inventory in Kesterson soils that is water-extractable is about 5%, indicating that only a limited amount of the selenium is currently mobile and available for plant uptake and dissolution in rainwater pools. No significant changes in total or water-extractable selenium concentrations have been observed between the 1989 and 1990 data sets.

The cumulative evidence available to date indicates that the total inventory of selenium, the fractions that are in water-soluble form, and the distribution within the soil profile will change slowly in the Kesterson environment. Processes contributing to this evolution include microbial transformation of organic and inorganic forms of selenium to volatile forms that may dissipate in the atmosphere, cyclic oxidation and reduction of selenium resulting from seasonal variations in soil moisture content, mineralization of soil organic matter, and physical redistribution resulting from root uptake of soil moisture and rainfall infiltration. The net effect of all these eventually will be to decrease the amount of selenium in this environment. However, in the

interim, increases in the quantities of readily available selenium may be observed. Nevertheless, these changes are expected to occur slowly. Under unmanaged conditions, measurable changes in mean selenium concentrations, fractions in the water-soluble form, and distribution within the soil profile are not expected to occur over the next 10 years in the areas covered by native Kesterson soil. Areas covered with fill are expected to undergo more rapid changes because of the large gradients in selenium concentrations at the fill/native soil interface.

During years with annual rainfall in excess of 350 mm (about 50% more than normal), surface water pools from several up to 20 cm deep are expected to form within the Reservoir. In the event of a 500-mm rainfall (100-year event), pools from 10 to 25 cm deep are expected to form over most of the Reservoir. The water in the pools will be derived from rainwater ponding at the soil surface. Selenium and salts present at the soil surface will dissolve in these pools, creating selenium concentrations ranging from less than detectable to several hundred µg/L. Estimates of a Reservoir-wide average selenium concentration have been made. For 20-cm-deep pools covering the entire Reservoir, estimates of the average selenium concentrations range from <5 to 30 µg/L. Given the sparsity of data from which these estimates were obtained, it is not possible to narrow the expected range of average concentrations. These concentrations are in the range of values measured in surface waters near Kesterson, including Mud Slough, Fremont Canal, and the San Luis Drain. However, they exceed the "safe levels" of 2 to 5 µg/L recommended for aquatic life.

To prevent formation of aquatic habitat at Kesterson that may attract nesting birds during spring, provisions for draining surface waters from the Reservoir are prudent. Direct discharge of surface drainage into Mud Slough or discharge through the San Luis Drain into Mud Slough would be the most practicable solutions for an emergency drainage plan. Given the high levels of selenium observed in Mud Slough over the past year (up to 50 µg/L), it is unlikely that the incremental loading of selenium due to surface drainage from Kesterson during unusually wet years would contribute significantly to degradation of this waterway.

An experiment is under way to evaluate the potential risks and benefits of land disposal of San Luis Drain sediments containing up to 100 mg/kg of selenium. This experiment demonstrates that applying a 7.5-cm-thick layer of these sediments to soils with low concentrations of selenium results in selenium concentrations in soil water and upland vegetation similar to levels observed throughout Kesterson. This indicates that San Luis Drain sediments are an effective soil supplement for increasing selenium concentrations in upland vegetation and may provide an economical soil supplement for the selenium-deficient east side of the San Joaquin Valley. At the same time, selenium concentrations may be elevated enough so that unmonitored exposure to such vegetation may pose a hazard to wildlife. Decreasing the application rate should result in lowering the quantity of selenium available for plant uptake. Monitoring at Kesterson will continue in order to establish time trends in soil water, soil, and biotic concentrations of selenium.

BIBLIOGRAPHY

Benson, S.M., Delamore, M., and Hoffman, S., 1990. Kesterson crisis: Sorting out the facts. *In* Proceedings, National Conference on Irrigation and Drainage Engineering, ASCE, Durango, Colorado, July 11–13, 1990 (LBL-30587).

Benson, S.M., Tokunaga, T.K., Zawislanski, P., Yee, A.W., Daggett, J.S., Oldfather, J.M., Tsao, L., and Johannis, P.W., 1990. Hydrological and geochemical investigations of selenium behavior at Kesterson Reservoir. Lawrence Berkeley Laboratory Report LBL-29689.

Benson, S.M., White, A., Halfman, S., Flexser, S., and Alavi, M., 1990. Groundwater contamination at the Kesterson Reservoir, California. Part I: Hydrological setting and conservative solute transport. Water Resour. Res. (in press) (LBL-29901).

Long, R.H., Benson, S.M., Tokunaga, T.K., 1990. Selenium immobilization in a pond sediment at Kesterson Reservoir. J. Environ. Qual., v. 19, no. 2, p. 302–311 (LBL-27807).

Poister, D., and Tokunaga, T., 1991. Selenium in Kesterson Reservoir ephemeral pools: 2. Laboratory experiments. Submitted to J. Environ. Qual. (LBL-30589).

Tokunaga, T.K., and Benson, S.M., 1991. Selenium in Kesterson Reservoir ephemeral pools: 1. A field study of ponding resulting from shallow water table rise. Submitted to J. Environ. Qual. (LBL-30588)

Tokunaga, T.K., Lipton, D.S., Benson, S.M., Yee, A.W., Oldfather, J.M., Duckart, E.D., Johannis, P.W., and Halvorsen, K.E., 1991. Soil selenium fractionation, depth profiles and time trends in a vegetated upland at Kesterson Reservoir. Water, Air and Soil Pollution (in press) (LBL-29049).

White, A., Benson, S.M., Yee, A., Wollenberg, H., and Flexser, S., 1991. Groundwater contamination at the Kesterson Reservoir, California. Part II: Geochemical parameters influencing selenium mobility. Water Resour. Res. (in press) (LBL-30385).

Evaluation of a Casting-and-Imaging Technique for Measuring Void Geometry of Fractured Rock Specimens

B. L. Cox, P. Persoff, and K. Pruess

The quantification of rock fracture void geometry is important in the study of geology, rock mechanics, and fluid flow. Natural fractures in rock have rough faces; besides being important indicators of the previous history of the fracture, the contact areas between the two faces can affect the present distribution of stresses along the fracture and can create tortuous pathways for fluids. Single- and multiphase flow of fluid in rock fractures is of great importance in the fields of waste storage and energy recovery. Our efforts have been focused on trying to quantify the geometry.

Previous quantification of void geometry by others included using sensitive paper to record contact areas (Iwai, 1976), measuring both sides of a fracture with a profilometer (Gentier, 1986), and injecting a low-melting-point metal into the fracture (Pyrak-Nolte et al., 1987). A new technique for quantifying void geometry has been developed jointly by Lawrence Berkeley Laboratory (LBL) and the Bureau de Recherches Geologiques et Miniers (BRGM); the technique involves (1) making a translucent silicone cast of the fracture, (2) photographing this cast by transmitted light to obtain a digitized map of the light intensities, and (3) converting the light intensity values to thickness (Gentier et al.,1989; Cox et al., 1990). We have improved and evaluated this technique in order to determine its reproducibility and to consider its use for quantifying fracture void geometry for flow visualization experiments. Our evaluation included a comparison of data from the casting technique with data from a profilometer measurement and an estimate of errors in the various steps of the casting-and-imaging technique.

FRACTURED ROCK SPECIMEN

A fractured rock sample was excavated from near the surface of a normal range-front fault in Dixie Valley, Churchill County, Nevada (Power, 1989; Power and Tullis, 1989). The fault contact separates metamorphosed Jurassic gabbro from alluvial fan sediments and consists of highly altered slickenside rock surfaces of predominantly quartz composition. The surface area of the fracture specimen is an irregular shape roughly 110×110 mm^2. Power (1989) measured the void geometry of this fracture using an automatic mechanical profiling system (Keller and Bonner, 1985). We measured the void geometry of this same fractured rock specimen using the casting-and-imaging technique of Gentier et al. (1989). We cast and imaged the fracture several times to obtain data sets to compare (1) the two measuring techniques and (2) the reproducibility of the casting technique.

COMPARISON OF MEASUREMENT TECHNIQUES

Power measured profiles in grids across both sides of the fracture. One hundred sixty-four traverses were made at a spacing of 0.51 mm, and measurements were taken at 0.51 mm along each traverse. This yielded raw topographic data for both surfaces. The corresponding points on the two surfaces were matched by optimizing the fit of the two surfaces, and the raw topographic data were subtracted to give the aperture, or "composite topography." We extracted a 1024×1024 pixel subset from the cast images, which corresponded approximately to the region covered by the mechanical profilometer. Each pixel represented an area approximately 0.07×0.07 mm, or more than seven times the spatial resolution (in each horizontal dimension) of the mechanical profilometer data set.

The data sets obtained by the two methods represent the pointwise aperture as a function of position in the fracture plane. We refer to this as the "aperture surface," not to be confused with the rough faces of the fracture. We compared aperture surfaces obtained by the two methods visually (i.e., by plotting) and statistically. Figures 1 and 2 show the aperture surface as measured by the profilometric and casting techniques, respectively. All three data sets show log-normal distributions.

Comparisons of Figures 1 and 2 show that the void geometry measured by the profilometric and casting techniques are quite similar. Table 1 shows the statistics for the profilometer data (P1) and two replicate castings (C1 and C2). These statistics, along with Figures 1 and 2, show that although the roughness of the aperture surface, as indicated by the standard deviation of apertures measured at individual pixels, is similar in all three measures, the absolute value of the aperture, as indicated by the mean, varies considerably, both between the two techniques (data sets C1 and P1) and between replicates of the casting technique (C1 and C2). Baseline in the profilometric technique is based upon setting the smallest aperture to zero. In the casting-and-imaging technique, it is determined by the amount of casting material that doesn't get squeezed out of the void space. The large discrepancy in the mean values between C1 and C2 impelled us to examine all steps in the casting-and-imaging process to

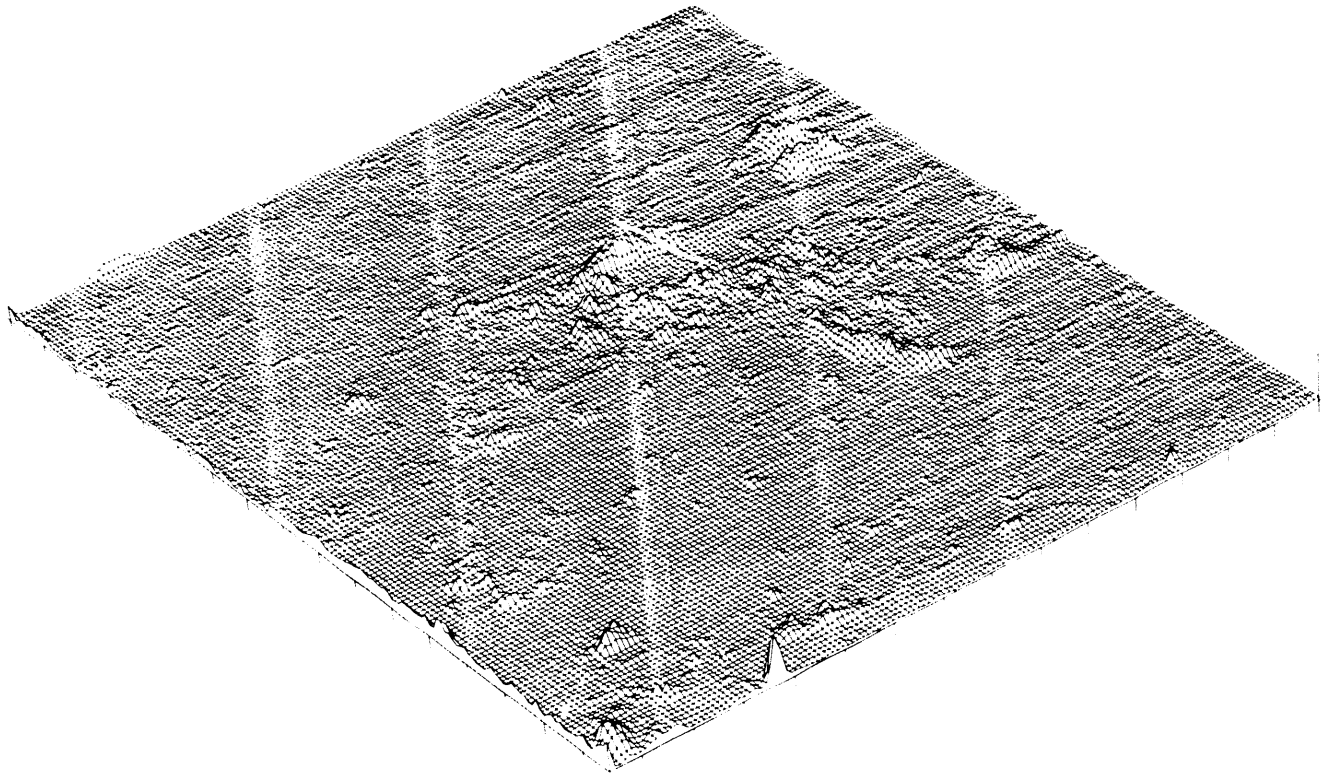

Figure 1. Aperture surface measured by profilometer technique (P1). [XBL 897-2541]

Figure 2. Aperture surface measured by casting-and-imaging technique (C1). [XBL 896-2198]

Table 1. Statistics for profilometer data and two replicate castings.

Data set	Area covered	Number of pixels	Spacing	Aperture mean	Std. deviation
P1	83.3 × 73.2 (mm)	164 × 144	0.508 mm	0.16 mm	0.076 mm
C1	69.8 × 69.8 (mm)	1024 × 1024	0.068 mm	0.090 mm	0.055 mm
C2	72.0 × 72.0 (mm)	1024 × 1024	0.070 mm	0.039 mm	0.069 mm

identify and quantify the sources of error and try to improve the reproducibility of the technique.

SOURCES OF ERROR IN THE CASTING PROCESS

The casting method is described by Gentier et al. (1989). The two sides of the fracture are fitted together to act as a mold in which the fracture itself is filled with a colored, translucent RTV (room-temperature-vulcanizing) silicone rubber (Rhone-Poulenc #1556). A calibration wedge of known varying thickness is cast at the same time by pouring the same batch of silicone material into a machined mold with a flat cover plate. We improved the design of the calibration wedge, replacing a ramp with steps. Each step can be precisely measured so that the resulting image can be calibrated exactly. We also improved the casting technique by minimizing variations in aperture due to differences in the way the two sides of the fracture are held together during curing. For each fracture, we used metal struts and bolts with pressure-sensitive washers and a torque wrench in order to hold together the two sides of the fracture with a reproducible pressure. The clamped fracture and cast, along with the calibration wedge, were then cured for 4 hours at 100°C.

The second step in the casting process requires the careful separation of one side of the fracture from the cast. A collar is then secured around the other side of the rock attached to the cast, and a clear RTV base is poured into the collar. This clear base acts as a support for the cast, facilitating the removal of the cast from the rock and supporting the cast during the imaging process.

There are many possible sources of error in the casting technique, and the most important of these are shown in Table 2. Some of these are systematic, affecting the whole fracture, and others are local. The mixing ratio errors refer to the mixing of the two parts of the RTV, requiring accurate weights and mixing. The shelf life of the RTV is nominally 6 months, and the material changes with time, becoming more viscous. This affects the filling of voids and the formation of bubbles. Fitting and filling errors are the most problematic and difficult to control. Curing errors refer to the possibility that the RTV may cure differently in the metal calibration mold than in the rock fracture. Cast removal errors refer to the tendency for the RTV material to tear or stick to the rock. Errors for the clear base refer to the difficulty in controlling the thickness of the base.

Table 2. Estimates of casting errors.

Variable	Error type	Error estimate
Mixing ratio	Systematic	Unknown
Filling of voids	Local	0.5 mm
Bubbles	Local	Up to 1 mm in size
Fitting	Systematic	0.05 mm
Curing	Systematic	0.02 mm
Cast removal	Local	0.6 mm
Clear base	Systematic	0.005 mm

SOURCES OF ERROR IN IMAGING AND CALIBRATION

The image of the translucent cast and calibration ramp is obtained using an image analyzer (Eiconix 78/99 AD2) located at the National Center for Electron Microscopy (NCEM). This camera uses a linear photodiode array to capture an image of 2048 × 2048 pixels, each having a light intensity digitized between 0 and 255. With the cast resting on a light table for imaging, we compared images obtained from both an incandescent and a fluorescent light source. The fluorescent light has an advantage in being a cooler light source with a lower overall range in intensity.

The calibration process requires a physical measurement of the heights of the calibration steps, since the nominal thickness of the steps will usually not be the same as the actual thickness. We measured the steps with a profilometer and then found the corresponding light intensities for each position measured. The actual value of the calibration wedge image was divided by the intensity of the background image. According to the Beer-Lambert law, the quotient of the incident and transmitted light should equal the negative exponent of the thickness times some constant. By plotting the log of the light intensity quotient versus the thickness, a calibration curve can be obtained for use in converting the cast image to apertures.

The errors estimated for the digitizing and calibration are shown in Table 3. An unknown but probably small error may be introduced by the focal length of the camera lens, which may distort images away from the center. Because the light source varies with time, small errors are introduced when correcting the cast and calibration wedge with a light source background that was photographed at a different time. Calibration errors are introduced by the physical measurement of the steps in the calibration wedge, by pixel image averaging, and by the curve-fitting used to convert the light intensities to thicknesses. We noticed a systematic difference in the resolution of the imaging technique due to calibration in the thick versus thin apertures.

CONCLUSIONS

Our improvements in cast-fitting and calibration may have improved the reproducibility by a factor of 3. Our best estimate of vertical resolution is on the order of 0.1 mm; of horizontal resolution, about 0.7 mm, for a pixel area of 0.07×0.07 mm. The casting technique does not seem to have the resolution and reproducibility that we had hoped for. The casting material very effectively reproduces the surfaces of the rock, but fitting problems and optical problems reduce the resolution of the thickness measurement. It is probably possible to reduce some of the optical problems with smoothing techniques, but this would be time-consuming, and the fitting problems would still be a major limitation.

The casting-and-imaging technique does produce a very nice physical model of the void geometry that can help in conceptualization of void geometry. The casting technique seems to have greatest value as a semiquantitative technique that shows the distribution or patterns of thick and thin apertures in different kinds of fractures. For flow visualization experiments, the casting technique could provide a useful map, but it is not precise or accurate enough for relative permeability determinations.

Table 3. Estimates of digitizing and calibration errors.

Variable	Error type	Error estimate
Camera	Local	Microns
Light source	Systematic	0.05 mm
Calibration	Systematic	Tens of microns
Averaging	Extreme values	Tens of microns

ACKNOWLEDGMENTS

Many people contributed to this work at different stages. Lisette van Vliet taught us the casting technique, which she and Sylvie Gentier had developed with Jane Long. Bill Power provided the Dixie Valley rock specimen and the profilometer data used in the comparison study. Hans Kraft helped us measure the calibration steps. Ed Sheena and Amy Davey provided computer assistance. The digitizing would have been impossible without the facilities of LBL's National Center for Electron Microscopy and the generous time and advice provided by John Turner and Michael O'Keefe.

REFERENCES

Cox, B.L., Pruess, K., and Persoff, P., 1990. A casting and imaging technique for determining void geometry and relative permeability behavior of a single fracture specimen. Presented at the Fifteenth Workshop on Geothermal Reservoir Engineering, Stanford, California, January 23–25, 1990 (LBL-28485).

Gentier, S., 1986. Morphologie et comportement hydromecanique d'une fracture naturell dans un granite sous contrainte normale (doctoral thesis). University d'Orleans, France, 640 p.

Gentier, S., Billaux, D., and van Vliet, L., 1989. Laboratory testing of the voids of a fracture. Rock Mech. Rock Eng., v. 22, p. 149–157.

Iwai, K., 1976. Fundamental studies of fluid flow through a single fracture (Ph.D. thesis). University of California, Berkeley.

Keller, K., and Bonner, B.P., 1985. Automatic, digital system for profiling rough surfaces. Rev. Sci. Instrum., v. 56, p. 330–331.

Power, W.L., 1989. Roughness of natural fault surfaces: Implications for friction and deformation in fault zones (Ph.D. thesis). Brown University, Providence, Rhode Island.

Power, W.L., and Tullis, T.E., 1989. The relationship between slickenside surfaces in fine-grained quartz and the seismic cycle. Submitted to J. Struct. Geol.

Pyrak-Nolte, L.J., Myer, L.R., Cook, N.G., and Witherspoon, P.A., 1987. Hydraulic and mechanical properties of natural fractures in low permeability rock. *In* P.G. Herget and S. Vongpaisal (eds.), Proceedings, Sixth International Congress on Rock Mechanics, Montreal, Canada, August 30–September 3, 1987. A.A. Balkema, Rotterdam, The Netherlands, p. 225–231 (LBL-22718).

An Application of the Simulated Annealing Fracture Flow Model at the Grimsel Rock Laboratory, Switzerland

A. Davey, K. Karasaki, J. C. S. Long, S. J. Martel, and M. Landsfeld

The disposal of nuclear waste is the subject of research internationally, and many countries are considering storage in underground facilities. The need to predict accurately the long-term effects of storing waste underground has led to greater effort in developing and validating models of fluid flow and transport in fractured rock. One of the major problems in analyzing flow and transport in fractured rock is that the flow may be largely confined to a poorly connected network of fractures. In these cases, the equivalent continuum models for flow and transport that were developed for porous media problems may not be reliable. Alternative modeling approaches have been explored for these cases. One approach is discrete fracture flow modeling, where every fracture that carries flow is explicitly represented in a stochastic model (e.g., Long, 1983; Billaux et al., 1989). A problem with these models is that they focus on determining the hydrologic behavior from a statistical description of the fracture geometry. This can be very difficult, because many fractures do not conduct fluid and because much of the flow may be carried by a few large features that are not well sampled.

To overcome some of these problems, Lawrence Berkeley Laboratory has been developing a new type of fracture hydrology model called an "equivalent discontinuum" model. In these models we represent the discontinuous nature of the problem through flow on a partially filled lattice. Essentially, we look at flow through the fractured rock as an equivalent percolation problem on a complex lattice. The lattice we choose, called a "template," is designed to contain a set of possibly important conductors. The choice of template depends on a geologic evaluation of the medium. If there is no information about the structure of the rock, the template could be a regular lattice in space.

A key step in constructing an equivalent discontinuum model from this lattice is to remove some of the conductive elements, so that the system becomes partially connected in the same manner as the fracture network. This is done through a statistical inverse technique called "simulated annealing" (Kirkpatrick et al., 1983; Press et al., 1986; Tarantola, 1987). The simulated annealing algorithm makes changes in the lattice and examines whether the changes cause the model to represent, more or less, the behavior of an in situ test. Changes are accepted according to a stochastic process that results in a model that can reproduce hydrologic data observed in the field.

This report gives a detailed description of simulated annealing and an example application of this technique. The example is based on data from the Migration Experiment (MI) at Grimsel Rock Laboratory in Switzerland. The MI experiment has been carried out by the Swiss Nationale Genossenschaft fur die Lagerung radioaktiver Abfälle (NAGRA) (Frick et al., 1988). The MI site consists of a simple, subvertical fracture zone that is intersected by several of the tunnels in the Grimsel Rock Laboratory in the Swiss Alps. From this tunnel, a series of boreholes were drilled into various parts of the fracture zone in order to carry out a series of hydraulic and tracer tests. The MI site provided a unique opportunity to develop a model using geological information and hydrologic field data. We were able to construct a model, identify possible solutions for the flow geometry given the hydrologic test results, assess the predictive performance of our solutions, and propose improvements for future use. The results of the analysis of the MI data are preliminary but offer encouragement for the utility of this new approach.

THE MIGRATION SITE CASE

Once we have developed a set of possible conductors in the fracture flow system and estimated the boundary conditions, we are ready to use the inversion algorithm. The hydrologic tests we use control the final result of the model-building procedure. The hydraulic inversion technique, using a simulated annealing algorithm, finds discontinuous flow geometries that behave like the real system. Since the problem is ill-posed and we do not make continuity assumptions for this media, we find multiple solutions. The resulting solutions are assessed using statistical methods and expert opinion. The MI study has allowed us to validate our inverse models and identify future improvements. We have modeled the MI zone as a two-dimensional system. We first developed a template that contains all the channels that our fracture flow model could possibly include. We then use the annealing algorithm to develop channel models for the steady-state and the transient case. Five solutions were found for the steady-state pressure case. A cross-validation study was done to estimate the prediction error associated with using the steady-state solutions to predict the steady-state head value at an arbitrary point in the channel model. For the transient case, only a single solution was found.

The template for the MI site was based on the geology of the MI zone. Geologic field investigations

indicated that the hydraulic conductivity of the MI zone was probably greatest in the dip direction of the zone. Accordingly, the template for the migration zone was constructed with straight channels in the dip direction. This assumption is based on geologic evidence for hydrologic anisotropy of the fracture zone. The grid has a coarse border that surrounds a fine mesh in the vicinity of the eight wells and the drift. The central region with the fine mesh is where we expect annealing to be able to resolve details in the pattern of conductance. The border region moves the boundary outside the region we modeled hydrologically and diminishes perturbation from the boundary effects. No meaningful resolution of pattern is expected in the border region. The template is a 50×42 m grid with a 30×22 m center region. The template has three fracture channel sets: the inclination from horizontal (as measured in the plane of the zone) are 30°, 90°, and 150°. Figure 1 shows the MI template. The spacing between fractures is 0.8 m in the center and 2.4 m in the border region. The eight boreholes are represented by marked nodes in the grid, and the drift is an open circle in the mesh.

We tried first to build the simplest possible model. Therefore, each channel in the template has the same conductance. We used a curve-shifting technique to estimate the value of this conductance at each iteration. The storativity of the channels in the border region is 3.0×10^{-5} L/m, and the center channels have a storativity of 1.0×10^{-5} L/m, so that the total storativity in each region is the same.

The steady-state pressure case was studied. In the steady-flow case, the head at the various wells was measured in response to drawdown to the drift running through the fracture. Figure 2 shows the head record in the wells during a pumping test (Solexperts, 1989). The heads at the end of the recovery period were used for the steady-state case.

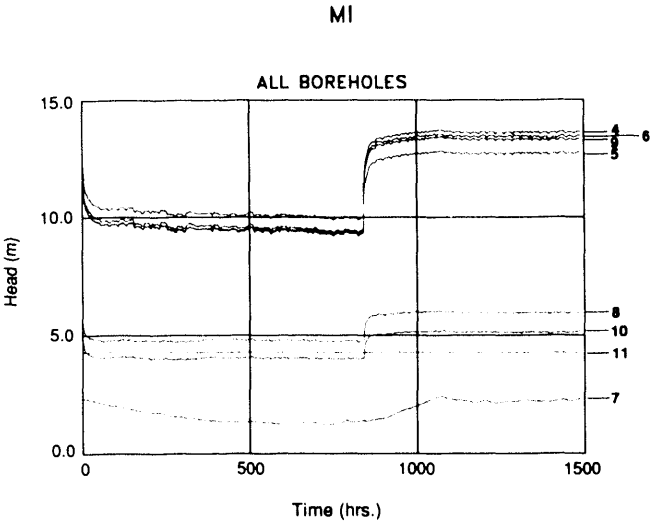

Figure 2. Pressure records from the constant flow withdrawal test followed by a buildup test (Solexperts, 1989). [XBL 8910-3872]

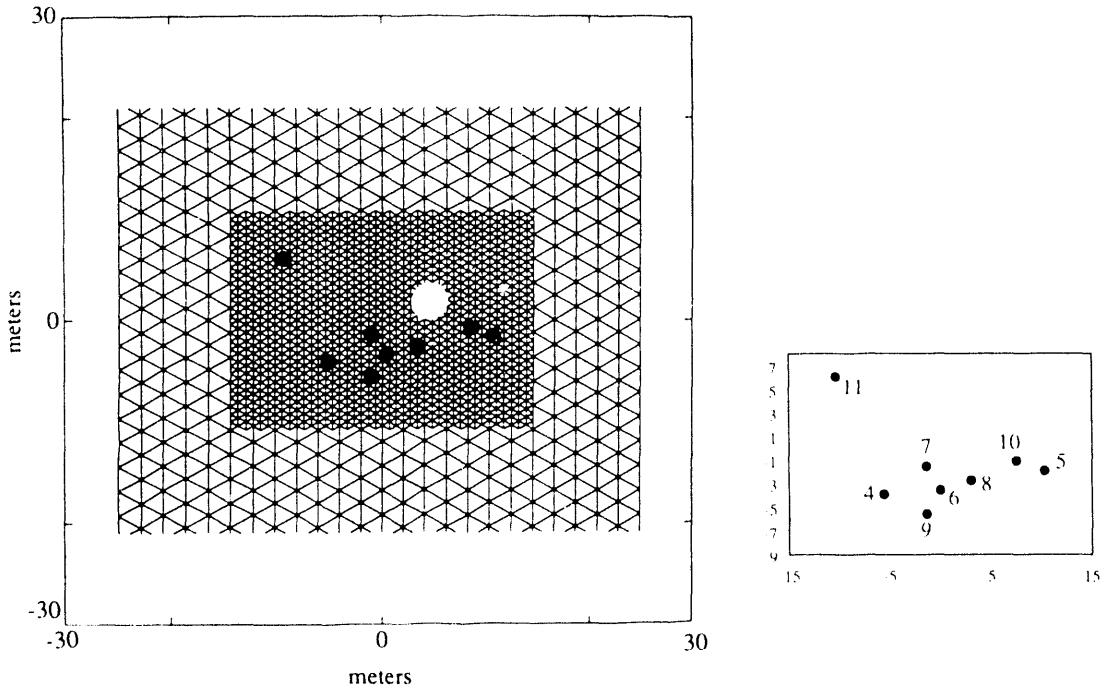

Figure 1. The MI template with three fracture sets. [XBL 8910-3873]

STEADY-STATE RESULTS

The annealing algorithm was used five times to find configurations that matched the observed data for heads at the end of the recovery period. Two configurations are given in Figures 3 and 4 (cases 1 and 2). The first solution was found starting from a configuration with 60% of the elements present; the second solution was found starting from a configuration with 70% of the elements present; and the third, fourth, and fifth were found starting from configurations with 80%, 90%, and 100% of the elements present, respectively. We refer to these as cases 1 through 5. Note that the annealed models show a lack of connection between wells 7, 11 and wells 4, 6, 9. Moreover, annealing has found a lack of connection between well 11 and the boundary; this is happening because well 11 had a very low head, close to zero. As the drift boundary is at atmospheric pressure and the outer boundaries are held at a higher head, steady-state annealing encourages a connection to the drift. Transient annealing might be used to see if this well is simply not connected to anything if the data are sufficient. These data should be collected sequentially, using different holes as different sources.

Each of the solutions was found using the same temperature schedule but starting from different configurations. This means that the number of changes the algorithm accepted at each temperature in the schedule is the same for all the solutions. The solutions are within the estimated measurement error of the observations, which we assumed to be on the order of 0.1 m, judging from the tolerance for similar instruments.

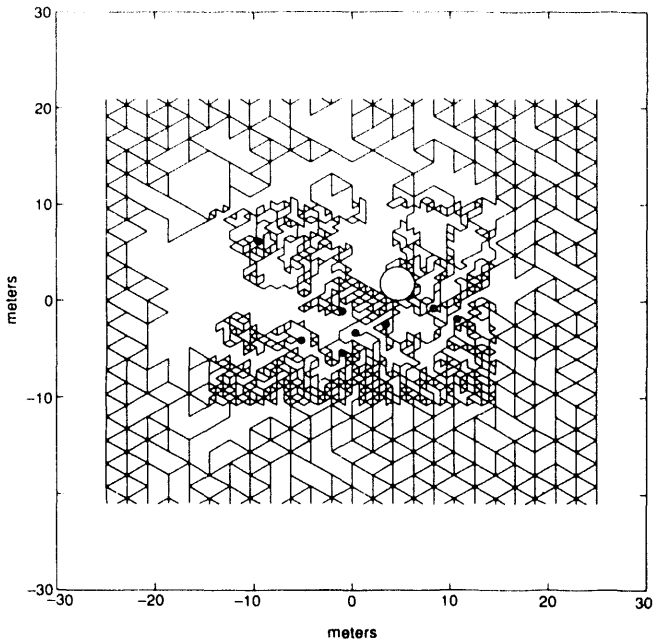

Figure 3. The first of five solutions that have similar geometries, case 1. [XBL 905-6399]

The prediction error for the steady-state head response is calculated using the statistical method called

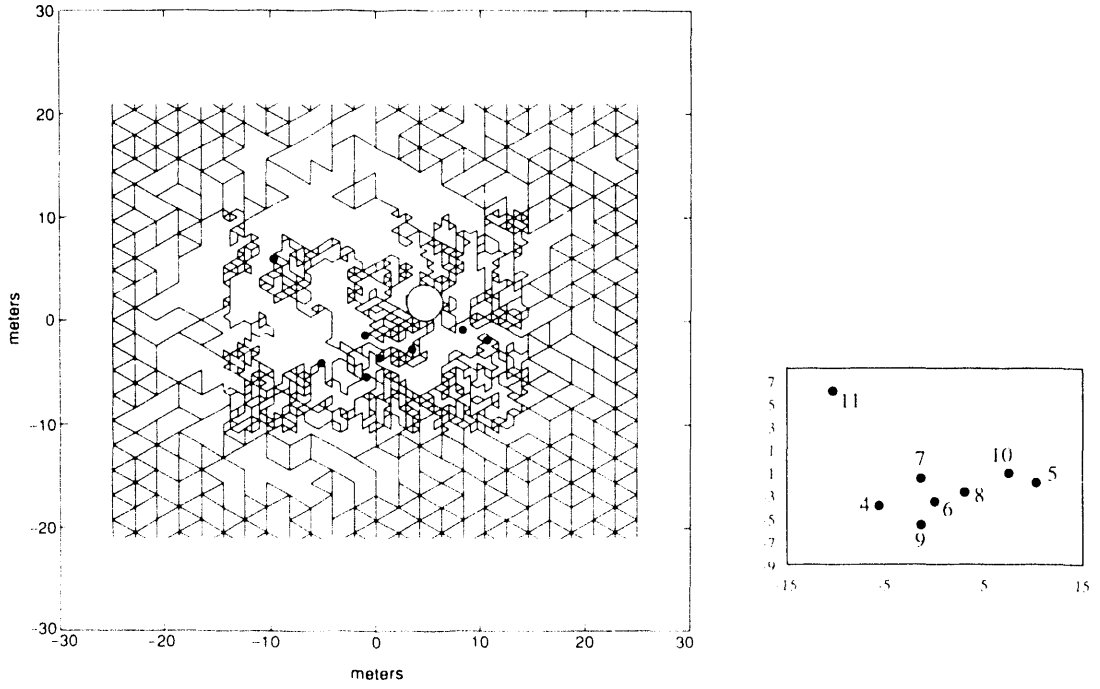

Figure 4. The second of five solutions that have similar geometries, case 2. [XBL 905-6386]

cross-validation (Stone, 1974). At the MI site, we have 8 wells and a drift. We use the steady-state observed pressure response H^i_{obs}, at each well, i, under conditions of steady flow to the drift. We would like to know the error associated with using our annealing model to predict the steady-state head response at an arbitrary nearby point. We do the following:

1. Leave the steady-state head value for well i out of the energy function.
2. Determine the annealing solutions for the starting configurations specified in cases 1 through 5.
3. For each end configuration, $C\bar{1}^i \ldots C\bar{5}^i$, calculate a predicted steady-state value for well i. These predicted head values are $H\bar{1}^i \ldots H\bar{5}^i$.
4. Calculate the mean-square prediction error for well i:

$$PE^2(i) = \frac{\sum_{j=1}^{5} \left| H_j^{-i} - H^i_{obs} \right|}{5} .$$

The estimated prediction error is

$$\widehat{PE} = \frac{\sum_{i=1}^{8} PE(i)}{8} .$$

$P\hat{E}$ is then an estimate of the error involved in using one annealing model to predict the head response of any other well in the vicinity.

Similarly, we can compute $P\hat{E}$ for the mean or median predicted head response of the five solutions for each well left out. We used the loss function to compare the mean and median predicted value of the five solutions and found that the median was a slightly better predictor of steady-state pressure at a given point on the grid. We then compared $P\hat{E}$ for predictions made using each solution independently with $P\hat{E}$ for predictions made by generating five solutions and using the median value as the prediction. The estimated prediction error found using a single solution was 4.3 m, and the estimated prediction error for using the median of five solutions was 3.3 m (Table 1). The estimated density of prediction error for the median of five solutions also shows that the median is expected to give a lower prediction error. We can make better predictions if we base them on multiple solutions instead of a single solution.

Table 1. The observed steady-state head values at each well and the predicted head values found using the median value for five annealing solutions. In each case the steady-state head at the indicated well was left out of the energy function.

Well left out	Obs. head	Median ($\hat{h}$) (m)	$PE\,(i)$ (m)	$PE\,(i,\hat{h})$ (m)
4	9.97	6.64	3.8	3.3
5	10.95	5.95	5.0	5.0
6	10.22	7.72	4.0	2.5
7	0.64	0.988	3.2	0.3
8	3.37	0.96	2.5	2.4
9	8.07	9.99	2.1	1.9
10	4.0	5.07	2.8	1.1
11	1.04	11.37	11.1	10.3

REFERENCES

Billaux, D., Chiles, J.P., Hestir, K., and Long, J., 1989. Three-dimensional statistical modeling of a fractured rock mass—An example from the Fanay-Augères mine. Int. J. Rock Mech. Min. Sci. & Geomech. Abstr., v. 26, no. 3/4, p. 281–299 (LBL-27030).

A. Davey, K. Karasaki, J.C.S. Long, M. Landsfeld, A. Mensch, and S.J. Martel, 1989. Analysis of the hydraulic data from the MI fracture zone at the Grimsel Rock Laboratory, Switzerland. Lawrence Berkeley Laboratory Report LBL-27864 (NDC-15).

Frick, U., Baertschi, P., and Hoehn, E., 1988. Migration investigations. NAGRA Special Bulletin, p. 23–34.

Kirkpatrick, S., Gelatt, C.D., Vecchi, M.P., 1983. Optimization by simulated annealing. Science, v. 220, p. 671–680.

Long, J.C.S., 1983. Investigation of equivalent porous medium permeability in networks of discontinuous fractures (Ph.D. thesis). University of California at Berkeley. Lawrence Berkeley Laboratory Report LBL-16259.

Press, W.H., Flannery, B.P., Teukolsky, S.A., and Vetterling, W.T., 1986. Numerical Recipes. Cambridge University Press, New York.

Solexperts, 1989. 566 NAGRA migration long term constant Q test in BOMI 87.009. Test Analysis and Description, 2/20/1989.

Stone, M., 1974. Cross-validatory choice and assessment of statistical predictions. J. Roy. Stat. Soc., Ser. B, v. 2, p. 111–147.

Tarantola, A., 1987. Inverse Problem Theory. Elsevier Scientific Publishing Company Inc., New York, p. 326,334.

Unsaturated-Zone Thermal-Energy Storage: Improvement and Validation of the Numerical Model of the 1989–1990 Field Experiment

C. Doughty, A. Nir, and C. F. Tsang*

Seasonal heat storage is an important element in the utilization of alternative energy sources with low-temperature heat supplies, as it addresses the common problem of out-of-phase energy supply and demand. Unsaturated-zone soils have been identified as the most suitable medium for this purpose in warm climatic zones, where the use of groundwater aquifers is generally not feasible (Nir et al., 1986). Since 1981 detailed mathematical modeling of a particular configuration for such a storage system has been under way in a cooperative effort between Lawrence Berkeley Laboratory (LBL) and Ben-Gurion University of the Negev (BGU) (Doughty et al., 1983; Nir et al., 1986). In 1987 a three-year Binational Science Foundation project began, aimed at validating the concept and mathematical model by means of a field experiment conducted at the Beer-Sheva campus of BGU.

In the field experiment, heat transfer to the soil is performed through a heat exchanger constructed of a 3-cm-diameter polybutylene pipe wound into a 1-m-diameter, 6-m-long vertical helical configuration and inserted into a 10-m-deep well. The top of the heat exchanger is 4 m below the ground surface. The well is then refilled with the original soil, which is subsequently saturated with water. During the charge period, warm water flows down a vertical center pipe to the bottom of the heat exchanger, then spirals up through the helix; heat is stored as the water cools via conduction to the adjacent soil. Figure 1 shows a schematic diagram of the heat exchanger, along with the temperature distribution in the surrounding soil at the end of the 1989 charge period, calculated with the mathematical model. During discharge the direction of flow is reversed and cool water is circulated down through the helix and then up through the center pipe, extracting heat from the soil as it warms. For full-scale operation, it is envisioned that a rectangular array of heat exchangers would be used, each 1.3 m in diameter and 18 m long, with an inter-helix spacing of 6 m.

From February to November 1989 a storage cycle was conducted that consisted of eight months of charge followed by one month of discharge. The mathematical modeling of this storage cycle, described in the 1989 Annual Report (Doughty et al., 1990), matched the observed response reasonably well. Subsequently, several improvements were made in the model. Some of the improvements were based on a more accurate representation of the physical processes occurring, and others were based on sensitivity studies motivated by the discrepancies between the observed and modeled results of the 1989 storage cycle. During February and early March 1990 a storage cycle consisting of 35 days of charge was conducted and modeled, using two versions of the improved model in order to validate the model.

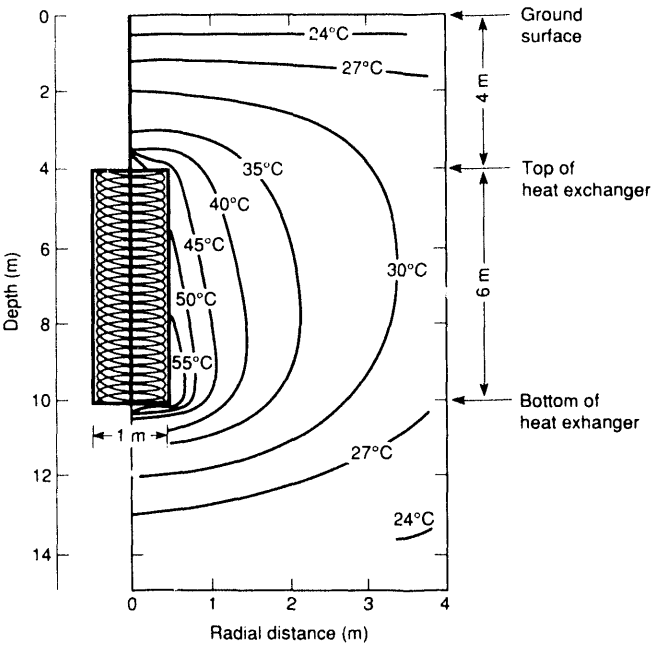

Figure 1. A schematic diagram of a vertical cross section of the heat exchanger, along with the calculated temperature distribution at the end of the 1989 charge period. [XBL 9011-6703]

MATHEMATICAL MODEL

The mathematical modeling studies done by LBL use the computer code PT (Bodvarsson, 1982). Although PT is designed to calculate coupled fluid and heat flows in a fully saturated medium, for the present work fluid flow is restricted to the heat exchanger and heat flow in the soil is purely by conduction, with constant thermal properties representative of a soil-water-air mixture.

Because the calculational mesh is axisymmetric (r, z), the helical heat exchanger is represented by a cylindrical conduit. For the 1989 storage cycle, a uniform temperature of 21.5°C was assumed for the soil initial condition. For the 1990 cycle initial condition, the calculated soil temperature distribution following the 1989 cycle and

* Also at Institute of Desert Research, Ben-Gurion University of the Negev, Israel.

subsequent months of inactivity was used. For both cycles, the heat exchanger inlet temperature and flow rate were time-averaged and specified as boundary conditions for the numerical model. The mesh extends far enough (well beyond the limits shown in Figure 1) in the radial direction and in the direction of increasing depth to represent a semi-infinite medium. The ground surface temperature provides the final boundary condition. It is assumed to vary sinusoidally, with parameters determined from a previous soil temperature profile analysis (Nir et al., 1988). This analysis also provided a value for soil thermal conductivity of $\lambda = 1.8$ W/mK.

The field observations available to compare with the output of the numerical model consist of the heat exchanger outlet temperature as a function of time and the temperatures measured via thermistors at various locations throughout the storage volume. Generally, the calculated temperatures for the 1989 storage cycle agree with the observed ones. Both the short-term and long-term changes in temperature are followed, but there is a systematic 1–2°C underprediction of the absolute value of the temperature at sensor locations within the heat exchanger.

SENSITIVITY STUDIES AND MODEL IMPROVEMENTS

To enable a convenient comparison between the output of various versions of the model and the field observations, we consider the time-average of the fractional difference between the observed and calculated temperatures:

$$\left\langle \Delta T_{frac} \right\rangle = \left\langle \frac{\left(T_{obs} - T_{calc}\right)}{\left(T_{obs} - T_{obs}^{init}\right)} \right\rangle ,$$

where T_{obs} and T_{calc} are observed and calculated temperatures, respectively, T_{obs}^{init} is the observed temperature at the start of the experiment, and $\langle\ \rangle$ denotes the time-average for days 160–290 for the 1989 run and the time-average for days 30–70 for the 1990 run (day 1 is January 1). $\langle \Delta T_{frac} \rangle$ is calculated for three values of temperature:

1. Ch0 – The heat exchanger outlet temperature (radial distance 0.5 m, depth 4 m).
2. Ch6 – The deepest observed temperature inside the heat exchanger (radial distance 0.3 m, depth 9 m).
3. A7 – The deepest observed temperature outside the heat exchanger (radial distance 1.68 m, depth 7 m).

Although the in situ value of soil thermal conductivity λ was estimated from the soil temperature profile studies mentioned above, the actual value of λ within the heat exchanger may differ because of variations in temperature, moisture content, or soil density resulting from the excavation and refilling procedure. It was therefore considered worthwhile to treat λ as an unknown parameter and model the 1989 storage cycle using a range of values for it. Results of such a sensitivity study are shown in Table 1. In each case, λ is constant in time and space. Increasing λ 25% above the base-case (U18) value results in larger fractional temperature differences (case U185), whereas decreasing it 20% results in smaller differences (case U21). Recent soil temperature profile analyses, using a wider range of data than the previous studies, yield values of λ closer to the lower value.

Three additional mechanisms can be included in PT to more accurately reflect physical processes occurring during the storage cycles. The results of calculations including these effects are summarized in Table 2.

1. It is generally accepted in the soil physics literature that soil thermal conductivity varies with temperature. For simplicity we consider a linear variation. Because λ increases with temperature, including this variation (case U19) has a similar effect to assuming a constant larger value of λ (case U185) and therefore produces a larger fractional temperature difference than does the base case (U18). For a temperature-dependent λ case to yield decreased fractional temperature differences, the base value of λ (λ at $T = 22$°C) must be smaller.

Table 1. Sensitivity studies.

Case	λ	Comments	$\langle \Delta T_{frac} \rangle$ (%)		
			Ch0	Ch6	A7
U18	1.8	Base case; most calculated T's too low	4.1	5.8	3.6
U185	2.25	Worse than U18	9.0	9.8	5.4
U21	1.44	Better than U18	-1.1	2.4	2.2

Table 2. Model improvements.

Case	Description	$\langle \Delta T_{frac} \rangle$(%)		
		Ch0	Ch6	A7
U19	$\lambda(T)$: linear variation $d\lambda/dT = 0.009$, $\lambda(22) = 1.8$	5.7	7.5	3.3
U20	C(r,z): duct interior, C = 3.2 elsewhere, C = 2.35	4.1	5.8	3.5
U218	Shallow heat flow included	3.3	5.1	3.0
U218-90	1990 run; same model as U218	5.0	3.7	1.8

2. Soil heat capacity C varies with soil moisture content, which is larger within the heat exchanger because the backfilled soil was saturated with water during heat exchanger construction. Allowing C to vary in space has a very small affect on fractional temperature difference (case U20).
3. In the original modeling, the center pipe was assumed to be perfectly insulated between the ground surface and the top of the heat exchanger (depth 0 to 4 m). Using realistic thermal properties for the insulation allows a small part of the heat stored to be deposited in the shallow soil overlying the heat exchanger. Including this effect decreases the fractional temperature differences (case U218). For the 1990 cycle, which was conducted with higher heat exchanger inlet temperature and flow rate, the fractional temperature differences are somewhat higher (case U218-90).

Shown in Table 3 for both the 1989 and 1990 storage cycles are the results of a new model that combines all the improvements shown in Table 2 and uses a smaller base value for thermal conductivity, as indicated in Table 1. The fractional temperature differences are much improved relative to the base case for the 1989 cycle (compare cases U18 and U301). For the 1990 cycle, the effect of decreasing the base value of λ, and allowing $\lambda(T)$ and $C(r, z)$ has mixed results (compare cases U218-90 and U301-90), but for the most important parameter, heat exchanger outlet temperature, Ch0, the fractional temperature difference is much smaller.

In conclusion, the combined experimental/modeling effort of the Binational Science Foundation project has been found very useful, both from the point of view of the experimenters and the modelers. Modeling results have been used to aid in experiment planning and design. Experimental results have provided both validation of model results and insight into the importance of various physical processes.

REFERENCES

Bodvarsson, G.S., 1982. Mathematical modeling of the behavior of geothermal systems under exploitation (Ph.D. thesis). University of California at Berkeley. Lawrence Berkeley Laboratory Report LBL-13937.

Doughty, C., Nir, A., Tsang, C.F., and Bodvarsson, G.S., 1983. Heat storage in unsaturated soils: Initial theoretical analysis of storage design and operational methods. *In* Proceedings, International Conference on Subsurface Heat Storage in Theory and Practice, June 6–8, Stockholm, p. 518–523 (LBL-14957).

Doughty, C., Nir, A., and Tsang, C.F., 1990. Unsaturated-zone thermal-energy storage: Modeling the 1989 module experiment. *In* Earth Sciences Division Annual Report 1989. Lawrence Berkeley Laboratory Report LBL-27900, p. 14–16.

Table 3. New model.

Case	Description	$\langle \Delta T_{frac} \rangle$(%)		
		Ch0	Ch6	A7
U301	Combine all 3 improvements; $\lambda(22) = 1.35$	-1.0	2.5	0.4
U301 90	1990 run; same model as U301	2.6	4.2	2.3

Nir, A., Doughty, C., and Tsang, C.F., 1986. Seasonal heat storage in unsaturated soils: Example of design study. *In* Proceedings, 21st Intersociety Energy Conversion Engineering Conference, August 25–29, San Diego, California, p. 669–675 (LBL-21016).

Nir, A., Doughty, C., and Tsang, C.F., 1988. Unsaturated-zone thermal-energy storage: model development and field validation. *In* Earth Sciences Division Annual Report 1987. Lawrence Berkeley Laboratory Report LBL-24200, p. 197–199.

Continued Development of a Semianalytical Solution for Two-Phase Fluid and Heat Flow in a Porous Medium

C. Doughty and K. Pruess

Over the past few years we have developed a semianalytical solution for transient two-phase water, air, and heat flow in a porous medium surrounding a constant-strength linear heat source, using a similarity variable $\eta = r/\sqrt{t}$. Although the similarity transformation approach requires a simplified geometry, all the complex physical mechanisms involved in coupled two-phase fluid and heat flow can be taken into account in a rigorous way, so that the solution may be applied to a variety of problems of current interest. Our work was motivated by a desire to predict the thermohydrological response to the proposed geologic repository for heat-generating high-level nuclear wastes at Yucca Mountain, Nevada, in a partially saturated, highly fractured volcanic formation.

THERMAL AND HYDROLOGIC CONDITIONS NEAR THE HEAT SOURCE

The ambient temperature in the partially saturated formation around the proposed nuclear waste repository at Yucca Mountain, Nevada ($T_0 \approx 20°C$), is well below the saturation temperature at ambient pressure ($T_{sat} \approx 96°C$ at $P_0 \approx 0.89$ bars), so that water is primarily in the liquid phase and the initial heat transfer in the host rock is mainly conductive. As the temperature around a waste package (the heat source) increases to the saturation temperature, evaporation increases and vapor partial pressure becomes appreciable. A convective heat-transfer mechanism known as a heat pipe may contribute to or even dominate heat transfer in this regime. Near the heat source, liquid water vaporizes, causing pressurization and an outflow of the gas phase. The water vapor condenses in cooler, more distant regions, depositing its latent heat of vaporization. This sets up a saturation profile, with liquid saturation increasing with distance from the heat source. The saturation gradient drives the counterflow of the liquid phase toward the heat source through capillary forces. The liquid then vaporizes again and repeats the cycle. With time the heat pipe moves away from the waste canister, leaving a gas-phase zone in which heat transfer is again dominated by conduction. The convective heat transfer of the heat-pipe region is accompanied by small temperature gradients, whereas in the conductive regions temperature gradients are large. Thus conditions at the waste package may vary greatly, depending on the relative importance of conductive and convective heat transfer. If an extensive heat pipe develops, two-phase conditions will persist for long times, with temperature remaining near the saturation temperature (about 100°C). Under these conditions, air will be purged from the near-canister region, eventually leaving a gas phase composed purely of water vapor. If heat transfer is primarily conductive, a gas-phase zone, or two-phase zone with only a small amount of immobile liquid, will develop around the waste package. Temperatures may be very high, and air is more likely to be present.

METHODOLOGY

The governing equations for two-phase fluid and heat flow for water and air in a porous medium are summarized in Doughty and Pruess (1991); the basic processes represented by the equations are outlined below. A conservation law balances accumulation and flux of each component (water, air, energy), assuming local thermodynamic equilibrium between water, air, and rock. The fluid flux terms include Darcy's law modified for two-phase flow using relative permeability and capillary pressure functions and binary diffusion between water vapor and air in the gas phase. The inclusion of capillary pressure ($P_c = P_l - P_g$) allows the possibility of liquid- and gas-phase counterflow. The heat balance includes conductive and convective terms with phase-change effects and transport of latent heat. The conservation laws form a set of three coupled nonlinear second-order partial differential equations, which are mathematically equivalent to a set of six nonlinear coupled first-order partial differential equations.

To achieve the symmetry required for the similarity solution approach, the geologic medium is assumed to be uniform and isotropic, the heat source is modeled as an infinitely long cylinder, and gravity is neglected. The geometry of the problem then reduces to radial symmetry, with just two independent variables, radial distance r and time t. If the medium is of infinite extent, with uniform initial conditions, and if boundary conditions are applied only at $r = 0$ (a line source) and $r = \infty$ and are time independent, the partial differential equations can be transformed into simpler ordinary differential equations (ODEs) through the use of a similarity variable, $\eta = r/\sqrt{t}$. This transformation is known as the Boltzmann transformation in the context of heat-conduction problems.

Because the resulting ODEs are still coupled and nonlinear, a numerical integration is required to solve them. The boundary conditions constitute a two-point boundary-value problem, in which three of the boundary conditions are specified at the $\eta = 0$ limit of integration and three at the $\eta = \infty$ limit, hence an iterative integration scheme, known as the shooting method (Press et al., 1986), is used. A more detailed discussion of the similarity solution methodology is given in Doughty and Pruess (1990a).

NEW FEATURES

Two previous Annual Report articles summarize the development of the similarity solution before 1990. The first (Doughty and Pruess, 1989) treats a one-component version of the problem (no air), in which the residual liquid saturation was constrained to be zero ($S_l = 0$). The second (Doughty and Pruess, 1990b) discusses the effect of adding air and allowing $S_{lr} > 0$. Both articles include comparisons between the results of the similarity solution and those of the numerical simulator TOUGH (Pruess, 1987), which show excellent agreement. In the present article we discuss the inclusion of vapor pressure lowering and the use of an effective continuum to represent a fractured/porous medium. The similarity-solution results presented here were all calculated using the computer program SIMSOL, which has been fully documented in a laboratory report (Doughty, 1991). In addition to the features described here, the similarity solution can include an enhanced vapor diffusion arising from pore-level phase-change effects and the Klinkenberg approximate treatment of Knudsen diffusion.

VAPOR PRESSURE LOWERING

Under two-phase conditions, the primary thermodynamic variables are gas-phase pressure P_g, gas saturation S_g, and air partial pressure P_a. When vapor pressure lowering effects are ignored, temperature is determined iteratively from the steam table saturation curve $P_v = P_{sat}(T)$. Since $P_v = P_g - P_a$, the functional dependence of temperature on the primary variables is $T = T(P_g, P_a)$. Vapor pressure lowering is modeled using the Kelvin equation, so that temperature becomes a function of saturation as well as vapor pressure, given implicitly by

$$P_v = P_{sat}(T) \cdot \exp\left[\frac{P_c(S_l)}{\rho_l R\,(T + 273.15)}\right] . \qquad (1)$$

Thus the functional dependence of temperature on the primary variables is $T = T(P_g, P_a, S_g)$.

Figure 1 shows results for two problems that are identical except for the presence or absence of vapor pressure lowering. Material properties and boundary conditions are given in Table 1. According to the definition of the similarity variable, $z = \ln(\eta) = \ln(r/\sqrt{t})$, Figure 1 represents both a spatial distribution at a given time, with distance from the heat source increasing from left to right, and a time sequence at a given point in space, with time increasing from right to left. The steep near-linear temperature profiles shown in Figure 1a indicate that heat transfer is primarily conductive for both cases.

The capillary pressure function, slightly modified from the van Genuchten (1980) formulation (Doughty and

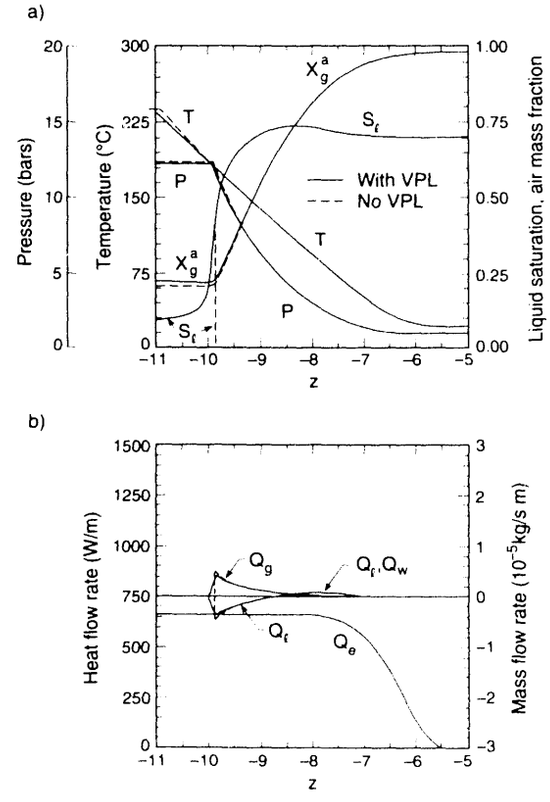

Figure 1. Results of the similarity solution for problems with and without vapor pressure lowering. [XBL 9012-5999]

Table 1. Parameters for problems illustrated in Figures 1 and 2. Parameters are typical of Yucca Mountain values (Tsang and Pruess, 1990).

Boundary and Initial Conditions	
$\eta = r/\sqrt{t} = 0$	$Q_{e0} = 667$ W/m*
	$Q_{w0} = 0$
	$Q_{a0} = 0$
$\eta = r/R(t) = \infty$	$P_0 = 1$ bar
	$T_0 = 22°C$
	$S_{l0} = 0.7$
Material Properties	
$k_m = 1.9 \times 10^{-18}$ m^2	$\tau = 0.25$
$\phi_m = 0.10$	$D^0_{va} = 2.14 \times 10^{-5}$ m^2/s
$\rho_s = 2480$ kg/m^3	$\theta = 2.334$
$c_s = 840$ J/kg K	$k_f = 10^{-11}$ m^{2†}
$\kappa = 1.9 - 2.34$ W/m K	$\phi_f = 1.0^\dagger$
	$V_f = 0.0018^\dagger$
Characteristic Curves‡	
$k_{rlm}(S_l) = \sqrt{S^*}\,[1-(1-(S^*)^{1/\Lambda})^\lambda]^2$	$S_{lr} = 8.01 \times 10^{-2}$
$k_{rgm}(S_l) = 1 - k_{rl}$	$\lambda = 0.4438$
$P_{cm}(S_l) = -P_{c0}[(S^*)^{-1/\Lambda} - 1]^{1-\lambda}$	$P_{c0} = 17.3$
$S^* = (S_l - S_{lr})/(1 - S_{lr})$	$P_{max} = 5000$ bars§

*This thermal power corresponds to high-level nuclear wastes approximately 10 years old.

†Not used for Figure 1.

‡Functional forms of van Genuchten (1980); P_{cm} has been modified slightly so that as $S^* \to 0$, $P_c(S_l) \to -P_{max}$ instead of approaching $-\infty$ (Doughty and Pruess, 1991). For Figure 1, a no-fracture problem, these characteristic curves are used directly. For Figure 2, a fracture/matrix problem, the characteristic curves given here refer to the matrix; Table 2 describes the complete effective-continuum formulation.

Pruess, 1991), has the feature that P_c becomes very large and negative as $S_l \to S_{lr}$ (see Table 1). Then, from Eq. (1), vapor pressure lowering effects become very strong for small S_l, and the two-phase region extends all the way to z_l, as is verified by Figure 1a. Except for this extension of the two-phase zone to small values of z, the results of the two problems are quite similar. The slope of the conductive temperature profile for $-11 < z < -10$ decreases slightly for the vapor-pressure-lowering case, reflecting the increase in thermal conductivity κ with liquid saturation ($\kappa \sim \sqrt{S_l}$. For these problems the intrinsic permeability is too small to allow enough fluid flow for much of a heat pipe to develop (Figure 1b); thus the air component of the gas phase is not completely purged from the region near the heat source ($-11 < z - 10$) (Figure 1a).

EFFECTIVE-CONTINUUM REPRESENTATION OF A FRACTURED/POROUS MEDIUM

In the effective-continuum approach, a single continuous medium incorporates features of both the fractures and the intact rock matrix. For example, under two-phase conditions, the primary variable S_g is replaced by $\tilde{S}_g$, where $\tilde{S}_g = 1 - \tilde{S}_l$ and $\tilde{S}_l$ is the effective-continuum liquid saturation, given by

$$\tilde{S}_l = \frac{S_{lm}\phi_m V_m + S_{lf}\phi_f V_f}{\phi_m V_m + \phi_f V_f}, \qquad (2)$$

where the subscripts m and f refer to matrix and fracture, respectively, ϕ is porosity, and V is fractional volume ($V_m + V_f = 1$).

In general, fracture capillary pressures are much weaker than those in the rock matrix. Thus during wetting the matrix will become almost completely saturated before any liquid enters the fractures; during drying the fractures will almost completely desaturate before any liquid leaves the matrix. Under these conditions, then, to a good approximation, one may consider that water will be present in the fractures only when the matrix is completely saturated. The value of $\tilde{S}_l$ at which liquid first enters the fractures is known as the threshold saturation, S_{lh}. This approach, described in detail in Doughty and Pruess (1991), is known as the sequential saturation model. When fracture and matrix capillary pressures are of comparable magnitude, the more complicated concurrent saturation model must be used (Doughty and Pruess, 1991).

Figure 2 shows results of the similarity solution for a problem identical to that shown in Figure 1, except that fractures are included, using the sequential saturation model. Effective-continuum characteristic curves are given in Table 2. The effective-continuum liquid saturation $\tilde{S}_l$ remains below the threshold value S_{lh} everywhere, so that liquid relative permeability is not enhanced by the fractures. Nonetheless, the fluid flow pattern changes markedly from the no-fracture case, with a short heat pipe now developing (compare Figures 1b and 2b). The enhanced gas-phase permeability not only allows increased gas-phase flow, but it substantially reduces the gas-phase pressure gradient, resulting in a large enough liquid-phase pressure gradient to drive a small liquid counterflow ($dP_l/dz = dP_g/dz - dP_c/dz \approx -dP_c/dz$). Although the heat pipe is too short to create much of a flattening in the temperature profile, the vapor flow effectively purges the air component of the gas phase from the region near the heat source, leaving a gas phase composed purely of water vapor. This could have important ramifications for waste-package design with regard to prevention of corrosion.

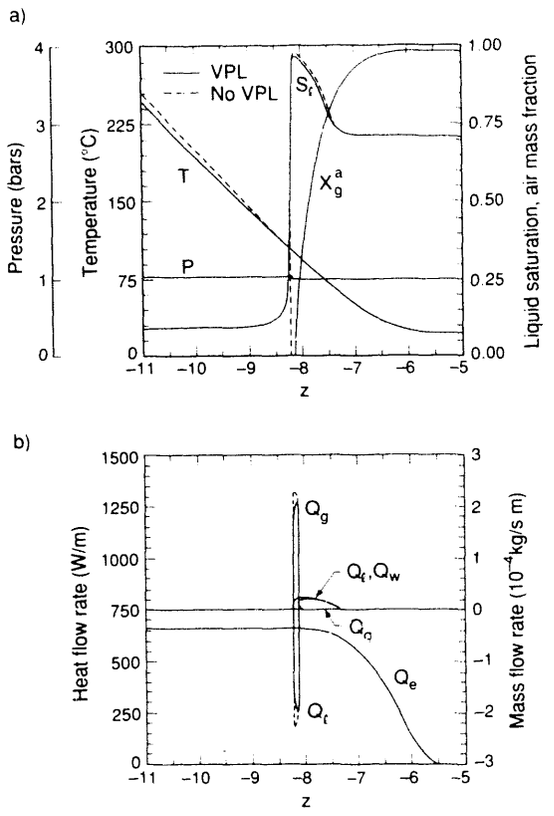

Figure 2. Results of the similarity solution for an effective-continuum representation of a fractured/porous medium. [XBL 9012-6002]

Table 2. Sequential-saturation-model characteristic curves.

P_c	$= P_{cm}\left[(1-\delta_s)\tilde{S}_l/S_{th}\right]$	$\tilde{S}_l < S_{th}$
	$= \frac{1-\tilde{S}_l}{1-S_{th}} \cdot P_{cm}(1-\delta_s)$	$\tilde{S}_l > S_{th}$
	with P_{cm} from Table 1, $\delta_s = 10^{-4}$	
	$\tilde{k}_{rl} = \frac{k_m V_m k_{rlm} + k_f V_f k_{rlf}}{k_m V_m + k_f V_f}$	
	$\tilde{k}_{rg} = 1 - \tilde{k}_{rl}$	
k_{rlm}	$= k_{rlm}(\tilde{S}_l/S_{th})$ from Table 1	$\tilde{S}_l < S_{th}$
k_{rlf}	$= 0$	
k_{rlm}	$= 1$	$\tilde{S}_l > S_{th}$
k_{rlf}	$= (\tilde{S}_l - S_{th})/(1-S_{th})$	

The much smaller gas-phase pressure greatly decreases T_{sat} compared with the no-fracture case (180 → 100°C), so that the location of the desaturation front (which occurs at $T = T_{sat}$) changes substantially, from $z = -10$ to $z = -8.2$ (compare Figures 1a and 2a). Because the far-field saturation is constrained by the boundary conditions to remain at $S_l = 0.7$, the larger dried region is balanced by a "condensation halo," or region of increased saturation coincident with the cold end of the heat pipe. The large contrast between Figures 1 and 2 illustrates the important effect fractures have on fluid and heat flow in partially saturated media.

REFERENCES

Doughty, C., 1991. SIMSOL users guide. Lawrence Berkeley Laboratory Report LBL-28384 (in preparation).

Doughty, C., and Pruess, K., 1989. A similarity solution for two-phase fluid and heat flow near buried nuclear waste packages. *In* Earth Sciences Division Annual Report 1988. Lawrence Berkeley Laboratory Report LBL-26362, p. 64–67.

Doughty, C., and Pruess, K., 1990a. A similarity solution for two-phase fluid and heat flow near high-level nuclear waste packages emplaced in porous media. Int. J. Heat Mass Transfer, v. 33, no. 6, p. 1205–1222 (LBL-26057).

Doughty, C., and Pruess, K., 1990b. The semianalytical similarity solution for two-phase fluid and heat flow: a tool for high-level nuclear waste studies. *In* Earth Sciences Division Annual Report 1989. Lawrence Berkeley Laboratory Report LBL-27900, p. 16–18.

Doughty, C., and Pruess, K., 1991. A similarity solution for two-phase water, air, and heat flow near a linear heat source in a porous medium. Lawrence Berkeley Laboratory Report LBL-30051.

Press, W.H., Flannery, B.P., Teukolsky, S.A., and Vetterling, W.T., 1986. Numerical Recipes: The Art of Scientific Computing. Cambridge University Press, New Rochelle, New York, Ch. 16.

Pruess, K., 1987. TOUGH user's guide. U.S. Nuclear Regulatory Commission Report NUREG/CR-4645, Washington, D.C. (Also available as Lawrence Berkeley Laboratory Report LBL-20700.)

Tsang, Y.W., and Pruess, K., 1990. Further modeling of gas movement and moisture migration at Yucca Mountain, Nevada. Lawrence Berkeley Laboratory Report LBL-29127.

van Genuchten, M.Th., 1980. A closed-form equation for predicting the hydraulic conductivity of unsaturated soils. Soil Sci. Soc. Am. J., v. 44, p. 892–898.

Numerical Simulation of Two-Dimensional Steam-Remediation Experiments

R. W. Falta, K. Pruess, I. Javandel, and P. A. Witherspoon

During the injection of steam into subsurface formations, significant multidimensional effects occur. In particular, gravitational forces tend to make the injected steam rise to the top of the formation. This phenomenon, known as steam override, can under certain conditions result in a premature breakthrough of steam at the producing location. The usefulness of steam injection as a method for remediating contaminated aquifers largely depends on the ability of the steam to completely sweep the contaminated region. In cases where severe steam override causes an early breakthrough of steam at the producing location, the efficiency of the steam in removing contaminants from the formation will be greatly reduced.

One of the major motivations for the development of the STMVOC simulator at Lawrence Berkeley Laboratory (Falta, 1990; Falta et al., 1990a,b) was recognition of the need for a comprehensive model that could be used to aid in the design of field-scale steam-injection remediation systems. For such a model to be useful, it must be demonstrated that the model accounts for the important physical processes taking place in the real situation. This article describes the use of the STMVOC simulator to model a series of two-dimensional laboratory-scale steam-injection experiments conducted by Basel and Udell (1989) in a clean sand. These experiments included the effects of gravity and were conducted with a variety of different initial and boundary conditions. The simulator was then used to model a two-dimensional xylene displacement experiment (K.S. Udell, personal communication, 1989).

DESCRIPTION OF EXPERIMENTS

Two-dimensional laboratory-scale steam-injection experiments were performed for the purpose of examining the shape of an advancing steam-condensation front under different flow conditions and for evaluating the displacement of a nonaqueous phase liquid (NAPL) by steam injection (Basel and Udell, 1989; K.S. Udell, personal communication, 1989). These experiments were conducted in a 5-cm-thick sand tank with a length of 91.5 cm and a height of 30.5 cm. The sand in the tank was very coarse, with an average permeability of 1×10^{-10} m^2 and a porosity of 0.4. The sides of the tank were made of glass with two additional layers of Lexan transparent plastic separated by an air space. The top of the sandpack was sealed and insulated. At either end of the apparatus, perforated copper tubes were installed, extending over the height of the sandpack. During the experiments, steam with a quality of about 1 (dry steam) was injected into one of the tubes while liquid and vapor were allowed to drain from the other tube against a certain backpressure. A diagram of the experimental apparatus is given in Figure 1.

Before each experiment, one of the glass panels was coated with a temperature-sensitive liquid crystal paint. The mixture used in this paint was calibrated so that it would turn from green to black at a temperature of 100°C. Photographs taken of the liquid crystal interface every 2 minutes during the experiment provided a complete record of the shape and location of the steam front. Further details of the experimental procedure are given by Basel and Udell (1989).

SIMULATION OF STEAM-INJECTION EXPERIMENTS IN A CLEAN SAND

Four experiments were conducted using the system described above (without the addition of a NAPL). The first experiment was performed with an initially dry sandpack. The three subsequent experiments were performed with the sandpack nearly saturated with water; in each of these experiments, a different steam-injection rate was used. The steam-injection experiments were simulated using STMVOC with a fairly coarse two-dimensional mesh. Except for the elements at either end of the mesh, the elements were 6 cm by 6 cm squares, with 15 elements in the horizontal direction and 5 elements in the vertical direction. The elements at each end of the mesh are rectangular, with a horizontal length of 1.5 cm and a height of 6 cm.

The material properties used in the simulations are described by Falta (1990); most were obtained from Basel and Udell (1989). Lateral heat losses from the experimental system made it necessary to use an artificially

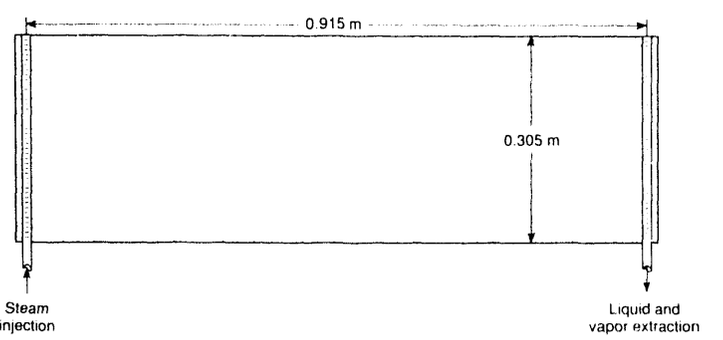

Figure 1. Schematic diagram of experimental apparatus used by Basel and Udell (1989). [XBL 902-5744]

large value of rock heat capacity in the two-dimensional numerical simulations. The value of this parameter was determined from preliminary simulations of the two-dimensional experiments, and the same value was used in all of the subsequent simulations.

The relative permeability curves used in the numerical simulations consisted of scaled cubic functions of saturation, assuming a residual water saturation of 0.1 (Falta, 1990). The gas-water capillary pressure function used the van Genuchten (1980) formulation. The values of the constants were chosen to produce a capillary rise of roughly 10 cm. This was done on the basis of visual observations by K.S. Udell (personal communication, 1989), which revealed a capillary fringe of about 10 cm for the sandpack. Because no direct measurements were made of either relative permeabilities or the capillary pressure, the particular choice of curves used in the simulations was somewhat arbitrary.

In each of the simulations, no-flow, insulated boundary conditions were used at the top and bottom edges of the mesh. The inlet boundary condition consisted of a constant-water-mass injection rate at the injection end of the mesh, with the overall water injection rate divided uniformly between the five injection elements. The injected water was assigned a specific enthalpy of 2676 kJ/kg, corresponding to steam with a quality of 1 and a temperature of 100°C. The water-mass injection rates used in each of the simulations were specified by Basel and Udell (1989). At the production end of the mesh, a well-deliverability model was used in the five production elements. With this arrangement, the outlet pressure at the top of the producing zone is specified, and the flowing "wellbore" pressure as a function of depth and time is computed numerically (Pruess, 1987; Falta, 1990).

In their first experiment, Basel and Udell (1989) injected steam into a dry sandpack at a rate of 5.33×10^{-4} kg/s. Figure 2a shows the experimental profiles for the steam-condensation front. Because the zone ahead of the steam front is not water saturated, the effects of gravity on the angle of the advancing steam front are very small, and the steam front is nearly vertical. As the steam-condensation front advanced through the sandpack, Basel and Udell (1989) observed the formation of a water bank at the bottom of the sand tank. This occurred as the injected steam condensed at the condensation front and drained downward due to gravity. Within this water bank, the steam-front profiles are slightly tilted. This experiment was numerically simulated with an initial water saturation of 0.01, an initial temperature of 22°C, and an initial pressure of 101.0 kPa in the top row of elements. The initial pressure distribution in the remaining elements was equal to the static equilibrium pressure as a function of depth. The calculated steam-condensation front profiles are shown in Figure 2b. As in the experiment, the front profiles are

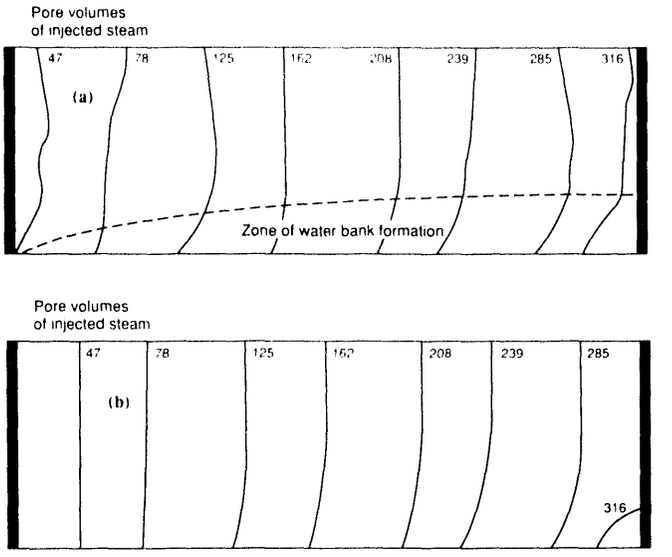

Figure 2. Experimental (**a**) and simulated (**b**) steam-condensation-front profiles. [Part a, XBL 902-5755; part b, XBL 902-5744]

nearly vertical except for some tilting in the lower part of the sandpack due to the formation of a water bank. The calculated profiles of the steam-condensation front shown in Figure 2b are in good agreement with the experimental profiles shown in Figure 2a.

Following the dry sandpack experiment, Basel and Udell (1989) flooded the sand with water in preparation for the next experiment. Unfortunately, this caused the sand in the tank to settle, resulting in a visible gap between the top of the sand and the top of the sand tank (M.D. Basel, personal communication, 1989). During the remaining experiments, this open space acted as a high-permeability zone, allowing the injected steam to preferentially invade the top of the sand tank. To approximately account for this effect in the numerical simulations, the permeability of the top row of elements was increased by a factor of 5 to 5×10^{-10} m^2 for the remaining simulations. It should be pointed out here that the presence of a high-permeability zone at the top of a formation undergoing steam treatment represents an extremely unfavorable condition for steam injection. The reason is that a high-permeability zone at the top of the formation greatly increases the natural tendency of the steam to rise to the top of the formation and override the lower part of the formation. This results in premature steam breakthrough at the producing location and a loss of steam sweep efficiency.

Figure 3a shows the experimental steam-front profiles for a steam-injection rate of 4.11×10^{-4} kg/s into a nearly saturated sand. The numerically calculated steam-front profiles for this case are shown in Figure 3b. Although there are differences in the experimental and computed profiles, the results are in fair agreement. The

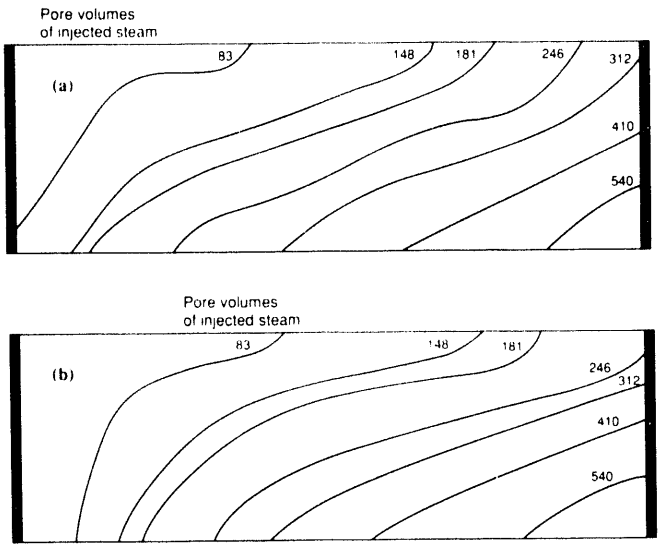

Figure 3. Experimental (**a**) and simulated (**b**) steam-condensation-front profiles. [Part a, XBL 902-5748; part b, XBL 902-5747]

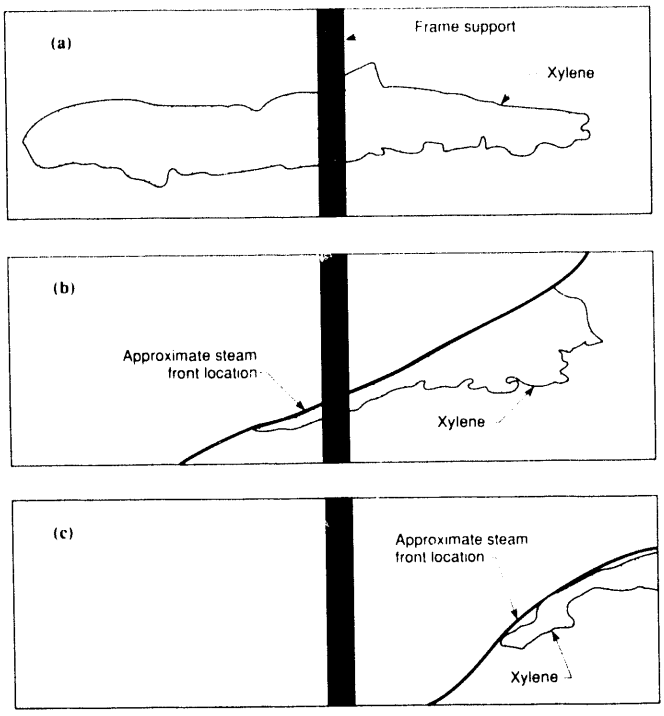

Figure 4. Experimental steam-condensation-front and separate-phase xylene locations (**a**) before steam injection, (**b**) after 15.1 minutes of steam injection, and (**c**) after 22.1 min. of steam injection. [Part a, XBL 904-5811; part b, XBL 904-5814; part c, XBL 904-5816]

influence of the air space at the top of the sandpack on the steam-front profiles is clearly seen in Figure 3a and is approximately accounted for by means of the high-permeability zone used in the simulation.

SIMULATION OF A NAPL STEAM-DISPLACEMENT EXPERIMENT

Following the clean-sand/steam-injection experiments, a xylene displacement experiment was conducted using the same experimental apparatus and sandpack (K.S. Udell, personal communication, 1989). Before adding the xylene to the sand tank, the sandpack was partly saturated with water so that about one-third of the sandpack height (~10 cm) was fully saturated. The resulting capillary fringe above the water table was also about one-third of the sandpack height. The remaining top third of the sandpack contained only the small water saturation remaining after the last steam-injection experiment.

At the top center of the sandpack, 100 ml of xylene was added and allowed to drain downward to the water surface, where it spread out horizontally. The xylene used in this experiment contained a red dye that allowed visual observation of the movement of the separate-phase xylene. During the experiment, photographs were taken at regular intervals, and a video cassette recording of the experiment was made. After the xylene distribution reached an equilibrium state, steam injection was started with a water-mass injection rate of 8.38×10^{-4} kg/s. Figure 4a shows the xylene profile in the sandpack before steam injection. Except for a very narrow vertical zone below the point of xylene injection (which is hidden from view by the frame support), the xylene is situated on top of the water table across the sandpack.

Parts b and c of Figure 4 show the xylene profile in the sandpack after 15.1 and 22.1 min of steam injection, respectively. From this series of xylene profiles, it is apparent that the xylene is effectively displaced ahead of the advancing steam-condensation front. This experiment was simulated using the STMVOC simulator with the same mesh and boundary conditions as were used in previous steam-injection simulations. The relative permeability curves for the gas phase and the water phase were identical to those used in the earlier steam-injection simulations; the NAPL relative permeability was calculated using Stone's first method (Stone, 1970). The NAPL residual saturation used in calculating the NAPL relative permeability was assumed to be equal to 0.05.

On the basis of the experimental observation that horizontal spreading of the xylene was not observed during the downward migration through the unsaturated sand, the gas-NAPL capillary pressure was assumed to be zero. The use of a significant gas-NAPL capillary pressure in the numerical simulation of this experiment results in an unrealistic horizontal spreading of the xylene in the unsaturated sand above the water table. The reasons for this are not obvious, but it is very possible that the NAPL

does not act as a strong wetting phase with respect to the gas phase under these conditions.

Because the gas-NAPL capillary pressure was assumed to be zero, the NAPL-water and the gas-water capillary pressures must be equal in order for the capillary pressures to be continuous during phase transitions. The gas-water capillary pressure function used in this simulation was identical to that used in the earlier two-dimensional steam-injection simulations.

The initial water saturation distribution was generated numerically and represents equilibrium conditions, with the bottom third of the sandpack being water saturated, the middle third variably saturated, and the top third nearly dry. The initial pressure distribution reflected static conditions, with a pressure of 101.0 kPa in the gas phase in the upper row of elements.

The simulation was begun by injecting 100 ml of o-xylene into the top center element at a constant rate (1.467×10^{-4} kg/s) for a period of 10 min. The specific enthalpy of the injected xylene was set equal to that of liquid xylene at a temperature of 22°C. During the simulation, the thermophysical properties of o-xylene were calculated using the NAPL/chemical equation of state described in Falta (1990) and Falta et al. (1990a).

After 100 ml of xylene was injected, the system was allowed to equilibrate for a period of 10 hr. The calculated separate-phase xylene (NAPL) saturation distribution in the sandpack after this 10-hr period is shown in Figure 5a. As in the experiment (Figure 4a), the liquid xylene has formed a floating lens on top of the water table. In the experiment, the xylene formed a rather narrow floating lens across almost the entire water table, whereas in the simulation, the xylene became distributed over a wider area vertically and a smaller area horizontally. This discrepancy is due in part to the coarse mesh spacing used in the simulation. It also suggests that the assumed NAPL relative permeability function tends to underpredict the true NAPL relative permeability in the sandpack. Although a finer numerical mesh would improve the simulated results, the ability of the numerical simulator to give reasonable projections of the true physical behavior using a coarse mesh is important. In large three-dimensional field-scale simulations there will be a limitation on the number of elements, and it will not be possible to use extremely fine meshes (at least in the near future).

Following the simulation of the xylene injection and equilibration for 10 hr, the boundary condition at the injection end of the sandpack was switched to the steam-injection condition. Steam was injected uniformly over the five injection elements at a total rate of 8.38×10^{-4} kg/s with a specific enthalpy of 2676 kJ/kg (steam with a quality of 1). In Figure 5 (b and c), the calculated steam condensation front locations and the separate-phase xylene saturations are shown after 15.1 and 22.1 min of steam injection, respectively. A comparison of Figure 5 with the corresponding experimental profiles in Figures 4 shows fairly good agreement of the simulation results with the experiment. The modeled saturation profiles have a shape and location similar to the experimental profiles, although the experimental profiles tend to be narrower and more sharply defined. Again, this is probably due in part to the coarse mesh spacing used in the simulation.

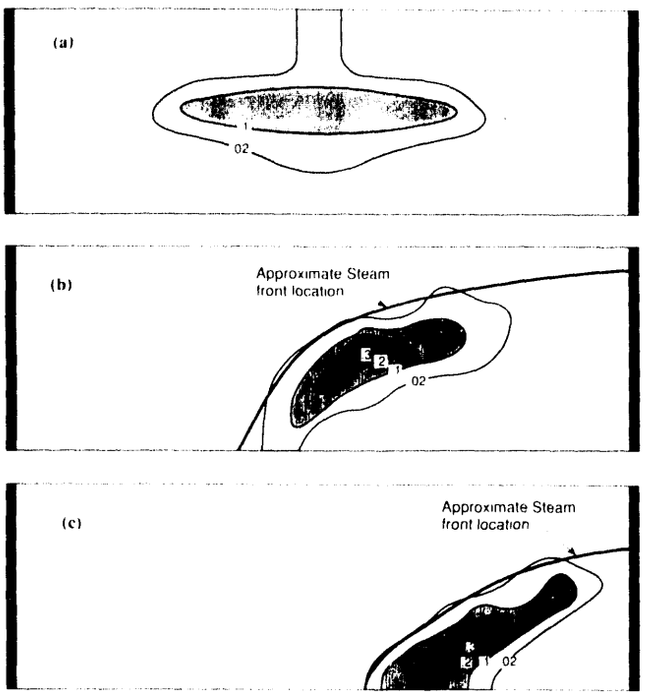

Figure 5. Simulated steam-condensation-front locations and separate-phase xylene-saturation distributions **(a)** before steam injection, **(b)** after 15.1 min. of steam injection, and **(c)** after 22.1 min. of steam injection. [Part a, XBL 903-5789; part b, XBL 903-5838; part c, XBL 903-5840]

SUMMARY

The STMVOC simulator was used to model a series of two-dimensional laboratory steam-injection experiments. The results of these simulations were in good general agreement with the experimental results and demonstrate the ability of the simulator to model the complex multiphase flow and heat transfer phenomena arising during steam displacement of NAPLs.

REFERENCES

Basel, M.D., and Udell, K.S., 1989. Two dimensional study of steam injection into porous media. Multiphase Transport in Porous Media, ASME HTD, v. 127, p. 39–46.

Falta, R.W., 1990. Multiphase transport of organic chemical contaminants in the subsurface (Ph.D. thesis). University of California at Berkeley.

Falta, R.W., Pruess, K., Javandel, I., and Witherspoon, P.A., 1990a. Numerical modeling of steam injection for the removal of nonaqueous phase liquids from the subsurface, 1. Numerical formulation. Lawrence Berkeley Laboratory Report LBL-29615.

Falta, R.W., Pruess, K., Javandel, I., and Witherspoon, P.A., 1990b. Numerical modeling of steam injection for the removal of nonaqueous phase liquids from the subsurface, 2. Code validation and application. Lawrence Berkeley Laboratory Report LBL-29616.

Pruess, K., 1987. TOUGH user's guide. U.S. Nuclear Regulatory Commission Report NUREG/CR-4645. Washington, D.C. Also available as Lawrence Berkeley Laboratory Report LBL-20700.

Stone, H.L., 1970. Probability model for estimating three-phase relative permeability. J. Pet. Technol., v. 22, no. 1, p. 214–218.

van Genuchten, M.T., 1980. A closed-form equation for predicting the hydraulic conductivity of unsaturated soils. Soil Sci. Soc. Am. J., v. 44, p. 892–898.

Economic Analysis of Alternate Development Strategies for the Ahuachapán Geothermal Field

C. Goranson,[†] M. Ripperda, M. J. Lippmann, and G. S. Bodvarsson

During previous years, a three-dimensional numerical model of the Ahuachapán geothermal field in El Salvador has been developed on the basis of geological, geochemical, geophysical and reservoir engineering data collected since the early 1970s (Aunzo et al., 1989, 1991; Ripperda et al., 1991; Steingrimsson et al., 1991). Validation of the model against well and reservoir data has been followed by evaluation of the response of the geothermal system to different assumed fluid production/injection scenarios.

Numerous cases were studied, ranging from letting the fluid production continue to decline without drilling any additional wells (the "declining power generation" case) to drilling enough new wells to bring the power generation up to the full installed capacity at Ahuachapán (95 MWe). The effects of reinjection on each of these development strategies—by way of four wells located in the northern part of the field—was also investigated.

The analysis indicated that maintaining 50 MWe will require four or five new production wells over the next 30 yr. Increasing the power production to 75 MWe will require 18 to 24 additional wells over the same time period. (The number of wells depends on whether injection was assumed or not.) The study also showed that the field could continuously support 90 MWe for only about 20 yr with the drilling of 24 new production wells. After that time the productivity of any additional well was very low, so the production was allowed to decrease with time. The purpose of this study is to evaluate from an economic point of view the alternate field management schemes considered by Ripperda et al. (1991).

ECONOMIC ANALYSIS

The economic analysis includes estimated costs for production and injection wells, pipelines, separation facilities, power plant operating conditions, and estimates for power sales and field development cost escalation rates. The cost, and therefore the economic impact, of power plant equipment was not included in the analysis because equipment for generating 95 MW of electrical power is in place at this time. The effects of land acquisition costs, taxes, interest, engineering and development costs, equipment acquisition, management overhead and costs, etc., were also not considered.

The analysis utilized predicted well flow rates and assumed locations for production and (for some cases) injection wells determined from the reservoir exploitation studies (Ripperda et al., 1991). Pipeline sizes were calculated assuming that large-diameter two-phase lines would extend from the power plant to areas central to the new production wells to be drilled in the southeast quadrant of the known geothermal area. Two-phase pipelines from the individual wells were then tied into these large-diameter pipelines (termed "trunk lines"). The time when wells were drilled and pipelines built were discretized in five-year increments to reflect an ordered field development program

[†] Consultant, Richmond, CA 94805.

to simplify the economic calculations and to assist in the representation of the economic comparisons.

The production and injection wells, pipelines, separation facilities, operating costs, and cash flows from power sales were used as input to a computer program to determine the cumulative cash flow versus time, using the inflation rate on costs and sales with an assumed plant operating factor. Comparison of the various development strategies was made with the cumulative cash flow versus time and on a net present value (NPV) calculation. The NPV calculation used a 10% return factor and represents the amount of money that would be needed as an investment in year zero to achieve the yearly cash flows that the project generates. Additional economic comparison methods are available, but since the cost of the power plant is neglected in this study, the number of available comparison methods is thereby reduced.

TWO-PHASE PIPELINE AND SEPARATOR DESIGN CALCULATIONS AND COST DETERMINATION

The homogeneous two-phase flow method was used to determine the size of the two-phase pipelines. The steam-water tables were digitized and fifth-order polynomials fitted to the pressure, temperature, and enthalpy data to allow iterative calculations to be performed with a personal computer. The pipelines were divided into 100-m lengths for the purpose of making pressure drop calculations. The pipeline size was adjusted to maintain the two-phase flow conditions in an annular regime. The Baker (1954) method was used to determine the pipeline flow conditions. The pipe sizes were further adjusted to limit the wellhead pressures to below 8.5 bars with a steam-water separator inlet pressure of 5.7 bars. The estimated length of the pipelines was increased by 25% to account for terrain and thermal expansion loops. The pipeline sizes are approximate, and no design safety factors are included. The sizes vary for each well and for the main trunk lines, depending on the flow rate and length of line (e.g., a 1500-m-long line carrying 250 kg/s requires a 30-in.-diameter line; a 1000-m-long line with a 40-kg/s flow rate requires a 16-in. line, etc.).

The cost of the pipelines was estimated as $\$685 \times d^2$ per km, where d is the pipeline diameter in inches. For example, the cost of a 30-in.-diameter pipeline is $620,000/km (all costs are in U.S. dollars). The costs are based on data from available handbooks and experience in other geothermal fields. However, it should be noted that most of the pipeline costs are small when compared to the well costs. The pipeline costs are included only to provide a more accurate comparison of the various development strategies.

The separator equipment sizes were designed using a combination of methods from Bangma (1961) and Lazalde-Crabtree (1984). The steam-water separator size was calculated for a design flow rate of 250 kg/s with an inlet pressure of 5.7 bars abs and an enthalpy of 1000 kJ/kg. This requires a separator with a 30-in.-diameter two-phase inlet and steam line outlet with a separator 10 m high and 2.5 m in diameter. The cost of the separator was estimated to be $250,000 in year zero based on vessel quotation and estimated associated costs f.o.b. Houston, Texas. For some of the development cases two separators are required. There has been no attempt at this time to determine what existing surface installations can be used for the various development strategies investigated in this study. Several of the cases show that the total mass flow rate will change with time and existing pipelines and separation facilities may be used in conjunction with the new wells to be drilled and required pipelines. The actual development strategy and the field behavior over time will determine the best use of the available facilities.

Several assumptions are used in the economic analysis (Table 1) and are based on experience and conversations with personnel involved with the Ahuachapán operations (G. Cuellar and C. Escobar, personal communications, 1989). Additional assumptions were made for inflation and operating factors.

Table 1. Assumptions used in the analysis.

Well costs	$1000/m per well ($1,500,000 per well)
Pipeline cost	$\$685 \times d^2$ per km, (d = diameter, inches)
Well dry hole ratio	1 : 4 (one out of four wells drilled are dry)
Inflation rate on costs	5%
Inflation rate on sales	5%
Operating factor	85% (plant operates 85% of the year)
Power sales rate	$0.035 per kW-hr
Operating costs	$0.015 per kW-hr

PRODUCTION DEVELOPMENT CASES STUDIED

Several power production development strategies were studied to determine the economics of future reservoir development. The cases studied (Table 2) include different levels of power generation with and without injection of 150°C separated water. We also considered the case of allowing the field to decline with the existing wells that are in place without injection or the drilling of make-up wells. The injection temperature of 150°C was considered appropriate for several reasons, including (a) past experience, (b) the need to inject at higher temperatures to reduce well scaling from silica deposition, (c) thermal breakthrough considerations and (d) the availability of injection fluid during long-term production. The power outputs are all estimated nominal power outputs. No correction to actual net power output has been used in these analyses.

DISCUSSION OF VARIOUS DEVELOPMENT STRATEGIES

Figure 1 shows the cumulative cash flow versus time for the various development scenarios for which economic aspects were studied. The 90 MWe case shows the largest cumulative cash flow, and the declining power generation (no wells drilled) case shows the lowest. The 75 MWe cases with and without injection show approximately similar cash flows versus time at levels somewhat below the 90 MWe cash flow. The 50-MWe cases with and without injection also show similar cash flows with respect to each other, with cash flows notably less than the 75 and 90 MWe cases. The reason for the similarity of the cash flows for the cases with and without injection is that, for the cases with injection, a greater amount of cash needs to be invested in year zero because of the injection wells. However, a smaller number of production wells are required during the project life for the case with injection when compared to the case without injection (Table 3).

Figure 2 gives the produced electrical output for the various cases as a function of time. This plot shows the reduction in output versus time for the declining power generation and the 90 MWe with 30% injection case. The other ones show constant power output over the 30-year project period.

Figure 3 presents the cumulative produced electrical energy versus time for the cases studied. The declining power generation and 90 MWe with 30% injection cases show a decreasing slope, indicating declining power production. The other cases show a constant slope, reflecting their respective uniform power outputs.

Figure 4 shows the cumulative number of new wells (including production, injection, and dry wells) drilled for all but the case of declining power generation (no drilling is assumed). From the graphs given in Figures 1 and 4 one concludes that the number of new production wells and dry holes drilled have a direct influence on the cash flow as a function of time.

Table 3 summarizes the economic and developmental information, including the total number of new wells required in each of the cases analyzed. The main difference between the various cases is the amount of investment required in year zero, due to the number of wells drilled at the beginning of the project.

CONCLUSIONS

As noted in Table 3 the difference between the 50, 75, and 90 MWe cases is small in terms of NPV but large in terms of the number of new wells drilled and the year zero investment. In this analysis this early investment is the main controlling factor on the NPV and in turn is governed by the number of wells needed initially to meet the production requirements and, for the cases with injection, the injection well requirements. From a NPV standpoint, each of the cases are justified for development because the project cash flow can easily cover the cost of development. From the standpoint of the number of new wells needed

Table 2. Production development strategies investigated.

Declining power generation		No new wells/no injection
50 MWe	New wells drilled	No reinjection
50 MWe	New wells drilled	60% of the produced fluid reinjected*
75 MWe	New wells drilled	No reinjection
75 MWe	New wells drilled	60% of the produced fluid reinjected*
90 MWe†	New wells drilled to year 20	30% of the produced fluid reinjected*

*Injection temperature: 150°C

†A nominal value of 90 MWe, instead of 95 MWe was considered for calculating steam requirements to account for occasional down-time of the power plants and wells.

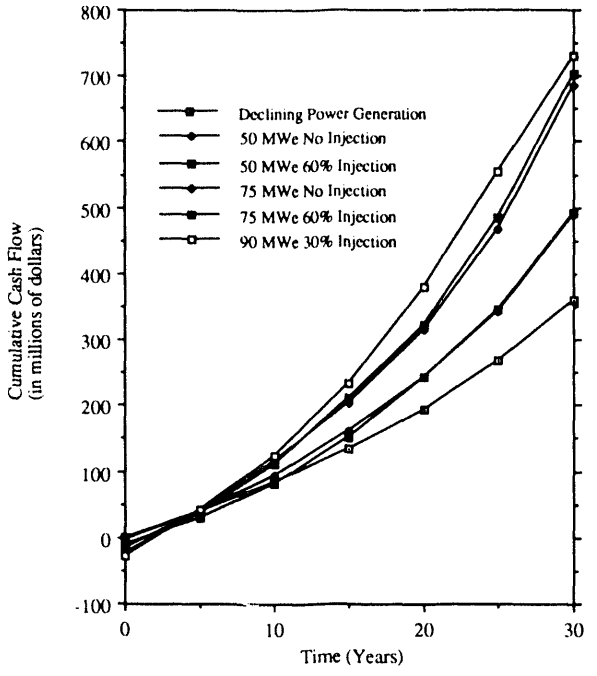

Figure 1. Cumulative cash flow versus time for various field development scenarios. [XBL 913-461]

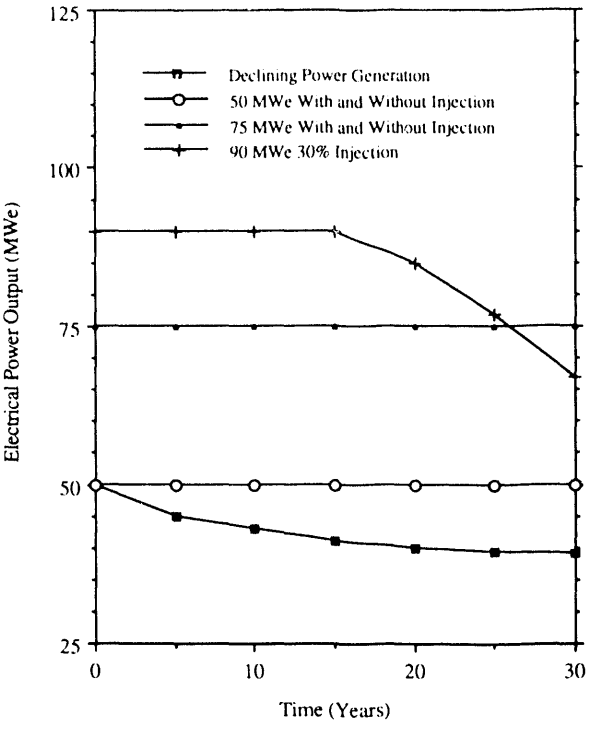

Figure 2. Produced power output versus time for various field development scenarios. [XBL 913-462]

Table 3. Summary of the economic calculations.

Case	Number of new wells				NPV*	Year zero investment*	Cumulative cash flow*
	Production	Injection	Dry	Total			
Declining Power generation	0	0	0	0	82	0	360
50 MWe No injection	5	0	2	7	100	3	489
50 MWe 60% injection	4	4	1	9	94	8	503
75 MWe† No injection	24	0	6	30	130	15	685
75 MWe 60% injection	18	4	5	27	128	24	704
90 MWe† 30% injection	24	4	7	35	141	29	731

*Millions of U.S. dollars.

†For these cases the targeted power generation is not possible for the entire 30-year period.

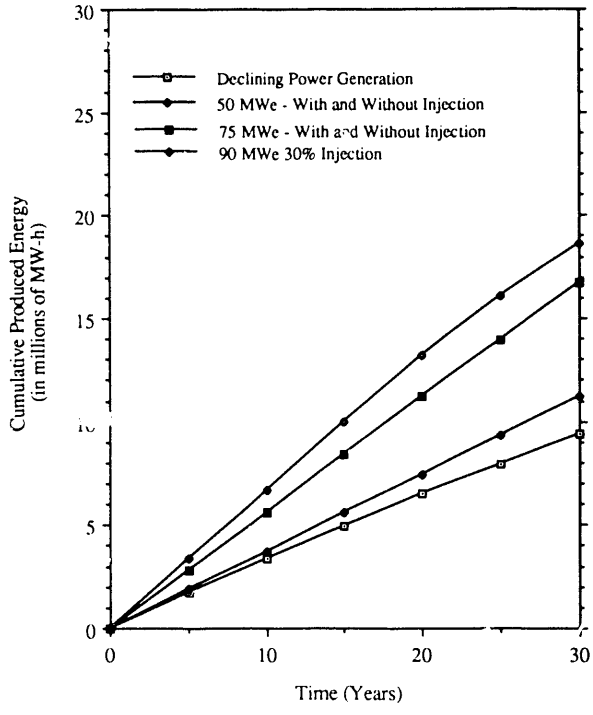

Figure 3. Cumulative produced electrical energy versus time for the various development scenarios. [XBL 913-463]

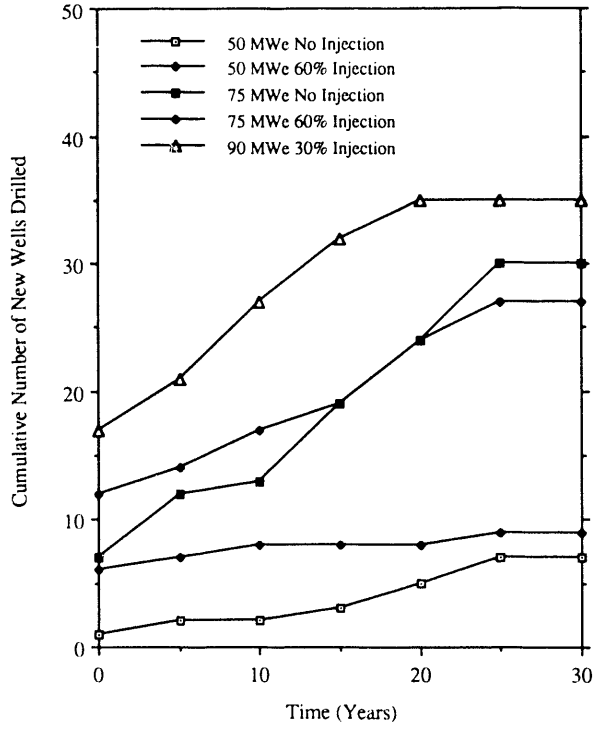

Figure 4. Cumulative number of (production, injection, and dry) wells drilled versus time for various development scenarios. [XBL 913-464]

there is a large difference between the 50, 75, and 90 MWe cases. This therefore leads to the conclusion that the magnitude of the development to be undertaken should be based on the confidence in the resource size and the ability of the resource to behave as the reservoir simulation has indicated.

The main reason that the economics indicate that each development case is warranted is that the cost of purchase and installation of the power plant is not included. This allows for the cost of the wells to easily be met by the cash flows. If the plants were not already in place, then a rate of return economic analysis (and other additional economic analyses) could then be performed. In any case, confidence in the reservoir size and reservoir simulation studies will always enter into the evaluation of development strategies.

REFERENCES

Aunzo, Z., Bodvarsson, G.S., Laky, C., Lippmann, M.J., Steingrimsson, B., Truesdell, A.H., and Witherspoon, P.A., 1989. The Ahuachapán geothermal field, El Salvador—Reservoir analysis (LBL-26612).

Aunzo, Z., Laky, C., Steingrimsson. B., Bodvarsson, G.S., Lippmann, M.J., Truesdell, A.H., Escobar, C., Quintanilla, A., and Cuellar, G., 1991. Pre-exploitation state of the Ahuachapán geothermal field, El Salvador. Geothermics, v. 20, no. 1/2, p. 1–22 (LBL-27704).

Baker, O., 1954. Design of pipelines for the simultaneous flow of oil and gas. Oil and Gas Journal, v. 53, p. 185.

Bangma, P., 1961. The development and performance of a steam-water separator for use on geothermal bores. Proc. U.N. Conference on New Sources of Energy, Rome, Italy, August 1961, v. 3, p. 60.

Lazalde-Crabtree, H., 1984. Design approach of steam-water separators and steam dryers for geothermal applications. Geotherm. Resour. Coun. Bull., v. 13, no. 9, p. 11–20.

Ripperda, M., Bodvarsson, G.S., Lippmann, M.J., Cuellar, G., and Escobar, C., 1991. An exploitation model and performance predictions for the Ahuachapán geothermal field, El Salvador. Accepted for publication in Geothermics (LBL-29879).

Steingrimsson, B., Aunzo, A., Bodvarsson, G.S., Truesdell, A , Cuellar, G., Escobar, C., and Quintanilla, A., 1991. Changes in thermodynamic conditions of the Ahuachapán Reservoir due to production and injection. Geothermics, v. 20, no. 1/2, p. 23–38 (LBL-27703).

The Use of Iterated Function Systems in Fracture Hydrology

K. Hestir, J. C. S. Long, and S. J. Martel

One approach to building hydrologic models for fractured rock is to use inverse methods to find equivalent discontinuum models. An equivalent discontinuum model is a simplified lattice model that can reproduce the observed hydrologic behavior (Long et al., 1991). A simulated annealing inversion, developed for this purpose by Davey et al. (1990), finds lattice configurations that reproduce observed well-test behavior. Another approach that holds promise is related to the observation that fracture networks may exhibit scaling behavior. We can find objects that exhibit self-similar properties and which also behave like the well tests we observe. This approach has tremendous appeal, for the simple reason that the self-similar properties provide a logical path for scaling up our understanding to larger regions.

Probably the simplest approach is to look for fractals that manifest the hydrologic behavior we require. Some work on this topic has begun and is discussed below. Fractals, however, are really a subset of a larger class of objects called "attractors" that can be generated with "iterated function systems" (IFS). Some new ideas for inverse techniques based on IFS are also briefly described.

FRACTAL APPROACH

It is not hard to believe that some fracture networks might form a type of fractal. In fact, the name "fractal" is derived from the word "fracture." We can consider that fluid flow in a fracture network is equivalent to the problem of percolation on a lattice (Hestir and Long, 1990). Then the network is characterized by clusters of conductors that form at scales that exhibit self-similar geometry (Orbach, 1986).

Barker (1988) has provided a technique for determining the fractional flow dimension of a network through a well test. He solved the generalized equation of flow to a well by letting the flow dimension be a variable. Thereby, the flow dimension is allowed to be fractional—say, a dimension of 1.6 or 1.8 (as opposed to integral dimension, i.e., two- or three-dimension space). Polek (1990) has shown that this "flow" dimension is closely related to the geometric fractal dimension.

Certain fracture systems may have fractal geometry (Barton et al., 1987). Therefore, use of fractal geometry for representing fracture systems may be quite plausible. Flow to wells in such geometry differs from that in Euclidian geometry. One should be able to calculate the corresponding fractal dimension from the well-test results if the straight-line portion of the response is present. This may be important information about the structure of the system. Fractal representation of fracture geometry may provide another way to find equivalent discontinuous models.

THE USE OF IFS MODELS IN FRACTURE NETWORK PROBLEMS

An iterated function system is a standard way to model self-similar geometrical structures (Barnsley, 1988). To create an IFS one first specifies a function f that maps sets to sets:

$$f(A_0) = A_1 , \tag{6}$$

where A_0 and A_1 are (compact) subsets of two- (or three-) dimensional space. A set A_∞ can then be defined by

$$A_{n+1} = f(A_n)\ n = 0,1, \ldots ,$$

$$A_\infty = \lim_{n \to \infty} A_n . \tag{7}$$

Given certain restrictions on the set function f, one can show (Barnsley 1988) that A_∞ exists, is independent of the starting set A_0, and generally has a fractional Hausdorff dimension (e.g., A_∞ is a fractal). Hence f determines a fractal, A_∞.

If we have a function f that is easily parameterized, then the fractal A_∞ is parameterized as well. This leads to a nice setup for modeling real-world problems, because a small number of parameters can characterize a complex geometry. One important example of a parameterized f used extensively by Barnsley (1988) is

$$f(A) = g_1(A) \cup g_2(A) \cup \ldots g_k(A) . \tag{8}$$

Here the g_i's are so-called affine transforms:

$$g_i(A) = \bigcup_{\vec{x} \in A} g_i(\vec{x}) ,$$

$$g_i(\vec{x}) = B\vec{x} + \vec{b}_i , \tag{9}$$

where B_i is a matrix and $\vec{b}_i$ a vector. The parameters characterizing f are the entries in the B_i's and $\vec{b}_i$'s. The B_i matrix serves to rotate and "shrink," and the $\vec{b}_i$ vector translates. Figure 1 shows an example pattern generated using $k = 3$ affine transformations, which results in a fractal called a Serpinski's gasket. Figure 2 shows another example pattern generated using $k = 4$ affine transforms,

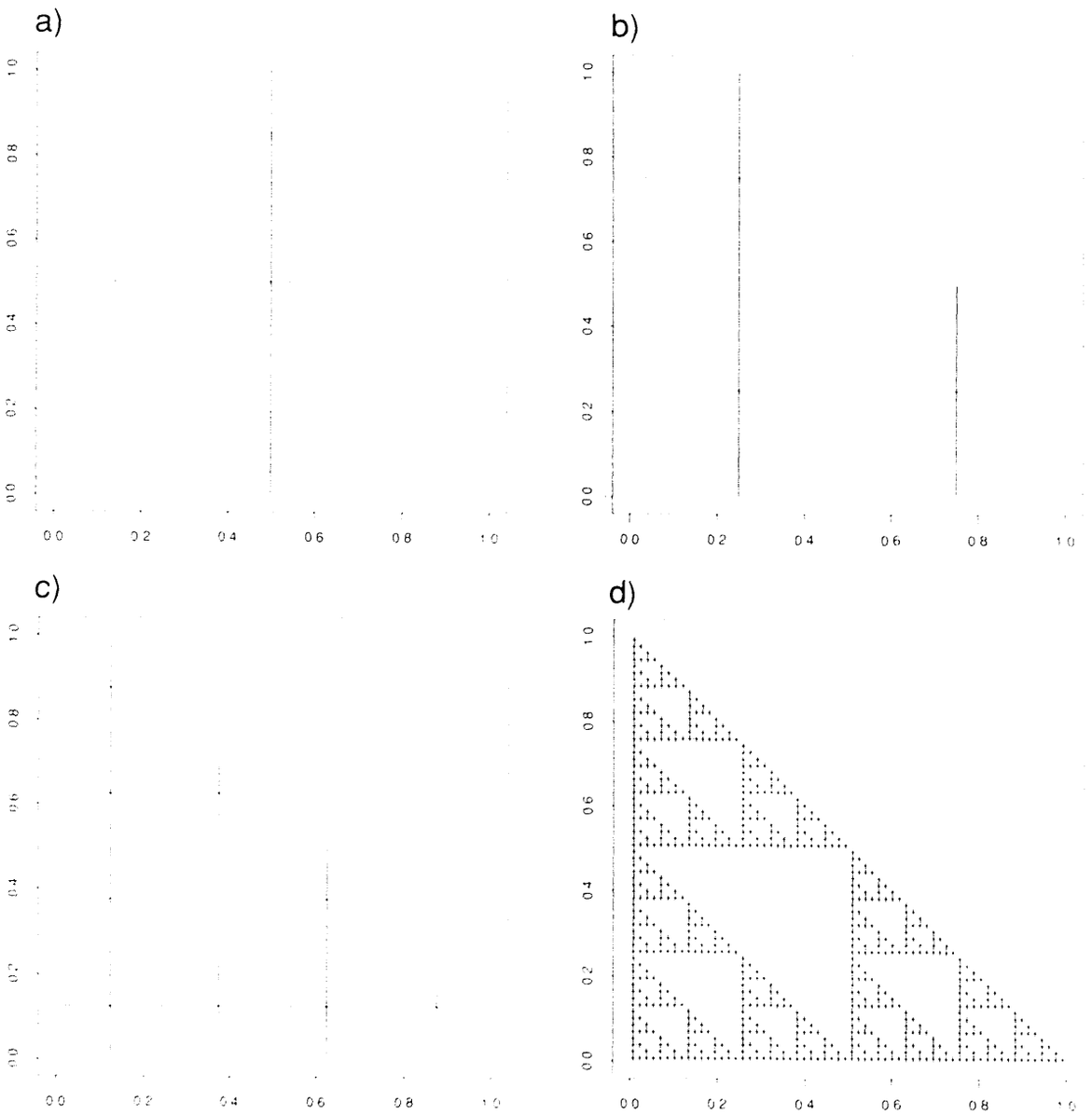

Figure 1. Generation of a Serpinski's gasket using three affine transformations. [XBL 911-5208]

with entries chosen randomly. In this figure, the beginning set was one horizontal line segment and the pattern shown resulted from six iterations of f.

One can exploit the IFS idea to generate sequences of fracture patterns that have self-similar properties and the complex geometries observed in the field. We have developed a way to do this with an iterative first-order growth scheme. To build a fracture pattern with this scheme, we can define a beginning set A_0, to be a given existing set of fractures in a mostly unfractured rock. The function f applied to a set A of fractures is defined to be a rule that grows new fractures from each of the existing fractures in A. This is done by looking at each fracture in A in its own local coordinate system (Figure 3a, the solid line) and growing one fracture from it using rules defined in that local coordinate system. The method is called first order because we grow new fractures without accounting for interaction between existing fractures. The new fracture growth is chosen at random from a finite number of possibilities (the dashed lines in Figure 3a), each with a given probability of occurring. The growth possibilities (with probability $p_1\ p_2\ \ldots$) shown in Figure 3a result in a fracture pattern given in Figure 3b. The rules governing fracture growth can be based on fracture mechanics. For

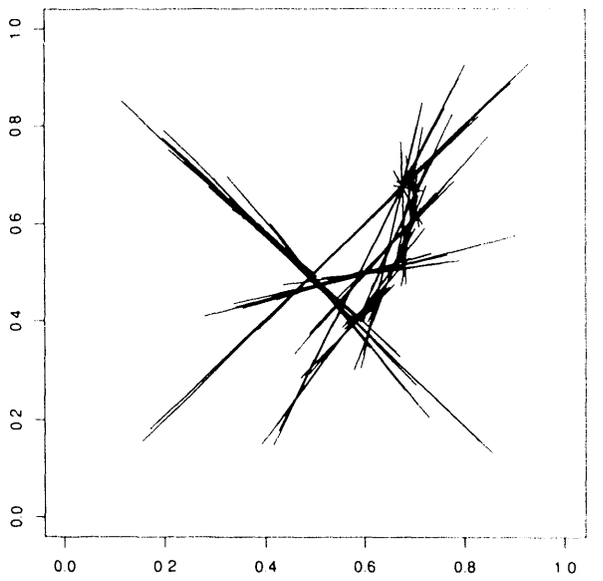

Figure 2. An attractor formed using a set of four random affine functions [XBL 911-5206]

example, the probabilities for growth are scaled to the size of the fracture, and the growth positions are approximately located where stress concentrations would be in the absence of interactions. Further growth orientations can be picked on the basis of stress trajectories. So far, we have been able to use this method to produce realistic sequences of two-dimensional fracture network patterns.

One can also use the geometries given by the IFS technique to define patterns of high and low permeability in a flow system. If there are hydrologic measurements on a system that can be numerically modeled, then inverse modeling techniques can be used to find an IFS for the system. This can be applied in porous media as well as fracture networks. In the fracture network case, this is an exciting idea, because we have a hydrologic model that could be coupled to a mechanically based model for fracture growth.

An example of the possibilities of using IFS for hydrologic inversion is given in Figure 4. Figure 4a shows a grid of points that are connected by equal conductance elements (not shown). A heterogeneous field is obtained by superimposing an attractor (Figure 4b) on the grid and increasing the conductance of those elements that are in the vicinity of points on the attractor. We then use an optimization technique to change the parameters of the attraction (Figure 4c,d) such that we find an attractor (Figure 4d) that matches the observed well-test behavior (Figure 5). Clearly this inversion could be refined to better match the early-time data, but the example as is illustrates the possibilities for using IFS to characterize heterogeneous hydrology.

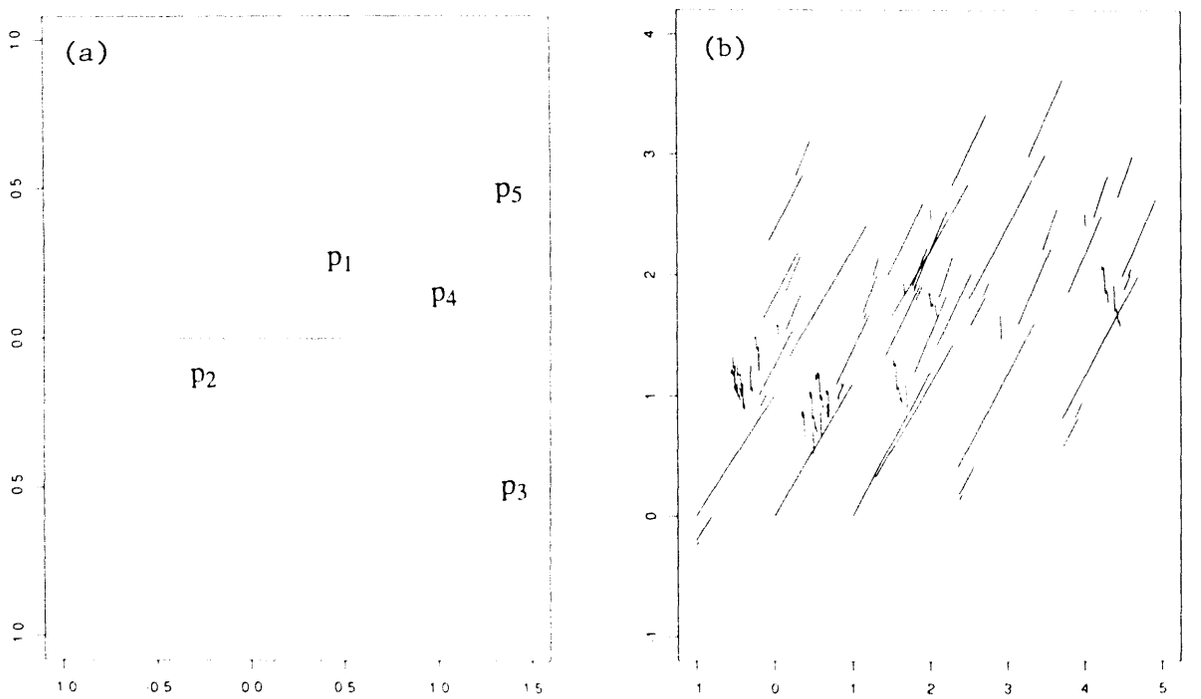

Figure 3. **(a)** A fracture (solid line) shown in its own coordinate system has the possibility of growing according to the dashed lines at each iteration. **(b)** Application of this growth scheme results in this fracture pattern. [XBL 911-5205]

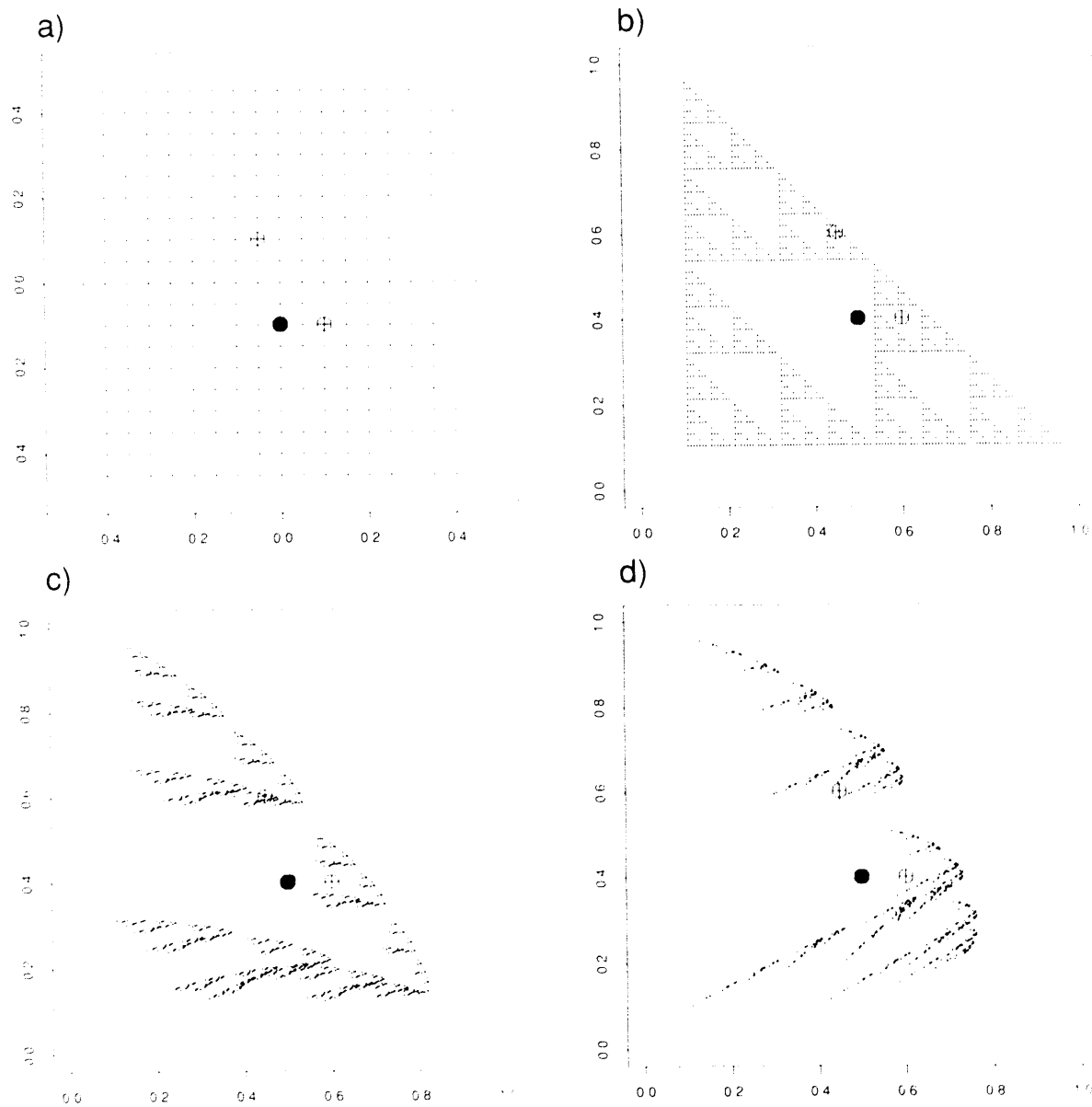

Figure 4. **(a)** A grid of equal conductance elements with three wells. The solid circle is the pumping well. The two open circles are the observation wells. **(b)** The conductance of elements that are near points in this attractor is increased. **(c)** The configuration at iteration 5. **(d)** The final configuration of attractor at iteration 993. [XBL 911-5209]

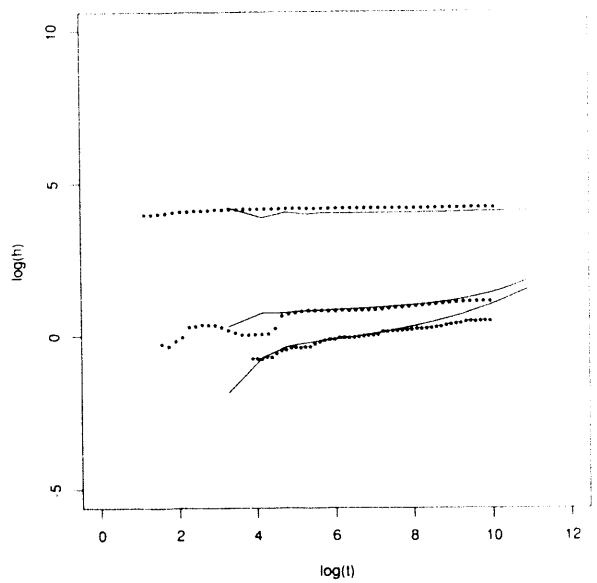

Figure 5. The-well test data as simulated on the lattice at iteration 993 compared with the real well-test data. Stars are data; solid line is the simulation. [XBL 911-5207]

REFERENCES

Barker, J., 1988. A generalized radial-flow model for pumping tests in fractured rock. Water Resour. Res., v. 24, no. 10, p. 1796–1804.

Barnsley, M., 1988. Fractals Everywhere. Academic Press, Inc., San Diego, California.

Barton, C.C., Schutter, T.A., Page, W.R., and Samuel, J.K., 1987. Computer generation of synthetic fracture networks for hydrologic-flow modeling. EOS: Trans., Am. Geophys. Union, v. 68, no. 44.

Davey, A., Karasaki, K., Long, J.C.S., Landsfeld, M., Mensch, A., and Martel, S.J., 1990. Analysis of hydraulic data from the MI fracture zone at the Grimsel Rock Laboratory. Lawrence Berkeley Laboratory Report LBL 27864 (NDC-15).

Hestir, K., and Long, J.C.S., 1990. Analytical expressions for the permeability of random two-dimensional Poisson fracture networks based on regular lattice percolation and equivalent media theories. J. Geophys. Res. (in press).

Long, J.C.S., Karasaki, K., Davey, A., Peterson, J.E., Landsfeld, M., Kemeny, J., and Martel, S.J., 1991. An inverse approach to the construction of fracture hydrology models conditioned by geophysical data—An example from the validation exercises at the Stripa Mine. Int. J. Rock Mech. Min. Sci. & Geomech. Abstr. (in press).

Mandelbrot, B.B., 1982. The Fractal Geometry of Nature. W.H. Freeman and Company, New York, 468 p.

Orbach, R., 1986. Dynamics of fractal networks. Science, v. 231, p. 814–819.

Polek, J., 1990. Studies of the hydraulic behavior of hierarchically fractured geometries. Lawrence Berkeley Laboratory Report LBL-28612, 72 p.

Preliminary Environmental Investigations at the Lawrence Berkeley Laboratory

I. Javandel

Lawrence Berkeley Laboratory (LBL) is a research facility managed by the University of California for the United States Department of Energy (DOE). It is located in the Berkeley Hills adjacent to the main campus of the University of California at Berkeley. Ernest Lawrence started the Laboratory in 1940 essentially as a center for nuclear physics research. Since then it has grown to 12 major research divisions and supporting organizations housed in more than 100 buildings. Out of necessity, most of these buildings have some shop facilities for manufacturing research instrumentation. Others have different physical, chemical, and biological laboratories. Over the years, many types of chemicals, some hazardous, have been used in these shops and laboratories.

In the summer of 1986, as a part of the environmental baseline study for the development of the East Canyon area within the site, LBL staff collected several samples of soil, groundwater, surface water, and vegetation from within the property's boundary, as well as from adjacent areas. Groundwater samples were collected from a few flowing horizontal drains (hydraugers). Chemical analysis of water samples from two adjacent hydraugers (1.3 and 1.4) east of Building 51 (see Figure 1) showed low levels of solvents (chlorinated hydrocarbons). Flow rates from these hydraugers are on the order of one or two liters per minute. Because of the persistence of these levels of chemical concentration in the effluent water from these two hydraugers and the observation of some contaminants

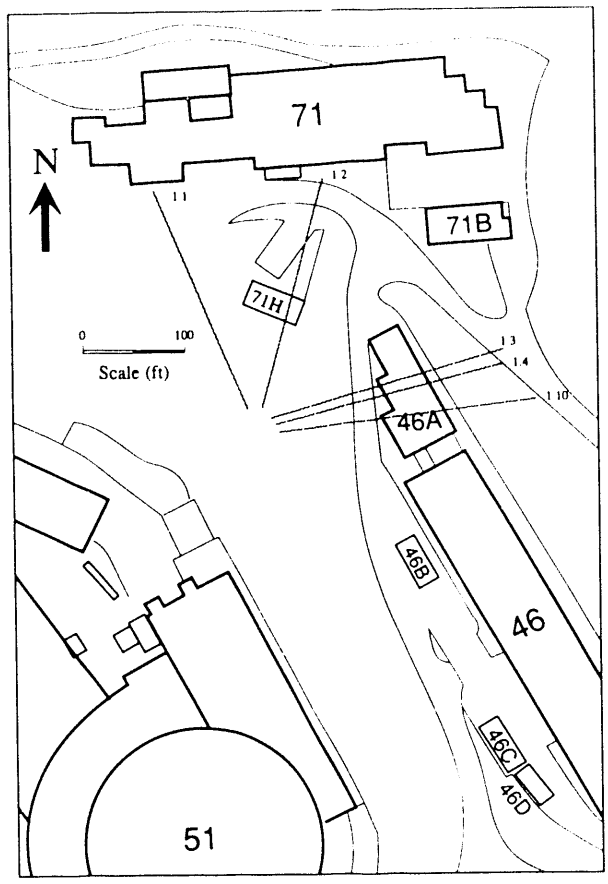

Figure 1. Approximate position of hydraugers 1.1, 1.2, 1.3, 1.4, and 1.10 of the Building 51 series. [XBL 913-465]

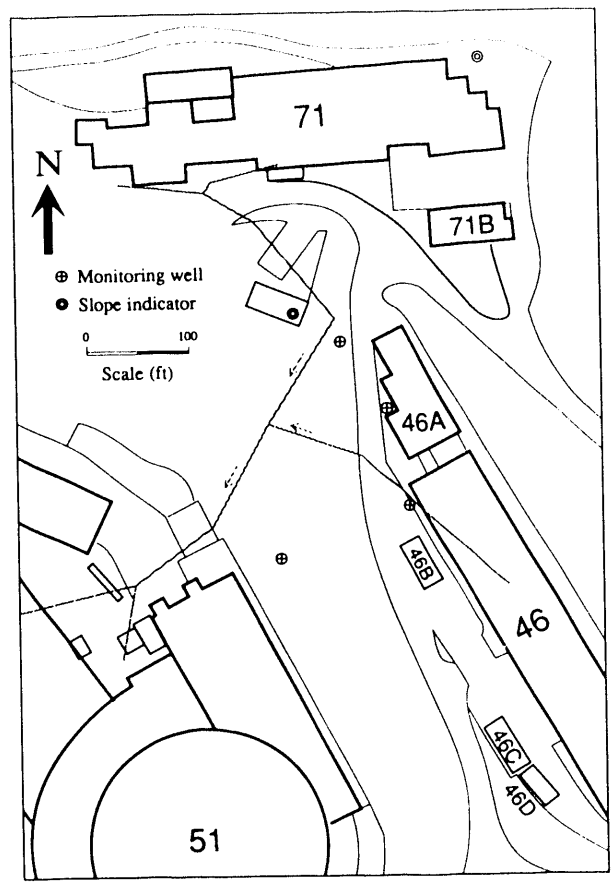

Figure 2. Sanitary sewer lines in the vicinity of Buildings 46, 51, and 71. [XBL 913-466]

elsewhere on the Laboratory site, LBL submitted in 1989 a proposal to the DOE for a site-wide environmental characterization and monitoring program. Meanwhile, during Fiscal Year 1990, using laboratory overhead resources, LBL carried out a preliminary investigation. The results of it are as follows:

1. The source of contamination observed in the effluent flowing in the hydraugers east of Building 51 is believed to be leakage from a sanitary sewer coming from Building 71 (see Figure 2). This sewer line was decommissioned during 1988. A few chlorinated hydrocarbons were also detected in a relatively narrow aquifer formed along the bed of the main branch of the original Blackberry Canyon Creek. A piezometric map of this narrow aquifer is shown in Figure 3. Observed concentrations of these chemicals in the groundwater never exceeded 0.1 mg/L during the course of this investigation. To investigate the extent of contamination, three new monitoring wells (90-4, 90-5, and 90-6) were constructed downstream from the observed position of the contaminant plume. Locations of these wells are shown in Figure 4. Chemical analyses of water samples from these wells indicate that the plume of contamination is contained in an area upgradient from these three wells.
2. Chemical analysis of "grabbed" samples from a few wells and slope indicators in the "old town" (area of Buildings 7, 52, and 53) showed chlorinated hydrocarbons ranging up to 2 mg/L. However, study of subsurface geologic information from past and recent drilling, as well as a single pumping test, indicates that the contaminated water is limited to a very thin saturated seam (about 4 in. thick) having a very low hydraulic transmissivity. Further studies will be carried out to check the validity of this conclusion.
3. Chemical analysis of water samples collected from three nearby wells in the Corporation Yard (area of Buildings 69 and 75) showed some low concentrations of chlorinated solvents (less than 0.1 mg/L). On the basis of current information, the plume of contamination in this area seems to be relatively small. A more detailed study is being carried out to characterize this contamination.

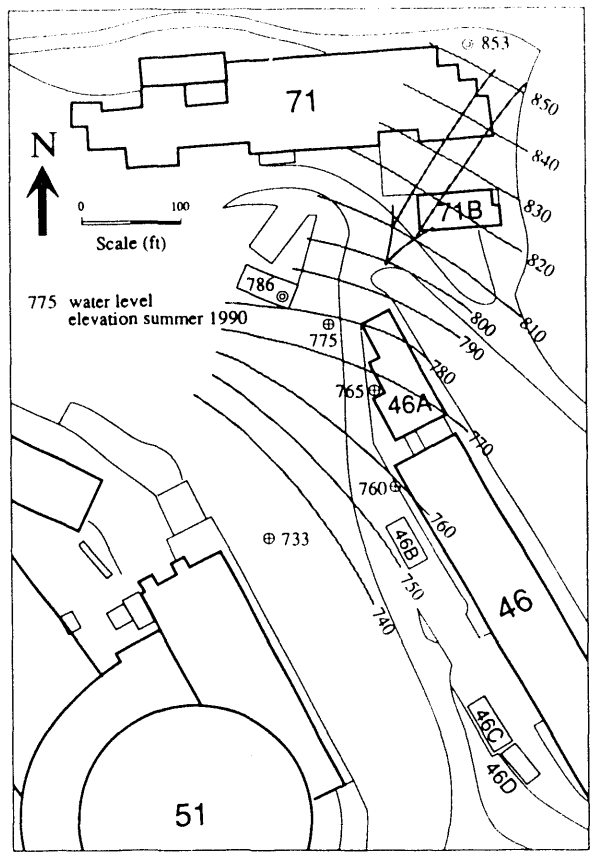

Figure 3. Piezometric map of groundwater in the vicinity of Buildings 46, 51, and 71 during the summer of 1990. [XBL 913-467]

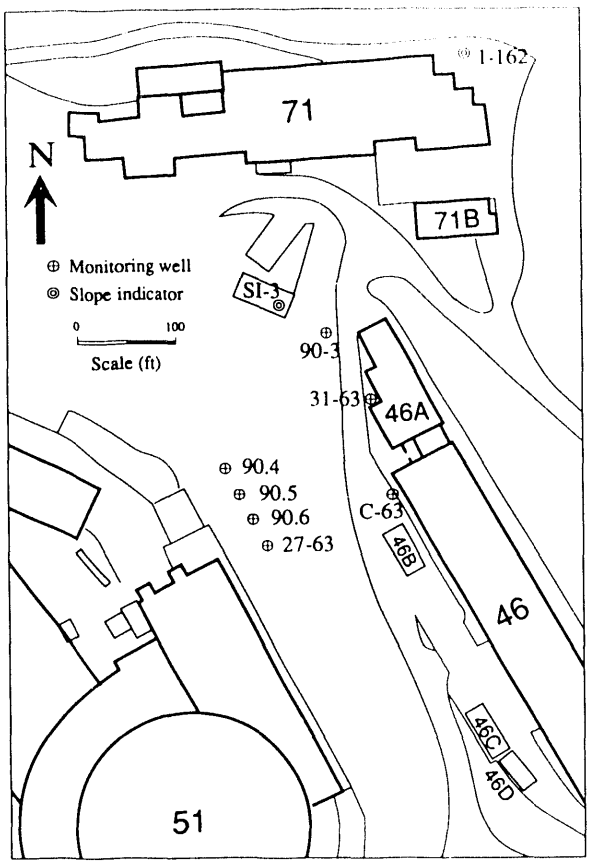

Figure 4. Location of monitoring wells and slope indicators in the vicinity of Buildings 46, 51, and 71. [XBL 913-468]

A site-wide program of investigation is being implemented during Fiscal Year 1991 to complete the characterization of the above three problem areas and to identify other possible environmental contamination at LBL. Specific attention will be paid to monitoring the presence of contamination at the property boundary. Some interim remedial actions may be proposed and, if approved, carried out during Fiscal Year 1991. More detailed discussion of this study can be found in Javandel (1990).

REFERENCE

Javandel, I., 1990. Preliminary environmental investigations at the Lawrence Berkeley Laboratory. Lawrence Berkeley Laboratory Report LBL-29898.

Method Development and Strategy for the Characterization of Complexly Faulted and Fractured Rhyolitic Tuffs, Yucca Mountain, Nevada

*K. Karasaki and D. Galloway**

The planned high-level nuclear waste repository at Yucca Mountain, Nevada (Figure 1a), would exist in unsaturated, fractured welded tuff. One possible contaminant pathway to the accessible environment is transport by groundwater infiltrating to the water table and flowing through the saturated zone. Therefore, an effort to characterize the hydrology of the saturated zone is being undertaken in parallel with that of the unsaturated zone. As a part of the saturated zone investigation, three wells—

* U.S. Geological Survey, Sacramento, CA.

UE-25c#1, UE-25c#2, and UE-25c#3 (hereafter called the c-holes)—were drilled to study hydraulic and transport properties of rock formations underlying the planned waste repository. The location of the c-holes is such that the formations penetrated in the unsaturated zone occur at similar depths and with similar thicknesses as at the planned repository site. The c-holes penetrate to a depth of approximately 914 m with separations of 30–75 m among the wells (Figure 1b). Geophysical logs (Muller and Kibler, 1984) and geologic logs (Richard W. Spengler, U.S. Geological Survey, written commun., 1989) are available for the c-holes, along with information on the degree of welding of the tuffs and formation stratigraphy. The surface geology has also been mapped (Scott and Bonk, 1984).

In characterizing a highly heterogeneous flow system, several issues emerge. (1) The characterization strategy should allow for the virtual impossibility to enumerate and characterize all heterogeneities. (2) The methodology to characterize the heterogeneous flow system at the scale of the well tests needs to be established. (3) Tools need to be developed for scaling up the information obtained at the well-test scale to the larger scale of the site. In the present paper, the characterization strategy and the methods under development are discussed with the focus on the design and analysis of the field experiments at the c-holes.

YUCCA MOUNTAIN

Yucca Mountain is a north-south-trending ridge bounded on the west by Solitario Canyon and Crater Flat and on the east by Fortymile Canyon and Jackass Flats (Figure 1a). The west face of Yucca Mountain is a scarp defined by the Solitario Canyon fault. The eastern flank slopes toward Fortymile Canyon and smaller intervening ridges and valleys. From the crest of Yucca Mountain eastward to Fortymile Wash, many other smaller north-south-trending faults bound individual blocks of mostly rhyolitic tuff. Among the larger of these are the Paintbrush Canyon, Ghost Dance, and Abandoned Wash faults. These are high-angle normal faults bounding blocks that dip eastward 5 to 20°. The tuffs, composed of thin beds of lava intercalated with bedded tuffs, were deposited unconformably upon Paleozoic bedrock between 15 and 11 million years ago. The thickness of the tuffs exceeds

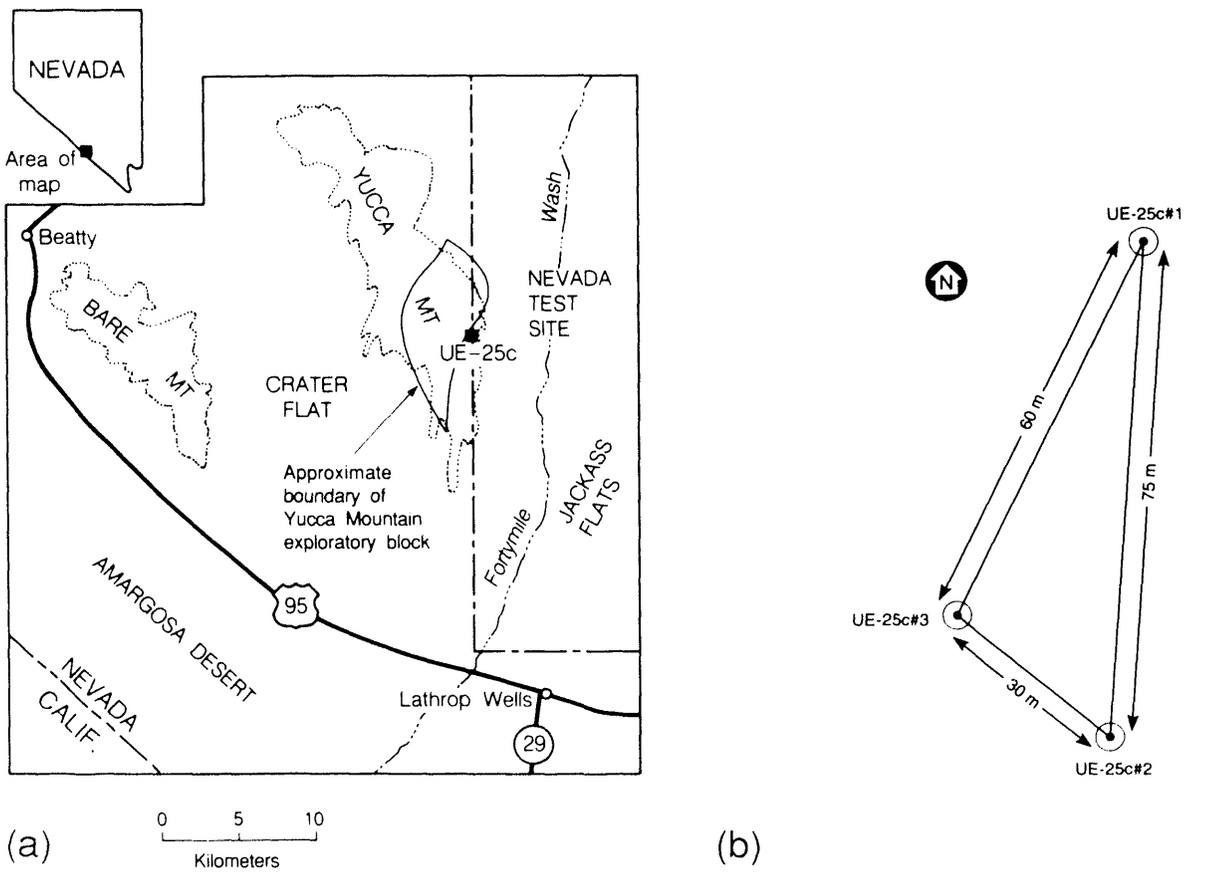

Figure 1. (a) Location map of Yucca Mountain and vicinity. (b) Surface layout of UE-25 c-holes. [a, XBL 862-10671A; b, XBL 9010-5946]

1200 m on the eastern flank of Yucca Mountain, where test well UE-25p#1 penetrated the Timber Mountain Tuff, the Paintbrush Tuff, the tuffaceous beds of Calico Hills, the Crater Flat Tuff, the Lithic Ridge Tuff, the Older Tuffs, and 500 m of Paleozoic carbonate rocks (Figure 2). Bedded tuffs were encountered between each of the major tuffs.

In the saturated zone, aquifer boundaries may not coincide with stratigraphic boundaries. Results from borehole geophysical surveys and well hydraulic tests suggest that a strict hydrostratigraphic categorization based on lithology and laboratory-derived hydraulic properties inadequately represents groundwater flow at the scale of the well tests (Waddell et al., 1984). Although fractures are the principal conduit for groundwater flow in the saturated zone, borehole flow-production surveys show that the majority of fractures mapped in boreholes do not contribute to flow. Flow is typically dominated by only a few fractures or groups of fractures.

Most hydraulic tests conducted at Yucca Mountain have been single-well tests conducted in thick composite sections of borehole, and most of these have been falling-head injection tests. The pressure-transient responses for most of the tests conducted in fractured intervals of boreholes cannot be explained by linear or radial flow models. Spherical flow models (Karasaki et al., 1988) and another model based on a noninteger-dimension flow field (Barker, 1988) can explain many of the pressure-transient responses. These models indicate that the flow geometry has a fractional dimension somewhere between 2 (radial) and 3 (spherical). Several tests conducted in unfractured sections of boreholes were indicative of poorly conductive units and displayed ideal radial flow behavior for the duration of the tests. Similarly mixed pressure-transient responses have been measured in single-well tests conducted in tuffs elsewhere at the Nevada Test Site (Charles Savard, U.S. Geological Survey, oral commun., 1990).

The frequency-dependent fluid-pressure responses measured in the c-holes can be explained by water-table drainage, indicating that the monitored intervals are in hydraulic connection with the water table. For the response measured below the packer in UE-25c#3, this means that the hydraulic connection between the lower Bullfrog member of the Crater Flat Tuff and the water table near the top of the tuffaceous beds of Calico Hills is realized over the 350-m thickness of saturated tuffs (Figure 2). Estimates of vertical hydraulic conductivity made on the basis of the frequency-dependent responses in the c-holes are on the same order of magnitude as those measured in cores from nonwelded units and are about two to three orders of magnitude larger than measurements made on cores from moderately to densely welded units (Galloway and Rojstaczer, 1988). If conductive fractures alone provide the hydraulic connection between the water table and deeper stratigraphic units, the in situ measurements would be much larger than the measurements from cores, which reflect matrix properties. This suggests that the vertical hydraulic connection in the stratigraphic section penetrated by the c-holes is limited by the matrix hydraulic conductivity of the nonwelded tuffs. Taken together with other information on fracture orientation and density and fault boundaries, these results indicate that an areal two-dimensional flow

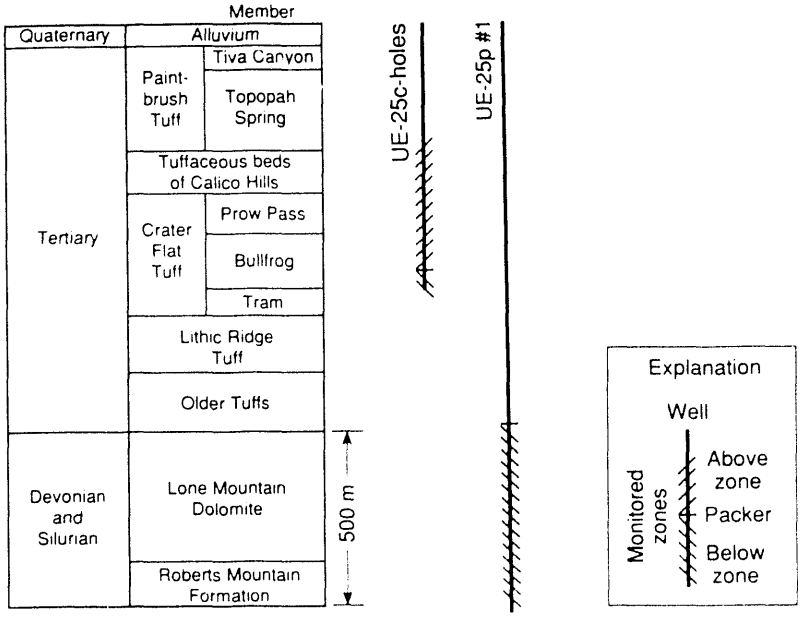

Figure 2. Schematic stratigraphic column of the rock units penetrated by UE-25p#1 and the c-holes. [XBL 913-469]

model cannot adequately represent the flow geometry at the scale of the well tests or at larger scales. Further, because of potential stratigraphic bounds on fracture connectivity, a combination of discontinuum and continuum flow mechanics may be required.

DESIGN OF FIELD EXPERIMENTS

The approach that is envisaged here is one of hypothesis testing and confidence building. One makes assumptions regarding the structure of the system using available data and then plans the next field experiment to test those assumptions. One then either rejects or modifies the assumptions on the basis of the new data. This process is repeated until sufficient confidence in those assumptions is obtained. Experiments planned at the c-holes are one step of this iterative process. In addition to collecting pertinent data for site characterization, the c-hole complex is also used as a method-development site. Because a limited number of tests are possible and because interpretation of hydraulic test data is inherently non-unique, a multidisciplinary approach is envisaged, where geologic, geochemical, geophysical, geomechanical, and hydrological investigations are combined.

Cross-borehole seismic tomography surveys will be conducted at the c-holes to help narrow the range of possible interpretations of geologic and hydrologic data (Majer et al., 1990). For example, these surveys may be able to confirm the existence of faults that thus far have not been confirmed using geologic data alone. The seismic tomography will also provide information on the structure of the fracture system, which will then be used to construct a fracture network model. The primary target of the tomography is the Bullfrog member of the Crater Flat Tuff, which has been identified as the most productive unit by the previous hydraulic tests and which at the c-holes contains the suspected fault. If a strong enough seismic source can be obtained, seismic tomography will also be conducted between one of the c-holes and UE-25p#1, which is located roughly 500 m east of the c-holes. The technique would provide a critically needed large-scale image of the geologic structure.

Multiple-zone, cross-borehole hydraulic, and conservative tracer tests are planned at the c-holes. Three five-packer strings are currently being constructed. Each string will allow water to be pumped from or injected into any one of the packed-off intervals. This is made possible through the use of mechanically controlled downhole valves fitted in each interval. Each interval is also equipped with an independently controlled solenoid attached to the tracer line so that a tracer can be released from any interval. The spacing between the packers is adjustable, and each interval is equipped with a pressure transducer and temperature sensor. By alternately stressing different intervals in all three holes and recording pressure transients in all the intervals in a crude tomographic fashion (Figure 3), it is expected that the hydraulic structure between the holes can be estimated. Conservative tracer tests will be carried out in much the same way by directing a convergent flow field into one interval and releasing

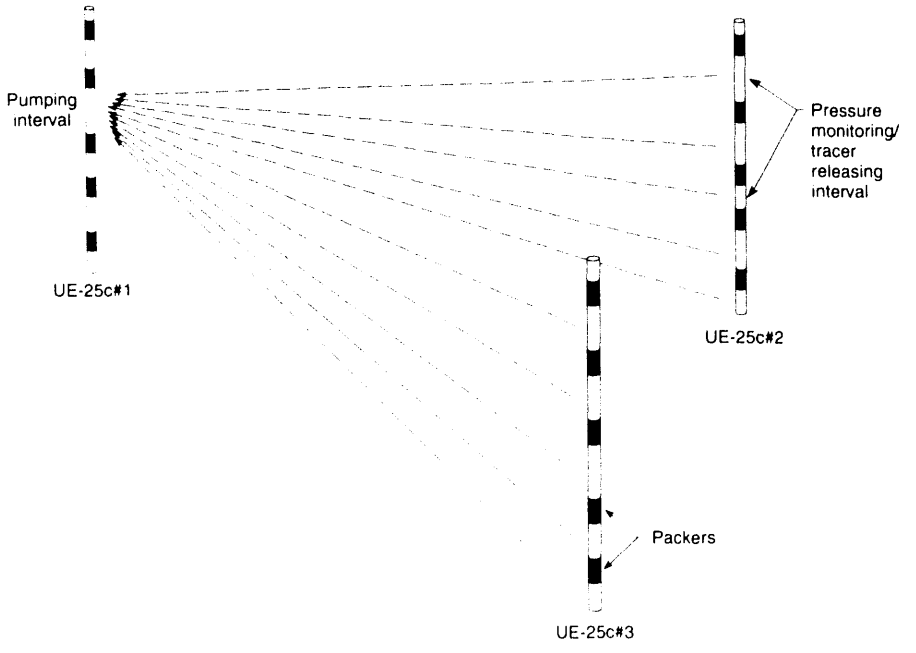

Figure 3. Tomographic configuration of multiple-level, cross-hole hydraulic, and tracer tests. [XBL 9010-5948]

various tracers from other intervals. Groundwater flow paths will be estimated by analyzing the tracer arrivals from the various release points. Both organic and inorganic tracers are planned for use, and the analytical methods are currently under development. Single-well hydraulic and tracer tests will also be conducted and the results compared with those of multiple-well tests to determine whether single-well tests can be reliably applied in fractured rocks.

Another objective of the experiments at the c-holes is to test the hydrologic significance of strata boundaries and the suspected fault(s). The knowledge obtained at the c-holes may provide a first approximation toward understanding these boundary influences that could be applied and tested elsewhere throughout the site. Scale dependency of the parameters will be addressed by conducting tests at various scales. For example, the distance between c#1 and c#3 is roughly twice that between c#2 and c#3, and a planned fourth c-hole would be drilled at a distance at least twice that between c#1 and c#2. Pumping tests are planned so that interference responses may be observed in the c-holes at these scales and in other boreholes located even farther away. Transient pressure data at the pumping well may also be used to assess the existence of a scale-dependent permeability structure.

DEVELOPMENT OF ANALYSIS METHODS

Heterogeneities exist at all scales. This is particularly true for fractured rocks. Simply stated, there are three different scales of interest: small, intermediate, and large. At the small (laboratory) scale, studies indicate that there is a large variation in the roughness within a single fracture and that fluid flows preferentially in tortuous channels of varying flow properties. This channeling effect is observed to be further enhanced when stress is applied across the fracture. At an intermediate scale, such as at the scale of a well test, the transmissivity is often observed to vary markedly along the length of a borehole and from borehole to borehole. The heterogeneous transmissivity observed at this scale is a compound effect of the variability in the fracture density, conductance, and connectivity. Intermediate-scale features, including faults and fracture zones, also affect the transmissivity. The large scale is the one at which well-test interference responses cannot be observed at distant observation wells. Heterogeneities at this scale can be attributed to large faults and changes in geologic settings. The overall flow system consists of the hierarchically structured heterogeneities of all scales. Therefore, the manner in which smaller-scale features affect those at the next larger scale must be understood. This is particularly true for the regional scale, because direct measurement of hydraulic properties at such a scale is not possible.

At the scale of well tests, a conventional porous medium model is likely to prove inappropriate to simulating groundwater flow. A model that accounts for the discontinuous and highly heterogeneous nature of fractured rocks is necessary. Because it is impossible to identify, characterize, and simulate every detail of the geometry and flow properties of small-scale heterogeneities such as fractures, it is necessary to make some simplifying assumptions. One such assumption is that geometric details of the fracture system are unimportant. An equivalent discontinuum model (EDM) is thus being investigated as an approach to model the c-hole hydrology. The EDM does not attempt to reproduce every geometrical detail of the real system. Instead, it attempts to reproduce the observed behavior of the fracture system using simplified geometry while preserving the system's inherent discontinuous nature.

The design and analysis of the hydraulic and tracer tests to be conducted at the c-holes and elsewhere in the Yucca Mountain area will include testing of the fractal hypothesis. Pumping tests will be conducted to estimate parameters at different scales. Preliminary analysis of past c-hole hydraulic tests indicate that the flow dimension is between 2 and 3. Although it is known that the flow dimension is always less than the geometric fractal dimension and that the flow geometry is a subset of the actual geometry (Polek et al., 1989), outcrop mapping is planned to obtain independent information regarding the fracture structure. One of the questions to be addressed is whether there is a consistent fractal dimension to describe the fracture system over a wide range of scales. More than one fractal dimension may exist, because various geologic features are generally caused by mechanisms acting on discrete scales. Nonetheless, if it can be shown that the system behaves like a fractal and that the structure of the system can be estimated through the use of well tests, fractal analysis will become a powerful tool in characterizing otherwise difficult heterogeneous systems.

REFERENCES

Barker, J., 1988. A generalized radial flow model for hydraulic tests in fractured rock. Water Resour. Res., v. 24, no. 10, p. 1796–1804.

Galloway, D., and Rojstaczer, S., 1988. Analysis of the frequency response of water levels in wells to earth tides and atmospheric loading. *In* B. Hitchon and S. Bachu (eds.), Proceedings, 4th Canadian/American Conference on Hydrogeology, Fluid Flow, Heat Transfer and Mass Transport in Fractured Rocks. National Water Well Association, Dublin, Ohio, p. 100–113.

Karasaki, K., Long, J.C.S., and Witherspoon, P.A., 1988. Analytical models of slug tests. Water Resour. Res., v. 24, no. 1, p. 115–126 (LBL-23948).

Majer, E., Myer, L., Peterson, J., Karasaki, K., Long, J., Martel, S., Blümling, P., and Vomvoris, S., 1990.

Joint seismic, hydrogeological, and geomechanical investigations of a fracture zone in the Grimsel Rock Laboratory, Switzerland. Lawrence Berkeley Laboratory Report LBL-27913.

Muller, D.C., and Kibler, J.E., 1984. Preliminary analysis of geophysical logs from drill hole UE-25p#1, Yucca Mountain, Nye County, Nevada. USGS Open-File Report 84-649.

Polek, J., Karasaki, K., Long, J., and Barker, J., 1989. Flow to wells in fractured rock with fractal structure. Presented at the Materials Research Society Fall Meeting, Boston, Massachusetts, November 27–30, 1989, Scientific Basis for Nuclear Waste Management XIII.

Scott, R., and Bonk, J., 1984. Preliminary geologic map of Yucca Mountain, Nye County, Nevada with geologic sections. USGS Open-File Report 84-494.

Waddell, R.K., Robison, J.H., and Blankennagel, R.K, 1984. Hydrology of Yucca Mountain and vicinity, Nevada-California—Investigative results through mid-1983. USGS Water-Resources Investigations Report 84-4267.

Fractal Characteristics of Fracture Roughness and Aperture Data

S. Kumar and G. S. Bodvarsson

Flow of fluids through fractures in rocks is a significant transport mechanism in geological systems. The rate of groundwater and contaminant migration and the extent of spreading are largely governed by fracture networks and corresponding fracture apertures. The variation of these apertures controls the transport properties of the fracture, such as its permeability and capillarity. The characteristics of this aperture variation are determined by the characteristics of the opposite surfaces of natural fractures and the correlation between them.

In this study apertures between fractal surfaces are analyzed. Mathematical expressions are developed that relate the aperture characteristics to those of the fracture faces. The characteristics of the aperture distribution depend on the fractal surfaces and their correlation (Brown and Scholz, 1985; Brown et al., 1986; Wang et al., 1988). If the two surfaces are uncorrelated, then the aperture distribution will have a fractal dimension that may or may not be different from that of the opposing faces. Conversely, if the the opposing faces are either displaced mirror images or are correlated at larger wavelengths, then the aperture distribution may not be a fractal or may be a fractal only over certain length scales.

Fracture tracings of intact fractures from cores from the Nevada Test Site are also examined. It is found that the roughness profiles exhibit fractal characteristics over certain frequencies, but the characteristics of the aperture cannot be clearly associated with a unique fractal dimension over all scales. This is indicative of fractures between surfaces that are correlated at higher wavelengths. Opposite surfaces of natural fractures in geologic media are expected to be correlated at higher wavelengths, leading to a mean value of aperture on which lower wavelength perturbations are superimposed.

SURFACE FRACTAL ANALYSIS

Self-affine or self-similar fractal distribution of heights of rough surfaces are characterized by correlation over many scales and by continuous, but not differentiable, profiles. Such profiles have a power spectrum given by (Hough, 1989; Kumar and Bodvarsson, 1990)

$$S(\omega) \propto \frac{1}{\omega^{5-2D}}, \quad 1 < D < 2, \tag{1}$$

where D is the fractal dimension of the profile. Equation (1) is a sufficient condition for fractality, i.e., if the power spectrum exhibits a linear variation in log-log representation and the slope is between –3 and –1, then the profile is a fractal.

APERTURE ANALYSIS

A schematic depiction of the surfaces and apertures is shown in Figure 1.

Uncorrelated Surfaces

If the opposing surfaces of the fracture are completely uncorrelated over all scales, the resultant aperture will be the difference between these two completely random uncorrelated height distributions. This implies that

$$\sigma_a^2 = \sigma_{s1}^2 + \sigma_a^2 = 2\sigma_s^2 \ (\text{if } \sigma_{s1} = \sigma_{s2} = \sigma_s), \tag{2}$$

where σ is the standard deviation of aperture and surface profile heights and σ^2 is the variance. Here subscripts a,

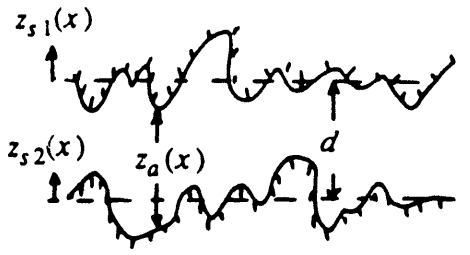

Figure 1. Schematic depiction of apertures. [XBL 913-470]

$s1$, $s2$ refer to aperture, surface 1, and surface 2, respectively. The variances σ_a^2 and σ_s^2 are proportional to the area under the power spectra $S_a(\omega)$ and $S_s(\omega)$, respectively, where ω is the angular frequency.

For apertures between completely uncorrelated similar surfaces of similar fractal dimension D_s, this yields

$$S_a(\omega) = 2S_s(\omega) \ , \tag{3}$$

i.e., $D_a = D_s$, where both S_a and S_s obey Eq. (1).

If the two uncorrelated fractal surfaces have different characteristics, then the fractal characteristics of the aperture are not as easy to obtain. For the case where $D_{s1} = D_{s2} = D_s$ and $C_{s1} \neq C_{s2}$, the value of C_a is $C_{s1} + C_{s2}$ and $D_a = D_s$. However, if the fractal dimensions of the two surfaces are not identical, the characteristics of the aperture are difficult to obtain. This is because the power spectrum, and hence the amplitudes, of the surface with lower fractal dimension fall faster with increasing frequency than those on the one with higher fractal dimension, and this leads to a nonunique determination of the aperture dimension.

Partially Correlated Surfaces

In a situation where a strong correlation exists between the opposite faces at small frequencies (large wavelengths), the fractal relation developed in the previous section will hold in the uncorrelated region. The aperture distribution will thus be a fractal only in the range where no correlation exists and the corresponding fractal dimensions of the surfaces and aperture will be the same as that obtained in the previous section. At the lower frequencies (larger wavelengths), where correlation between the opposing surfaces is strong, the surfaces will still be a fractal but the aperture distribution will not be. Because of correlation, the power spectrum $S_a(\omega)$ of the aperture distribution over the correlated range will be smaller in magnitude than if it were a fractal.

For opposing similar surfaces ($D_{s1} = D_{s2} = D_s$, $C_{s1} = C_{s2} = D_s$) that are correlated at smaller frequencies (larger wavelengths), the following relation is proposed:

$$S_a(\omega) = 2[1 - \langle \cos \phi(\omega) \rangle] S_s(\omega) \ , \tag{4}$$

where $\phi(\omega)$ is the phase difference between the opposing faces at the frequency ω. The value of $\langle \cos \phi \rangle$ is obtained as

$$\langle \cos \phi(\omega) \rangle = \int_{-\pi}^{\pi} \cos(\phi) P_\omega(\phi) \, d\phi \ . \tag{5}$$

Here $P_\omega(\phi)$ is the probability of the phase difference of the Fourier components of the opposite faces to be ϕ at frequency ω. For completely uncorrelated frequencies, $P_\omega = 1/2\pi$; i.e., any angle between $-\pi$ and π can be found with equal probability. In such a case Eq. (4) reduces to Eq. (3). If the phase difference is zero, implying that the two surfaces are identical at the frequency ω and that the amplitudes of the two surfaces will cancel, then $P_\omega(\phi) = 2\pi\delta(\phi)$, where δ is the Dirac delta function. This leads to $\langle \cos \phi \rangle = 1$, and thus $S_a(\omega) = 0$ for this frequency ω.

Surfaces with Displacement

Yet another case is possible, one in which the two surface profiles are mirror images of each other but are displaced by a small displacement distance x_c. This distribution can be shown to have the following power spectrum (Wang et al., 1988):

$$S_a(\omega) = 2(1 - \cos \omega x_c) S_s(\omega) \ , \tag{6a}$$

$$\approx \omega^2 x_c^2 S_s(\omega) \ , \quad \omega x_c \to 0 \ . \tag{6b}$$

Clearly the aperture distribution is not a fractal, since its power spectrum $S_a(\omega)$ does not follow the functional form required by Eq. (1). From Eq. (6b) and using the functional form of the power spectrum $S_s(\omega)$ of the fractal surface from Eq. (1) yields

$$S_a(\omega) \to C_s \frac{x_c^2}{\omega^{(3-2D)}} \ , \ \omega \to 0, \ D = D_s. \tag{6c}$$

This implies that, if the fractal dimension D_s is less than 1.5, the power spectrum of the aperture at small ω increases with decreasing ω, and, if D_s is greater than 1.5, the power spectrum decreases with decreasing ω. For fractal dimension D_s equal to 1.5, the power spectrum of the aperture approaches a constant value as ω decreases.

INTACT FRACTURE DATA

Rock samples were obtained from the G-tunnel of the Nevada Test Site. The imprints of the intact fracture traces

were obtained by using pencil lead on paper pressed against the core surface. This method was employed because measurements of in situ apertures of intact fractures were desired and the fractures could not be opened to expose their surfaces. Only the visually exposed traces of the fracture on the core surfaces were available for measurement. Other sophisticated measurement techniques, such as using profilometers and castings, can be used only if the surface of the fracture is available, and such was not possible for this analysis. The tracings obtained were digitized using a thousand line per inch digitizing board and a contouring program. More than fifty such tracings were obtained from five different cores. However, most were hair-line fractures and were not considered for this study, since they did not yield any measurable aperture. Some other large-aperture fractures were damaged by the coring process. Of the remaining, two representative aperture data sets corresponding to fractures with measurable apertures and no discernable damage are presented here. They are from one fracture, and each set was measured from diametrically opposite parallel locations on cylindrical core surfaces (Figure 2). The circumference of the first core (U12G-AF-7) was approximately 31.8 in. The second core (U12G-AF-8) had a circumference of approximately 31.6.; the tracings are presented in Figure 2.

The apertures from core U12G-AF-8 appear visually to be correlated at large wavelengths. This is reflected in the power spectrum of the aperture distributions, where a fall-off is obtained at smaller frequencies (larger

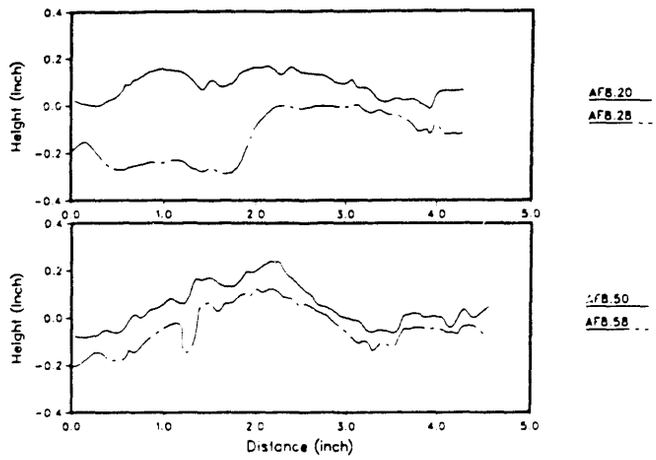

Figure 2. Two aperture tracings from a single fracture in core U12G-AF-8. [XBL 913-471]

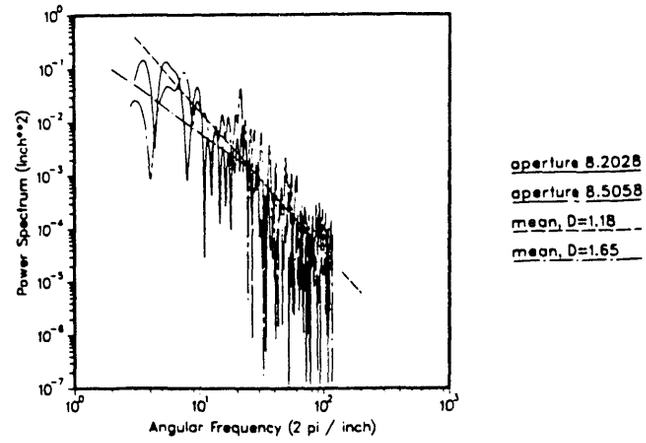

Figure 3. Power spectrum of the two apertures from U12G-AF-8. [XBL 913-472]

wavelengths; see Figure 3). The fractal dimension of the aperture at larger frequencies is approximately 1.2, whereas that of the surface profiles is 1.35. The characteristics of the two apertures from core AF-8 follow the results predicted by the mathematical model developed for partially correlated surfaces.

ACKNOWLEDGMENTS

The authors thank Edward Kwicklis and Gary Severson of the U.S. Geological Survey, Denver, and Jim Boernge of the U.S. Bureau of Reclamation, Denver, for providing the fracture data.

REFERENCES

Brown, S.R., and Scholz, C.H., 1985. Broad bandwidth study of the topography of natural rock surfaces. J. Geophys. Res., v. 90, p. 12575–12582.

Brown, S.R., Kranz, R.L., and Bonner, B.P., 1986. Correlation between the surfaces of natural rock joints. Geophys. Res. Lett., v. 13, p. 1430–1433.

Hough, S.E., 1989. On the use of spectral methods for the determination of fractal dimensions. Geophys. Res. Lett., v. 16, p. 673–676.

Kumar, S., and Bodvarsson, G.S., 1990. Fractal study and simulation of fracture roughness. Geophys. Res. Lett., v. 17, p. 701–704 (LBL-29171).

Wang, J.S.Y., Narasimhan, T.N., and Scholz, C.H., 1988. Aperture correlation of a fractal fracture. J. Geophys. Res., v. 93, p. 2216–2224 (LBL-22494).

The NAGRA-DOE Cooperative Project

J. C. S. Long

The NAGRA-DOE Cooperative (NDC-I) research program was sponsored by the U.S. Department of Energy (DOE) through the Lawrence Berkeley Laboratory (LBL) and the Swiss Nationale Genossenschaft für die Lagerung radioaktiver Abfälla (NAGRA). Scientists participating in this project explored the geological, geophysical, hydrological, geochemical, and structural effects anticipated from the use of a rock mass as a geologic repository for nuclear waste. The principal investigators for LBL were Jane C.S. Long, Ernest L. Majer, Karsten Pruess, Kenzi Karasaki, Chalon L. Carnahan, and Chin-Fu Tsang for LBL and Piet Zuidema, Peter Blümling, Peter Hufschmied, and Stratis Vomvoris for NAGRA.

Six joint tasks were defined and are described briefly below. Tasks 1, 2, 3, and 5 were concerned with the characterization of rock. Task 5 in particular was focused on investigations at the Grimsel Underground Laboratory in the Swiss Alps (Figure 1). Tasks 2 and 6 focused on the phenomenology associated with storing nuclear materials underground.

TASK 1. DETERMINATION OF FRACTURE HYDRAULIC PARAMETERS BY MEANS OF FLUID LOGGING IN BOREHOLES

—C. F. Tsang

In many cases, previously unexplored rocks at depth are candidates for nuclear waste repositories. Fractures in these rocks are considered to be the main conduits through which nuclear waste can escape containment and reach the accessible environment. The only way to gain access to

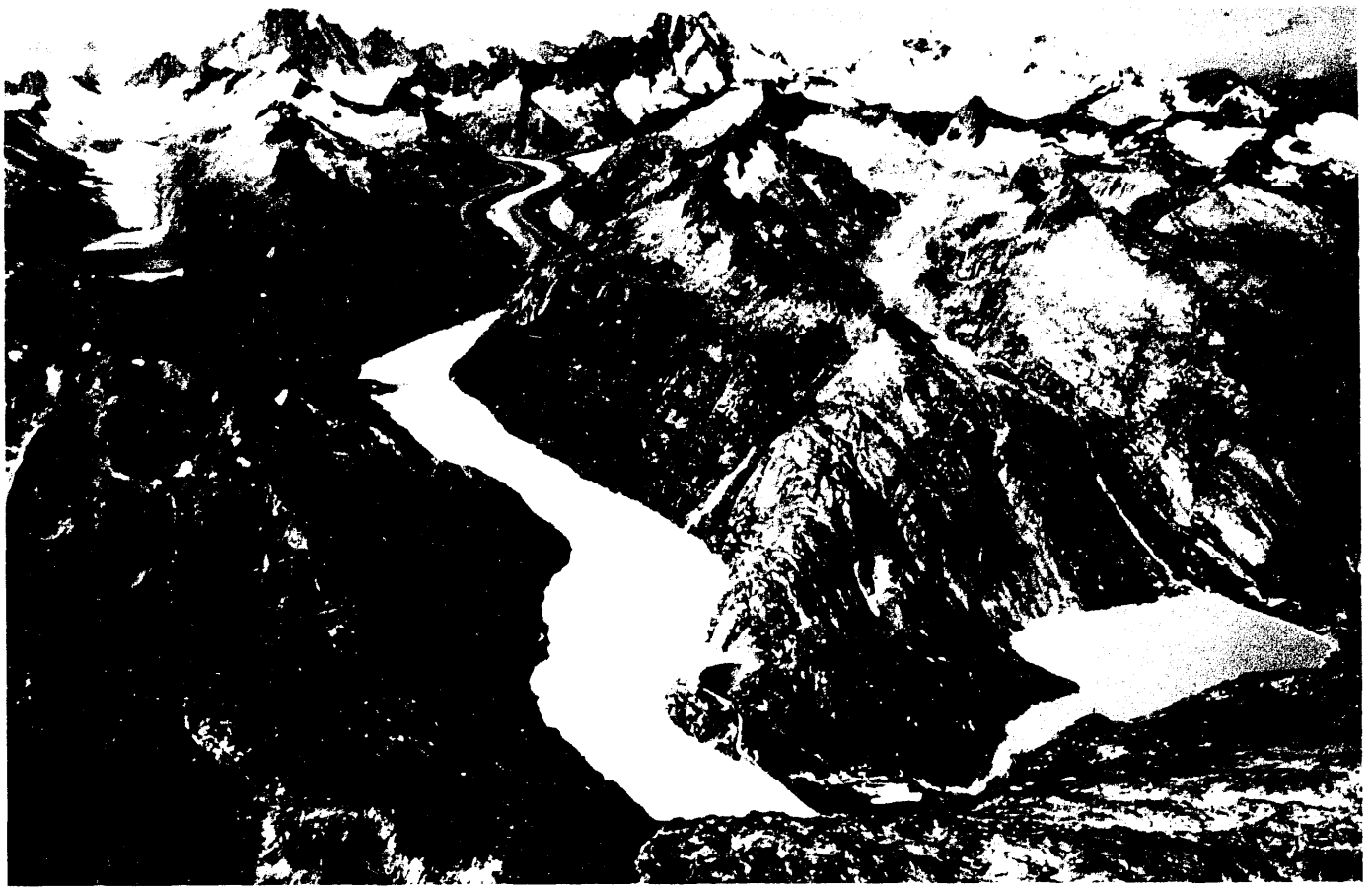

Figure 1. A view to the south of the Swiss Alps in the vicinity of the Grimsel Underground Laboratory. The laboratory lies under the mountain situated behind the lake on the right. [CBB 8811-11064]

these rocks and characterize the fractures is through boreholes. The purpose of this study was to develop well-test interpretation methods to determine key fracture parameters. In particular, a fluid logging interpretation technique was developed. In this technique, the borehole is flushed with deionized water and the resistivity of the borehole fluids is monitored as the more saline native waters flow into the borehole through the fractures. The analysis gives the location and permeability of the fractures intersecting the borehole.

TASK 2. DEVELOPMENT AND APPLICATION OF NEW SOLUTIONS FOR WELL-TEST ANALYSIS IN FRACTURED MEDIA

—K. Karasaki

Slug tests are widely used to estimate the flow parameters of rocks in the field because they are relatively inexpensive and easy to conduct. However, in low-permeability rocks, it takes a long time to complete these tests, hence they are often terminated prematurely. This task developed a solution to this well-test behavior and an analysis method for interpreting prematurely terminated slug-test data. This interpretation was applied to available data from the deep boreholes in Northern Switzerland, giving a much improved fit to the data than is otherwise available.

TASK 3. INTERDISCIPLINARY METHODOLOGY FOR CHARACTERIZING FRACTURE HYDROLOGY

—J. C. S. Long

Efforts to develop an interdisciplinary approach to the characterization of fracture hydrology have been in progress at LBL over the past several years. The methodology incorporates the many kinds of geological, geophysical, and hydrological data into models of the fracture hydrology. This task documented the methodology in its current state and provided examples of applications at several sites, including the Grimsel Rock Laboratory in Switzerland.

TASK 4. INVESTIGATION OF TWO-PHASE GAS-LIQUID FLOW IN FRACTURED MEDIA

—K. Pruess

Natural gas has been observed to occur at the Oberbauenstock site in Switzerland. This task helped to develop an interpretation of all the available information on natural gas from this site using a multiphase code. This effort in modeling unsaturated conditions is useful for understanding the behavior of the unsaturated zone at Yucca Mountain, where two fluid phases (liquid water and formation gas) are present under natural conditions. Similar effects are expected to arise from corrosive gas releases in a proposed low-level waste repository at Oberbauenstock. Such release is expected to take place for all forms of nuclear waste, regardless of whether they are high level or low level.

TASK 5. UNDERGROUND ROCK LABORATORY STUDIES

—E. L. Majer, L. R. Myer, K. Karasaki, and J. C. S. Long

This task had several sub-tasks, the largest of which was concerned with an experiment called the Fracture Research Investigation (FRI). This project centered on a clearly identifiable and accessible fracture zone that was subjected to geological, geophysical, geomechanical, and hydrological characterization in an effort to assess our ability to find and understand fracture zones. The largest part of the effort was extensive geophysical imaging with seismic techniques that gave insight into how hydrologically significant features can be seen with geophysics. Another project focused on an inverse analysis of hydrological interference data taken within a fracture zone (the MI zone) similar to the FRI zone. A new inverse technique based on simulated annealing was applied to those data to develop equivalent discontinuum models of the fracture hydrology. A third effort focused on a joint geological and geophysical interpretation of data from a site called the US/BK site. This effort showed how conceptual models can be developed from a combination of geologic mapping and geophysical tomography.

TASK 6. COUPLING OF TRANSPORT AND GEOCHEMISTRY

—C. L. Carnahan and J. Jacobsen

When waste is emplaced in the ground, the waste itself causes changes in the transport properties of the surrounding material. The objectives of this task were to evaluate the changes in the chemical properties of packing and backfill materials caused by post-emplacement interactions with major dissolved components of ambient groundwaters and to evaluate the effects of these changes on subsequent migration of waste radionuclides. In addition the uptake and distribution of water by packing and backfill materials in contact with partially or completely saturated porous matrix in the presence of thermal gradients was evaluated.

A series of sixteen technical reports document the results of the 3-year NDC-I project, which concluded in 1990. The reports in this series are listed below.

1. Determination of Fracture Inflow Parameters with a Borehole Fluid Conductivity Logging Method, by Chin-Fu Tsang, Peter Hufschmied, and Frank V. Hale (NDC-1, LBL-24752).
2. A Code to Compute Borehole Fluid Conductivity Profiles with Multiple Feed Points, by Frank V. Hale and Chin-Fu Tsang (NDC-2, LBL-24928; also NTB 88-21).
3. Numerical Simulation of Alteration of Sodium Bentonite by Diffusion of Ionic Groundwater Components, by Janet S. Jacobsen and Chalon L. Carnahan (NDC-3, LBL-24494).
4. *P*-Wave Imaging of the FRI and BK Zones at the Grimsel Rock Laboratory, by Ernest L. Majer, John E. Peterson Jr., Peter Blümling, and Gerd Sattel (NDC-4, LBL-28807).
5. Numerical Modeling of Gas Migration at a Proposed Repository for Low and Intermediate Level Nuclear Wastes at Oberbauenstock, Switzerland, by Karsten Pruess (NDC-5, LBL-25413).
6. Analysis of Well Test Data from Selected Intervals in Leuggern Deep Borehole—Verification and Application of PTST Method, by Kenzi Karasaki (NDC-6, LBL-27914).
7. Shear Wave Experiments at the U.S. Site at the Grimsel Laboratory, by Ernest L. Majer, John E. Peterson Jr., Peter Blümling, and Gerd Sattel (NDC-7 LBL-28808).
8. The Application of Moment Methods to the Analysis of Fluid Electrical Conductivity Logs in Boreholes, by Simon Loew, Chin-Fu Tsang, Frank V. Hale, and Peter Hufschmied (NDC-8, LBL-28809).
9. Numerical Simulation of Cesium and Strontium Migration through Sodium Bentonite Altered by Cation Exchange with Groundwater Components, by Janet S. Jacobsen and Chalon L. Carnahan (NDC-9, LBL-26395).
10. Theory and Calculation of Water Distribution in Bentonite in a Thermal Field, by Chalon L. Carnahan (NDC-10, LBL-26058).
11. Prematurely Terminated Slug Tests, by Kenzi Karasaki (NDC-11, LBL-27528).
12. Hydrologic Characterization of Fractured Rocks—An Interdisciplinary Methodology, by Jane C.S. Long, Ernest L. Majer, Stephen J. Martel, Kenzi Karasaki, John E. Peterson Jr., Amy Davey, and Kevin Hestir, (NDC-12, LBL-27863).
13. Exploratory Simulations of Multiphase Effects in Gas Injection and Ventilation Tests in an Underground Rock Laboratory, by Stefan Finsterle, Erika Schlueter, and Karsten Pruess (NDC-13, LBL-28810).
14. Joint Seismic, Hydrogeological, and Geomechanical Investigations of a Fracture Zone in the Grimsel Rock Laboratory, Switzerland, by Ernest L. Majer, Larry R. Myer, John E. Peterson Jr., Kenzi Karasaki, Jane C.S. Long, Stephen J. Martel, Peter Blümling, and Stratis Vomvoris (NDC-14, LBL-27913).
15. Analysis of Hydraulic Data from the MI Fracture Zone at the Grimsel Rock Laboratory, Switzerland, by Amy Davey, Kenzi Karasaki, Jane C.S. Long, Martin Landsfeld, Antoine Mensch, and Stephen J. Martel (NDC-15, LBL-27864).
16. Use of Integrated Geologic and Geophysical Information for Characterizing the Structure of Fracture Systems at the US/BK Site, Grimsel Laboratory, Switzerland, by Stephen J. Martel and John E. Peterson Jr. (NDC-16, LBL-27912).

Generation of Fracture Patterns Using Self-Similar Iterated Function System Concepts

S. J. Martel, K. Hestir, and J. C. S. Long

Scaling (i.e., using data collected from a small volume of rock to help characterize a much larger volume) is an issue of widespread interest in the earth sciences. There is especially great interest in scaling fracture information from drill cores and outcrop mapping to help characterize petroleum reservoirs and rock masses being considered as hosts for radioactive waste repositories. One approach to scaling is to numerically generate a suite of different synthetic fracture distributions that have a common appearance over the scales at which data are available. The range of behaviors at the scale of interest can then be examined. In these cases, the type of synthetic fracture generator to use becomes a key issue. A variety of numerical techniques that are based on fracture mechanics are available for simulating fracture growth. Unfortunately, the most rigorous techniques require prohibitively large amounts of computer power, memory, and time in order to track the growth of even a single array containing many fractures. Fractal concepts provide a much simpler way to extrapolate data from one scale to another. Systems that

have fractal characteristics have recurring geometric patterns that are scale independent. If a system has fractal characteristics, then its large-scale features can be predicted from knowledge of its small-scale features. Recent measurements of fracture trace patterns and fracture surface roughnesses have indicated that some fracture attributes can be described as a fractal over a fairly broad range of scales. However, it has not been demonstrated (1) how recognized processes of fracture would lead to a fractal distribution of fractures in space or (2) whether there is a mechanical basis for determining when a fractal approach is (or is not) appropriate. We are investigating how concepts from fracture mechanics and fractal theory can be blended to help address scaling problems. Work to date indicates that this joint approach may provide an efficient, physically based way to generate synthetic fracture distributions.

ITERATED FUNCTION SYSTEMS

One way to generate fractal patterns is through the use of an iterated function system, or IFS (Barnsley, 1988). An IFS consists of a selection of rules that maps (i.e., scales, distorts, rotates, translates, and/or reflects) elements from one set into another. These rules, when applied recursively, lead to the formation of a fractal pattern. A mathematically perfect fractal pattern is approached as the number of iterations becomes infinite and the replicated pattern is produced at infinitely finer scales. Only a few IFS rules may be necessary to produce an exceedingly intricate fractal pattern. The way a fractal pattern changes from one scale to another can be described quantitatively by a term called the fractal dimension. The dimension of a fractal pattern can be calculated or bounded directly from the IFS rules.

A MECHANICALLY BASED, RECURSIVE FRACTURE-GENERATION SCHEME

An IFS-like process can be used to grow fracture patterns in a visually realistic sequence by using growth rules based on fracture mechanics concepts. We begin with a starter set of line segments that represent fracture traces and add new short-line segments or extend some of the pre-existing ones to simulate the evolution of a fracture pattern. Intricate fracture patterns can be generated using this technique in much less time than by using a pure mechanistic approach. However, because the growth rules are based on mechanical principals, this procedure also allows an opportunity to tie fractal concepts to mechanical principals that govern fracture growth. We are evaluating what kinds of probabilistic growth rules will produce fractal patterns and whether a fractal dimension can be determined directly from the growth rules. The two-dimensional cases we consider below correspond to fracture growth in homogeneous, isotropic elastic materials under plane strain. We focus on mode I fractures, fractures whose walls move apart, rather than faults, whose walls slide past each other.

A key tenet of fracture mechanics is that the stress field near the tip of a fracture will dictate how the fracture may propagate. Two important simplifying assumptions we make are (1) that the stress field near the tip of an isolated crack is suitable for predicting the growth of each crack in an array and (2) that all fractures will grow parallel to one another. In light of these assumptions, our current models would most appropriately apply to cases in which the far-field stress state (rather than crack interactions) dictates the fracture growth pattern (Olson and Pollard, 1989). These conditions require that the regional stress field be significantly anisotropic, that is, that the difference in magnitude between the remote principal stresses be large relative to the driving pressure σ (the driving pressure is the difference between the internal fluid pressure and the least-compressive remote principal stress). The fractures in many natural fracture sets are nearly planar and parallel, indicating that strongly anisotropic stress conditions commonly exist when macroscopic fractures grow in rock. A commonly used fracture mechanics criterion for fracture propagation is that fracture growth will occur in a way that minimizes the fracture energy release rate G,

$$G = c_1 (K_I^2 + K_{II}^2) + c_2 K_{III}^2 , \quad (1)$$

where K_I, K_{II}, and K_{III} are the respective stress intensity factors corresponding to opening, sliding, and tearing displacements of the crack walls, and c_1 and c_2 are elastic constants. For an isolated mode I crack, K_{II} and K_{III} equal zero and

$$K_I = \sigma\sqrt{A} , \quad (2)$$

where σ is the driving pressure and A is the half-length of the crack. Expressions (1) and (2) lead to

$$G \propto A . \quad (3)$$

We assume that the relative probability of fracture growth (either by propagation of a pre-existing fracture or by growth of a new "daughter fracture" near the tip of a pre-existing parent fracture) is proportional to G. On the basis of Eq. (3), we scale the relative growth probabilities to the fracture length:

$$\text{Prob(fracture growth)} = (1/L)\, A . \quad (4)$$

The constant of proportionality $(1/L)$ in Eq. (4) acts as a cutoff parameter. During a given iteration through the fracture-generating program, growth *may* occur for fractures with a half-length below L. Growth *will* occur for fractures with half-lengths greater than L. In each iteration

through the algorithm, each fracture is checked for growth using Eq. (4). Fracture growth stops when the desired number of iterations is reached.

Fracture growth is allowed only where stresses are particularly favorable—near the tip of a pre-existing fracture. Fracture growth can occur either by propagation of the parent fracture or by growth of a parallel daughter crack near the tip of the parent (Figure 1). In either event fracture growth is parallel to the most-compressive far-field principal stress. The relative probability of in-plane propagation of the parent is P; the relative probability of a daughter growing is $(1 - P)$. If a daughter crack grows, the cylindrical coordinates of its center (r,θ) relative to the parent fracture tip are located probabilistically using the equation for the crack-perpendicular stress near the tip of a fracture:

$$\sigma_{yy}(r, \theta) = (K_I/\sqrt{r})(\cos\theta/2)[1 + \sin(\theta/2)\sin(3\theta/2)]$$

$$-\pi < \theta < \pi, 0 < r < B. \quad (5)$$

The terms that contain r and θ in Eq. (5) can be isolated and integrated to yield probability distributions for daughter crack locations. The highest probabilities are for locations near the crack tip, where σ_{yy} is greatest. The distance over which the near-tip field is allowed to operate is B. The maximum length of a daughter crack relative to the parent or the maximum relative growth increment of a parent crack is given by B. The actual length or growth increment is a product of A, B, and a random number between 0 and 1.

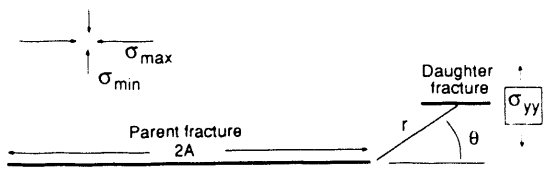

Figure 1. Diagram showing the relative positions of a parent fracture and a daughter fracture and the orientations of the most-compressive and least-compressive far-field stresses. [XBL 913-473]

In summary, the recursive algorithm is simple to implement. A starter set of fractures must be defined, along with the number of iterations, a seed number for the random number generator, and the parameters P, B, and L. Although the most realistic patterns are expected with small growth increments ($B < 0.02$) and a large number of generations, similar patterns can be produced rapidly for trial comparisons by decreasing the number of generations and increasing B.

RESULTS TO DATE

The approach outlined here can generate realistic-looking fracture growth sequences (Figure 2) that compare favorably with detailed outcrop maps (e.g., Figure 3). Note

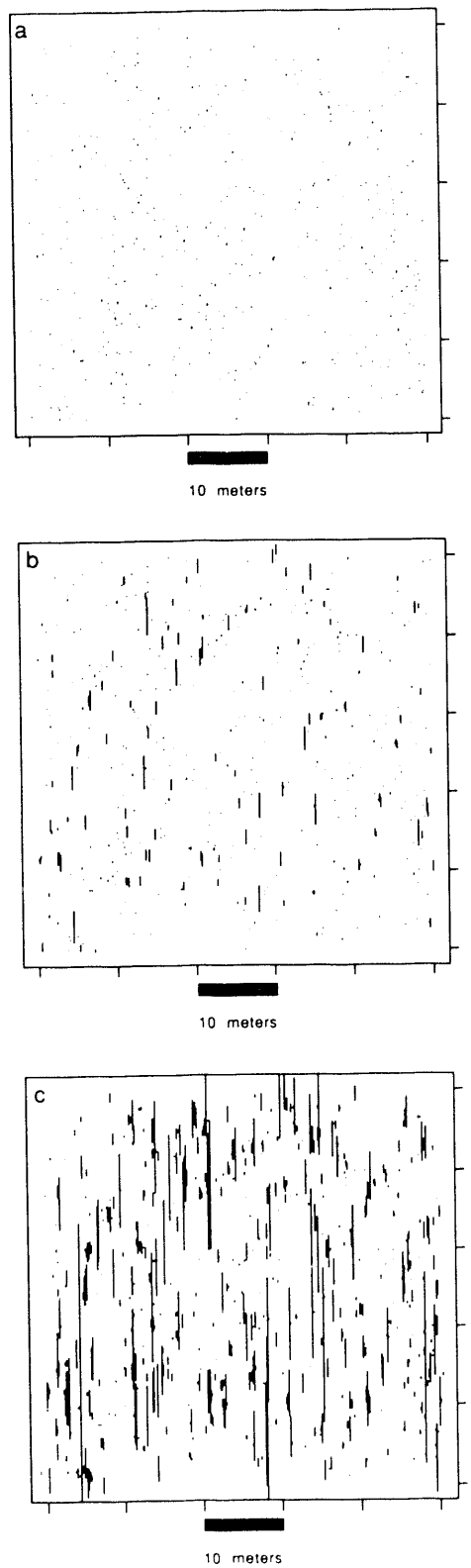

Figure 2. Development of a fracture pattern from 500 randomly located starter cracks after (**a**) 0, (**b**) 5, and (**c**) 10 iterations. Each starter crack in (a) is 1 cm long, a distance corresponding to the likely initial crack length of Figure 4. $P = 0.8$, $L = 5$ cm. [a, XBL 913-474; b, XBL 913-475; c, XBL 913-476]

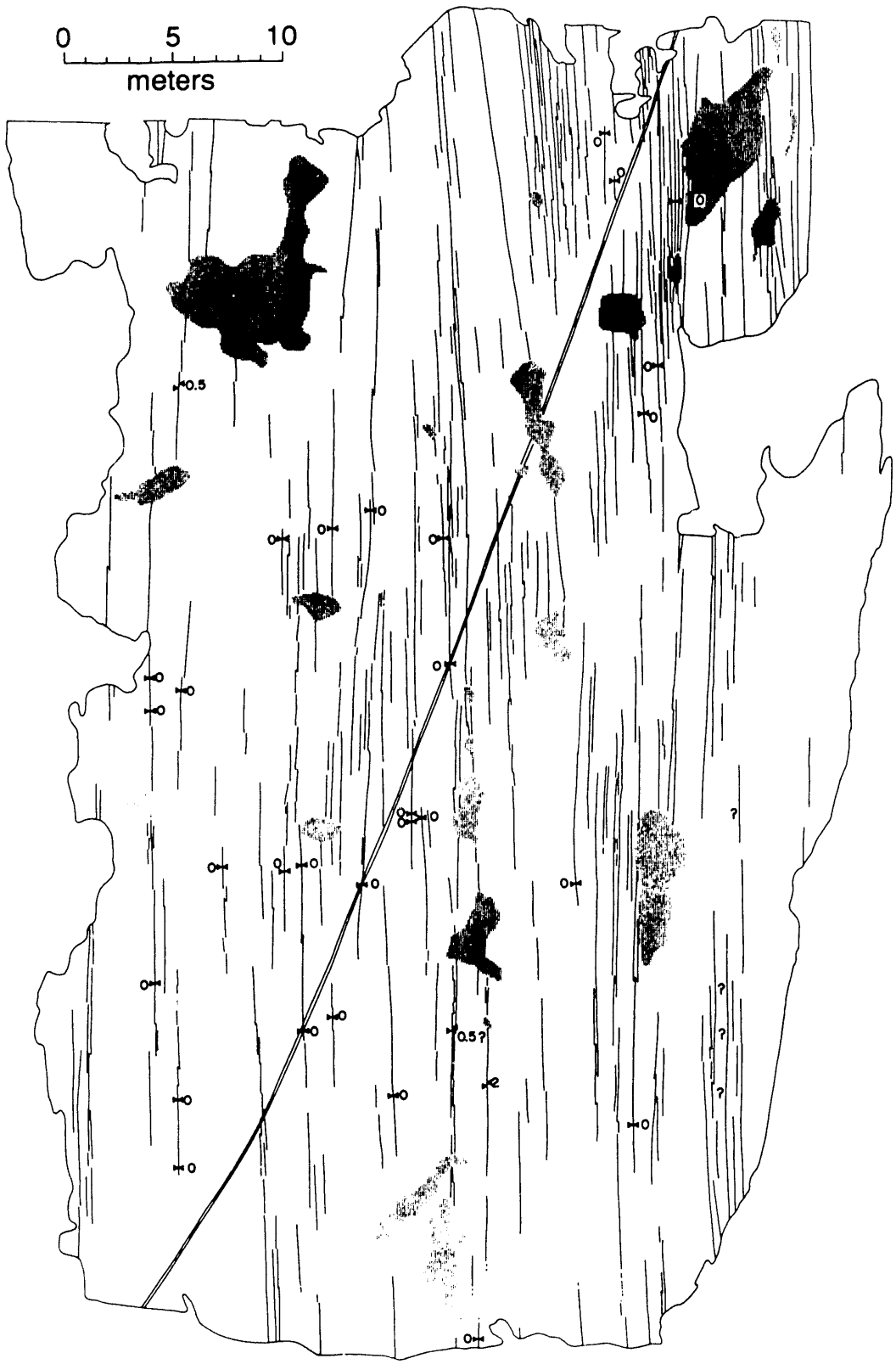

Figure 3. Map of fracture traces in a granite outcrop (modified from Segall and Pollard, 1983). The fractures dip steeply. Numbers indicate amount of lateral separation (in centimeters) across fractures. The feature marked by a double line is a vein. Areas where the outcrop is covered are shown in gray. The pattern here is visually similar to that in Figure 1c. [XBL 913-477]

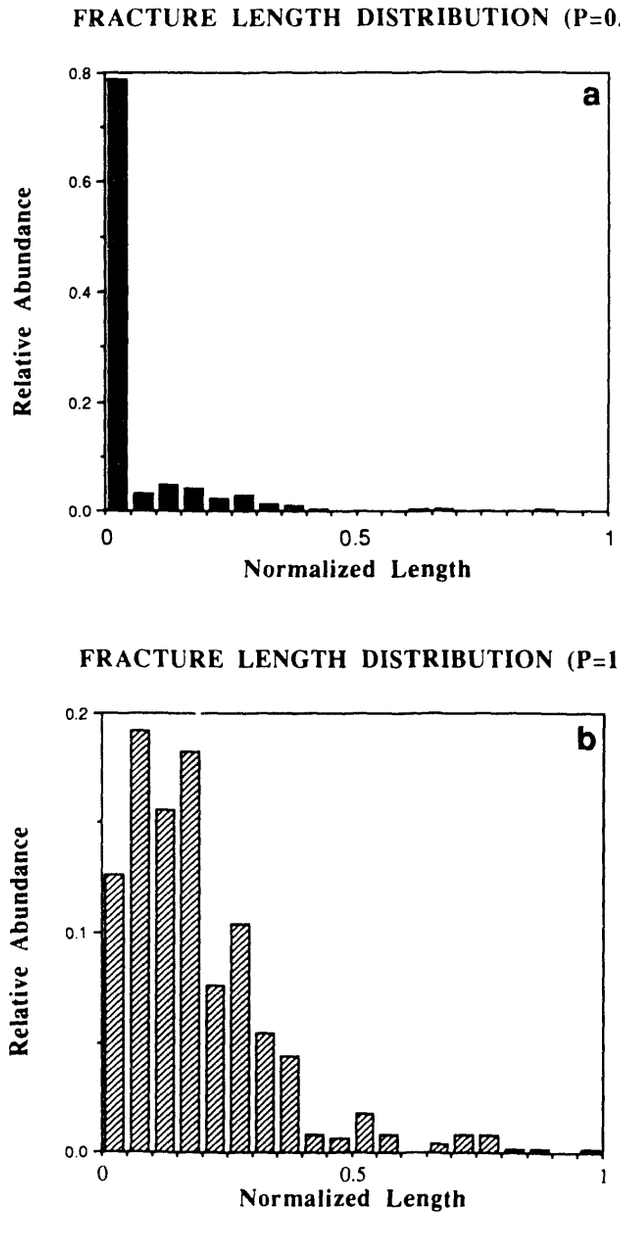

Figure 4. Comparison of fracture length distributions for patterns grown with (a) $P = 0.8$ and (b) $P = 1.0$ using the distribution of starter cracks in Figure 1a. The length distribution in (a) is approximately a power law distribution, whereas the distribution in (b) is approximately log-normal. [XBL 913-478]

that the pattern evolves in a reasonable progression, rather than "flashing" to a realistic-looking final image from an unusual-looking intermediate step. This is important; there is no way to know in advance the exact number of iterations that would correspond to a natural fracture pattern.

Realistic-looking patterns are produced if the probability that daughter fractures will grow is low and the probability that pre-existing fractures will lengthen is high (i.e., $P > 0.8$). The two most common types of fracture length distributions reported in the literature (log-normal and power-law) can be produced using our scheme (Figure 4). The type of distribution produced is highly sensitive to P. Log-normal distributions develop for P values near 1; power-law distributions develop for P values near 0.8. Power-law (fractal) distributions will not be produced by our scheme if daughter cracks cannot grow, implying that, if natural fractures do form fractal patterns, large numbers of small new fractures must develop during the growth of a fracture set. Many starter cracks are needed to produce realistic-looking patterns. If the probability of pre-existing fractures extending in their own plane is zero (i.e., $P = 0$), then the resulting pattern shows a strong scale-independent (i.e., "fractal") pattern of small fractures being clustered near the ends of fractures that are roughly two orders of magnitude larger. Such a pattern is not observed in nature and is unrealistic. This problem is especially acute for cases with a low areal density of starter cracks.

As a final note, the fractal dimension of a fracture set changes as a function of scale for sets formed by a finite number of iterations. The dimension approaches 1 for small scales. Cases in nature that correspond closely to an infinite number of iterations may be rare. The rate at which the "apparent" fractal dimension changes as a function of scale may therefore be useful to know when extrapolating information on natural fractures from one scale to another.

REFERENCES

Barnsley, M., 1988. Fractals Everywhere. Academic Press, New York, 394 p.

Olson, J., and Pollard, D.D., 1989. Inferring paleostresses from natural fracture patterns: A new method. Geology, v. 17, p. 345–348.

Segall, P., and Pollard, D.D., 1983. Joint formation in granitic rock of the Sierra Nevada. Geol. Soc. Am. Bull., v. 94, p. 563–575.

Toward Self-Verifying Numerical Models of Groundwater Flow

T. N. Narasimhan

Numerical models are now extensively used to solve steady-state as well as transient groundwater flow problems. An important limitation of such models is that solutions generated with them cannot normally be verified for internal mathematical consistency except in the case of problems for which closed-form analytical solutions are available. In such cases, the numerical solutions can be verified by comparison with the known analytical solutions. Considering the fact that numerical models are powerful tools capable of solving problems for which analytical solutions are very difficult or even impossible to obtain, it is of major conceptual and practical interest to explore approaches by which a numerical solution to any groundwater problem can be verified in itself. Arguments are presented below to suggest that it is logically possible to verify *any* steady-state groundwater solution generated by a numerical model. This report is a summary of recent work by Narasimhan (1991).

FORMULATION OF NUMERICAL MODELS

In general, three different approaches are available to pose and numerically solve steady-state groundwater problems. The first is to integrate the partial differential equation and numerically evaluate the discretized integrals—e.g., the Integral Finite Difference Method (IFDM) or the Finite Element Method (FEM).

The second, the variational approach, is to intrinsically state the problem in terms of energy minimization rather than mass conservation. Nevertheless, the way the variational principle is implemented in the literature, the final discretized equations turn out to be exactly the same as those obtained by integrating the differential equation. Recently Narasimhan et al. (1991) have shown that it is possible to enunciate the variational statement differently, in terms of flow geometry rather than in terms of gradients of potential, as is the case with the classical Euler integral.

The third approach is to make use of the knowledge that mass flux is constant through a flow tube and that potential must be continuous across a point on a flow line. This approach has been successfully implemented by civil engineers to draw flow nets to solve seepage problems. It must be recognized that the basic ideas of this approach can be readily extended to a generalized flow net philosophy that can be implemented numerically to solve practical problems of interest.

VERIFICATION OF STEADY-STATE SOLUTIONS

The Classical Solution

The term "classical solution" is here intended to mean the solution obtained with any of the three techniques popularly known as the Finite Difference Method: FDM, IFDM, and FEM. In the finite difference technique, the second derivative of potential is directly evaluated at discrete points in the domain by linearly approximating gradients between points. In the IFDM and FEM, the second derivative of potential of the partial differential equation is dispensed with and the steady-state flow problem is expressed as an integro-differential equation defined over discrete subdomains of space. In either case, whether one uses the differential approach or the integro-differential approach, the solution process involves at least one task of approximately evaluating the spatial gradient of potential on the basis of information known at points separated by finite distances.

Regardless of whether the system is linear or nonlinear, the potential gradient (or, equivalently, fluid flux or fluid velocity) has to be continuous at each point in a homogeneous medium. In a heterogeneous medium, the gradient of potential will be discontinuous at a material interface. At the interface between materials, the disposition of the magnitude of the deflection (refraction) of the gradient vector is dependent on the contrast in permeability across the interface. For heterogeneous media with isotropic materials, Hubbert (1940) showed that the refraction of the gradient vector (the flow path) follows a tangent law,

$$\frac{k_1}{k_2} = \frac{\tan \theta_1}{\tan \theta_2},$$

where k_1 and k_2 are intrinsic permeabilities of the materials and θ_1 and θ_2 are the angles of incidence.

Subject to the above constraints, and the criteria of mass balance, continuity of gradients and the refraction law for flow lines are fully sufficient for verifying the numerical solution to any arbitrary steady-state groundwater flow problem. These criteria should be amenable to implementation in existing numerical algorithms for verifying any solutions generated by these models.

The Variational Method

The variational principle appropriate for the steady-state groundwater problem is the Euler Integral, which may be written as

$$U(\phi) = \int_V \rho g\, K(\nabla\phi)^2\, dV\,, \tag{1}$$

where ρ is fluid density $[M/L^3]$, g is acceleration due to gravity $[L/T^2]$, K is hydraulic conductivity $[L/T]$, ϕ is potentiometric head $[L]$, and V is volume $[L^3]$. The postulate of variational calculus is that for the correct distribution of potential, ϕ, over the domain V, $U(\phi)$ will be an extremum (a maximum or a minimum). It can be shown that one can obtain the partial differential equation characterizing steady-state flow by differentiating $U(\phi)$ with reference to ϕ and setting the derivative to zero.

The integrand in (1) has dimensions of energy per unit time. Physically, therefore, the variational integral can be interpreted to mean that in response to the conditions on the boundaries, the system will choose a pattern of potential distribution in such a way that the energy expended over the entire flow domain by the flowing water to overcome frictional resistance is an extremum. Conceivably, one can use this postulate as a basis of verifying a numerical solution obtained with any of the three numerical methods under consideration here.

In practice, the variational approach is implemented by algebraically extremizing the variational principle using trial functions and numerically evaluating the resulting extremized equations to calculate the distribution of potentials.

Alternate View of the Variational Approach Based on Flow Geometry

In the conventional variational procedure, one defines the integral in terms of the potential ϕ. However, note that the steady-state flow problem is described by two characteristics: isopotential surfaces and flow lines. Therefore, it is equally possible to state the variational principle in terms of flow geometry, rather than the distribution of potentials. Indeed, one can easily understand this if one recognizes that in two dimensions, the steady-state flow problem can be stated either in terms of fluid potential or in terms of stream functions according to Cauchy-Riemann conditions.

In order to state the variational problem in terms of flow geometry, we first conceptualize the flow system as being made up of a bundle of flow tubes. In a heterogeneous flow domain or in a domain of complex geometric shape, the flow tubes will have nonuniform cross-sectional areas due to convergent and divergent patterns. The rate at which energy is expended in overcoming friction within a section of a flow tube is given by

$$Q_m \Delta\Phi = Q_m g \Delta\phi\,, \tag{2}$$

where Q_m is the mass flux through the tube $[M/T]$ and $\Delta\Phi$ is the drop in potential $[L^2/T^2]$ between the inlet and the outlet. Given this, we may now state the variational postulate as follows: In response to conditions imposed on the boundaries, the flow system will adjust itself in such a way that if there are $i = 1, 2, 3, \ldots, I$ flow tubes, then the rate at which energy is expended in overcoming friction is an extremum; that is,

$$U(\phi) = \sum_{i=1}^{I} g Q_{m,i} (\Delta\phi)_i\,. \tag{3}$$

Note that for a flow tube of nonuniform cross-sectional area we may write the equation of motion in the format of Ohm's law (Narasimhan, 1985),

$$\sigma Q_{m,i} = \frac{\rho(\Delta\phi)_i}{R_i} = \rho(\Delta\phi)_i \Big/ \int_{x_{in}^i}^{x_{out}^i} \frac{dx}{K(x)A(x)} \sqrt{A} \tag{4}$$

where x_{in}^i and x_{out}^i are the coordinates of the inlet and the outlet of the flow tube along a properly chosen curvilinear axis. We see from (4) that the flow resistance of a segment of a flow tube is a function of the hydraulic conductivity of the material constituting it as well as the geometry of the flow tube, characterized by $A(x)$.

In principle it should be possible to develop an algorithm that is capable of implementing the variational logic using an adequate number of flow tubes. For example, such an algorithm may consist of the following. First, start with a set of flow tubes whose disposition (or geometry) is estimated. Then, using the assumed geometry of each tube as known, compute its flow resistance, R_i, on the basis of (4). Following this, calculate $U(\phi)$ either as

$$U(\phi) = \sum_{i}^{i=1} g Q_m (\Delta\phi)_i$$

or as

$$U(\phi) = \sum_{i}^{i=1} \frac{\rho g (\Delta\phi)_i^2}{R_i}\,,$$

depending on the manner in which boundary conditions are prescribed (i.e., prescribed flux or prescribed potential

conditions). Following this, one can iteratively adjust the flow geometry in such a way that $U(\phi)$ ultimately attains an extremum. As far as is known, this view of the variational statement has not been expressed in the literature. Although the above reasoning is logically consistent, its practical implementation will require the imaginative use of new multidimensional graphing capabilities currently available in the computing world. Note that in this approach one avoids the discretization errors characteristic of conventional numerical methods. Rather, reliance is placed on accurately calculating flow resistances of macroscopic flow tubes of known geometry.

Generalized Flow Nets

In addition to numerically approximating the governing equation or extremizing the variational integral, a third way to solve the steady-state flow problem is to make use of the two interrelated continuity conditions relating to flux through a flow tube and potential across a flow line. Traditionally this approach has been restricted in practice to the graphical solution of two-dimensional problems—that of drawing flow nets. Nevertheless, this philosophy of solution is broader in scope and can be generalized, to facilitate development of novel numerical approaches for solving the steady-state groundwater flow problem.

Recall that two notions are fundamental to the steady-state groundwater flow problem. First is the equation of motion, which states that the mass flux through a flow tube is equal to the potential drop between entry and exit times the reciprocal of the flow tube resistance. The flow tube resistance is a function of the material contained in the tube as well as the shape (geometry) of the tube. Second, across any point on a flow line, the potential must be continuous. To implement this approach in practice, one would start with a set of estimated flow tubes whose geometry is assumed known. By cumulative integration of resistances along flow tubes, one could then calculate the location of any desired isopotential value. If the flow tubes have been accurately chosen, isopotential surfaces of a chosen value, calculated for two adjoining tubes, must be continuous at the common flow line separating them. Any mismatch in this regard will indicate that the flow tubes will have to be adjusted. By progressive adjustment of the flow tubes, one can iteratively obtain a self-consistent solution.

DISCUSSION

For solving steady-state groundwater flow problems in heterogeneous media, numerical models are widely used. The conventional wisdom is to treat these models as approximate solvers of partial differential equations. Nevertheless, solutions generated by these models can be verified for internal mathematical consistency, regardless of the availability of analytical solutions. Such self-verification of individual solutions should be based on a combination of mass balance, continuity of gradients, and refraction of flow lines at interface between materials. Note that the verification logic combines a global criterion (mass balance) with local criteria (continuity of gradients; refraction of flow lines).

In these models, it is customary to approximate gradients using a priori chosen trial functions that have a polynomial form (linear, quadratic, or cubic functions). However, it appears desirable to use trial functions that inherently incorporate information on the flow geometry. Should such trial functions be successfully developed, the accuracy of solutions can be iteratively improved by progressively refining the trial function over a mesh of given coarseness, rather than improving accuracy by mesh refinement.

The paradigm that numerical models of groundwater flow approximately solve the partial differential equations takes a narrow view of the overall problem. It is possible, in principle, to develop self-verifying numerical models on the basis of alternate integral perspectives. Two such approaches are presented in this work. The first of these involves the variational principle, defined in terms of flow geometry (a collection of flow tubes). Although this approach is mathematically consistent, it does not offer any special advantages from the viewpoint of developing practical tools of problem solving. The second approach, involving the notion of generalized flow nets, is far more straightforward to understand, while yet being robust in its logic.

The generalized flow net approach consists in idealizing the multidimensional flow system as a bundle of flow tubes. The geometrical disposition of these flow tubes is iteratively adjusted in such a way that the constancy of flux through a flow tube and the continuity of potential at a flow line are everywhere satisfied over the flow domain within acceptable error. This approach, which requires neither the constraint of mass balance nor the extremization of expended energy, is equivalent to the other two approaches to a solution.

For solving linear problems (those in which permeability is independent of potential), the higher-order finite element approach may become specially advantageous, provided that improved trial functions can be devised that take into account the shape of the element as well as known information on flow geometry. However, when permeability is dependent on potential, integration of the equation of motion even in two dimensions may become so cumbersome that the finite element method is likely to be less advantageous to obtain verifiable solutions. Therefore, for solving nonlinear problems the generalized flow net approach may prove to be a more efficient method of solution than the techniques currently being used.

REFERENCES

Hubbert, M.K., 1940. The theory of ground-water motion. J. Geol., v. 48, p. 785–944.

Narasimhan, T.N., 1991. Toward self-verifying numerical models of groundwater flow. To be submitted to Water Resour. Res. (LBL-30600).

Narasimhan, T.N., 1985. Geometry-imbedded Darcy's law and transient subsurface flow. Water Resour. Res., v. 21, no. 8, p. 1285–1291.

Narasimhan, T.N., Perrochet, P., and Wang, J.S.Y., 1991. On the variational principle for steady state groundwater flow. To be submitted to Water Resour. Res. (LBL-30601).

Coupled Thermo-Hydro-Mechanical (THM) Behavior around a Repository

J. Noorishad and C. F. Tsang

Because of the radioactive decay of the stored waste, a nuclear waste repository in rock can be expected to release considerable energy over the thousands of years following its closure. This energy will give rise to mechanical stress changes and hydrologic buoyancy flow in the geologic formation. To be able to model such coupled thermo-hydro-mechanical (THM) processes in order to carry out repository performance assessment presents a considerable challenge.

Coupled processes around a nuclear waste repository (Tsang, 1987) have been the subject of active research during the last few years. Recently a far-field regional analysis was made, illustrating the advancing state of the art on the subject. The numerical code used is the ROCMAS code (Noorishad et al., 1984), which has continued to be improved and enhanced since its early development. The code has been verified against a number of known solutions.

A repository is assumed to be located at a depth of 600 m, with a length and width of 3 km. The analysis of the coupled processes is performed on the two-dimensional vertical cross section of the rock-repository system, which is capable of simulating a worst case scenario. The modeled section has a vertical dimension of 2.2 km and a horizontal dimension of 18 km. Figure 1 shows the cross section with the vertical scale exaggerated fivefold. We include two major fractures in this section; one fracture intercepts the repository (represented by a thin disk) in its horizontal plane, and the other fracture cuts through the repository along a vertical plane of symmetry. Both fractures extend to the model boundaries. A regional hydraulic gradient of 0.1% and a geothermal gradient of 30°C/km were assumed to exist in the model. Material properties assumed are shown in Table 1. The repository is assumed to possess a decaying thermal power output; the power decay curve is adapted from Wang and Tsang (1980), with a 10-year cooled down power output of 14.4 W/m^2 gross thermal loading for the spent fuel. This selected power is chosen in some level of conformity with one of the scenarios of the Atomic Energy of Canada (Acres, 1978). A study of a modified Rayleigh number for a laterally infinite system, with characteristics similar to the waste repository model, indicates the possibility for development of a natural thermal circulation pattern in the absence of the regional hydrologic gradient.

Simulation times of interest for the performance assessment of a repository range to thousands of years. This immediately brings out the difficulty of obtaining a time marched solution of the THM processes occurring in the host geologic system. There is a large discrepancy in the time constants of the heat transport and the mass flow phenomena since the flow processes take place rather fast compared to the slowly changing temperature field. Following an approach used by Runchal and Maini (1980), for investigation of the role of convection in the evolution of temperature field around a repository, we adapted a snapshot approach for the solution of the fluid flow part of the THM processes. Within this strategy, the evolution of the quasi-static thermomechanical processes was followed by a time-marched simulation of the THM phenomena, which uses a steady-state solution of the coupled flow-deformation equations at each time increment. This approach not only provides a reasonably correct picture of the thermohydromechanical state of the problem, it also saves very effectively on the computation cost.

The nonlinearity introduced in the model is that of the two extensive fractures that pass through the model. The results reveal significant effects. We present here an example of the thermal, flow, and stress patterns 1000 years after repository closure. Figure 2 gives the temperature contours. Far away from the repository, the temperature field follows the initial geothermal gradient. The presence of the repository is accompanied by a local high-temperature region. Figure 3 shows the distribution of fluid flow directions, which includes the initial regional flow from left to right and the induced buoyancy flow due to the

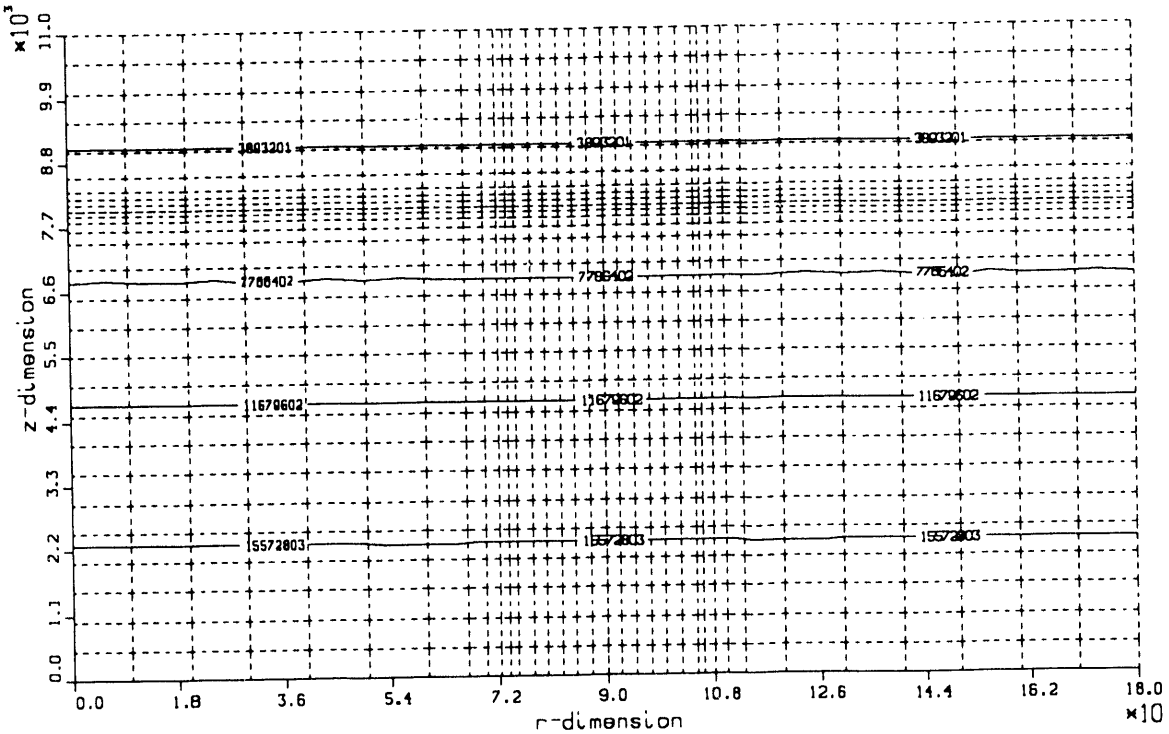

Figure 1. Diagram of model with vertical scale exaggerated fivefold. [XBL 913-483]

Table 1. Material properties used for various runs with ROCMAS.

Material	Parameter	Laboratory/field* data	Modeling data
Fluid:	Mass density, r_l		997 kg/m^3
	Compressibility, b_p		5.13×10^{-1} GPa^{-1}
	Dynamic viscosity at 20°C, n_l		1×10^{-3} N/m^2
	Thermal expansion coefficient		3.17×10^{-4}°C^{-1}
	Specific heat		1.0 kcal/kg
Rock:	Young's modulus, E_s	80 GPa	35 GPa
	Poisson's ratio, v_s	0.25	0.25
	Mass density, ρ_s	2.9×10^3 kg/m^2	2.9×10^3 kg/m^3
	Porosity, ε		0.015
	Intrinsic permeability, k		10^{-20} m^2
	Biot's constant, M		130 GPa
	Biot's constant, α		1.0
	Thermal expansion coefficient		1.1×10^{-5}°C^{-1}
	Specific heat		2×10^{-1} kcal/kg
	Solid-fluid thermal conductivity		6.9×10^{-4} kcal/m·s·°C
*Fracture:	Initial normal stiffness, K_n	1620 GPa/m	1620 GPa/m
	Initial tangential stiffness, K_s		3 GPa/m
	Initial aperture, b	17 microns	17 microns
	Porosity, ε		1.0
	Biot's constant, M		2 GPa
	Biot's constant, α		1.0
	Radius, r		1.2 m
	Initial normal stress, σ_0	10.2 MPa	8.6 mpa

*Energy transport in fractures are presumed to be negligible.

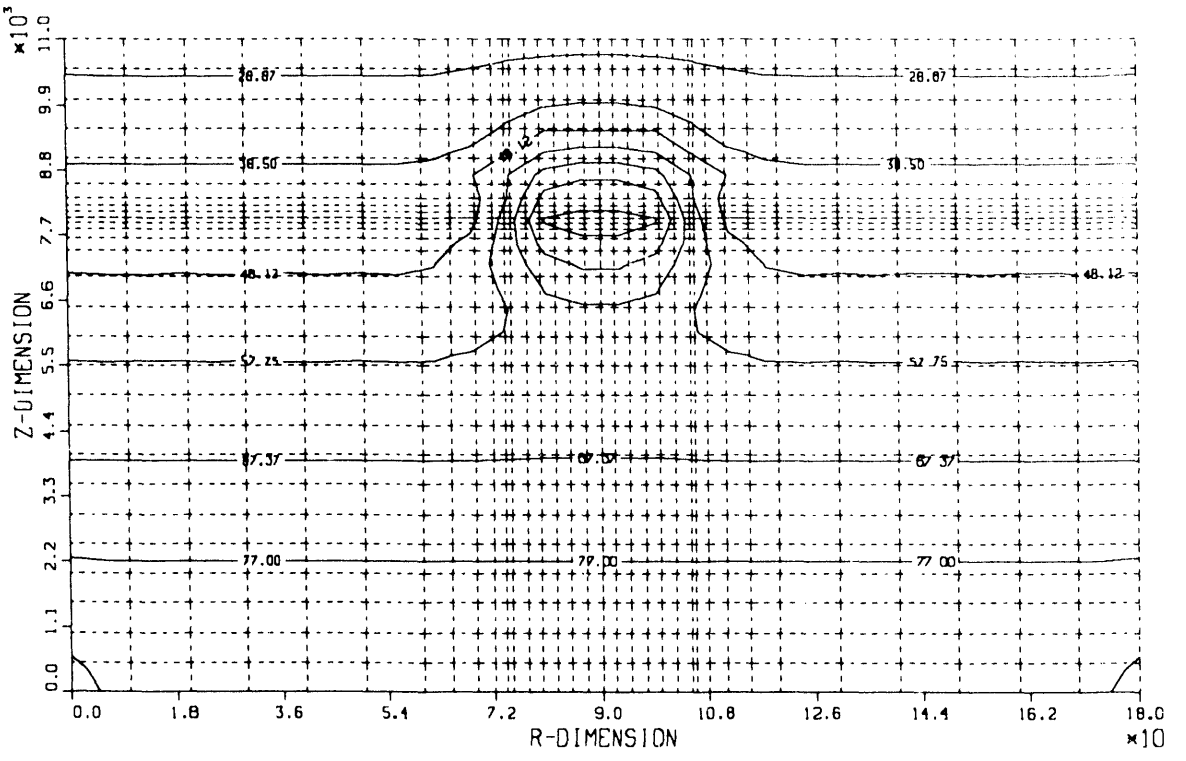

Figure 2. Temperature contours at 1000 yr. [XBL 913-484]

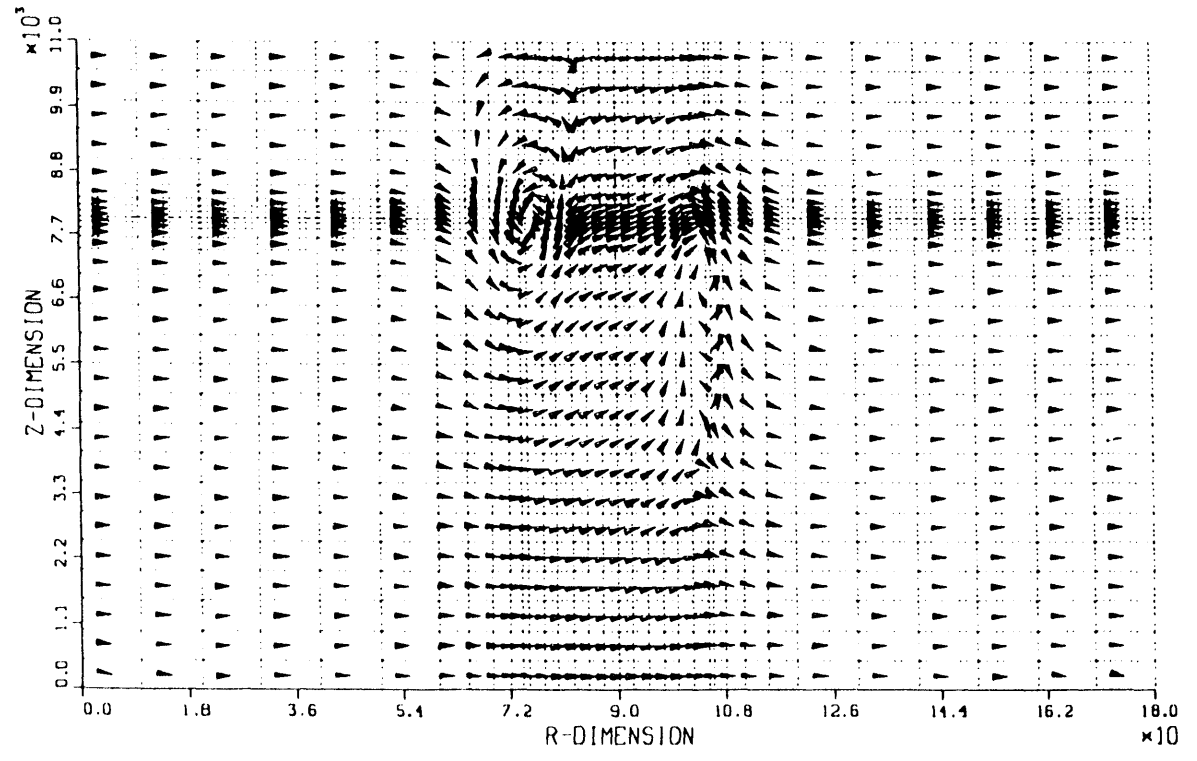

Figure 3. Flow direction at 1000 yr. [XBL 913-485]

thermal output from the repository. The buoyancy flow velocity is generally larger in magnitude in the fractures. However, the quantity of water involved is small and is thus not noticed in this figure. The principal stresses at 1000 years are shown in Figure 4. Originally they are parallel to the *r* and *z* directions and increase in magnitude as a function of depth. The influence of heating from the repository and of the presence of the major horizontal and vertical fracture can be seen in this figure. The normal stress changes along the vertical fracture from the repository to the land surface ranges over two orders of magnitude, resulting in aperture increases near the surface and aperture decreases near the repository.

These results are shown to demonstrate the advancing capability of performing more realistic calculations. Further studies are underway to apply these capabilities to repository performance assessment, and to identify critical phenomena involved, important parameters to be measured, and key elements that may impact repository safety.

REFERENCES

Acres Consulting Company, Ltd., 1978. Radioactive Waste Repository Study — Technical memoranda 3-3, 4-1, AECL-6415.

Noorishad, J., Tsang, C.F., Witherspoon, P.A., 1984. A coupled thermal-hydraulic-mechanical finite element model for saturated fractured porous rocks. J. Geophys. Res., v. 89, no. B12, p. 10365–10373 (LBL-16513).

Runchal, A., and Maini, T., 1980. The impact of a high-level nuclear waste repository on the regional groundwater flow. Int. J. Rock Mech. Min. Sci. & Geomech. Abstr., v. 17, p. 253–264.

Tsang, C.F. (ed.), 1987. Coupled Processes Associated with Nuclear Waste Repositories. Academic Press, Orlando, Florida.

Wang, J.S.Y., and Tsang, C.F., 1980. Buoyancy flow in fractures intersecting a nuclear waste repository. *In* F.A. Kulacki and R.W. Lyczkowski (eds.), Heat transfer in nuclear waste disposal. Proceedings, Winter Annual Meeting of ASME, Chicago, Illinois, HTD, v. 1, p. 105–112. Also published as Lawrence Berkeley Laboratory Report LBL-11112.

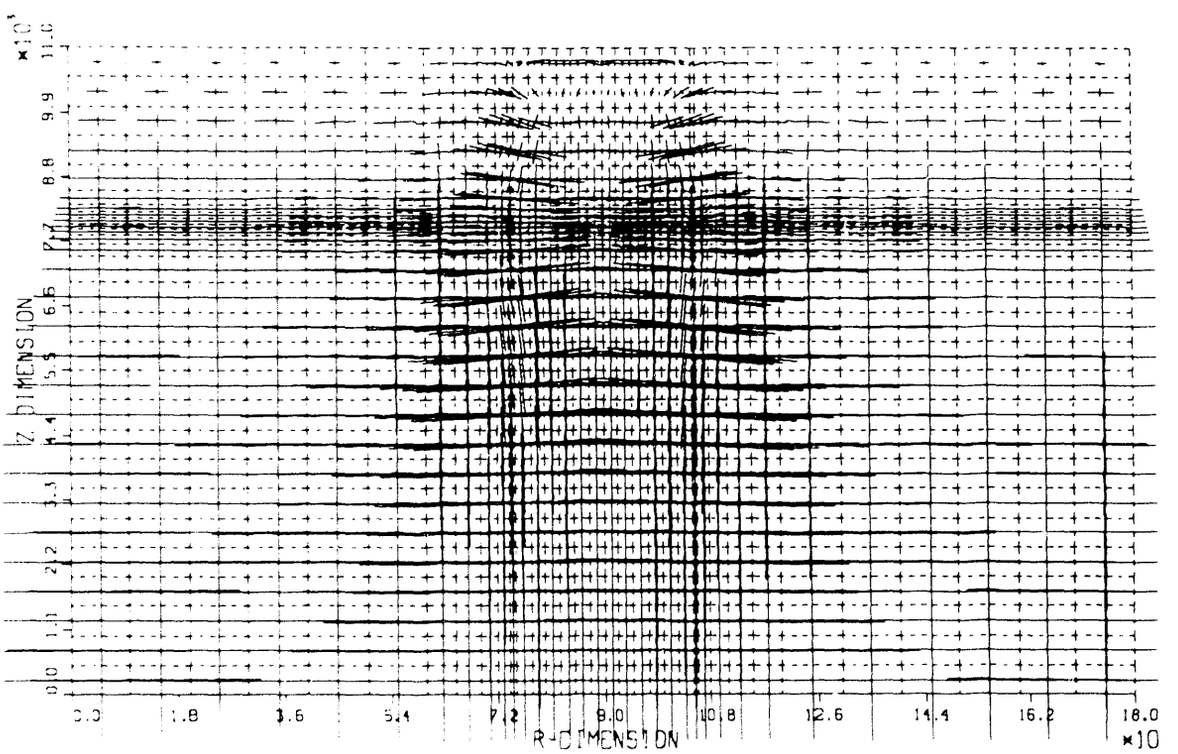

Figure 4. Principal stresses at 1000 yr. [XBL 913-486]

A Wellbore Fluid Logging Method for Characterizing Bedrock Aquifers

W. H. Pedler, C. F. Tsang, and F. V. Hale*

One of the most challenging tasks faced by environmental engineers is cost-effective hydraulic and hydrochemical characterization of a fractured bedrock aquifer by means of exploratory wellbores. To address this problem, a new borehole fluid logging method for rapidly and efficiently determining the vertical distribution of hydraulic conductivity in fractured bedrock aquifers has been developed (Tsang et al., 1990). The technique involves replacing the standing column of water in a borehole with a uniformly deionized fluid and then profiling the changes in fluid electrical conductivity (FEC) in the borehole. These changes occur when the contrasting formation water is drawn back into the borehole by continuous low-flow-rate pumping. The resulting FEC logs are then analyzed to estimate the interval-specific flow rate and the electrical conductivity of the associated formation water.

Previous field validation of this method was described by Tsang et al. (1990) for the Leuggern well, a deep borehole (2700 m) drilled through granite and biotite gneiss in Switzerland for research related to nuclear waste isolation. The objective of the DOE-Industry Technology Transfer Exchange Program under which this work was done was to validate this technique in the shallow environment (Pedler and Urish, 1988; Pedler et al., 1989, 1990), which is more typically associated with hazardous waste characterization. During this program, thirteen shallow wellbores (< 500 ft deep) were analyzed to determine the range of applicability of this new technique. The results presented here were obtained from one of these wellbores, a 200-ft-deep borehole in discretely fractured crystalline bedrock located near an active landfill in Rhode Island.

FIELD STUDIES

The technique employs wellbore fluid logging to record induced changes in fluid electrical conductivity (FEC) of deionized water emplaced in the wellbore. The field methodology is summarized in the following steps. First, a solid riser is deployed to the bottom of the wellbore to emplace a uniformly deionized fluid (DI) and replace the standing column of formation water. The DI consists of either formation water or potable water, with the dissolved ionic species removed. A continuous pumping test is then conducted to induce electrically contrasting formation water into the wellbore. Changes in FEC of the emplaced DI water occur as a result of mixing of (and subsequent displacement by) the contrasting formation water. Wireline water quality instrumentation is employed to log the wellbore fluid column and record the resulting FEC profile. The FEC logs and results from analysis using the code BORE (Hale and Tsang, 1988; Tsang et al., 1990) are then used in conjunction with the pumping test data to (1) identify the producing intervals, (2) determine depth-specific hydraulic conductivity, and, (3) estimate the electrical conductivity of the associated formation waters.

The Rhode Island wellbore (PAO-1) was a 200-ft-deep, 6-in.-diameter open bore in discretely fractured Scituate granite. The well was of relatively low yield and was previously used for residential water supply. Procedures after emplacement were similar to standard pumping tests: a constant rate of fluid extraction was maintained, and measurements of the piezometric surface were recorded. Changes in the wellbore fluid conditions were logged as a function of depth at different times during pumping. The resulting time-sequential FEC logs and the short-term pumping test data were then analyzed to determine the hydraulic conductivity of the individual producing intervals. Temperature, pH, and Eh logs were contemporaneously obtained to evaluate the hydrochemical conditions of the formation water.

ANALYSIS AND RESULTS

The locations of individual fractures and/or fracture zones were determined by comparing the initial baseline FEC log to the subsequent logs, which were obtained after emplacement of the DI water. Figure 1 shows these data for borehole PAO-1. The left side of Figure 1 (logs PAO1223, PAO1345, and PAO1406) depicts early-time logs and clearly shows four distinct spikes, indicative of hydraulically conductive intervals (inflow locations) at 16 m, 26 m, 29 m, and 54 m. These spikes represent a location where formation water associated with a hydraulically conductive interval has entered the wellbore and mixed with the emplaced DI water. The result is a dramatic increase in electrical conductivity of the fluids at that location. The right side of Figure 1 illustrates late-time logs (PAO1406, PAO1428, and PAO1623). These FEC logs show the continued advancement of the ionically contrasting formation water up the well and the establishment of a saturated interval from 10 m to 31 m. A saturated interval is defined as a constant FEC value between inflow locations and occurs when the emplaced DI water has been replaced by produced formation water. The FEC values exhibited in PAO1623 for the interval 10 m to 31 m will remain unchanged until the front associated with

* GZA GeoEnvironmental, Inc., Newton Upper Falls, MA.

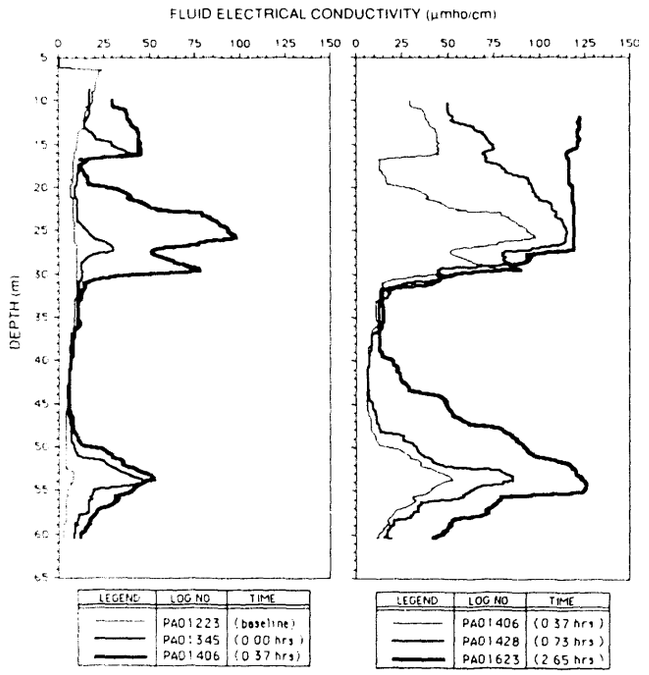

Figure 1. Time series of fluid electrical conductivity profiles. [XBL 913-479]

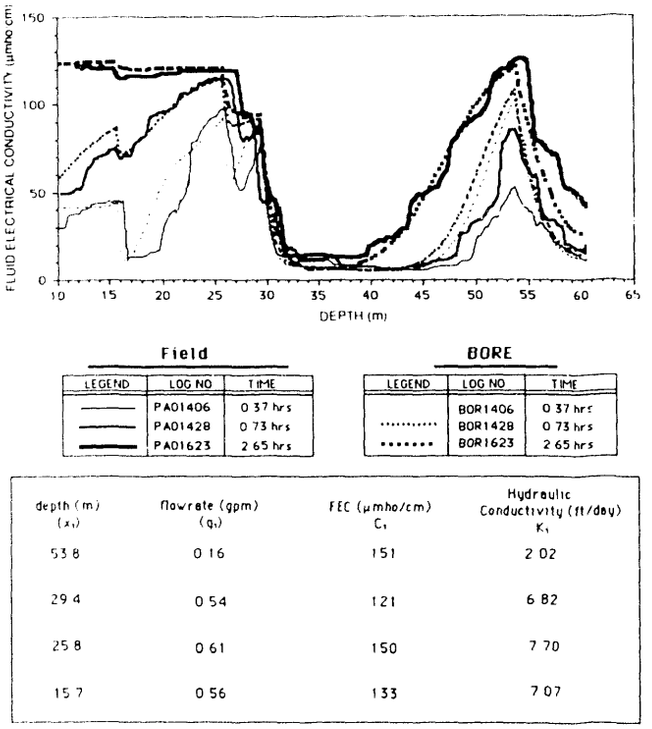

depth (m) (x_i)	flowrate (gpm) (q_i)	FEC (μmho/cm) C_i	Hydraulic Conductivity (ft/day) K_i
53.8	0.16	151	2.02
29.4	0.54	121	6.82
25.8	0.61	150	7.70
15.7	0.56	133	7.07

Figure 2. Comparison of field fluid electrical conductivity logs with corresponding logs generated by code BORE. Input parameters and derived hydraulic conductivity for 10-ft sample interval. [XBL 913-480]

the inflow location at 53 m has progressed through this interval.

To analyze these data the techniques described in Hale and Tsang (1988) and Tsang et al. (1990) were applied. Tsang and coworkers have developed a computer program called BORE, which performs a multi-parameter fit of the FEC logs to determine values of q_i (inflow rate) and C_i (FEC) for each of the producing fractures and associated formation water. Figure 2 shows the BORE input parameters and the resulting match to the field data obtained for wellbore PAO-1. For the producing fracture zones at 15 m, 25 m, and 29.5 m, BORE accurately simulated the field data for both early and late times. The lowermost producing fracture at 53 m yields the poorest match between the code-generated early-time logs and the corresponding field logs. The late-time logging (2.65 hr) provides the best fit for this interval. The suspected cause for the poor match was fluid dispersion by the logging tool.

Once q_i is determined for each producing interval, the corresponding hydraulic conductivity can be determined from review of the drawdown data recorded during pumping. A solution for hydraulic conductivity after Hvorslev (1951) was applied to each q_i using a sample interval of 10 ft and the observed drawdown data (Figure 2). These results for shallower wells are being validated by means of independent straddle packer testing and downhole flow metering. This current study will also determine the efficacy and cost-benefit ratio of this technique in the relatively shallow fractured bedrock aquifer environment.

The hydrochemical parameters of pH and oxidation-reduction potential (Eh) were also recorded. Figure 3 shows the data obtained during log PAO1623. A review of these data gives a qualitative estimate of the variability of water types present in the wellbore. A better understanding of these results is currently being developed.

On the basis of the work to date, it appears that further development of the instrumentation is needed to provide stabilized readings of pH and Eh in formation waters of low ionic strength. It is anticipated that with forthcoming instrumentation developments, fracture specific values for other water quality parameters (pH, oxidation-reduction potential, nitrite, dissolved oxygen and fluoride) can be obtained by application of mass balance principles similar to those employed for determining fracture specific fluid electrical conductivity.

SUMMARY AND CONCLUSIONS

A DOE-Industry Technology Transfer Exchange Program was undertaken to apply and validate a new borehole method for the purpose of characterizing groundwater flow in fractured bedrock aquifers. During this exchange thirteen wellbores were evaluated by this technique. These wells exhibited a wide range in aquifer parameters and well hydraulics. The results presented here

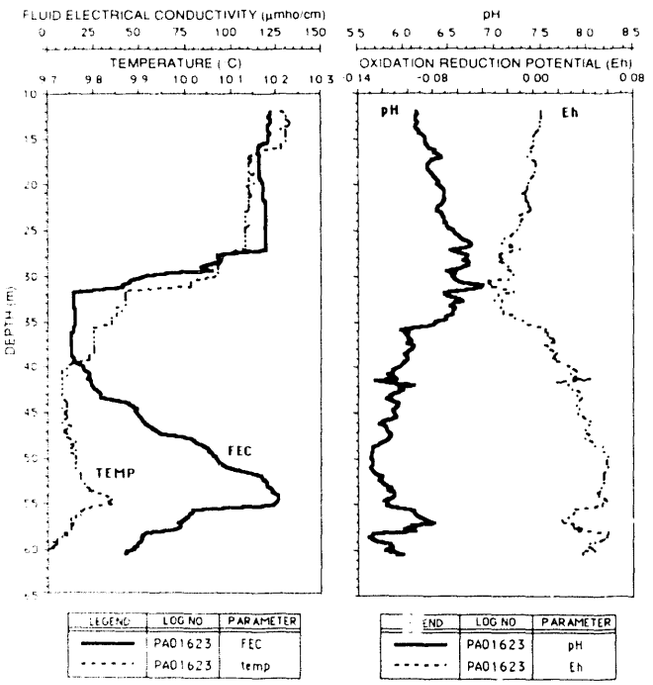

Figure 3. Fluid electrical conductivity, temperature, pH, and oxidation-reduction potential (Eh) logs for late-time logging. [XBL 913-481]

were obtained from a low-yield wellbore in discretely fractured crystalline bedrock near an active landfill in Rhode Island.

The technique combines standard pumping methodologies with fluid logging in wellbores where the water column has been replaced with an environmentally safe deionized fluid (DI). Fluid electrical conductivity (FEC) logging is used to elucidate zones of contrast between the emplaced fluid and the formation water that invades the borehole under pumping. These FEC logs are then evaluated to determine hydraulic conductivity as a function of depth for the bedrock aquifer. Application of the previously verified numerical code BORE to the existing data demonstrates the usefulness and capability of this new technique.

The data appear to support the following conclusions:

1. The tested aquifer is subjected to minimal disturbance during testing. The hydraulic and hydrochemical characterization was typically achieved with the net removal of only one wellbore volume of fluid.
2. Time-dependent wellbore fluid logging, during continuous low-rate DI emplacement or after completion of DI emplacement, has been employed to observe and quantify vertical flow in the wellbore under ambient pressure conditions.
3. With continued downhole instrument improvement, this new technique has the potential of estimating additional hydrochemical parameters (pH, oxidation-reduction potential, nitrite, dissolved oxygen, and fluoride) of fracture-specific formation water.
4. The technique can yield information commonly obtained with injection/extraction packer testing but in a much shorter time and at a significantly reduced cost.

Further description of this validation study is currently under way. However, it already appears that this investigatory tool may be particularly valuable for the hazardous waste engineer involved in projects where an understanding of bedrock contaminant transport mechanisms is critical for site remediation.

REFERENCES

Hale, F.V., and Tsang, C.F., 1988. A code to compute borehole fluid conductivity profiles with multiple feed points. Lawrence Berkeley Laboratory Report LBL-24928.

Hvorslev, M.J., 1951. Time lag and soil permeability in ground-water observations. Waterways Experiment Station, Corps of Engineers, U.S. Army, Vicksburg, Miss.

Pedler, W.H., and Urish, D.W., 1988. Detection and characterization of hydraulically conductive fractures in a borehole: The emplacement method. Eos, Trans. Am. Geophys. Union, v. 69, no. 44, p. 1186.

Pedler, W.H., Barvenik, M.J., Gardner, G.W., and Urish, D.W., 1989. Detection and characterization of hydraulically conductive fractures by geophysical logging after fluid emplacement. Proceedings, Second Annual Hazardous Materials Management Conference/Central, Rosemont, Illinois, March 14–16, 1989. Tower Conference Management Company, p. 121–129.

Pedler, W.H., Barvenik, M.J., Tsang, C.F., and Hale, F.V., 1990. Determination of bedrock hydraulic conductivity and hydrochemistry using a wellbore fluid logging method. Proceedings, Fourth National Outdoor Action Conference on Aquifer Restoration, Groundwater Monitoring and Geophysical Methods, Las Vegas, Nevada, May 4–10, 1990. National Water Well Association. Lawrence Berkeley Laboratory Report LBL-30713.

Tsang, C.F., Hufschmied, P., and Hale, F.V., 1990. Determination of fracture inflow parameters with a borehole fluid conductivity logging method. Water Resour. Res., v. 26, no. 4, p. 561–578 (LBL-24752).

TOUGH2: A General-Purpose Numerical Simulator for Multiphase Nonisothermal Flows

K. Pruess

Numerical simulators for multiphase fluid and heat flows in permeable media have been under development at Lawrence Berkeley Laboratory for more than 10 yr. The initial focus of this work was mostly on geothermal reservoir simulation, but efforts later broadened to include flow problems arising in the context of high-level nuclear waste isolation, oil and gas recovery and storage, and the management and protection of groundwater resources.

Several interrelated numerical codes have been developed. The first of these was SHAFT79, which was designed for simulating water/vapor flows in geothermal reservoirs, including heat flows and phase change effects. Real geofluids, however, contain noncondensible gases and dissolved solids in addition to water, and the desire to model such "compositional" systems led to the development of a flexible multicomponent, multiphase simulation architecture known as "MULKOM" (Figure 1). The design of MULKOM was based on the recognition that the mass- and energy-balance equations for multiphase fluid and heat flows in multicomponent systems have the same mathematical form, regardless of the number and nature of fluid components and phases present. Hence MULKOM can simulate flows in which an arbitrary number of components is distributed among several coexisting fluid phases. Application of MULKOM to different fluid mixtures, such as water and air, or water, oil, and gas, is possible by means of appropriate "equation-of-state" (EOS) modules, which provide all thermophysical and transport parameters of the fluid mixture and the permeable medium as a function of a suitable set of primary thermodynamic variables. Although the design of MULKOM is based on simple and straightforward concepts, the code has never been easy to use because various research applications have led to a proliferation of specialized program modules and options. Investigations of thermal and hydrologic effects from emplacement of heat-generating nuclear wastes into partially water-saturated formations prompted the development and release of a specialized version of MULKOM for nonisothermal flow of water and air, named TOUGH (Pruess, 1987). TOUGH is an acronym for "transport of unsaturated groundwater and heat" and is also an allusion to the tuff formations at Yucca Mountain, Nevada, which are presently being evaluated by the U.S. Department of Energy for their suitability as a host medium for a high-level nuclear waste repository.

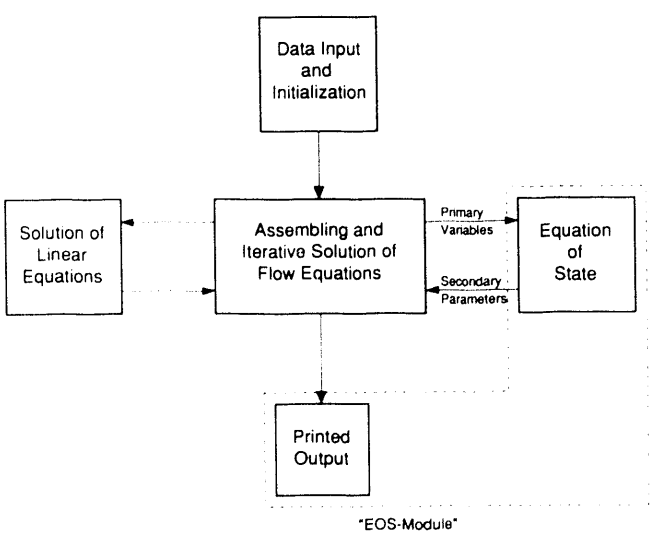

Figure 1. Modular architecture of MULKOM and TOUGH2. [XBL 908-2883]

The TOUGH2 code is intended to supersede TOUGH. It offers all the capabilities of TOUGH and includes a considerably more general subset of MULKOM modules with added capabilities. TOUGH2 can interface with different EOS modules and thereby model different fluid mixtures that consist of a variable number of components distributed among several phases. It also contains facilities for mesh generation and internal processing of geometric data, including multiple interacting continua discretization of fractured media, and it provides a tight and visible version control system for meeting stringent demands on reliability and referenceability of code applications. Except for the added flexibility and user features, TOUGH2 is — subroutine for subroutine — actually very similar to TOUGH. TOUGH2 input formats are similar to and upwardly compatible with those of TOUGH, facilitating the maintenance of existing TOUGH applications. A detailed documentation is available (Pruess, 1990a).

SIMULATION METHODOLOGY

For a multiphase flow system with NK mass components and one heat "pseudo-component," the $(NK + 1)$ coupled mass- and energy-balance equations can all be written in the following general form.

$$\frac{d}{dt}\int_{V_n} M^{(\kappa)}dV = \int_{\Gamma_n} \mathbf{F}^{(\kappa)}\cdot n\,d\Gamma + \int_{V_n} q^{(\kappa)}dV$$

$$\kappa = 1, \ldots, NK + 1 . \qquad (1)$$

The integration is over an arbitrary subdomain V_n ("grid block" in finite difference parlance) of the flow system under study, which is bounded by the closed surface Γ_n. The left-hand side represents the "accumulation term," with M denoting the amount of component κ (κ = water, air, heat, . . .) present per unit volume of the flow system. **F** is the flux of component κ entering V_n on the closed surface Γ_n around V_n, and q represents sinks and sources, through which mass or heat is injected into or removed from the system.

Thus Eq. (1) expresses the simple fact that the rate of change in the amount of κ within V_n is equal to the total rate at which κ flows across the surface Γ_n of V_n, plus the contribution of sinks and sources from within V_n. The accumulation term M is a sum over contributions from the various phases (liquid, gaseous, solid) in which component κ is present. This formulation automatically includes the description of phase change processes subject to the constraint of "local thermodynamic equilibrium" between all phases. The flux terms **F** are likewise sums of the separate contributions made by the different flowing phases, the main term being a multiphase version of Darcy's law that includes relative permeability and capillary pressure effects. In addition, diffusive and dispersive mass fluxes can be present. Heat flux includes conductive and convective components; the latter includes latent heat effects represented by different specific enthalpies of different phases.

The transport equations (Eq. 1) need to be complemented with constitutive relationships, which express all thermophysical parameters as functions of a set of primary thermodynamic variables. Thermophysical property modules developed for MULKOM are listed in Table 1; modules included in the present TOUGH2 package are marked with an asterisk.

For numerical solution, the mass and energy balance equations (Eq. 1) must be discretized in space and time. In MULKOM and TOUGH2, space discretization is made directly from the integrals, without first converting Eq. (1) into partial differential equations. This "integral" finite difference method, pioneered by Edwards (1972) and Narasimhan and Witherspoon (1976), avoids any reference to a global system of coordinates and thus offers the advantage of being applicable to regular or irregular discretizations in one, two, or three dimensions. It also facilitates implementation of higher-order differencing methods and applications to fractured media. For systems of regular grid blocks referred to global coordinates, the integral finite difference method is equivalent to conventional finite differences. Time is discretized fully implicitly as a first-order backward finite difference. This together with 100% upstream weighting of flux terms at interfaces is necessary to achieve unconditional stability and to avoid impractical time-step limitations for multiphase flow problems in fractured media with their usually small but highly active fracture volume. Space and time discretization results in a

Table 1. MULKOM/TOUGH2 fluid property modules.

Number of components	Components	Applications
1	Water*	Hydrology
2	Water, heat*	Geothermal, lab experiments
	Near-critical water, heat	Geothermal
3	Water, tracer, heat*	Geothermal, hydrology
	Water, CO_2, heat*	Geothermal
	Water, air, heat*,†	Nuclear waste, geothermal compressed air energy storage
	Water, H_2, heat*	Nuclear waste
	Water, SiO_2, heat	Nuclear waste, geothermal
	Water, NaCl, heat	Geothermal
	Water, CH_4, foam	Aquifer gas storage, environmental
	Water, NAPL,‡ heat	Environmental
4	Water, CO_2, NaCl, heat	Geothermal
	Water, light oil, heavy oil, heat	Enhanced oil recovery (steam flooding)
$N + 1$	Water, N-component NAPL‡	Environmental

*TOUGH2.

†TOUGH.

‡NAPL = nonaqueous phase liquid, such as organic solvents or fuels.

set of nonlinear algebraic equations. These are usually strongly coupled and are solved completely simultaneously by means of Newton/Raphson iteration. If convergence is not achieved within a predetermined number of iterations (typically eight), the time step size is automatically reduced. The linear equations arising at each iteration step are solved with a sparse version of LU-decomposition and backsubstitution (Duff, 1977).

TOUGH2 USER FEATURES

TOUGH2 input formats are upwardly compatible with those of TOUGH. Much of the available parameter choices is documented in the printed output, which otherwise is similar to that of TOUGH. Several additional parameters are provided through TOUGH data blocks for modeling additional processes and effects. These include a provision for the Klinkenberg effect, an account of vapor diffusion enhancement from pore-level phase change effects, and a capability to model heat exchange with impermeable confining layers by means of a semianalytical method.

A new feature in TOUGH2 is the concept of "inactive elements." For the inactive elements no mass or energy balance equations are set up, and their primary thermodynamic variables are not included in the list of unknowns. Otherwise, however, inactive elements can appear in flow connection and initial condition specifications like all other elements. This feature can be conveniently used to specify Dirichlet boundary conditions. TOUGH2 features flexible dimensioning of major (problem-size dependent) arrays, by means of PARAMETER statements in the main program. Allowable problem size data are printed in the output.

Further enhancements in comparison to TOUGH can be invoked by means of new data blocks. The keyword 'MESHM' calls up a MESHMAKER module for mesh generation and processing, which itself has a modular structure and can call several submodules. Present capabilities include generation of two-dimensional *R-Z* grids, and one-, two-, or three-dimensional rectilinear grids. MESHMAKER can also be used to subgrid a porous medium mesh for fractured media according to the method of "multiple interacting continua," which includes double-porosity and dual-permeability models as special cases.

A new data block 'MULTI' can be used for various choices in the EOS modules. The balance equations solved by TOUGH2 are ordered in such a fashion that, for a system with *NK* mass components, the *NK* mass balance equations appear first, followed by an energy balance. For nonisothermal problems, therefore, the number of equations per grid block is $NEQ = NK + 1$. In many problems heat effects are unimportant, however, and it would be desirable to avoid the expenditure of computing resources on solving a system of equations in which the energy balance reduces to the trivial statement $dT/dt = 0$. For several of the EOS modules it is possible to specify $NEQ = NK$, in which case no energy balances will be set up. As computing work typically is proportional to *NEQ***2, this can provide substantial savings.

In addition to specifying initial conditions by default for the entire flow domain, or in element-for-element fashion, TOUGH2 permits specification of default initial conditions for reservoir subdomains (data block 'INDOM').

TOUGH2 features a version control system. On first call to each subroutine, a one-line informative message will be printed to unit 11 (disk file 'VERS'), identifying the program unit, its version number and date, and the function performed by the program unit. At the end of a TOUGH2 simulation run, the contents of file 'VERS' will be copied to (default) OUTPUT; see the example in Figure 2. Besides documenting the versions and dates of subroutines used, this listing is instructive as a record of the calling sequence of program units during execution.

Keyword 'ENDFI' can be used as an alternative to 'ENDCY' for terminating input data. 'ENDFI' will cause the flow simulation to be bypassed; this option is useful when only mesh processing is desired.

CONCLUDING REMARKS

TOUGH2 is a more powerful successor to TOUGH. The code implements the general MULKOM architecture that separates and interfaces the flow and transport aspects of the problem (which do not depend on the nature and number of fluid components and phases) from the fluid property and phase composition aspects (which are specific to the particular fluid mixture under study).

The emphasis in the development of the MULKOM concept, and its implementation in the TOUGH2 code, has been on flexibility and robustness. TOUGH2 is an adaptable research tool; in its present form the TOUGH2 package includes the "core" modules of MULKOM for simulation studies in the fields of geothermal reservoir engineering, nuclear waste isolation, and hydrology. Examples of applications can be found in several papers presented at the TOUGH Workshop (Pruess, 1990b). MULKOM fluid property modules to be included in future releases would allow applications to problems in petroleum engineering, natural gas recovery and storage, and environmental monitoring and remediation. Further enhancements of the code are desirable, including a more comprehensive description of multiphase processes, improved execution speed, and a simpler more graphically oriented user interface.

```
                    SUMMARY OF PROGRAM UNITS USED

UNIT      VERSION      DATE                    COMMENTS
--------  -------  ---------------  ----  ------------------------------------------------------------

TOUGH2    1.0      6 JUNE           1990  MAIN PROGRAM
IO        1.0     22 JANUARY        1990  OPEN FILES *MESH*, *INCON*, *GENER*, *SAVE*, *LINEQ*, AND *TABLE*

INPUT     1.0     24 MAY            1990  READ ALL DATA PROVIDED THROUGH FILE *INPUT*

MESHM     1.0     24 MAY            1990  EXECUTIVE ROUTINE FOR INTERNAL MESH GENERATION
RZ2D      1.0     22 JANUARY        1990  CALCULATE 2-D R-Z MESH FROM INPUT DATA
WRZ2D     1.0     25 MAY            1990  WRITE DATA FOR 2-D R-Z MESH ON FILE *MESH*
RFILE     1.0     24 MAY            1990  INITIALIZE DATA FROM FILES *MESH* OR *MINC*, *GENER*, AND *INCON*

CYCIT     1.0     22 JUNE           1990  EXECUTIVE ROUTINE FOR MARCHING IN TIME

EOS       1.0      5 FEBRUARY       1990  *EOS3* ... THERMOPHYSICAL PROPERTIES MODULE FOR WATER/AIR
SAT       1.0     22 JANUARY        1990  STEAM TABLE EQUATION: SATURATION PRESSURE AS FUNCTION OF TEMPERATURE
COWAT     1.0     22 JANUARY        1990  LIQUID WATER DENSITY AND INT. ENERGY AS FUNCTION OF TEMPERATURE AND PRESSURE
SUPST     1.0     29 JANUARY        1990  VAPOR DENSITY AND INTERNAL ENERGY AS FUNCTION OF TEMPERATURE AND PRESSURE
VISW      1.0     22 JANUARY        1990  VISCOSITY OF LIQUID WATER AS FUNCTION OF TEMPERATURE AND PRESSURE

VISCO     1.0      1 FEBRUARY       1990  CALCULATE VISCOSITY OF VAPOR-AIR MIXTURES

COVIS     1.0      1 FEBRUARY       1990  COEFFICIENT FOR GAS PHASE VISCOSITY CALCULATION
VISS      1.0     22 JANUARY        1990  VISCOSITY OF VAPOR AS FUNCTION OF TEMPERATURE AND PRESSURE
RELP      1.0     25 JANUARY        1990  LIQUID AND GAS PHASE RELATIVE PERMEABILITIES AS FUNCTIONS OF SATURATION
PCAP      1.0     22 JANUARY        1990  CAPILLARY PRESSURE AS FUNCTION OF SATURATION

BALLA     1.0      1 FEBRUARY       1990  PERFORM SUMMARY BALANCES FOR VOLUME, MASS, AND ENERGY
TSTEP     1.0     22 JANUARY        1990  ADJUST TIME STEPS TO COINCIDE WITH USER-DEFINED TARGET TIMES

MULTI     1.0     24 MAY            1990  ASSEMBLE ALL ACCUMULATION AND FLOW TERMS
QU        1.0     22 JANUARY        1990  ASSEMBLE ALL SOURCE AND SINK TERMS
LINEQ     1.0     22 JANUARY        1990  INTERFACE FOR THE LINEAR EQUATION SOLVER MA28
MC19A                                   HARWELL SUBROUTINE FOR SCALING MATRIX
CONVER    1.0     22 JANUARY        1990  UPDATE PRIMARY VARIABLES AFTER CONVERGENCE IS ACHIEVED

PP        1.0      1 FEBRUARY       1990  CALCULATE VAPOR PRESSURE, DENSITY, INT. ENERGY AS F(P,T,X)

OUT       1.0      1 FEBRUARY       1990  PRINT RESULTS FOR ELEMENTS, CONNECTIONS, AND SINKS/SOURCES
WRIFI     1.0     22 JANUARY        1990  AT THE COMPLETION OF A TOUGH2 RUN, WRITE PRIMARY VARIABLES ON FILE *SAVE*

END OF TOUGH2 SIMULATION RUN --- ELAPSED TIME =  159.015 SEC-- CALCULATION TIME =  158.726 SEC-- DATA INPUT TIME =    0.289 SEC
```

Figure 2. An example of the version identification printout from TOUGH2. [XBL 913-482]

REFERENCES

Duff, I.S., 1977. MA28—A set of FORTRAN subroutines for sparse unsymmetric linear equations. AERE Harwell Report R 8730.

Edwards, A.L., 1972. TRUMP: A computer program for transient and steady state temperature distributions in multidimensional systems. National Technical Information Service, National Bureau of Standards, Springfield, Virginia.

Narasimhan, T.N., and Witherspoon, P.A., 1976. An Integrated finite difference method for analyzing fluid flow in porous media. Water Resour. Res., v. 12, no. 1, p. 57–64.

Pruess, K., 1987. TOUGH user's guide. U.S. Nuclear Regulatory Commission Report NUREG/CR-4645. (Also available as Lawrence Berkeley Laboratory Report LBL-20700.)

Pruess, K., 1990a. TOUGH2—A general purpose numerical simulator for multiphase fluid and heat flow. Lawrence Berkeley Laboratory Report LBL-29400.

Pruess, K. (Ed.) 1990b. Proceedings of the TOUGH Workshop. Lawrence Berkeley Laboratory Report LBL-29710.

Soil Selenium Depth Profiles and Time Trends in a Vegetated Site at Kesterson Reservoir

T. K. Tokunaga, D. S. Lipton, S. M. Benson, A. W. Yee, J. M. Oldfather, E. C. Duckart,† P. W. Johannis, and K. E. Halvorsen*

Kesterson Reservoir, once a set of evaporation ponds for agricultural drain waters, is situated in the southern portion of the Kesterson National Wildlife Refuge, on the west side of the San Joaquin Valley, California. The Reservoir consisted of 12 ponds, totaling 520 ha. Seleniferous drain waters were delivered to Kesterson via the San Luis Drain from farmlands approximately 140 km further south in the western San Joaquin Valley. Approximately 9 Mg of Se and 3×10^5 mg of salts were delivered to Kesterson between 1981 and 1986 (USBR, 1986). Selenium in drain water and pond water was primarily in the form of selenate (Se(VI)) under the prevailing oxidizing, neutral to slightly alkaline surface water environment. The salt composition of these waters was dominated by Na^+, SO_4^{2-}, and Cl^-. Although approximately 50% of the salt load was diminished through seepage losses, Se inputs were largely confined to the surface and near-surface environment (Weres et al., 1989). Reducing conditions that developed during drain-water ponding removed Se from solution by transforming the highly soluble pool of Se(VI) to a combination of less-soluble species, including selenite (Se(IV)), elemental Se, and various organic associations (Weres et al., 1989).

A large inventory of Se remains in Kesterson soils, where approximately 75% is concentrated in the upper 0.15 m of soils (Weres et al., 1989). Se concentrations in the surface soils ranged from 1 to over 100 mg kg^{-1}, with a Reservoir-wide average concentration of 5 mg kg^{-1}. Only 5 to 20% of Se in the detrital layer and surface soils is readily water soluble. Nevertheless, extremely high concentrations of dissolved Se (100 to 10,000 µg L^{-1}; the EPA drinking water standard for Se is 10 µg L^{-1}) are present in soil solutions under present conditions, down to depths of 1 m below the soil surface. The objectives of the investigations described here include (1) monitoring temporal and spatial trends in soil Se concentrations and (2) determining the distribution of Se within various soil fractions. This paper focuses on distributions of Se in a *Distichlis spicata*-dominated upland environment, one of the more stable and common upland environments at Kesterson. These data will provide information useful in assessing processes contributing to the future evolution of the Se inventory at Kesterson Reservoir.

* Levine-Fricke Inc., Emeryville, CA.

† Dept. of Soil Science, University of California at Berkeley.

METHODS

Characterization of Se in this upland habitat was initiated in January 1987 in a region of Pond 11. These soils formed on old alluvial floodplains (of primarily Sierran granitic parent material, low in Se) of the San Joaquin River. The soils are generally associated with poorly drained, saline, and occasionally sodic conditions. Low mean annual precipitation (290 mm), high potential evaporation (1800 mm y^{-1}), and the presence of a shallow water table commonly associated with saline soils are characteristic of the Reservoir. At the Pond 11 (P11) study area, the water table has fluctuated annually between 1.0 and 2.5 m below the soil surface during the interval spanning summer 1986 to spring 1990. These annual water table fluctuations have been correlated with winter flooding and spring draining of adjacent wetlands. The soils in the Kesterson area were diagnosed as being saline long before development of the Reservoir and subsequent accelerated importation of salts (Cole et al., 1952). Although the area soils have historically been saline, the high concentrations of Se in these soils are solely due to the recent influx of drain waters.

Soil samples used for Se extraction studies were obtained at 0.10-m intervals down to 1.70 m below the soil surface. Physical characterization of the soils included particle-size analyses, identification of evaporite and clay minerals, and measurements of hydraulic conductivities. The monitoring of soil solution profiles began in late January 1987, using tensiometers and soil solution samplers (0.15, 0.30, 0.46, 0.61, 0.91, and 1.22 m). Three similar test plots, designated P11C, P11D, and P11H, were instrumented in this manner. Additional test plots were constructed in which the surface soils were removed to depths of 0.15 m and 0.30 m (designated P11S1/2 and P11S1 respectively). Previously installed shallow wells were used to monitor depths to the water table. In subsequent years, instrumentation at one plot was expanded to include additional soil solution samplers down to 1.50 m, and a set of three neutron probe access tubes (down to at least 1.50 m) for monitoring changes in soil water content. Soil solution collections were generally limited to the months of January through April, during which time the soil profiles were sufficiently saturated by rainfall and by the seasonal rise of the shallow water table. Soil solution samples were analyzed for Se(IV) and total solution Se by hydride-generation atomic absorption spectrometry, HGAAS (Weres et al., 1989).

RESULTS AND DISCUSSION

The soils in the P11 test area were relatively homogeneous with respect to physico-chemical, characteristics when compared with other Reservoir sites. Clay and silt contents throughout the profile were in the range of 23 ± 4 and $24 \pm 5\%$, respectively (sandy loam to sandy clay loam USDA textures). Field-saturated hydraulic conductivities ranged from 2×10^{-8} to 6×10^{-7} m s^{-1} in 15 replicated measurements within the upper 1.3 m of the site. The site is very saline, with all soil solutions and the shallow groundwater characterized by electrical conductivity (EC) values exceeding 14 dS m^{-1}, sodium adsorption ratios (SAR) exceeding 30, and slightly alkaline pH. Gypsum and calcite are distributed over the upper 1.2 m of the profile (Flexser, 1988). Roots of *Distichlis*, *Cressa*, and *Frankenia* permeate the upper 1.0 m of the soil. A distinct surface salt crust was absent at the P11 area, in contrast with the more frequently ponded areas of the Reservoir.

Figure 1 shows depth profiles of soil solution Se concentrations obtained through in situ soil water samplers during the months of January through May from 1987 through 1990 at the P11C site. Figure 2 shows similar data from a site in which the upper 0.15 m of soil surface has been removed. Soil solution Se in all of these profiles occurred primarily as Se(VI), with usually minor amounts of Se(IV) (<10%). Although the volumetric soil water content profiles were not identical from year to year, their differences are judged to be minor on the basis of a combination of data from gravimetric moisture content determinations, neutron probe readings, and tensiometer data. Concentration changes, therefore, are interpreted as reflecting solution inventory changes. Nonuniformities in the soluble Se depth distributions (e.g., Figure 1) make interpretation of these data difficult. However, time trends in Se concentrations obtained by averaging data within particular profiles permit detection of general patterns, especially when several different profiles are simultaneously evaluated in this manner.

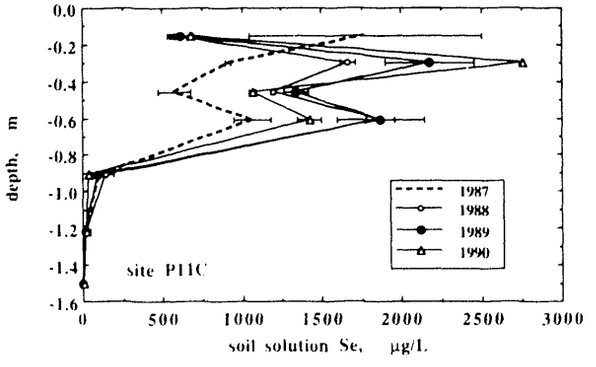

Figure 1. Soil solution selenium concentration profiles at site P11C, from 1987 to 1990. [XBL 913-487]

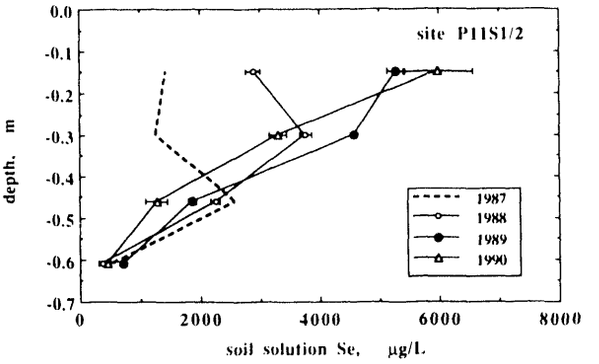

Figure 2. Soil solution selenium concentration profiles at site P11S1/2, from 1987 to 1990. [XBL 913-488]

Thus several general observations concerning the soil solution Se inventory at this upland site can be made, as discussed below.

The major changes in observed Se concentrations occurred during the first 2 yr of monitoring, whereas the most recent (1990) data show little overall difference from the preceding year. The three unexcavated upland plots exhibited 37 to 129% increases in average solution Se from 1987 to 1989. Incomplete sample collections during 1990 prevented meaningful averaging for two of these sites. However, the available data are indicative of relatively minor changes during the 1989 to 1990 period. From 1987 to 1989, average soil solution Se concentrations in the sites that have had surface soils removed to depths of 0.15 m and 0.30 m increased by 108 and 320%, respectively. No significant changes in profile-averaged Se concentrations were observed between the 1989 and 1990 data from these sites.

The increase in solution Se concentrations cannot be explained from external inputs, either from above or from below the sampling zone. Although downward leaching of Se from the soil surface (0 to ~ 0.10 m depths) by rainfall will provide some inputs into the strata monitored by the soil solution samplers, data from the excavated sites indicate that such a process appears inadequate for explaining the magnitude of the concentration changes. In the two excavated sites, where the most seleniferous surface soils have been completely removed, even greater increases in the profile-averaged Se concentrations were measured through 1987–1989 (e.g., Figure 2). It also should be noted that increases in Se concentrations in these soil solution profiles cannot be attributed to Se inflows from the shallow water table. As is evident from Figure 1, Se concentrations in soil solutions at depths below 1 m are too low to provide significant relative changes within the upper soil profile over the monitored history (unless implausibly high flow rates, ranging from 3 to 50 m yr^{-1}, were assumed).

The general time trends of initially rapid increases in soil solution Se concentrations, followed by more recent minor fluctuations is consistent with the expected behavior of a seleniferous soil that has experienced a transition from reducing to oxidizing conditions. Although this upland site was last flooded approximately 1 yr before the initiation of this study, it is conceivable that the increases in soil solution Se concentration observed during 1987 to 1989 represented the end of a period in which rapid release of a portion of the total Se inventory took place during a return to a more oxidizing soil environment. The present, relatively stable, high concentrations of Se in the soil solution do not appear to represent a solubility limit reached with respect to a Se(VI) pure solid phase.

Most of the increase in the soil solution Se concentration profiles appears to represent the release of Se from the *adsorbed*, *carbonate*, and *soil organic matter* (*SOM*) associated fractions. The dynamic nature of the soluble Se fraction evident from the soil solution sampler data, as well as the presence of a much larger proportion of the Se that is currently not freely mobile in the soil solution, have motivated the detailed analyses of these other pools of upland soil Se at the Reservoir by Lipton (1991). Figure 3 shows the depth distribution of the major Se fractions at site P11C. Total extractable Se is presented along with *soluble*, *soluble + adsorbed*, *soluble + adsorbed + carbonate*, and *SOM* associated pools of Se so that the relative importance of the soil fractions can be visualized throughout the profile.

The general decrease in the quantities of Se with depth reflects the practice by which Se was introduced into this site, i.e., from surface applications of drainage waters, and the capacity of the Kesterson soil environment to immobilize large amounts of Se, most notably in the *SOM*. In the top 0.2 m, more than 70% of the total Se inventory was observed to be associated with the *SOM* fraction,

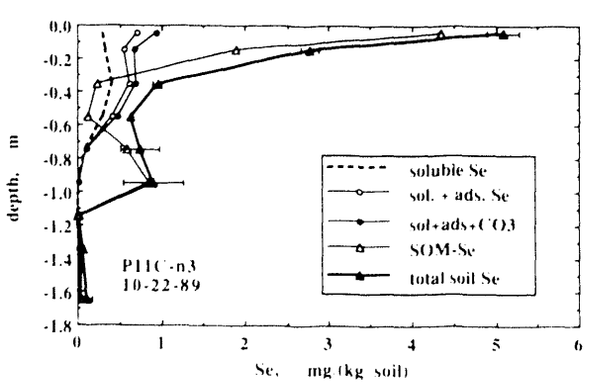

Figure 3. Depth profiles of soil Se concentrations at site P11C, from various extracted fractions. [XBL 913-489]

highlighting the importance of the *SOM* in the biogeochemistry of Se. The relative significance of *SOM*-Se at about 0.5 m depth, however, declined markedly (to about 20%) as the *soluble* and *adsorbed* pools of Se increased proportionally. Interestingly, this trend was reversed deeper in the profile (0.7 to 1.0 m) as Se in the *soluble* and *adsorbed* pools were found in small amounts while *SOM*-Se was observed to reach a second maximum of almost 1.0 mg kg^{-1} soil. As previously noted, this portion of the profile corresponds to the region influenced by the annual maximum height of the water table. Preliminary investigations, using a combination of methods developed by Weres et al. (1989) and Lipton (1991), have indicated that the *SOM*-Se at the 0.7 to 1.0 m depth was largely elemental Se though at the surface it was primarily organic Se and *SOM*-associated Se(IV) (data to be presented in a future paper). This apparent increase in the percentage of elemental Se relative to the total Se inventory with depth and may have resulted from more reducing conditions at the fluctuating water table.

ACKNOWLEDGMENTS

We thank Susan Hoffman, Jim Esget, and Mike Delamore of the U.S. Bureau of Reclamation for enthusiastic support of these experiments. We thank Oleh Weres (presently at Sonoma Research Company, Vineburg, California) and Robert Giauque of Lawrence Berkeley Laboratory for assistance in various aspects of this work.

REFERENCES

Cole, R.C., Gardner, R.A., Harradine, F.F., Kissling, R.O., Kingsbury, J.W., and Thompson, L.G., 1952. Soil survey of the Los Banos area, California. United States Department of Agriculture, Soil Conservation Service, Series 1939, no. 12.

Flexser, S., 1988. Lithologic composition and variability of the sediments underlying Kesterson Reservoir as interpreted from shallow cores. Lawrence Berkeley Laboratory Report LBL-25586.

Lipton, D.S., 1991. Associations of selenium in inorganic and organic constituents of soils from a semi-arid region (Ph.D. thesis). University of California at Berkeley.

U.S. Bureau of Reclamation, 1986. Final environmental impact statement, Kesterson program (Vol. 2). U.S. Bureau of Reclamation, Sacramento, California.

Weres,O., Jaouni, A.-R., and Tsao, L., 1989. The distribution, speciation and geochemistry cycling of selenium in a sedimentary environment, Kesterson Reservoir, California, U.S.A. Appl. Geochem., v. 4, p. 543-563.

Interaction of Groundwater Aquifers with Geothermal Reservoirs at Cerro Prieto, Mexico

A. H. Truesdell and M. J. Lippmann*

The Cerro Prieto geothermal field in northern Baja California, Mexico, is developed in the deltaic sands and shales of the southern Salton trough (Figure 1). Extensive drilling by the Comisión Federal de Electricidad (CFE) has provided fairly detailed information concerning lithology and temperatures from about 800 to 3000 m depth in the upper part of the system. Cerro Prieto has two thoroughly explored geothermal reservoirs and another that is less well known. These reservoirs differ from some other exploited reservoirs (The Geysers, Wairakei) in having "leaky" boundaries where the hot geothermal fluids exist in dynamic equilibrium with much cooler waters. Originally the boundaries of the system were maintained by an upward flow of hot water that eventually emerged at the surface or dispersed into surrounding cold aquifers.

In the natural state, heat in high-temperature hot-water reservoirs is supplied by an upward flow of hot fluid. This fluid must cool by boiling or by mixing with cooler water (dilution) to eventually reach surface temperatures. These processes have been described for the shallow Cerro Prieto α (alpha) reservoir and for Wairakei and Broadlands by Grant et al. (1984). At Wairakei boiling occurred at the top of the reservoir, but dilution was prevented by relatively well-sealed margins. At Broadlands boiling took place throughout the reservoir and dilution was very limited. In contrast, the α Cerro Prieto reservoir showed strong dilution, which produced temperature and salinity gradients and limited boiling. This reservoir, unlike the New Zealand systems, was not well sealed, and connections to cooler aquifers must have been relatively open. Bixley (1990) showed that under exploitation Wairakei and other New Zealand reservoirs were increasingly invaded by cooler water entering along conduits that originally fed surface discharges.

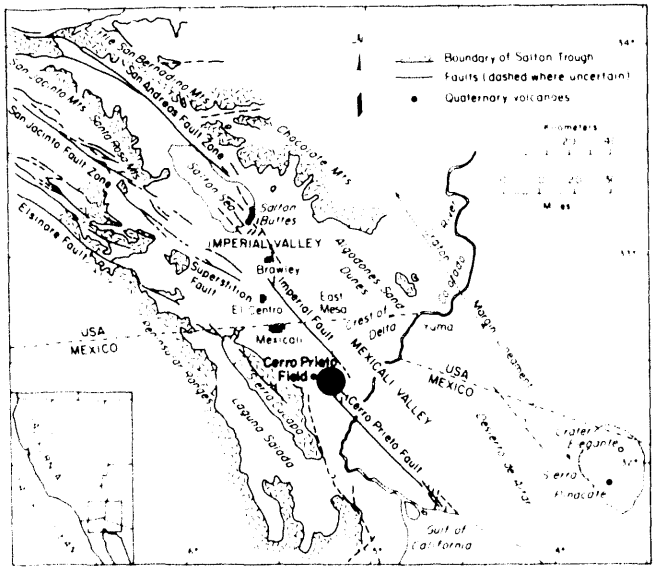

Figure 1. 9 Regional geological map of the Salton trough, showing the location of the Cerro Prieto field. [XBL-801-6718A]

NATURAL-STATE BOILING AND DILUTION

Boiling and dilution in the natural state differ from the same processes during exploitation. In the natural state, steam resulting from boiling may remain with liquid or separate to form a steam zone. The flow of mixtures of steam and water through pores (or small fractures) may be restricted by relative permeability effects and possibly by permeability reduction due to mineral precipitation. The results of these processes is to hinder fluid flow. Under exploitation high-enthalpy fluids may be locally generated by boiling and removed through drill holes, so that long-distance transport of steam-water mixtures does not occur.

In the natural state, dilution within a reservoir requires that cooler water enter along the same permeable connections through which hot fluids discharge. This counterflow of hot and cold fluids was shown in the natural-state simulations of Cerro Prieto by Lippmann and Bodvarsson (1983). The competition of boiling and dilution may act to hold temperatures at the boiling point to depth without much boiling. Hotter, less-diluted liquid would boil, and its upward flow would be impeded by relative permeability and mineral deposition. Fluids diluted just enough not to boil would not be hindered by these effects but would be more buoyant than cooler, more-diluted fluid. This could explain the adherence to boiling temperatures in the shallow α reservoir (Grant et al., 1984) even though little boiling occurs.

NATURAL-STATE HOT AND COLD AQUIFERS AT CERRO PRIETO

Halfman et al. (1986) and Lippmann et al. (1989) have described the natural-state hydrology of Cerro Prieto. These descriptions are based on lithologic and temperature logs and on modeling of heat and fluid flows. The general pattern of circulation in each of the Cerro Prieto reservoirs

* U.S. Geological Survey, Menlo Park, California, 94025, USA.

is similar. Hot fluids enter each reservoir from below and flow upward and toward the margins.

In the natural state the Cerro Prieto reservoirs are fed by hot brine from a deep source. These fluids appear to be heated by intrusion of igneous dikes into the sediments. It has been suggested from geochemical arguments that the deep recharge to the Cerro Prieto system consists of hypersaline brines of marine origin that mix with Colorado River water in several stages (Truesdell et al., 1981). This mixing was, as will be described later, the major cooling process for the Cerro Prieto brines in the natural state.

The hot brine (at 350°C where first encountered) flows up normal fault H (Figure 2) and, as discussed next, enters the deep γ (gamma) and β (beta) reservoirs and then flows through part of the β reservoir to the shallow α reservoir. Each of these reservoirs has complex connections through more-or-less permeable interbedded sandstones and shales to the hot brine and in most parts to cooler water.

The γ reservoir has been found only SE of fault H at depths greater than 3300 m. Very few wells produce from this aquifer. We do not know its extent and have no information on connections with cold-water aquifers. The entry of hot water suggests connection and flow to cold aquifers to maintain temperatures.

The β reservoir is the largest in the exploited field. It underlies the entire α reservoir and extends 3–4 km to the NE of the railroad (Figure 2). The depth to this reservoir is about 1500 m in the W to more than 2700 m in the E. It is divided by the SE-dipping fault H into upthrown and downthrown blocks. Fluids ascending along fault H flow NW and SE into these two parts of the β reservoir. About

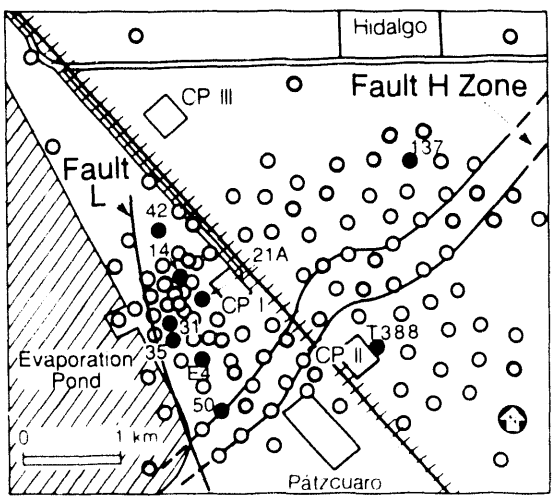

Figure 2. Location of Cerro Prieto wells discussed in the paper (filled circles) and faults H and L. Fault H zone is shown at the β reservoir level; fault L is subvertical (after Halfman et al., 1986). [XBL-904-6342]

two thirds of the β reservoir lies in the upthrown block. Fluid temperatures range from 320° to 340°C in the central reservoir and decrease to 240°C toward the margins.

The β reservoir is connected with cold-water aquifers to the S and W. Wells near these boundaries show evidence of chemical breakthrough of lower Cl, lower $\delta^{18}O$ waters (Stallard et al., 1987; Truesdell et al., 1989), indicating dilution. Wells in the N and NE, however, do not show dilution but present high excess steam, indicating reservoir boiling. Modeling by Lippmann et al. (1989) shows that most of the fluid entering the β reservoir from fault H enters the upthrown block (to the NW). A large proportion of this fluid flows into the α reservoir, but part is dispersed into cold aquifers within the thick sandstones present along the western edge of the field (Halfman et al., 1986). Probably all of the flow out of the downthrown block is into an adjacent cold-water aquifer. The edge of the β reservoir is defined by decreases in temperature and alteration. There is no evidence of self-sealing by mineral deposition at any of the lateral boundaries.

Most of the hot fluid leaving the E part of the β reservoir flows upward into the α reservoir through a gap in the shale overlying the β reservoir (Halfman et al., 1986). Modeling by Lippmann and Bodvarsson (1983) indicates that the fluid boils as it ascends through this gap. Flow into the α reservoir is from both fault H and the E part of the β reservoir.

The shallow α reservoir is found in the W part of the field (W of the railroad in Figure 2). It extends from 1000 to 1500 m depth and originally had temperatures from 260° to 310°C. Unlike the β reservoir, the α reservoir is not confined to a single sand unit but resides in mixed sands and shales. Flow upward may be limited by more shaley layers or by precipitation of calcite or quartz. The sandstone above it carries cooler waters with temperatures < 100°C in the E, increasing to 250°C in the W, where hot waters enter from fault L (Figure 2). Fault L is the major outflow conduit for fluids from the α reservoir, as indicated by the pattern of cold-water entry under exploitation (Stallard et al., 1987; Lippmann et al., 1989).

From the α reservoir some fluids flow to the W and S margin, but probably most flow up the subvertical normal fault L into the overlying cooler sandstone aquifer. At shallower depths the path is not certain, but eventually most of the hot fluid feeds the springs and fumaroles W of the field. Solute concentrations in the spring waters suggest boiling and dilution of hot brine originally at a temperature and chloride concentration (300°C and 9000 mg/kg) similar to those of brine in the α reservoir.

In systems such as Cerro Prieto, where the hottest fluids are significantly saline and cooler fluids are more dilute, most ascending fluid is cooled by dilution. Complex exchange between hot and cold aquifers occurs in the natural state. Cold water must enter hot aquifers and mix

with hot fluid to produce the gradients in temperature and chlorinity observed in the earliest samples from the field (Truesdell et al., 1979; Grant et al., 1984). Cooling by dilution rather than boiling must be favored by a decrease in effective permeability in zones of boiling. Relatively free access of cooler water aquifers to geothermal reservoirs in the natural state has provided a mechanism for the throughflow of hot water to maintain reservoir temperatures and has limited boiling through cooling by dilution.

RESPONSE OF CERRO PRIETO RESERVOIRS TO EXPLOITATION

Production of fluid from the α reservoir causes pressure drawdown and a deficit of mass. Without injection of liquid to replace the fluid deficit and maintain pressures, surrounding cooler water will be drawn into the reservoir or fluid will boil so that the volume of fluid removed is filled by vapor or cooler liquid.

At Cerro Prieto the chemistry of produced fluids, along with measured enthalpy, has been used to indicate processes in the reservoir (Truesdell et al., 1989; Lippmann and Truesdell, 1990). Near-well fluid temperatures are indicated by the quartz-saturation geothermometer and distant temperatures by the Na-K-Ca geothermometer. The comparison of these temperatures (or equivalent liquid enthalpies) with measured total enthalpy indicates excess steam. Changes in aquifer chloride indicate dilution and boiling.

Exploitation of Cerro Prieto reservoirs started in 1973, with the α reservoir supplying steam to the CPI power plant (Figure 2). Electrical power production from this part of the field increased from 75 MWe initially to 180 MWe in 1981. Declining production from the α reservoir led to drilling the deeper E-series wells that produce from the β reservoir in the same area. Production from E-wells within the CPI area started in 1981. The CPII and CPIII power plants (each 220-MWe capacity) went on line during 1986 and 1987. These plants were fed with fluids from the β reservoir (and to a small extent, the γ reservoir) in the E part of the field (E of the railroad in Figure 2). Thus experience with reservoir behavior is longest for the α reservoir, shortest for the β reservoir in the E, and intermediate for wells in the W part of the β reservoir.

The Cerro Prieto reservoirs have shown quite different behavior under exploitation. The α reservoir presented strong localized drawdown within a short time after the start of production. Almost all wells showed near-well boiling, with excess steam that decreased exponentially with time. After this initial boiling, wells in the N part of the α reservoir away from intense exploitation showed no boiling or dilution, with near-constant liquid and total enthalpies (Figure 3).

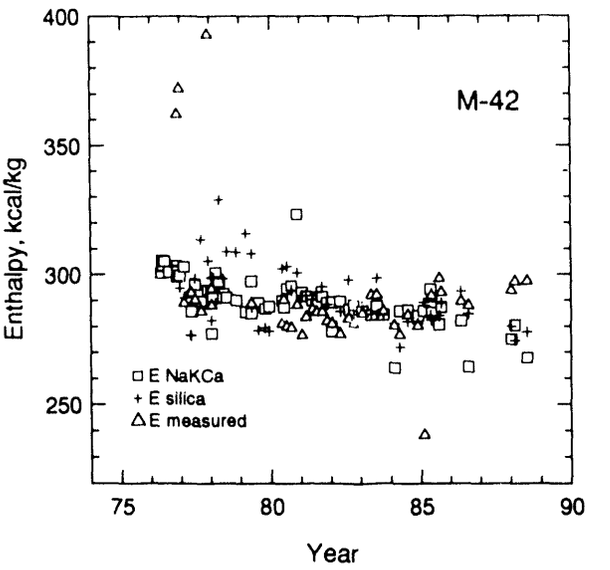

Figure 3. Indicated aquifer liquid enthalpy values and measured wellhead total fluid enthalpy values for well M-42. E Na-K-Ca is the enthalpy of liquid calculated from the Na-K-Ca geothermometer temperature; E silica is the enthalpy of liquid calculated from the quartz saturation geothermometer temperature. [XBL 913-492]

Wells near the edge of the field show chemical and thermal breakthrough of cooler, lower-Cl waters. Wells near fault L show sharp breakthrough (Figure 4), but wells in the W and S of the α reservoir and in the downthrown S block of the β reservoir show more gradual decreases in temperature (Figs. 5 and 6), as well as in Cl.

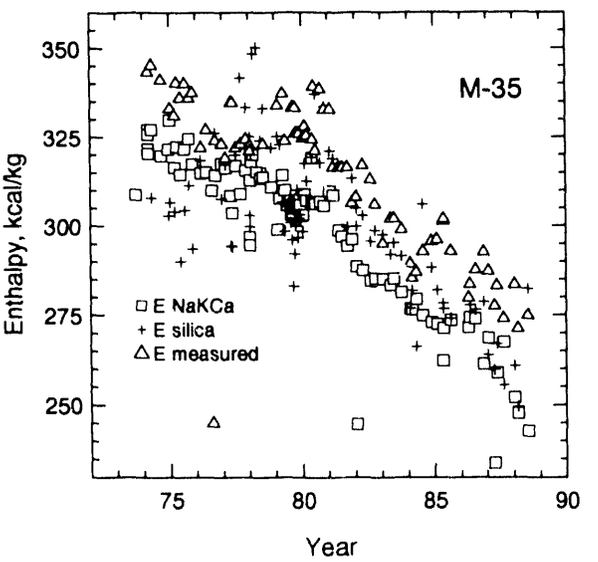

Figure 4. Indicated aquifer liquid enthalpy and wellhead total fluid enthalpy values for well M-35 (see caption of Figure 3). [XBL 913-493]

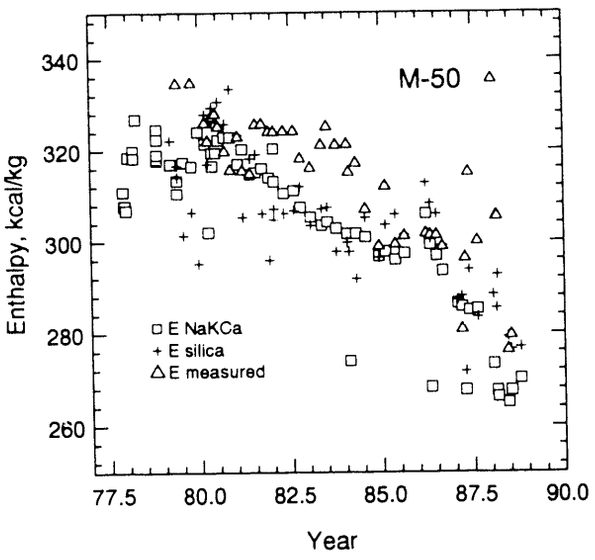

Figure 5. Indicated aquifer liquid enthalpy and wellhead total fluid enthalpy values for well M-50 (see caption of Figure 3). [XBL 913-494]

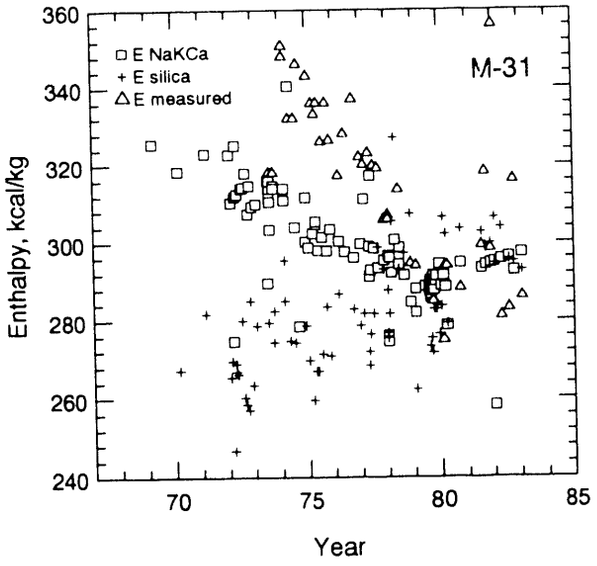

Figure 7. Indicated aquifer liquid enthalpy and wellhead total fluid enthalpy values for well M-31 (see caption of Figure 3). [XBL 913 496]

Wells with pronounced near-well boiling exhibit significant excess steam that decreases exponentially and lowered near-well temperatures (Figure 7). This has been shown by Lippmann and Truesdell (1990) to result from boiling in a reservoir with a constant-pressure boundary. This near-well boiling in the α reservoir was characteristic of the first 6 yr of production of wells in the central part of this reservoir, where connection to cooler aquifers through fault L probably provided the constant pressure. Near-well boiling and resulting mineral deposition may lead to formation plugging (Truesdell et al., 1984).

Boiling of a different sort is shown by wells in the β reservoir. These wells are not as closely connected to cool aquifers, and boiling is more widespread, not limited to individual wells. Almost all wells in the NW part of the β aquifer (N of fault H) show high excess enthalpy, which has increased with time rather than decreasing exponentially (Figure 8). Although these wells have been

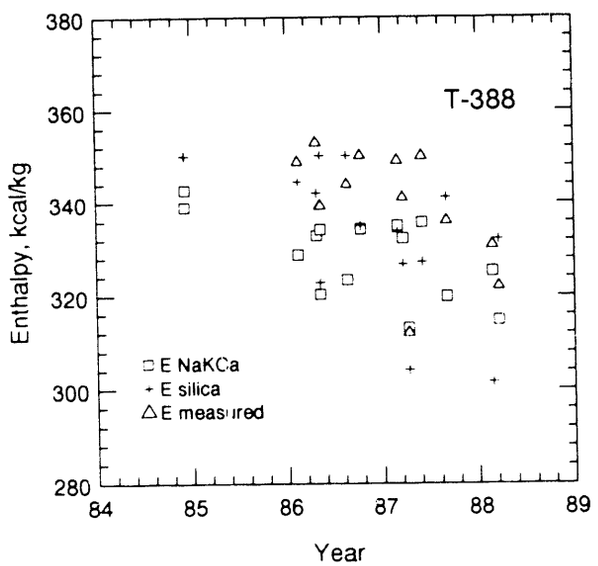

Figure 6. Indicated aquifer liquid enthalpy and wellhead total fluid enthalpy values for well T-388 (see caption of Figure 3). [XBL 913-495]

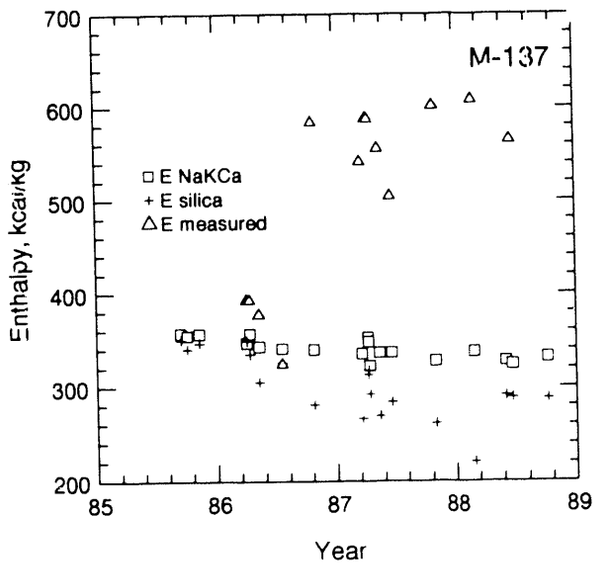

Figure 8. Indicated aquifer liquid enthalpy and wellhead total fluid enthalpy values for well M-137 (see caption of Figure 3). [XBL 913-497]

produced for only 3 yr, it appears that declining pressure has caused nearly reservoir-wide boiling with gravity segregation of steam and brine. As the brine level drops and steam flow to the wells increases, both enthalpy and whole-fluid gas concentrations increase. The β reservoir wells in the W part of the upthrown block (CPI area) also show general boiling but with cold sweep superimposed (Figure 9). Temperature and enthalpy decrease with the arrival of the thermal front, presumably as a result of replacement of vapor with cooler water.

EFFECTS OF COOL-WATER ENTRY ON PRODUCTION

Cerro Prieto has been a very productive field. This productivity has been achieved without liquid injection and with wells located on a grid pattern. We suggest that this success is due in part to the entry of cooler waters that have maintained pressures, prevented boiling, and swept heat to the wells. Only in the N part of the β reservoir, where access of cool water is most limited, could liquid injection benefit the field.

The comparison of well productivity and longevity in different parts of the Cerro Prieto reservoirs is instructive. The α reservoir has been produced for the longest time and in the S and W has the strongest connections to cooler aquifers. Wells in this part of the field have shown early chemical and thermal breakthrough and little boiling. The enthalpy of the wells has decreased slowly, however, and these wells have produced high steamflow over long lifetimes.

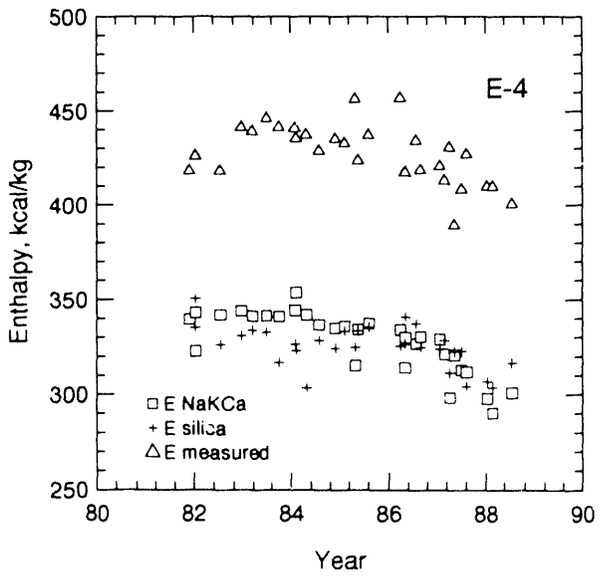

Figure 9. Indicated aquifer liquid enthalpy and wellhead total fluid enthalpy values for well E-4 (see caption of Figure 3). [XBL 913-498]

Wells in the N part of the α reservoir show little drawdown because this area has not been extensively drilled. These wells show only slight initial boiling and no dilution. They have relatively long lives with moderately low steam flow.

The behavior of wells in the central, heavily exploited zone of the α reservoir has been varied. Some wells on the N edge of this zone (e.g., M-14) behave like those in the N part of the reservoir. Others are close to the L fault and have shown early chemical and thermal breakthrough, sometimes combined with moderate initial boiling. Their steam production has been high and their longevity has been exceptional. Other wells (e.g., M-31, M-21A), perhaps less well connected to cool water, have high excess enthalpy and reduced fluid silica contents, indicating near-well boiling and mineral precipitation in the reservoir. These wells were initially high steam producers but have shown rapid declines and relatively short lives.

The deeper E-wells in the CPI area are on the average more productive than the shallower M-wells but only because they are younger. Some of the E-wells show excess enthalpy after a few years and some almost immediately upon start of production (Figure 9). The excess enthalpy generally does not decrease but remains high or increases, except in the few wells that show thermal breakthrough. Since none of these wells were produced before 1981, we cannot compare their longevity to that of M-wells. Silica in the fluid from the E-wells is not depressed, suggesting that mineral deposition and plugging may not become a problem.

Wells in the eastern CPII and CPIII areas have been producing in most cases since 1986 or 1987 but many only since 1988 or 1989, and as a result the average steam production is high. The record is too short to show clearly the influence of cool-water access on longevity. As in the α reservoir, the downthrown block of the β reservoir (S of fault H in the CPII area) shows progressive dilution but no excess enthalpy (boiling). The wells in the center of the CPII area show high steam productivity, but a few of those in the far S show low enthalpy and low steam.

Finally, considering the upthrown block of the β reservoir N of fault H in the CPIII area, we find unusually high excess enthalpy, which has increased in the few years of production. Wells adjacent to fault H produce unusually large flows. The lack of cool-water entry and the intense boiling in this part of Cerro Prieto suggest that liquid injection might be advantageous.

CONCLUSIONS

The observations presented here suggest that cool-water entry has increased the average longevity of Cerro Prieto wells. Some wells at the extreme edges of the field have been cooled so that they now produce less steam, but

pressures throughout the α reservoir and the S part of the β reservoir have been maintained. In these areas boiling has been prevented in most wells, and the total amount of heat extracted from the reservoir has probably been increased relative to the amount expected without natural recharge. The future productivity of the N part of the β reservoir, which shows little or no cool-water recharge, will be an interesting test of these ideas. The present management of the Cerro Prieto field has produced good results, which probably could not have been improved upon. A question for the future is the behavior of the β reservoir in the N part of the field that might benefit from liquid injection. Reinjection into other parts of Cerro Prieto might be less cost-effective, since there is already natural recharge of groundwater, mainly from the W and S.

REFERENCES

Bixley, P., 1990, Cold-water invasion in producing liquid-dominated systems. *In* Proceedings 15th Workshop on Geothermal Reservoir Engineering, Stanford, California, January 23–25, 1990 (in press).

Grant, M.A., Truesdell, A.H., and Mañón M., A., 1984. Production induced boiling and cold-water entry in the Cerro Prieto geothermal reservoir indicated by chemical and physical measurements. Geothermics, v. 13, no. 1/2, p. 117–140.

Halfman, S.E., Mañón M., A., and Lippmann, M.J., 1986. Update of the hydrogeologic model of the Cerro Prieto field based on recent well log data. Geotherm. Resour. Counc. Trans., v. 10, p. 369–375.

Lippmann, M.J., and Bodvarsson, G.S., 1983. Modeling studies on Cerro Prieto. Water Resour. Res., v. 19, p. 753–767.

Lippmann, M.J., and Truesdell, A.H., 1990. Reservoir simulation and geochemical study of Cerro Prieto I wells. *In* Proceedings, 15th Workshop on Geothermal Reservoir Engineering, Stanford, California, January 23–25, 1990 (in press).

Lippmann, M.J., Truesdell, A.H., Mañón M., A., and Halfman, S.E., 1989. The hydrogeologic-geochemical model of Cerro Prieto revisited. *In* Proceedings, 14th Workshop on Geothermal Reservoir Engineering, Stanford, California, January 24–26, 1989, p. 163–172.

Stallard, M.L., Winnett, T.L., Truesdell, A.H., Coplen, T.B., Kendall, C., White, L.D., Janik, C.J., and Thompson, J.M., 1987. Patterns of change in water isotopes from the Cerro Prieto geothermal field, Baja California, Mexico: 1977–1986. Geotherm. Resour. Counc. Trans., v. 11, p. 203–210.

Truesdell, A.H., Mañón M., A., Jiménez, M.E., Sánchez, A., and Fausto, J.J., 1979. Geochemical evidence of drawdown in the Cerro Prieto geothermal field. Geothermics, v. 8, p. 257–265.

Truesdell, A.H., Thompson, J.M., Coplen, T.B., Nehring, N.L., and Janik, C.J., 1981. The origin of the Cerro Prieto geothermal brine. Geothermics, v. 10, p. 225–238.

Truesdell, A.H., D'Amore, F., and Nieva, D., 1984. The effects of localized boiling on fluid production at Cerro Prieto. Geotherm. Resour. Counc. Trans., v. 8, p. 223–229.

Truesdell, A.H., Terrazas, B., Hernández, L., Janik, C., Quijano, L., and Tovar, R., 1989. The response of the Cerro Prieto reservoir to exploitation as indicated by fluid geochemistry. *In* Proceedings, Final Symposium Agreement US/DOE and CFE Mexico in the Field of Geoth. Energy, San Diego, California, April 4–5, 1989, p. 123–132.

Modeling Studies of Gas Movement and Moisture Migration at Yucca Mountain, Nevada

Y. W. Tsang and K. Pruess

Modeling studies on moisture redistribution processes that are mediated by gas phase flow and diffusion have been carried out (Tsang and Pruess, 1990). The problem addressed is the effect of a lowered humidity of the soil gas at the land surface on moisture removal from Yucca Mountain, the potential site for a high-level nuclear waste repository. At the land surface, humid formation gas contacts much drier atmospheric air. Near this contact, the humidity of the soil gas may be considerably lower than at greater depth, where we expect equilibrium with the liquid phase and close to 100% humidity. The lower relative humidity of the soil gas may be modeled by imposing, at the land surface, an additional negative capillary suction corresponding to vapor pressure lowering according to

Kelvin's Equation (Edlefsen and Anderson, 1943), thus providing a driving force for the upward movement of moisture in both the vapor and liquid phases. Sensitivity studies show that moisture removal from Yucca Mountain arising from the lowered-relative-humidity boundary condition is controlled by vapor diffusion. The lowered-humidity boundary condition implies a composition gradient in the gas phase, giving rise to a downward diffusive flux of air and an upward flux of vapor. The binary diffusion gas flux is described by

$$F^{\kappa} = -D_{va}\,\rho_g\,\nabla X_g^{\kappa}\,, \qquad (1)$$

where κ is the component index for the gas phase (κ = air or vapor), X_g^{κ} is the mass fraction of the κ^{th} component in the gas phase, and D_{va} is the diffusion coefficient for the vapor-air mixture in a porous medium, given by (Vargaftik, 1975; Walker et al., 1981)

$$D_{va} = \tau\phi S_g D_{va}^0 \frac{P_0}{P}\left(\frac{T}{T_0}\right)^{\theta}\,. \qquad (2)$$

Here D_{va}^0 is the diffusion coefficient in free gas phase at standard conditions of P_0 = 1 bar and T_0 = 273.15 K. The parameter group $\beta = \tau\phi S_g$, where S_g is the gas saturation, τ is the tortuosity, and ϕ is the porosity, specifies properties relevant to binary diffusion in a porous medium. For typical values of porosity and saturation in geological formations, β falls in the range of 0.001 to 0.01. However, there is much experimental evidence in the soil literature (e.g., Jury and Letey, 1979) that diffusion of vapor is enhanced due to pore-level phase change effects by a few orders of magnitude, so that β may take on values on the order of 1 regardless of media properties and gas saturation. Modeling results presented here will account for this enhancement in vapor diffusion.

SIMULATION RESULTS FOR A MEDIUM WITH UNIFORM HYDROLOGICAL PROPERTIES

Calculations were carried out by means of an in-house version of the numerical simulator "TOUGH" (transport of **u**nsaturated **g**roundwater and **h**eat; Pruess, 1987), which includes vapor pressure lowering effects. To focus on the vertical movement of fluxes, the simulation was carried out in one dimension, in a vertical tuff column of 600 m, which is the approximate distance from the land surface to the water table at the proposed repository site. We first employed a highly simplified stratigraphic description, assuming uniform hydrologic parameters that were representative of the proposed repository host formation (the Topopah Spring welded unit). The welded tuff unit is intensely fractured, with an average continuum fracture permeability about four orders of magnitude larger than the matrix permeability. An effective continuum approximation (Pruess et al., 1990) was employed, which allowed the use of one set of hydrological parameters for the description of fluid flow in both the fractures and matrix. This is accomplished by coding effective continuum characteristic curves into TOUGH. The numerical computation is first carried out without the imposition of a lowered-humidity boundary condition. The ground surface and the water table serve as constant temperature boundaries maintained at 286 K and 304 K, respectively. The water table serves also as a pressure boundary with the constant pressure P_0 of 1 bar, while a "no flow" boundary is imposed at the top, so that the gas pressure at each elevation will adjust itself to $P_0 - \rho_g g z$, whereas the equilibrium liquid pressure depends also on the capillary suction. Then the lowered-humidity boundary condition is implemented at the land surface for the second part of the calculations.

Figure 1 shows the fluxes in the liquid and gas phases. Results obtained prior to imposition of reduced-humidity boundary conditions are labeled "reference case," and those with imposed-humidity boundary conditions are labeled accordingly as "50% humidity." Units of flux are in both kg/m^2-s (bottom scale) and mm/yr of water (top scale). The label "vapor" in the figures denotes the total vapor flux arising from binary diffusion, as represented by Eq. (1), as well as pressure-driven Darcy flow. The figures display the fluxes as a function of elevation, with positive values for upward fluxes and negative values for downward fluxes. Figure 1 shows results for the enhanced value of β = 1 for vapor diffusion and the value corresponding to material properties $\tau\phi S_g$ = 0.0018 for air diffusion. For the "reference case," the upward vapor flux is balanced by the downward flow of the condensed liquid, resulting in zero net moisture migration. The larger magnitude of the vapor fluxes at depth is due to the geothermal gradient. With the imposition of a 50% relative-humidity boundary condition, both the liquid flux and the vapor flux are upward, resulting in a net upward migration of moisture. Vapor flux first decreases with elevation from the water table because of the decrease of temperature; at 300 m above the water table, vapor pressure lowering effects come into play because of the lowered-humidity boundary condition applied at the land surface, and the magnitude of vapor flux increases with elevation. The moisture flux from the upper portion of the formation consists almost entirely of vapor. The decrease of liquid flux with elevation arises from nonlinear liquid-flow effects, since the lower liquid saturation with elevation from the imposed boundary condition, while giving rise to a stronger upward capillary driving force, also results in a rapid decrease in liquid relative permeability. The total upward moisture flux is seen to be approximately 0.04 mm/yr in Figure 1b.

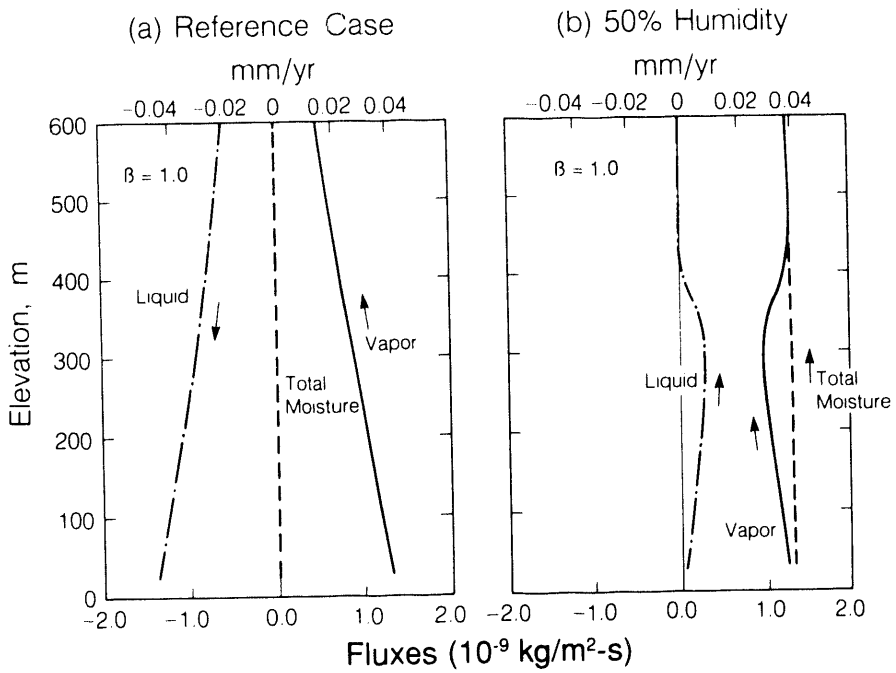

Figure 1. Fluxes in a column of welded tuff with vapor diffusion strength $\beta = 1$ and air diffusion strength $\beta = 0.0018$. [XBL 891-7440]

Simulations were also carried out for three other values, $\beta = 0.0018$, 0.05, and 0.33. The simulated results are summarized in Figure 2, which is a log-log plot of fluxes versus the vapor diffusion strength β. The upward vapor fluxes are the simulated values at 2.5 m below the land surface. When no lowered-humidity boundary condition is present, the vapor fluxes fall on a straight line of unit slope on the log-log plot, illustrating the linear dependence of the diffusion vapor flux on β, which follows from Eqs. (1) and (2). With the 80% humidity boundary condition at the land surface, the upward moisture flux is predominantly carried by the vapor phase when β is larger than 0.05. Only for the smallest value of $\beta = 0.0018$ does the liquid phase flux contribute significantly to the total upward moisture flux. For the range of values of β examined, the rate of moisture removal ranges from about 0.002 mm/yr to 0.04 mm/yr with the lowered humidity boundary condition of 80%. Similar results were obtained for the humidity boundary condition of 50%. Figure 2 therefore summarizes the following: (1) For the reference case, the vapor flux increases linearly with β. In the absence of an imposed lowered-humidity boundary condition, the upward vapor flux is balanced by the downward condensed liquid flux, resulting in no net loss of moisture from the formation. (2) With the lowered-humidity boundary condition at the surface, the magnitude of the total moisture flux is larger than, but of the same order of magnitude as, the vapor flux of the reference case. Hence the strength of the vapor diffusion both controls and gives a good estimate of the amount of moisture that is removed from the formation under an imposed lowered relative-humidity-boundary condition.

By varying β over a large range up to the greatly enhanced value of 1, the possible range of magnitude of moisture flux out of a column of welded tuff has been bracketed. Since the value of β dictates the rate of vapor-dominated moisture removal from humidity boundary conditions, our estimates for a column of welded tuff remain pertinent to the actual formation with layers of different hydrological properties. To substantiate our

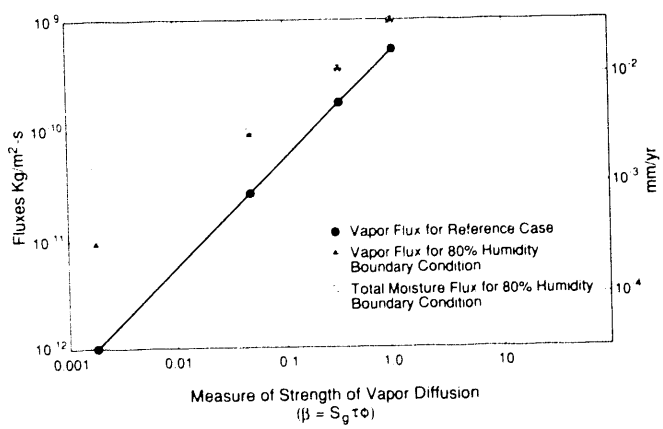

Figure 2. Fluxes at land surface as a function of vapor diffusion strength. [XBL 899-7751]

claim, sample calculations are presented that include the effects of stratigraphy.

INCLUSION OF STRATIGRAPHY IN 1-D COLUMN SIMULATIONS

We included in our calculations a simplified stratigraphy consisting of alternating layers of welded and nonwelded tuff Figure 3a shows the division of hydrologic units and spatial discretization for numerical simulation. The nonwelded units of tuff are only sparsely fractured and may be treated as a porous medium, and the effective continuum approximation still applies for the highly fractured welded units. For choice of layer thickness, material properties and characteristic curves, we refer the reader to our detailed report (Tsang and Pruess, 1990). Figure 3b shows the steady-state liquid saturation profile for the reference case, which clearly demonstrates the effects due to different hydrological properties in the alternating layers. Figure 4 shows the simulated results for fluxes; part (a) shows those for the "reference case" prior to the imposition of humidity boundary conditions, and part (b) shows those for an imposed boundary condition of 50% humidity. Figure 4b also shows that, whereas in the welded unit both liquid and vapor flow contribute to the upward transport of moisture, in the top 250 m the removal of moisture from the formation comes mostly from vapor flow. In comparing the fluxes for the layered column, in which the layers have different characteristic curves (Figure 4), with the fluxes for the 1-D welded column, which lacks stratigraphy (Figure 1), it is clear that the moisture removal from the formation is of the same order of magnitude, confirming our earlier claim that vapor diffusion strength is the controlling factor for the amount of moisture that is removed from the formation with a lowered-humidity boundary condition.

These results show that the presence of a realistic stratigraphy of alternating layers of nonwelded and welded units with very different hydrological properties has minor effects on the magnitude of moisture removal due to the "humidity" boundary condition. With a typical enhanced vapor diffusion strength of $\beta = 1$, our studies show that the amount of upward moisture flux (predominantly vapor) from the tuff column is equivalent to ≈0.04 mm/yr of water. We therefore conclude from our calculations that the rate of moisture removal from vapor transport has an upper limit of about 0.1 mm/yr.

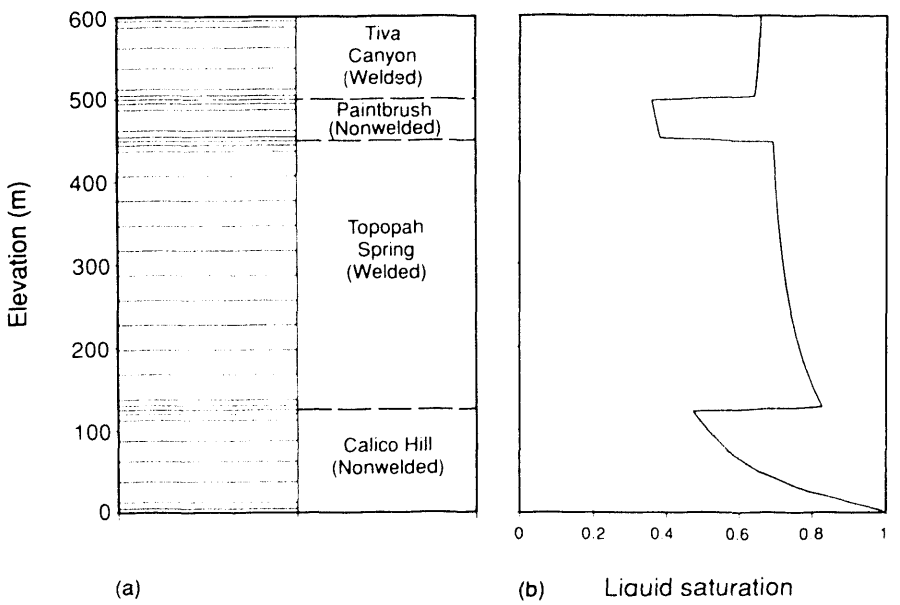

Figure 3. (a) Division of hydrologic units and spatial discretization for numerical simulation and (b) liquid saturation profile for a layered column of welded and nonwelded tuff. [XBL 904-6358A]

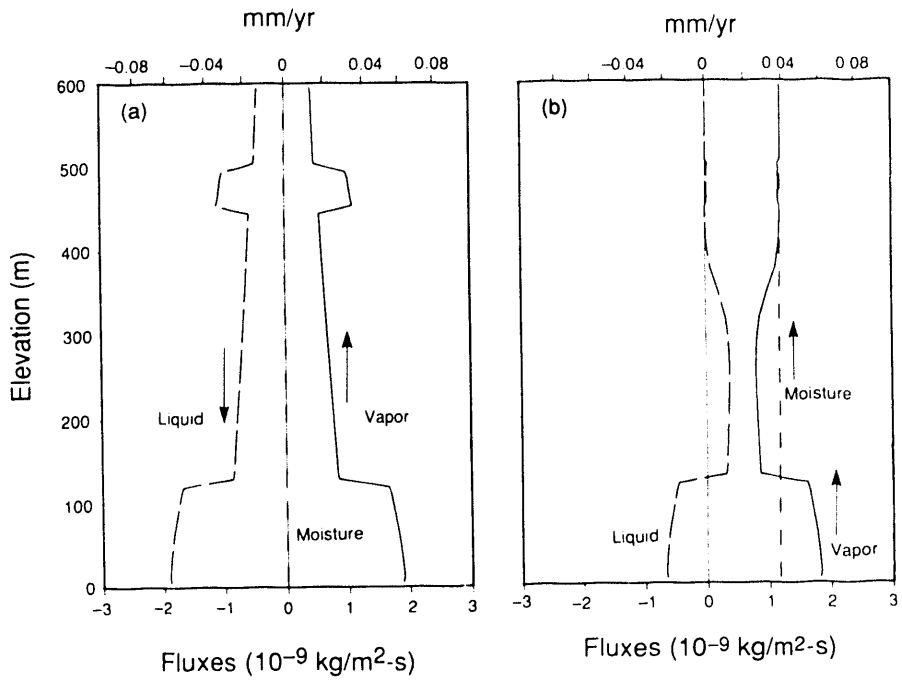

Figure 4. Fluxes for a layered column in (**a**) the "reference case" and (**b**) with 50% humidity boundary condition imposed. Vapor diffusion strength is $\beta = 1$. [XBL 913-555]

REFERENCES

Edlefsen, N.E., and Anderson, A.B.C., 1943. Thermodynamics of soil moisture. Hilgardia, v. 15, no. 2, p. 31–298, 1943.

Jury, W.A., and Letey, J., Jr., 1979. Water vapor movement in soil: Reconciliation of theory and experiment. Soil Sci. Am., v. 43, no. 5, p. 823–827.

Pruess, K, 1987. TOUGH users' guide. Lawrence Berkeley Laboratory Report LBL-20700.

Pruess, K.,Wang, J.S.Y., and Tsang, Y.W., 1990. On thermohydrologic conditions near high-level nuclear wastes emplaced in partially saturated fractured tuff, 2. Effective continuum approximation. Water Resour. Res., v. 26, no. 6, p. 1249–1261.

Tsang, Y.W., and Pruess, K., 1990. Further modeling studies of gas movement and moisture migration at Yucca Mountain, Nevada. Lawrence Berkeley Laboratory Report LBL-29127.

Vargaftik, N.B., 1975. Tables on the Thermophysical Properties of Liquids and Gases (2nd ed.). John Wiley, New York,.

Walker, W.R., Sabey, J.D., and Hampton, D.R., 1981. Studies of heat transfer and water migration in soils. Final report. Department of Agricultural and Chemical Engineering, Colorado.

A Variable-Aperture Channeling Model and Its Application to Field Data

C. F. Tsang, Y. W. Tsang, and F. V. Hale

The concept of flow channels was introduced to the study of fractured rocks by Neretnieks and coworkers (Neretnieks, 1983, 1987; Abelin et al., 1985). Motivated by this, Tsang and Tsang (1987) developed the model in which transport through fractured rocks is controlled by a number of channels, each of which has variable apertures along its length. Later, Tsang and Tsang (1989) pointed out that these channels are not physical pipes in the fracture plane but instead arise directly from the wide range of apertures distributed over each fracture. Figure 1 shows schematically a square section of fracture with a spatial distribution of apertures and the flow channeling that

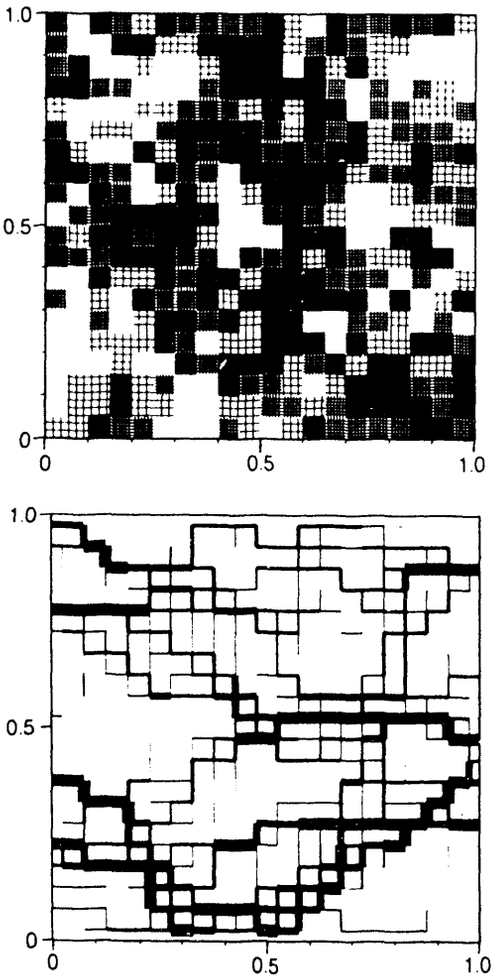

Figure 1. A discretized representation of apertures in a fracture plane is shown above. The magnitudes of the apertures are indicated by shading, with lighter shading corresponding to larger apertures. Relative flow rates for the apertures are shown below, assuming constant-pressure boundaries on the left and right, and no-flow boundaries for the top and bottom. Thicker lines indicate larger flow rates. [XBL 905-1748]

results by imposing a potential difference from left to right. Thus flow channeling is manifested by the occurrence of a few tortuous channels, each of which is composed of a number of flow paths of comparable mean velocities.

Flow and transport through a system of fractures can be envisioned as occurring through these tortuous channels of flow paths from fracture to fracture in three-dimensional space. The hydraulic conductivity of each channel is controlled by constrictions along the channel and is therefore not directly related to the volume or average aperture value of the channel. Transport in the system is then hypothesized to be dependent on the aperture probability density distribution, with a mean aperture value $\overline{b}$ and a spread or standard deviation σ_b, and on the spatial arrangement of the apertures characterized by the spatial correlation length λ. In many tracer transport experiments the measuring scale is such that the transport distances cover only a few fracture spacings in a fracture network, in which case transport can be studied as flow through a number of fractures in series. A large number of fractures may be generated by a geostatistical method with a specified aperture probability density distribution and a spatial correlation length, and the local flow rates in each of these fractures may be solved separately (Moreno et al. 1988).

EXPERIMENT AND CONCEPTUAL MODEL

The channeling model described above was applied to data from the Stripa mine in Sweden. The experiment was carried out in two drifts in the form of a cross, with lengths of 75 and 25 m. Each drift is 4.5 m in width and 3 m in maximum height. Three vertical boreholes drilled into the ceiling of the drifts were packed off to form nine sections 1 m in length with sufficient local hydraulic conductivity to be suitable for tracer injection. A different tracer was injected into each section, and tracers were collected in plastic sheets (1×2 m) covering the ceiling and sides of the drifts. The flow rates at the collection sheets were approximately constant in time, indicating that steady-state flow conditions prevail. However, of the more than 300 sheets, only a small number received significant flow, and tracer mass tended to concentrate at discrete regions of the drift (Figure 2). Only five of the nine tracers were found in significant concentrations in the collection sheets during the first 30 months of the experiment.

The characteristics of the variable-aperture channel model allow us to consider that the tracers travel along several tortuous channels in 3-D space, each of which is composed of a number of flow paths of comparable mean velocities, thus giving rise to some kind of dispersion within the flow channel. Of the flow paths that make up the channel, each one has variable apertures along its length. Within each flow path, we ignore dispersion

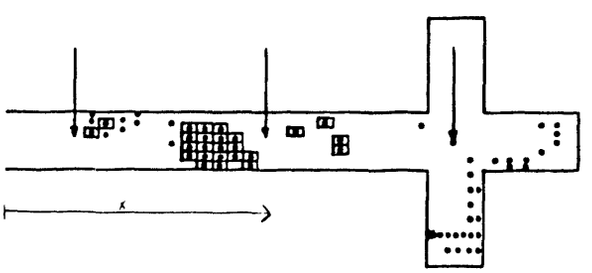

Figure 2. Tracer distribution in the Stripa 3-D test site. The arrows indicate the positions of the injection holes; dots indicate sheets with significant water flow; squares indicate sheets where tracers were collected. [XBL 905-1750]

(Taylor dispersion), and we ignore possible matrix diffusion and chemical retardation processes, with the implicit assumption that the tracers used are conservative over the relatively small travel times. We also assume that the travel distances cover only a few fracture spacings, so that the 3-D fracture network effects are not important. Under these assumptions, flow velocities and dispersion measures of these 1-D channels will be obtained and will be shown to be related to each other and to the basic fracture parameters $\overline{b}$ and σ_b, characterizing the variable-aperture channel model.

Our conceptual model of the Stripa 3-D experiment is as follows. The underground drift is maintained at atmospheric pressure and is a major sink for water from the rock around it. The majority of flow takes place in only selected flow paths of least flow resistance, which constitute only a small fraction of the total 3-D flow region. When a tracer is injected, the solution moves downstream along these preferred flow paths toward the drift and emerges in a number of collection sheets. From the experimental measurements, we do not have knowledge of the actual flow paths connecting the tracer injection and the particular collection sheet of tracer emergence. However, from the time dependence of the tracer collection, it will be shown below that we can identify channels or groups of flow paths that have comparable residence times.

Dilution of the tracers is apparent because the tracer injection flow rate is much smaller than the total exit flow rates at the drift, and the injection flow rate is strongly varying while the collection flow rate is fairly constant. Because of the dilution effect, the absolute value of the concentration of the breakthrough curves will not be investigated; this is not needed to obtain the relevant parameters such as mean and standard deviation of aperture values along the flow paths that govern and characterize the advective transport in the fractured medium. In our analysis, summarized below, we used the rate of tracer mass accumulation as the observed quantity rather than the more commonly used tracer concentration.

In this conceptual picture, one has a flow channel with emerging flow rate at the collection location while tracer is injected with a given mass per unit time at an upstream location. The tracer mass injected per unit time is proportional to injection flow rate because the injected tracer concentration is constant. Assuming that the one-dimensional advective-diffusive transport equation holds in the 1-D channels, well-known analytic solutions are available for the analysis of tracer transport data.

DATA ANALYSIS

The main complication with the present data set is the strong temporal variation of the tracer injection flow rate (Figure 3). For this a deconvolution method was developed

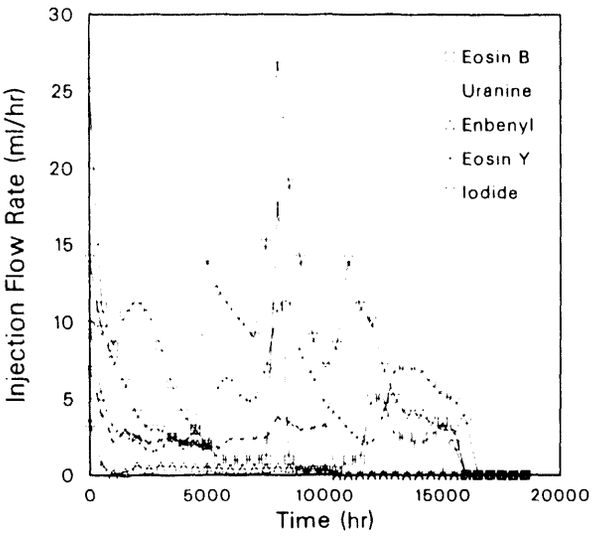

Figure 3. Injection flow rates in ml/hr for the five tracers; points are estimates for average flow rates over 500-hr intervals. [XBL 905-1732]

by Tsang et al. (1990), who called it the Toeplitz method. The Toeplitz method deconvolutionizes the field data to a_i's, which are the tracer breakthrough curves if the tracer injection were a delta function pulse input. All results for the five tracers are analyzed, and a typical example is shown in Figure 4 for the case of eosin B. The four peaks clearly show the multiple-channel nature of the tracer transport in the Stripa 3-D data. Note that we have defined a channel as a group of nearby flow paths with comparable

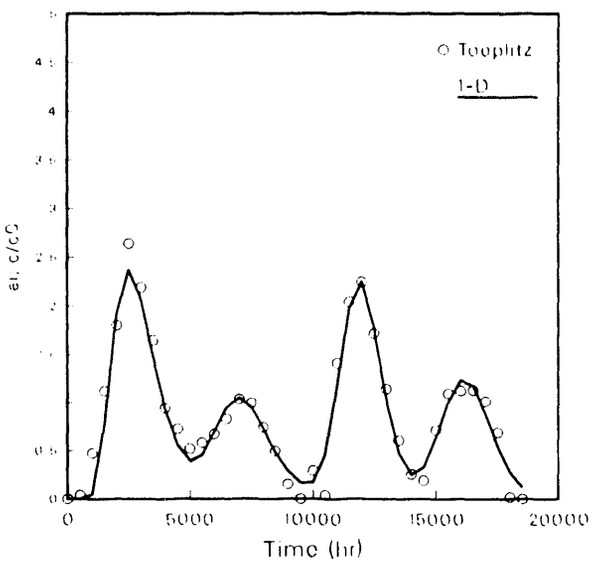

Figure 4. Results of Toeplitz analysis method for eosin B. The circles are the results of the Toeplitz analysis, and the solid line is the fit of the 1-D advection-diffusion equation to the results, separated into distinct peaks. [XBL 913-490]

mean velocities. These results were obtained by applying the Toeplitz analysis to the mean concentration breakthrough curves averaged over all the collection sheets where the tracer arrived. The same analysis was also applied to tracer breakthrough curves for a few specific collection sheets at a single distance along the experimental drift. Similar results were obtained. Thus the channels do not correspond to different flow tubes arriving at different collection sheets, but rather all sheets appear to display the same multiple-channel structure in their respective tracer breakthrough curves.

To quantitatively characterize the channels, we fit the solution of the 1-D advective diffusive equation with a delta function tracer injection to each of these peaks. Thus we can obtain the mean tracer velocity v and dispersion coefficient D for each peak, and the "channel dispersivity" α is then given by D/v. The results are plotted in Figure 5, which shows the surprising trend of α decreasing with the mean travel time $\overline{t} = x/v$, where x is the transport distance of the tracer. Very roughly, the figure appears to show that $\alpha \approx \overline{t}^{-2}$.

DISCUSSION

The surprising result that $\alpha \approx \overline{t}^{-2}$ is a direct result of the analysis of the field data. It is in contrast to the case of a porous medium, where α is usually assumed to be constant with respect to mean travel time $\overline{t}$. It is also different from the result for flow in a constant-diameter pipe, where the time dependence is given by the Taylor's dispersion, which for small molecular dispersion is $\alpha \approx \overline{t}^{-2}$. In the Stripa 3-D data, we find a much stronger $\overline{t}$ dependence for transport through variable-aperture fractures. The basis and implication of this interesting result are yet to be studied. One possible explanation is that the standard deviation σ_t of tracer particle arrival times for

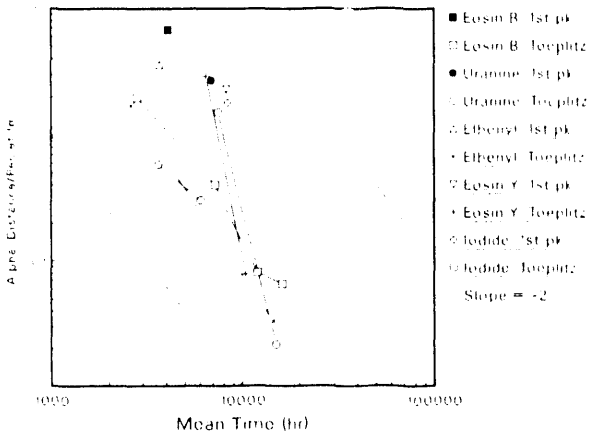

Figure 5. Log-log plot of $\alpha = D/v$ versus mean arrival time of each channel. The broken lines indicate a slope of –2. [XBL 913-491]

each of the peaks is about the same as for the other peaks in each case; i.e., σ_t appears to be independent of the mean travel times of the peaks. Since the Peclet number for 1-D transport along a channel may be expressed (Levenspiel, 1972) as $\alpha = 2x(\sigma_t^2/\overline{t}^2)$, then $\alpha \approx \overline{t}^{-2}$. Thus, σ_τ is dependent on the variance of fracture apertures or local permeabilities over the 2-D fracture plane. For tracer transport along different channels between injection and collection points, this may be approximately the same. However, the mean travel times of these channels may be strongly affected by the local heterogeneity. Thus a local constriction or a relatively large local aperture volume along a flow channel will strongly affect the mean travel times. In other words, for a strongly 2-D heterogeneous system, as in our case, the mean travel time and the travel time standard deviation may be decoupled. If we extrapolate this line of reasoning, we may conjecture that for the type of system under study, we should not focus on the dispersivity. Rather, we should determine the travel time standard deviations σ_t and mean travel times $\overline{t}$ of the groups of flow paths, or channels. The former, σ_t, is closely correlated to aperture or permeability variance and can be estimated for the Stripa 3-D data discussed above. The latter, $\overline{t}$, is strongly affected by the local heterogeneity around the injection location and is not correlated to aperture distribution parameters in our case study. However, if one is able to study the $\overline{t}$ values for a larger number of such transport channels, we expect that the mean of these $\overline{t}$ values can be correlated to the basic aperture probability distribution parameters.

ACKNOWLEDGMENTS

We have benefited from the careful review and comments of G.S. Bodvarsson and C.L. Carnahan of Lawrence Berkeley Laboratory and L. Moreno and I. Neretnieks of the Royal Institute of Technology, Stockholm, Sweden.

REFERENCES

Abelin, H., Neretnieks, I., Tunbrant, S., and Moreno, L., 1985. Final report on the migration in a single fracture. Experimental results and evaluations. Svensk. Kärnbränsleförsorjning Tech. Report 85-03, Nucl. Fuel Safety Project, Stockholm.

Levenspiel, O., 1972. Chemical Reaction Engineering (2nd ed.). John Wiley, New York, p. 275.

Moreno, L., Tsang, Y.W., Tsang, C.F., Hale, F.V., and Neretnieks, I., 1988. Flow and tracer transport in a single fracture: A stochastic model and its relation to some field observations. Water Resour. Res., v. 24, no. 12, p. 2033–3048.

Neretnieks, I., 1983. A note on fracture flow dispersion mechanisms in the ground. Water Resour. Res., v. 19, no. 2, p. 364–370.

Neretnieks, I., 1987. Channeling effects in flow and transport in fractures rocks—Some recent observations and models. Proceedings, GEOVAL-87, International Symposium, Stockholm, Sweden, April 7–9, 1987.

Tsang, Y.W., and Tsang, C.F., 1987. Channel model of flow through fractured media. Water Resour. Res., v. 23, no. 3, p. 467–479.

Tsang, Y.W., and Tsang, C.F., 1989. Flow channeling in a single fracture as a two-dimensional strongly heterogeneous permeable medium. Water Resour. Res., v. 25, no. 9, p. 2076–2080.

Tsang, C.F., Tsang, Y.W., and Hale, F.V., 1990. Tracer transport in fractures: Analysis of Field data based on a variable-aperture channel model. Submitted to Water Resour. Res. (LBL-29474).

Variation and Correlation of Hydrologic Properties

J. S. Y. Wang

Hydrological properties vary within a given geological formation and even more so among different soil and rock media. The variance of the saturated permeability is shown to be related to the variance of the pore-size distribution index of a given medium by a simple equation. This relationship is deduced by comparison of the data from Yucca Mountain, Nevada (Peters et al., 1984), Las Cruces, New Mexico (Wierenga et al., 1989), and Apache Leap, Arizona (Rasmussen et al., 1990). These and other studies in different soils and rocks also support the Poiseuille-Carmen relationship between the mean value of saturated permeability and the mean value of capillary radius. Correlations of the mean values and variances between permeability and pore-geometry parameters can lead us to better quantification of heterogeneous flow fields and better understanding of the scaling laws of hydrological properties.

Figure 1 is the scatter plot of saturated permeability values versus the capillary radius values from the three sites. The capillary radii are deduced from the desaturation curves, which are fitted by the van Genuchten (1980) equation. The capillary radius is a good measure of the effective hydraulic radius. Among very different soil and rock media, the mean value of permeability is approximately proportional to the square of the mean value of capillary radius. Within a given medium, there is no apparent correlation between these two parameters from the data sets.

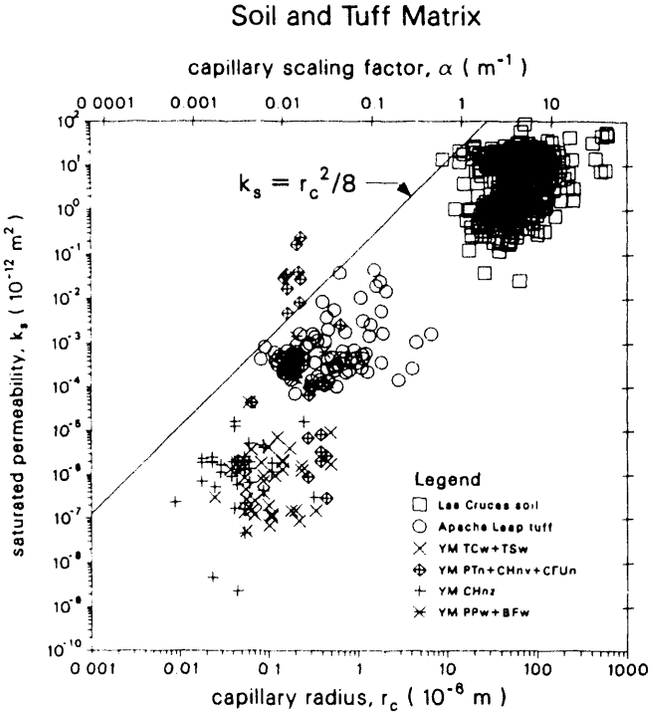

Figure 1. Correlation between saturated permeability and capillary radius. [XBL 914-743]

Figure 2 is the scatter plot of saturated permeabilities k_s versus the pore-size distribution indices λ. We do not expect from physical models, and do not observe from experimental data, any correlation between the mean values of these two parameters. However, the standard deviation of $\log(k_s)$ is proportional to the standard deviation of $\log(\lambda)$, as shown in Figure 3. The simple equation

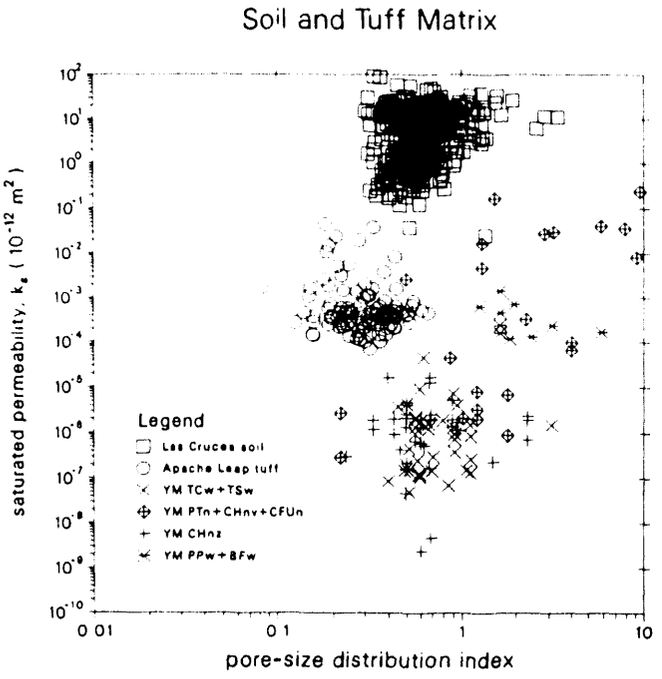

Figure 2. Correlation between saturated permeability and pore-size distribution index. [XBL 913-744]

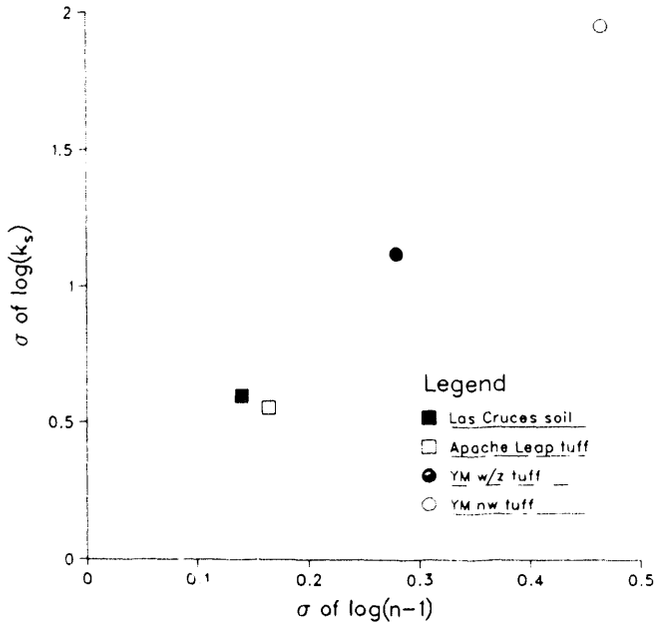

Figure 3. Correlation between standard deviation of saturated permeability and standard deviation of pore-size distribution index. [XBL 914-745]

$\sigma_{log(k_s)} = 4\ \sigma_{log(l)}$ is proposed. There is no similar relationship between $\sigma_{log(k_s)}$ and $\sigma_{log(r_c)}$, even through the mean values are correlated.

For N samples of a given medium, we have $3N$ parameters, with each characteristic curve fitted by two parameters, r_c and λ, and one k_s value. In the Miller and Miller (1956) scaling theory for porous media, the relative pore structures at different magnifications are assumed to be the same. This is equivalent to the assumption that the pore-size distribution index is a constant for a given medium. Then for N samples, we have $2N + 1$ parameters and one λ value for all samples. The results presented in this study suggest that the pore-size distribution index does vary within a given medium. It is correlated with the variation in permeability. Such correlations between the variances of different parameters are not generally obvious from multivariance correlation analyses with traditional statistical programs. The simple relationships among the permeability and pore-geometry parameters, in inter-medium mean values and in intra-medium variances, will motivate more general scaling theories and approaches to quantify hydrological processes through heterogeneous geological formations.

REFERENCES

Miller, E.E., and Miller, R.D., 1956. Physical theory for capillary flow phenomena. J. Applied Phys., v. 27, no. 4, p. 324–332.

Peters, R.R., Klavetter, E.A., Hall, I.J., Blair, S.C., Heller, P.R., and Gee, G.W., 1984. Fracture and matrix hydrologic characteristics of tuffaceous materials from Yucca Mountain, Nye County, Nevada. Sandia National Laboratories Report SAND84-1471, Albuquerque, New Mexico, 188 p.

Rasmussen, T.C., Evans, D.D., Sheets, P.J., and Blanford, J.H., 1990. Unsaturated fractured rock characterization methods and data sets at the Apache Leap tuff site. U.S. Nuclear Regulatory Commission Report NUREG/CR-5596, 125 p.

van Genuchten, M.Th., 1980. A closed-form equation for predicting hydraulic conductivity of unsaturated soils. Soil Sci. Soc. Am. J., v. 44, p. 892–898.

Wierenga, P.J., Hudson, D., Vinson, J., Nash, M., Toorman, A., and Hills, R.G., 1989. Soil properties at the Las Cruces trench site, U.S. Nuclear Regulatory Commission Report NUREG/CR-5441.

Geological Problems in Radioactive Waste Isolation—A World Wide Review

P. A. Witherspoon

The problem of isolating radioactive wastes from the biosphere presents specialists in the earth sciences with some of the most complicated problems they have ever encountered. This is especially true for high-level waste (HLW), which must be isolated in the underground and away from the biosphere for thousands of years. The most widely accepted method of doing this is to seal the radioactive materials in metal cannisters that are enclosed by a protective sheath and placed underground in a repository that has been carefully constructed in an appropriate rock formation.

The HLW problem is complicated because of the heat generated during the decay process. If the HLW is not stored at the surface for a lengthy period of time so as to lose much of its thermal generating capacity, the heat released in the underground can raise the temperature of the repository over a long period of time with a maximum increase of as much as 200°C. The projected size of a repository involves a rock volume on the order of a cubic kilometer, and to predict the effects of significantly raising the temperature of the rock by this amount involves a number of complicated questions. To simplify this problem, several countries have decided to store their HLW at the surface for 40 to 50 yr to dissipate the generated heat and minimize the temperature increases in the underground repository.

The first investigations on storing radioactive waste underground were started in the United States in the early 1960s in a salt mine near Lyons, Kansas, and in West Germany in 1965 using an underground laboratory in the Asse salt mine. The early work at Asse was concerned mainly with various disposal techniques for isolating low-level and medium-level radioactive wastes in rock salt. Later investigations concentrated on problems concerned with high-level waste (Langer et al., 1990). The first effort to study the problems of isolating HLW in granitic rock was initiated in late Spring 1977, when another underground laboratory was set up in an abandoned iron ore mine at Stripa, Sweden. This program was accomplished as part of a Swedish-American cooperative program that was initiated by a bilateral agreement between the U.S. Energy Research and Development Administration (now the U.S. Department of Energy) and the Swedish Nuclear Fuel Supply Company (Witherspoon and Degerman, 1978). The Earth Sciences Division played a lead role in getting this field work started and in bringing to the attention of the international community the importance of investigating waste isolation problems in the underground. This bilateral program was later expanded into the International Stripa Project, which is still operating today.

Essentially every country that is generating electricity in nuclear power plants is faced with the problem of isolating the radioactive wastes that are produced. The general consensus is that this can be accomplished by selecting an appropriate geologic setting and carefully designing the rock repository. Much new technology is being developed to solve the problems that have been raised, and there is a continuing need to publish the results of new developments for the benefit of all concerned.

The 28th International Geological Congress, held July 9–19, 1989, in Washington, D.C., provided an opportunity for earth scientists to gather for detailed discussions on these problems. Workshop W3B, on the subject "Geological Problems in Radioactive Waste Isolation—A World Wide Review," was organized by Paul A. Witherspoon and Ghislain deMarsily and convened July 15–16, 1989. Fifty-eight persons were in attendance from the following 16 countries:

Belgium	The Netherlands
Canada	Soviet Union
China	Spain
France	Sweden
East Germany	Switzerland
West Germany	Taiwan
Italy	United Kingdom
Japan	United States

Reports from all of these countries, except the Soviet Union, have been gathered for publication. Contacts were also made with workers in Argentina, Finland, India, and Yugoslavia, and these contacts have resulted in reports from four additional countries. Representatives from the U.S. Nuclear Regulatory Commission, the OECD Nuclear Energy Agency, the Commission of the European Communities, and the International Atomic Energy Agency were also invited to participate in the workshop. Reports from each of these agencies were also submitted to provide a description of their national and international activities. All of this material was published January 1991 in LBL-29703, a report entitled *Geological Problems in Radioactive Waste Isolation—A World Wide Review*, edited by P.A. Witherspoon.

Table 1. Geologic formations under investigation for radioactive waste isolation projects.

	Sedimentary					
	Clay	Salt	Other	Granitic	Metamorphic	Tuff
Argentina				I†		
Belgium	URF*					
Canada				URF		
China	I		I	I	I	
Finland				I	I	
France	I	I		I	I	
East Germany		I				
West Germany		URF				
India	I			I	I	
Italy	I					
Japan			URF	I	I	
Netherlands		I				
Spain				I		
Sweden				URF		
Switzerland	I			URF		
Taiwan				I	I	
United Kingdom				I	I	
USA		‡				I§
Yugoslavia	I			I	I	

Note:

*Underground research facility.

†Under investigation.

‡Underground research facility currently in operation at WIPP site in New Mexico for military waste.

§Unsaturated zone .

Table 1 presents a summary of the various formations under investigation according to the reports submitted for this world wide review. It can be seen that in those countries that are searching for repository sites, granitic and metamorphic rocks are the prevalent rock type under investigation. Six countries have developed underground research facilities that are currently in use. All of these investigations are in saturated systems below the water table, except the United States project, which is in the unsaturated zone of a fractured tuff.

REFERENCES

Langer, M., Schneider, H., and Kuhn, K., 1990. The salt dome of Gorleben—Target site for the German radioactive waste repository. *In* P.A. Witherspoon (ed.), Geological Problems in Radioactive Waste Isolation—A World Wide Review. Lawrence Berkeley Laboratory Report LBL-29703, p. 57–63.

Witherspoon, P.A., and Degerman, O., 1978. Swedish-American cooperative program on radioactive waste storage in mined caverns. Program summary. Lawrence Berkeley Laboratory Report LBL-7049, 26 p.

Sorptivity of Rocks and Soils of the van Genuchten-Mualem Type

R. W. Zimmerman and G. S. Bodvarsson

One hydrological process that will have great relevance to the performance of the proposed underground radioactive waste repository at Yucca Mountain, Nevada, is that of the absorption of water from a water-filled fracture into the adjacent unsaturated rock formation. The rate at which water is imbibed by a rock depends on the hydrological properties of the rock and on the initial saturation (or initial capillary suction) of the formation. The hydrological properties that affect imbibition are the relative permeability function $k_r(\psi)$ and the capillary pressure function $S(\psi)$, where ψ is the capillary potential, S is the liquid saturation, and k_r is the relative permeability. These functions are often collectively referred to as the "characteristic functions" of the porous medium. For one-dimensional absorption, it can be shown (Zimmerman and Bodvarsson, 1989) that, regardless of the details of the characteristic functions, the total amount of water imbibed by the formation, per unit surface area, will be proportional to the square root of the elapsed time. Hence the ability of a rock or soil to imbibe water can be quantified by a parameter known as the sorptivity **S**, which is defined such that the cumulative volumetric liquid influx per unit area is given by $Q = \mathbf{S}\sqrt{t}$.

One set of characteristic functions that has been frequently used to model the hydrological behavior of rocks and soils, in particular the volcanic tuffs at Yucca Mountain, is that suggested by van Genuchten (1980) and Mualem (1973):

$$k_r(\psi) = \frac{\{1 - (\alpha|\psi|)^{n-1}[1 + (\alpha|\psi|^n)]^{-m}\}^2}{[1 + (\alpha|\psi|)^n]^{m/2}} \quad , \tag{1}$$

$$S(\psi) = S_r + (S_s - S_r)[1 + (\alpha|\psi|)^n]^{-m} \quad , \tag{2}$$

where α is a parameter that has dimensions of 1/pressure, and m, n are parameters related by $m = 1 - 1/n$. A discussion of the physical significance of these parameters is given by Zimmerman and Bodvarsson (1989).

In order to efficiently study the effect that the hydrological parameters and the initial saturation have on the sorptivity, the governing equation for imbibition (see Hillel, 1980) can be simplified by defining a normalized saturation $\hat{S} = (S - S_i)/(S_s - S_i)$, a normalized capillary potential $\hat{\psi} = \alpha\,\psi$, a normalized distance into the formation $\hat{x} = \sqrt{(\alpha\mu\phi/k)}x$, and a reduced time $\hat{t} = t/(S_s - S_i)$. In these transformations, k is the absolute (single-phase) permeability of the medium, ϕ is the porosity of the medium, μ is the viscosity of the pore water, and S_i is the initial saturation of the formation before imbibition begins. The governing equation can then be written as (Zimmerman and Bodvarsson, 1991)

$$\frac{\partial \hat{S}}{\partial \hat{t}} = \frac{\partial}{\partial \hat{x}}\left[D(\hat{S})\frac{\partial \hat{S}}{\partial \hat{t}}\right] , \tag{3}$$

in which the effective diffusion coefficient is related to the characteristic functions by

$$D(\hat{S}) = k_r(\hat{S})\frac{d\hat{\psi}}{d\hat{S}} \quad . \tag{4}$$

The boundary and initial conditions for the imbibition problem are $\hat{\psi}(\hat{x} = 0, \hat{t}) = 0$, $\hat{\psi}(\hat{x}, \hat{t} = 0) = \hat{\psi}_i$, and $\hat{\psi}(\hat{x} \to \infty, \hat{t}) = \hat{\psi}_i$, where the normalized initial potential $\hat{\psi}_i$ is related to the normalized initial saturation $\hat{S}_i$ by Eq. (2).

Depending on the degree of accuracy and detail required for a particular application, various types of exact and approximate methods exist for finding the sorptivity. Zimmerman and Bodvarsson (1989) presented an approximate solution to this problem by applying the "integral" or "boundary-layer" approach, which consists of assuming a saturation profile that depends upon the initially unknown wetting-front location and then determining the location of the wetting front by requiring the profile to satisfy the integrated form of the governing Richards equation. This analysis produced an approximate solution for the sorptivity in a very simple algebraic form, with an accuracy that was typically about 5–10%. For many purposes, such as incorporation into a double-porosity model, such accuracy should suffice. If exact results for the sorptivity and the saturation profile are needed, these can be found with the program BOLTZ, developed by Zimmerman and Bodvarsson (1989), which uses the Boltzmann transformation to convert Eq. (3) into an ordinary differential equation and then performs fourth-order Runge-Kutta integration. This program leads to essentially exact values of the sorptivity, although it does require exceedingly small integration steps when the initial saturation is very close to the irreducible value. In some situations, an accurate estimate of the sorptivity may be required, but detailed knowledge of the saturation profile may not be needed. For such cases, we have found that the sorptivity approximation proposed by Youngs and Parlange (see Brutsaert, 1976) is convenient.

The Youngs-Parlange sorptivity approximation can be expressed as

$$\mathbf{S}_{YP}^2 = 2(S_s - S_i)\int_0^{\chi_i} k_r(\chi)\,d\chi \quad , \tag{5}$$

where, since the capillary potential is inherently < 0, we use the dummy variable $\chi = |\hat{\psi}|$. For a van Genuchten-Mualem medium, this approximation takes the form

$$S_{YP}^2 = 2(S_s - S_i)$$

$$\times \int_0^{\chi_i} \left[\frac{1}{(1+\chi^n)^{m/2}} - \frac{2\chi^{n-1}}{(1+\chi^n)^{3m/2}} + \frac{\chi^{2(n-1)}}{(1+\chi^n)^{5m/2}} \right] d\chi \quad , \quad (6)$$

which can be evaluated to yield

$$S_{YP}^2 = \frac{2(S_S - S_i)}{n} \left[B_\omega\left(\frac{1}{n}, \frac{m}{2} - \frac{1}{n}\right) \right.$$

$$\left. - 2B_\omega\left(1, \frac{3m}{2} - 1\right) + B_\omega\left(2 - \frac{1}{n}, \frac{5m}{2} - 2 + \frac{1}{n}\right) \right] \quad , \quad (7)$$

where $\omega = |\hat{\psi}_i|^n/(1 - |\hat{\psi}_i|^n)$ and $B_\omega(p,q)$ is the incomplete Beta function (Erdelyi, 1953).

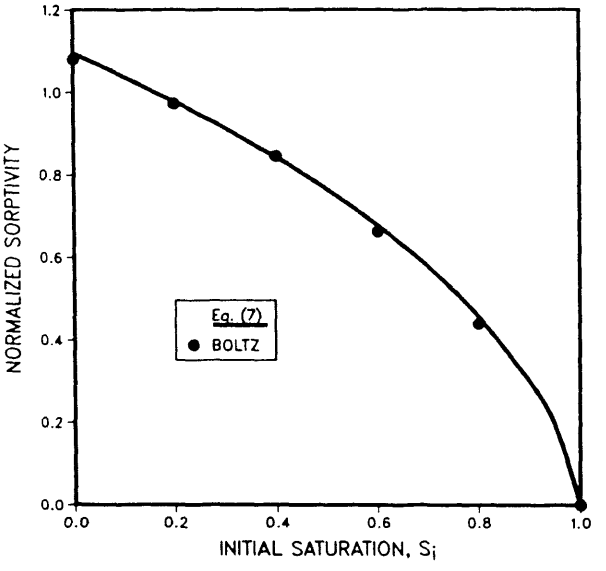

Figure 1. Normalized sorptivity of a rock or soil of the van Genuchten-Mualem type as a function of the initial saturation S_i, with $n = 3$, $S_s = 1$, and $S_r = 0$. [XBL 913-499]

As an example of the accuracy of this sorptivity approximation, consider the case $n = 3$, which is close to the value estimated for the Topopah Spring welded tuff at Yucca Mountain (see Zimmerman and Bodvarsson, 1989). To simplify the display of the data, we take $S_s = 1$ and $S_r = 0$. Figure 1 shows the sorptivity predicted by Eq. (7), compared with a few values calculated by the BOLTZ program. Equation (7) is seen to be accurate to within about 1% over the entire range of initial saturations. Hence, if an accurate estimate of the sorptivity is required, Eq. (7) can be used in place of explicit Runge-Kutta integration. Although Eq. (7) also requires numerical integration, it has the advantage that the integrals involved do not become singular as the initial saturation approaches the irreducible value. If, however, precise knowledge of the full saturation profile is needed, the BOLTZ program should be used.

REFERENCES

Brutsaert, W., 1976. The concise formulation of diffusive sorption of water in a dry soil. Water Resour. Res., v. 12, p. 1118–1124.

Erdelyi, A., 1953. Higher Transcendental Functions (Vol. I). McGraw-Hill, New York, p. 87.

Hillel, D., 1980. Fundamentals of Soil Physics. Academic Press, San Diego, California.

Mualem, Y., 1973. Modified approach to capillary hysteresis based on a similarity hypothesis. Water Resour. Res., v. 9, p. 1324–1331.

van Genuchten, M.Th., 1980. A closed-form equation for predicting the hydraulic conductivity of unsaturated soils. Soil Sci. Soc. Am. J., v. 44, p. 892–898.

Zimmerman, R.W., and Bodvarsson, G.S., 1989. An approximate solution for one-dimensional absorption in unsaturated porous media. Water Resour. Res., v. 25, p. 1422–1428.

Zimmerman, R.W., and Bodvarsson, G.S., 1991. Reply to "Comment on 'An approximate solution for one-dimensional absorption in unsaturated porous media' by R.W. Zimmerman and G.S. Bodvarsson," by Parlange et al. Submitted to Water Resour. Res. (LBL-29912).

Lubrication Theory Analysis of the Permeability of Rough-Walled Fractures

R. W. Zimmerman, S. Kumar, and G. S. Bodvarsson

The flow of fluid through rock fractures is an important geophysical phenomenon that has much relevance to problems such as the underground disposal of radioactive wastes, enhanced oil recovery, and the production of geothermal energy. To simplify the mathematical analysis, rock fractures have often been modeled as consisting of smooth, parallel walls. This leads to the well-known "cubic law," in which the permeability k is related to the aperture d by $k = d^2/12$ (Snow, 1966). However, real fractures are "rough-walled," with apertures that vary from point to point. The flow of a fluid between the rough surfaces of a rock fracture is very complex, because of the tortuous paths followed by the fluid particles. Exact analytical modeling of these flows is made difficult by the irregular geometry, and full three-dimensional numerical simulations of these flows are as yet still impractical. To overcome the difficulties of working with the three-dimensional Navier-Stokes equations, the simpler Reynolds lubrication equation is sometimes used. This equation is easier to solve than are the full three-dimensional Navier-Stokes equations, yet it still allows variations in aperture to be accounted for.

We have carried out a detailed mathematical analysis of the applicability of the lubrication equation to flow in rough-walled fractures. First, we applied the theory to two simplified aperture profiles, sinusoidal and "sawtooth," and found analytical expressions for the permeabilities. The predicted permeabilities depend on the mean and the standard deviation of the aperture but are otherwise somewhat insensitive to the precise details of the aperture distributions. The predicted permeabilities were also very similar to numerical results (Patir and Cheng, 1978; Brown, 1987) that had previously been obtained by solving the lubrication equation for fractures with "random" surfaces, implying some universal validity to the relationships. Second, the validity of the lubrication equations for modeling flow in rough fractures was studied by examining higher-order perturbation solutions, as well as numerical solutions, to the full Navier-Stokes equations. A criterion was developed for the applicability of the lubrication approximation in terms of the ratio of the standard deviation of the aperture to the dominant wavelength of the roughness. Fortunately, this criterion seems to be met by most naturally occurring rock fractures.

LUBRICATION THEORY EQUATIONS

The flow of a Newtonian fluid through a rock fracture is governed by the nonlinear Navier-Stokes equations of fluid mechanics (Schlichting, 1968). Under certain geometric and kinematic conditions, which usually are assumed to hold for rock fractures, the Navier-Stokes equations can be reduced to the simpler Reynolds equation. One requirement for the Reynolds equation to be valid is that viscous forces dominate the inertial forces. The other main requirement is that, in some sense, the aperture variations are not too "rapid." If these dynamic and geometric conditions hold, the flow can be described by the Reynolds lubrication equation:

$$\frac{\partial}{\partial x}\left(d^3(x,y)\frac{\partial P}{\partial x}\right)+\frac{\partial}{\partial y}\left(d^3(x,y)\frac{\partial P}{\partial y}\right)=0\,. \tag{1}$$

where (x,y) are orthogonal coordinates in the plane of the fracture and $d(x,y)$ is the local aperture of the fracture. Equation (1) is a single, linear partial differential equation that describes the pressure field in the fracture plane. The volumetric flow of liquid is then related to the pressure by

$$\vec{Q}=\frac{-d^3(x,y)}{12\mu}\nabla P\,. \tag{2}$$

EFFECT OF APERTURE VARIATIONS

We have used the lubrication equation to analyze the flow in fractures whose profiles are simple enough to allow analytical treatment, but which still capture some of the flavor of "rough-walled" fractures. To accomplish this, we first restrict Eq. (1) to one dimension. Although this is an approximation, we note that the flow will always be locally one-dimensional; furthermore, the two-dimensional character of the flow field can be accounted for by an averaging procedure. If the x axis is chosen so as to coincide with the macroscopic pressure gradient, then the one-dimensional version of Eq. (1) is simply

$$\frac{d}{dx}\left(d^3(x)\frac{dP}{dx}\right)=0\,. \tag{3}$$

Two integrations of Eq. (3), when combined with Eq. (2), yield

$$Q=\frac{d_h^3}{12\mu}\frac{\Delta P}{L},\quad \text{where}\quad d_h=\left[\frac{1}{L}\int_{x_1}^{x_2}\frac{dx}{d^3(x)}\right]^{-1/3}, \tag{4}$$

and $L = x_2 - x_1$. Using angle brackets to denote the "mean value," Eq. (4) can be expressed as $d_h = \langle d^{-3}\rangle^{-1/3}$.

One of the simplest aperture profile functions that has some of the geometrical properties of a "rough-walled" fracture is a constant aperture with a sinusoidal perturbation (Figure 1):

$$d(x) = d_m [1 + \delta \sin(2\pi x/\lambda)] , \quad (5)$$

where d_m is the mean aperture, δ is the magnitude of the "roughness," and λ is the wavelength of the aperture oscillations. First we imagine that all cross sections parallel to the plane of Figure 1 are identical. If the flow is in the direction transverse to the aperture oscillations (i.e., the x direction), then the hydraulic aperture can be found by considering Eq. (4) over one spatial wavelength. After evaluating the resulting integral, we find

$$d_h^3 = d_m^3 \frac{(1 - \delta^2)^{5/2}}{1 + (\delta^2/2)} . \quad (6)$$

Equation (6) assumes that the resistances due to each aperture element are in series, since the flow through each element is the same. The other extreme assumption would be that all of the resistances are in parallel. This would correspond to flow "into the page" of Figure 1, and would be equivalent to an hydraulic aperture given by

$$d_h^3 = \langle d^3 \rangle,$$

that is,

$$d_h^3 = d_m^3 [1 + (3\delta^2/2)] . \quad (7)$$

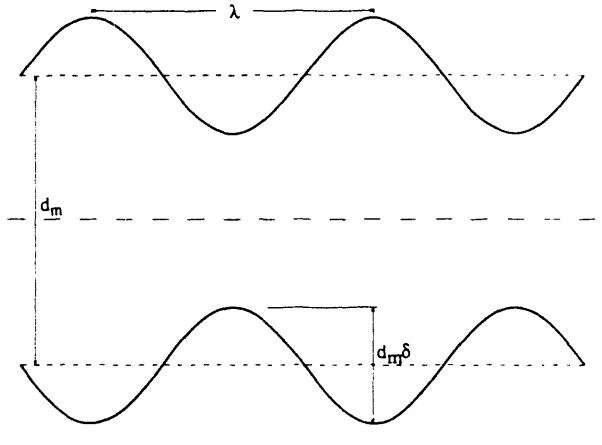

Figure 1. Fracture with a sinusoidal variation in aperture; d_m is the mean aperture, δ is the relative amplitude of the aperture variation, and λ is the wavelength of the aperture variation. [XBL 913-500]

It is known from network theory that the assumption that all of the resistors in a random resistor network are in series (or parallel) provides lower (or upper) bounds, respectively, to the actual effective conductivity. In our problem, we know that at some points the fluid will be flowing parallel to the aperture oscillations, while in some cases it will be flowing transverse to the oscillations. One simple way to arrive at an estimate of the effective conductivity of a "random mixture" of these two cases is to use the geometric mean of the conductivities given by Eqs. (6) and (7):

$$d_h^3 = \sqrt{d_h^3(\text{series}) \times d_h^3(\text{parallel})}$$

$$= d_m^3 \left\{ \frac{[1 + (3\delta^2/2)](1 - \delta^2)^{5/2}}{1 + (\delta^2/2)} \right\}^{1/2} . \quad (8)$$

The permeabilities predicted by Eq. (8) are plotted in Figure 2 as a function of d_m/σ, where $\sigma = d_m\delta/\sqrt{2}$ is the standard deviation of the aperture distribution. The predictions are similar to the numerical values found by Patir and Cheng (1978) and Brown (1987), who numerically solved the lubrication equation for randomly distributed apertures.

We have also investigated the extent to which additional roughness with higher spatial frequencies alters the results. This was done by using a profile that contains two sinusoidal components; the analysis showed that the addition of this "smaller scale roughness" has only a minor effect on the relationship between d_h/d_m and d_m/σ (see

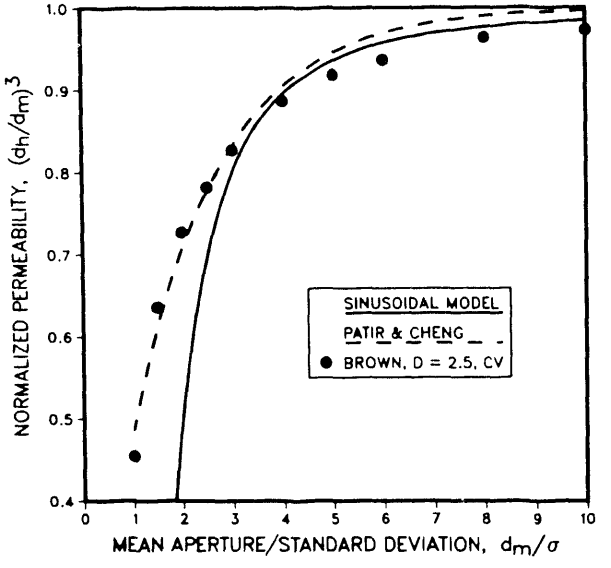

Figure 2. Permeability of a fracture as a function of the mean and the standard deviation of the aperture distribution. Analytical values for the sinusoidal model are similar to numerical values for fractures with random aperture distributions. [XBL 913-501]

Zimmerman et al., 1991). A similar analysis was also carried out for a fracture with a "sawtooth" profile, such as that used by Elsworth and Goodman (1986). This analysis leads to a different expression for the d_h/d_m vs. σ/d_m relationship; however, if plotted as in Figure 2, the permeability of the sawtooth profile would be very close to that of the sinusoidal profile. In fact, the two expressions agree exactly to "first order": $(d_h/d_m)^3 = 1 - 1.5(\sigma/d_m)^2$. The dependence of d_h/d_m on the single parameter σ/d_m therefore appears to be somewhat insensitive to shape.

ACCURACY OF LUBRICATION APPROXIMATION

Strict "error estimates" for the lubrication theory approximation to the Navier-Stokes equations are difficult to derive. A more tractable approach is to focus on a specific geometry, such as that shown in Figure 1, and examine the solutions to higher-order approximations to the Navier-Stokes equations. In this way we can find the range of values for the parameter σ/λ for which the lubrication approximation is "valid." This will provide us with a rough rule of thumb that should apply to more general fracture aperture profiles. Hasegawa and Izuchi (1983) performed a perturbation analysis of the problem of flow between a smooth wall and a wall with sinusoidal roughness. Although this geometry is slightly different from that shown in Figure 1, it can still serve to demonstrate the influence of the effects of roughness, wavelength, etc., on permeability. When translated into the present notation, their results can be put into the following form:

$$d_h^3 = d_m^3 \frac{(1-\delta^2)^{5/2}}{1+(\delta^2/2)}\left[1 - \frac{6\pi^2(1-\delta^2)\delta^4}{10[1+(\delta^2/2)]}\left(\frac{d_m}{\lambda}\right)^2\right]. \qquad (9)$$

The second term in brackets in Eq. (9) is the correction due to nonzero values of σ/λ. In order to understand the implications of this equation, we first note that the amplitude of the roughness usually drops off rapidly with increasing spatial frequency. It is typically found (Kumar and Bodvarsson, 1990) for rock fracture profiles that $\delta \approx C\lambda^s$, where s lies between 1.0 and 1.5. Hence if λ is small, δ will necessarily be small also, and the correction term will remain bounded. For example, consider the "worst case," $s = 1$, for which $\delta = C\lambda$. The correction term in Eq. (9) then scales as $\lambda^4/\lambda^2 = \lambda^2$ and will therefore be very small for small spatial wavelengths.

The most stringent condition that we can derive by requiring the correction term to be small is found by considering the largest wavelength roughness. We first replace d_m with $\sqrt{2}\sigma/\delta$ and note that, over the physically meaningful range $0 < \delta < 1$, the maximum value of the term that multiplies $(\sigma/\lambda)^2$ is 2.39. Therefore, if we want to restrict the relative magnitude of the correction term to 10% of the value predicted by lubrication theory, we must have $2.39(\sigma/\lambda)^2 < 0.10$, which implies $\lambda > 5\sigma$. This condition is much less restrictive than the condition that was postulated by Brown (1987), which was $\lambda > 50\sigma$. If we agree that a sinusoidal surface can be considered "smooth" over lengths not greater than about $\lambda/10$, this new criterion can (very roughly) be viewed as requiring the surfaces to be smooth over lengths on the order of σ.

REFERENCES

Brown, S.R., 1987. Fluid flow through rock joints: The effect of surface roughness. J. Geophys. Res., v. 92, no. B2, p. 1337–1347.

Elsworth, D., and Goodman, R.E., 1986. Characterization of rock fissure hydraulic conductivity using idealized wall roughness profiles. Int. J. Rock Mech. Min. Sci. & Geomech. Abstr., v. 23, no. 3, p. 233–243.

Hasegawa, E., and Izuchi, H., 1983. On steady flow through a channel consisting of an uneven wall and a plane wall, Part 1, Case of no relative motion in two walls (sic). Bull. Jap. Soc. Mech. Eng., v. 26, p. 514–520.

Kumar, S., and Bodvarsson, G.S., 1990. Fractal study and simulation of fracture roughness. Geophys. Res. Lett., v. 17, no. 6, p. 701–704.

Patir, N., and Cheng, H.S., 1978. An average flow model for determining effects of three-dimensional roughness on partial hydrodynamic lubrication. ASME J. Lubr. Technol., v. 100, no. 1, p. 12–17.

Schlichting, H., 1968. Boundary-Layer Theory (6th ed.). McGraw-Hill, New York.

Snow, D.T., 1968. Rock fracture spacings, openings, and porosities. J. Soil Mech. Found. Div. ASCE, v. 94, no. SM1, p. 73–91.

Zimmerman, R.W., Kumar, S., and Bodvarsson, G.S., 1990. Lubrication theory analysis of the permeability of rough-walled fractures. Int. J. Rock Mech. Min. Sci. & Geomech. Abstr. (in press) (LBL-30534).

GEOLOGY AND GEOCHEMISTRY

Investigators in the Geology and Geochemistry group primarily study causes and results of chemical reactions in the earth's crust. These reactions result from interactions between subsurface aqueous fluids and the surrounding soil and rock, causing chemical alteration of the solids and changes in the chemistry of the fluids. Since many of these reactions occur during the movement of fluids, our studies are quite germane to the disposal and isolation of radioactive and toxic wastes. Successful containment of waste species depends strongly on arresting the movement of dissolved chemical species in groundwater. In this respect, specific investigations in areas of isotope geochemistry, radiochemistry, inorganic chemistry, and surface chemistry are all applicable to reactive chemical transport models. Field-oriented research pertinent to chemical transport encompasses the coupling of hydrology with isotope geology, aqueous analytical chemistry, chemical-species modeling, and hydrochemistry. Projects emphasizing geochemical and chemical modeling of nuclear waste repositories focus on how both radionuclide and major groundwater species react and migrate under conditions close to and away from the repository.

The group also conducts basic research on processes that occur in the earth's crust and oceans, including examination of isotopic evidence for interactions of components within the crust and between the crust and mantle and studies of the thermodynamics of high-temperature brines at mid-ocean ridges. The geochemistry of geothermal systems and the paleoclimatic implications of isotopic variations are also under investigation. Members participate in the Continental Scientific Drilling program and in studies to define the occurrence and movement of radon and its parent radioisotopes in rock and soil. Research is also in progress on interfacial chemical reactions that address both solid-liquid and solid-gas reactions on mineral surfaces.

On the Treatment of Oxidation-Reduction Reactions in a Numerical Simulator of Reactive Chemical Transport

C. L. Carnahan

The computer program THCC is a numerical simulator of the advective/diffusive transport of reactive chemicals and heat in saturated porous media (Carnahan, 1987, 1988a,b). THCC directly couples solute transport processes to chemical reactions at equilibrium, in the sense that numerical solutions of the transport equations are obtained while simultaneously the chemical mass action relations are satisfied. Chemical reactions included in THCC are complexation and pH changes in the aqueous phase, reversible precipitation/dissolution of minerals, and homogeneous and heterogeneous oxidation-reduction reactions. A variant, THCCIX, treats ion exchange in addition to the other reaction types (Jacobsen and Carnahan, 1988, 1989). This discussion is concerned with the treatment of oxidation-reduction reactions in THCC.

Two methods for treating oxidation-reduction reactions are available in THCC. The "direct" method assumes that the oxidation potential is controlled directly by chemical reactions included in the simulation. The "indirect," or "electron activity," method assumes that the oxidation potentials of initial and boundary systems are controlled either by one or more dominant oxidation-reduction couples or by processes external to the simulation, such as an externally imposed electrical potential. This article briefly describes the principles underlying each method. Four example simulations illustrate the differences between the methods. It is seen that if one oxidation-reduction couple dominates the chemical system, certain results of the two methods become indistinguishable.

ANALOGY BETWEEN COMPLEXATION AND OXIDATION-REDUCTION REACTIONS

In THCC, the reduction of a species in a high oxidation state by a reductant to form a species in a low oxidation state (the high- and low-oxidation state species being the members of an oxidation-reduction couple) is analogous to the reaction between two or more basis species to form an aqueous complex. [The set of basis species is the minimum set of aqueous species required to define all other species (aqueous, sorbed, and solid) in the chemical system. The required number of basis species equals the number of chemical "components" in the sense of the Gibbs phase rule.] For example, chloride complexation of the Fe^{3+} ion can be written

$$Fe^{3+} + 6\,Cl^- = FeCl_6^{3-} ,$$

and a hydrolysis reaction can be written

$$Fe^{3+} + 2\,H_2O - 2\,H^+ = Fe(OH)_2^+ .$$

Here, Fe^{3+}, Cl^-, and H^+ are basis species and $FeCl_6^{3-}$ and $Fe(OH)_2^+$ are complexes. A similar convention is adopted in THCC for oxidation-reduction reactions, in that the high-oxidation state members of oxidation-reduction couples are treated as basis species and the low-oxidation state members are treated as "complexes." This implies that at least one basis species must be designated a reductant. In the direct method the reductant is a low-oxidation state member of one of the oxidation-reduction couples, whereas in the indirect method the reductant is a hypothetical free electron, e^-, an imaginary surrogate for the reducing potential of the system. Consider a system containing the oxidation-reduction couples $A^{2+} - A^+$, $B^{2+} - B^+$, and $C^{2+} - C^+$. In the indirect method, the oxidation-reduction reactions would be posed as

$$A^{2+} + e^- = A^+,$$
$$B^{2+} + e^- = B^+,$$
$$C^{2+} + e^- = C^+.$$

Here, A^{2+}, B^{2+}, C^{2+}, and e^- (the reductant) are basis species, and A^+, B^+, and C^+ are "complexes." In the direct method, e^- is replaced by, say, C^+, and the reaction set becomes

$$A^{2+} + C^+ - C^{2+} = A^+,$$
$$B^{2+} + C^+ - C^{2+} = B^+.$$

Here again, A^{2+}, B^{2+}, and C^{2+} are basis species and A^+ and B^+ are "complexes," but now C^+ (the reductant) is another basis species.

THCC uses well-established thermodynamic relations to relate activities of members of oxidation-reduction couples to the oxidation potential and the hypothetical electron activity. Consider a reduction half-cell reaction in which a species "ox" reacts with transfer of n electrons to form a reduced species "red," thus:

$$ox + n\,e^- = red.$$

The oxidation potential, Eh, referred to the hydrogen electrode, of the "ox-red" couple is given by

$$Eh = E^0 + \frac{RT}{nF} \ln \frac{[ox]}{[red]} , \qquad (1)$$

where the [ ] denote activities, E^0 is the standard electrode potential (on the hydrogen scale) for the reaction, R is the gas constant, F is the Faraday constant, and T is the absolute temperature; E^0 is related to the equilibrium constant, $K(T)$, for the reaction by

$$E^0 = \frac{RT}{nF} \ln K(T) \quad . \tag{2}$$

The hypothetical electron activity, a_e, is related to the Eh by

$$a_e = [e^-] = \exp\left(-\frac{EhF}{RT} \right). \tag{3}$$

EXAMPLE SIMULATIONS

Four example simulations were run with the THCC program to illustrate differences between the two oxidation-reduction options and the effects of one oxidation-reduction couple dominating the chemical system. In all four cases, fluid flows into a porous-medium spatial domain at the boundary $x = 0$. The pore fluid velocity of the influent fluid is 1×10^{-6} m/s, and the coefficient of hydrodynamic dispersion in the spatial domain is 5×10^{-8} m^2/s. The Eh of the fluid initially occupying the spatial domain is –0.2 V, and the Eh of the influent fluid is +0.2 V. The chemical system is composed of two oxidation-reduction couples, $A^{2+} - A^+$ and $B^{2+} - B^+$. In all cases, the total concentration of substance A, denoted (A), is the same in both initial and influent fluids and is equal to 1×10^{-8} M. In two cases, the total concentration of substance B, denoted (B), is equal to 1×10^{-8} M in both fluids [the same as (A), the "low-(B)" cases], whereas in the other two cases (B) equals 1×10^{-3} M in both fluids [the "high-(B)" cases]. The low-(B) and high-(B) cases were treated by both the direct and indirect methods. The following reaction schemes and thermodynamic data were used:

Reaction	E^0 (V)	log K
Indirect method		
$A^{2+} + e^- = A^+$	+0.178	+3.00
$B^{2+} + e^- = B^+$	–0.118	–2.00
Direct method		
$A^{2+} + B^+ - B^{2+} = A^+$	+0.296	+5.00

Results of the simulations at the simulated elapsed time of 1×10^6 s are shown in Figures 1–5. Figure 1 shows spatial profiles of concentrations of higher oxidation-state species (A^{2+}, B^{2+}). The direct method produces slightly sharper B^{2+} profiles than the indirect method in both high- and low-(B) cases. The A^{2+} profiles generated by the direct method are very sharp for low (B) and tend toward the

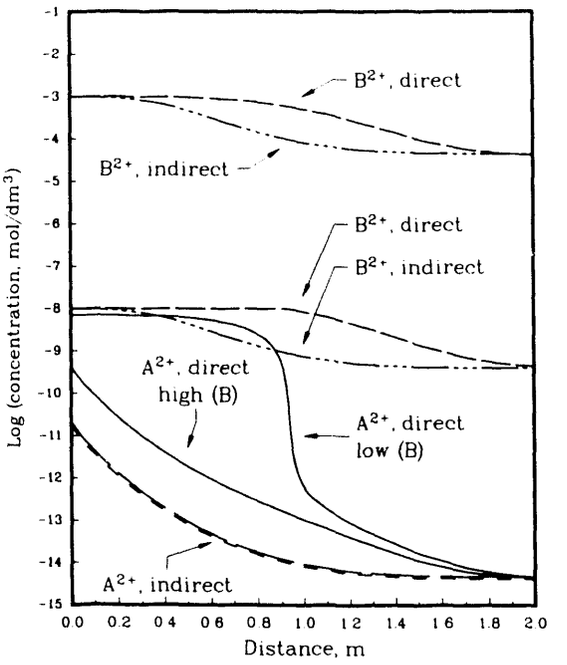

Figure 1. Concentration profiles of oxidized species at simulated time 1×10^6 s. [XBL 913-561]

profiles generated by the indirect method as (B) increases. The high- and low-(B) profiles generated by the indirect method are almost indistinguishable. Figure 2 shows profiles of concentrations of lower oxidation-state species

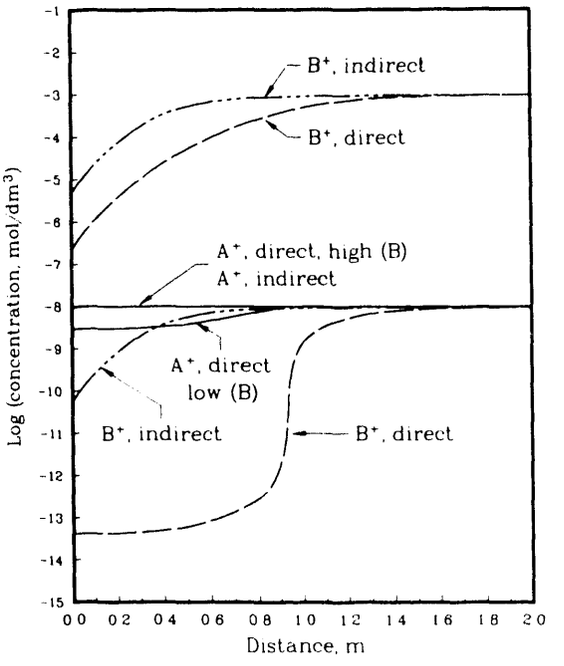

Figure 2. Concentration profiles of reduced species at simulated time 1×10^6 s. [XBL 913-562]

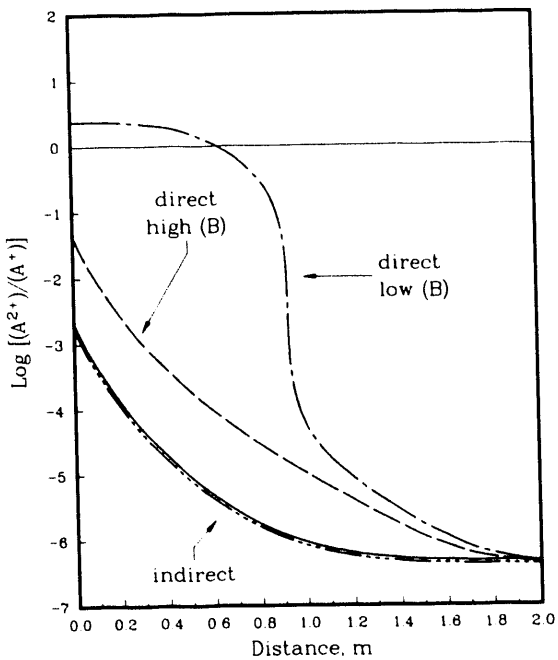

Figure 3. Profiles of ratio $(A^{2+})/(A^{+})$ at simulated time 1×10^{6} s. [XBL 913-563]

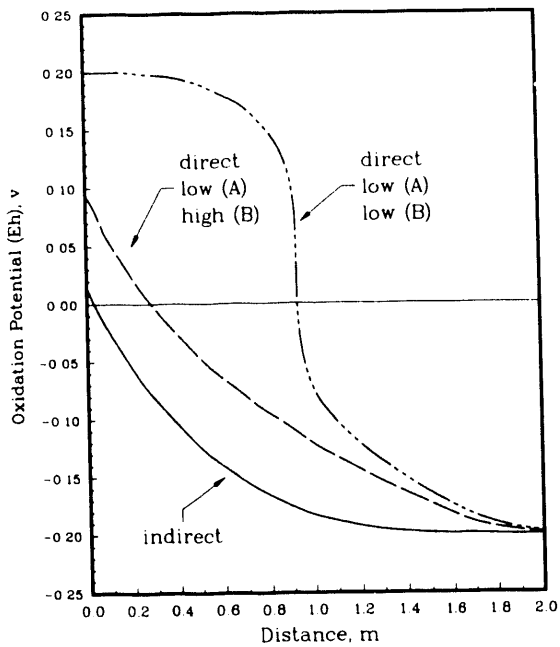

Figure 5. Profiles of oxidation potential (Eh) at simulated time 1×10^{6} s. [XBL 913-565]

(A^{+}, B^{+}). Noteworthy features here are the contrast in sharpness between the direct-method B^{+} profiles for the high- and low-(B) cases, and the similarity in shape of the high- and low-(B) profiles of B^{+} for the indirect method.

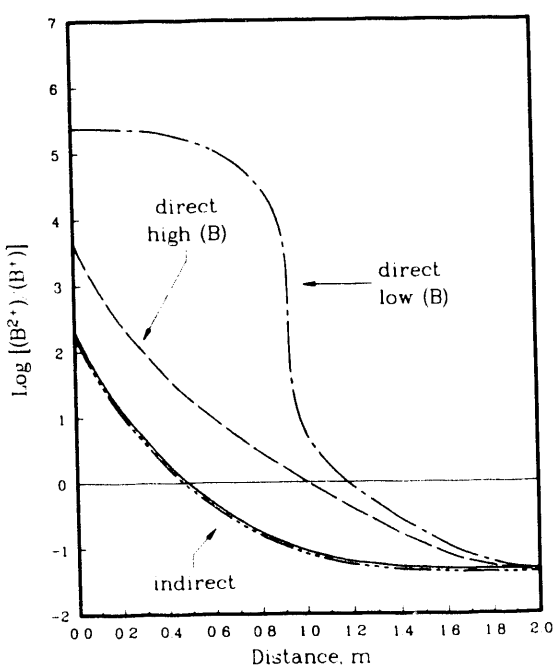

Figure 4. Profiles of ratio $(B^{2+})/(B^{+})$ at simulated time 1×10^{6} s. [XBL 913-564]

Moreover, the profiles of A^{+} for the direct, high-(B) case and both indirect cases are indistinguishable from each other but are distinct from the profile of A^{+} for the direct, low-(B) case. Figure 3 shows profiles of the ratio of concentrations, $(A^{2+})/(A^{+})$, for the four cases. As (B) increases, the direct-method profiles tend toward the indirect-method profiles, the latter two being almost indistinguishable. Figure 4 is similar to Figure 3 but is for the $(B^{2+})/(B^{+})$ ratio. Features similar to those in Figure 3 are observed here. Figure 5 shows profiles of Eh generated in the four cases. The indirect method produces the same Eh profile regardless of the value of (B). Again, the tendency of the direct-method profiles to approach the indirect-method profiles with increasing (B) is evident.

CONCLUSIONS

The results of these simulations, and of others not discussed here, lead to the following general observations:

1. In the indirect method, the explicitly specified oxidation-reduction system behaves as if a very large excess of another hypothetical oxidation-reduction couple were present. Oxidation-reduction behavior of the hypothetical couple is specified implicitly by initial and boundary values of oxidation potential.
2. In the direct method, the oxidation-reduction behavior of the system is determined solely by the simulated species.

3. Results of simulations using the direct method approach those of the indirect method if one oxidation-reduction couple becomes dominant.

Thus, in simulations of oxidation-reduction behavior during transport of trace-level species in the presence of relatively high concentrations of other oxidation-reduction couples (the latter controlling the oxidation potential of the chemical system), considerable savings of computer time and array storage can be realized by use of the indirect method in THCC.

REFERENCES

Carnahan, C.L., 1987. Simulation of uranium transport with variable temperature and oxidation potential: the computer program THCC. *In* J.K. Bates and W.B. Seefeldt (eds.), Scientific Basis for Nuclear Waste Management X (Materials Research Society Symposium Proceedings, Vol. 84). Materials Research Society, Pittsburgh, Pennsylvania, p. 713–721.

Carnahan, C.L., 1988a. Simulation of effects of redox and precipitation on diffusion of uranium solution species in backfill. *In* M.J. Apted and R.E. Westerman (eds.), Scientific Basis for Nuclear Waste Management XI (Materials Research Society Symposium Proceedings, Vol. 112). Materials Research Society, Pittsburgh, Pennsylvania, p. 293–302.

Carnahan, C.L., 1988b. Some effects of data base variations on numerical simulations of uranium migration. Radiochimica Acta, v. 44/45, p. 349–354.

Jacobsen, J.S., and Carnahan, C.L., 1988. Numerical simulation of alteration of sodium bentonite by diffusion of groundwater components. *In* M.J. Apted and R.E. Westerman (eds.), Scientific Basis for Nuclear Waste Management XI (Materials Research Society Symposium Proceedings, Vol. 112). Materials Research Society, Pittsburgh, Pennsylvania, p. 415–424.

Jacobsen, J.S., and Carnahan, C.L., 1989. Numerical simulation of cesium and strontium migration through sodium bentonite altered by cation exchange with groundwater components. *In* W. Lutze and R.C. Ewing (eds.), Scientific Basis for Nuclear Waste Management XII (Materials Research Society Symposium Proceedings, Vol. 127). Materials Research Society, Pittsburgh, Pennsylvania, p. 749–754.

Laboratory for Spatially Resolved Texturally Controlled Microsampling of Minerals and Rocks

S. G. Borg, D. J. DePaolo, and B. M. Smith

A microsampling laboratory has been developed in the Berkeley Center for Isotope Geochemistry to facilitate acquisition of small samples of solid materials for earth science research. The facility is designed for precise sampling from specimen slabs in a clean laboratory that is kept at positive pressure with a HEPA-filtered air supply. The central feature of the initial facility is a microdrill apparatus equipped with an optical microscope/video monitor system (MAS: Microsample Acquisition System), which is designed for acquiring samples ranging from < 1 microgram up to several milligrams in mass. A spatial resolution of 25 μm can be achieved with textural control. When combined with isotope-dilution mass spectrometry, MAS constitutes a high-precision chemical-isotopic microprobe with the capability of measuring trace element concentrations to ±0.1% relative precision and isotopic abundance ratios to 0.005% relative precision The laboratory is also equipped with a high-quality research petrographic microscope, a low-power reflected-light binocular microscope, a laminar flow work bench, a semimicro balance, a micro-balance, and equipment for obtaining samples weighing up to several tens of milligrams by drilling.

DESCRIPTION OF MAS

The MAS consists of (1) a precision drill press, (2) an electronically controlled moveable sample stage, (3) a light source for transmitted light, (4) a binocular microscope with mirror assembly and video camera, (5) a solid-optics borescope with fiber-optic light source and video camera, (6) a video tape recorder, and (7) two color video monitors. Items (1)–(4) are attached to a custom designed frame to facilitate their interaction. The frame, the mirror assembly, and the sample stage were manufactured at Lawrence Berkeley Laboratory. The MAS is shown schematically in Figure 1.

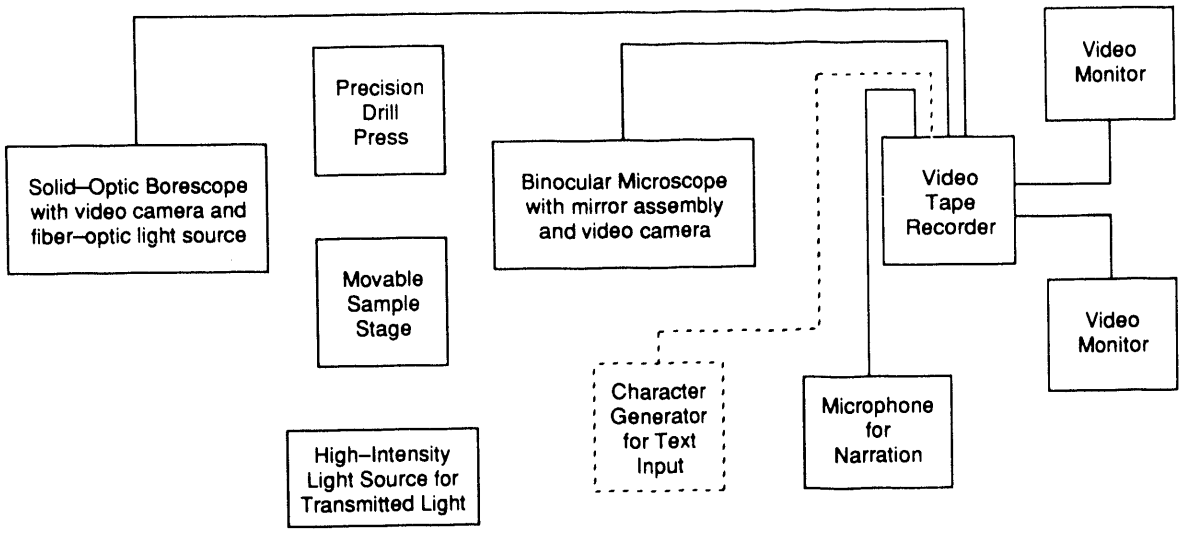

Figure 1. Schematic diagram of MAS (Microsample Acquisition System). Broken lines indicate that the character generator is a planned component. [XBL 913-566]

The precision drill press was acquired from a commercial source. Drill speed is fully adjustable up to 20,000 rpm (no load), and the drill accepts bits with shank diameter up to about 5 mm. It has a micrometer (smallest increment is 0.05 mm) to measure downward drill movement and an adjustable stop to limit drill penetration. Size, shape, and material of the drill bit cutting surface can vary according to sample hardness and research needs. Tungsten carbide and hardened steel tips are used mainly, but composite tips with diamond or carbide particles embedded in ceramic, epoxy resin, or metal alloy can be used as well. Drill bits used so far have tip diameters in the range of 0.2–1 mm: bits are available with diameters down to 25 μm.

The sample stage is motor-driven with joy-stick control of movement in the horizontal plane to adjust sample position so that the desired site is directly under the drill bit. The stage assembly can be manually raised and lowered for ease of inserting or removing samples. The stage has a clear glass plate in the work surface area to allow use of transmitted light from a high-intensity light source. For thin slabs, transmitted light is useful for mineral identification and to ensure that the desired material is present at depth in the sample.

A binocular microscope with zoom magnification of 7.5× to 64× provides the main viewing port. It is set up in a side-looking configuration (i.e., the view is parallel to the stage surface) with the stage and sample surface visible in the lower portion of the field of view. An adjustable mirror assembly allows viewing of the drill bit and drill site from above the sample, approximately parallel with the bit. A slot in the mirror allows the drill bit to make contact with the sample. A solid-optic borescope with a high-intensity fiber-optic light source can also be used for observing the drill site and the drilling procedure. It is not attached to the frame and can therefore be adjusted to whatever view is desired. Both the microscope and the borescope are equipped with video cameras. A 35 mm camera can also be attached to the microscope and used simultaneously.

The video cameras feed signals to video monitors and a video recorder, which can be used to obtain a permanent record of sampling procedures. A microphone can be attached for narrative description. A character generator to record text on the video tape will be added in the future.

PRESENT AND ANTICIPATED APPLICATIONS

The MAS and other equipment in the microsampling laboratory can be used for any research where small samples are required from research materials in which precise location within a specimen is important. So far, MAS has been used for (1) sampling portions of pelecypod shells in support of research in Sr isotope stratigraphy (DePaolo and Capo, 1990), (2) sampling quartz from phenocrysts and veins in a fracture/fault system in granitic host rock to study hydrothermal alteration effects with oxygen isotopic data, and (3) sampling cores and rims of

quartz phenocrysts from a compositionally zoned granite pluton to look for compositional zoning on a phenocryst scale with oxygen isotope data. Anticipated uses include studies of element partitioning between adjacent mineral grains, trace element diffusion coefficients, micro-distribution of chemical and isotopic species in permeable geologic media, and geochronology.

REFERENCES

DePaolo, D.J., and Capo, R.C., 1990. Paleoclimatic implications of oceanic strontium isotopic variations over the past 2.5 million years. *In* Earth Sciences Division Annual Report 1989. Lawrence Berkeley Laboratory Report LBL-27900, p. 111-114.

The Rate and Timing of Garnet Growth in the Upper Schieferhülle, Tauern Window, Eastern Alps

J. N. Christensen, J. L. Rosenfeld, and D. J. DePaolo*

Metamorphic rocks provide a partial record of the processes, such as deformation, recrystallization/reaction, heating and burial, that are related to the formation of mountain belts. The rates of these processes are fundamental to an understanding of metamorphism and its relationship to tectonism. Though progress has been made in estimating rates of cooling and uplift, there are few direct constraints on the rates of processes acting during the prograde history of a metamorphic rock. We have demonstrated that it is possible to measure the growth rate of garnet in metamorphic rocks (Christensen, et al., 1989), providing the means to determine the rates of processes, such as deformation, heating, and pressure change, that are recorded by garnet during its growth. In addition it is possible to place absolute ages on their operation. In this article we summarize the method used to determine the timing and rate of garnet growth associated with the Alpine orogeny.

THEORY

The growth rate of garnet is determined from the measured radial variation of $^{87}Sr/^{86}Sr$ within single garnet crystals. This variation is produced during garnet growth by decay of ^{87}Rb within the surrounding matrix. The essential aspects of the method are illustrated in Figure 1, a Sr isotopic evolution diagram. The slopes of evolution lines (arrows) are proportional to the $^{87}Rb/^{86}Sr$ of the sample. In this example a mineral with low Rb/Sr grows from a matrix with higher Rb/Sr. The mineral grows continuously from t_A to t_B. The mineral begins to grow at t_A, incorporating Sr of isotopic composition A. At a later time t_B the rim of the mineral grows incorporating Sr of isotopic composition B, the matrix having changed because of ^{87}Rb decay. After their formation, the core and rim isotopic compositions evolve along lines of low slope. The time interval of growth is recovered from the measured isotopic compositions of the core, rim, and matrix. The time resolution depends on the $^{87}Rb/^{86}Sr$ of the matrix and the resolution of Sr isotopic differences by the mass spectrometer. With a $^{87}Rb/^{86}Sr$ of 5 and a resolution of 2×10^{-5} in $^{87}Sr/^{86}Sr$, a time resolution of 2.8×10^5 yr is possible

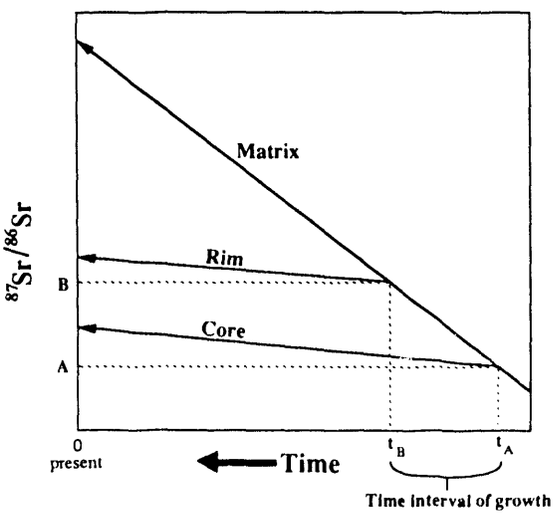

Figure 1. Hypothetical plot of $^{87}Sr/^{86}Sr$ versus time for a mineral growing continuously between times t_A and t_B from a matrix with a much higher $^{87}Rb/^{86}Sr$ than that of the mineral. Shown are evolution lines for core and rim of the mineral and the matrix. Slopes of evolution lines are proportional to their $^{87}Rb/^{86}Sr$ ratios. [XBL 913-567]

The two most critical assumptions of this method are that (1) the matrix domain from which growth occurred was homogeneous with respect to $^{87}Sr/^{86}Sr$ and $^{87}Rb/^{86}Sr$ and

* Department of Earth and Space Sciences, University of California at Los Angeles.

(2) $^{87}Sr/^{86}Sr$ of the matrix changed during garnet growth by ^{87}Rb decay but not by exchange with fluids or adjacent lithologies with contrasting $^{87}Sr/^{86}Sr$ or $^{87}Rb/^{86}Sr$. From previous work (Christensen et al., 1989) we believe these are reasonable assumptions, though we are currently carrying out work to test them further.

GEOLOGIC SETTING

The sample we analyzed is from the eastern Alps, within the Tauern Window, Austria. This tectonic window exposes the Penninic series from beneath the Austroalpine nappes, which were emplaced during the Alpine orogeny. The Penninic nappes are made up of three units (Selverstone, 1988): (1) the Zentralgneis, consisting of Hercynian crystaline rocks, (2) the lower Schieferhülle, consisting of the Paleozoic and parautochthonous Permo-Mesozoic cover to the Zentralgneis, and (3) the upper Schieferhülle, an allochthonous Mesozoic series of greenstones and pelitic schists. The sample we have analyzed is from the upper Schieferhülle.

The sample is a schist consisting predominantly of paragonite along with biotite, quartz, ilmenite, and porphyroblasts of garnet. The garnet we analyzed was 8 mm in diameter. A rectangular prism was cut through the center of the garnet and divided into 2.3 × 2.5 × 3.5 mm core and rim segments for Rb and Sr isotopic analysis. A 1-g sample of the matrix surrounding the garnet was also analyzed.

RESULTS

The core and rim of the garnet have resolvable $^{87}Sr/^{86}Sr$ and indicate the expected increase in $^{87}Sr/^{86}Sr$ from core to rim (Figure 2). The core and matrix give an age of 39.9 ± 0.4 Ma while the rim sample gives an age of 34.8 ± 0.3 Ma. These ages are plotted against distance within the garnet in Figure 3. Assuming a constant growth rate indicates that the garnet grew at a rate of 0.54 ± 0.06 mm/Ma. Extrapolation to the true rim of the garnet indicates a total growth time of 7.4 ± 0.7 Ma and an age of 32.5 ± 0.8 Ma for the cessation of garnet growth.

DISCUSSION

The rate of garnet growth found here is approximately a factor of 3 lower than the growth rate found for garnet that grew during Acadian metamorphism in SE Vermont (Christensen et al., 1989). The total growth times of the Vermont garnets (av = 10.5 ± 4.2 Ma), however, agree well with the growth time calculated above. This indicates that the difference in size between the Vermont garnets (3 cm diameter) and the garnet from the Tauern is due mostly to differences in growth rate rather than growth time.

The sample we analyzed comes from an outcrop from which pressure and temperature history has been obtained from garnet (Selverstone and Spear, 1985). Garnet from this outcrop grew over an interval of 20°C to a maximum of 475°C, while pressure increased by 2.5 kb from the core to half way to the rim of the garnet and then decreased by 2.5 kb to the rim. These data can be used to calculate rates of heating and pressure change, assuming that the smaller (2-mm diameter) garnets analyzed by Selverstone and Spear took 7.4 ± 0.7 Ma to grow. The above data imply a rate of heating of approximately 3°C/Ma during garnet growth. The barometric data imply first burial or tectonic loading at a rate of 2.3 km/Ma followed by a decompression equivalent to an exhumation rate of 2.3 mm/yr.

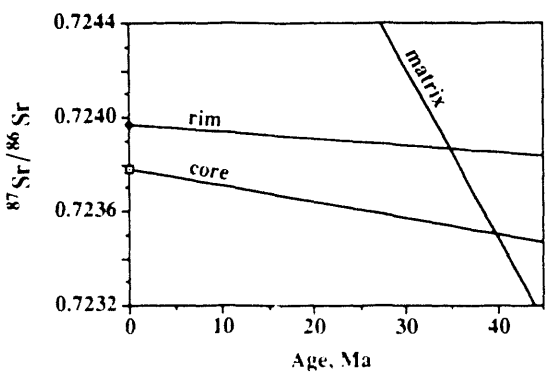

Figure 2. The $^{87}Sr/^{86}Sr$ evolution lines of garnet core and garnet rim and matrix. The measured $^{87}Sr/^{86}Sr$ of the garnet rim and core are plotted on the ordinate; errors are smaller than the symbols. [XBL 913-568]

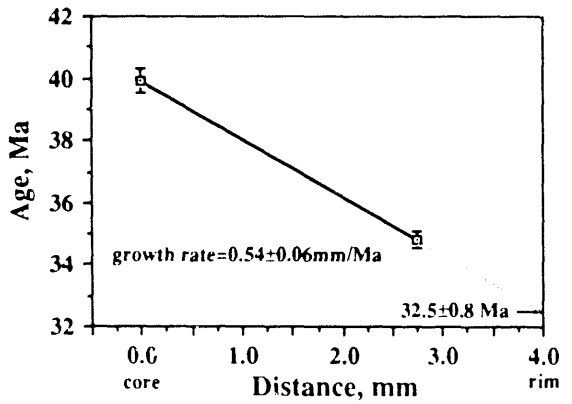

Figure 3. Time versus distance, core to rim, for the analyzed garnet. The age of each segment is plotted against the position of its center within the garnet. The errors shown in age are at the ~95% confidence level on the basis of the errors in the isotopic analyses. A constant growth rate is assumed for the calculation. [XBL 913-569]

The upper Schieferhülle reached its maximum temperature at 32.5 ± 0.8 Ma (see above), but it has been estimated (Selverstone, 1988) that the lower Schieferhülle reached its maximum temperature of 550°C perhaps 10 Ma later. Garnet from the lower Schieferhülle will be measured to test this proposition.

ACKNOWLEDGMENT

We wish to thank Jane Selverstone for kindly providing the sample analyzed for this paper.

REFERENCES

Christensen, J.N., Rosenfeld, J., and DePaolo, D.J., 1989. Rates of tectonometamorphic processes from rubidium and strontium isotopes in garnet. Science, v. 224, p. 1465–1469.

Selverstone, J., 1988. Evidence for east-west crustal extension in the eastern Alps: Implications for the unroofing history of the Tauern Window. Tectonics, v. 7, no. 1, p. 87–105.

Selverstone, J., and Spear, F., 1985. Metamorphic *P-T* paths from pelitic schists and greenstones from the south-west Tauern Window, Eastern Alps. J. Metamorphic Geol., v. 3, p. 439–465.

Temporal Variations in the Isotopic Compositions of Volcanic Rocks from the Southeastern Great Basin: A Clue to Processes in the Lower Crust and Subcontinental Mantle during Continental Extension

E. E. Daley and D. J. DePaolo

In many regions of old continental crust, the subcontinental lithospheric mantle has been enriched in incompatible elements for sufficient time to develop an isotopic composition distinct from that of the asthenospheric (depleted) mantle. Thus the boundary between continental lithosphere and asthenosphere separates mantle regions with contrasting isotopic and incompatible element compositions. It is possible to study the behavior of this boundary during extension by examining temporal patterns of variation in the chemical and isotopic compositions of extension-related volcanic rocks. Ultimately this information can provide clues to processes operating in the mantle and lower crust during extension and help characterize the nature of the boundary between lithosphere and asthenosphere.

MODEL

During extension, thinning of the continental crust and lithosphere is accompanied by upwelling of the underlying asthenospheric mantle. As this occurs, the mantle source of magmas will change from primarily lithospheric to primarily asthenospheric (Figure 1). This transition will be reflected in a change with time in the Nd and Sr isotopic character of these magmas (Perry et al., 1987, 1988). In the simplest model; that of simple thinning of the lithosphere in response to stretching (analogous to pure shear), the thickness of the lithosphere would be equal to the original lithospheric thickness divided by the stretching factor β (β = extended length of crust/original length of crust). Thus, if the original thickness of the lithosphere is D, and the depth of magma generation is d, the lithosphere-asthenosphere boundary would intersect the zone of melting when $\beta = D / d$. For example, if the lithospheric thickness were 120 km and the depth of magma generation were 60 km, the lithosphere-asthenosphere boundary should intersect the zone of magma generation when $\beta = 2$. If the transition occurred earlier than predicted by simple stretching, attenuation recorded by the the entire lithospheric column was faster than that recorded by the upper crust. One process that might cause this is erosion of the base of the lithosphere by the convecting asthenosphere. If this transition occurred later than predicted, the upper crust thinned faster than the entire lithospheric column beneath it. One possible explanation is that deformation in the upper crust can be transferred laterally through the lithosphere by simple shear (Wernicke, 1984), and thus the magnitude of the strain in the upper crust does not necessarily reflect strain in the entire lithospheric column beneath it. A further possibility is that strain in the lithosphere is distributed over a larger area than strain in the more brittle upper crust.

Comparison of the age and geometry of this transition in isotopic character with details of the timing and magnitude of extension recorded by upper crustal rocks on a regional scale can provide other clues to processes

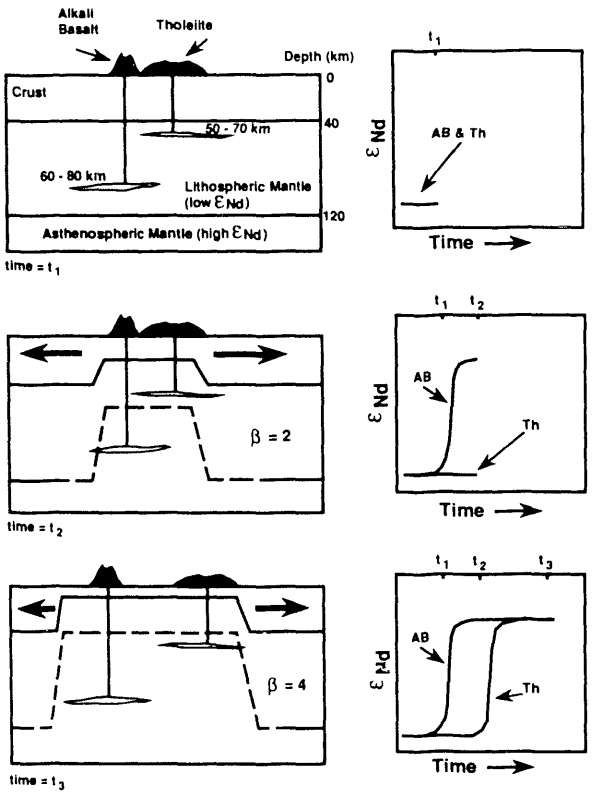

Figure 1. A simple model for how the lithosphere may become thinned during extension, causing a change from a primarily lithospheric source for magmas to a primarily asthenospheric source. Diagrams at the right illustrate how the ε_{Nd} of magmas would change through time to reflect the changing source. Magma types derived from deeper in the mantle, such as alkali basalt, would record the passage of the lithosphere-asthenosphere boundary later than magma types derived from shallower depths, such as tholeiitic basalt. [XBL 913-570]

occurring in the lower crust and mantle. For example, if the locus of maximum thinning corresponds to the earliest transition from a lithospheric to an asthenospheric source on a regional scale, the lower crust may be deforming by a process of pure shear; and if the locus of maximum thinning and the earliest isotopic transition are offset, it is more plausible that simple shear is the mode of deformation in the lower crust (Farmer et al., 1989). If there is large-scale mixing at the boundary between the lithospheric and asthenospheric mantle during extension, there may be a long time during which the isotopic character of the magmas is transitional between the two end members.

DATA

The timing and magnitude of extension in a transect across the southern Great Basin at the latitude of Las Vegas has been well characterized by Anderson (1971) and by Wernicke et al. (1988; see also references therein). Extension began in the east at about 15 Ma and progressed westward from a well-developed breakaway zone (the edge of the Colorado Plateau), leaving blocks of the upper crust stranded above a mid-crustal decollement. Wernicke et al. (1988) estimate that the net extension along this transect has been 247 ± 56 km, with the most intense stretching occurring at the margins of the Great Basin: in the Death Valley region to the west, and in the Las Vegas area to the east, where Wernicke et al. (1988) estimate the extension factor to be 3–4.

A sequence of volcanic rocks ranging in age from 18 to 5 Ma along the Arizona-Nevada border near Lake Mead was erupted during active extension in that area. Compositions of most units in the sequence range from basaltic to dacitic, and units become progressively less deformed higher in the section. The last volcanic activity, at about 5 Ma, produced ridge-capping basalts (now tilted at most 35 degrees) and alkalic dikes.

We have analyzed a preliminary suite of samples from this section for Sr, Nd, and O isotopes. There is a remarkably good correlation between $^{87}Sr/^{86}Sr$ and ε_{Nd} in these samples and a complete lack of correlation between the radiogenic isotopes and $\delta^{18}O$. ε_{Nd} ranges from values around −10, similar to other estimates of the lithospheric mantle compositions in the region, to +6.4, approaching values found in magmas derived from the asthenospheric mantle (+8 to +10). $^{87}Sr/^{86}Sr$ ranges from 0.709 to 0.703. Oxygen has a limited range in these samples, from $\delta^{18}O$ = +5.9 to +7.3, similar to typical depleted mantle values (+5.5 to +6.0). Both Nd and Sr isotopic systems show a change from more enriched lithospheric values to more depleted asthenospheric values during extension (Figure 2). Surprisingly, the large change in ε_{Nd} (and $^{87}Sr/^{86}Sr$) occurs entirely within the ridge-capping basalts (~5 Ma) and *postdates* most of the extension recorded by deformation of

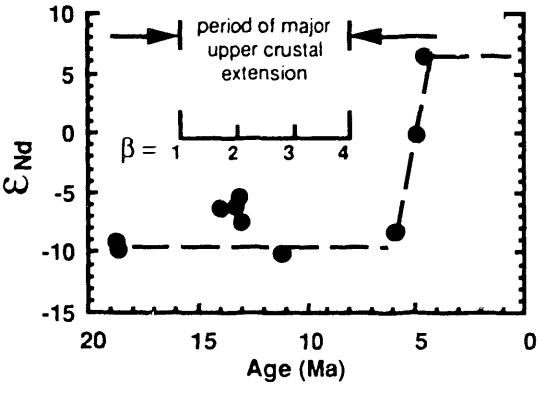

Figure 2. Preliminary Nd isotopic data from the Las Vegas sample suite show an abrupt change from an enriched (low ε_{Nd}) to a depleted (high ε_{Nd}) mantle source for magmas at around 5 Ma. Individual units have been dated by K-Ar (Anderson et al., 1972). Error bars are smaller than the symbols. [XBL 913-571]

the upper crustal rocks. It is possible that there is a small increase with time in the ε_{Nd} of the older sequence of rocks, but a more extensive data set is needed to determine if this is systematic.

DISCUSSION

Preliminary results indicate that there is indeed a change through time from a lithospheric to an asthenospheric source for magmas erupted in the SE Great Basin. On the basis of the probable pre-extension crustal thickness, and minimum depth of alkali basalt genesis, we would expect this transition to be complete by the time the stretching factor (β) reached approximately 2. Assuming simple stretching, and a constant rate of extension, β should have reached 2 between 14 and 13 Ma (Figure 3). That the transition from a lithospheric source to an asthenospheric source for these magmas is recorded at approximately 5 Ma, after the bulk of the extension, and when β had reached 3–4, indicates that attenuation in the lower lithosphere beneath this area is not as rapid as that in the upper crust. Extension of the lithosphere by simple shear (Wernicke, 1984) is one mechanism by which this could occur.

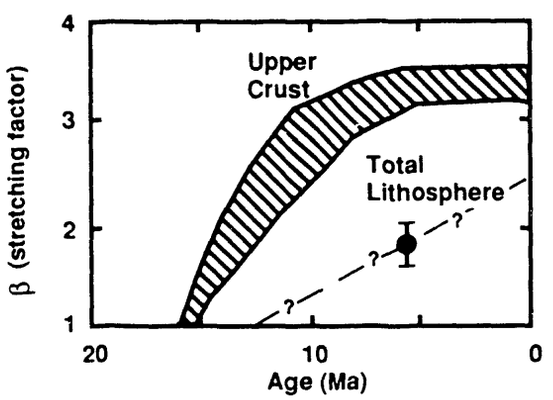

Figure 3. The discrepancy between extension (β) for the upper crust (ruled pattern) and the apparent β for the entire lithosphere (data point) determined by the time at which the source for mantle-derived magmas changed from primarily lithospheric to primarily asthenospheric. By the time upper crustal extension had reached β = 3 – 4 (by 5 Ma), the entire lithospheric column had reached only β = 2. [XBL 913-572]

REFERENCES

Anderson, R.E., 1971. Thin skin distension in Tertiary rocks of southeastern Nevada. Geol. Soc. Am. Bull., v. 82, p. 43–58.

Anderson, R.E., Longwell, C.R., Armstrong, R.L., and Marvin, R.F., 1972. Significance of K-Ar ages of Tertiary rocks from the Lake Mead region, Nevada-Arizona. Geol. Soc. Am. Bull., v. 83, p. 273–288.

Farmer, G.L., Perry, F.V., Semken, S., Crowe, B., Curtis, D., and DePaolo, D.J., 1989. Isotopic evidence on the structure and origin of subcontinental lithospheric mantle in southern Nevada. Geol. Soc. Am. Bull., v. 94, no. B6, p. 7885–7898.

Perry, F.V., Baldridge, W.S., and DePaolo, D.J., 1987. The role of asthenosphere and lithosphere in the genesis of Late Cenozoic basaltic rocks from the Rio Grande Rift and adjacent regions of the Southwestern United States. J. Geophys. Res., v. 92, no. B9, p. 9193–9213.

Perry, F.V., Baldridge, W.S., and DePaolo, D.J., 1989. Chemical and isotopic evidence for lithospheric thinning beneath the Rio Grande Rift. Nature, v. 332, no. 6163, p. 432–434.

Wernicke, B., 1984. Uniform-sense normal simple shear of the continental lithosphere. Can. J. Earth Sci., v. 22, p. 108–125.

Wernicke, B., Axen, G.J., and Snow, J.K., 1988. Basin and Range extensional tectonics at the latitude of Las Vegas, Nevada. Geol. Soc. Am. Bull., v. 100, p. 1738–1757.

Numerical Model of Oxygen Exchange between Seawater and Oceanic Crust

D. P. Schrag, D. J. DePaolo, F. M. Richter, and B. M. Smith

Chemical reactions between seawater and oceanic crustal rocks influence the chemistry of the oceans and hence are important in global cycling of elements. In addition, understanding the nature and style of alteration of the oceanic crust is important in assessing the potential for subsea radioactive waste disposal. Although it has been argued that seawater-basalt interaction at high temperatures (200–350°C) at mid-ocean ridges is the most important factor in controlling the composition of seawater (Muehlenbachs and Clayton, 1972), chemical and isotopic gradients in interstitial waters of sediments and low-temperature alteration assemblages in basalt indicate that

chemical exchange persists long after basalt has moved away from the spreading ridge (e.g., Lawrence et al., 1975). Many studies have discussed low-temperature alteration of basalt as an important process in the chemical interaction between the oceans and the oceanic crust, but none have successfully quantified the rates of such alteration. To adequately describe the chemical and isotopic evolution of the oceans, the rate as well as the duration of such low-temperature alteration must be understood.

It is difficult to arrive at an estimate for the rates of low-temperature alteration of basalt from experimental data on the kinetics of the relevant mineral reactions because the *in situ* reactions are numerous and occur under a variety of chemical conditions (e.g., variable oxygen fugacity). Moreover, the actual rate of exchange of any element between basalt and seawater depends on both the kinetics of individual reactions and the effects of local equilibrium.

We quantify the rate of low-temperature alteration of submarine basalt using constraints imposed by oxygen isotopic gradients in interstitial waters. Studies of pore fluid chemistry from Deep Sea Drilling Project (DSDP) cores demonstrate a global trend of decreasing $\delta^{18}O$ profiles with depth, corresponding with an increase in Ca and a decrease in Mg. The $\delta^{18}O$ typically decreases downsection by about 3–9‰ per km of depth from the modern seawater value of about 0‰ (Lawrence and Gieskes, 1981). McDuff and Gieskes (1976) have shown that these $\delta^{18}O$ gradients in deep sea pore fluids result from extended, slow alteration underlying basaltic basement. This alteration mainly involves the replacement of original igneous material of $\delta^{18}O \approx +6$ with smectite having a much higher $\delta^{18}O$ (depending on temperature and pore fluid composition). This process represents a sink for ^{18}O below the sediment layer, supplied by the coexisting pore fluid with a synchronous release of Ca and uptake of Mg. The uptake of ^{18}O by weathering basalt is balanced by supply of ^{18}O from seawater by diffusion through the sedimentary column, so that the $\delta^{18}O$ of the interstitial water decreases with depth (McDuff and Gieskes, 1976; McDuff, 1981).

Diffusion of water molecules from seawater above results in the maintenance of a near-steady-state isotopic gradient in the pore fluids between the underlying basalt and the overlying ocean. Using an approach similar to that of Richter and DePaolo (1987,1988) in calculations of reaction rates for carbonate diagenesis, analyses of interstitial waters from Ocean Drilling Program (ODP) cores have been incorporated into a mathematical model that describes the transport of oxygen both by diffusion and by advection due to compaction.

MODEL

Our model considers the basalt and the sediment together as one system. Solids are treated as fluid-saturated porous media with vertical transport of oxygen occurring by diffusion and advection in the pore fluid. The model simulates the sedimentation process by successively adding boxes of sediment, initially 10 m thick, to a 1-km-thick section of basalt. Compaction is simulated by allowing the porosity of each box to decrease as it is buried successively deeper by other boxes. The height of each box is then calculated on the assumption that the mass of solid in each box is conserved.

In mathematical terms, the transport of oxygen by diffusion and advection in the pore fluid and by reaction between fluid and solid are described by equations of mass conservation for the bulk solids and fluid. Following Richter and DePaolo (1987), the conservation equation for a chemical species $C_{i,f}$ (i.e., the concentration of ^{16}O or ^{18}O in mass per unit mass of fluid) in the pore fluid is

$$\frac{\partial C_{i,f}}{\partial t} = \nabla(\phi D \cdot \nabla C_{i,f}) + U \cdot \nabla C_{i,f} + \frac{(1-\phi)\rho_s}{\phi \rho_f} R(C_{i,s} - kC_{i,f}) .$$

The terms on the right-hand side of the equation represent, respectively, diffusion, advection, and the source or sink of C_{if} due to chemical reaction of basalt to clay minerals. Similarly, the conservation equation for a chemical species C_{if} (i.e., the concentration of ^{16}O or ^{18}O in mass per unit mass of solid) in the bulk solid is

$$\frac{\partial C_{i,s}}{\partial t} = U \cdot \nabla C_{i,s} + R(C_{i,s} - kC_{i,f}) .$$

This equation ignores the effect of diffusion in the solid.

As the oxygen isotopic compositions of geologic materials are reported by $\delta^{18}O$ values, it is useful to express the conservation equations also in terms of $\delta^{18}O$. Converting the above equations, and defining Δ_{s-f} as the difference between $\delta^{18}O_s$ and $\delta^{18}O_f$ at equilibrium, yields the equations for fluid,

$$\frac{\partial(\delta^{18}O_f)}{\partial t} = \nabla\left(\phi D \cdot \nabla(\delta^{18}O_f)\right) + U\nabla\delta^{18}O_f + \frac{(1-\phi)\rho_s}{\phi\rho_f}\frac{O_s}{O_f} R\left(\delta^{18}O_s - \delta^{18}O_f - \Delta_{s-f}\right) + \frac{2D}{^{16}O_f}\nabla{}^{16}O_f \nabla\delta^{18}O_f ,$$

and for solid,

$$\frac{\partial(\delta^{18}O_s)}{\partial t} = U\nabla\delta^{18}O_s + R\left(\delta^{18}O_s - \delta^{18}O_f - \Delta_{s-f}\right) .$$

The last term in the equation for conservation of fluid arises from the expression for the derivative of an isotopic ratio. However, because

$$\frac{2D}{^{16}O_f} \nabla {}^{16}O_f \nabla \delta^{18}O_f \ll \nabla(\phi D \cdot \nabla(\delta^{18}O_f)),$$

this term can be ignored in the model calculations (F. Richter, personal communication, 1990). In our model, the equations are solved numerically for one-dimensional transport.

The reaction term in the conservation equations represents low-temperature basalt alteration, which is modeled as conversion to smectite with $\Delta_{smectite\text{-}H_2O}$ calculated from experimental data using model thermal gradients. R is the reaction rate of basalt, expressed in mass fraction reacted per unit time. As the low-temperature alteration of basalt is an irreversible process, once basalt has been converted to smectite in the model, it is no longer allowed to react. This is consistent with Rb-Sr dates of vein smectites, which suggests that the smectite, once formed, is not subject to later solution-reprecipitation (Richardson et al., 1980). Reactions in the sediment involving oxygen exchange are neglected in this version of the model, as such reactions contribute only a minor amount to the oxygen composition of the pore fluids (McDuff and Gieskes, 1976). Oxygen exchange between pore fluids and sediments may significantly alter the composition of the sediments, however, and this process can be explored using a similar approach (Schrag et al., 1990).

Parameters

For initial runs of the model, we use generalized parameters, constrained by observations from DSDP and ODP cores. Most of the parameters including porosity, diffusivity, and sedimentation rate can be customized for investigation of a specific site. The model porosity of the sediment varies linearly with depth from an initial value of 0.7 to a minimum value of 0.3 at a depth of 600 m. The porosity in the basalt also varies linearly with depth from 0.1 at the basalt-sediment interface to 0.01 at 1000 m deeper in the basalt. Diffusion coefficients are calculated from the porosities to account for tortuosity in the sediment, where $D = D_0\phi$. For the sediment, diffusion coefficients vary linearly with depth from 14×10^{-6} cm^2 s^{-1} at the seafloor to a minimum value of 6×10^{-6} cm^2 s^{-1} at a depth of 500 m. These values are typical of diffusion coefficients estimated from electrical conductivity measurements of DSDP cores (McDuff and Gieskes, 1976). Diffusion coefficients for the basalt are calculated as above, but D_o is increased by a factor of 4 because of the lower tortuosity of fractured basaltic crust. Advection in the system, apart from that due to compaction of sediment, is neglected ($U = 0$). The sedimentation rate in the model is fixed at 20 m Ma^{-1} (uncompacted), the temperature gradient is fixed at 40°C km^{-1}.

The reaction rate for the conversion of basalt to smectite is treated as a fit parameter, adjusted to produce model pore fluid profiles compatible with observations from DSDP and ODP cores.

Boundary Conditions

The initial $\delta^{18}O$ of the basalt is set at the beginning of each run to +6.0, the approximate value of fresh, unaltered mid-ocean ridge basalt. The pore fluid has an initial $\delta^{18}O = 0$, as might be expected following extensive hydrothermal circulation of seawater. The $\delta^{18}O$ of the fluid at the top of the sediment is fixed at zero to simulate the composition of seawater. Changes in the oxygen isotopic composition of seawater can easily be accommodated by allowing this boundary condition to vary with time. At the base of the basalt, we apply a no-flux boundary condition. At the basalt-sediment interface, where there are discontinuous changes in porosity and diffusivity, we use a condition satisfying the continuity of flux and isotopic composition of the fluid (Crank, 1956).

RESULTS

Model outputs for the pore fluid and basalt are shown in Figure 1. For these runs, $R_{basalt} = 0.01$ (1% Ma^{-1}). Outputs from run times of 25, 50, and 100 Ma are displayed. This generalized model illustrates the behavior of the system and is useful in estimating the magnitude of isotopic shifts.

Model Pore Fluids

The pore fluid profiles are compatible with observations from DSDP cores, with $\delta^{18}O$ decreasing with depth in the sediment column. As sediment is added to the column, the $\delta^{18}O$ of the pore fluid at the basalt-sediment interface decreases. The pore fluid profile for the 100-Ma run time is peculiar in that the slope of the profile decreases with depth. This is produced by continued sedimentation, which causes the sediment thickness to exceed the diffusion length scale. If the model sedimentation rate decreased with age, as is typical of pelagic sections, diffusion would achieve a near steady-state profile, more closely resembling observed pore fluid compositions.

Increasing the reaction rate for the basalt by a factor of 2 does not significantly change the pore fluid profiles, lowering the $\delta^{18}O$ at the basalt-sediment interface by less than 1‰. For reaction rates less than 0.005 (0.5% Ma^{-1}), isotopic gradients in the model pore fluid could not be maintained. This constrains the reaction rate in natural systems to between 0.005 and 0.02. This range is

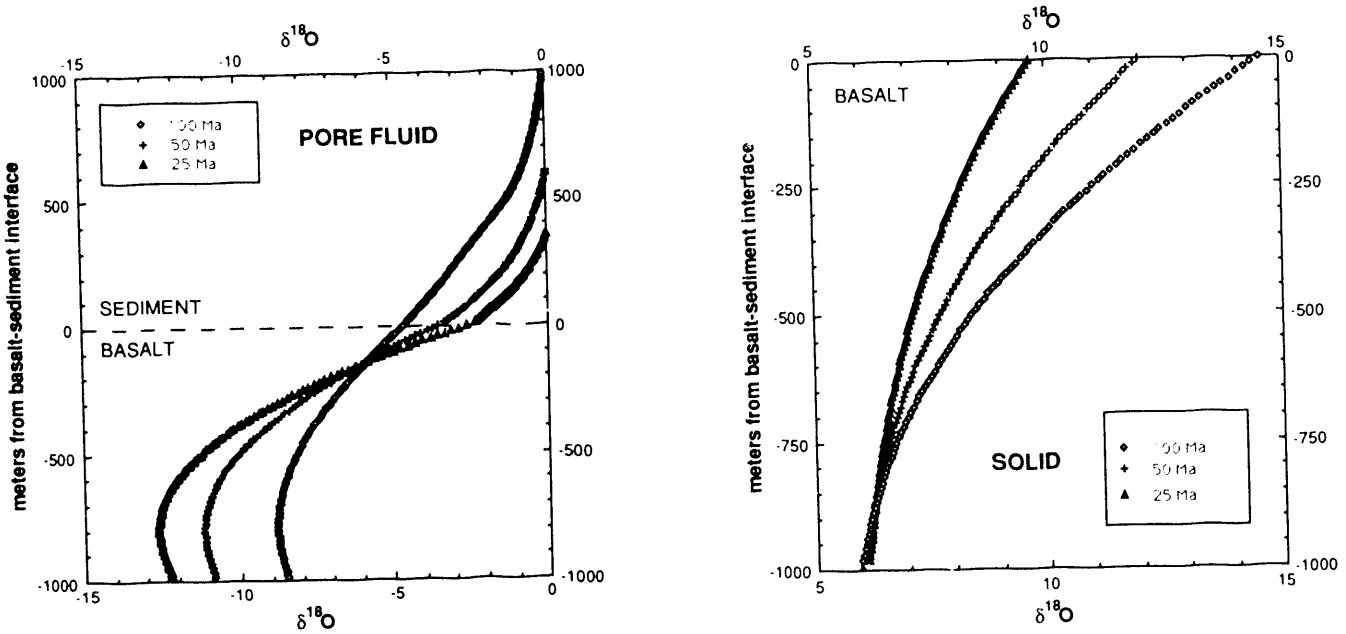

Figure 1. Model outputs for 25, 50, and 100 Ma of pore fluid and solid basalt. [left, XBL 913-573; right, XBL 913-574]

compatible with the duration of low-temperature alteration estimated from the ages of oceanic crust for which isotopic gradients in pore fluids have been observed.

Varying the porosity of the basalt produces the largest changes in pore fluid composition. Increasing ϕ_{basalt} in the upper 500 m of oceanic crust lowers the $\delta^{18}O$ of the pore fluid at the basalt-sediment interface. Changing the porosity affects the system in two ways. First, the porosity is proportional to the diffusivity, which controls transport of oxygen in the basalt. Second, the porosity at the basalt–sediment interface regulates the flow of oxygen into and out of the basalt. If the change in porosity across the interface is very large, the ^{18}O-depleted fluid diffusing up from the basalt is effectively diluted by the greater amount of pore fluid in the sediment.

The model produces basalt pore fluids that have extremely low $\delta^{18}O$ values. Once any convection of seawater has ceased, the fluids deep in the basalt are only in diffusive contact with seawater. Increasing the reaction rate at depth in the basalt, as might be expected with increasing temperature, does not significantly affect the pore fluids in the sediment because the system is already near isotopic equilibrium.

Model Basalt

The corresponding $\delta^{18}O$ profile of the altered basalt shows extreme isotopic enrichment in the upper hundreds of meters, where the pore fluids are drawn by diffusion toward the seawater value. The general geometry of this alteration is similar to the $\delta^{18}O$ profiles observed in ophiolites, which have previously been ascribed to temperature gradients in ridge-proximal hydrothermal systems (Gregory and Taylor 1981). This pattern of alteration is different from that observed at DSDP Site 504B, where drilling penetrated more than 1 km through young oceanic crust (Alt et al., 1986). The thickness of this zone of ^{18}O enrichment in the model is highly dependent on the porosity structure given to the basalt. If the basalt is made more permeable by increasing the porosity, the zone of enrichment extends deeper. Repeated runs of the model, varying porosity and diffusivity, suggest that natural variations in the porosity of the oceanic crust between locations can explain the differences in the depth and extent of alteration.

DISCUSSION

The model runs illuminate many aspects of the nature of alteration of oceanic crust. The model successfully produces isotopic gradients in pore fluids through slow (~1% Ma^{-1}), extended low-temperature alteration of the basalt away from the ridge crest. The strong dependence of the isotopic compositions of the model pore fluids on porosity of the basalt suggests that site-specific modeling efforts could be used to constrain the porosity of the upper oceanic crust, which is difficult to measure in natural systems because of poor recovery and statistical problems. The model demonstrates that the pattern of alteration observed in ophiolites can be produced by slow alteration of the basalt, where the dominant transport mechanism is diffusion. Future modeling efforts to examine the effect of

convection in the basalt during low-temperature alteration may help assess the extent and duration of large convective cells in older oceanic crust.

REFERENCES

Alt, J.C., Muehlenbachs, K., and Honnorez, J., 1986. An oxygen isotopic profile through the upper kilometer of the oceanic crust, DSDP hole 504B. Earth Plan. Sci. Lett., v. 80, p. 217–229.

Crank, J., 1956. The Mathematics of Diffusion. Oxford University Press, New York.

Gregory, R.T., and Taylor, H.P., Jr., 1981. An oxygen isotope profile in a section of Cretaceous oceanic crust, Samail Ophiolite, Oman: Evidence for $\delta^{18}O$ buffering of the oceans by deep (>5 km) seawater-hydrothermal circulation at mid-ocean ridges. J. Geophys. Res., v. 86, no. B4, p. 2737–2755.

Lawrence, J.R., and Gieskes, J.M., 1981. Constraints on water transport and alteration in the oceanic crust from the isotopic composition of pore water. J. Geophys. Res., v. 86, no. B9, p. 7924–7934.

Lawrence, J.R., Gieskes, J.M., and Broecker, W.S., 1975. Oxygen isotope and cation composition of DSDP pore waters and the alteration of layer II basalts. Earth Plan. Sci. Lett., v. 27, p. 1–10.

McDuff, R.E., 1981. Major cation gradients in DSDP interstitial waters: the role of diffusive exchange between seawater and upper oceanic crust. Geochim. Cosmochim. Acta., v. 45, p. 1705–1713.

McDuff, R.E., and Gieskes, J.M., 1976. Calcium and magnesium profiles in DSDP interstitial waters: Diffusion or reaction? Earth Plan. Sci. Lett., v. 33, p. 1–10.

Muehlenbachs, K., and Clayton, R.M., 1972. Oxygen isotope studies of fresh and weathered submarine basalts. Can. J. Earth Sci., v. 9, p. 172–184.

Richardson, S.H., Hart, S.R., and Staudigel, H., 1980. Vein mineral ages of old oceanic crust. J. Geophys. Res., v. 85, no. B12, p. 7195–7200.

Richter, F.M., and DePaolo, D.J., 1987. Numerical models for diagenesis and the Neogene Sr isotopic evolution of seawater from DSDP Site 590B. Earth Plan. Sci. Lett., v. 83, p. 27–38.

Richter, F.M., and DePaolo, D.J., 1988. Diagenesis and Sr isotopic evolution of seawater using data from DSDP 590B and 575. Earth Plan. Sci. Lett., v. 90, p. 382–394.

Schrag, D.P., DePaolo, D.J., and Richter, F.M. 1990. Numerical model for low-temperature oxygen exchange between ocean floor basalt, sediment and pore fluids: Implications for paleotemperature studies. EOS Trans. Am. Geophys. Union, v. 71, no. 43, p. 1704.

Nd Isotope Chronostratigraphy of Colorado Plateau Lithosphere: Implications for Magmatic and Tectonic Underplating of Continental Crust

E. Wendlandt and D. J. DePaolo

Determining the age and composition of the lower continental crust is critical for evaluating crustal growth processes and global crustal age distribution models. The "crustal age" of a region generally refers to radiogenic isotope age determinations of mid- to upper crustal granitic rocks and is likely to date the main crust-forming episode for the region. This age, however, may have no bearing on the age of the lower crust in that region. Areas that have undergone magmatic or tectonic underplating (addition to the lower crust by mantle-derived mafic intrusions or tectonically emplaced material) could have significantly different lower crustal and upper crustal ages. Dating the time that lower crustal rocks were extracted from the mantle is thus one means of evaluating whether there have been significant additions to the lower crust at times more recent than the main crust-forming event.

The purpose of this study is to determine if crust-formation ages vary with depth in the crust, in order to evaluate whether magmatic and tectonic underplating are indeed viable processes for contributing significantly to crustal volume. To investigate the systematic vertical distribution of mantle extraction ages, it is necessary to be able to sample a virtual cross section of normal-thickness continental lithosphere. The available means of sampling the lower crust are limited. Exposed granulite terranes, although perhaps once residing at lower crustal depths, generally do not show a complete crustal profile and are potentially complicated by chemical and thermal

reequilibration to upper crustal conditions. Xenolith suites are often limited by samples that originate from a restricted depth range and are often found in regions of high heat flow and anomalous, thinned continental crust.

We have chosen to investigate the age relationships in a vertical column of lithosphere sampled by xenoliths from the Colorado Plateau. Diatremes and minettes in the Four Corners region of Utah, Arizona, New Mexico, and Colorado host a large variety of xenolith lithologies that sample upper crustal to upper mantle depths in a region of normal-thickness lithosphere. This unique opportunity to sample such a lithospheric section at these localities was recognized by McGetchin and Silver (1977), but virtually no geochronologic information is available regarding crust formation and subsequent stabilization of the crust and mantle lithosphere. Although the Colorado Plateau has been relatively quiescent during the Phanerozoic, there are reasons that age variations with depth might exist in this region.

Bird (1979) suggested that delamination of the continental lithosphere and subsequent replacement of asthenospheric mantle in this region was consistent with existing petrologic and geophysical data to explain the uplift of the Colorado Plateau and the Tertiary volcanic events. Thus the Colorado Plateau might be a logical place to look for asthenosphere-derived mafic underplate in the xenolith assemblage.

High-grade metapelitic xenoliths indicate that tectonically emplaced material has also been added to the lower crust in the Colorado Plateau. This material may not be of the same age as the upper crust currently above it. In addition, it has become accepted that eclogite xenoliths from the Colorado Plateau, on the basis of compositional and Sr isotope similarities to Franciscan eclogites, are remnants of subducted Mesozoic oceanic crust (Helmstaedt and Doig, 1975). However, while the Nd isotope system might be most useful in unraveling their petrogenesis, virtually no Nd isotope or geochronologic data exist for the eclogite xenoliths.

APPROACH

Nd model ages, calculated using present-day Nd isotopic compositions and Sm/Nd ratios, have been interpreted as dating the mantle extraction of high-grade metamorphic terranes in Norway (Jacobsen and Wasserburg, 1978) and Antarctica (DePaolo et al., 1982) and a number of xenolith suites (e.g., Stolz and Davies, 1989). The technique determines the time when the Nd evolution curve of the sample intersects the evolution curve of the depleted mantle reservoir and is therefore dependent on a valid model for the evolution of the mantle source of continental crust. As pointed out by many authors, interpretations of Nd model ages must be made with caution (Arndt and Goldstein, 1987; Rudnick, 1990). In particular, mixing of mantle-derived magma with pre-existing older crust can produce a mixed Nd model age in the hybrid rock (Ruiz et al., 1988; Rudnick, 1990). This age would have no significance in terms of dating the time of extraction from the mantle, but would still indicate younger mantle-derived additions. Likewise, high-grade metamorphism can cause metamorphic differentiation or mineral enrichment, which, if sampling were nonrepresentative, could change the Sm/Nd ratio from that of the true whole-rock protolith. Such wholesale Sm/Nd fractionation in the analyzed sample could result in erroneous model age determinations (Rudnick, 1990).

However, in spite of these potential complications in the interpretation of Nd model ages, they are nonetheless useful in determining whether any newer mantle-derived material exists at deep crustal levels. That is, any *pattern* of "anomalous" T_{DM} ages, or those that are not the accepted age of the upper crust in a region, is instructive because they may trace involvement of different age mantle-derived material. The calculated ages may or may not be interpreted as true mantle-extraction ages, depending on other geochemical and petrographic criteria. If the model ages are interpreted as mixed ages, mixing models could constrain the age and isotopic compositions of the melt or assimilant. In reality, the results are likely to be complicated, especially if only some parts of the lower crust show anomalous ages.

The Nd isotopic system has been shown to remain unusually robust even under high-grade metamorphic conditions (DePaolo et al., 1982). A systematic study of xenoliths from a lithospheric column, however, also allows a unique opportunity to investigate the behavior of the Nd isotopic system during progressively higher-grade metamorphism and the temporal relationship between whole-rock model ages and mineral cooling ages for this region.

RESULTS AND DISCUSSION

The Nd isotope and model age results for upper crustal, lower crustal, and eclogite xenoliths from the Colorado Plateau are shown in Figure 1. Each ε_{Nd} vs. model age (T_{DM}) plot traces the evolution of the sample's Nd isotope value back from its present-day value to its intersection with the depleted mantle evolution line (bold). The time of this intersection is the Nd model age. The plot of upper crustal ages includes data from Bennett and DePaolo (1987) for exposed upper crustal rocks from regions bordering the Colorado Plateau. The ages defined by the exposed granitic rocks, which are the accepted ages of the upper crust in the region, are shown by the two vertical lines between ~1.7 and 2.1 Ga. The eclogite

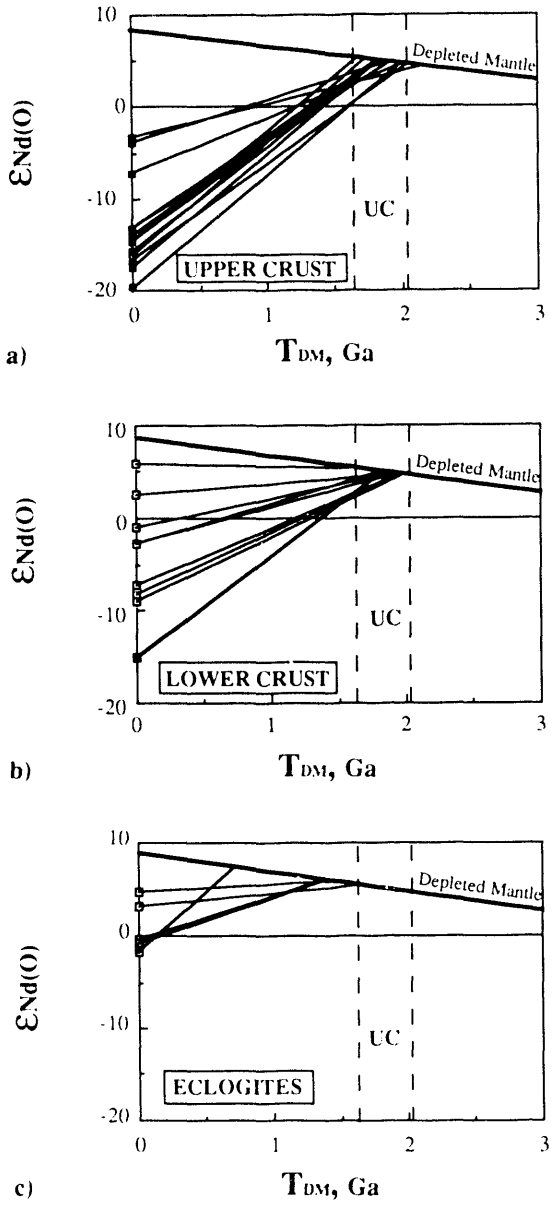

Figure 1. ε_{Nd} vs. age diagrams showing Nd model age determinations for **(a)** upper crustal Colorado Plateau xenoliths and regional granitoids (from Bennett and DePaolo, 1987), **(b)** lower crustal xenoliths, and **(c)** eclogite xenoliths. Vertical lines between 1.7 and 2.1 Ga on all the diagrams indicate the upper crustal age determined by granitoids.

xenoliths are likely part of the lower crustal assemblage but are presented here separately.

Of particular significance in Figure 1a and b is the remarkable coherence of Nd model ages between upper and lower crustal rocks. When the eclogite xenoliths are excluded, the lower crustal garnet amphibolites, granulites, and metapelites display Nd model ages between 1.63 and 1.98 Ga, thus indistinguishable from the ages of the upper crustal rocks. The range of ε_{Nd} and Sm/Nd ratios is much more variable for lower crustal xenoliths than for the felsic upper crustal rocks, in some cases even approaching mantle values.

The model ages, however, are unexpectedly consistent, especially when considering that there is no a priori reason to expect that metamorphic differentiation has not occurred, resulting in unrepresentative whole-rock sampling. A preliminary garnet whole-rock isochron from a granulite xenolith indicates that the sample last passed through the garnet blocking temperature at ~1.2 Ga, which probably dates some part of the cooling history from the granulite facies metamorphism. If there were significant garnet enrichment or depletion in the xenoliths at this time, the ages could deviate significantly from the true age of the protolith. However, because the model ages are so consistently that of the upper crustal rocks, it appears that the lower crustal samples have retained the identity of their protolith and that the ages are meaningful.

These results suggest that old crustal material is found at all levels of the crust in the Colorado Plateau. The major and trace element compositions of the high-grade amphibolites and granulites (not presented here) are consistent with mafic meta-igneous protoliths, but the Nd isotopic data do not indicate that there has been a significant mantle contribution to the lower crust by igneous processes since the main crust-forming event at ca. 1.9 Ga.

The garnet, sillimanite-bearing gneiss xenoliths have peraluminous compositions and REE patterns indicative of sedimentary protoliths. The Nd model ages of these metapelites, which are between 1.84 and 1.86 Ga, show that, before being tectonically emplaced to lower crustal depths, the sediments had clearly sampled a source region that was itself extremely homogeneous with respect to age.

The Nd isotope data of the eclogite xenoliths from the Colorado Plateau are much more complex (Figure 1c). ε_{Nd} values range from −1.8 to +5.8, and the calculated model ages are variable but all younger than 1.64 Ga. The sample with the lowest Sm/Nd ratio that could theoretically determine an accurate model age has the youngest age (0.73 Ga). This same sample has a negative ε_{Nd} value that is farthest away from that expected for Mesozoic MORB.

There is no significant overlap between Nd isotope values for Colorado Plateau eclogites and Nd values for Franciscan eclogite blocks (Figure 2). The Franciscan eclogites (data from Nelson, 1985) have ε_{Nd} values indistinguishable from those of mid-ocean ridge basalt (MORB), indicating that the high-grade metamorphism of oceanic crust does not erase the isotopic signature of MORB in eclogitic facies rocks. This important observation, as well as the Proterozoic model ages and relatively low ε_{Nd} of the eclogite xenoliths, argues strongly against these eclogites being Mesozoic oceanic crust.

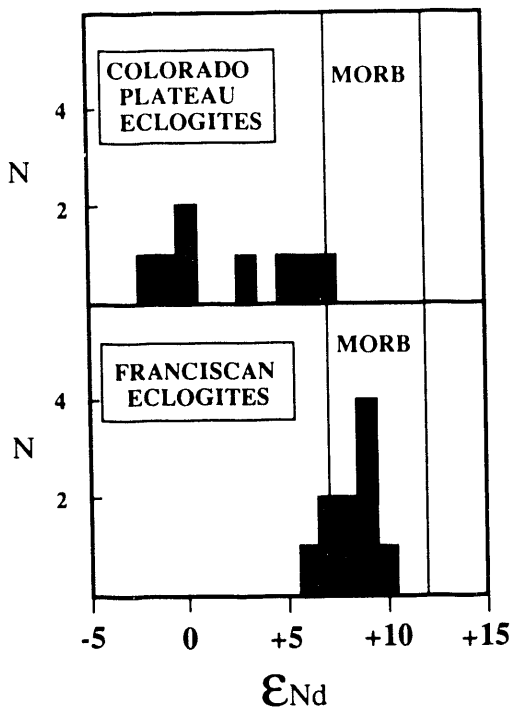

Figure 2. Histogram plot comparing Nd isotopic compositions of Colorado Plateau eclogite xenoliths with those of Franciscan eclogite blocks (from Nelson, 1985). Nd values for MORB modified from Morris and Hart (1983).

An alternate explanation for the origin of the eclogite xenoliths that is consistent with current theories for the Precambrian crustal assembly for this region of the western United States is that they represent *Proterozoic* oceanic crust metamorphosed at eclogite facies conditions. Ongoing work with the eclogite xenoliths includes mineral geochronology, which will better constrain their petrogenesis by dating their cooling history.

REFERENCES:

Arndt, N.T., and Goldstein, S.L., 1987. Use and abuse of crust-formation ages. Geology, v. 15, p. 893–895.

Bennett, V.C., and DePaolo, D.J., 1987. Proterozoic crustal history of the western United States as determined by neodymium isotopic mapping. Geol. Soc. Am. Bull., v. 99, p. 674–685.

Bird, P., 1979. Continental delamination and the Colorado Plateau. J. Geophys. Res., v. 84, no. B13, p. 7561–7571.

DePaolo, D.J., Manton, W.I., Grew, E.S., and Halpern, M., 1982. Sm-Nd, Rb-Sr and U-Th-Pb systematics of granulite facies rocks from Fyfe Hills, Enderby Land, Antarctica. Nature, v. 298, p. 614–618.

Helmstaedt, H., and Doig, R., 1975. Eclogite nodules from kimberlite pipes of the Colorado Plateau—Samples of subducted Franciscan-type oceanic lithosphere. Phys. Chem. Earth, v. 9, p. 95–111.

Jacobsen, S.B., and Wasserburg, G.J., 1978. Nd and Sr isotopic study of the Permian Oslo Rift. *In* R.E. Zartman (ed.), Short Papers of the 4th International Conference on Geochronology, Cosmochronology, Isotope Geology. USGS Open-File Rept. 78-701, p. 194–196.

McGetchin, T.R., and Silver, L.T., 1972. A crustal–upper mantle model for the Colorado Plateau based on observations of crystalline rock fragments in the Moses Rock Dike. J. Geophys. Res., v. 77, p. 7022–7037.

Nelson, B., 1985. Samarium–neodymium and rubidium–strontium isotopic studies of the origin and evolution of continental crust (Ph.D. thesis). University of California at Los Angeles.

Rudnick, R.L., 1990. Nd and Sr isotopic compositions of lower-crustal xenoliths from north Queensland, Australia: Implications for Nd model ages and crustal growth processes. Chem. Geol., v. 83, p. 195–208.

Ruiz, J., Patchett, P.J., and Ortega-Gutierrez, F., 1988. Proterozoic and phanerozoic basement terranes of Mexico based on Nd studies. Geol. Soc. Am. Bull., v. 100, p. 274–281.

Stolz, A.J., and Davies, G.R., 1985. Metasomatized lower crustal and upper mantle xenoliths from north Queensland: Chemical and isotopic evidence bearing on the composition and source of the fluid phase. Geochim. Cosmochim. Acta, v. 53, p. 649–660.

X-Ray Fluorescence Microprobe Studies of the Sorption of Chromium Colloids on Galena

D. L. Perry

As part of the Basic Energy Sciences program at DOE, this author, at the Lawrence Berkeley Laboratory (LBL), has been applying synchrotron radiation to the study of natural geologic materials and their associated sorption chemistry. One area that has been especially fruitful is the study of interfacial reactions between sulfide minerals and metal ions in aqueous solutions. The studies of these reactions provide many new data concerning the production of reaction compounds that form on mineral surfaces. Measurements of the reaction mechanisms, kinetics, and end products will help develop a chemical understanding of these geologic material/aqueous interfaces, with one of the major areas of understanding being the interaction of toxic metals with geologic media.

An improved understanding of the reactions between aqueous metal ions and sulfides can also help to improve the processing of metal ores. The extractive metallurgy industry makes use of metal ion reagents in many aqueous reactions to recover strategic metals from their ores. These reactions are dependent on the surface chemical conditions of the ore that reacts with the reagents, and therefore a detailed understanding of these reaction systems is critical in planning better processing schemes.

The high intensity, tunability, and small beam spot size of x-ray beams from synchrotron radiation facilities provide a variety of powerful techniques for studying these reactions. For example, an x-ray microprobe can measure the spatial distribution of trace elements with a spatial resolution of 5 μm × 5 μm (and even smaller) and an elemental sensitivity of as little as several femtograms/μm^2. At LBL, one of the areas this author is currently studying is the segregation and clustering of chromium ions on a PbS surface. With synchrotron radiation, it is also possible to measure the interfacial solution species in situ, using extended x-ray absorption fine structure. Overall, synchrotron radiation has afforded an exciting opportunity to expand research in geologic surface sorption and metallurgical processing development. The enhanced understanding of chemical interfacial (and concomitant surface) reactions will allow researchers to design better metallurgical processing schemes for strategic metals. Even very small increases in recovery of these metals would produce large energy savings to U.S. industry.

Under geologic conditions, chromium can exist in both the hexa- and trivalent oxidation states. Previous work in our laboratory (Perry et al., 1984) has shown that the dichromate ion, $Cr_2O_7^{2-}$, a major chemical species in some Department of Energy toxic waste sites, can undergo two processes in its interaction with reducing geologic substrates such as galena, PbS.

Process I: $Cr_2^{VI}O_7^{2-}$ reduced to $Cr_2^{III}O_3 \cdot xH_2O$ (CrOOOH)

Process II: $Cr_2^{VI}O_7^{2-}$ monomerized to $Cr^{VI}O_4^{2-}$ ($PbCrO_4$)

Such reduction-oxidation systems produce a layering and mixing (Perry, 1990) of colloid reaction products, the distribution and morphology of the products being dependent on the precise chemical state of the reducing sulfide surface. Reduction of the Cr(VI) to Cr(III) species and its deposition on the surface results in a passivation of the reducing sulfide, followed by the subsequent chemisorption of the chromate species. The use of scanning electron microscopy studies has confirmed that the resulting colloid-covered surface can only be modeled as a heterogeneous array of chemical components available for undergoing subsequent dissolution by groundwater. The second process, in addition to the reduction-oxidation one, involves the alteration of the dichromate ion to the chromate ion.

This surface heterogeneity of the galena is manifested both chemically and morphologically. The dichromate ion, with a formed electronic configuration of [Ar] $3d^0$, undergoes a three-electron reduction to the paramagnetic [Ar] $3d^3$ configuration in forming hydrated Cr_2O_3. In the presence of a carbon dioxide/carbonate source, a second phase—a hydrated oxide/carbonate—is formed. This secondary reaction is analogous to that reaction previously reported as occurring in both hydrated oxides of lead (Perry and Taylor, 1984) and uranium (Perry et al., 1984).

The present research addresses the use of synchrotron radiation at the Brookhaven National Synchrotron Light Source for extracting x-ray fluorescence microprobe data for chromium colloids generated on the surface of natural galena. Lateral elemental profiles have been obtained, and the x-ray fluorescence data are comparable with those resulting from previous spectroscopic studies. Various intermediates in the reaction pathway to the final products have implications that are important for construction of realistic models.

Figure 1 shows the image of a galena surface that has been reacted with sodium dichromate. The chromium is unevenly distributed, with some areas having no appreciable chromium. Other areas, however, have high concentrations (in the μg range). As shown previously

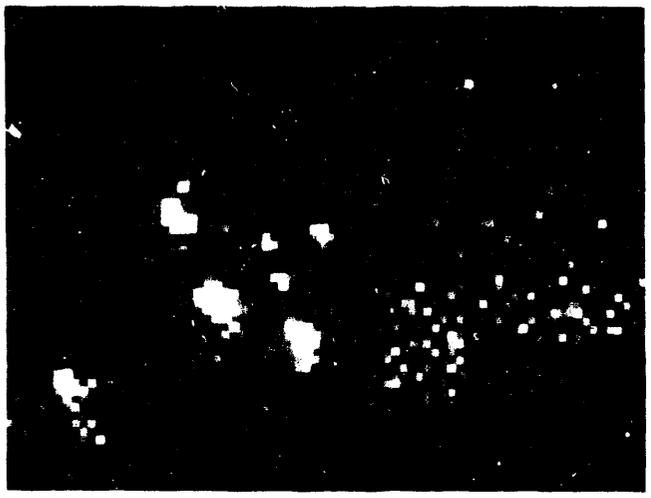

Figure 1. X-ray fluorescence microprobe image of chromium on galena, PbS. The lightest areas represent the highest chromium concentrations on the surface. [CBB 905-4453]

(Perry et al., 1984), these areas of chromium are a composite of both chromium(III) and chromium(VI); Figure 2 clearly indicates the presence of both oxidation states. The chromium $2p_{3/2,1/2}$ spin-orbit doublet spectrum of the reacted galena is shown in Figure 2. Each of the two photoelectron lines consists of obvious doublets, one line in each doublet representing chromium(III) and the other line representing chromium(VI). Binding energies and spin-orbit splittings for the chromium(VI) lines are in good agreement with an assignment of $PbCrO_4$ as previously reported.

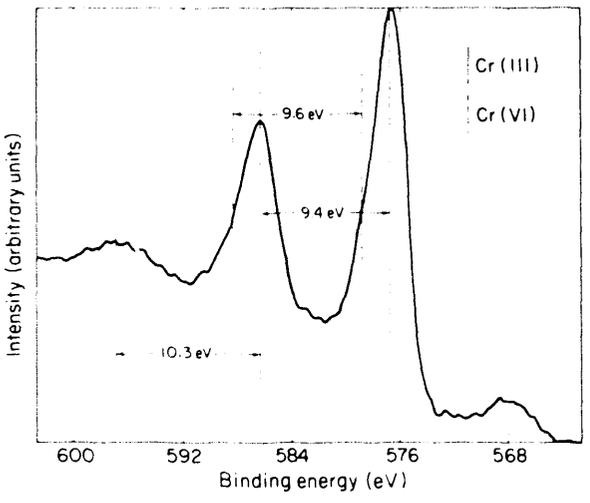

Figure 2. The chromium $2p_{3/2,1/2}$ photoelectron spectrum of galena that has been reacted with an aqueous solution of $Na_2Cr_2O_7$. [XBL 839-2218]

The chromium(III) portion of the spectrum, however, represents a much more complex situation, since chromium(III), with its $3d^3$ electronic paramagnetic configuration [as opposed to the diamagnetic $3d^0$ state of chromium(VI)], exhibits (1) a broader $2p$ core line, (2) associated "shake-up" satellite lines to the high-binding-energy side of the main photoelectron lines, and (3) multiplet splitting of the $3s$ core levels by the $3d$ valence electrons. Additionally, special characteristics and parameters resulting from these effects can be altered by such factors as sample hydration.

The two chromium(III) lines shown in Figure 2 have binding energies of 577.0 and 586.4 eV, respectively, for the $2p_{3/2}$ and $2p_{1/2}$ lines. These values are very similar to those exhibited by $Cr(OH)_3$ and hydrated $Cr_2(CO_3)_3$ as well as those previously reported for the natural mineral CrOOH, a hydrated chromium(III) oxide. The spin-orbit splitting between the Cr $2p_{3/2}$ and $2p_{1/2}$ lines is 9.4 eV, within experimental error, also quite close to the splitting of 9.8 eV exhibited by hydroxide and carbonate chromium(III) models. The seeming discrepancy of 0.4 eV between the two values can probably be attributed to the inability to locate the exact centroids of the chromium(III) peaks accurately. While these splittings also compare favorably with the value of 9.7 eV previously reported for Cr_2O_3, it is highly unlikely that any Cr_2O_3 formed in an aqueous reaction medium would be anhydrous.

An examination of the carbon 1s line (not shown here) reveals not only the adventitious carbon line at 284.6 eV but also a line at 288.0 eV for the dichromate-treated galena sample, $Cr(OH)_3$, and $Cr_2(CO_3)_3 \cdot nH_2O$. This line indicates the presence of the carbonated species, which undoubtedly results from chemisorption (and subsequent reaction) of CO_2 from the reaction solution with the hydrated chromium oxide. This reaction, forming a mixed hydrated oxide/carbonate complex, has been documented for several other metal oxide (and "hydroxide") systems, including lead (Taylor and Perry, 1984) and uranium (Perry et al., 1984). While one cannot assign the carbonate species to the chromium(III) exclusively, such an association is reasonable in light of the chemisorption of CO_2 by all the anhydrous Cr_2O_3 samples prepared and studied in this investigation. Previous workers have indicated that Cr_2O_3 often has a coating of $Cr(OH)_3$, or CrOOH, on its surface, which would act as a reaction substrate for CO_2. The extreme similarities in the XPS spectral parameters of Cr_2O_3 and CrOOH have also been compared previously. Strong evidence has been observed for the presence of the analogous lead(II) hydroxide/carbonate complex (Taylor and Perry, 1984) on the galena surface on the basis of the lead core photoelectron lines.

On the basis of the x-ray photoelectron data, the reaction between galena and an aqueous solution of sodium dichromate is shown to yield both chromium(III) and

chromium(VI) species. The chromium(III) complex is actually hydrated chromium(III) oxide, $Cr_2O_3 \cdot nH_2O$, with a layer of chemisorbed CO_2 on the surface, thus forming a mixed complex of the type $Cr_2O_3 \cdot nH_2O \cdot xCO_2$. This product is a result of the hydration of chromium(III) oxide, which in turn adsorbs (and subsequently reacts with) CO_2. There is, however, no way of determining the amount of carbon dioxide adsorbed from the air or solution during the process of the chemical reaction occurring on the surface of the galena.

REFERENCES

Perry, D.L., Tsao, L., and Taylor, J.A., 1984. The galena/dichromate solution interaction and the nature of the chromium(III) species. Inorg. Chim. Acta, v. 85, p. L57–L60 (LBL-17517).

Perry, D.L., 1990. Instrumental Surface Analysis of Geologic Materials. VCH Publishers, Chap. 1.

Perry, D.L., and Taylor, J.A., 1984. An x-ray photoelectron and electron energy loss study of the oxidation of lead. J. Vac. Sci. Technol., ser. A, v. 2, p. 771–774 (LBL-17515).

Perry, D.L., Tsao, L., and Brittain, H.G., 1984. Photophysical studies of uranyl complexes. 4. X-ray photoelectron and luminescence studies of hydrolyzed uranyl salts. Inorg. Chem., v. 23, p. 1232–1237 (LBL-16975).

A Study of the Oxidation of Europium(II) Sulfide by Europium-151 Mössbauer Spectroscopy

*D. L. Perry and F. J. Berry**

Although the existence of the europium sulfides of composition EuS and Eu_2S_3 has been known for many years (Greenwood and Earnshaw, 1984), there appears to be a surprising sparsity of information concerning their behavior under mild conditions in air. The authors have initiated a study of such systems and, in this article, describe how the oxidation of europium(III) sulfide appears to be a more complex process than might be initially imagined. This work is an extension of the study of the oxidation of both synthetic and naturally occurring mineral sulfides.

Commercially prepared high-purity europium(II) sulfide (Alfa Venton, 99.99%) was exposed to the atmosphere for various lengths of time and heated in air at temperatures not exceeding 250°C. ^{151}Eu Mössbauer spectra were recorded at 298 K with a microprocessor-controlled Mössbauer spectrometer using a 25-mCi $^{151}SmF_3$ source. The drive velocity was calibrated with a ^{57}Co/Rh source and iron foil. All the spectra were computer fitted. The ^{151}Eu chemical isomer shift data are quoted relative to europium(III) oxide.

The ^{151}Eu Mössbauer spectra recorded in situ europium(II) sulfide in an atmosphere of argon as shown in Figure 1a. The ^{151}Eu Mössbauer parameters are collected in Table 1. The results confirm the data reported previously (Gerth et al., 1968). The ^{151}Eu Mössbauer spectrum recorded from europium(II) sulfide following exposure to the atmosphere for periods up to 48 hours showed (Figure 1b and Table 1) only the presence of Eu^{2+} and was similar to that recorded from pure europium(II) sulfide. After prolonged exposure to air at 25°C for periods between 72 and 90 hours, some partial oxidation of Eu^{2+} to Eu^{3+} was observed (Figure 1c and Table 1). Although the chemical isomer shift of the Eu^{3+} species resembles that reported for $Eu_2(SO_4)_3$ (Deeney et al., 1967; Greenwood and Gibb, 1971), the relatively narrow range of chemical isomer shifts spanned by different Eu^{3+} species (Greenwood and Gibb, 1971) requires great caution in interpretation without evidence from complementary techniques. Indeed, the authors found that x-ray powder diffraction was insensitive to the nature of the oxidized product. Taken together the results show that europium(II) sulfide is remarkably stable to atmospheric oxidation at 25°C.

The ^{151}Eu Mössbauer spectrum recorded from europium(II) sulfide following treatment in air at 50°C for 6 hours (Figure 1d and Table 1) showed a single absorption characteristic of Eu^{2+}. Treatment at 250°C in air for 6 hours induced the partial oxidation of Eu^{2+} to Eu^{3+} (Figure 1e and Table 1). The extent of oxidation is only slightly greater than that achieved when europium(II) sulfide is exposed to air at 25°C for 90 hours. The results show that

* School of Chemistry, University of Birmingham, U.K.

Table 1. ^{151}Eu Mössbauer parameters recorded from europium(II) sulfide following treatment in air.

Treatment	Assignment	$\delta(Eu_2O_3)$ $\pm$ 0.8 /mms^{-1}	Spectral peak area (% $\pm$ 8)
Argon, in situ	Eu^{2+}	–12.72	100
Air, 25°C, 48 h	Eu^{2+}	–12.94	100
Air, 25°C, 90 h	Eu^{2+}	–13.09	92
	Eu^{3+}	–0.59	8
Air, 50°C, 6 h	Eu^{2+}	–13.07	100
Air, 250°C, 6 h	Eu^{2+}	–12.99	85
	Eu^{3+}	–0.50	15

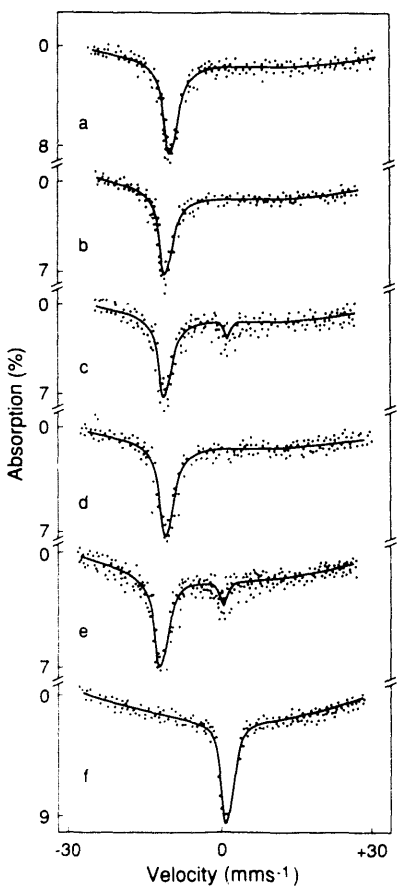

Figure 1. ^{151}Eu Mössbauer spectra recorded from europium(II) sulfide (a) in situ under argon and following treatment in (b) air at 25°C (48 h), (c) air at 25°C (90 h), (d) air at 50°C (6 h), (e) air at 250°C (6 h). The spectrum recorded from europium(III) oxide is shown in (f). [XBL 912-6041]

the treatment of europium(II) sulfide at temperatures greater than 25°C does not necessarily induce facile oxidation.

The oxidation of europium(II) sulfide is therefore a nontrivial process. Whether the oxidation proceeds through the formation of a surface phase—such as an oxysulfide, sulfate, or some other species that is not sensitive to characterization by x-ray powder diffraction (which essentially examines the bulk properties of a solid)—is unclear, as are the kinetics of the oxidation process. This nontriviality of the mechanism and products of the oxidation of europium(II) sulfide may not be unexpected when considered in the light of previous studies of other metal sulfides. For example, the oxidation of lead(II) sulfide has been shown to be exceedingly complex (Zingg and Hercules, 1978) and to involve the initial formation of a thin overlayer of lead(II) oxide, which is subsequently converted to lead sulfate, $PbSO_4$. The oxidation of lead(II) sulfide with mixtures of oxygen and sulfur dioxide gives the additional formation of $PbSO_3$ (Zingg and Hercules, 1978). These results have been confirmed by more recent studies (Perry et al., 1984a,b), which have also indicated that the interaction of oxidized and unoxidized surfaces of lead(II) sulfide with aqueous solutions of metal ions such as copper(II) and chromium(VI) gives surface products that depend on the degree of lead(II) sulfide oxidation and the nature of the experimental conditions. The oxidation of the surface of the zinc(II) sulfide (sphalerite) by air oxidation and by interaction with aqueous solutions of metal ions has also been found to be a complex process (Perry et al., 1984b). Hence the results of the work reported here suggest that the oxidation of lanthanide sulfides is no less trivial.

REFERENCES

Deeney, F.A., Delaney, J.A., and Ruddy, V.P., 1967. Isomer shifts in trivalent compounds of europium. Phys. Lett., v. 25A, p. 370–371.

Gerth, G., Kienle, P., and Luchner, K., 1968. Chemical effects of the isomer shift in ^{151}Eu. Phys. Lett., v. 27A, p. 557–558.

Greenwood, N.N., and Earnshaw, A., 1984. Chemistry of the Elements. Pergamon, Oxford, p. 1438.

Greenwood, N.N., and Gibb, T.C., 1971. Mössbauer spectroscopy. Chapman and Hall, London, p. 548.

Perry, D.L., Tsao, L., and Taylor, J.A., 1984a. The galena/dichromate solution interaction and the nature of the resulting chromium(III) species. Inorg. Chim. Acta, v. 85, p. L57–L59 (LBL-17517).

Perry, D.L., Tsao, L., and Taylor, J.A., 1984b. Surface studies of the interaction of copper ions. *In* P.E. Richardson, S. Srinivasan, and R. Woods (eds.), Proceedings, International Symposium on Electrochemistry in Mineral and Metal Processing (Vol. 84–10). 165th National Meeting of the Electrochemical Society, Cincinnati, Ohio, U.S.A., p. 169 (LBL-17912).

Zingg, D.S., and Hercules, D.M., 1978. Electron spectroscopy for chemical analysis of lead sulfide oxidation. J. Phys. Chem., v. 82, p. 1992–1995.

Thermodynamics of High-Temperature Brines

K. S. Pitzer and S. M. Sterner

Equilibrium considerations based on various types of experimental measurements interrelated and extended by thermodynamic calculations provide an important basis for understanding and prediction in a variety of geochemical systems. This article presents two new equations of state, one for very concentrated NaCl-KCl brines extending to the anhydrous fused salts and a second for NaCl-KCl solid solutions. The experimental data base includes new and unpublished measurements for the ternary system from I.M. Chou of the USGS, Reston, Virginia, who will be a co-author of the published paper. Described below are the modeling equations developed here at Lawrence Berkeley Laboratory, which are valid over the temperature range 600–1100 K and to at least 2 kb pressure.

For multicomponent systems miscible in all proportions or with wide ranges of miscibility, equations of the Margules type are usually the most successful. Terms from binary systems are directly applicable to ternary or higher-order solutions. For the three-component liquid with the mole fractions of NaCl, KCl, and H_2O given as x_1, x_2, and x_3, respectively, the excess Gibbs energy (G_L^{ex}) is given by

$$G_L^{ex} = x_1^L x_2^L (w_{12}^L + w_{112}^L x_1^L)$$

$$+ x_1^L x_3^L w_{13}^L + x_2^L x_3^L w_{23}^L + x_1^L x_2^L x_3^L w_{123}^L. \qquad (1)$$

All of the Margules parameters w^L are, in principle, functions of temperature and pressure, but constant values sufficed for w_{12}^L and w_{112}^L. Simple temperature and pressure dependencies were required for w_{13}^L and w_{23}^L.

The general three-suffix treatment would include terms in w_{113}^L and w_{223}^L, but these were not needed. Appropriate differentiation yields the chemical potentials for NaCl and KCl, which are simultaneously equal to the corresponding chemical potentials for the solid. The excess Gibbs energy for the solid is given by

$$G_S^{ex} = x_1^S x_2^S (w_{12}^S + w_{112}^S x_1^S) , \qquad (2)$$

with both w_{12}^S and w_{112}^S temperature and pressure dependent.

The thermodynamic properties of pure NaCl and KCl were taken from Robie et al. (1979), and the parameters for the solid solution system were evaluated using data from Vesnin and Zakovsyashin (1979), Barrett and Wallace (1954), and Bhardwaj and Roy (1971). For the anhydrous NaCl-KCl binary there are enthalpy data for the liquid from Hersh and Kleppa (1965), as well as solid-liquid phase composition data from Chou (1982) and Chou (unpubl.). For the aqueous binaries there are differential thermal analysis (DTA) data for the NaCl-H_2O system from Gunter et al. (1983) and for the KCl-H_2O system from Chou (unpubl.).

Iterative methods were developed to solve for both the solid and liquid compositions that would make equal the chemical potentials of both NaCl and KCl. In the evaluation of the Margules parameters a stepwise process

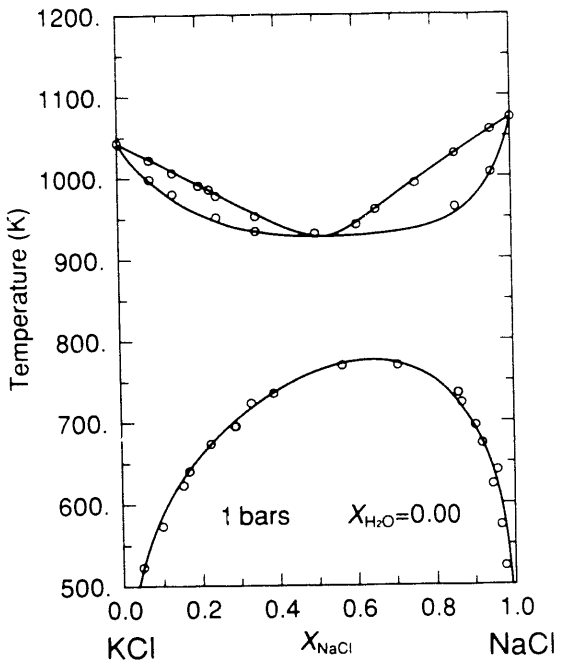

Figure 1. Phase relations in the anhydrous NaCl-KCl binary system at 1 bar. Open circles are experimental determinations of the solvus from Vesnin and Zakovsyashin (1979) and Barrett and Wallace (1954); the solidus from Chou (unpubl.); and the liquidus from Chou (1982). Equilibrium phase boundaries were calculated using Eqs. (1) and (2) by equating the chemical potentials of NaCl and KCl in the coexisting phases. [XBL 913-577]

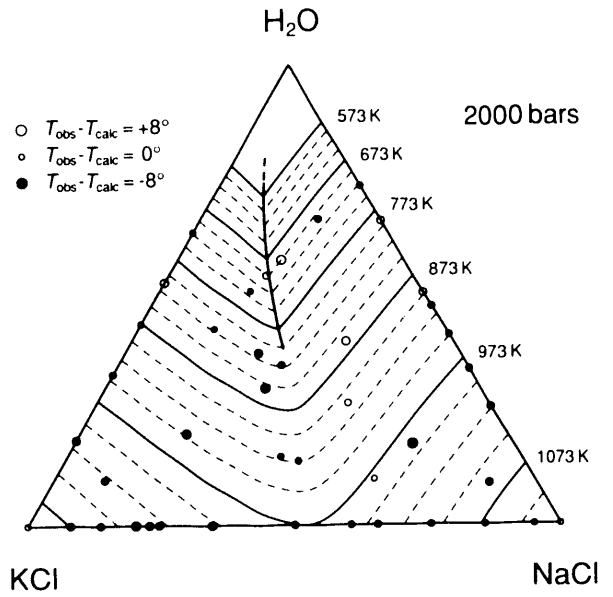

Figure 2. Phase relations in the NaCl-KCl-H_2O system. Subparallel solid and broken curves are isotherms on the ternary liquidus at 2 kb constructed by equating the chemical potentials of NaCl and KCl in the coexisting liquid and solid phases. The near-vertical curve, broken at the extreme water-rich end, is the cotectic boundary that divides the halite (NaCl) and sylvite (KCl) liquidus at sub-solvus temperatures and represents the composition of the liquid phase coexisting simultaneously with the two solid solutions. Circles are experimental determinations of the 2 kb liquidus from Chou (1982, and unpubl.) and Gunter et al. (1983). Deviations between measured liquidus temperatures and those derived using Eqs. (1) and (2) are indicated by the relative size of the circle. Positive values of observed minus calculated temperatures are shown by open circles, whereas negative deviations are indicated by filled symbols. [XBL 913-578]

was followed in which the three binaries NaCl-KCl, NaCl-H_2O, and KCl-H_2O were first treated independently. The parameters obtained for the salt-H_2O binaries were found to be directly applicable to the ternary solution, whereas the anhydrous binary liquid parameters were modified somewhat in a global regression, which included ternary liquid and binary solid data as well. Finally, a single ternary interaction parameter w^L_{123} having a simple pressure and temperature dependence was added to yield satisfactory agreement with experimental data. Additional parameters proved unnecessary. Phase equilibria predicted from the above equations of state are shown in Figures 1 and 2.

REFERENCES

Barrett, W.T., and Wallace, W.E., 1954. Studies of NaCl-KCl solid solutions. I. Heats of formation, lattice spacings, densities, Schottky defects and mutual solubilities. J. Am. Chem. Soc., v. 76, p. 366–369.

Bhardwaj, M.C., and Roy, R., 1971. Effect of high pressure on crystalline solubility in the system NaCl-KCl. Phys. Chem. Solids, v. 32, p. 1603–1607.

Chou, I.M., 1982. Phase relations in the system NaCl-KCl-H_2O. Part I: Differential thermal analysis of the NaCl-KCl liquidus at 1 atmosphere and 500, 1000, 1500, and 2000 bars. Geochim. Cosmochim. Acta, v. 46, p. 1957–1962.

Gunter, W.D., Chou, I.M., and Girsperger, S., 1983. Phase relations in the system NaCl-KCl-H_2O. Part I: Differential thermal analysis of the halite liquidus in the NaCl-H_2O binary above 450°C. Geochim. Cosmochim. Acta, v. 47, p. 863–873.

Hersh, L.S., and Kleppa, O.J., 1965. Enthalpies of mixing in some binary liquid halide mixtures. J. Chem. Phys., v. 42, p. 1309–1322.

Robie, R.A., Hemingway, B.S., and Fisher, J.R., 1979. Thermodynamic properties of minerals and related substances at 298.15 K and 1 bar (10^5 Pa) pressure and at higher temperatures. USGS Bull. 1452, p. 456.

Vesnin, Y.I., and Zakovsyashin, S.P., 1979. About decay of solid solutions of KCl-NaCl. Solid State Comm., v. 31, p. 635–639. [in Russian]

Studies of the Mobility of Uranium and Thorium in Nevada Test Site Tuff

*H. A. Wollenberg, S. Flexser, and A. R. Smith**

Hydro-geochemical processes must be understood if the movement of radionuclides away from a breached radioactive waste canister is to be modeled and predicted. In this respect, occurrences of uranium and thorium in hydrothermal systems are under investigation in tuff and in rhyolitic tuff that was heated to simulate the effects of introduction of radioactive waste (Wollenberg et al., 1991). In these studies, high-resolution gamma spectrometry and fission-track radiography are coupled with observations of alteration mineralogy and thermal history to deduce the evidence of, or potential for movement of, U and Th in response to the thermal environment.

At the G-tunnel test facility, Nevada Test Site, core obtained for mineralogical, geochemical, and geomechanical studies of welded tuff from the unsaturated zone has been artificially heated to repository temperature. The mineralogical and physical properties of this tuff, the Grouse Canyon, are similar to those of the densely welded Topopah Springs tuff, the candidate repository medium (Connolly et al., 1983). In an experiment conducted by Lawrence Livermore National Laboratory, an electric heater simulated the localized thermal field caused by introduction of high-level waste (Ramirez et al., 1990). The heater was at full power for 4 months, with a temperature of 240°C at the heater edge and 120°C in rock at a distance of 0.7 m. A small steam-dominated system developed in the rock within 0.6–0.7 m of the heater and lasted for at least 70 days.

To provide baseline data, we selected unheated core from a hole, designated NE-2, that passes within 1 m of the electric heater (Figure 1). The distribution of radioelements in this core was investigated by gamma spectrometry, and results showed a relatively even distribution of U and Th over the length of the core (mean values: U = 3.4+/–0.4 ppm, Th = 15.6+/–2.1 ppm). More detailed gamma spectrometry indicated high concentrations of U and Th associated with an open fracture, coated partially with amorphous silica. This occurrence was examined by fission-track radiography, disclosing that U, at ~20 ppm, is concentrated by a factor of 5 in the silica coating relative to the tuff matrix. The U-rich coating could have been associated with the hydrothermal system that developed soon after deposition of the tuff or with a cooler, fracture-controlled groundwater system that subsequently developed.

Investigations of heated core obtained by drilling through the heater hole are presently underway. We are examining the core from sites where localized heating may have affected fracture-lining and rock-matrix constituents; preliminary results are presented here. Five subcores perpendicular to the axis of the 30-cm-diameter drillback core and one core parallel to the axis were obtained, covering a span of 30 cm from the edge of the heater hole. Whole-rock gamma spectrometry of these subcores indicates a slightly lower U concentration (3.3 ppm) in the core closest to the heater hole (3.5 cm) than in the more distant cores, which average 3.5 ppm U. Thorium, averaging 16.5 ppm, is nearly the same in all cores, with only a small depletion (to 16.2 ppm) evident in the subcore at 10 cm from the heater hole. The mean concentrations of U and Th in the heated subcores are similar to those of the unheated core. Preliminary comparison of radioelement correlations in heated and unheated rock (Table 1) indicates that U and Th are correlated similarly, whereas U and K are more strongly correlated in the heated than in the unheated rock. Th and K are strongly correlated in both the heated and the unheated rock.

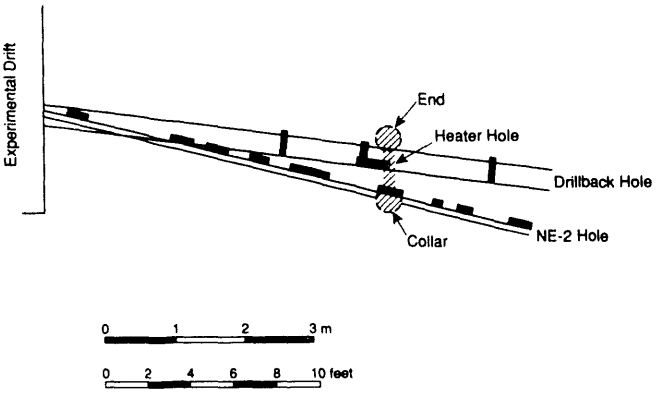

Figure 1. Vertical section perpendicular to heater hole in G-tunnel, Nevada Test Site, showing sampled intervals in core from the NE-2 hole, drilled prior to the heater hole, and the "drillback" hole that intersected the heater hole. The heater hole projects into the figure, with the end of the hole ~1 m above the elevation of its collar. [XBL-8910-7806]

The apparently more independent behavior of U than of Th and K in both heated and unheated tuff might be influenced by the loci of U in the rock. This is indicated by

Table 1. Correlations (r^2) between radioelements.

	U with Th	U with K	Th with K
Heated tuff	0.47	0.59	0.96
Unheated tuff	0.43	0.28	0.93

* Engineering Division, Lawrence Berkeley Laboratory.

the aforementioned association of U with fracture-lining silica and also by the results of fission-track radiography of tuff close to the heater. Radiography in combination with x-ray spectroscopy (EDAX) on the scanning electron microscope show that U is associated both with primary magnetite and ilmenite and with secondary disseminated Mn-oxyhydroxide minerals (Figure 2). Uranium has probably been localized in the secondary minerals by adsorption, although it appears to be incorporated in the grains and on the surfaces of the primary minerals. Fission-track determinations of U in five thin sections from within 10 cm of the heater hole (Figure 3) show that U is concentrated 8 to 10 times above whole-rock values where it is associated with the primary Fe-Ti-oxide minerals and 4 to 5 times whole-rock values where it is associated with secondary, mainly Mn-oxide minerals. Where U is associated with Fe-Ti-oxide minerals in unheated core from the NE-2 hole, U concentrations are ~85 ppm, considerably higher than the concentrations in similar minerals in the heated tuff. This,

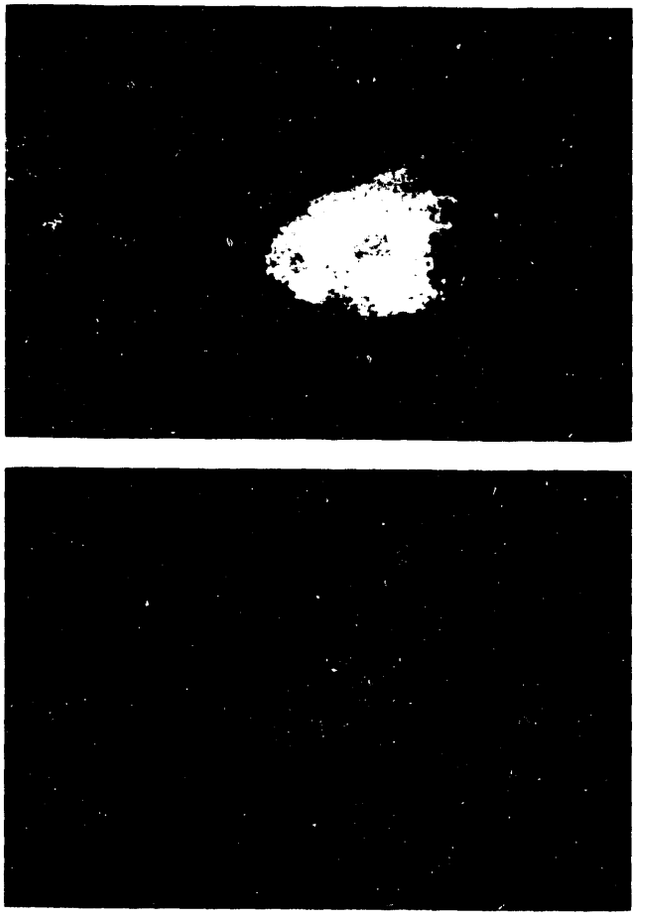

Figure 2. Uranium associated with primary and secondary opaque minerals in heated tuff. **(Top)** Backscattered electron image of primary Fe-rich grain (center) and secondary disseminated Mn-rich mineral (left). **(Bottom)** Associated fission tracks. Length of field 1.3 mm. [XBB-9011-9412]

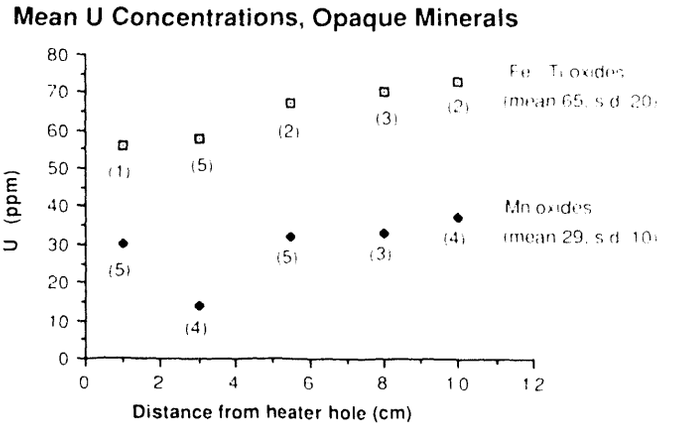

Figure 3. Uranium concentrations, by fission-track radiography, in primary Fe-Ti and secondary Mn-oxyhydroxide minerals in welded tuff within 10 cm of the heater hole. Numbers of observations are shown in parentheses. [XBL-908-2897]

together with the apparent gradient in U shown in Figure 3, suggests a relative depletion of U associated with Fe-Ti-oxide minerals close to the heater. Electron microscopy with EDAX is being used to determine more accurately the composition of these opaque minerals. Detailed fission-track radiography and EDAX are proceeding as well on thin sections from the five subcores, covering a broader range (30 cm) of distance from the heater.

Observations to date suggest that U was mobile in the vicinity of the heater but that localized reducing environments provided by Fe-Ti-Mn-oxide minerals concentrated U and thus attenuated its migration.

REFERENCES

Connolly, J., Mansker, W., Hicks, R., Carlton, C., Husler, J., Keil, K., and Lappin, A., 1983. Petrology and geochemistry of the Grouse Canyon member of the Belted Range tuff, rock mechanics drift, G-tunnel, Nevada Test Site. Sandia National Laboratories Report SAND 81-1970.

Ramirez, A., Buscheck, T., Carlson, R., Daily, W., Latorre, V., Kenrick, L., Lin, W., Mao, N., Towse, D., Ueng, T., and Watwood, D., 1990. Prototype heater test of the environment around a simulated waste package. *In* Proceedings, International Topical Meeting on High Level Waste Management. Am. Nuc. Soc., Las Vegas, Nevada.

Wollenberg, H., Flexser, S., and Smith, A.R., 1991. Radionuclides in hydrothermal systems as indicators of repository conditions. *In* Scientific Basis for Nuclear Waste Management XIV. Proceedings, Materials Research Society Fall Meeting, November 26–29, 1990. Materials Research Society, Boston, Massachusetts (LBL-29857).

GEOPHYSICS AND GEOMECHANICS

The Geophysics and Geomechanics group conducts basic and applied research relevant to the nation's energy development programs and helps train the next generation of scientists and engineers in the geosciences. The research utilizes unique facilities at Lawrence Berkeley Laboratory and is directed toward the solution of problems related to the disposal of nuclear and toxic wastes, the exploration for and recovery of fossil fuels, the definition of fundamental properties and processes in the earth's crust, and the development of geothermal energy. The aim is to address not only today's needs, but also needs that will arise from the ever-increasing pressures placed upon the earth's resources. The group has focused, and will continue to focus, on a collaborative approach, not only between geophysical and geomechanical disciplines, but with other disciplines in government and industry as well. The thrust is for a strong theoretical foundation coupled with laboratory, numerical, and field-based studies. We are unique in that this group has a strong emphasis in all three areas. The overall philosophy is to address broad research bases rather than individual program areas. The group draws upon the unique resources within other divisions at the Laboratory and the various earth sciences departments on the U.C. Berkeley campus. Current emphasis is on the development of techniques for characterizing and monitoring processes in heterogeneous rock and soils using high-resolution seismic and electrical imaging. Future growth will come about only through a coordinated and balanced program based on solid research principles—one that can respond to changing needs in the earth sciences and new objectives of DOE programs in a timely and efficient manner.

Cross-Borehole Scale-Modeling Experiment

D. L. Alumbaugh and A. Becker

Scale modeling makes use of the law of similitude to relate a small laboratory system to a large-scale field experiment. In electromagnetic scale modeling the frequency and/or conductivity is increased to maintain the field relationships while reducing the size. Frischnecht (1988) describes in detail the theoretical and practical aspects of scale modeling.

In the past, scale modeling provided the only means to simulate field situations and thus in many cases the only method to interpret electromagnetic data. However, with the advancement of fast digital computers, scale modeling is being used more to check numerical algorithms and to inexpensively develop and test field systems rather than to interpret data. The purpose of this experiment was threefold: (1) to show that accurate measurements can be made in a simulated borehole environment, (2) to check existing forward numerical computer codes with data resulting from a known model, and (3) to provide a data set for various inversion routines.

MATHEMATICAL BASIS FOR SCALE MODELING

Spies (1980) describes two types of scale modeling using either geometric scaling or absolute scaling. In geometric scaling only field ratios are obtained, and it is required that a dimensionless parameter δ be the same for the natural and man-made systems. Because the actual field value is needed in absolute scaling, an additional scale factor must be applied. In the experiment described below, absolute scaling was employed, partly for comparison with the numerical results and partly because of the input requirements of the various inversion routines.

The scale model relationships are derived by requiring that both the model system, denoted by the subscript m, and the natural system, denoted by subscript n, obey Maxwell's equations (Grant and West, 1965). Manipulation of the equations yields

$$l^2 \sigma_n \mu_n \omega_n = \sigma_m \mu_m \omega_m \,, \tag{1}$$

where σ is the conductivity, μ is the magnetic permeability, ω is the frequency, and l is the scale factor defined by

$$l = \frac{x_n}{x_m} = \frac{y_n}{y_m} = \frac{z_n}{z_m} \,. \tag{2}$$

Thus the dimensionless parameter δ is defined by

$$\delta = \sigma \mu \omega l^2 \,. \tag{3}$$

In most cases, $\mu_n = \mu_m = \mu_0$, the magnetic permeability of free space, and thus δ simplifies to $\delta = \sigma\omega l^2$. The absolute scaling factor a, which is used in the experiment, is defined below.

DESCRIPTION OF THE SCALE MODELING SYSTEM

The scale model facility at the University of California's Richmond Field Station has previously been described by Morrison et al. (1982). The models are located within a 3-m by 5-m by 2-m tank filled to a depth of 1.4 m with salt water of conductance 12.8 S/m. Targets composed of graphite-epoxy composite are hung from the wooden support beam that straddles the tank and also supports the fully automated transmitter and receiver positioning systems. Low noise measurements are made by keeping all cables in constant tension and the receiver in a fixed position while data is collected with the transmitter moving. The scale factors for this experiment are: geometrical, 1/100; conductivity, 1000; and frequency, 10.

The receiver and transmitter coils are identical in size (5-cm radius) and windings (100 turns of #18 wire) and are both shielded to protect the receiver from electrostatic coupling. The only difference between the coils is that the transmitter has been tuned to 98.6 kHz. Unfortunately the coil radius scales to field size of 5 m, which is much larger than the natural borehole size. However, Spies and Frischnecht (1988) indicate that transmitter-receiver separations of 10 coil radii are sufficient to approximate the coils as dipoles. The effect of the target location and size relative to the coil position and size is unknown. However, if induction dominates the secondary response such that the target acts as a dipole, then the above rule should be observed.

The transmitter is mounted on a vertically translating tower that has a maximum vertical displacement of 1.0 m. The tower position is controlled by a variable speed motor that drives a screw upon which the tower is suspended. The transmitter depth is determined by means of a pulse encoder that triggers the data acquisition system at 0.5-mm increments of tower movement. The receiver coil is mounted on a similar screw, which is driven by a stepping motor. Because the screw is calibrated and we know the number of steps per revolution, we can use a stepping controller to move the coil up or down at a constant increment, which was 2.5 cm for the experiment described here.

The transmitter and receiver instrumentation is composed mostly of off-the-shelf components. A Hewlett

Packard 3325A synthesizer/function generator supplies the reference signal to both the transmitter and the receiver systems. The transmitter power is supplied by an ENI model 2100L RF amplifier, and the current is monitored by a Hewlett Packard 3457A multi-meter.

The output signal from the receiver coil is amplified by an EG&G Parc model 113 pre-amp before being input into an Ithaco Dynatrack 393 Lock-In amplifier upon which the receiver system is centered. An optical isolator designed and built by Gayle Holladay at Lawrence Livermore National Laboratory (LLNL) is used on the reference signal to minimize the chance of ground loops. The lock-in decomposes the signal into real and quadrature components, which are monitored by a Hewlett Packard 3495A scanner in series with a Hewlett Packard 3456A voltmeter.

A Hewlett Packard 9000-300 computer controls the data acquisition. The scanner alternately reads real and quadrature voltages at 0.5-mm transmitter depth intervals as triggered by the pulse encoder, which yields a real and an imaginary component every 1 mm. The computer stores these values and also monitors the transmitter current at 5-mm intervals. At the end of the acquisition, the computer averages 5 successive real and quadrature data points to yield a final data set consisting of 200 real and imaginary voltages and 200 transmitter currents at 5-mm transmitter intervals from a depth of 0.25 cm to 99.75 cm.

SYSTEM CALIBRATION AND NOISE DETERMINATION

The system was calibrated component by component in the lab and then the whole system compared with an analytic solution for a layered earth by placing the coils in the tank in the absence of a target. This analysis also provided the correction factors needed to calculate the absolute scaling factor a. The coils are rigidly mounted in the tank and thus are not easily removeable for recalibrating and referencing in a free space. This problem was solved by positioning both coils at the surface of the water, zeroing the quadrature component with the lock-in amplifier and using the resulting real component as the reference value. This reference value was checked not only at the beginning and end of each day but also at various intervals throughout the day in order to determine if any system drift had occurred. However, because the phase is set to zero, calibration not only requires multiplying the data by the scale factor but also implies rotating the phase. Calibration was accomplished by comparing the tank data with results calculated by program EM1D (K.H. Lee, personal communication, 1984), which is an analytic solution to the one-dimensional layered earth problem. Laboratory measurements of the water indicated a conductivity of 14.1 S/m at 21°C. Using a nomogram we determined the conductivity to be between 12.5 and 13.0 S/m for a tank temperature of 17°C.

The voltages collected in the tank are corrected to field values to compare with EM1D in the following manner. All voltages are first normalized by the reference voltage measured with both coils on the surface. Next a correction is applied to account for changes in the transmitter current observed as the coil descends into the medium. The phase and amplitude of these normalized voltages are then calculated.

A field model consisting of a 140-m-thick layer of conductivity between 0.0125 and 0.013 S/m overlying a resistive half-space was used as the input to EM1D. Results were calculated with the transmitter at the surface and receiver positioned at 5-m intervals from 0 to 100 m depth. The reference phase and amplitude for the EM1D results were calculated with both the transmitter and receiver at the surface; this numerical phase was added to the tank phase data and the tank amplitudes multiplied by the EM1D reference amplitude. Thus the scaling factor a is given by

$$a = \frac{H_{em1d}^{z=0}}{V_m^{z=0}} \frac{I_{Tx}^{z=0}}{I_{Tx}^{z}}, \tag{4}$$

where $H_{em1d}^{z=0}$ is the vertical magnetic field with both transmitter and receiver on the surface as calculated by program EM1D, $V_m^{z=0}$ is the measured voltage in the scale model with both coils on the surface, $I_{Tx}^{z=0}$ is the current in the transmitter coil with both coils on the surface, and I_{Tx}^{z} is the current in the transmitter coil for at transmitter depth z.

The results were converted to real and imaginary components and compared with the analytic results provided by EM1D. The layer conductivity was changed, and the process repeated until a best fit was observed in a least-squares sense. The final value was 0.0128 S/m for the layer conductance. Figure 1 shows a comparison of the tank and analytical results for two different receiver depths.

The measurement error for the scale modeling experiment is dependent on the coil configuration employed as well as external and system noise. In this case the primary sources for error were (1) uncertainty in the transmitter and receiver positions, (2) low-signal levels at large separations, and (3) drift in the instrumentation. The total error was determined by repeating measurements over various periods of time. This involved moving both the transmitter and receiver coils and then returning to occupy the positions a few hours later. In general, the error was found to be less than 1% of the primary field, although this error tended to increase with the amount of time between measurements.

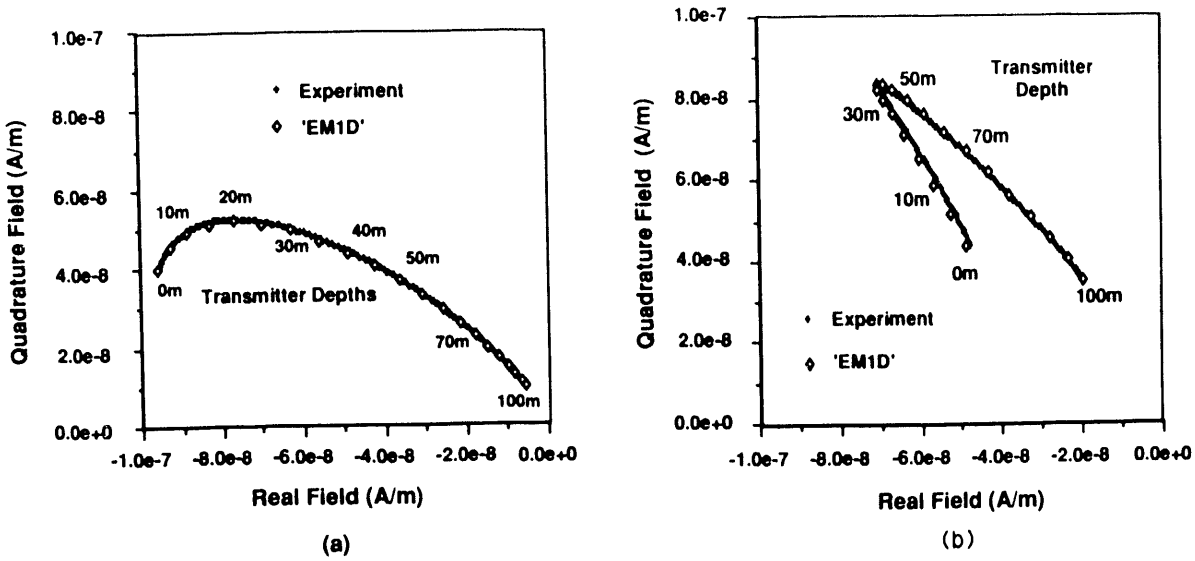

Figure 1. Tank data compared with program EM1D. A 140-m thick 0.0128 S/m layer was used as the model input. (a) Receiver at 0 m depth. (b) Receiver at 40 m depth. [XBL 913-579]

THE MODEL

The model was constructed to simulate an e.o.r. project, or a salt-water injection experiment like the one planned for the Richmond Field Station. Figure 2 shows the model consisting of two 100-m-deep wells separated by 100 m in an 80-Ωm half-space. A 10-m-thick tabular conductive body is situated between the two wells at 54 m depth.

The tank results were compared with two numerical solutions to determine their accuracy. Program SHEET is a integral equation solution for a thin sheet located in a full space originally published by Weidelt (1981) and modified for multiple targets in a half-space by Zhou (1989). The solution labeled "3D" is an integral equation solution for three-dimensional bodies located in a layered half-space developed by A.C. Tripp at the Utah Research Institute (1990, personal communication).

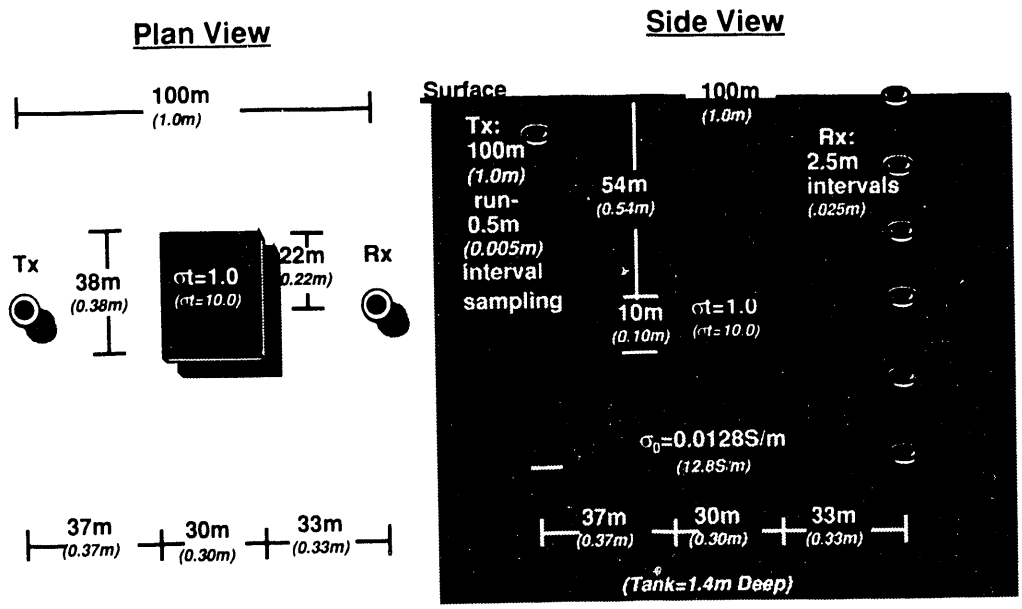

Figure 2. Field situation simulated in the scale model experiment. Scaled values are given in italics. [XBL 913-580]

The conductance of the block was originally measured in the laboratory using a Wenner resistivity array to have a field conductance of 5.2 S. However, comparing the tank results with the numerical solutions indicates the conductance to be between 1.0 S and 2.0 S. It is the author's opinion that this discrepancy is caused by an error in the resistivity measurements rather than the numerical solutions. Two possible explanations for this error are surface effects of the graphite composite and contact resistance between the graphite and the metal tacks used as electrodes.

Comparisons with the two numerical solutions are shown in Figure 3 for two different receiver positions (0 and 40 m depth). The first conclusion drawn from the secondary fields is that the block is too thick to be simulated by a thin sheet. A comparison between SHEET and 3D shows that the two solutions give nearly identical results for thin bodies, and thus the larger amplitudes shown both by the tank results and 3D are due to the thickness of the block.

The best fit to the tank data for the models that were run occurs for a 10-m-thick block with a conductance of 1.0 S. Although the fit between the numerical solution and the tank data is not exact, these results are considered accurate because the measured secondary fields approach the noise level of the system and the total and primary fields that were needed to calculate the secondary fields were measured over the period of 1 week.

INVERSION RESULTS

A linearized inversion routine proposed by Zhou (1989) was tested with the scale model data. This method employs a quadratic programing scheme to invert for a two-dimensional model. Both a Born approximation and a Rytov approximation are used to linearize the problem.

The inverted results are shown in Figure 4. Although the geometry of the model is recovered fairly well, the conductivity of the target body is poorly resolved. One probable source of error is the violation of the Born approximation due to the thickness of the block and the 10-to-1/target-to-host conductivity contrast. In addition, Zhou (1990, personal communication) has shown that using program SHEET as a forward solution gives much better target resolution when the vertical coverage in the boreholes is 150 m rather than 75 m, as was the case here. Thus this audio-frequency tomographic method does show some promise, although more work is needed to improve it.

CONCLUSIONS

The scale modeling at the Richmond Field Station salt water tank has proved (1) accurate measurements can

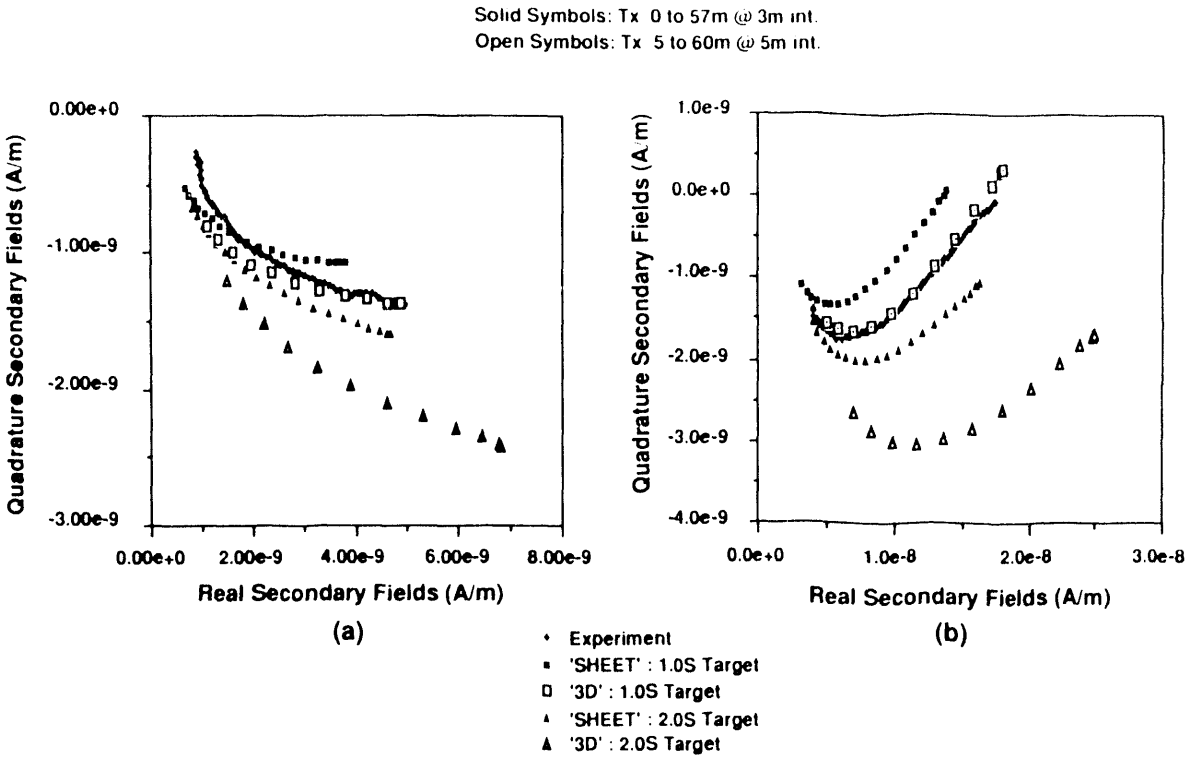

Figure 3. Secondary field tank data compared to programs SHEET and 3D. Background conductivity = 0.0128 S/m. (a) Receiver at 0 m depth. (b) Receiver at 40 m depth. [XBL 913-581]

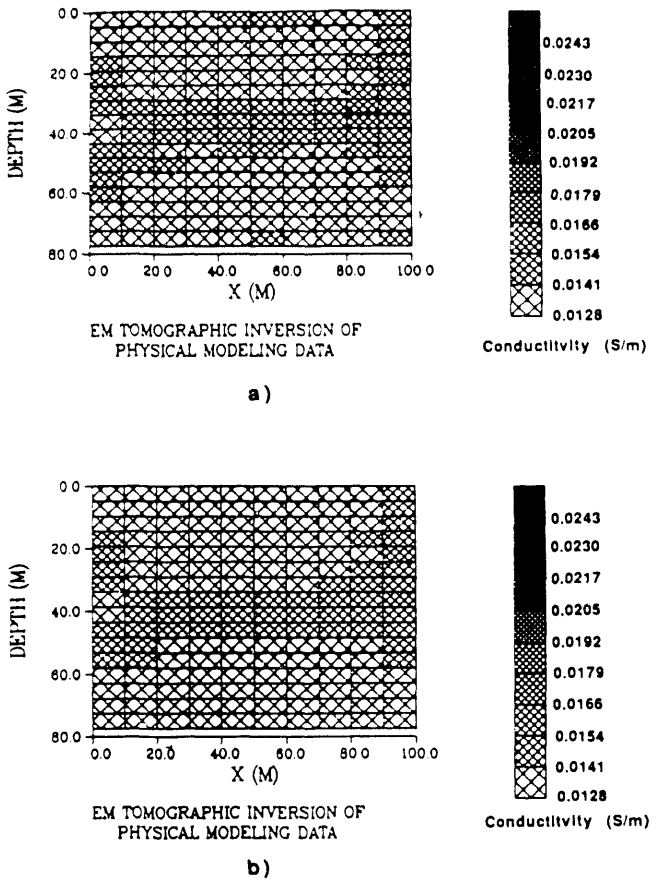

Figure 4. Linearized inversion results using the method proposed by Zhou (1989). (a) Rytov approximation. (b) Born approximation. [XBL 913-582]

be made in a cross-borehole environment and (2) existing forward numerical solutions are accurate within the noise range of the scale modeling system. In addition it has been shown that although the existing linearized inversion routine does recover the geometry of the model, the conductivity resolution is poor. Because the forward numerical solutions are much quicker and easier to use compared with the scale model system, we propose to use these algorithms to provide synthetic data for more complex model geometries. These results will in turn be used to test the limitations of existing inversion codes and to test new inversion routines that better resolve the conductivity distribution.

REFERENCES

Frischnecht, F.C., 1988. Electromagnetic scale modeling. *In* M.N. Nabighian (ed.), Electromagnetic Methods in Applied Geophysics (Vol I). Society of Exploration Geophysics.

Grant, F.S., and West, G.F., 1965. Interpretation Theory in Applied Geophysics. McGraw-Hill, New York.

Morrison, H.F., Clarke, A.J., Hanson, W.D., and Becker, A., 1982. A versatile EM scale modeling system (abstr). Geophysics, v. 47, p. 435.

Spies, B.R., 1980. The application of the transient EM method in Australian conditions—Field example and model studies (Ph.D. thesis). Macquerie University.

Spies, B.R., and Frischnecht, F.C., 1988. Electromagnetic sounding. *In* M.N. Nabighian (ed.), Electromagnetic Methods in Applied Geophysics (Vol II). Society of Exploration Geophysics (in preparation).

Weidelt, P., 1981. Report on dipole induction by a thin plate in a conductive half-space with and without overburden. Federal Institute for Earth Science and Raw Materials, Hannover, Germany.

Zhou, Q., 1989. Audio-frequency electromagnetic tomography for reservoir evaluation (Ph.D. thesis). Department of Material Sciences and Mineral Engineering, University of California at Berkeley. Lawrence Berkeley Laboratory Report LBL-28171.

Resistivity Logging through Metal Casing

C. J. Schenkel and H. F. Morrison

In recent years, there has been an increased interest in measuring formation resistivity through metal casing. Measurements made through casing can aid in characterizing existing reservoirs for effective recovery of oil and gas, as well as geothermal heat, without the cost and time of drilling new wells. Measuring the resistivity of adjacent formations may be useful to locate oil that was missed during the original logging prior to insertion of the casing. The method may also monitor changes in resistivity caused by subsurface processes such as injection or leakage

of contaminants from a waste site, flooding operations for enhanced oil recovery, or extraction processes of geothermal production.

Several patents have recently been issued that describe methods and devices that are capable of measuring formation resistivity through casing (Kaufman, 1989; Vail, 1989a,b; Gard et al., 1989). Currently, it is only known that Vail has developed and tested such a device, called Through-Casing Resistivity Tool (TCRT).

Kaufman (1990) investigated the behavior of the potential and its derivatives for a borehole with casing based on models of an infinite-length conductive pipe in a homogeneous medium. He showed that the second vertical derivative of the potential only varies with the casing conductance and formation resistivity for receivers located in the "intermediate zone" from the source. From his analysis, he concluded that if the casing conductance (S_C) is known, then the formation resistivity (ρ_f) measurements taken at that depth can be calculated by the expression

$$\rho_f = (\phi S_c)^{-1} \frac{d^2\phi}{dz^2}, \qquad (1)$$

where ϕ is the potential.

FORMULATION OF THE PROBLEM

A surface integral equation approach (Eloranta, 1986) is used to calculate the potentials in a finite-length borehole. In this numerical analysis, the borehole fluid, casing, and layer are modeled as inhomogeneities in the host or background medium. It is assumed that the sources are coaxial on the vertical axis and the inhomogeneities have axial symmetry so that the cylindrical coordinate system can be used. Because of the axisymmetry, the field can be described by its radial (ρ) and vertical (z) components.

Application of Green's theorem to Poisson's equation will result in an expression of the potential as the superposition of a single-layer and double-layer potential. By employing the boundary conditions, a Fredholm integral equation of the second kind is obtained, which is

$$\phi(\mathbf{r}) = \phi_0(\mathbf{r}) + C \int_S \phi(\mathbf{r}^*) \frac{\partial}{\partial n^*} g(\mathbf{r}, \mathbf{r}^*)\, ds^*, \qquad (2)$$

where $\mathbf{r}$ and $\mathbf{r}^*$ are the field point and the source density point on S, respectively.

In this integral equation, the potential function, $\phi(\mathbf{r})$, is expressed as the sum of the external source(s), $\phi_0(\mathbf{r})$, and the product of a double-layer potential and a normalized conductivity contrast, $C = \Delta\sigma/\sigma_0$. The conductivity contrast is given by $\Delta\sigma = \sigma_0 - \sigma_1$, where σ_0 and σ_1 are the background and disturbing body conductivities, respectively. The double-layer potential, which is distributed over the surface of the inhomogeneity, contains the unknown boundary values, $\phi(\mathbf{r}^*)$ and the normal derivative of the Green's function. The axisymmetric half-space Green's function, used for this problem, was derived in Schenkel and Morrison (1990) and can be written as

$$g(\mathbf{r}, \mathbf{r}^*) = \frac{1}{4\pi} \int_0^\infty J_0(\lambda\rho) J_0(\lambda\rho^*) \left[e^{-\lambda|z-z^*|} - e^{-\lambda(z+z^*)} \right] d\lambda, \qquad (3)$$

where $J_0(x)$ is the Bessel function of order zero and the primed and unprimed values are the locations of the source and field points, respectively.

When the field point approaches the surface of the disturbing body, the surface integral is improper and must be evaluated at the singular point. This evaluation can be found in Brebbia et al. (1984). This results in an additional term to integral equation (2) for $\mathbf{r} = \mathbf{r}^*$:

$$\phi(\mathbf{r}) = \phi_0(\mathbf{r}) + C \left[\int_S \phi(\mathbf{r}^*) \frac{\partial}{\partial n^*} g(\mathbf{r}, \mathbf{r}^*)\, ds^* + \frac{1}{2}\phi(\mathbf{r}^*)\, \delta(\mathbf{r}, \mathbf{r}^*) \right], \qquad (4)$$

where $\delta(\mathbf{r}, \mathbf{r}^*)$ equal one for $\mathbf{r} = \mathbf{r}^*$ and zero elsewhere.

The integral equation (4) is solved by the approximation method of moments (Harrington, 1968). This method involves the expansion of the unknown function into a series of weighting and basis functions at N discrete points on the region of interest. Each basis function exists only over a subsection in the region, and the corresponding weighting function will only affect the approximation of the unknown function over that subsection. The integral over the region is then approximated as a summation of integrals over the subsections. By using piecewise constant-basis and Dirac delta-weighting functions, Eq. (4) can be approximated by

$$\phi(\mathbf{r}) = \phi_0(\mathbf{r}) + C \left[\sum_{n=1}^{N} K(\mathbf{r}, \mathbf{r}_n^*)\, \phi(\mathbf{r}_n^*) + \frac{1}{2}\phi(\mathbf{r}_n^*)\delta(\mathbf{r}, \mathbf{r}_n^*) \right], \qquad (5)$$

where:

$$K(\mathbf{r}, \mathbf{r}_n^*) = \int_{S_n} \frac{\partial}{\partial n^*} g(\mathbf{r}, \mathbf{r}_n^*)\, ds^*.$$

This linear form of the integral equation must now be satisfied at each of the N discrete points. As a result, a matrix equation is obtained and can be solved to determine the unknown potential functions. Once the surface potentials are found, Eq. (5) is used to calculate the potential at the field point.

NUMERICAL RESULTS

Figure 1 illustrates the model used for this analysis. The simplified model consists of a finite-length conductive casing filled with fluid embedded in a three-layer medium. For simplicity, the resistivity of 10 Ω·m was used for the top layer, bottom layer, and borehole fluid. The casing has a resistivity of 10^{-6} Ω·m and length of 100 m. The target layer was 3 m thick with its top located 49 m below the surface. To approximate a layer of infinite extent, the outer boundary of the layer placed at 5000 m. The equally spaced potential electrodes, M, N, and M′, are straddled by two current electrodes, A and B. All electrodes are placed in contact with the casing. For models with a single current source, electrode B is placed at "infinity," the remote position.

The calculated voltage difference for a lateral-log configuration is shown in Figure 2. These voltage differences, which are normalized by the potential electrode separation (MN = 0.5 m), represent an estimate of the electric fields on the casing and are proportional to the current leakage. The separation from the source-to-center

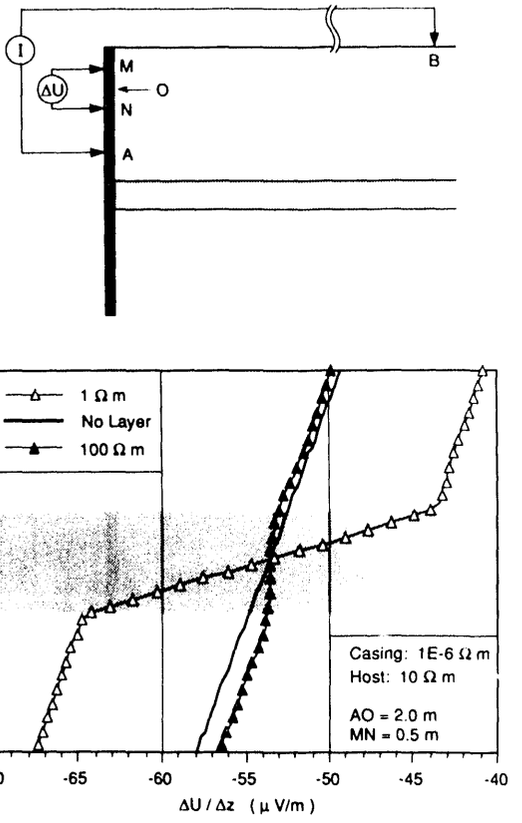

Figure 2. (Top) Electrode array used for electric field calculation. **(Bottom)** Electric field response with increasing depth for a 1-Ω·m and 100-Ω·m layer (dark area). [XBL 913-584]

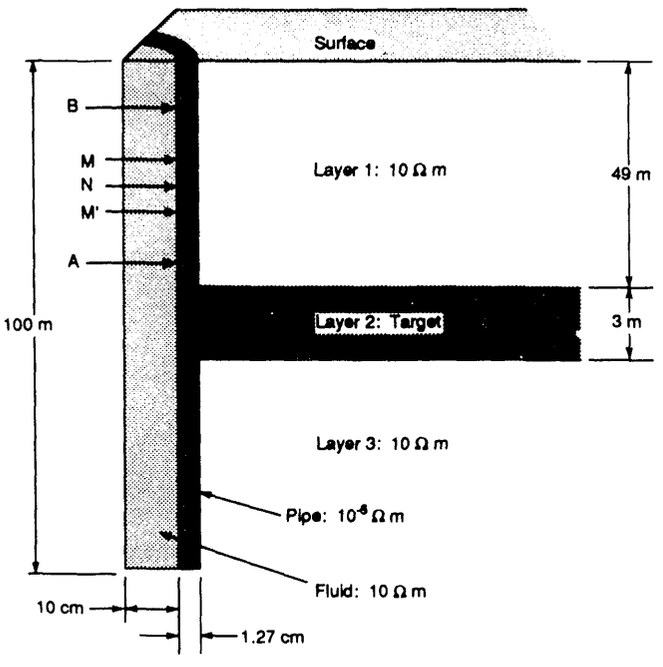

Figure 1. Model and electrode array configuration. [XBL 913-583]

potential array, AO, was 2.0 m. The resistivities of ! Ω·m and 100 Ω·m were used for the target layer. The discontinuity of the curves corresponds to the change in resistivity. For the conductive layer, the increased rate of voltage drop is due to the increased current leakage into the adjacent formation. A resistive formation has the opposite effect, and a decrease rate of change is observed through the target layer.

A well-log of through-casing measurements with unknown casing conductivity is simulated using the parameters in Figure 1. For an unknown casing conductance, two electrode configurations were used to obtain the formation resistivity by Eq. (1). In Figure 3a, the top electrode configuration estimated the casing conductance and the bottom configuration was used to calculate the formation resistivity. To estimate the second derivative, three potential electrodes, M, M′, and N, were needed. The current, I, is applied at the source electrodes, A and B, which are close to the potential electrodes. Because of the large casing-formation conductivity contrast, the voltage across the electrode pair, MN or NM′, is mainly dependent on the casing resistance between the pair. From the voltage and current strength, the casing conductance can be calculated. Moving electrode B to the

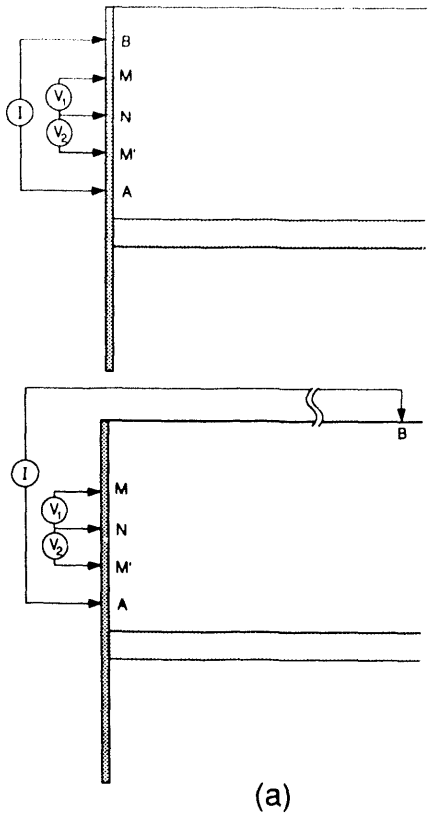

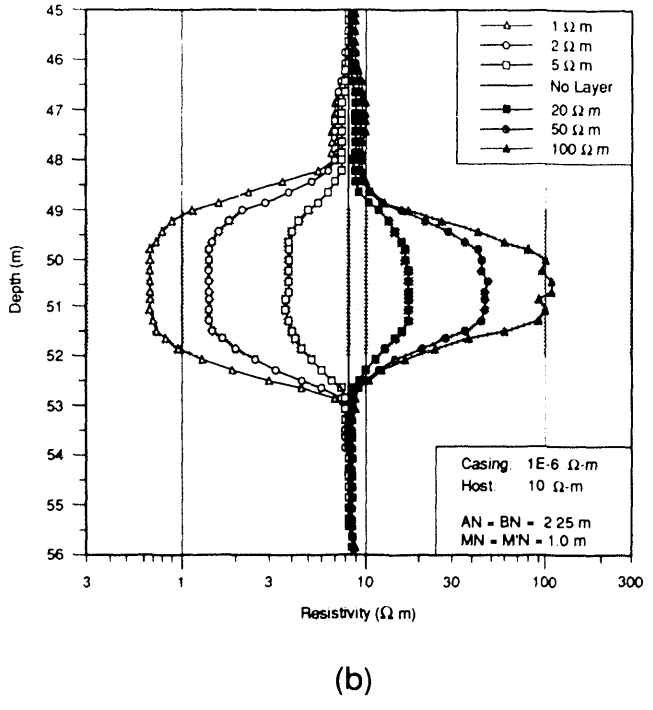

Figure 3. (a) Electrode array used to calculate formation resistivity. The casing conductance is estimated from the top array, and the second derivative of the potential is approximated with the bottom array. (b) The resistivities calculated from the model of Figure 1 using Eq. (1). Several resistivities were used for the target layer (dark area). [XBL 913-585]

remote position, the current must now flow through the casing and the formation. The voltage differences, V_1 and V_2, at their respective electrode pair, MN and NM′, will reflect both the casing and formation resistances. By subtracting the two voltages, a second-derivative approximation is obtained.

With the estimate of the casing conductance and second derivative, the formation resistivity is calculated from Eq. (1). The numerical results for several resistivities of the target layer are illustrated in Figure 3b. The resistivity values for the target layer ranged from 1 Ω·m to 100 Ω·m. For this analysis, the separation between the current electrode and the center potential electrode, AN, was 2.25 m. The potential electrode spacings, MN and NM′, were 1.0 m. From the plot, the calculated resistivity values are slightly lower than those of the model with no layer (homogeneous) and the model with the low-resistivity layer (1 Ω·m to 5 Ω·m). This discrepancy decreases with increasing resistivity. The effects on the formation resistivity for various borehole fluids is shown in Figure 4. The spacings of the current and potential electrodes are the same as those in Figure 3. A resistivity of 1 Ω·m was used for the target layer. The borehole fluid resistivity ranged from 1 Ω·m to 20 Ω·m. The figure indicates that varying the borehole fluid resistivity has a very small or no influence on the resistivity measurement. Figure 5 illustrates the effects of the electrode separation on the layer boundary resolution. The target layer and fluid have

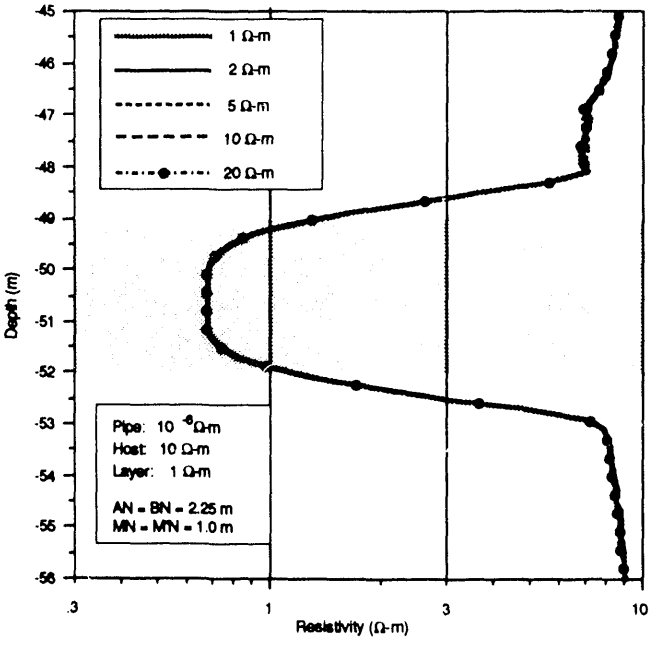

Figure 4. The formation resistivity calculated for various borehole fluid resistivities. The electrode array is the same as Figure 1. The resistivity of the target layer (dark area) is 1 Ω·m. The fluid resistivities ranged from 1 Ω·m to 20 Ω·m. [XBL 913-586]

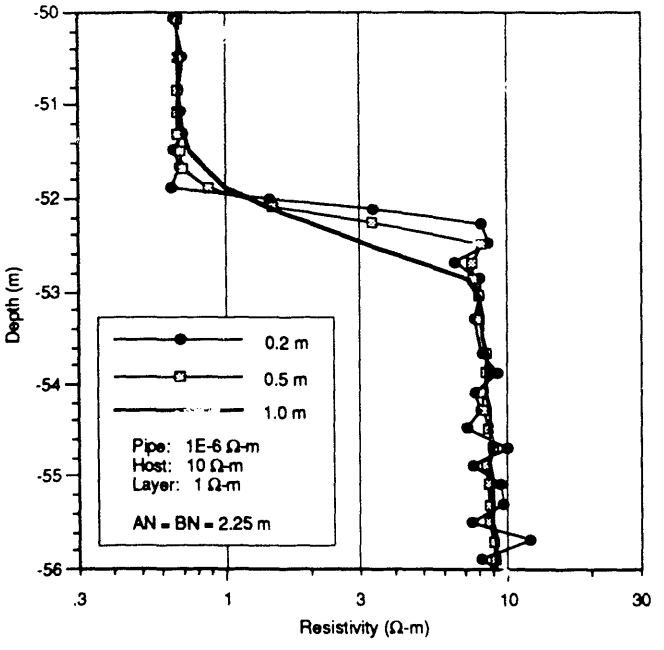

Figure 5. The formation resistivity calculated with different potential electrode arrays. The current electrode array is the same as Figure 1. The resistivity of the target layer (dark area) is 1 Ω·m. The electrode separation ranged from 0.2 m to 1.0 m. [XBL 913-587]

resistivities of 1 Ω·m and 10 Ω·m, respectively. The separations of 0.2 m, 0.5 m, and 1.0 m show that the boundary resolution improves as the electrode separation becomes smaller. It appears that the resolution of the boundaries is dependent on the electrode spacing needed to approximate the second derivative.

SUMMARY

These numerical results clearly show the feasibility of determining formation resistivity through metal casing. For the situation of the unknown casing conductance, two measurements with different electrode configurations are needed to determine the formation resistivity for a given depth. One calculates the casing conductance, and the other estimates the second derivative of the potential. A three-point measurement on the inner surface of the metal casing is needed to approximate the second derivative of the potentials. Using Eq. (1), the formation resistivity can be calculated from the three-point measurement, the potential, and the estimate of the casing conductance.

The analysis of electrical logging through metal casing was for the situation of a finite-length casing in a layered medium. A surface integral equation approach was used to determine the potentials on the casing. The casing, borehole fluid, and layers were modeled as inhomogeneities in the background medium. It was assumed that the sources and the inhomogeneities had axial symmetry. For the simulations, all electrodes were in contact with the inner wall of the casing.

It appears that the discontinuity of the electric field corresponds to the boundaries of the layer and that the rate of change of the field is proportional to the resistivity of the adjacent formation. The calculated values of formation resistivity compared closely with the resistivities of the layer model. The borehole fluid appears to have little or no influence on the the formation resistivity measurements. The vertical resolution of the layer boundaries is dependent on the potential electrode spacing needed to approximate the second derivative.

The discrepancy observed between the calculated results and the model resistivity may be attributed to numerical errors, such as discretization of the model and approximating derivatives with differences.

REFERENCES

Brebbia, C.A., Telles, J.C.F., and Wobel, L.C., 1984. Boundary Element Techniques; Theory and Applications in Engineering. Springer-Verlag, New York, 464 p.

Eloranta, E.H., 1986. Potential field on a stationary electric current using Fredholm's integral equations of the second kind. Geophysical Prospecting, v. 34, p. 856–872.

Gard, M.F., Kingman, J.E.E., and Klein, J.D., 1989. Method and apparatus for measuring the electrical resistivity of geological formations through metal drill pipe or casing. U.S. patent 4,837,518.

Harrington, R.F., 1968. Field Computation by Moment Methods. The MacMillian Company, New York, 229 p.

Kaufman, A.A., 1989. Conductivity determination in a formation having a cased well. U.S. patent 4,796,186.

Kaufman, A.A., 1990. The electric field in a borehole with a casing. Geophysics, v. 55, p. 29–38.

Schenkel, C.J., and Morrison, H.F., 1990. Effects of well casing on potential field measurements using downhole current sources. Geophys. Prospect., v. 38, p. 663–686.

Vail, W.B., 1989a. Methods and apparatus for measurement of the resistivity of geological formations from within cased boreholes. U.S. patent 4,820,989.

Vail, W.B., 1989b. Methods and apparatus for measurement of electronic properties of geological formations through borehole casing. U.S. patent 4,882,542.

Predicting Hydraulic Conductivity of Sedimentary Rocks from Microgeometry

E. M. Schlueter, R. W. Zimmerman, N. G. W. Cook, and P. A. Witherspoon

The macroscopic transport properties of porous and fractured media depend critically upon processes at the pore level, which are very dependent on the connectivity and geometry of the pore space. The primary focus of this research is (1) to understand, through analysis and experiment, how fluids in pores affect the hydraulic properties of rocks and (2) to develop equations relating these macroscopic properties to the microscopic geometry and structure of the pore space. It has been our aim to assemble a comprehensive picture of a rock based on a geologically sound and physically accurate framework. The theoretical analysis has been useful in defining and ranking needed experiments and has been successful in correlating measurements of important transport properties such as intrinsic permeability of sandstone to the microgeometry of the pore space.

For this study, rock cross sections have been prepared for imaging with the scanning electron microscope (SEM). The resulting 2-D SEM micrographs have been employed to infer the hydraulic conductance of the individual pores. We assume that the pores are cylindrical tubes of varying radius and that they are arranged in a cubic lattice, so that the coordination number of the network is 6. The hydraulic conductance of each tube is estimated from its area and perimeter, using the hydraulic radius approximation and the Hagen-Poiseuille equation. In the section under consideration, the pore cross sections are assumed to be randomly oriented with respect to the directions of the channel axes. The orientation effect has been corrected by means of geometrical and stereological considerations. Account is also taken of possible variation of the cross-sectional area along the length of each tube, e.g., pore necks and bulges. The effective-medium theory of solid-state physics is then used to replace each individual conductance with an effective average conductance. Finally, a unit cubic cell is extended to relate the effective-hydraulic-tube conductances to the continuum values of permeability. Preliminary results, using Berea, Boise, Massilon, and Saint-Gilles sandstones, yield very close agreement between the predicted and measured permeabilities, with essentially no arbitrary parameters in the model.

EFFECTIVE MEDIUM THEORY

Consider an inhomogeneous, disordered, continuous composite system (conductive/nonconductive) in which one can locally define a given conductive property, e.g., hydraulic conductance, which can be calculated from the geometry of the conductive element (e.g., the coefficient in Poiseuille's law for cylindrical tubes). This is possible as long as the dimensions of the local elements are large with respect to the scale of the conduction process involved. According to Kirkpatrick (1973), such a medium can be approximated by a 3-D network with the same topology in which all the conductances have a single effective value. The effective medium can be defined as one in which the macroscopic conductance is the same as for the heterogeneous system, and the effective conductance can therefore be considered as the mean value controlling the physical property of concern. Since we are concerned with a random medium, it is assumed that no spatial correlation exists between the individual conductances. The theory leads to the requirement that the perturbation introduced when each individual conductance is replaced by the effective conductance must average to zero. The resulting implicit equation defining the effective conductance is

$$\left\langle \frac{c_{eff} - c_i}{[z/2 - 1]c_{eff} + c_i} \right\rangle = 0 , \qquad (1)$$

where the angle brackets indicate the average with respect to the probability distribution function $p(c)$ of the individual conductances, c_i, and z is the average coordination number of the network (the number of branches meeting at a node). The effective-medium theory coupled with a network of resistors has been used by Koplik et al. (1984) to predict permeability of Massilon sandstone, although the predicted value was 10 times higher than the measured value. Doyen (1988) calculated the transport properties of Fontainebleau sandstone and predicted permeability within a factor of 3 of the measured value. These models do not account for the fact that the 2-D section under consideration slices each pore at a random angle to its axis or for the variation of the cross-sectional area along the length of each tube, both of which are significant effects.

METHOD OF ANALYSIS

The concept of permeability allows a macroscopic description of the fluid flow phenomena in porous media under a regime of sufficiently low fluid velocities (Scheidegger, 1974). This property is linked to other properties of porous media, such as capillary pressure and relative permeability. In order to understand the relationships, one has to understand how all those properties are conditioned by the connectivity and geometrical properties of the pore space. The simplest model that can be constructed is one representing a porous

medium by a bundle of straight, parallel cylindrical capillaries of uniform diameter that extend from one face of the porous medium to the other. Equations based on a 1-D model of this type are called Kozeny equations. The opposite extreme of this parallel case would be to assume a serial model in which all the pores are connected in series. Obviously, this model is as unrealistic as the parallel model, and a realistic model lies somewhere between these extremes.

Figure 1, an SEM micrograph of a pore cast of Berea sandstone, reveals a 3-D network of irregularly shaped pores. Although an exact description of key pore space morphological characteristics is rather complex, it is possible to isolate three main features: (1) multiple connectivity of pore segments, (2) cross sections of converging-diverging pores, and (3) roughness and irregularity of pore walls.

Since the actual rock geometry is too complex for any quantitative study, we have replaced it by a standard model geometry that preserves the main observed morphological features. The local conductive elements have been obtained from 2-D SEM micrographs of Berea, Boise, Massilon, and Saint-Gilles sandstone (Figure 2). Typical pore-space contours obtained from serial sections are shown in Figure 3. The hydraulic conductance of each tube of varying radius is estimated from its area and perimeter, using the hydraulic radius approximation and Poiseuille's law, and the electrical conductance is related only to the cross-sectional area of the tube.

According to the Hagen-Poiseuille equation, the volumetric flux of fluid through a cylindrical tube of radius r is

$$q = \frac{\pi r^4}{8\mu} \nabla P , \tag{2}$$

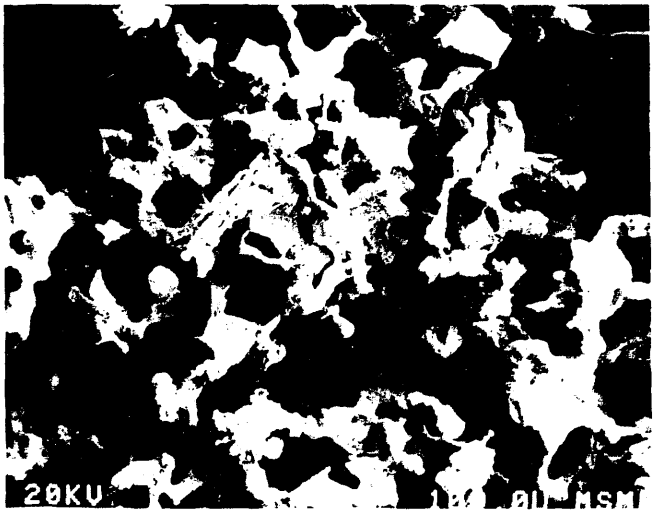

Figure 1. SEM micrograph of Berea sandstone. [XBB 905-4402]

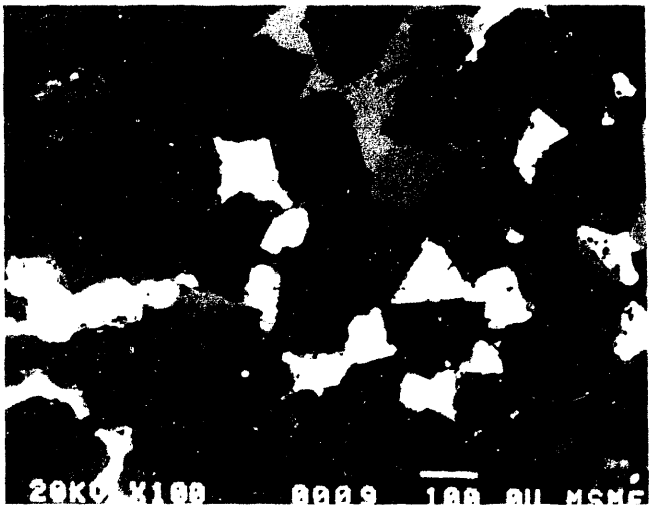

Figure 2. Typical serial section of Berea sandstone. [XBB 908-6348]

where μ is the absolute viscosity and ∇P is the pressure gradient. We now use the hydraulic radius concept to rewrite Eq. (2) in a form that is applicable to noncircular pores. The hydraulic radius R_H of the tube is defined as

$$R_H = \frac{\text{area}}{\text{wetted perimeter}} = \frac{r}{2} . \tag{3}$$

Using Eq. (3), we can rewrite Eq. (2) as

$$q = \frac{R_H^2 A}{2\mu} \nabla P , \tag{4}$$

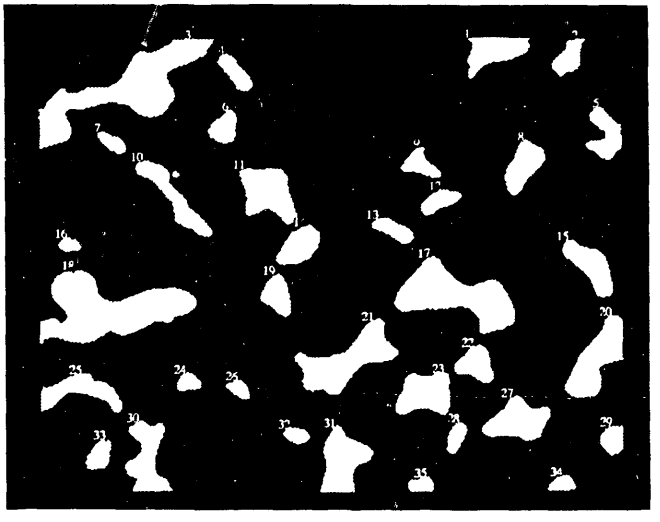

Figure 3. Pore-space contours obtained from serial section of Figure 1. [XBB 908-6348A]

where A is the area of the tube. The hydraulic conductance per unit length of each tube is therefore given by

$$C_h = \frac{R_H^2}{2} A \,. \tag{5}$$

In the 2-D section under consideration, however, the pore cross sections are randomly oriented with respect to the directions of the channel axes. The orientation effect has been corrected by means of the following geometrical and stereological considerations (Underwood, 1970), which are exact for the case of circular cross sections,

$$(R_H^2 A)_{actual} = \frac{1}{2} \left\langle \frac{1}{\cos\theta(1+\cos^2\theta)} \right\rangle^{-1} (R_H^2 A)_{measured} \,, \tag{6}$$

where the angle-bracketed expression is the spherical average for pores of random orientation,

$$\left\langle \frac{1}{\cos\theta(1+\cos^2\theta)} \right\rangle = \frac{1}{\pi} \int_0^{\pi} \int_0^{\theta_{max}} \frac{\sin\theta \, d\theta \, d\phi}{\cos\theta(1+\cos^2\theta)} \,, \tag{7}$$

with θ_{max} = arctan (L/D) and L/D being the maximum ratio of pore length to diameter. Using an average value of L/D = 5, as estimated from the micrographs, we find that

$$(R_H^2 A)_{actual} = 0.32 (R_H^2 A)_{measured} \,. \tag{8}$$

(Evaluation of the integral in Eq. (7) shows that the factor 0.32 in Eq. (8) is very insensitive to the value chosen for L/D.) In addition, constrictions within the individual branch channels, i.e., pore necks and bulges, have been taken into account using an analysis based on a sinusoidal variation of cross section. In the permeability analysis, for example, the factor accounts for the ratio of $\langle R^{-4} \rangle^{-1}$, which governs the conductance of a tube of varying radius, to $\langle R \rangle^4$, which is the value estimated from the micrographs. Throat-to-pore ratios given by this analysis have been verified by direct micrograph measurements for Berea sandstone. We have estimated a throat-to-pore radius ratio of 0.5 from a pore cast of Berea sandstone and tentatively use this value for each rock. This ratio indicates a hydraulic constriction factor of 0.55. Although some sandstones also exhibit roughness at scales much smaller than the average pore diameter, it is known that such roughness has little effect on the hydraulic conductance (Berryman and Blair, 1987) and can therefore be ignored. Study of SEM micrographs of Berea sandstone has indicated the presence of a statistically isotropic 3-D pore structure, which is well represented by Figure 4. These

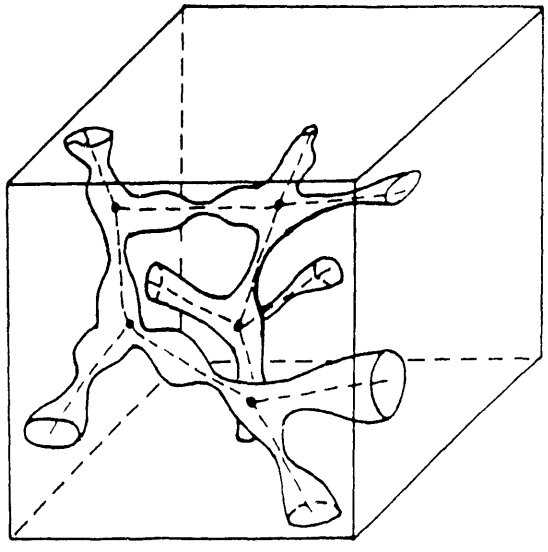

Figure 4. Microscopically inhomogeneous pore system and its skeleton (after Doyen, 1988). [XBL 913-588]

observations have led to the assumption that the pores of varying size are arranged in a cubic lattice, so that the coordination number of the network is 6. The effective-medium theory from solid-state physics is then used to replace each individual conductance with an effective average conductance as follows. For a general discrete distribution of conductances, Eq. (1) takes the form

$$\sum_{i=1}^{N} \frac{c_{eff} - c_i}{[z/2 - 1]c_{eff} + c_i} = 0 \,, \tag{9}$$

where the sum is over all N conductive elements. For a coordination number of z = 6, Eq. (9) has been solved numerically to allow for the calculation of the effective-medium conductance, given the individual conductances.

Finally, a unit cubic cell is extended to relate the effective-hydraulic-tube conductance to the continuum values of permeability by the expression

$$k = \frac{N C_{eff}}{A_{ph} \tau} \,, \tag{10}$$

where C_{eff} is the effective conductance of the cubic network of coordination number 6, N is the number of pore elements in the micrograph, A_{ph} is the area of the photograph, and τ is the tortuosity of a cubic lattice, which is 3.

RESULTS AND DISCUSSION

Preliminary results are presented in Table 1. Good agreement was found between measured and predicted hydraulic conductivity for a variety of sandstones when using the cubic lattice model, with essentially no arbitrary

Table 1. Intrinsic permeability of sedimentary rocks.

Rock	Measured	Predicted ($z = 6$)
Berea	462 md	670 md
Boise	1.30 d*	1.35 d
Massilon	2.50 d†	3.10 d
Saint-Gilles	170 md*	370 md

*Persoff et al. (1990).
†Koplik et al. (1984).

adjustable parameters. If a Kozeny-type parallel or serial model is applied instead, permeability is overpredicted or underpredicted, respectively. This study marks the beginning of our effort to understand how the important single-phase and multiphase transport parameters are related to the topology and geometry of the pore structure in reservoir rocks. Future extensions of this work will be to predict such properties as electrical conductivity and relative (two-phase) permeability.

REFERENCES

Berryman, J.G., and Blair, S.C., 1987. Kozeny-Carman relations and image processing methods for estimating Darcy's constant. J. Appl. Phys., v. 62, no. 6, p. 2221–2228.

Doyen, P., 1988. Permeability, conductivity, and the geometry of sandstone. J. Geophys. Res., v. 93, no. B7, p. 7729–7740.

Kirkpatrick, S., 1973. Percolation and conduction. Rev. Mod. Phys., v. 45, no. 4, p. 574–587.

Koplik, J., Lin, C., and Vermette, M., 1984. Conductivity and permeability from microgeometry. J. Appl. Phys. v. 56, no. 11, p. 3127–3131.

Persoff, P., Pruess, K., Benson, S.M., Wu, Y.S., Radke, C.J., Witherspoon, P.A., and Shikari, Y.A., 1990. Aqueous foams for control of gas migration and water coning in aquifer gas storage. Presented at the 1989 International Gas Research Conference, Tokyo, Japan, November 6–9, 1989. Lawrence Berkeley Laboratory Report LBL-27274.

Scheidegger, A.E., 1974. The Physics of Flow through Porous Media. University of Toronto Press.

Underwood, E.E., 1970. Quantitative Stereology. Addison-Wesley, Reading, Massachusetts.

Fractal Dimensions of Pores in Sedimentary Rocks

E. M. Schlueter, R. W. Zimmerman, N. G. W. Cook, and P. A. Witherspoon

When the microstructure of a typical sedimentary rock is examined under an optical microscope at low resolution, the pore-grain interfaces appear to be smooth. However, when the scanning electron microscope (SEM), with its higher resolution, is used instead (see Figure 1), the pore-grain interface commonly appears rough, and fractal surface behavior has often been found to span all length scales below the pore size (Katz and Thompson, 1985; Krohn, 1988). We have examined SEM micrographs of various reservoir-type sedimentary rocks and found that they satisfy the perimeter-area relation for fractal islands derived by Mandelbrot (1982), in which $P \approx A^{D/2}$. The fractal dimensions of four sandstones (Berea, Boise, Massilon, and Saint-Gilles) were found to lie between 1.31 and 1.40, whereas that of an Indiana limestone was found to be 1.20. Since the fractal dimension is a parameter that quantifies the roughness of the pore surfaces, it is reasonable to expect that it has some influence on the permeability. Models that will allow the permeability to be

Figure 1. SEM micrograph of Saint-Gilles sandstone at 160× magnification. [XBB 911-125].

predicted from the fractal dimension and pore-size distribution, as measured from thin sections, are currently under development.

FRACTAL GEOMETRY

For each family of standard planar shapes, geometrically similar but of different sizes, one can define a characteristic length as (Feder, 1988)

$$\varepsilon = \frac{\text{Perimeter}}{\text{Area}^{1/2}} . \tag{1}$$

The ratio ε is the same for each of the similarly shaped features and is independent of their size. For example, since the perimeter of a circle of radius r is equal to $2\pi r$, and the area of the disk bounded by such a circle is πr^2, it follows that

$$\varepsilon(\text{circle}) = \frac{\text{Perimeter}}{\text{Area}^{1/2}} = \frac{2\pi r}{\sqrt{\pi r^2}} = 2\sqrt{\pi} . \tag{2}$$

Similarly, the ratios $\varepsilon = 4$ and $\varepsilon = 6/3^{1/4}$ can be found for squares and equilateral triangles, respectively. Hence each of these shapes obeys a relationship of the form $P = \varepsilon A^{1/2}$, where ε is some constant.

Consider now a collection of similar "islands" with fractal "coastlines" of length $P(\alpha)$ and area $A(\alpha)$. Mandelbrot (1982) has shown that for each island whose boundary is a fractal curve, there exists an analogue of ε that can be defined by

$$\varepsilon = \frac{\text{Perimeter}^{1/D}}{\text{Area}^{1/2}} , \tag{3}$$

where D is the fractal dimension of the coastlines of the similarly shaped islands. The area and length of each of the islands is measured by using an area-dependent yardstick $\alpha^* = \rho\sqrt{A_i(\alpha)}$ for the ith island, with ρ being an arbitrary but fixed small parameter and α a fixed yardstick. The length of the coastline of the ith island is $P_i(\alpha^*) = N_\rho \alpha^*$, where N_ρ is the number of segments of length α^* needed to traverse the perimeter. For similarly shaped islands, N_ρ is independent of the size of the island. From the definition of the Hausdorff-Besicovitch fractal dimension in the limit of small α, it can be shown that (see Feder, 1988; Rys and Waldvogel, 1986)

$$P_i(\alpha) = \varepsilon^D A_i(\alpha)^{D/2} , \tag{4}$$

where the parameter ε depends on the length of the measuring yardstick, α. This equation holds for any given yardstick α that is small enough to measure the smallest island accurately.

MEASUREMENT TECHNIQUE

In order to study the pore structure of the rock samples, specimens of cylindrical shape were first impregnated with a blue-dyed epoxy. Thin sections were then prepared and imaged (Figure 1) by SEM. The basic method involves counting size and perimeter pixel units for every feature in a standard SEM micrograph of some fixed magnification. The field imaged by the micrograph must contain a large enough number of pores to ensure a statistically representative sample; we have found that 30–40 pores suffices for this purpose. The analysis was carried out using both a manual and an automated image analysis procedure. The manual technique involved overlaying a square grid, with grid size of 2.54 mm, and visually counting the number of grid blocks occupied by the area of each pore, as well as the number of grid blocks that the perimeter passes through. Digital images with typical image sizes of 482×640 pixels, and 8 bits per pixel to quantify the darkness level, were used for comparison with the manual technique. The size of each pixel was about 3 μm on a side. The image analysis program sets a threshold level of darkness to distinguish between pore space and mineral grains. The digitized thin section (Figure 2) then shows mineral grains in black and pore space in white. This method was used to estimate the area-perimeter statistics for groups of pores in a thin section. Individual pores were also studied by changing the magnification of the SEM to cover feature sizes from approximately 10 μm to sizes larger than the typical grain size.

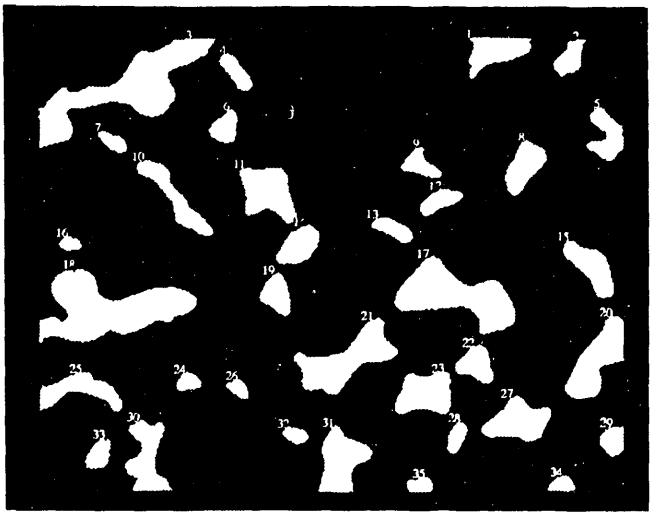

Figure 2. Pore-space contours obtained from computerized image analysis of a Berea sandstone thin section. [XBB 908-6348A]

DATA AND FRACTAL ANALYSIS

According to Eq. (4), the fractal dimension D can be estimated from the slope of a plot of ln P vs. ln A, since $d \ln P/d \ln A = D/2$. Analysis of the perimeter-area data from several reservoir rocks confirms their fractal nature (see Figures 2 and 3). The constants D and ε appearing in Eq. (4) were found by performing a linear regression on the log perimeter-log area data. From this analysis we find pore fractal dimensions ranging from 1.31 to 1.40 for the four sandstones examined and 1.20 for Indiana limestone (Table 1). The fractal nature of the pore cross sections was also verified by examining a single pore (Figure 4) from a Berea sandstone thin section at different levels of magnification, from 54× to 120×. The fractal dimension thus determined (Figure 5) was very close to the value estimated from a suite of pores examined at the same magnification, which verifies that the cross sections are indeed fractals.

SUMMARY

Digitized image analysis has been performed on SEM micrographs of thin sections of five sedimentary rocks. The pore cross sections were found to have fractal dimensions ranging from 1.20 to 1.40. This indicates a much rougher pore surface than would be be the case for a pore with a Euclidean shape, such as a circle or ellipse, for which the fractal dimension would be 1.0. We are currently developing a model that will relate the fractal dimension to the hydraulic permeability.

Table 1. Area–perimeter fractal data.

Rock	D	r*
Berea sandstone	1.34	0.99
Boise sandstone	1.40	0.98
Massilon sandstone†	1.40	0.98
Saint-Gilles sandstone	1.34	0.98
Indiana limestone	1.20	0.99

* Correlation coefficient.

† From Koplik et al. (1984).

Figure 4. Pore-space contours from a Berea sandstone pore at different magnifications. [XBB 911-127]

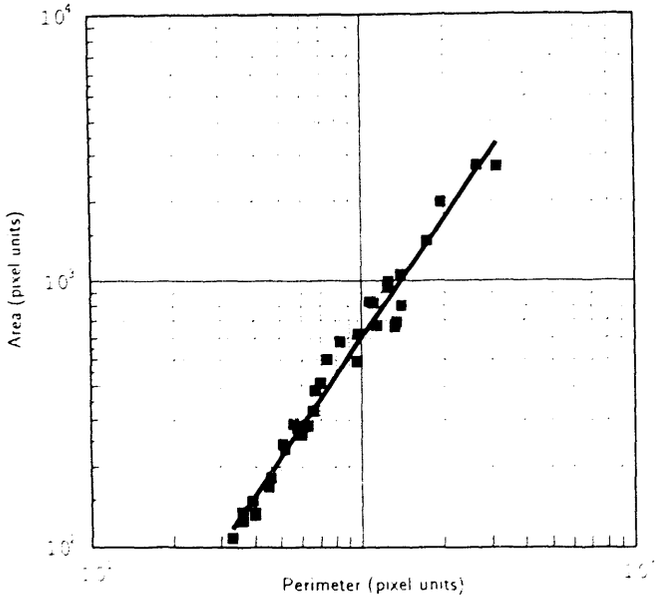

Figure 3. Fractal area-perimeter relationship for Berea sandstone. The fractal dimension D is equal to twice the slope $d \ln P/d \ln A$. [XBB 913-556]

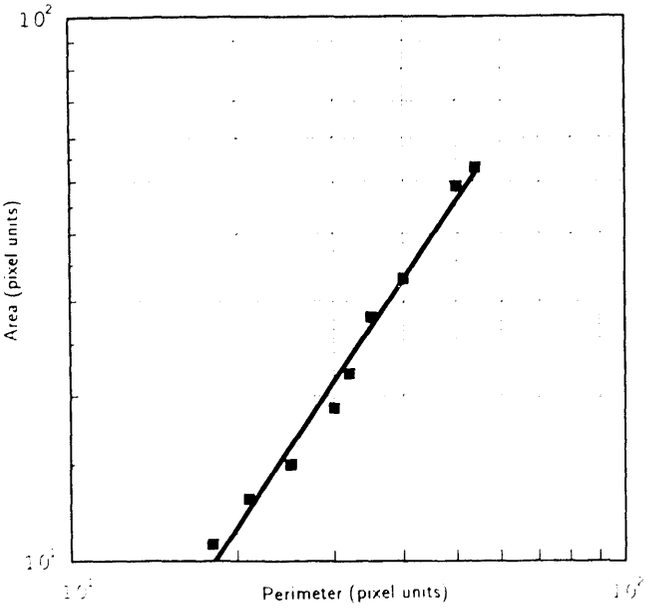

Figure 5. Fractal area-perimeter relationship for a Berea sandstone pore at different magnifications. [XBB 913-557]

REFERENCES

Feder, J., 1988. Fractals. Plenum Press, New York.

Katz, A.J., and Thompson, A.H., 1985. Fractal sandstone pores: Implications for conductivity and pore formation. Phys. Rev. Lett., v. 54, no. 12, p. 1325–1328.

Koplik, J., Lin, C., and Vermette, M., 1984. Conductivity and permeability from microgeometry. J. Appl. Phys., v. 56, no. 11, p. 3127–3131.

Krohn, C.E., 1988. Sandstone fractal and Euclidian pore volume distributions. J. Geophys. Res., v. 93, no. B4, p. 3297–3305.

Mandelbrot, B.B., 1982. The Fractal Geometry of Nature. W.H. Freeman, San Francisco.

Rys, F.S., and Waldvogel, A., 1986. Fractal shape of hail clouds. Phys. Rev. Letts., v. 56, no. 7, p. 784–797.

Laboratory Mercury Porosimetry Studies on a Single Fracture

L. R. Myer, A. M. Cook, and L. J. Pyrak-Nolte[†]

The transport of fluids in porous fractured media is of particular interest in the areas of oil, natural gas, geothermal energy, and groundwater contamination. The relationship between pore structure and the transport properties of these media has been an area of study for some time. While mercury porosimetry is a well-established method for determining pore structure of porous materials, it has not been applied to characterization of pore space in fractures. In this study mercury porosimetry techniques were used to study the distribution of apertures in a single natural fracture and the hydraulic conductivity of the fracture as a function of capillary pressure. The emphasis of the work is on the effects of changing stress on these characteristics. A numerical model incorporating changes in void volume with stress has been used to analyze the results.

EXPERIMENTAL APPARATUS AND PROCEDURES

The sample used in this experiment was a section of granite core of diameter 11.54 cm with a single natural fracture through it, roughly normal to the core axis. To keep the mercury from leaking out of the fracture, a nylon jacket was glued around the sample using a thin layer of silicon glue. A steel jacket was fitted over the nylon jacket and bolted in place so as to provide additional confinement to the nylon. Two ports were provided for entry and exit of the mercury.

The experimental setup consisted of a reservoir to hold the mercury, an inlet capillary tube to measure the volume of mercury that flowed into and out of the fracture, and an exit capillary tube to measure the flow rate of mercury across the fracture (Figure 1). The reservoir and the two capillary tubes were connected to each other and to the sample by means of 3.2-mm diameter, high-pressure, clear plastic tubing. The mercury in the reservoir, capillary tubes, and high-pressure tubing was kept under a constant injection pressure using nitrogen gas. The capillary tubes used to measure mercury volume changes and flow rates had an inside diameter of 0.5 mm, permitting resolution of volume changes as small as 2×10^{-10} m^3

The mercury injection tests were carried out over a range of load conditions and injection pressures. The injection pressures used were 0.1, 0.2, 0.4, and 0.8 MPa. For each injection pressure, the sample was subjected to a vertical loading sequence, with measurements of volume change, and flow being carried out at axial stresses of 2.8, 5.7, 11.4, 17.1, 22.8, and 47.6 MPa. The sample was first loaded to the maximum axial stress level, then unloaded sequentially to the minimum levels, and finally loaded again through the reverse sequence back to maximum.

DATA RESULTS AND INTERPRETATION

Mercury Volume Changes

Figure 2 shows the mercury volume changes measured during the tests at injection pressures of 0.1, 0.2, 0.4, and 0.8 MPa. Each curve represents only the volume change due to the change in axial load at one value of injection pressure. The curves are offset vertically by the volume of mercury remaining in the fracture after completion of the loading cycle. The injection pressure was increased after each cycle while the sample was under 47.6 MPa axial stress. The injected volumes resulting from these increases in injection pressure are not shown in the

[†] Earth and Atmospheric Sciences, Purdue University, W. Lafayette, Indiana.

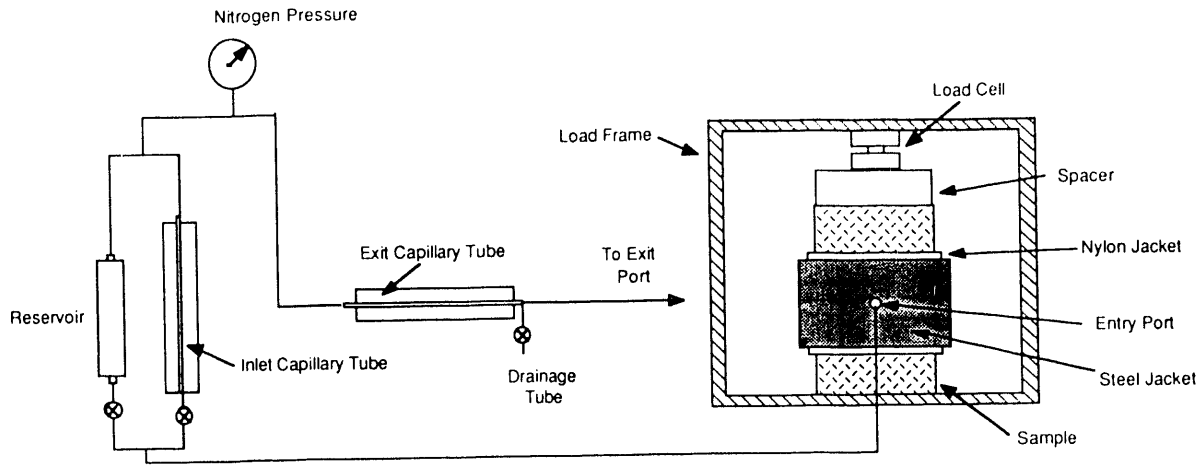

Figure 1. Schematic illustration of apparatus for mercury porosimetry and flow measurements. [XBL 913-558]

figure because of the unknown compressibility of the system plumbing and seals. Had these injected volumes been included, the result would differ only by a vertical translation of the curves; the shape of the curves would not change. The cycle at 0.8 MPa injection pressure is shown as a dashed line because mercury was lost during the cycle, either because a fracture opened in the intact rock or a leak developed in the seal system. The measurements were therefore subject to an unknown error.

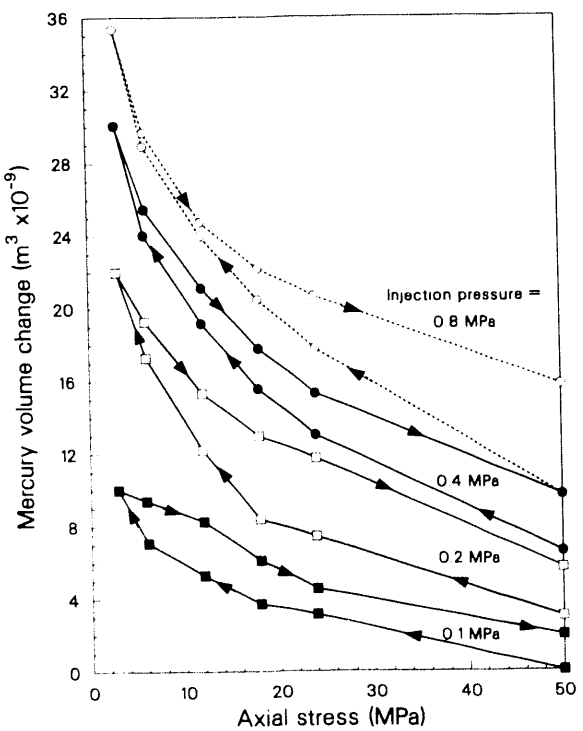

Figure 2. Change in mercury volume in the fracture in response to unloading and reloading of the fracture at different injection pressures. [XCG 884-6629A]

The curves in Figure 2 reveal several important characteristics of the change in void geometry as axial load is changed. First it is seen that the total amount of mercury injected under any axial load increases at higher injection pressures. Since mercury is nonwetting, smaller and smaller voids are penetrated by the mercury as injection pressure increases. The relationship between injection pressure, P, and pore radius, r, is given by Laplace's equation:

$$P = 2\frac{T}{r}\cos\alpha ,$$

where T is surface tension and α is the contact angle. Using Eq. (1), and assuming that cos α = 1 for flow of mercury in air, then at $P = 0.1$ MPa mercury would penetrate all cylindrical voids with diameters greater than about 19.2 μm and all flat voids with apertures greater than 9.6 μm. The size of the void penetrated is inversely proportional to the injection pressure, so that at $P = 0.8$ MPa all tube-like voids with diameters greater than 2.4 μm and all flat voids with apertures greater than 1.2 μm would be filled. Results shown in Figure 2 indicate that the process of unloading the sample from an axial stress of approximately 48 MPa to 3 MPa resulted in opening of voids with apertures ranging from at least 1 μm to 19 μm.

As seen in Figure 2 the volume injected increases nonlinearly with decreasing axial stress. This means that the areal extent of voids exceeding a certain aperture increased as the axial stress decreased. If, on the contrary, the areal extent had remained constant, the volume injected would have increased linearly as a function of decreasing axial load. These results corroborate conclusions of

previous studies (Pyrak-Nolte et al., 1987) that the nonlinearity observed in the deformation of fractures under normal loads is due in large part to the change in geometry and distribution of the fracture voids.

Hysteresis is also observed in the curves in Figure 2; that is, when the axial stress was increased from 3 MPa back to 48 MPa, less mercury came out of the fracture than had gone in. The hysteresis is due to entrapment of mercury by necks located along flow paths.

Mercury Flow Measurements

The volume flow per unit time was measured using the 0.5-mm-diameter exit capillary tube. The volume data were plotted against time for all loads in the unloading and loading sequences and at all injection pressures. The slope for each curve was divided by the gradient to normalize the flow rates. These normalized flow rates, Q, were plotted against load to evaluate the effects of normal stress and injection pressure.

Figure 3 shows that the permeability of the fracture to mercury decreased in a nonlinear fashion with increasing axial stress. As can be seen, there is considerable difference between the flow behavior at P = 0.8 MPa and that at lower injection pressures for a given axial stress. At the lower injection pressures, increases in axial stress had much less effect on the flow than would have been expected if water had been used. In studies of the flow of water through natural fractures in Stripa granite, Pyrak-Nolte et al. (1987) observed a decrease of more than two orders of magnitude in the flow of water over the same stress range, as compared with a factor of four decrease observed for mercury at the lower injection pressures. At an injection pressure of 0.8 MPa, however, the flow decrease for mercury over the range of applied axial stress is about an order of magnitude. The 0.8-MPa injection pressure also corresponds to nearly saturated conditions. At low injection pressures the voids and flow paths penetrated by mercury apparently undergo little change with increasing axial load. However, under nearly saturated conditions at low axial stress levels, many voids that close easily with stress must be contributing to the flow.

In Figure 4 the flow data are combined with the volume-change data to produce plots of permeability as a function of percent saturation in the fracture. Values of percent saturation were obtained by assuming that the volume of mercury in the fracture at each axial stress level during loading at P = 0.8 MPa represented 100% saturation of the fracture. Saturation levels at each axial stress level were determined by dividing the volume measurements by the mercury volume at P = 0.8 MPa. Because mercury is nonwetting, these curves represent the relative permeability of the fracture to the nonwetting liquid. The general shape of the curves appears similar to the relative permeability curves often obtained for porous media, but there are significant differences between the curves at different stress levels. At low normal stresses the reduction in nonwetting-phase permeability with decreasing saturation occurs much more rapidly than at high stress levels. It is also significant that at saturations of about 20–35% there was no flow.

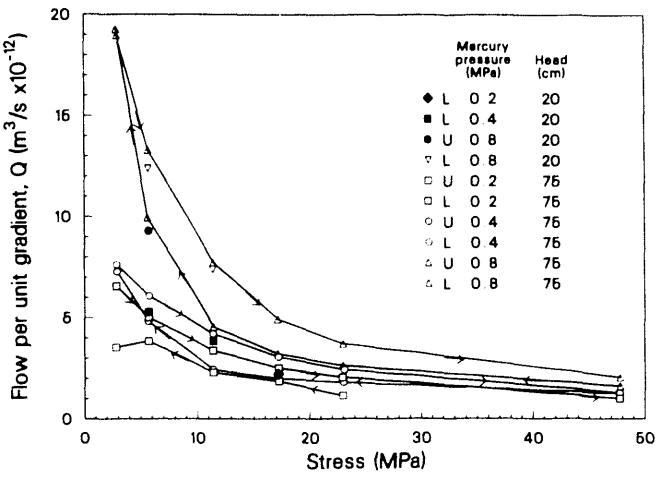

Figure 3. Fracture permeability expressed as mercury flow rate per unit gradient, Q, for head differences of 20 and 75 cm of mercury. Arrows indicate loading direction; L means increasing load on fracture, and U means decreasing load. [XCG 885-6666]

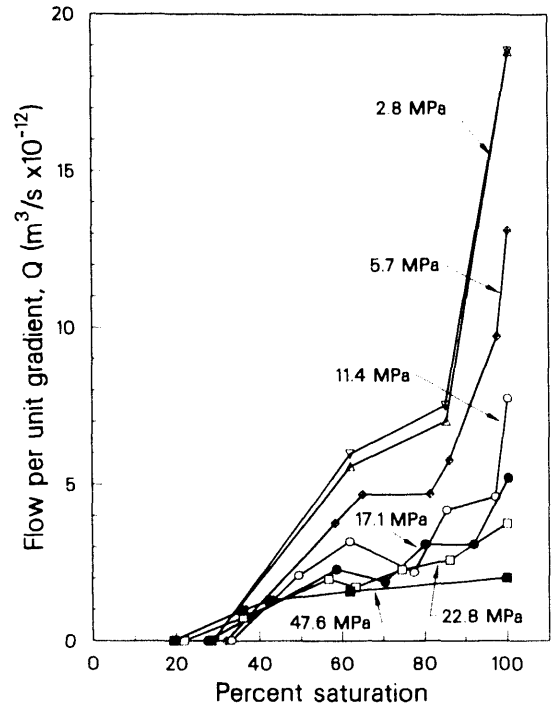

Figure 4. Fracture permeability, Q, as a function of saturation for various axial stress levels. [XCG 885-6663]

Even though mercury entered the fracture, a connected path between inlet and outlet was not present.

The results shown in Figure 4 are qualitatively very similar to those obtained by Pyrak-Nolte et al. (1990) in a theoretical study of two-phase flow in a single fracture. In the theoretical study a stratified percolation model (Pyrak-Nolte et al., 1988) was used to generate realistic, spatially correlated variable-aperture patterns. A zeroth order approach to calculation of relative flow of each phase assumed, at a local level, "cubic law" dependence of flow with aperture and tortuosity described by a simple scaling law. Assuming linear elasticity, under changing normal stress, the average measured fracture displacement, integrated over the plan area of the fracture, must be equal to the change of void volume in the fracture. In the model this volumetric change in the fracture voids was distributed equally among all apertures. Figure 5 shows the effects of stress on relative permeability of a fracture as calculated from the theoretical model. In the figure, stresses are referred to by the amount of aperture closure (0, 5, 20, 50 units). A closure of 50 units of aperture is about one-third of the largest apertures in the pattern. Two similarities with the experimental data are observed. First, the model predicts a more rapid decrease in nonwetting-phase permeability with saturation at low stress than at high stress. Second, the model also predicts that the relative permeability of the nonwetting phase drops to zero at a critical saturation, through this level was higher in the model than observed experimentally. These results indicate that the changes in geometry of fracture voids and, in particular, the presence of critical necks along the flow path have a dominant effect on the two-phase flow behavior in a single fracture.

The stratified percolation model can also be used to study the effects of stress on the void occupancy characteristics of the different phases. Figure 6 is a plot of the change in volume of voids in a pattern with apertures greater than some minimum value. Data points are the void volumes calculated for the displacement values. It is seen that predicted void volume decreases rapidly with fracture closure and does so with increasing nonlinearity as the minimum aperture increases. These theoretical curves will be compared with data from the mercury porosimetry experiments as a measure of the effects of a single fracture. In this first-order analysis the effects of entrapment have not been included.

CONCLUSIONS

Mercury porosimetry measurements on a single fracture showed that unloading the sample from an axial stress of 48 MPa to 3 MPa resulted in opening of voids with apertures ranging from at least 1 m to 19 m. The measurements provide data on the effects of stress on the capillary pressure characteristics of a natural granitic fracture. Flow measurements performed with mercury as the flowing fluid indicated that the effects of stress on flow of the nonwetting phase differs from the effects of stress on wetting-phase flow. Numerical simulations of two phase flow based on fractal construction of the void space (stratified percolation model), conservation of volume of rock, and dominance of the critical neck, yield results very similar to those observed in the laboratory. Numerical modeling to analyze the effects of stress on capillary pressure characteristics is currently underway.

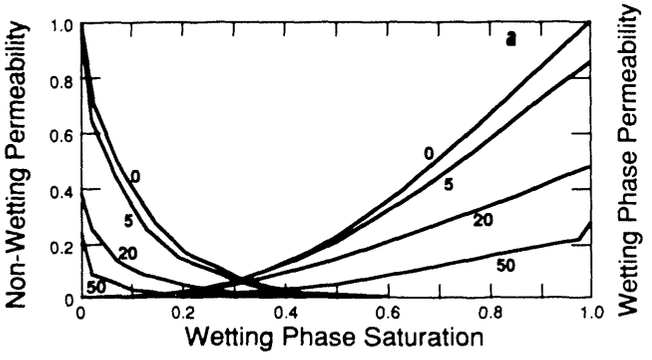

Figure 5. Prediction of effect of stress on relative permeability of a single fracture using stratified percolation model. Numbers on curves represent units of aperture reduction. [XCG 8912-4767A]

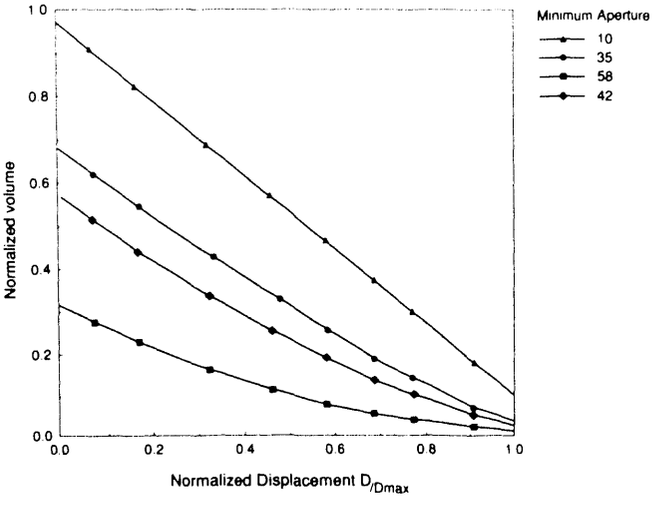

Figure 6. Prediction of change in volume of voids greater than a minimum aperture for a stratified percolation model. Volume is normalized to total void volume, and D_{max} represents maximum fracture closure. [XBL 913-559]

REFERENCES

Pyrak-Nolte, L.J., Myer, L.R., and Cook, N.G.W., 1987. Seismic visibility of fractures. *In* I.W. Farmer et al (eds.), Proceedings, 28th U.S. Symposium on Rock Mechanics, University of Arizona, Tucson. A.A. Balkema, Rotterdam, Netherlands, p. 47–56 (LBL-25310).

Pyrak-Nolte, L.J., Cook, N.G.W., and Nolte, D., 1988. Fluid percolation through single fractures. Geophys. Res. Lett., v. 15, no. 11, p. 1247–1250 (LBL-25714).

Pyrak-Nolte, L.J., Cook, N.G.W., and Myer, L.R., 1990. Stratified percolation model for saturated and unsaturated flow through natural fractures. *In* Proceedings, First Annual International High-Level Radioactive Waste Management Conference. Trans. Am. Nucl. Soc., v. 1, p. 551–558 (LBL-28334).

Removal of Ground-Induced Vibroseis Correlation Artifacts by Frequency-Uncorrelated Time Filtering

D. A. Okaya, E. D. Karageorgi, T. V. McEvilly, and P. E. Malin†*

The CALCRUST consortium collected a Vibroseis multichannel reflection profile in the southern San Joaquin Valley-Tehachapi Mountains in order to examine the crustal relationship between these structures and the adjacent Garlock transform fault (Figure 1). The survey was conducted using a 400-channel MDS-16 and four

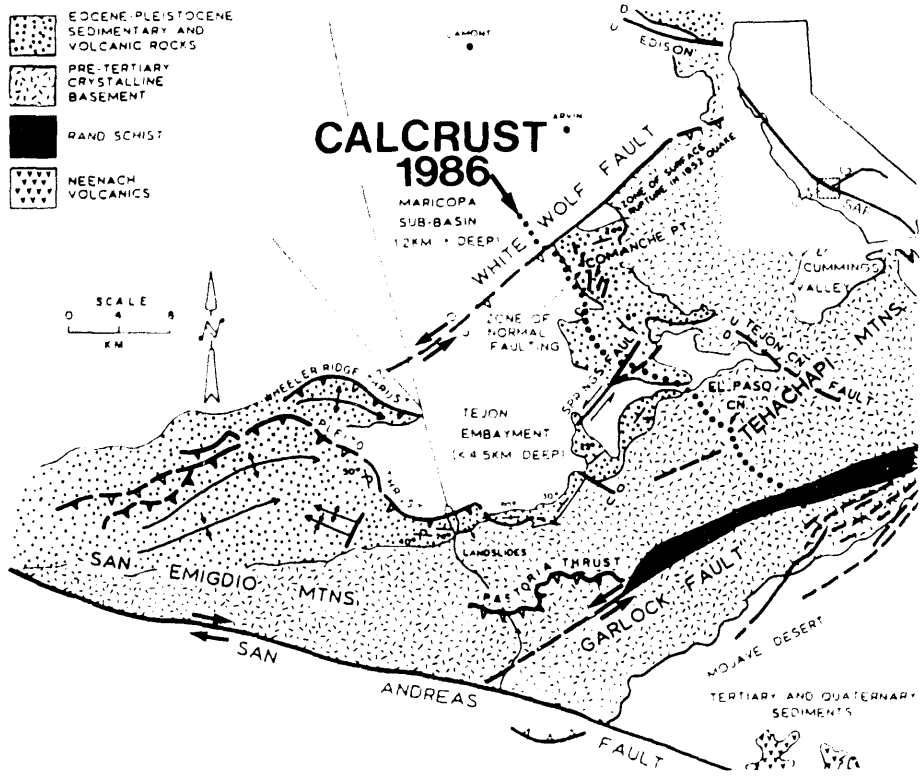

Figure 1. Map of southern San Joaquin Valley region. Reflection profile shown as dotted line. [XBL 913-424]

* Dept. of Geological Sciences, University of Southern California.

† Institute for Crustal Studies, University of California at Santa Barbara.

40,000-lb vibrators generating 32-sec sweeps from 8 to 32 Hz with a 13-sec listen time. Both the field-correlated and uncorrelated shot gathers were recorded for subsequent processing. In the crustal-scale correlated shot gather shown in Figure 2, expected events are visible, such as the first arrivals, surface waves/ground roll, and shallow reflections; additionally, strong energy that mimics the moveout of the first arrival can be seen between 5 and 11 sec. These coherent large-amplitude artifacts are identified as by-products of the cross-correlation operator. Using frequency-time displays of uncorrelated seismograms, the artifacts are identified to occur within specific frequency and time intervals.

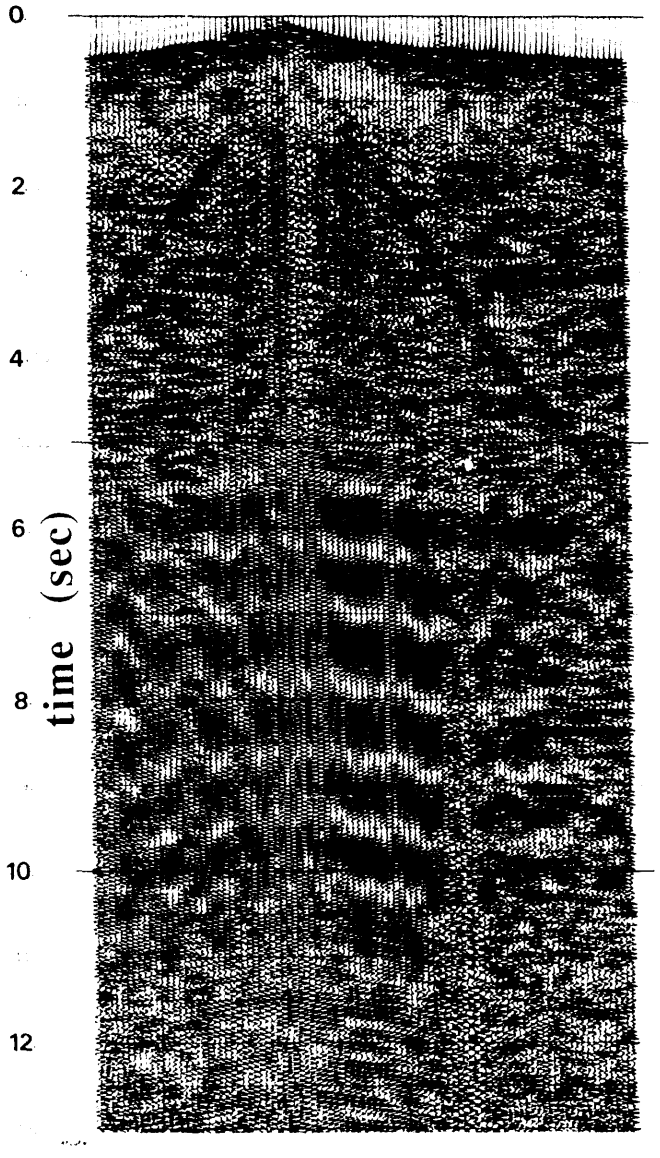

Figure 2. Correlated shot gather. Note the strong energy (at 5–11 sec) that mimics the first arrival. [XBL 913-417]

FREQUENCY-TIME DOMAIN REPRESENTATION OF ARTIFACTS

The transformation of a seismogram into the frequency-time (ω-T) domain reveals the changing behavior of the frequency content along the seismogram. This decomposition of a time series into its frequency components along discrete moving windows is the principle of short-time Fourier analysis (Nawab and Quatieri, 1988). The seismogram $y(t)$ is modified into a series of windows $y(t,T)$, where T represents the times of the window centers. After proper tapering and zero-padding of the windowed seismograms, one-dimensional Fourier transformations convert them into their frequency spectra:

$$y(t,T) \rightarrow Y(\omega,T) = R(\omega,T)e^{i\theta(\omega,T)}, \qquad (1)$$

where $R(\omega,T)$ is the frequency-time modulus function and $\theta(\omega,T)$ is the phase function.

The modulus of an uncorrelated seismogram from the Tehachapi Mountains is shown in Figure 3. The first arrival (r), which is the strongest event, looks similar to the ω-T signature of the source sweep (8–32 Hz over 32 sec; sweep gradient 0.75 Hz/sec). The first- and higher-order harmonics (h) of the first arrival are clearly present. In addition, an event (a) with slope less steep than the source sweep appears between (18 Hz, 21 sec) and (26 Hz, 30 sec). This event is the cause of the correlation artifact. Within ω-T space, both source and reflected sweep energy have similar slopes, and excellent correlation is obtained. Artifact energy with slope different from the slope of the sweep operator creates a narrow-band correlated signature different from that of reflected events. In the correlated shot gathers, the unwanted energy can obscure reflections if the reflected sweeps that are within the zone of the artifact have a lower amplitude.

FREQUENCY-TIME FILTERING

Alteration of the amplitude spectra prior to inverse ω-T transformation is equivalent to frequency filtering in ω-T space. Using the definition of a seismogram in ω-T space (Eq. 1) and a real-valued weighting coefficient function, $c(\omega,T)$, the expression for frequency filtering in ω-T space is $Y'(\omega,T) = c(\omega,T)R(\omega,T)e^{i\theta(\omega,T)}$. Inverse transformation of $Y'(\omega,T)$ back to $y'(t)$ is performed by (a) inverse one-dimensional transformations to convert $Y'(\omega,T)$ to $y'(t,T)$, (b) removing from $y(t,T)$ the effects of applied tapers and zero-padding, and (c) reconstructing the seismogram by undoing the initial windowing. For the San Joaquin Valley data, tapered pie-slice and box mutes were designed and used to partially suppress the harmonics and the artifact energy associated with the first-arrival sweep. However, because subsequent reflected sweeps contain similar artifact energy, this approach cannot treat such subsequent artifacts.

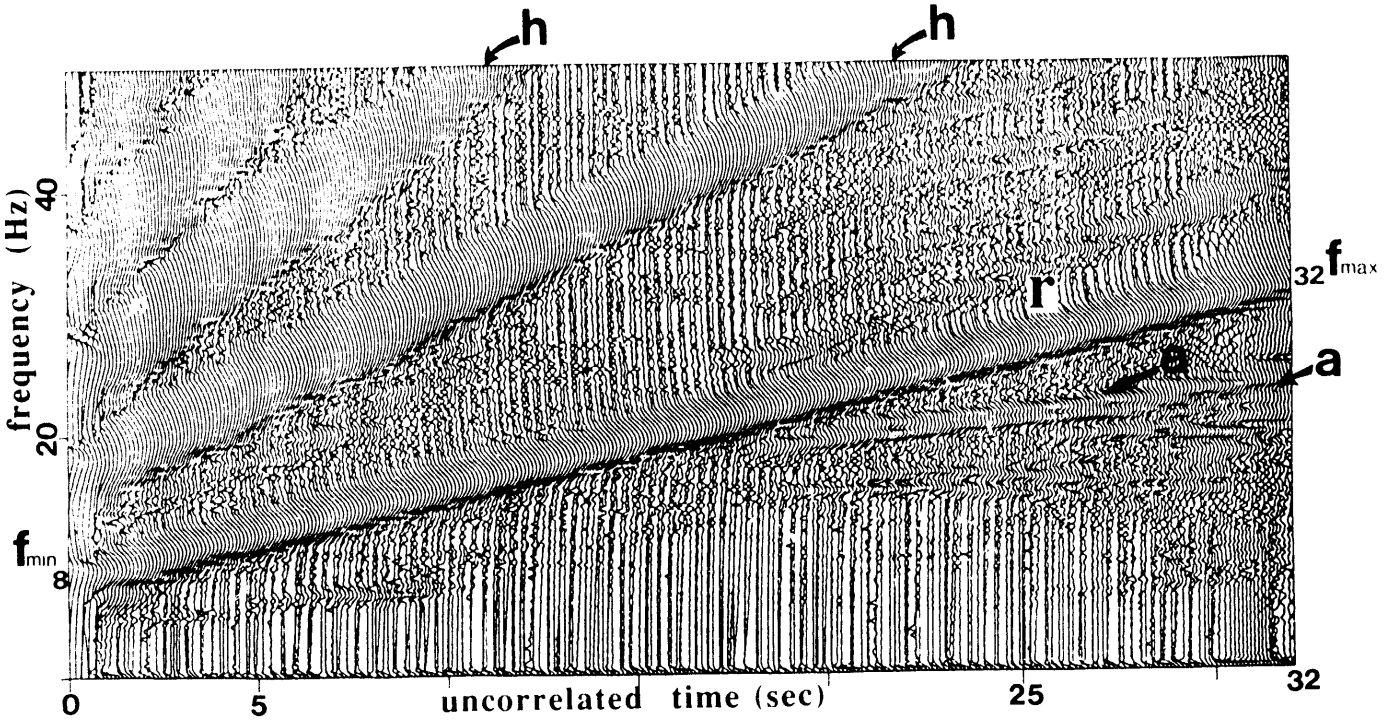

Figure 3. ω-T display of a single uncorrelated seismogram from the field gather that produced Figure 2; r = first arrival, h = harmonics, a = artifact. [XBL 913-419]

Moreover, a new box mute must be designed for other seismograms of the shot gather, because the length and slope of the artifact energy in the ω-T domain change with offset. Finally, for downsweep data, harmonics and reflected sweeps are present in the same ω-T zone, making the filtering impossible. Therefore, although the decomposition of a seismogram into ω-T space makes possible the identification of reflected and nonreflected energy, it is not as effective in suppressing artifact energy with slope other than the slope of the reflected sweeps.

K_Ω-K_T DOMAIN AND FILTERING

A procedure to separate the reflected sweeps and possible unwanted energy by slope differentiation is provided by two-dimensional Fourier analysis, which can localize all events with similar slopes. The first-arrival and reflected sweeps are mapped into one zone (r) (Figure 4); first- and higher-order harmonics (h) map into separate zones; artifacts (a) with different slopes map into separate regions of the k_ω-k_T space. The two-dimensional Fourier transformation of the real-valued modulus $R(\omega,T)$ is expressed as $R(k_\omega k_T)$. As in f-k filtering of x-t field of Common Depth Point (CDP) gathers, filtering within $R(k_\omega,k_T)$ will preserve events of specified slope and suppress other events that have different slopes in ω-T space. Separation of modulus and phase of twice-transformed data is found in homomorphic time series analysis (Oppenheim and Tribolet, 1979; Tribolet, 1988). A set of k_ω-k_T weighting coefficients was designed for the Tehachapi data in order to suppress all events other than those mapped in region (r) of Figure 4. Inverse k_ω-k_T and ω-T transformations (Figure 5), and subsequent cross-correlation yielded shot gathers in which the correlation artifact energy has been significantly reduced (Figure 6).

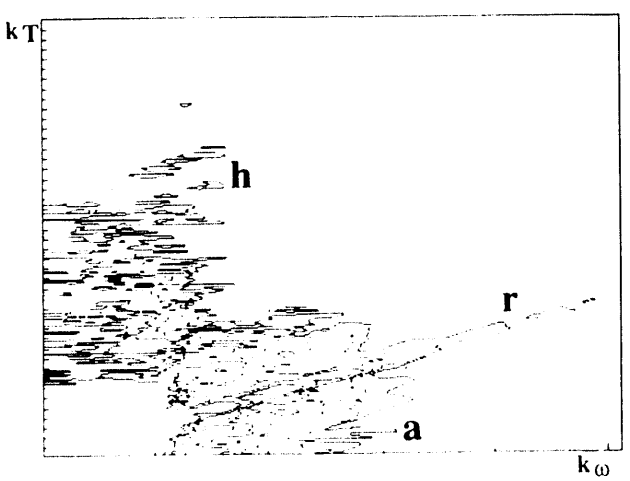

Figure 4. k_ω-k_T transformation of the modulus of ω-T transformation (Figure 3). The modulus of the complex transform is shown; r = first arrival and all reflections, h = harmonics, a = artifact. [XBL 913-421]

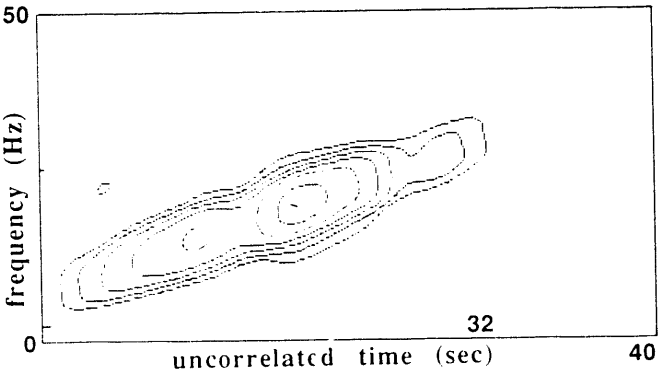

Figure 5. ω-T display of seismogram shown in Figure 3 after filtering in k_ω-k_T domain. [XBL 913-420]

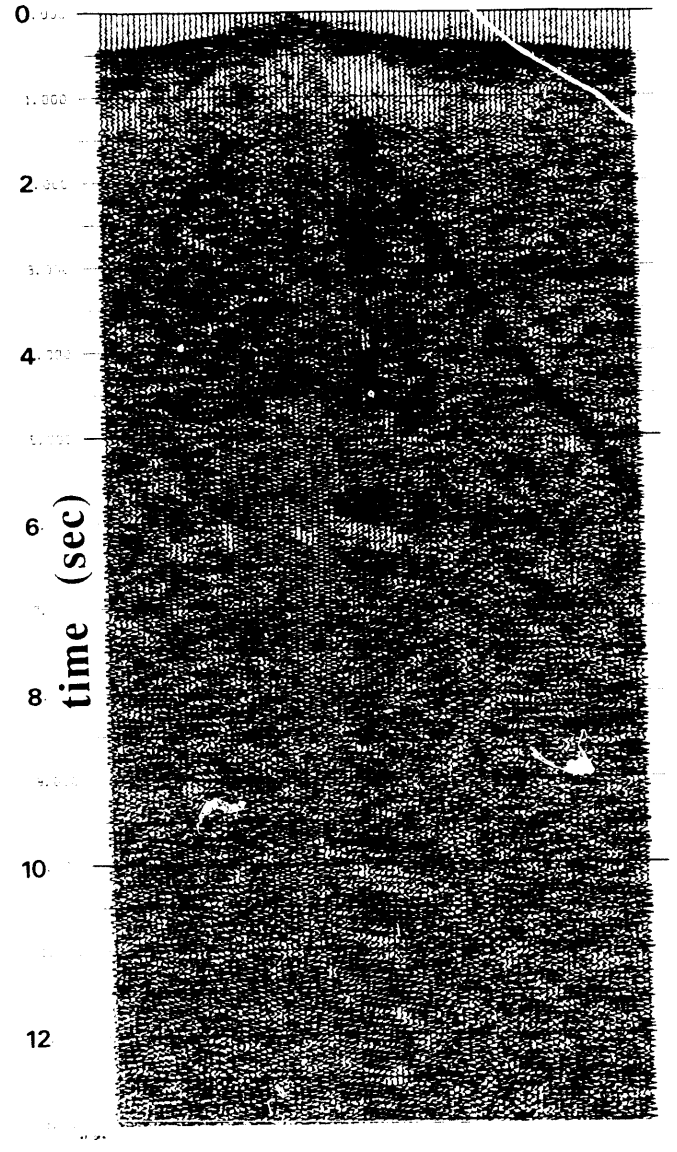

Figure 6. Filtered version of correlated shot gather shown in Figure 2. [XBL 913-418]

DISCUSSION-RESULTS

The use of ω-T and k_ω-k_T decomposition and filtering methods in uncorrelated Vibroseis seismograms can suppress undesired coherent events. Subsequent cross-correlated filtered shot gathers provide substantially improved stacked CDP sections. For the San Joaquin Valley Tehachapi crustal profile, unfiltered stacked CDP sections show little reflectivity between 5 and 11 sec (Figure 7a). The pre-correlation k_ω-k_T filtering of the field data suppressed the artifact and allowed for the emergence of significant lower crustal reflectivity (Figure 7b).

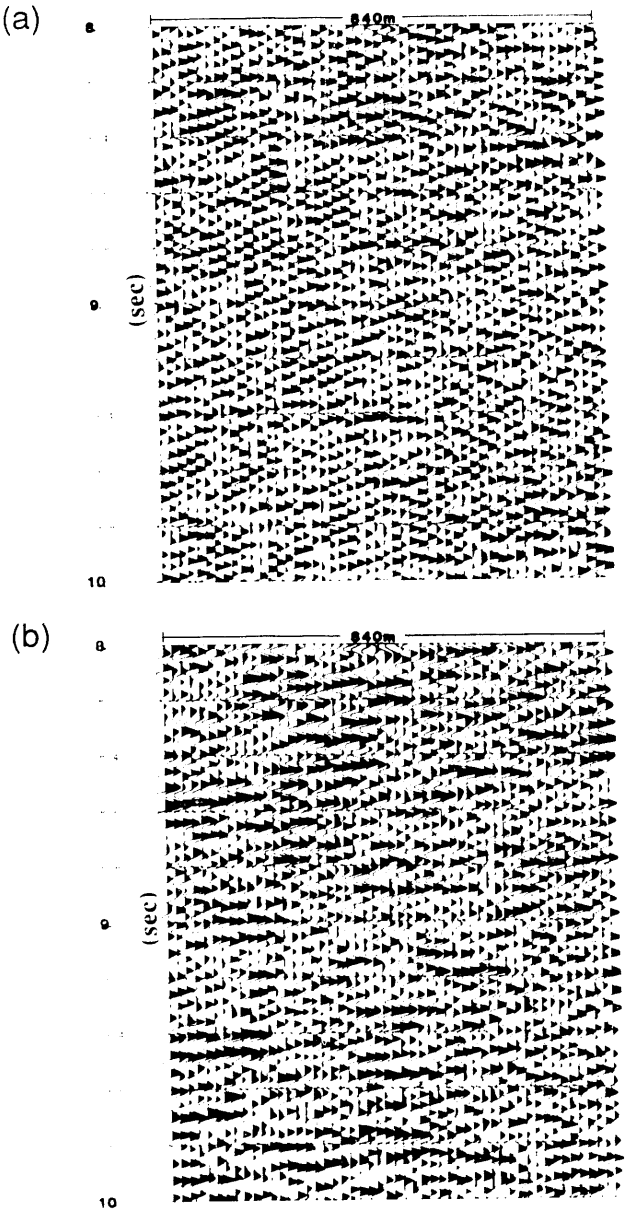

Figure 7. Comparison of lower crustal section of CDP stack of San Joaquin Valley data: (a) No filtering. (b) k_ω-k_T filtering. [a, XBL 913-422; b, XBL 913-423]

REFERENCES

Oppenheim, A., and Tribolet, J., 1987. Application of homomorphic filtering to seismic data processing; Applied time series analysis. *In* D.E. Findley (ed.), Proceedings, First Applied Time Series Symposium. Academic Press, New York.

Nawab, S.H., and Quatieri, T.F., 1988. Short-time Fourier transform. *In* J.S. Lim and A.V. Oppenheim (eds.), Advanced Topics in Signal Processing. Prentice-Hall Signal Processing Series, Prentice-Hall, Englewood Cliffs, New Jersey.

Tribolet, J.M., 1979. Seismic applications of homomorphic signal processing. Digital signal processing series advanced monograph. Prentice-Hall, Inc., Englewood Cliffs, New Jersey.

Shear-Wave Anisotropy in the Parkfield Varian Well VSP

T. M. Daley and T. V. McEvilly

The method of vertical seismic profiling (VSP) has been applied in many different types of geophysical investigations (Hardage, 1985; Oristaglio, 1985). The VSP method, when used with variably polarized shear-wave sources and 3-component receivers, yields information on the anisotropic nature of the earth's elasticity. In particular, this type of VSP survey has been used extensively in quantitative studies of shear-wave velocity anisotropy. Robertson and Corrigan (1983) recorded signals from orthogonal orientations of a shear-wave vibrator to measure velocity anisotropy in shale, and Majer et al. (1988) and Daley et al. (1988a) used similar methods in studies of geothermal reservoir rocks. Although earthquake studies have previously indicated the presence of shear-wave anisotropy (Crampin and Booth, 1985; Peacock et al., 1988), the VSP method has not generally been applied to the investigation of seismically active fault zones.

The research reported here was motivated by the potential use of stress-induced shear-wave anisotropy as an indicator of accumulated stress on a seismogenic fault segment. The VSP work was made possible by the availability of the 1500-m Varian well, situated 1.4 km from the San Andreas fault near Parkfield, California. The Parkfield segment of the San Andreas fault is the location of an intensive and multi-faceted experimental study of earthquake prediction methodology (Bakun and Lindh, 1985) because of regularly recurring magnitude 6 earthquakes there (McEvilly et al., 1967; Bakun and McEvilly, 1981, 1984). We use the shear-wave VSP method to show that a polarization-dependent shear-wave velocity is seen near the borehole, and we argue that this anisotropy is most likely due to effects of the nearby San Andreas fault, although the exact mechanism cannot be determined with this limited data set.

THE EXPERIMENT

The Varian well, drilled to 1500 m depth, is located 1.4 km northeast of the San Andreas fault near the town of Parkfield, California. The Varian array contains a variety of seismometers; strong-motion accelerometers, conventional high-sensitivity geophones, and high-frequency acoustic emission sensors. The 42 individual sensor packages (36 are 3-component units) were fabricated into a 1400-m molded cable with 120 conductor pairs, and the cable was cemented in the well.

The three VSP source locations are shown in Figure 1, with the two shear-wave excitation orientations assumed by the vibrator at each location. A Texas Instruments DFS-

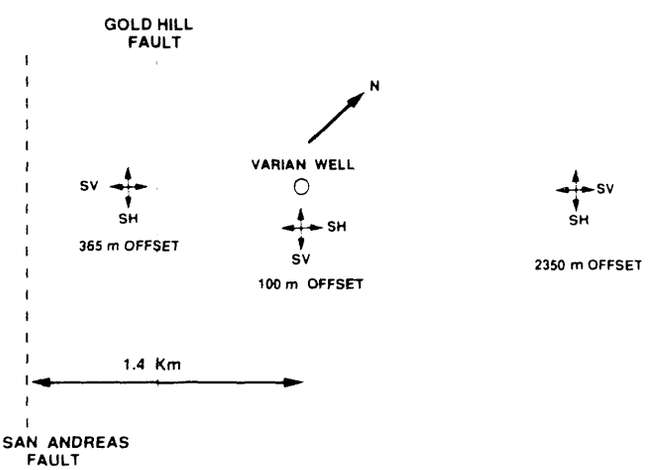

Figure 1. Layout of the VSP survey into the Varian well, showing source polarizations and azimuths used in the survey. Offset distances are not to scale. [XBL 913-547]

IV 48-channel recording system (courtesy of University of California at Santa Barbara) was used, recording half of the 96 channels (3 components at 32 depths) for each sweep. Sets of 5 or 6 sweeps were recorded at each source location. A 6- to 48-Hz sweep of 16-sec length and a 20-sec listening time were used. The shear-wave vibrator is from the Geophysical Measurements Facility of the University of California at Berkeley and Lawrence Berkeley Laboratory.

DATA ANALYSIS

The controlled orientations of the shear-wave source provide a direct measurement of the more subtle shear-wave velocity anisotropy expected near the San Andreas fault (e.g., Crampin, 1985). We have previously experimented with the shear-wave VSP method at the Geysers geothermal field (Majer et al., 1988), at the Salton Sea Drilling Project (Daley et al., 1988a), and at the Cajon Pass Deep Drillhole (Daley et al., 1988b), developing procedures both for the use of variable source orientations and for signal processing and data display in the study of shear-wave velocity anisotropy.

The raw three-component data are difficult to interpret because of the nonuniform orientation of the horizontal-component geophones in the borehole. To display the data in a more useful way, we perform an eigenvalue decomposition of the waveform (Daley et al., 1988a) based upon the direction of the linear particle motion of the *P*-wave arrival and reconstitute (or "rotate") the 3-component traces in this "wavefront-based" coordinate system. Figure 2 shows the rotated 3-component data for both source orientations at the 365-m offset. The 2350-m offset data were rotated in a similar fashion. For the 100-m offset data, the raypaths are nearly vertical, precluding accurate definition of the horizontal components of the *P*-wave motion, so these data were rotated into a "borehole" coordinate system with the horizontal components specified by adding 90 degrees to the azimuths obtained for the 365-m offset data (Figure 1).

At each of the three source offsets, the vibrator was positioned twice to generate separate, orthogonally polarized horizontal forces. This exercise, an attempt at the direct measurement of *S*-wave velocity anisotropy, has been found useful in previous investigations of anisotropy in the shallow (0–2 km) crust (Majer et al., 1988; Daley et al., 1988a,b; Leary et al., 1988). In our conventional VSP processing for anisotropy in shear-wave propagation, we define arbitrarily and independently the two horizontal force orientations at the surface and the two orthogonal polarizations of the "rotated" data. These coordinate directions are labeled "*SH*" (for the source, *SH* indicates the horizontal force oriented transverse to a line from the well to the vibrator; for particle motion, *SH* indicates a horizontal direction orthogonal to the *P*-wave) and "*SV*" (the horizontal source force oriented radially toward the well; and particle motion orthogonal to *P* and *SH* in a vertical plane). The two *S*-wave coordinate directions thus lie in a plane normal to the *P*-wave as defined by eigenvector decomposition of the three-component *P*-wave data. For an isotropic, horizontally layered subsurface, this convention would define the standard *P*-, *SV*-, and *SH*-waves, respectively. We compare travel times at various depths of the *SV* arrival for the *SV* source and the *SH* arrival for the *SH* source, searching for evidence of velocity anisotropy.

Inspection of the rotated data from the 365-m offset shows a clear difference in travel time between the *SV* and *SH* components (Figure 3). The possibility that the variation is due to a slight difference in source position is eliminated by the identical *P*-wave travel times for the two sources and by the absence of the *S*-wave time difference at shallow depths. In practice, the vibrator baseplate is repositioned as closely as possible onto the impression from the previous orthogonal alignment, and the two baseplate center points should not differ more than 20–30 cm. The travel-time difference as a function of depth (Figure 4) indicates anisotropic material beginning around 400 m and producing a maximum travel-time difference of about 8%. A change in velocity gradient is seen at that depth in Figure 4. The faster polarization, *SH*, has particle motion nearly parallel to the San Andreas fault (see Figure 1). Similar analysis of the 2350-m offset data also shows a difference in travel time between *SV* and *SH*, but the variation with depth is not seen. At this offset the *S*-wave arrivals are propagating upwards in the well above 850 m, indicating relatively deep turning points, so that even the shallow arrivals appear to penetrate the anisotropic material. The *S*-wave velocity gradient in Figure 4 would have even the shallowest arrival (surface geophone) at the 2350-m offset propagating below the gradient change at 400 m depth, so that most of the raypaths at this offset represent largely horizontal propagation, whereas the short offsets yield near-vertical raypaths. At 2350-m offset, the source and particle motion orientations roughly parallel to the San Andreas fault (*SH-SH*) again yield the faster *S*-wave arrival, although the travel-time difference is only 2–3%. This apparent decrease in the degree of anisotropy away from the fault zone is suggestive of a mechanism closely related to the San Andreas fault zone, and we are tempted to attribute the anisotropy to fault-zone processes. However, it must be realized that secondary phenomena, such as the complex geological structure near the fault zone at this site, must also be considered as possible causes.

DISCUSSION

Geological studies of Sims (personal communication, 1990; 1991) in the area place the Varian well on the west limb of the narrow thrust-fault bounded Parkfield syncline, which parallels the San Andreas fault. The well penetrates

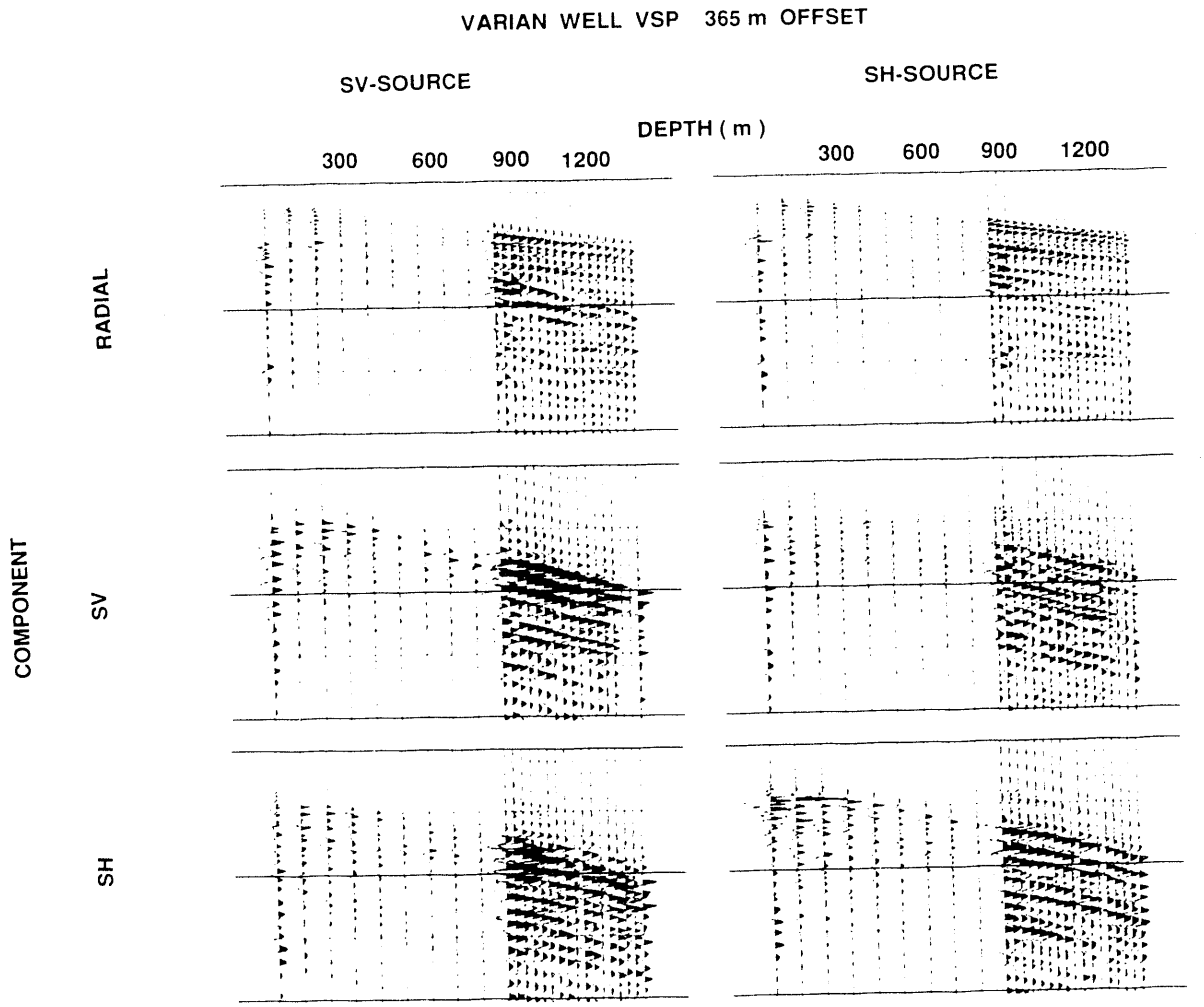

Figure 2. VSP data for both polarizations of the source at the 365-m offset displayed in the wavefront coordinate system (see Figure 5). All traces are plotted at true relative amplitude. The *P*-wave energy is well confined to the radial component for both sources. The *SV*-source produces maximum energy on the *SV*-component, and the *SH*-source puts maximum energy on the *SH*-component. The lower signal levels of the accelerometers (overdamped phones above 850 m) are apparent. [XBL 894-1348]

the Miocene Etchegoin, Monterey, and Temblor formations, bottoming in rocks of the Franciscan assemblage. The Etchegoin/Monterey contact may control the velocity-gradient change at 400–600 m depth, and the anisotropy appears to be developed within the Monterey formation. Dips are about 45 degrees to the east at the well. The 365-m offset vibrator source position, to the west of the well, is just west of the Gold Hill fault, a steeply west-dipping reverse fault that bounds the Parkfield syncline on its west limb. Raypaths showing the anisotropy are thus propagating obliquely across the bedding of the Monterey, and this may be a source of the observed phenomenon. However, raypaths from the source offset 2350 m to the east appear to be similar in length and geometry to raypaths from the 365-m offset for those ray segments within the Monterey formation (much of the added path length is confined to the Etchegoin). Therefore, the difference in shear-wave splitting between the 2350-m and 365-m offsets suggest that proximity to the San Andreas fault zone and sampling of its "fabric" (which can include the near-vertical Gold Hill fault) may be the controlling factor in the observed shear-wave anisotropy.

Thus it appears that transverse isotropy, with a horizontal axis of symmetry normal to the San Andreas fault zone, does provide a first-order model for propagation of shear waves near the San Andreas fault. Assuming two intrinsic polarizations for the "split" quasi shear-waves, the model predicts faster propagation for waves polarized as *SH* (parallel to the fault) and slower propagation for waves polarized as *SV* (perpendicular to the fault). A simple model of thin vertical layers or cracks, aligned parallel to

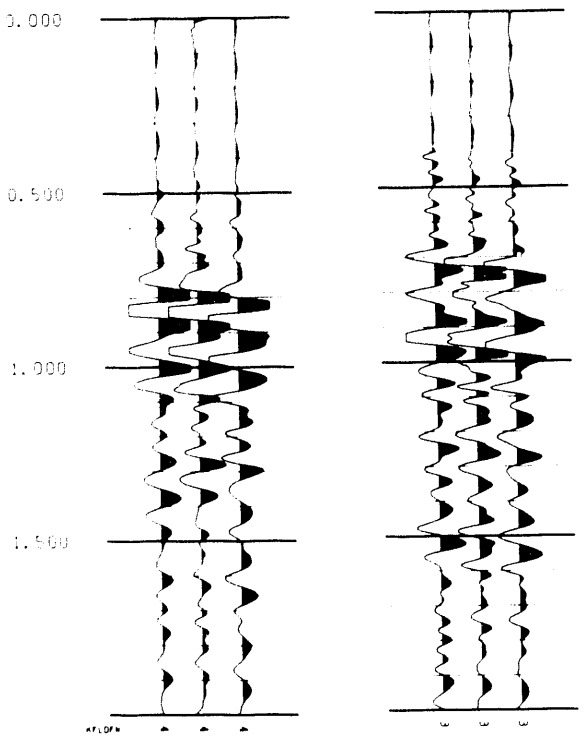

Figure 3. Data from the *SV*-component for the *SV* source **(left)** and the *SH* component for the *SH* source **(right)**. These *SV* and *SH* first arrivals show clear difference in travel-times for two orthogonal polarizations propagating between the same source and receiver points. The three depths plotted are 905, 934, and 966 m. [XBL 894-1347A]

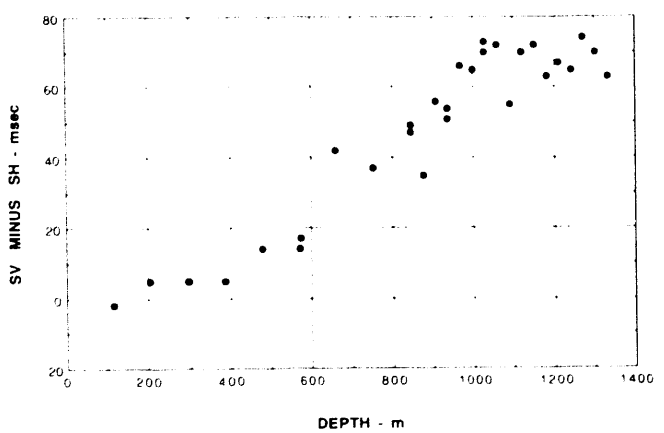

Figure 4. Travel-time difference between *SV* and *S H* polarizations as a function of depth. The sources were at the 365-m offset. Times were picked using the *SV* and *SH* components. Isotropic propagation will have zero travel-time difference, as is seen above 400 m. Below 400 m, the travel-time difference increases, implying anisotropic propagation Times are *SV* minus *SH*. [XBL 913-548]

the fault, could give this result. The degree of anisotropy appears to increase toward the fault zone, implying that the fault is controlling the phenomenon. Assuming fault-controlled velocity anisotropy, our data suggest a physical model involving a zone of vertically oriented shear fabric near the fault, probably developed from the long-term continuing slip. The extent of this shearing would decrease away from the fault, and the fabric orientation would be parallel to the fault. Although this simple model cannot explain all of the observed particle motion phenomena in the wavefield, it does provide an initial hypothesis that can be tested in continuing experiments in the Parkfield area. To this end, a more complete multi-azimuth, multi-offset VSP survey has been conducted to the currently accessible depth of about 1 km, which will sample the upper half of the Monterey formation, and it may provide a more definitive interpretation on the nature and mechanism for the anisotropy.

ACKNOWLEDGMENTS

The National Earthquake Hazards Reduction Program of the U.S. Geological Survey (USGS) provided financial support for the VSP survey under Grant 14-0001-G1703. This study was made possible only through an effective cooperation among scientists from several institutions. Peter Malin of the University of California at Santa Barbara (UCSB) is responsible for initiating interest in the plugged and abandoned Varian A1 well and for securing National Science Foundation support for the borehole seismic cable. The USGS funded cleanout of the well and the installation of the instrumentation under the capable and helpful direction of Tom Moses. The VSP survey used the recording system of UCSB. The shear vibrator used in this and other studies was donated by Amoco to UC Berkeley. Data processing was carried out in the Center for Computational Seismology at Lawrence Berkeley Laboratory. We are thankful to John Sims for helpful discussions and access to his work in progress.

REFERENCES

Bakun, W.H., and Lindh, A.G., 1985. The Parkfield, California, prediction experiment. Earthquake Predict. Res., v. 3, p. 285–304.

Bakun, W.H., and McEvilly, T.V., 1981. *P* spectra for M 5 foreshocks, aftershock and isolated earthquakes near Parkfield, California. Bull. Seismol. Soc. Am., v. 71, p. 423–436.

Bakun, W.H., and McEvilly, T.V., 1984. Recurrence models and Parkfield, California earthquakes. J. Geophys. Res., v. 89, p. 3051–3058.

Crampin, S., 1985. Evaluation of anisotropy by shear-wave splitting. Geophysics, v. 50, p. 142–152.

Crampin, S., and Booth, D.C., 1985. Shear-wave polarizations near the North Anatolian fault - II. Interpretation in terms of crack-induced anisotropy. Geophys. J. R. Astron. Soc., v. 83, p. 75–92.

Daley, T.M., McEvilly, T.Y., and Majer, E.L., 1988a. Analysis of *P*- and *S*-wave vertical seismic profile data from the Salton Sea Scientific Drilling Project. J. Geophys. Res., v. 93, p. 13025–13036 (LBL-22246).

Daley, T.M., McEvilly, T.Y., and Majer, E.L., 1988b. Multiply-polarized shear-wave VSPs from the Cajon Pass drillhole. Geophys. Res. Lett., v. 15, p. 1001–1004 (LBL-25289).

Hardage, B.A., 1985. Vertical Seismic Profiling - Part A: Principles. Geophysical Press, London.

Leary, P.C., Henyey, T.L., and McEvilly, T.V., 1988. A pilot vertical seismic profiling experiment in the Cajon Pass deep scientific drillhole. *In* Deep Drilling in Crystalline Bedrock (Vol. 2), Springer-Verlag, New York, p. 417-427.

Majer, E.L., McEvilly, T.V., Eastwood, F.S., and Myer, L.R., 1988. Fracture detection using *P*- and *S*-wave vertical seismic profiles at The Geysers. Geophysics, v. 53, p. 76–84.

McEvilly, T.V., Bakun, W.H., and Casaday, K.B., 1967. The Parkfield, California earthquakes of 1966. Bull. Seismol. Soc. Am., v. 57, p. 1221–1244.

Oristaglio, M.L., 1985. A guide to the current uses of vertical seismic profiles, Geophysics, v. 50, p. 2473–2479.

Peacock, S., Crampin, S., Booth, D., and Fletcher, J., 1988. Shear wave splitting in the Anza gap, Southern California: Temporal variations as possible precursors. J. Geophys. Res., v. 93, p. 3339–3356.

Robertson, J.D., and Corrigan, D., 1983. Radiation patterns of a shear-wave vibrator in near-surface shale, Geophysics, v. 48, p. 19–26.

Sims, J.D., 1991. Geologic map of the San Andreas fault in the Parkfield 7–1/2-minute quadrangle, Monterey and Fresno counties, California, unpublished USGS map and description (in preparation).

Seismological Studies at Parkfield: Shear-Wave Monitoring with Vibroseis

E. D. Karageorgi, R. Clymer, and T. V. McEvilly

Several lines of evidence support the concept of "characteristic" earthquakes of about magnitude 6 recurring at roughly 22-year intervals on the San Andreas fault at Parkfield in central California, the last having occurred in 1966. Seismologists have suggested that the next member of the sequence is imminent (Bakun and McEvilly, 1984; Segall and Harris, 1987; Wyss et al., 1990), hence the intense research activity focused on the area by the U.S. Geological Survey through numerous investigations supported by the National Earthquake Hazards Reduction Program (NEHRP). The University of California at Berkeley (UCB)/Lawrence Berkeley Laboratory (LBL) contribution to this "Parkfield Prediction Experiment" (Bakun and Lindh, 1985) is twofold: (1) High-resolution studies of the earthquake failure process as expressed in the background seismicity during the nucleation period of the expected magnitude 6 earthquake and (2) a search for temporal precursory variations in the characteristics of waves—generated both by earthquakes and by a controlled source—that sample multiple paths through the presumed nucleation zone. To these ends, an ongoing program of seismic wave measurements has been carried out by UCB/LBL since early 1987 using a High-Resolution Seismic Network (HRSN) consisting of ten, 3-component, 2-Hz, borehole (~300 m) seismometers in a network surrounding the expected nucleation zone (Figure 1). The acquisition system, featuring high bandwidth (125 Hz), wide dynamic range (16 bits), and digital telemetry to a central recording site, records both earthquakes and the controlled-source data. Installation of the HRSN was a truly cooperative effort involving groups from several institutions, including the Geophysical Measurements Facility (GMF) at LBL. The controlled source is a shear-wave hydraulic vibrator ("Vibroseis") developed for oil exploration and donated to UCB by Amoco Production Company.

The program is funded through the UC Seismographic Station on the Berkeley campus by USGS/NEHRP. The LBL Earth Sciences Division (ESD) has responsibility, through GMF, for carrying out the field program, including maintaining and operating the vibrator (for this as well as other research projects at LBL) and the HRSN, and, through the ESD Center for Computational

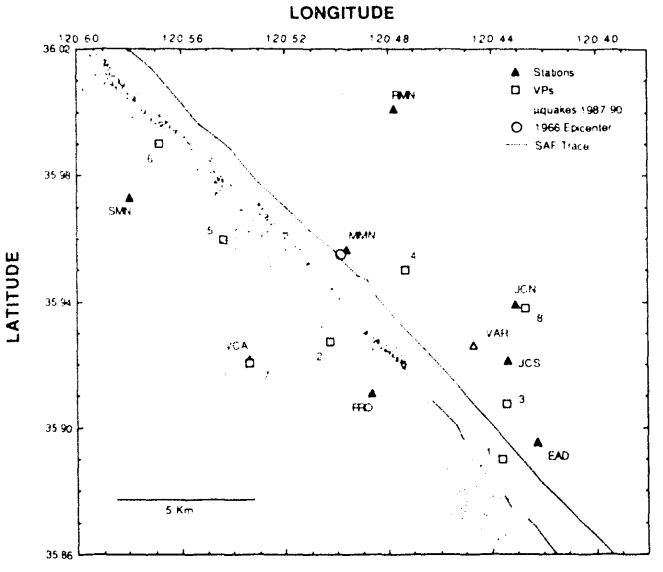

Figure 1. Base map of Parkfield *S*-wave monitoring study showing the ten stations of the High-Resolution Seismic Network (receivers) and eight vibrator source points (VPs). The San Andreas fault trace and microearthquake epicenters are also shown, along with the epicenter of the 1966 earthquake. [XBL 913-411]

Seismology (CCS), for data processing and analysis. The research supports three graduate students and a research seismologist.

The remainder of this report concerns the controlled-source studies. Other aspects of the work are reported in Daley and McEvilly (1990), Michelini and McEvilly (1991), and W. Foxall (personal communication, 1991).

The concept of very large changes in *P*-wave velocity precursory to earthquakes was investigated in central California in the 1970s and early 1980s with the maximum resolution provided by the networks of the time by, among others, McEvilly and Johnson (1974) and Boore et al. (1975). Clymer and McEvilly (1981), in the antecedent to the present project, used repeated measurements of travel times from a *P*-wave vibrator source on the San Andreas fault near Hollister, California. None of these studies produced evidence for the large and extensive precursory changes in *P*-wave velocity that had been reported widely in the previous decade (e.g., Scholz et al., 1973; Whitcomb et al., 1973).

The development of the Parkfield Prediction Experiment in the 1980s gave the opportunity to carry out an experiment incorporating state-of-the-art network design and a shift of emphasis from *P*- to *S*-wave properties made possible by the donation of the Amoco vibrator. Shear-wave parameters (velocity, attenuation, and anisotropy) are expected to be more sensitive than *P*-waves to stress-driven changes in material properties in the nucleation zone of an impending earthquake.

Controlled-source measurements at Parkfield were made at roughly six-week intervals through FY90, and have since been repeated every 2–3 months. At each of the eight source positions (VPs, Figure 1) the vibrator is operated at three orientations, two orthogonal and a third at 45 degrees to the others, in order not to miss one of the preferred *S*-wave polarizations, should the medium be anisotropic. Multiple records are summed in the field to improve signal-to-noise ratio. Eight VPs at three source polarizations recorded at ten sites with 3-component sensors, yields 720 traces each field session. Since June 1987, when the HRSN network was fully operational, 30 repeated data sets have been collected. These form the data base for this study.

The well-developed trace-manipulation software available at CCS provides a framework for processing and displaying the large data "gathers" and their attributes. The initial data reduction procedure includes editing of noisy traces, stacking, and correlation with the vibrator control signal, yielding 20-sec records at 2-msec sampling. Since the primary purpose of this exercise is the search for temporal variations, calendar time (as opposed to recording time) becomes a key independent variable, and analysis is concentrated on "time-gathers" (repeated traces for one of the 720 source-receiver pairs). These generally exhibit arrivals with usable signal-to-noise ratio that are coherent across calendar time throughout most of the 20-sec records (Figure 2).

These data sets, by virtue of the precise controls maintained in the field on source amplitude, location, and timing, allow analysis of temporal variations of waveform in the repeated signals. We have chosen to develop graphical procedures to display changes in four parameters: travel-time, amplitude, spectral content, and particle motion. Two approaches have been used. The first calculates changes in a parameter characterizing one phase (arrival) in a specific time window through calendar-time. The second approach extends the first to a moving-window scan of the entire travel-time axis, defining the parameter continuously along the trace. Temporal changes in anisotropy may be monitored by polarization analysis of the three-component seismograms for individual arrivals.

INITIAL RESULTS

Selected examples of the types of analysis mentioned above are presented in Figures 3–6. They represent interesting variations and anomalies occurring on particular source-receiver pairs.

Figure 3 is a display of travel-time changes for path VP7-JCN (see Figure 1). The changes are calculated across calendar time with respect to an arbitrarily chosen reference trace in a 300-msec window. The window is then shifted down the traces of the time gather in 16-msec steps. This path shows well-defined seasonal variations due to the

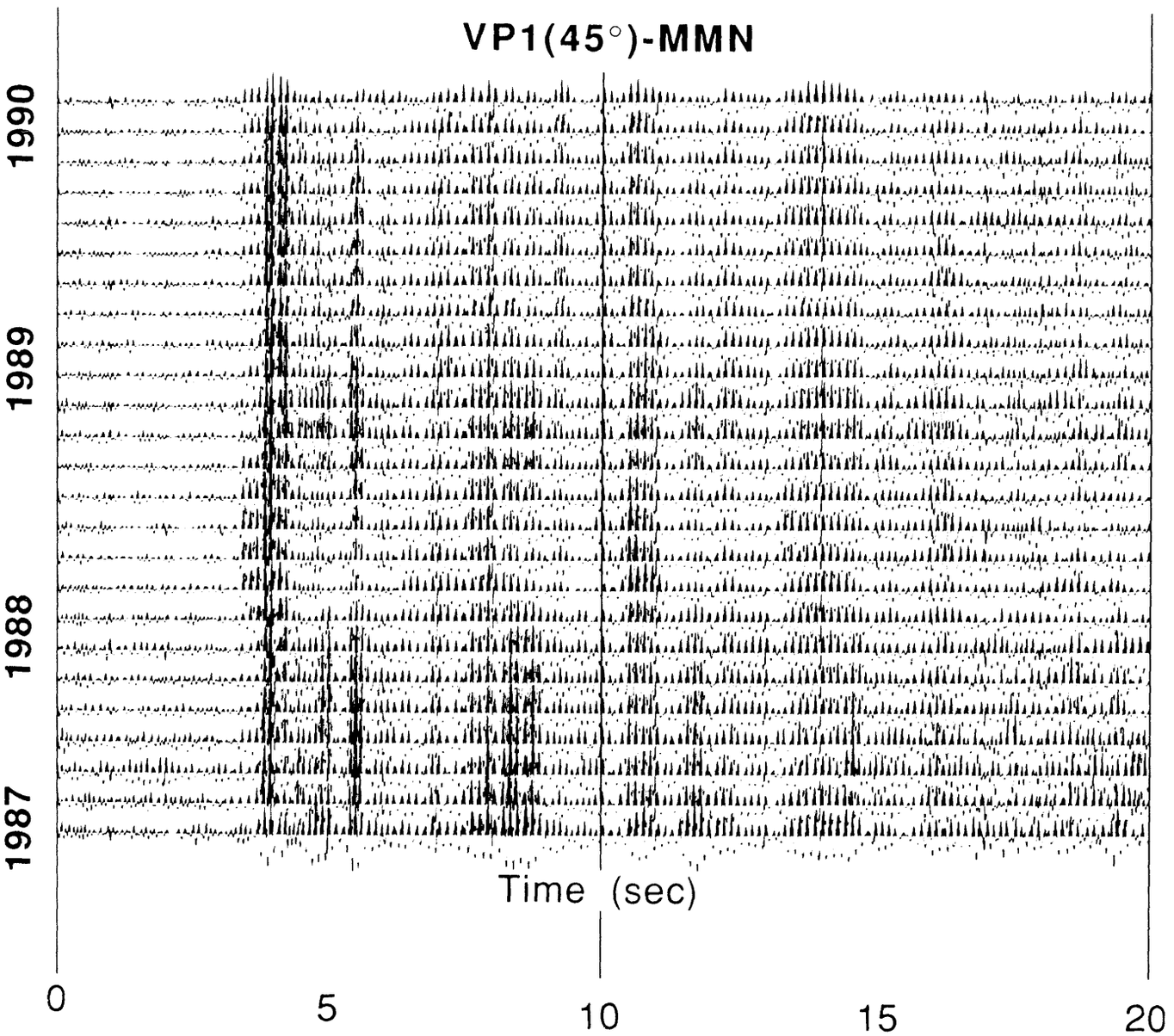

Figure 2. Example of a gather across calendar time for path from VP1 (45° source orientation) to MMN(H2 component). [XBL 913-412]

effects of the local climate of wet winters and dry summers on the coupling of the vibrator to the ground. Corrections were developed to remove this "noise" phenomenon.

In Figure 4, a collection of observations of anomalies in travel time for the paths VP2 to both MMN (3.3 km) and VCA (2.9 km), and for VP1-MMN (9.1 km), is presented along with other measured data. For VP2, the clear and continuing travel-time decrease in the later phases is not seen in the direct *S* arrivals. The path VP1-MMN, along the San Andreas fault zone, reveals an interesting 40-msec swing (May-June 1989) in two direct-*P* phases; this feature is not seen in the direct or later *S* arrivals and is roughly coincident with a magnitude 4 event just south of VP1. These travel-time anomalies cannot be ascribed to the seasonal effect. Also shown are seismic moment rate, water level, creep rate, and rainfall sampled along that stretch of the fault zone.

In the frequency-domain analysis, Fourier amplitude spectra were computed for both the windowed phases and for a moving window. Examples for the windowed phases are shown in Figure 5. They show spectra for *P*, *S*, and late (*L*) phases from a wet and dry month of the time-gather

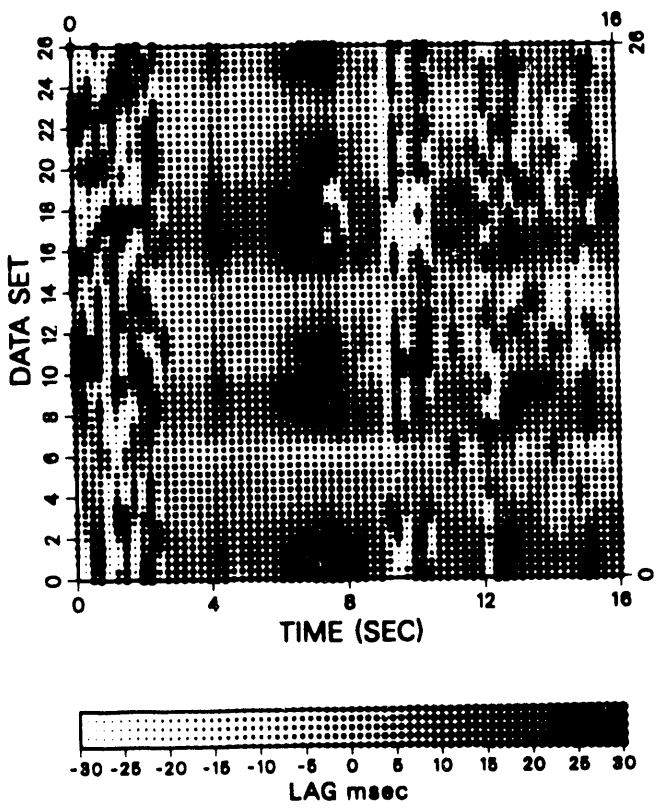

Figure 3. Gray-scale display of continuous travel-time changes of VP7-JCN. The scale displays 30-msec variations. [XBL 913-413]

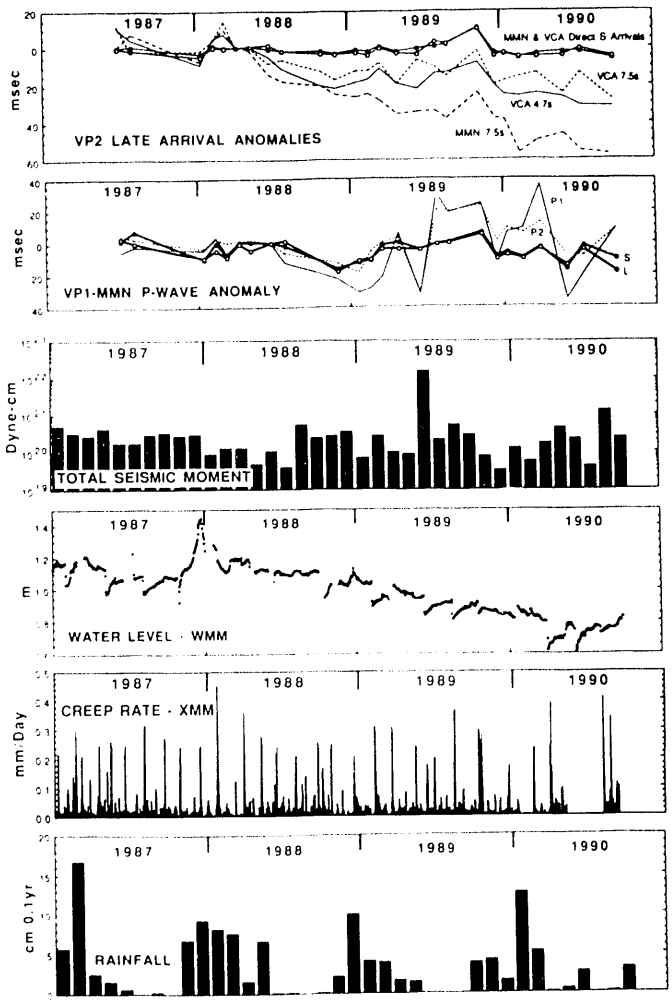

Figure 4. VP2 and VP1 anomalous travel-time data, shown along with examples of other data. **(Top two frames)** Later phases from VP2 to both MMN and VCA, where the continuing travel-time advance in the later phases is not seen in the direct *S* arrivals. Data for the path VP1-MMN, showing the anomalous 40-msec swing (may-June 1989) in the two direct *P* phases that is not seen in the direct *S* or later arrivals. **(Lower four frames)** Seismic moment, estimated from magnitudes and summed over 0.1-year intervals; water level; 3-day smoothed creep rate (derivative of daily readings); and local rainfall in 0.1-year increments. [XBL 913-414]

over two paths of different distances passing near the 1966 epicenter. The frequency content for the path 7-JCN illustrates seasonal changes and spectral differences between *P*- and *S*-waves. The *P*-wave exhibits more spectral structure than the *S*-wave, with a peaked spectrum at about 10 Hz. The S-wave spectrum is smoother, with a broad peak at 8–9 Hz. The late phase appears in its spectral character to be more like a *P*-wave. The seasonal effect for this path is a strong attenuation in the 7- to 11-Hz band under wet conditions. Path 2-MMN is a short offset SSW of the 1966 epicenter. The late arrival used here is the same event that shows the travel-time anomalies illustrated in Figure 4. In this window, bandwidth is quite broad and the late arrival has the characteristic spectrum of the direct *S*-wave. As Figure 4 shows, however, the direct *S* arrival does not display the travel-time advance of the late phase.

In general, the *P*- and *S*-wave spectra display differences in character, the *S*-wave frequency content being usually lower than that seen for *P*. This rough frequency discriminate between *P*- and *S*-waves can be of value in guiding the analyses of specific phases.

The results from VP2 to both MMN and VCA (Figures 4, 5) show very little apparent seasonal effect. It is possible that the late-arrival travel-time anomaly represents a deep-seated change in shear-wave velocity occurring near the M6 nucleation zone. Figure 6 shows further evidence for this. Travel-time changes are calculated for late phases from paths of various VPs to VCA. All of the arrivals showing progressive travel-time advances must follow paths not far from the vicinity of VP2. This volume of the crust has become the focus of intense study for the duration of the experiment.

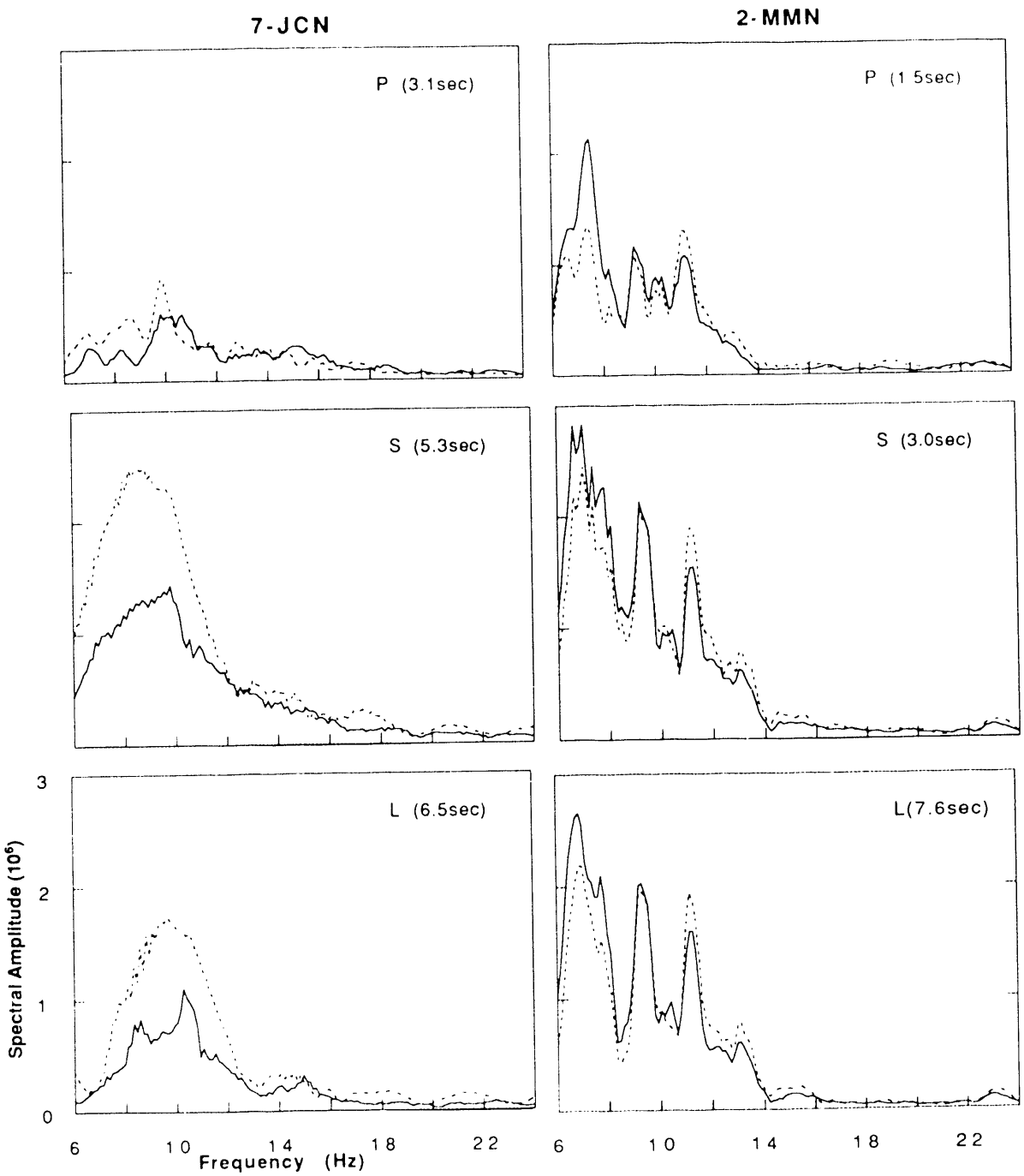

Figure 5. Examples of variations seen in frequency for three phases (*P*, *S*, Late) along two paths. **(Left)** 7-JCN, 9.5-km offset distance across the fault, 3 km SE of MMN. **(Right)** 2-MMN, 3.3-km offset, on SW side of fault zone near 1966 epicenter; solid lines indicate wet (winter) conditions, and broken lines indicate dry (summer) conditions. Vibrator sweeps were 6–24 Hz. Note the path-specific spectral signatures, which generally shift toward lower frequencies with distance, and also the wet-dry spectral effects, which differ for the various paths but are similar for all phases from a given source-receiver pair. [XBL 913-416]

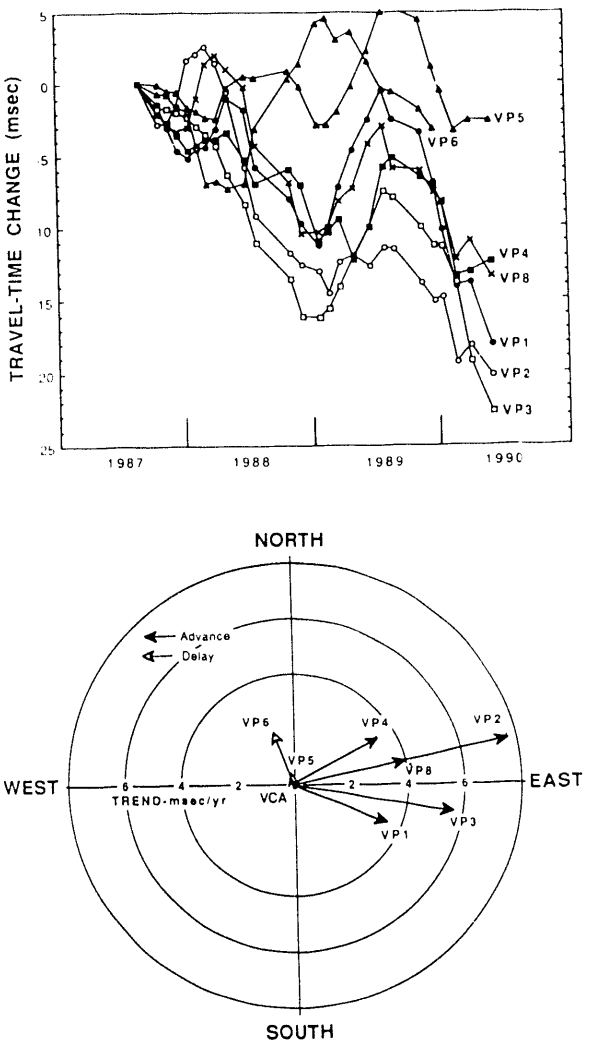

Figure 6. Late-phase anomalies seen at VCA from several VPs. (Top) Relative arrival time changes for late arrivals from seven VPs. Note differences in rates of decreasing time over the 3-year period. (**Bottom**) Path-azimuthal representations of the various trends of travel-time decrease seen in the late-phase data above. Arrow lengths are proportional to the rates of change for the various paths, whose receiver-source azimuths are as plotted. Note the apparent azimuth dependence of the trends. [XBL 913-415]

REFERENCES

Bakun, W.H., and Lindh, A.G., 1985. The Parkfield, California, prediction experiment. Earthquake Predict. Res., v. 3, p. 285–304.

Bakun, W.H. and McEvilly, T.V., 1984. Recurrence models and Parkfield, California earthquakes. J. Geophys. Res., v. 89, p. 3051–3058.

Boore, D.M., Lindh, A.G., McEvilly, T.V., and Tolmachoff, W., 1975. A search for travel-time changes associated with the Parkfield, California earthquake of 1966. Bull. Seismol. Soc. Am., v. 65, p. 1407–1418.

Clymer, R.W., and McEvilly, T.V., 1981. Travel-time monitoring with Vibroseis. Bull. Seismol. Soc. Am., v. 71, p. 1903–1927.

Daley, T.M., and McEvilly, T.V., 1990. Shear-wave anisotropy in the Parkfield Varian Well VSP. Bull. Seismol. Soc. Am., v. 80, p. 857–869,.

McEvilly, T.V., and Johnson, L.R., 1974. Stability of *P* and *S* velocities from central California quarry blasts. Bull. Seismol. Soc. Am., v. 64, p. 343–353.

Michelini, A., and McEvilly, T.V., 1991. Seismological studies at Parkfield: I. Simultaneous inversion for velocity structure and hypocenters using B-splines parameterization. Bull. Seismol. Soc. Am., v. 81, no. 2, p. 524–552 (LBL-28770).

Scholz, C.H., Sykes, L.R., and Aggarwal, Y.P., 1973. The physical basis for earthquake prediction. Science, v. 181, p. 803–810.

Segall, P., and Harris, R., 1987. Earthquake deformation cycle on the San Andreas fault near Parkfield, California. J. Geophys. Res., v. 92, p. 10511–10525.

Whitcomb, J.H., Garmany, J.D., and Anderson, D.L., 1973. Earthquake prediction: Variation of seismic velocities before the San Fernando earthquake. Science, v. 180, p. 632–635.

Wyss, M., Bodin, P., and Habermann, R.E., 1990. Seismic quiescence at Parkfield: An independent indication of an imminent earthquake. Nature, v. 345, p. 426–428.

VSP Site Characterization at NTS: OSSY '90

T. M. Daley, T. V. McEvilly, and A. Michelini

In late 1989 a site characterization study using the Vertical Seismic Profile (VSP) method was conducted as part of the On Site Seismic Yield (OSSY) experiment organized by Lawrence Livermore National Laboratory at well UE-10 ITS #3 located in Yucca Valley inside the Nevada Test Site (NTS). The OSSY experiment fired 10-

and 100-lb explosive sources at several depths in the hole, with multiple 3-component receivers on the surface to test the nature of seismic signal scaling with source size and the accuracy in the near field of source modeling algorithms. Shear waves in particular are influenced strongly by both the source mechanism and the properties of the propagation path. The multi-component OSSY VSP (3-component receivers at several depths, with *P*, *SV*, and *SH* surface sources) measured the seismic-wave transmission separately for three source types. The VSP surface-source to borehole-receiver acquisition geometry was reversed in the subsequent explosion phase of the experiment, in which the explosion-generated waves presumably experienced the same propagation effects as did the waves generated by the VSP sources.

The 1990 OSSY VSP experiment had the following goals:

1. Record waveforms along reciprocal raypaths of the OSSY explosions, with 3-component sensors and for three source-force orientations.
2. Develop a 3-D *P*- and *S*-velocity model for source modeling of subsequent explosions in the borehole.
3. Investigate possible seismic anisotropy in the explosive source region and near the well.
4. Detect and map in 3-D any strong structural heterogeneity near the well.
5. Measure the attenuation (Q) near the well and its frequency dependence if evident.

The multi-offset VSP survey was designed to address these goals.

DATA ACQUISITION AND PROCESSING

The VSP sources, located at the same surface sites as receivers for the subsequent OSSY explosions, were offset 0 to 1200 m on four azimuths, with at least two source points on each azimuth (Figure 1a). At each source point we acquired three vibrator data sets, *P*, *SV*, and *SH* source, using an 8- to 80-Hz sweep with 4 sec of correlated data at 2-msec sampling. The 3-component VSP receiver was positioned at recording depths clustered around the planned explosion depths to a maximum depth of 600 m (Figure 1b). Initial processing, including correlation and sorting into depth-ordered common source point data sets, was performed by the contractor, Seismograph Service Corporation. Further processing at the Center for Computational Seismology (CCS) at Lawrence Berkeley Laboratory (LBL) included editing of bad traces, sorting by source type at each source location, stacking of individual sweeps, and converting horizontal components to a consistent coordinate system.

For the OSSY experiment's multiple source-receiver paths, we computed an average orientation at each receiver depth using *P*-waves from all the source points, since the receiver remained clamped while all the sources were vibrated. This joint solution yielded a horizontal orientation at all 35 receiver depths with an average standard deviation of 9.5 degrees. The orientation analysis allows the data from three orthogonal sensor components to be rotated into a consistent coordinate system. After rotation, each source offset point yields a 9-component VSP with *P*, *SV*, and *SH* sources each recorded by vertical,

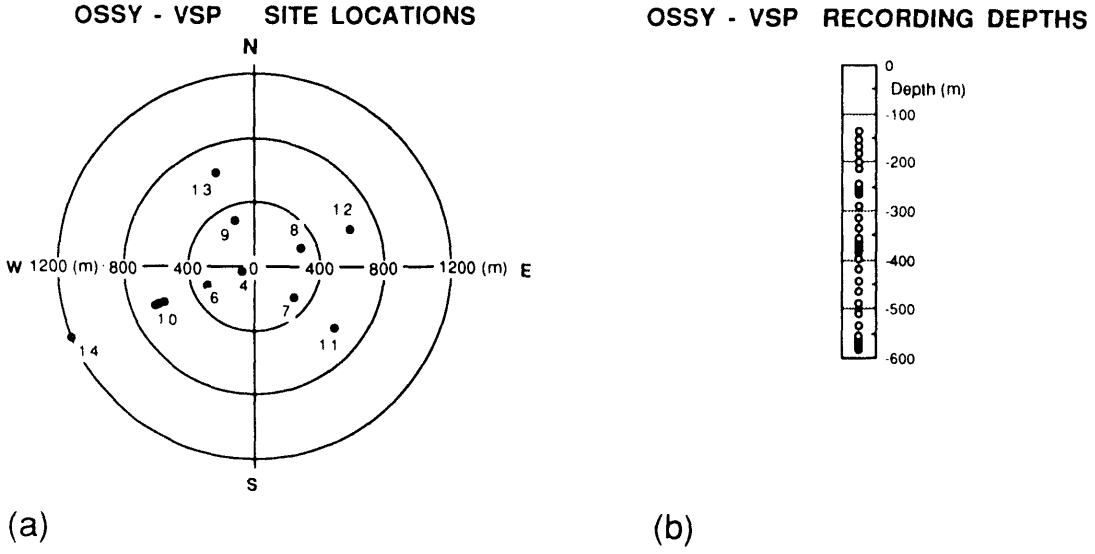

Figure 1. (a) The source locations for each of the 10 sites. Note that site 10 has three closely spaced source points. The coordinate system is centered at well UE-10 ITS #3. (b) Receiver depths for VSP data. Note that not all receivers were recorded for every source because of acquisition time limitations and raypath consideration. [XBL 913-549]

horizontal-radial, and horizontal-transverse receivers. An example of a 9-component data set is shown in Figure 2. The ten 9-component VSPs (one from each source site) form the survey data base. An interesting result of the orientation exercise was the apparent bending of raypaths out of the azimuthal plane (as defined by the other eight sites) for arrivals from the northwest sites (9 and 13, Figure 1a). This finding indicates subsurface lateral heterogeneity to the northwest.

After the data are sorted and rotated, *P*, *SV*, and *SH* travel times are picked for first arrivals on the appropriate seismograms (the panels that form a diagonal from top left to lower right in Figure 2). All times are picked from the peak or trough of the zero-phase Vibroseis wavelet (depending on polarity) using interactive graphics software. This travel-time information forms a data base for two studies, the velocity inversion and the anisotropy measurement.

ANISOTROPY MEASUREMENT

The anisotropy is quantified by comparing the travel times for shear-wave arrivals from the *SH* and *SV* source at every depth for each site (Majer et al., 1988; Daley et al., 1988). A difference in travel time is evidence of shear-wave splitting, which is caused by anisotropic *S*-wave

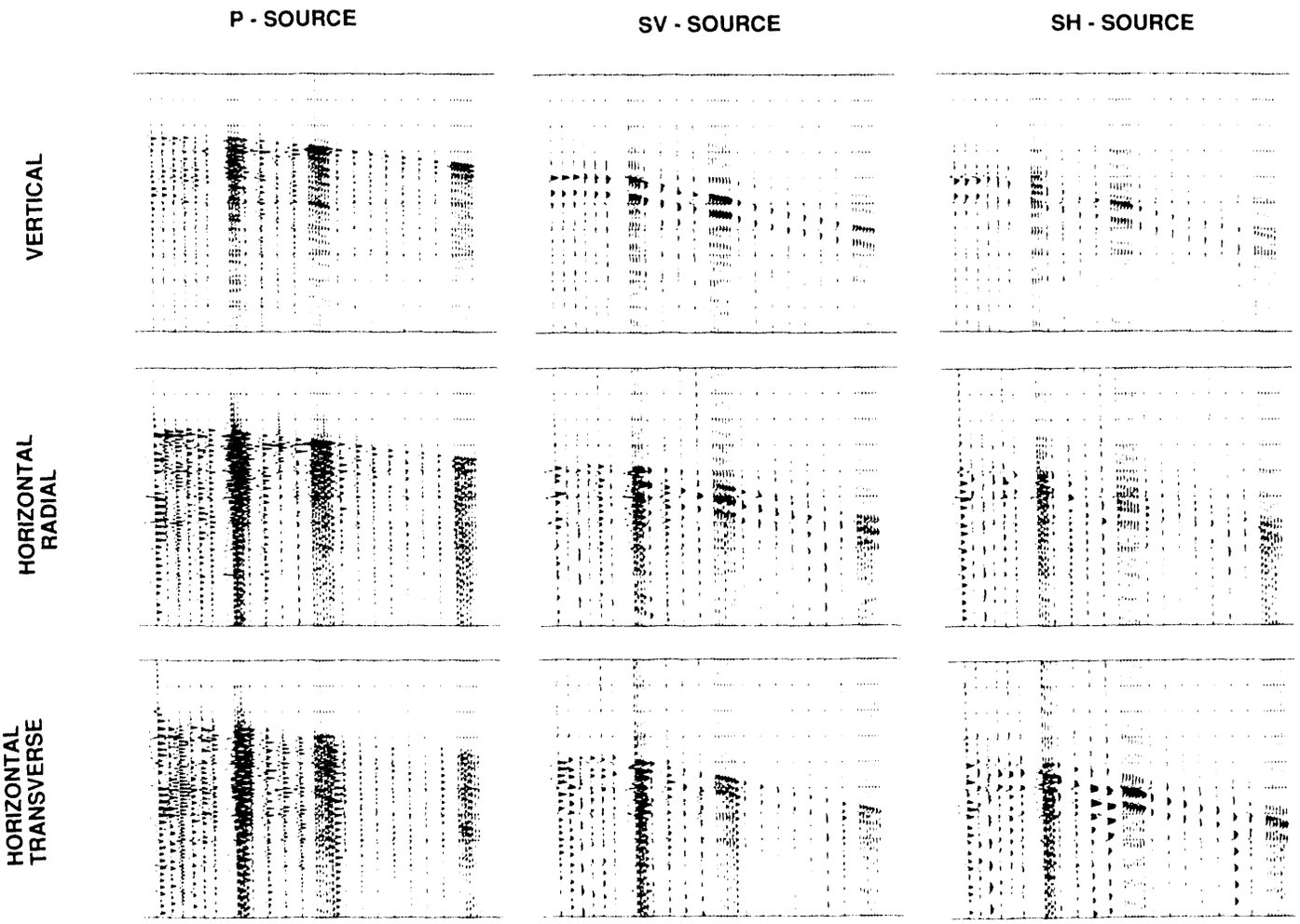

Figure 2. Nine-component VSP from site 6. All traces are plotted with true relative amplitude. The *P*-wave arrival (0.25 to 0.35 sec) is best seen on the *P*-source vertical component, whereas the *S*-wave arrival (0.38 to 0.6 sec) is clearly seen on both *SV*-source and *SH*-source data. A surface-wave arrival is seen on shallow traces at about 0.48 sec. The higher frequency content of the *P*-wave as compared to the *S*-wave can be seen along with the unexplained high noise level on the *P*-source horizontal components. The anisotropy study compares travel times of first shear-wave arrival on the horizontal radial component of the *SV* source with those on the horizontal-transverse component of the *SH* source (the lower two panels in the diagonal). This data set (site 6) had no significant difference in the *S*-wave travel times. [XBL 904-1527]

propagation. Only two sites, 8 and 12, which are offset to the northeast, showed such a difference. At both sites the *SH*-source generates the faster shear wave. The depth dependence of the 40- to 50-msec differences indicates that the shear-wave splitting occurs predominantly at very shallow depths (less than 150 m). Assuming 150 m of anisotropic material with an *S*-wave travel time of about 350 msec, we find a minimum of about 11% shear-wave anisotropy. Apparently a shallow section to the NE is highly anisotropic. A possible cause is shallow horizontal bedding, with large variations in seismic velocity, localized to the northeast. An additional 10- to 15-ms time difference appears to be accumulated below 350–400 m, allowing for possible anisotropy of about 5% in the deeper tuffs. Since only the NE azimuth shows this small effect, the medium at all explosive source levels is considered to be isotropic (an anisotropic medium at depth would show a continual increase in *SV-SH* travel-time difference with depth).

VELOCITY INVERSION

For the velocity inversion the travel-time data were projected onto two nearly perpendicular planes, and independent 2-D inversions were computed for each plane. The inversion method is based on the technique proposed by Thurber (1983), which determines the velocities at a set of discrete nodes by minimizing the travel-time residuals. Velocities between nodes are calculated by linear interpolation, and raytracing is used to produce travel times. The damped least-squares method is used in this nonlinear iterative inversion to solve for velocity perturbations at each node for each iteration. The method is described in detail by Michelini and McEvilly (1991). Separate inversions were performed for *P*- and *S*-wave velocity. For the anisotropic *S*-wave data (sites 8 and 12), the earliest shear-wave arrival was used. The separate determinations for *P*- and *S*-wave velocities provide a measure of the *Vp/Vs* ratio for the 2-D sections. As part of the velocity inversion the raypath coverage for each cross section is determined. The raypaths are determined separately for *P*- and *S*-waves, and they indicate the density of sampling within a given zone. Figure 3 shows the *P*-wave raypaths and velocity contours for the SW-NE cross section.

The rock volume imaged by the velocity inversion contains four major geologic units, as shown in Figure 4. The basement Paleozoic rocks are overlain by two tuff units, the Tertiary Tunnel Bed tuff and the younger Paintbrush tuff, and the shallow sediments are Quaternary alluvium. *P*-wave velocities determined by inversion are 1.0 to 1.7 km/sec in the alluvium and 1.6 to 2.1 km/sec in the tuffs. *S*-wave velocities are 0.5 to 1.0 km/sec in the alluvium and 0.9 to 1.4 km/sec in the tuffs. Within the Paintbrush and Tunnel Bed tuff formations we observe a west-dipping low-velocity zone (about 1.9 km/sec *P*-wave and 1.1 km/sec *S*-wave) in both sections east of the well at depths between 300 and 500 m.

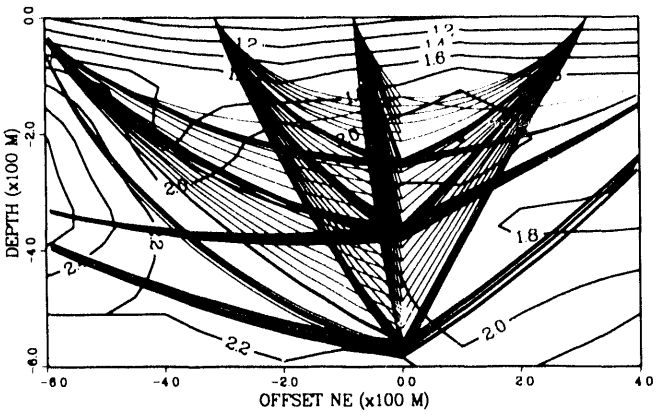

Figure 3. Raypaths and results from *P*-wave velocity inversion in the vertical SW-NE section using data from sites (left to right) 14, 10, 6, 4, 8, and 12. Sites 14, 10, and 12 are outside the cross section. The horizontal axis is centered at the well (offset = 0) and extends 400 m NE and 600 m SW. The alluvium is seen as the steep gradient from 1.0 to 1.7 km/sec, and a SW-dipping low-velocity zone is apparent to the NE. This low-velocity zone is within the Paintbrush and Tunnel Bed tuffs. The high-velocity zone to the extreme SW in the model is probably an artifact of poor ray coverage. Contour interval is 0.2 km/sec. [XBL 913-550]

Inferred faults, based on gravity and well control in the survey area, can be partially located using the velocity inversion results. One such fault has more than 100 m of basement offset SE of the survey well. The SE-NW velocity cross section indicates the location of this fault as high-velocity material between 0.3 km and 0.6 km depth and 0.2 km to 0 km SE offset from the well. A similar velocity increase is suggested in the SW-NE velocity section at 0 to 1 km offset to the NE.

COMPARISON OF VSP AND EXPLOSION DATA

The VSP sources occupied the same locations as the explosion receivers to provide data along reciprocal raypaths. Although this aspect of data analysis has just begun, one example demonstrates the potential for decomposition of the recorded explosion waveform into separate arrivals using the VSP information. Figure 5 shows data for a 10-lb explosion and for the VSP sources. The explosion receivers and VSP sources are at surface site 8, and the explosive source and VSP receivers are at about 360 m depth in the well. We see the effect of *S*-wave anisotropy on this path in the difference in arrival time for the direct shear wave from the *SV* and *SH* sources. We can also identify both the *SH* and *SV* arrivals in the explosion waveform.

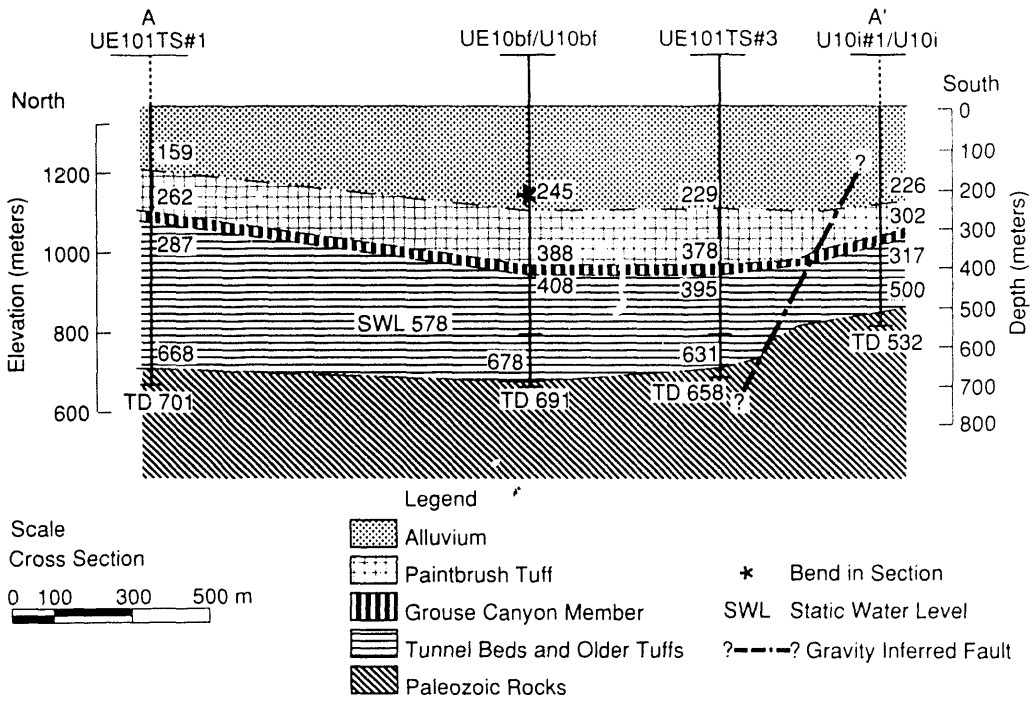

Figure 4. Geologic cross section *A-A'*, showing major formations in CSSY-VSP well UE10 ITS #3. [XBL 909-5743]

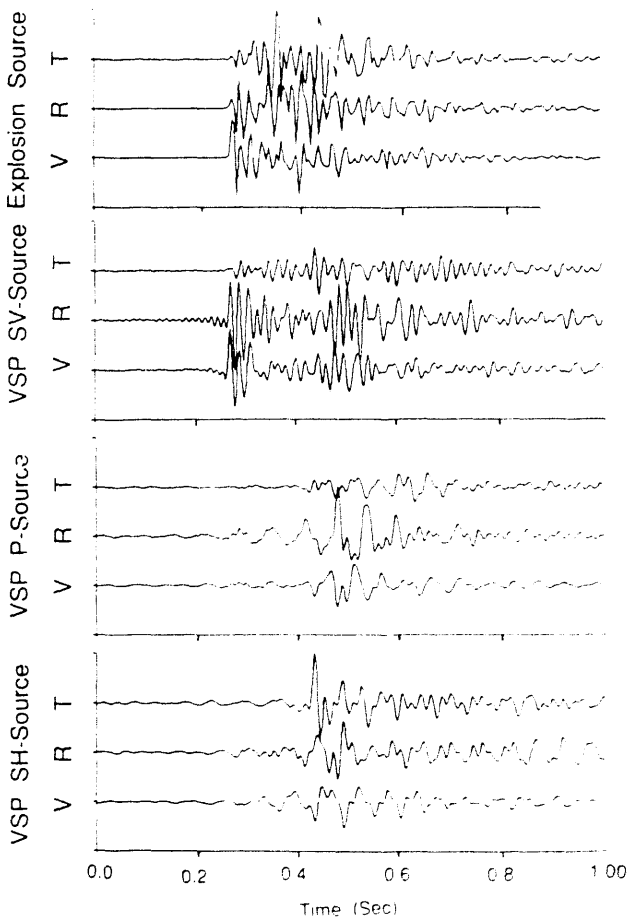

Figure 5. Comparison of 3-component data for reciprocal raypaths. The VSP data are from site 8 to a receiver at 361 m for all 3 sources. The explosion data are from a 10-lb source at 359 m to a receiver at site 8. The components are vertical (V), horizontal-radial (R), and horizontal-transverse (T). Each set of 3 components is normalized to the maximum of the 3 components. The *SH*-source data show a shear-wave arrival at 0.44 sec with large amplitude on the transverse component and a similar arrival is seen from the explosion source. The *SV*-source data have a shear-wave arrival at 0.48 sec (0.04 sec later than *SH*), demonstrating the shear-wave anisotropy. The explosion source also has an arrival at 0.48 sec on the vertical and radial components. The VSP data allows accurate identification of these later arrivals in the explosion data. The explosion source data display a large arrival on the transverse component at about 0.35 sec, which is not seen on the VSP data shown here; this may be a *P*-to-*S* conversion related to an *S*-to-*P* observed in another VSP section. [XBL 913-551]

CONCLUSION

The initial data analysis described here produced velocity models from travel-time inversion, defined the extent of shear-wave anisotropy, and identified reflections and mode-conversions. The initial velocity model and structure are input data for the associated study of the explosion source functions. The results, representing the first phase of data analysis, show that valuable information on subsurface properties around UE-10 ITS #3 have been obtained with the VSP survey.

REFERENCES

Daley, T.M., McEvilly, T.V., and Majer, E.L., 1988. Analysis of *P*- and *S*-wave vertical seismic profile data from the Salton Sea Scientific Drilling Project. J. Geophys. Res., v. 93, B11, p. 13025–13036 (LBL-22246).

Daley, T.M., and McEvilly, T.V., 1990. NTS seismic yield experiment: VSP site characterization study (Abstract). Seismol. Res. Lett., v. 61, p. 11.

Majer, E.L., McEvilly, T.V., Eastwood, F., and Myer, L., 1988. Fracture detection using *P*- and *S*-wave vertical seismic profiles at The Geysers geothermal field. Geophysics, v. 53, p. 76–84 (LBL-20100).

Michelini, A., and McEvilly, T.V., 1991. Seismological studies at Parkfield: I. Simultaneous inversion for velocity structure and hypocenters using cubic B-splines parameterization. Bull. Seismol. Soc. Am., v. 81, no. 2, p. 524–552 (LBL-28770).

Thurber, C.H., 1983. Earthquake locations and three-dimensional crustal structure in the Coyote Lake area, Central California. J. Geophys. Res., v. 88, p. 8226–8236.

Microseismic Monitoring of the Northwest Geysers

E. L. Majer, A. Schultz, and R. Haught

Lawrence Berkeley Laboratory (LBL), in conjunction with Cold Water Creek Operating Company (CCOC), has undertaken the collection, analysis, processing, and interpretation of the microearthquake (MEQ) data from the 16-station CCOC array now in place at the Northwest Geysers geothermal field (Figure 1). This array is unique in that it is a high-frequency (400 samples/sec) digital (16-bit) system collecting and processing data from 3-component borehole stations. To our knowledge there is no other array in the world that is providing data of this quality and quantity in a producing geothermal field. The work began in March of 1990. The first priority of the work was to bring the MEQ array into a stable state of operation in order to ensure the routine collection of data. The second task was to start processing existing data in order refine the velocity model for precision location of the microearthquakes. Precision locations will be needed to aid in the design of future injection tests and calibration studies.

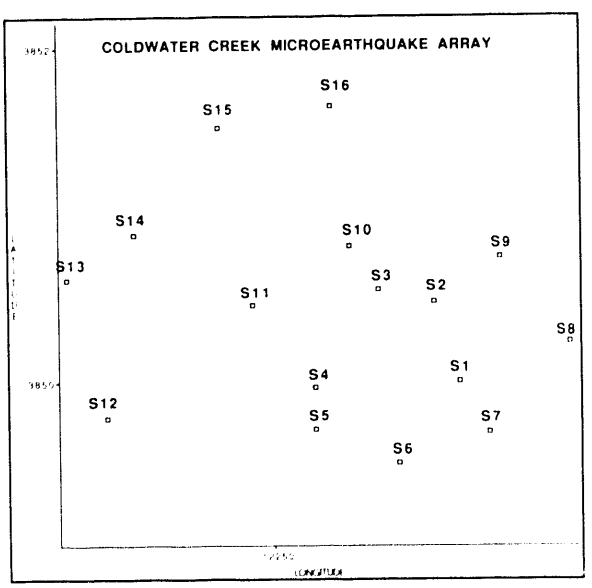

Figure 1. The 16 stations of the Coldwater Creek microearthquake array. [XBL 913-552]

OBJECTIVES

1. Demonstrate the utility of high-resolution microearthquake data (MEQ):
   - To locate high-permeability paths in the reservoir.
   - To aid in the location of in-fill well drilling.
   - To monitor the effect of condensate injection in real time.
2. Develop 3-D model of reservoir:

P- and *S*-wave velocity structure.

Poisson's ratio model.

3-D structural model using MEQ location for inferring flow paths.

APPROACH

1. Short Term:

   Ensure that hardware and software are operational.

   Upgrade software for modern picking, location, and inversion codes.

   Process existing data for software testing and MEQ technique evaluation.

   Monitor several injection processes for 6-12 weeks to understand relation between seismicity and injection.

2. Long Term:

   Stabilize software for streamlining data collection, processing and interpretation.

   Link hydrological/geological/geochemical data to MEQ processes.

   Provide high-precision location for reducing uncertainty in well siting.

PROGRESS TO DATE

The microearthquake array at the Coldwater Creek geothermal field (operated by GEO) has been brought up to operating conditions by LBL personnel over the past 7 months. Almost all parts of the system needed repair or maintenance to bring it back on line.

In terms of data processing, a considerable effort was expended on converting the existing data tapes into a format that was compatible with LBL processing codes. The first step in the processing was to select events for deriving a 3-D velocity model of the CCOC region. Over one hundred events with high-quality *P*-and *S*-waves were selected to form the initial velocity model. The MEQs selected are shown in Figure 2. The events were selected in order to have the raypaths between the source and receivers cover the CCOC geothermal field uniformly in depth and in extent. All *P*- and *S*-waves were carefully picked by hand. The next step in the process was the inversion of the arrival times for the velocity model. The inversion was done using a modified version of a program originally written by several different people (Ebberhart-Phillips, Thurber, Prothro). The program is based on a progressive inversion scheme to jointly determine the velocity structure (*P*- and *S*-wave) and location of the events.

The inversion is based on a technique proposed by Thurber (1983), which determines the velocities at a set of discrete nodes by minimizing the travel-time residuals. Raytracing is used to produce travel-time data in the

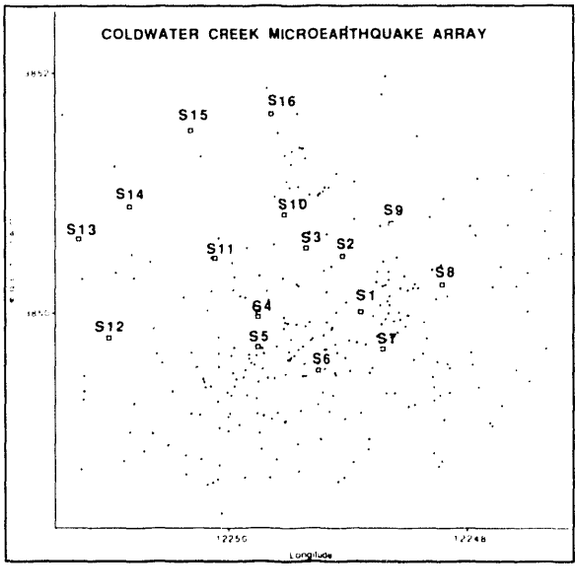

Figure 2. The MEQs selected for the 3-D velocity model. [XBL 913-553]

iterative procedure until the solutions converge. Damped least-squares solutions are used in this nonlinear iterative inversion to solve for velocity perturbations at each node for each iteration. Velocities between nodes are calculated by linear interpolation. This method is also described in detail in Michelini and McEvilly (1991).

For the initial study an $10 \times 5 \times 5$ (depth, X, Y,) grid of nodes was used, plus edge nodes. The initial velocity model was based on O'Connell's (1986) thesis work in this area. Separate inversions were performed for the *P*-wave velocity and for the *S*-wave velocity.

Figure 3 shows one of the results of the inversions: cross sections of the *P*- to *S*-wave velocity (*Vp/Vs*) velocity

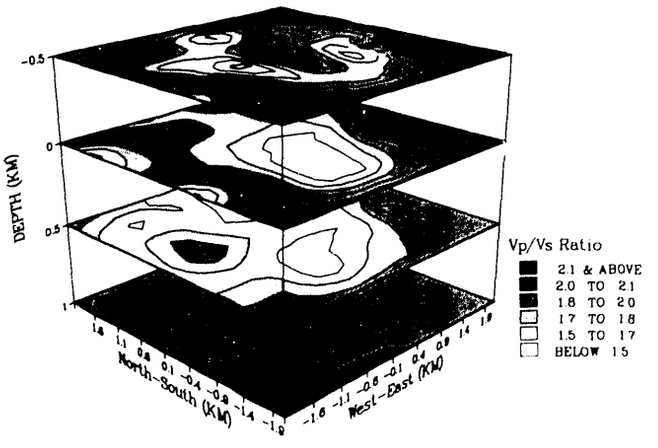

Figure 3. Horizontal cross sections of the *Vp/Vs* ratio (top 1.5 km). [XBL 913-554]

structure for the volume in Figure 1. These results are very encouraging in that once the station corrections and proper times were selected, stable velocity models were obtained. Future work will be focused on refining the velocity model and using the velocity model to start locating sets of events associated with injection activities. As can be seen from Figure 3 there is considerable lateral variation in the velocity structure. A second inversion was done using a totally different set of events, and the results were very similar, thus providing a measure of confidence that this is a good velocity model to be using for precision locations. Given a good velocity model it is now possible to start to analyze the MEQ data for subtle fault and fracture planes that may be apparent in precise event locations. This will be useful for in-fill well drilling.

REFERENCES

Michelini, A., and McEvilly, T.V., 1991. Seismological studies at Parkfield: I. Simultaneous inversion for velocity structure and hypocenters using cubic B-splines parameterization. Bull. Seismol. Soc. Am., v. 81, no. 2, p. 524–552 (LBL-28770).

O'Connell, D.R., 1986. Seismic velocity structure and microearthquake source properties at The Geysers, California, geothermal area (Ph.D. thesis). Lawrence Berkeley Laboratory Report LBL-22280.

Thurber, C.H., 1983. Earthquake locations and three-dimensional crustal structure in the Coyote Lake area, Central California. J. Geophys. Res., v. 88, p. 8226–8236.

Three-Dimensional Velocity Structure of the Long Valley Region, Eastern California, from the Inversion of Local Earthquakes

A. E. Romero, T. V. McEvilly, and E. L. Majer

The Long Valley caldera (LVC) was formed as a result of the eruption of the voluminous Bishop tuff 730,000 years ago. Since then, it has been the site of several episodes of intra-caldera volcanism, the most recent being around 500 years ago (Bailey, 1976). Numerous scientific investigations have been focused on the region since the onset of intense seismic activity in 1980, accompanied by almost 0.5 m of surface uplift at the resurgent dome.

A number of seismic studies argue for the existence of a magma body at shallow to mid-crustal depths beneath LVC. Refraction surveys (Hill et al., 1985) showed seismic reflectors from 7 to 8 km beneath the western margin of the resurgent dome; these were interpreted as the top of a magma chamber. Other studies (e.g., Luetgert and Mooney, 1985; Zucca et al., 1987) interpreted deeper reflectors as the bottom of the magma chamber. In a more recent study, Dawson et al. (1990) used teleseismic *P*-wave residuals to obtain a 3-D velocity structure, finding a low-velocity body between 7 and 20 km depth beneath the resurgent dome, which they interpret to be a magma body of approximately 20% partial melt. On the basis of *S*-wave shadowing, Sanders (1984) defines a possible magma body between 5 and 8 km depth beneath the central part of the caldera, with the top possibly as shallow as 4 km. However, Hauksson (1988) suggested that the observed *P* and *S* amplitude variations could be explained by radiation pattern effects. A large-scale tomographic study by Kissling (1988) found no evidence for a low-velocity region that would indicate the presence of a magma body beneath LVC.

In an attempt to resolve these contrasting results, a high-resolution tomographic study of the region of the proposed magma body was proposed by Lawrence Berkeley Laboratory (LBL) and the U.S. Geological Survey (USGS). With the installation of a fan array of eight 3-component borehole receivers (80- to 160-m depths) on the northwestern rim of the caldera, it was intended for the high seismic activity—in the South Moat, in the Sierran Block south of the caldera, and in Chalfant Valley—to illuminate the central part of the caldera as viewed from the array. The data acquisition rate was 480 16-bit gain-ranged samples per second per component, and the data were telemetered digitally to a local event-recording PC-based data acquisition system. Initial results from this experiment, which provide constraints on the structure, are presented here.

The array operated from June 1989 through August 1990. Some 2100 local microearthquakes were recorded. The purpose of the fan array was to provide the data necessary for a three-dimensional joint inversion for hypocenters and the crustal structure in and below the caldera, specifically in the region of the proposed magma chamber, by complementing coverage of existing USGS and University of Nevada at Reno (UNR) networks with

the specially focused, wideband borehole array. Seismicity during the period of operation concentrated beneath Mammoth Mountain, in the South Moat zone and at Chalfant Valley, but there were sufficient events recorded from other regions to yield fairly uniform coverage for the inversion. Figure 1 shows the station distribution and the epicenters of the 280 earthquakes used in the inversion.

MODEL GRID

We solved the joint problem for 3-D velocity distribution and hypocenter locations using the progressive inversion scheme proposed by Thurber (1983). A detailed discussion of this method is given by Michelini and McEvilly (1991). The region was parameterized into a 3-D rectangular grid with velocities assigned to each grid point. Two parameterizations shown in Figure 2 were adopted: (1) a coarse grid with an average node spacing along the x, y, and z directions, respectively, of 12 km (×7 nodes), 13 km (×7 nodes), and 2 km (×6 nodes) and (2) a fine grid with an average spacing of 5 km (×7 nodes), 4 km (×7 nodes), and 2 km (×6 nodes). Starting hypocenter locations were fixed arbitrarily near the center of the caldera. The joint inversion using the coarse grid was carried out and the resulting fairly smooth regional velocity model was used as the background starting model for the finer grid, to allow for more resolution within and beneath the heterogeneous caldera structure.

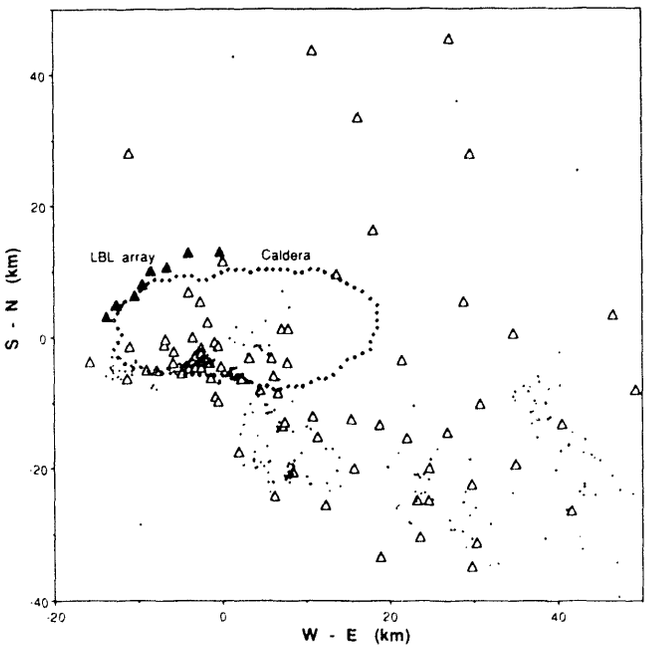

Figure 1. Map of Long Valley region showing the location of the LBL array (solid triangles) and other stations operated by UNR and USGS (open triangles). Also shown are the epicenters of the 280 microearthquakes used in the inversion (small crosses). [XBL 913-539]

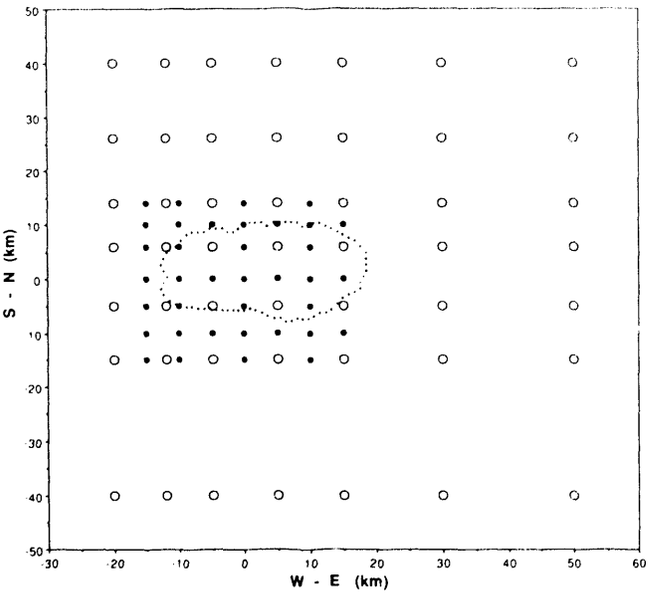

Figure 2. Location of 294 inversion nodes at which the P- and S-wave velocities are specified. The local reference grid is centered on the resurgent dome at 37° 40' N, 118° 54' W. The coarse grid (open circles) is used to determine a regional background model that is then used in an inversion with the fine grid (solid circles) for maximum resolution in the caldera itself. Both grids have vertical nodes at z = 2 km (average surface elevation), 1, 0, –2, –5, and –10 km. [XBL 913-540]

Fine grid spacing in the upper 2 km modeled the steep velocity gradient near the surface. We used the P-wave velocity model from the refraction work of Hill et al. (1985) to provide a starting model with lateral velocity variations. However, both the 1-D and the 3-D (Hill's velocities) starting models produced solutions with comparable variances and resolutions. The problem seems to be well-posed, at least for the P-waves. We calculated an initial S-wave velocity model by assuming a constant Vp/Vs ratio of 1.73.

SYNTHETIC TESTS

Tests with synthetic data used the actual source-receiver geometries to check the resolving capability of the data set. We used the model resolution matrix (R) as an aid in evaluating the features of the resulting model. The model resolution matrix, defined in

$$\hat{m} = R\, m$$

shows how close a model estimate ($\hat{m}$) is to an ideal earth model (m) in the absence of error and limited by the model parameterization. Each row of R is an averaging kernel of a single model parameter (m). If R is equal to an identity matrix I, then each ($\hat{m}$) is determined uniquely, independent of all other model parameters. Model resolution is

measured using the resolving width function, as defined by Michelini and McEvilly (1991). A perfectly resolved model parameter has zero resolving width. A large value indicates a broad resolving kernel shape. We used this measure with the data variance to select the appropriate damping parameter for the inversion. Our tests suggested a value of 0.25 sec/km as the optimum damping value, given the trade-off between data variance and model resolution.

We first generated arrival times from a model consisting of a checkerboard pattern of alternating high and low velocities (20% velocity contrast) on two horizontal planes at $z = 0$ and $z = -5$ km, embedded in a 1-D "background" model, as shown in Figure 3. Starting with the 1-D model used routinely by USGS in locating LVC hypocenters, we attempted to recover the initial synthetic structure. The resulting velocity distributions, shown in Figure 4, are virtually identical to the originals except in some regions to the north of the caldera with low resolution due to poor data coverage. The caldera region is well resolved to a depth of 7 km. We conclude that the inverse problem as posed can define heterogeneity within and beneath the caldera at a resolution of a few kilometers, sufficient to test the various magma chamber hypotheses.

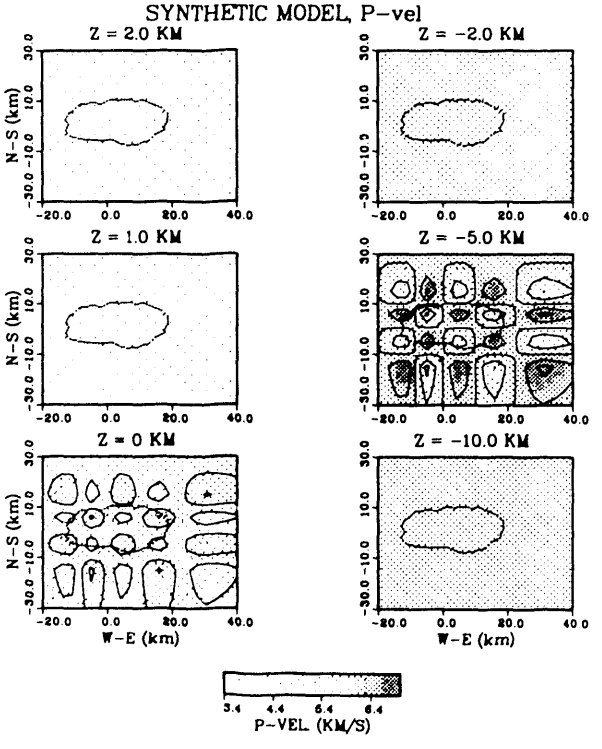

Figure 3. Horizontal cross sections of the synthetic *P*-wave velocity structure taken at several depths. Note the alternating patterns of high and low velocities (20% variation from background velocity) at $z = 0$ and $z = -5$ km. Contour interval is 1 km/sec. [XBL 913-541]

RESULTS AND DISCUSSION

The final model is based on the inversion of data from 280 well-distributed local earthquakes with about 7000 arrival times, including almost 1000 *S*-wave times from the 3-component stations. The model is presented together with the resolving width function to indicate regions of low resolution. The final rms residual of arrival times is 73 msec. The resulting velocity model, shown in Figures 5 and 6, defines an upper crustal structure consistent with refraction studies and geologic data. Low velocities mark the caldera fill, in contrast to the higher velocities of the Sierran basement to the south and west and to the highland terranes to the north and east. The caldera fill is discernible down to the basement, around 2 km depth. Sharp velocity contrasts at the western edge of the caldera delineate the caldera wall. Low velocities to the northeast are associated with the Mono Lake sediments and to the southeast with the Bishop tuff deposits of the Volcanic Tableland.

In the joint inversion results the hypocenters did not shift appreciably from those originally determined by USGS. For example, in the southern part of the caldera the relocated hypocenters were within about 2 km of their original USGS locations.

The *Vp/Vs* ratios show a remarkable low value beneath the South Moat, above the zone where dike injection has been postulated as the cause for the high seismicity there (Smith, 1984). This low ratio may indicate the presence of dry steam in fractures near the caldera wall. A possible zone of low *Vp/Vs* ratio at shallow depths beneath the West Moat is poorly resolved by the data. A high *Vp/Vs* ratio is seen near Casa Diablo at shallow depth in the caldera, a condition often found in fluid-saturated fractured rocks at elevated pore pressure (O'Connell and Budiansky, 1974; Moos and Zoback, 1983; Christensen, 1984).

There is no significant lateral velocity variation beneath the caldera, although velocities there are somewhat lower than in the surrounding regions. This low-velocity feature is diffuse and appears more likely related to hydrothermal alteration and fracturing rather than to the presence of a sizeable and distinct magma chamber. This conclusion is also supported by the absence of significant *S*-wave velocity anomalies beneath the caldera and by the normal values of *Vp/Vs* ratio (Figure 7). These tentative results are in agreement with Kissing's conclusion on the lack of evidence for any pervasive low-velocity body at shallow crustal depths. Our results do not rule out the possible presence of dike or sill intrusions of melt with dimensions below the resolution of this study, except in their total fractional volume as constrained by the averaged *Vp/Vs* values. The effects of melt geometry and physical properties on seismic wave velocities are poorly known, so that it is difficult to estimate melt fraction in such

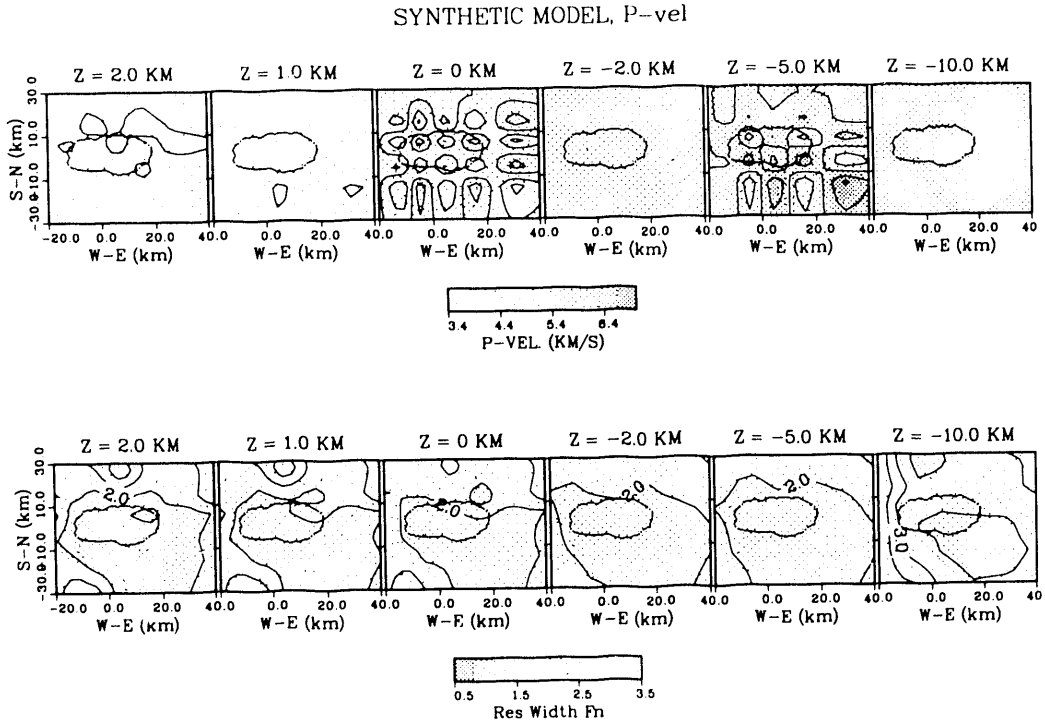

Figure 4. Plots of the recovered synthetic P-wave velocity structure and the resolving width function presented in the same manner as for Figure 3. [XBL 913-542]

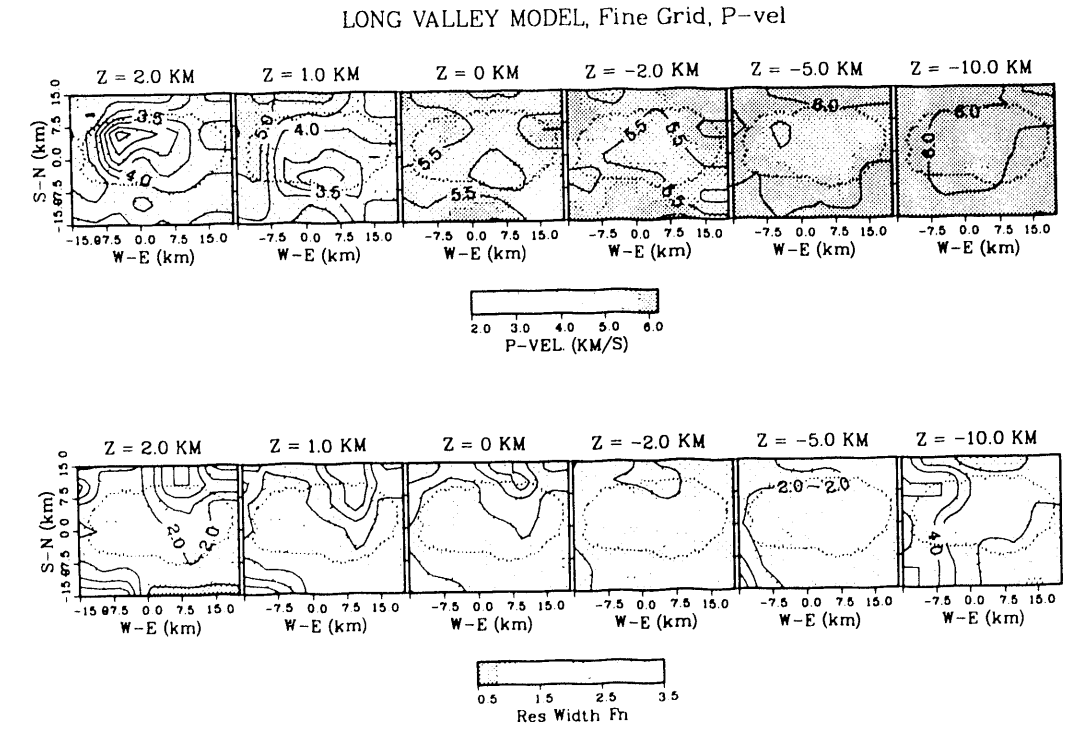

Figure 5. Plots of the *P*-wave velocity model and the resolving width function obtained from the inversion for the fine grid. [XBL 913-544]

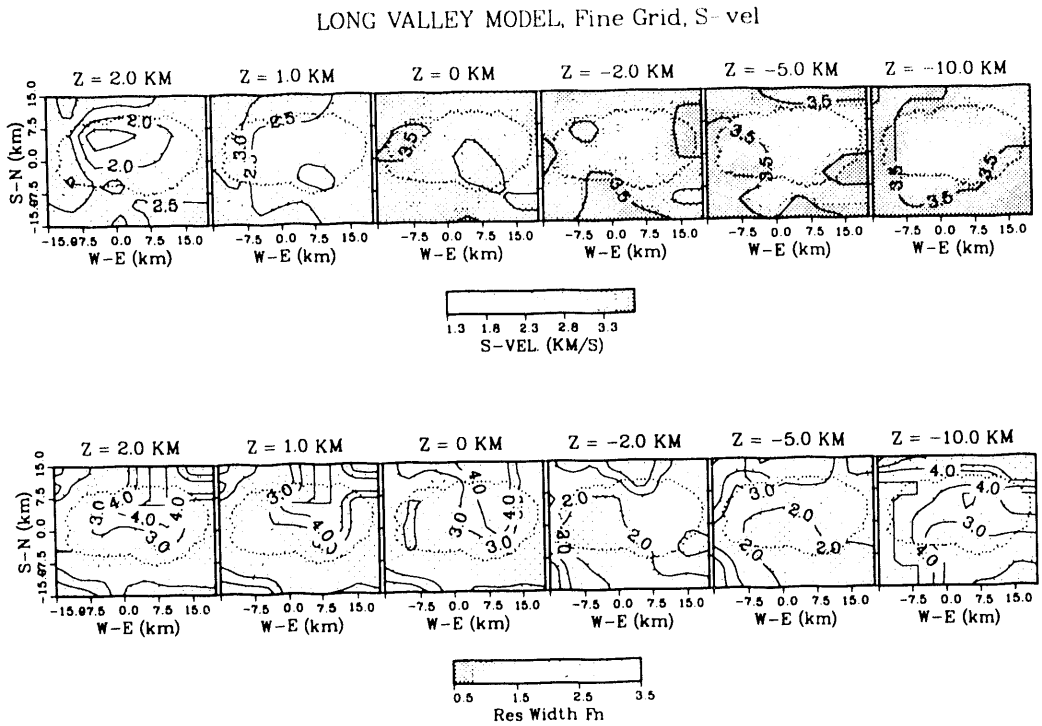

Figure 6. Plots of the *S*-wave velocity model and the resolving width function obtained from the inversion for the fine grid. [XBL 913-545]

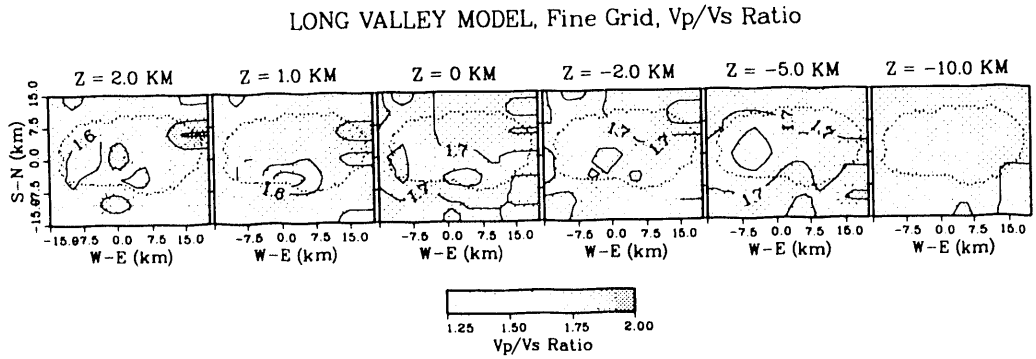

Figure 7. Plots of the *Vp/Vs* ratio obtained from the inversion for the fine grid. [XBL 913-546]

intrusions. Based on the theoretical study of Mavko (1980), the *Vp/Vs* ratio of 1.6–1.7 seen at 4–7 km depth beneath the caldera constrains the melt fraction to a few percent, if the melt is largely in a film configuration.

CONCLUSIONS

The velocity models determined by joint inversion of *P*- and *S*-wave arrival times from 280 earthquakes, with the velocity parameterized on 294 grid points, reflect the surface geology, defining the caldera fill to 2 km depth, and the contrast with the surrounding higher velocity Sierran block and highland topography. No isolated low-velocity anomalies are seen beneath the caldera floor, although a diffuse zone of reduced velocity persists to a depth of about 7 km. The *Vp/Vs* ratio shows intriguing variations within the caldera fill and above the south moat zone of high seismicity. We hope to improve the *Vp/Vs* resolution with more *S*-wave data from the recent UNR survey using portable 3-component recorders.

This exercise shows that the microearthquake data set and the available station distribution (including the special

fan array and the 3-component data) constitute a fairly well-conditioned inverse problem, capable of resolving velocity anomalies with dimensions of 3–5 km to a depth of about 10 km. The presence of a well-defined magma chamber between 4 and 7 km depth is not supported in this tomographic study, although the presence of magma in a pervasive set of fractures is allowed if the total melt fraction remains small enough to permit the *Vp/Vs* ratio of 1.6–1.7 at 7 km depth.

REFERENCES

Bailey, R.A., Dalrymple, G.B., and Lanphere, M.A., 1976. Volcanism, structure, and geochronology of Long Valley caldera, Mono County, California. J. Geophys. Res., v. 90, p. 725–744.

Christensen, N.I., 1984. Pore pressure and the oceanic crustal structure. Geophys. J. R. Astron. Soc., v. 79, p. 411–424.

Dawson, P.B., Evans, J.R., and Iyer, H.M., 1990. Teleseismic tomography of the compressional wave velocity structure beneath the Long Valley Region, California. J. Geophys. Res., v. 95, p. 11021–11050.

Haukkson, E., 1988. Absence of evidence for a shallow magma chamber beneath Long Valley caldera, California, in downhole and surface seismograms. J. Geophys. Res., v. 93, p. 13251–13264.

Hill, D.P., Kissling, E., Luetgert, J.H., and Kradolfer, U., 1985. Constraints on the upper crustal structure of the Long Valley–Mono craters volcanic complex, Eastern California, from seismic refraction measurements. J. Geophys. Res., v. 90, p. 11135–11150.

Kissling, E., 1988. Geotomography with local earthquake data. Rev. Geophys., v. 26, p. 659–698.

Luetgert, J.H., and Mooney, W.D., 1985. Crustal refraction profile of Long Valley caldera, California, from the January 1983 Mammoth Lakes earthquake swarm. Bull. Seismol. Soc. Am., v. 75, p. 211–221.

Michelini, A., and McEvilly, T.V., 1991. Seismological studies at Parkfield. I. Simultaneous inversion for velocity structure and hypocenters using cubic B-splines parameterization. Bull. Seismol. Soc. Am., v. 81, no. 2, p. 524–552 (LBL-28770).

Mavko, G.D., 1980. Velocity and attenuation in partially molten rocks. J. Geophys. Res.,v. 85, p. 5173–5189.

Moos, D., and Zoback, M.D., 1983. In situ studies of velocity in fractured crystalline rocks. J. Geophys. Res., v. 88, p. 2345–2358.

O'Connell, D.R., and Budiansky, B., 1974. Seismic velocities in dry and saturated cracked solids. J. Geophys. Res.,v. 79, p. 5412–5426.

Sanders, C.O., 1984. Location and configuration of magma bodies beneath Long Valley, California determined from anomalous earthquake signals. J. Geophys. Res., v. 89, p. 8287–8302.

Smith, A.T., 1984. High-Resolution microseismicity study of possible magmatic intrusion in Long Valley caldera. UCRL-90278 preprint.

Thurber, C.H., 1983. Earthquake locations and three-dimensional crustal structure in the Coyote Lake area, Central California. J. Geophys. Res., v. 88, p. 8226–8236.

Zucca, J.J., Kasameyer, P.W., and Mills, J.M., Jr., 1987. Observation of a reflection from the base of a magma chamber in Long Valley caldera, California. Bull. Seismol. Soc. Am., v. 77, p. 1674–1687.

High-Frequency Seismic Tomographic Imaging for Hydrologic Properties of Near-Surface Materials

E. L. Majer, J. E. Peterson Jr., S. M. Benson, and J. C. S. Long

Subsurface imaging for near-surface applications (less than 100 m) is becoming increasingly important for environmental remediation. Noninvasive monitoring and characterization methods are needed to reduce the cost of mitigation activities, increase worker safety, and provide 3-D information. Described here is a project to examine the relationship between seismic and hydrologic properties that may control contaminant transport in the near surface as part of the Department of Energy's Subsurface Science Program (SSP). Small-scale (approximately 10 m) controlled seismic and hydrologic experiments are being carried out in situ to determine the sensitivity and resolution of seismic methods for mapping porosity, structure, and soil composition to determine the permeability of the subsurface. One- to 10-kHz seismic energy is used to tomographically map the velocity and

attenuation properties with resolution of a few centimeters at spacings up to 10 m. Results to date indicate that if one uses the velocity and attenuation differences in the data, then it is possible in some cases to distinguish such factors as clay content, degree of permeability, and porosity. In this ongoing project work is being carried out in dispersive media, where matrix flow is dominant, and in channel conditions, where flow is dominated by discrete flow patterns. Results presented here are from the dispersive media. Shown in Figure 1 is the experimental field site used to study dispersive media. The site is located in the San Joaquin Valley of California. The site has previously been the subject of many different geological, hydrological, and geochemical investigations. The tomographic imaging work described here was carried out below the water table in well pairs, LBL-I1 to well 4, LBL-I1 to well 8, well 8 to well 4, and LBL-I1 to well 5. The geologic column deduced from core samples is a clay layer over a porous sand and gravel. Previous to this work a tracer study was carried out to determine the hydrologic behavior between wells LBL-I8A and LBL-I4. The results of the tracer study in the porous layer were somewhat unexpected in that the permeability varied much more than expected from the first examination of the core. Prior to the tracer tests it was assumed that the sand layer was almost uniform in permeability. As can be seen from the results of the tracer work in Figure 2, this is not the case. There is a high-permeability zone half way in the sand layer. Therefore a tomographic survey was carried out over this section to determine if subtle lithologic changes could be seen in the seismic data. If so, then what was the relationship between velocity, attenuation, and the physical properties (in this

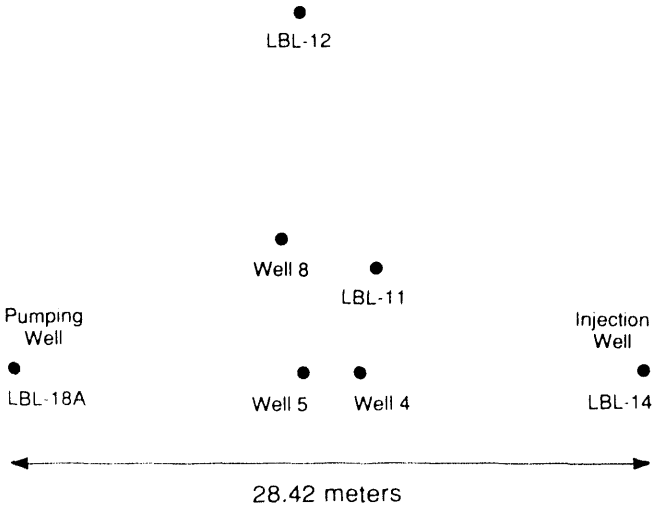

Figure 1. The experimental layout of the field site in the Central Valley of California. [XBL 913-528]

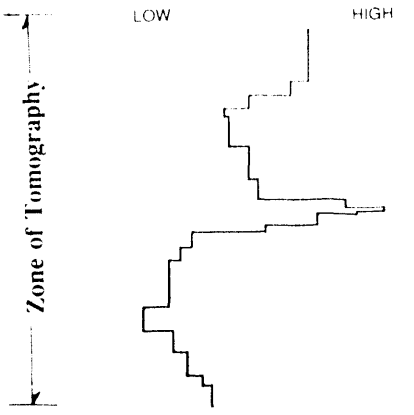

Figure 2. The results of a tracer test between wells LBL-I4 and LBL-I8A, showing the relative tracer velocities. [XBL 913-529]

case grain size, clay content, and porosity) as a function of frequency and hydrologic properties?

This experiment was somewhat unique because of the high frequencies used for the tomographic imaging. Using a piezoelectric pulse system, frequencies from 6 to 10 kHz were obtained between the wells. The data were collected at 0.3 m intervals in all well pairs. The source and electronics used for producing the signals was a high-voltage (4000 V) high-frequency (pulse widths of 50 to 1000 μsec) system powering a cylindrical piezoelectric transducer. A string of unclamped accelerometers lowered into the water-filled boreholes was used to collect the data; the source was also unclamped. This was done to improve repeatability of the data and to ensure that the only clamping of the source and receivers was through the water-filled boreholes.

Shown in Figures 3 to 5 are examples of the results of inverting the data from the cross-well surveys. The velocity data were corrected for anisotropy and inverted using a simple straight-ray ART algorithm. The attenuation data were also inverted using an ART algorithm with a constant-width window to calculate the power of the first arrival. The zone at the top of each plot was the zone of no data due to extreme attenuation in the clay layer. The most obvious feature is the large degree of heterogeneity associated with the results in the supposedly homogeneous "sand section" in which data were obtained. The velocity varies from 1.6 km/sec (water velocity is approximately 1.45 km/sec) to 1.75 km/sec throughout the section. For the section from LBL-I1 to well 5 there is a direct correlation between the permeable zone, as inferred from the tracer data, and the low-velocity section. However, it must be kept in mind that the tracer test was carried out between wells I8A and I4 and that the results are an average. It is also interesting to note the variability in the section from well 8 to well 4 versus the sections from I1 to well 5 and from well I1 to well 5. The attenuation results

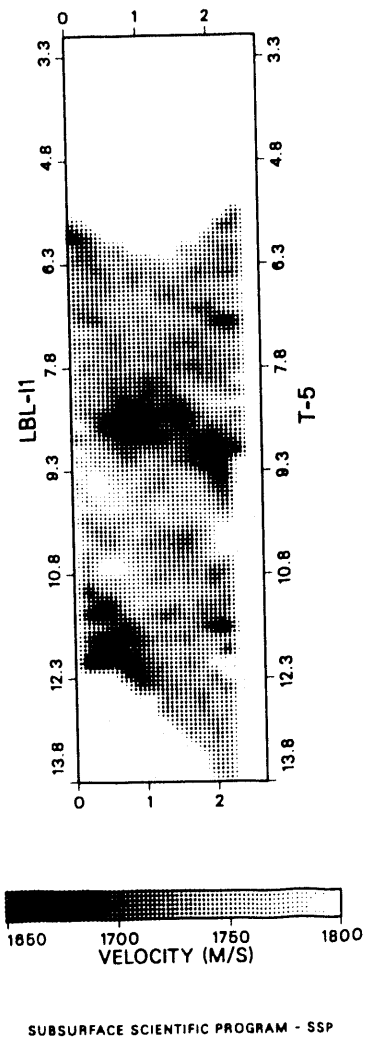

Figure 3. The velocity tomogram between wells LBL-I1 and 5. [XBL 913-530]

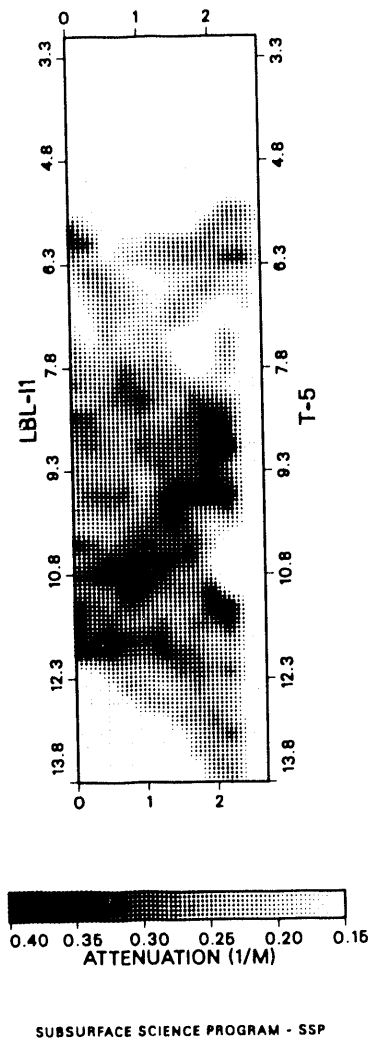

Figure 4. The amplitude or attenuation tomogram between wells LBL-I1 and 5. [XBL 913-531]

are also interesting: for the case of well 5 to LBL-I1, the zone of high attenuation corresponds to a high-velocity zone, i.e., almost the opposite of what is expected from traditional rock physics. Obviously water (porosity) and clay content are playing a controlling role in the velocity and attenuation, i.e., a zone of higher permeability is also a zone of low velocity and low attenuation.

It is obvious that the results cannot be interpreted with simple elastic theory of wave propagation. An elastic behavior is evident by the attenuation and velocity results. It also useful to note that at the frequencies used (6,000 to 10,000 Hz), the soil may exhibit behavior not usually seen at a few tens of hertz. Although the soil is totally saturated in this section, there is a strong relationship between the porosity, clay content, and seismic properties. The general distribution of grain size versus depth is shown in Figure 6 (Benson et al., 1989). Also shown is the relative content of clay (grain size less than 2 μ), silt (grain size from 2 to 50 μ) and sand (grain size greater than 50 μ). From the seismic data taken in these three compositions, it is evident that there is a relationship, though complex. The seismic traces shown in Figure 6 are absolute amplitude (753 counts and 12 counts). Shown in Figure 7 is a tomogram of porosity. The transformation that was used is from Klimentos and McCann (1990). Although Klimentos and

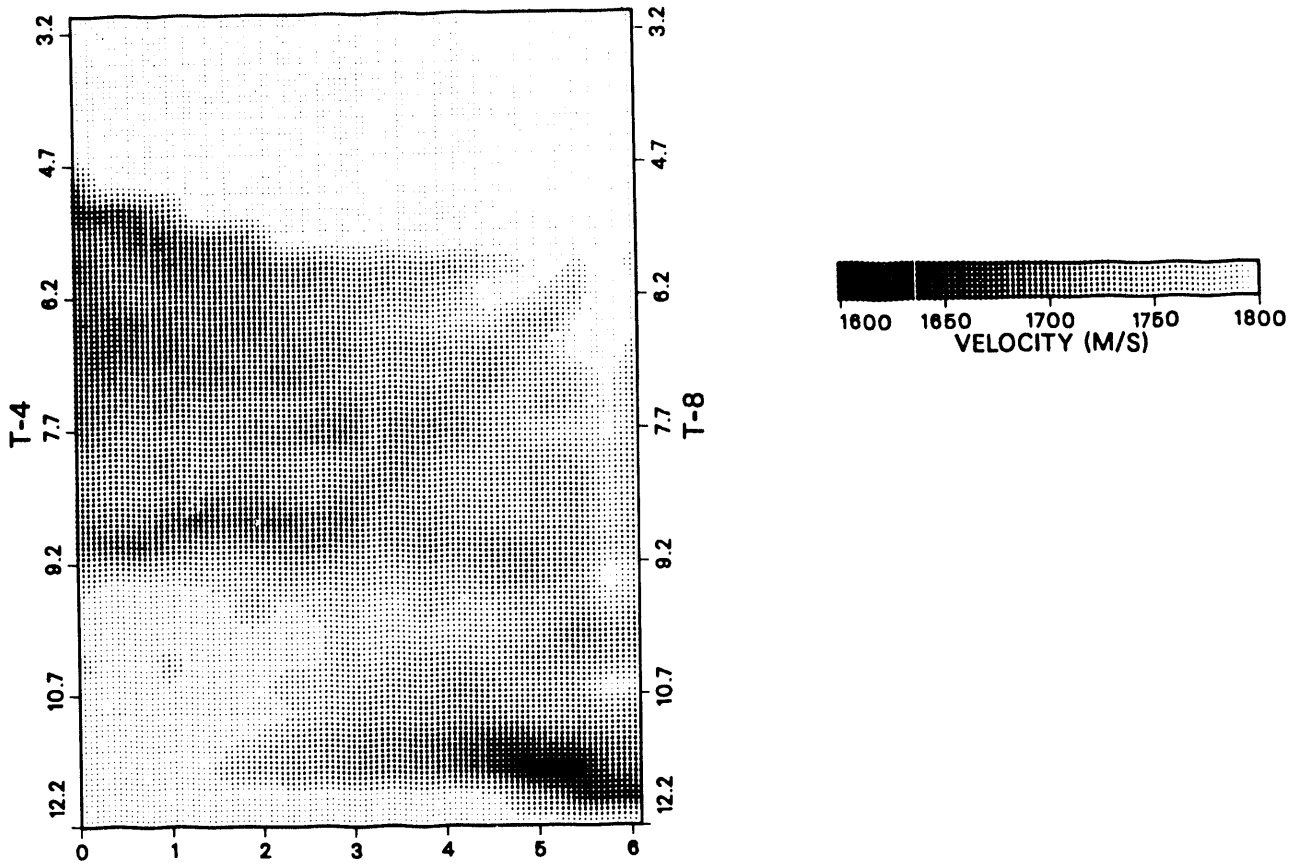

Figure 5. The velocity tomogram between wells LBL-I4 and 8. [XBL 913-532]

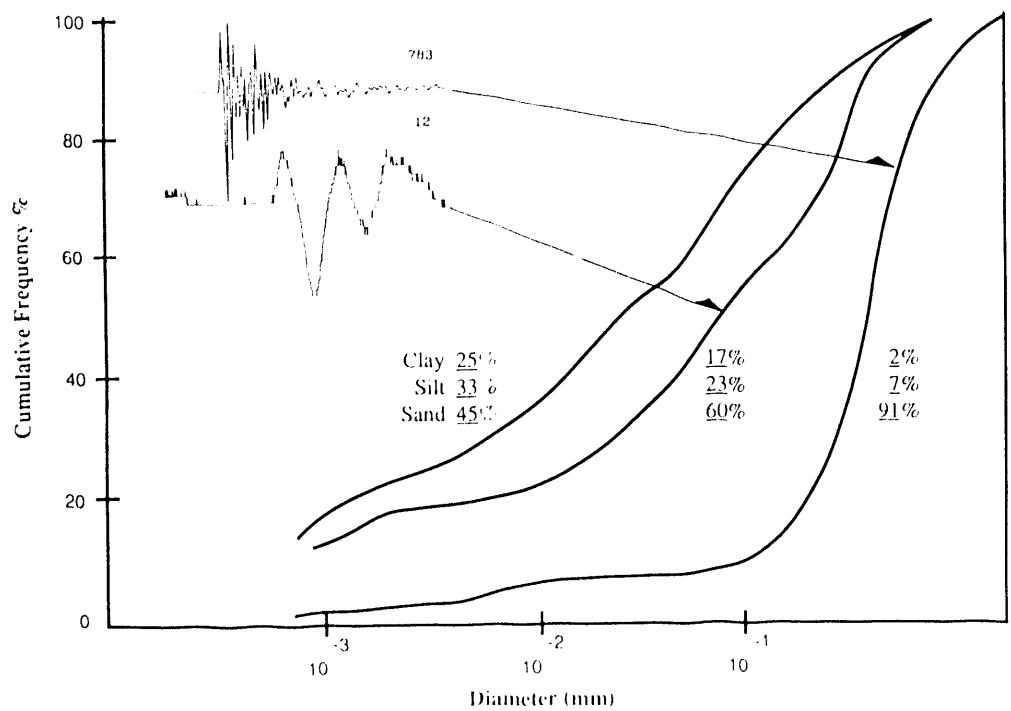

Figure 6. Particle size distribution as a function of clay and sand content. The two seismic traces show the attenuation effects of increasing clay content. [XBL 913-533]

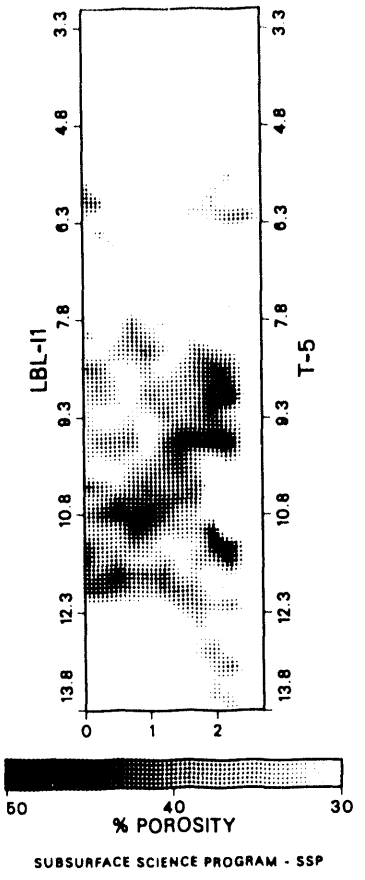

Figure 7. The porosity tomogram calculated from the clay content and the attenuation measurements. [XBL 913-534]

McCann focused their work in rock (a rigid matrix material), it is interesting to apply their results to soil. The equation used was attenuation = 0.031 porosity in percent plus 0.241 percent clay content by volume minus 0.132. Therefore, we fixed clay content at 2% and solved for porosity using attenuation. The results shown in Figure 7 are for the section between well 5 and LBL-11. The results should probably be viewed as more of a relative porosity than absolute. In any case it is obvious that there is a complex relationship between clay content, grain size, porosity, and seismic properties, continued work will focus on improving our understanding of the relationship of these parameters in soils in order to provide input to hydrologic models.

REFERENCES

Benson, S.M., Horne, A., Weres, O., Tokunaga, T.K., and Yee, A., 1989. Geochemical, biological, and hydrological research at Kesterson Reservoir: An update. Earth Sciences Division Annual Report 1988. Lawrence Berkeley Laboratory Report LBL-26362, p. 46–50.

Klimentos, T., and McCann, C., 1990. Relationships among compressional wave attenuation, porosity, clay content, and permeability in sandstones. Geophysics, v. 55, no. 8, p. 998–1014.

Hayward Fault Mechanics and Paleoseismicity

P. L. Williams

The Hayward fault produced two large earthquakes in the 19th century and thus is a key focus of concern with respect to the imminence of future damaging earthquakes. This study represents the first direct measurement of the frequency of Hayward fault ruptures. Surprisingly, basic parameters of the Hayward fault's mechanical behavior, including slip rate, rate of elastic loading, constitutive properties, geometry, and characteristic earthquake displacement, remain relatively poorly known. Anticipation of the fault's recurrence behavior requires either known or assumed values for these parameters (e.g., Working Group, 1990) or direct recovery of recurrence evidence from the geological record. Knowledge of characteristic Hayward fault behavior remains poor. This suggests that current estimates of its recurrence rate should be regarded with caution. Research outlined here provides direct evidence of past recurrence behavior from the geological record. These measurements provide a critical test of the assumptions made in current analyses of Hayward fault rupture hazard.

THE MOWRY SITE

Substantial evidence of the timing of Hayward fault slip over the past 1700 years has been recovered in excavations near Mowry Street (the "Mowry site") in Fremont. Recurrent motion of the fault is recorded by offset, tilt, and liquefaction of late Holocene pond and fluvial deposits at the northern end of Tule Pond (Figure 1). The pond is contained in a 100-m-wide pull-apart graben

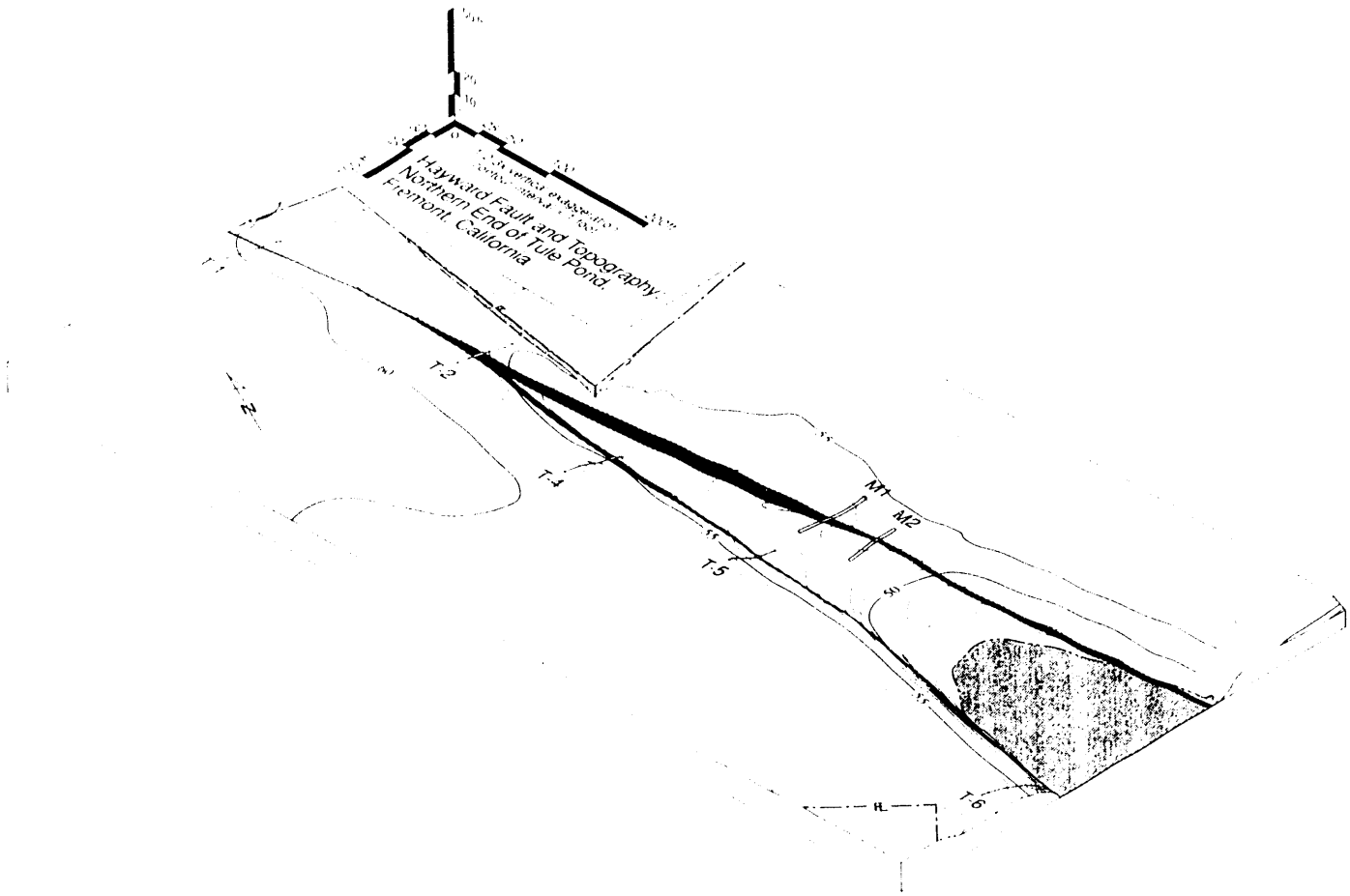

Figure 1. Orthometric map of Mowry site and locations of trenches M1 and M2. Map shows the topographic expression of the northern end of the Tule Pond graben. The graben results from extension across a right double-bend of the west trace. Note the shallow swale intersecting the Tule Pond depression from the east near trench M1. This probably expresses an intersecting buried channel that followed the fault between trenches M1 and M2. Artificial fill and warping subdues topographic expression of the graben north of the 47-ft contour. [XBL 913-535]

cut into the Holocene alluvial fan complex of Alameda Creek. The pond is fault-bounded on the west and east. The eastern surface trace dies southward into folding and thus, on the basis of observations of creep around fault bends in southern California, is unlikely to accommodate creep. During 1990 two trenches were excavated across the eastern trace, revealing evidence for five Hayward fault ruptures in the past 1800 years (Figures 2 and 3). Evidence for two additional events within this time is somewhat equivocal and requires corroboration. Significant gaps were also identified in the sedimentary record, thus some late Holocene ruptures are almost certainly not recorded at this site.

DATA

Evidence for up to seven past Hayward fault ruptures has been identified as follows. Additional discussion of the involvement of specific strata with faulting can be found in the figure captions. In trench M1 **Event F** is expressed by a sand eruption that passed through and mantles strata dated $\leq 1780 \pm 180$ calendar years before present (CYBP) [A dendrochronologic calibration was applied using the time series of Stuiver and Pearson (1986). The standard deviation includes an interlaboratory error multiplier = 1.60.] Event F appears to be corroborated in trench M2 by the similar stratigraphic position of independently dated faulting in the interval 2120 ± 210 CYBP $\geq$ (Event F age) $\geq$ 1230 ± 115 CYBP (Figure 2). If these are indeed the same events, the combined event age is $1780 \pm 180 \geq$ (Event F age) $\geq 1230 \pm 115$ CYBP. In trench M1 **Event I-I'** is indicated by upward truncation of offset along two fault branches. In trench M2 Event I-I' is again indicated by ephemeral upward truncation of offset along two fault planes. In both trenches the I' offset cuts farther upsection than the I offset (Figure 3). Corroboration of this observa-

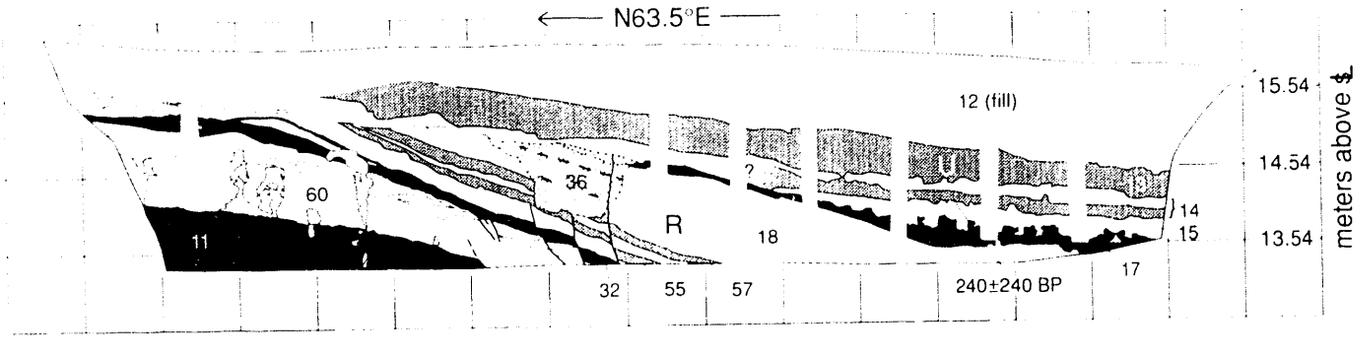

Figure 2. Trench M2 overview, south wall. Shaded layers are composed of silt- to clay-sized particles. The darker tones represent higher clay, and to a lesser extent, organic fractions. The light gray vertical features at the east end of the trench are liquefaction structures that consist primarily of fine- to medium-grained sand. The stippled feature near the middle of the trench is a channel-fill deposit. Event R is indicated by 19° westward dip of unit 17 and subsequent onlap of units 14 and 15. The 9° westward dip of units 13, 14, and 15 suggests that the 19° dip of unit 17 was produced in two events. The tabular geometry of unit 13 suggests deposition on a flat-lying surface and tilt in the latest (presumably 1868) fault rupture. Unit 13 contains historical artifacts. [XBL 913-536]

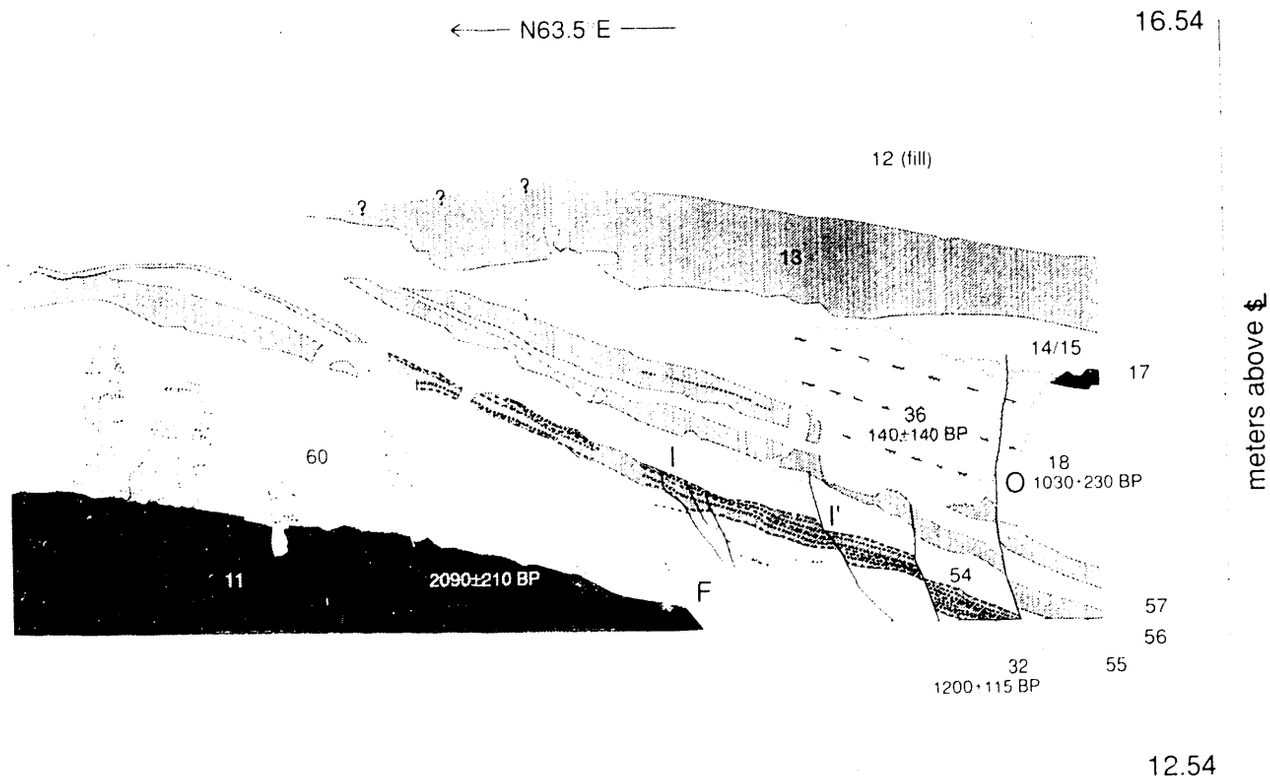

Figure 3. Detailed log of trench M2. The dark gray bed (unit 32) is laminated and has a high organic content consisting primarily of charcoal. This figure illustrates evidence for events F, I, I', and O. Event F is expressed by offset of unit 11 and lack of offset of overlying units. Event I-I' is indicated by upward truncation of offsets. The I' offset cuts farther upsection than the I offset. Corroboration of this observation in both trenches supports interpretation of the I and I' offsets as representative of two independent ruptures. Event O is supported the offset of units 33–58 across the western fault, but is less-well bracketed here than in trench M1. Note the different orientations of the liquefaction structures. The easternmost set is perpendicular relative to the matrix strata, which are not horizontal. The western liquefaction feature is vertical. Note also that the bedding of the channel feature indicates that it has been tilted by an amount similar to that of surrounding tabular strata. [XBL 913-537]

tion in two exposures supports the interpretation that the I-I' offsets are each representative of two fault ruptures. The offset strata defining events I and I' are not separately dated. Their combined interval age is 1230 ± 115 ≥ (Event I-I' age) ≥ 1060 ± 230 CYBP. The relatively tight time bracketing suggests interpreting the I-I' offsets as successive ruptures. **Event O** is recorded by a large stratigraphic separation of units dated at ≤ 1060 ± 230 CYBP and ≥ 270 ± 240 CYBP in trench M1. Because this separation decreases in the younger offset strata along the break, two ruptures (O and O') may be recorded. **Event R** is indicated by a 19° dip of bedding within and around a channel fill dated at 170 ± 140 CYBP in trench M2 (Figures 2 and 3). The 9° westward dip of overlying units suggests the 19° dip of the channel bedding was produced in two events, event R followed by event U (Figure 2). **Event U** is supported by the 9° dip of pond bedding already mentioned and the vertical orientation of liquefaction dikes that break pond strata dipping about 19° (Figure 2). The tabular geometry of the unit experiencing the latest tilting event (probably the 1868 fault rupture) suggests deposition on a nearly flat surface (Figure 2).

DISCUSSION

The two latest ruptures identified (events R and U) are recorded by 19° and 9° tilts of successive pond strata and tilting of a channel-filling deposit by 19° (Figures 3 and 4). Strata across the length of trenches M1 and M2 were folded in a monocline with a vertical amplitude of 2 to 2.5 m during this period. The minimum calendar age of the youngest unit deposited prior to events R and U, the channel fill, is approximately AD 1680. If event U is the 1868 event, this indicates the *maximum* renewal time is on the order of 190 years. The record summarized in Figure 4 continues to require corroboration and development; it represents the only known data on the timing of Hayward fault rupture prior to the ca. 150-year period of local historical record. The record of faulting recovered thus far can be improved by exposing the fault where it has a different relationship to the 170 ± 140-year-old cross-cutting channel. This channel is beneficial in that it records fault slip after ca. 310 CYBP but detrimental in that it has cut away information on earlier displacement. In 1991 we plan to trench 120 ft NW of trench M1 in order to step past a swale intersecting the Tule graben that may correspond with the upstream extension of the buried channel. Additional constraint of the *average* recurrence time of these and earlier fault ruptures is expected from backhoe exposures and radiocarbon analyses planned for spring of 1991.

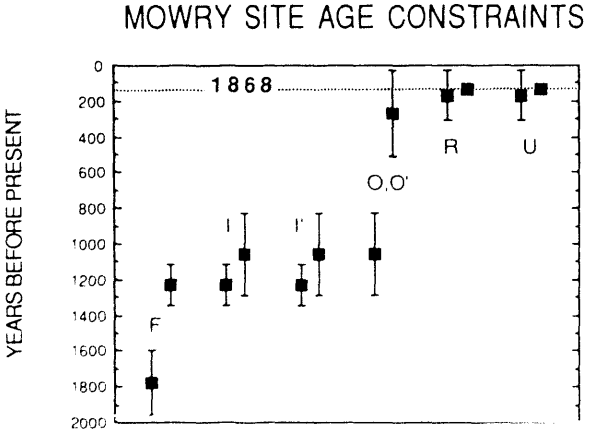

Figure 4. Calendar ages of faulting events relative to AD 1990. Large letters indicate postulated Hayward fault ruptures. [XBL 913-538]

SUMMARY

Additional trench exposures are needed to confirm several ruptures, and additional, more precise radiocarbon analyses are required to improve the resolution of rupture ages. The evidence recovered to date suggests a 190-year *maximum* recurrence interval.

ACKNOWLEDGMENTS

Research Technician P. Holland and Research Assistants M. Wopat and F. Yeates contributed substantially in the field and laboratory to the progress of this investigation. AMS age dating for this project was performed at the Center for Atomic Mass Spectrometry at Lawrence Livermore National Laboratory. This project is supported by the Lawrence Berkeley Laboratory Exploratory Research and Development Fund.

REFERENCES

Stuiver, M., and Pearson, G.W., 1986. High precision calibration of the radiocarbon time scale, AD 1950–500 BC. Radiocarbon, v. 28, p. 805–838.

Williams, P.L., Holland, P., and Yeates, M.F., 1990. Preliminary evidence of Hayward fault paleoseismicity (abstract). EOS Trans. AGU, v. 71, p. 1560.

Williams, P.L., 1991. Evidence of late Holocene ruptures, southern Hayward fault, California. GSA Abstracts with Programs, Spring 1991 SSA/GSA-Cordilleran meeting (abstract).

Working Group: Dietrich, J.H., Allen, C.R., Cluff, L.S., Cornell, C.A., Ellsworth, W.L., Johnson, L.R., Lindh, A.G., Nishenko, S.P., Scholz, C.H., Schwartz, D.P., Thatcher, W., and Williams, P.L., 1990. Probabilities of large earthquakes in the San Francisco Bay Region, California. USGS Circ. v. 1053, p. 51.

APPENDIXES

APPENDIX A: ABSTRACTS OF JOURNAL ARTICLES

Bjornsson, G., and Bodvarsson, G.S., 1990. A survey of geothermal reservoir properties. Geothermics, v. 19, no. 1, p. 17–27 (LBL-26892).

This paper presents results of a literature survey on thermal, hydrological and chemical characteristics of geothermal reservoirs. The data are presented in a table summarizing important fluid and rock parameters. The primary parameters of interest are the permeability, permeability-thickness, porosity, reservoir temperature and concentration of dissolved solids and non-condensible gases. Some preliminary correlations between these parameters are given

Bodvarsson, G.S., Bjornsson, S., Gunnarsson, A., Gunnlaugsson, E., Sigurdsson, O., Stefansson, V., and Steingrimsson, B., 1990. The Nesjavellir geothermal field, Iceland. Part 1. Field characteristics and development of a three-dimensional numerical model. Geotherm. Sci. & Technol., v. 2, no. 3, p. 189–228 (LBL-28760).

A three-dimensional model of the Nesjavellir geothermal field is described in two technical papers. This first paper summarizes the current knowledge of the field, emphasizing the complex thermodynamic conditions, the well characteristics and flow histories. The development of the numerical model is discussed, in terms of the natural state conditions of the field and the exploitation history. The model results indicate that the permeability of the subsurface rocks varies between 1 and 50 md and the porosity between 1 and 10 percent. The recharge rate is estimated to be 65 kg/s, with a fluid enthalpy of about 1850 kJ/kg. An extensive vapor zone is believed to exist underneath the nearby Hengill volcano. The thermal evolution time for the system is estimated to exceed 10,000 years.

Bodvarsson, G.S., Pruess, K., Haukwa, C., and Ojiambo, S.B., 1990. Evaluation of reservoir model predictions for the Olkaria East geothermal field, Kenya. Geothermics, v. 19, no. 5, p. 399–414 (LBL-26771).

In 1984 a detailed three-dimensional well-by-well model was developed for the Olkaria geothermal field in Kenya. The model was calibrated against the production history of the field over the period 1977–1983, using porosity and permeability as adjustable parameters. During this period two 15-MW_c Units were put on-line at Olkaria; the third 15 MW_c Unit commenced operation in March, 1985. The numerical model was used to predict the performance of the Olkaria wells, and these predictions have been compared with the observed well behavior for the period 1984–1987. In general, the model predictions show satisfactory agreement with the observed well behavior, especially for those wells that had production histories exceeding two years. The predicted steam rates for most of the wells were accurate to within 1 kg/s for the period considered, and the steam rate decline was well-predicted by the model. Some differences between the observed and predicted total flow rates and enthalpies of individual wells were seen, especially in those wells with large enthalpy variations or unorthodox increases in total flow rate. The model also predicted that three make-up wells would be needed by the end of 1987, which is consistent with the observed decline in total steam rates. New performance predictions have been made using an updated model, including the effects of wastewater reinjection.

Borg, S.G., DePaolo, D.J., and Smith, B.M., 1990. Isotopic structure and tectonics of the central Transantarctic Mountains. J. Geophys. Res., v. 95, no. B5, p. 6647–6667 (LBL-30803).

Regional patterns of Nd, Sr, and O isotopic ratios of ~500 Ma granitic rocks are used to identify the ages and areal extents of three crustal provinces in the central Transantarctic Mountains. One of the provinces is the edge of the East Antarctic Craton, which isotopic analyses show is composed of Archean rocks thrust over Proterozoic rocks. The other two provinces compose the Beardmore microcontinent, which we deduce was allochthonous to East Antarctica and was emplaced in late Precambrian or early Paleozoic time. Evidence for a former ocean basin between the Beardmore microcontinent and East Antarctica is provided by basalt and gabbro of mid-ocean ridge character, dated by Sm-Nd at ~760 Ma, associated with marine sediments now located at the suture. The granitic rocks formed over a westward-dipping subduction zone that was active at ~500 Ma. The East Antarctic Craton is exposed in the Miller Range, which is a tectonic composite of reworked Archean and early Proterozoic material containing ~500 Ma peraluminous granites with model ages (T_{DM}) of 2.0 Ga, high $\delta^{18}O$ (+11 to +12‰) and high initial $^{87}Sr/^{86}Sr$ (0.7324 to 0.7417). East of the Marsh Glacier the granitic rocks are metaluminous to weakly peraluminous with model ages of 1.3 to 1.8 Ga, high $\delta^{18}O$ (+9 to +13‰) and lower $^{87}Sr/^{86}Sr$ (0.7068 to 0.7191). East of the Shackleton Glacier, gabbro, tonalite, diorite, and granodiorite have low $\delta^{18}O$ (+6 to +7‰), low initial $^{87}Sr/^{86}Sr$ (0.7045 to 0.7059) and high ε_{Nd} (+0.4 to +1.7). These isotopic provinces correspond to differences in age and composition of the middle and lower crust at the time of formation of the granitic magmas. The boundaries of the isotopic provinces also correspond to discontinuities in provenance, lithology, structural style, and grade of metamorphism of prebatholithic metasedimentary rocks. The isotopic data indicate that the granitic magmas were formed mostly by crustal anatexis in the areas west of the Shackleton Glacier. This is typical of early Paleozoic granitic batholiths elsewhere in the world and has led to speculation that subduction was not involved in granitic magmatism at that time of earth history. However, the granitic rocks located west of the Shackleton Glacier, by virtue of their mantle-like isotopic compositions and their association with metavolcanic rocks, appear to be subduction-related. The tectonic history deduced for the Gondwana margin, as represented in the central Transantarctic Mountains, began with deposition of sediments on an Atlantic-type rifted margin at ~760 Ma. The Beardmore microcontinent was most likely accreted in association with folding of the clastic sedimentary rocks before middle Early Cambrian time (550 Ma). Carbonate sedimentation and volcanism along the eastern margin of the Beardmore microcontinent commenced in Cambrian time. Folding and metamorphism of all older units occurred in late Cambrian time followed by emplacement of granitic rocks at ~500 Ma.

Capo, R.C., and DePaolo, D.J., 1990. Seawater strontium isotopic variations from 2.5 million years ago to the present. Science, v. 249, p. 51–55 (LBL-29187).

Measurements of marine carbonate samples indicate that during the past 2.5 million years the $^{87}Sr/^{86}Sr$ ratio of seawater has increased by 14×10^{-5}. The high average rate of increase of $^{87}Sr/^{86}Sr$ indicates that continental weathering rates were exceptionally high. Nonuniformity in the rate of increase suggests that weathering rates fluctuated by as much as ±30 percent of present-day values. Some of the observed shifts in weathering rates are contemporaneous with climatic changes inferred from records of oxygen isotopes and carbonate preservation in deep sea sediments.

Cox, B.L., and Pruess, K., 1990. Numerical experiments on convective heat transfer in water-saturated porous media at near-critical conditions. Transp. Porous Media, v. 5, p. 299–323 (LBL-26060).

Fluid and heat flow at temperatures approaching or exceeding that at the critical point (374°C for pure water, higher for saline fluids) may be encountered in deep zones of geothermal systems and above cooling intrusives. In the vicinity of the critical point the density and internal energy of fluids show very strong variations for small temperature and pressure changes. This suggests that convective heat transfer from thermal buoyancy flow would be strongly enhanced at near-critical conditions. This has been confirmed in laboratory experiments. We have developed special numerical techniques for modeling porous flow at near-critical conditions, which can handle the extreme nonlinearities in water properties near the critical point. Our numerical simulations show strong enhancements of convective heat transfer at near critical conditions; however, the heat transfer rates obtained in the simulations are considerably smaller than data reported from laboratory experiments by Dunn and Hardee. We discuss possible reasons for this discrepancy and develop suggestions for additional laboratory experiments.

Daley, T.M., and McEvilly, T.V., 1990. Shear-wave anisotropy in the Parkfield Varian well VSP. Bull. Seismol. Soc. Am., v. 80, no. 4, p. 857–869 (LBL-28398).

A vertical seismic profile (VSP) survey was run to 1334 m depth in the instrumented Varian well, 1.4 km from the San Andreas fault trace at Parkfield, California, to test the sensor string shortly after its permanent installation. The cable subsequently failed near the 1000 m level, so the test survey represents the deepest data acquired in the study. A shear-wave vibrator source was used at three offsets and two orthogonal orientations, and the data have been processed for *P*- and *S*-wave velocities and for *S*-wave velocity anisotropy. Velocities are well-determined (3.3 and 1.9 km/sec, respectively, at the deeper levels), and the *S*-waves are seen clearly to be split by anisotropy below about 400 m. Some 8 per cent velocity difference is apparent between polarizations parallel to and perpendicular to the San Andreas fault (faster and slower, respectively), and the difference seems to decrease with distance from the fault, suggesting that the cause may be the fabric of the fault zone. Repeated surveys at the 1000 m depth are being conducted as part of the Parkfield monitoring program.

Doughty, C., and Pruess, K., 1990. A similarity solution for two-phase fluid and heat flow near high-level nuclear waste packages emplaced in porous media. Int. J. Heat & Mass Transfer, v. 33, no. 6, p. 1205–1222 (LBL-26057).

The emplacement of a heat source, such as a high-level nuclear waste package, into a geologic medium causes strongly coupled thermal and hydrologic behavior. Under certain conditions, a heat pipe may develop, with significant impact on conditions at the heat source. In an infinite, homogeneous, permeable medium with a constant-strength linear heat source, the partial differential equations governing fluid and heat flows in a radial geometry can be converted to ordinary differential equations by using a similarity variable, $\eta = r/\sqrt{t}$. These equations are numerically integrated using an iterative 'shooting' method to provide a description of temperature, pressure, saturation, heat flow, gas flow, and liquid flow conditions around a heat source such as a nuclear waste package. The similarity solution is verified by numerical finite-difference simulations. Illustrative solutions are given for a range of hydrologic and thermal parameters, and the likelihood of heat-pipe development for conditions at several proposed repository sites is discussed.

Gajewski, D., and Pšenčík, I., 1990. Vertical seismic profile synthetics by dynamic ray tracing in laterally varying layered anisotropic structures. J. Geophys. Res., v. 95, no. B7, p. 11,301–11,315 (LBL-27739).

Dynamic ray tracing (DRT) is important in evaluating high-frequency seismic wave fields in complicated structures. Two formulations of the DRT equations for inhomogeneous anisotropic media are presented. One of them is represented by the classical DRT system, suggested by Červený 15 years ago. Both systems are specified in Cartesian coordinates. The DRT equations are supplemented with formulae for the transformation of DRT across a smoothly curved interface between two inhomogeneous anisotropic media. Červený's formulation of the DRT is applied to the computation of vertical seismic profile (VSP) synthetics. The results of DRT are used for the evaluation of the geometrical spreading and of the coefficients of the paraxial ray approximation for travel times and ray amplitudes. In addition, the DRT is also used in the interval ray tracing procedure, a procedure searching for rays starting from the source and terminating in a specified interval on a profile. Results of numerical modeling of VSP measurements in a three-dimensional laterally varying structure consisting of isotropic and anisotropic layers separated by curved interfaces are presented. Ray diagrams of selected elementary waves, time-distance curves, and multisource three-component VSP synthetics generated for two different source locations calculated for the anisotropic model are compared with the results determined for a reference isotropic model. The latter is obtained by averaging phase velocities of the anisotropic model. This comparison clearly shows the effects of anisotropy and the lateral variation of the model on seismic wave fields. The reliability of the ray synthetics is briefly discussed.

Gauglitz, P.A., and Radke, C.J., 1990. The dynamics of liquid film breakup in constricted cylindrical capillaries. J. Colloid & Interface Sci., v. 134, no. 1, p. 14–40 (LBL-29145).

To understand form generation in porous media, this work considers the dynamics of a wetting viscous film forming an unstable collar (or collars) in a constricted cylindrical capillary. A nonlinear evolution equation is derived and solved numerically to determine the evolution in time of a liquid film deposited by a bubble after it has moved through a constricted capillary. Results show that time to break up depends on the initial film profile, the film thickness, the pore geometry, and also on the fluid viscosity, interfacial tension, and unconstricted capillary radius which combine to form a characteristic scaling time. Excellent agreement is found between breakup times predicted from the hydrodynamic analysis and experimental breakup time data over a wide range of initial film thicknesses and fluid properties. New data for the dynamic collar shape also agree well with the theoretical results.

Hestir, K., and Long, J., 1990. Analytical expressions for the permeability of random two-dimensional Poisson fracture networks based on regular lattice percolation and equivalent media theories. J. Geophys. Res., v. 95, no. B13, p. 21,565–21,581 (LBL-27625).

The permeability of random two-dimensional Poisson fracture networks can be studied using a model based on percolation theory and equivalent media theory. Such theories are usually applied on regular lattices where the lattice elements are present with probability p. In order to apply these theories to random systems, we (1) define the equivalent to the case where $p = 1$, (2) define p in terms of the statistical parameters of the random network, and (3) define the equivalent of the coordination number z. An upper bound for permeability equivalent to the case of $p = 1$ is found by calculating the permeability of the fracture network with the same linear fracture frequency and infinitely long fractures. The

permeability of networks with the same lineal fracture frequency and finite fractures can be normalized by this maximum. An equivalent for p is found as a function of the connectivity ζ, which is defined as the average number of intersections per fracture. This number can be calculated from the fracture density and distributions of fracture length and orientation. Then the equivalent p is defined by equating the average run length for a random network as a function of ζ to the average run length for a lattice as a function of p. The average run length in a random system is the average number of segments that a fracture is divided into by intersections with other fractures. In a lattice, it is the average number of bonds contiguous to a given bond. Also, an average coordination number can be calculated for the random systems as a function of ζ. Given these definitions of p and z, expressions for permeability are found based on percolation theory and equivalent media theory on regular lattices. When the expression for p is used to calculate the correlation length from percolation theory, an empirical formula for the size of the REV can be developed. To apply the models to random length systems, the expression for ζ must be modified to remove short fractures which do not contribute to flow. This leads to a quantitative prediction of how permeability decreases as one removes shorter fractures from a network. Numerical studies provide strong support for these models. These results also apply to the analogous electrical conduction problem.

Hovey, J.K., Pitzer, K.S., Tanger, J.C., IV, Bischoff, J.L., and Rosenbauer, R.J., 1990. Vapor–liquid phase equilibria of potassium chloride–water mixtures: Equation-of-state representation for KCl–H_2O and NaCl–H_2O. J. Phys. Chem., v. 94, p. 1175–1179 (LBL-27558).

Measurements of isothermal vapor–liquid compositions for KCl–H_2O as a function of pressure are reported. An equation of state, which was originally proposed by Pitzer and was improved and used by Tanger and Pitzer to fit the vapor–liquid coexistence surface for NaCl–H_2O, has been used for representation of the KCl–H_2O system from 300 to 410°C. Improved parameters are also reported for NaCl–H_2O from 300 to 500°C.

Hwang, Y., Chambré, P.L., Pigford, T.H., and Lee, W.W.-L., 1990. Brine migration in a salt repository. Nucl. Technol., v. 90, p. 205–214 (LBL-26748).

Salt is a candidate rock to host nuclear waste repositories in many countries. Brine exists in natural salt as inclusions in salt crystals and in grain boundaries. Brine inclusions in crystals move to nearby grain boundaries when subjected to a temperature gradient, because of the temperature-dependent solubility of salt. Brine in grain boundaries moves under the influence of a pressure gradient. Brine consolidates around high-level waste packages in a few years after emplacement. Heated salt near the waste package expands against the waste package and surrounding salt, creating high compressive stresses near the waste package and resulting in pressure above the lithostatic pressure. Brine pressure increases because grain-boundary brine expands more than does the salt. This increased pressure gradient causes brine to flow outward into the cooler salt. Outward flow of brine relieves the pressure gradient on the fluid, which finally relaxes to near-lithostatic pressure. Outward brine movement can become a mechanism for radionuclide transport. To determine the extent to which advection by brine in grain boundaries is an important transport mechanism for released radionuclides, it is necessary to estimate the time-dependent migration of brine.

The possible role of brine migration in radionuclide transport in a nuclear waste repository is studied. Mathematical derivation of the analysis is given, along with numerical illustrations using parameter values typical of a nuclear waste repository. For heat-emitting wastes and the parameters studied here, brine migration in salt is minuscule, of the order of micrometres per year, localized within a few metres from the waste package, and highly transient, fading away within a few years of waste emplacement.

Javandel, I., Tsang, C.F., and Witherspoon, P.A., 1990. Reply to Voigt and Wagner. Water Resour. Res., v. 26, no. 8, p. 1859–1860 (LBL-29168).

Karasaki, K., 1990. A systematized drillstem test. Water Resour. Res., v. 26, no. 12, p. 2913–2919 (LBL-29504).

A solution of the well response to a drillstem test (DST) is presented. The advantages of a DST over conventional slug tests are discussed. A systematized procedure of a DST is proposed, where a slug test is terminated in the midpoint of the flow period, and the subsequent shut-in data are recorded and analyzed. This method requires a downhole shut-in device and a pressure transducer, which is no more than the conventional deep-well slug testing. As opposed to slug tests, which are ineffective when a skin is present, more accurate estimate of formation permeability can be made using a DST. Premature termination also shortens the test duration considerably. Because in most cases no more information is gained by completing a slug test to the end, the author recommends that conventional slug tests be replaced by the premature termination technique.

Kumar, S., and Bodvarsson, G.S., 1990. Fractal study and simulation of fracture roughness. Geophys. Res. Lett., v. 17, no. 6, p. 701–704 (LBL-29171).

This study examines the roughness profiles of the surfaces of fractures and faults by using concepts from fractal geometry. Relationships between fractal characteristics of profiles and isotropic surfaces are analytically developed and a deterministic representation of the roughness is examined.

Light, W.B., Chambré, P.L., Pigford, T.H., and Lee, W.W.-L., 1990. Contaminant dissolution and diffusional transport with a stationary precipitation front. Water Resour. Res., v. 26, no. 7, p. 1681–1685 (LBL-26674).

Waste material in a geologic repository will eventually dissolve and migrate away, degrade by chemical reaction or radioactive decay, or become part of the basic rock material. For many waste components these processes will be limited by the dissolution rate of the waste matrix. The precipitation may be due to local geochemical changes such as changes in temperature, pH, or redox potential, caused by nearby geologic features or the waste itself. In this paper we analyze the effect of contaminant precipitation caused by a drop in the solubility at some specified location away from the waste. Transport is by diffusion only; advection is neglected. Analytical solutions are presented for the contaminant concentration in ground water and the mass-transfer rate as functions of space and time for regions on both sides of the precipitation front. Numerical illustrations are made applicable to nuclear waste in a geologic repository.

Long, R.H.B., Benson, S.M., Tokunaga, T.K., and Yee, A., 1990. Selenium immobilization in a pond sediment at Kesterson Reservoir. J. Environ. Qual., v. 19, no. 2, p. 302–311 (LBL-27807).

Kesterson Reservoir, Merced County, CA, a disposal facility for agricultural drain water, became the object of intense scientific investigation following discovery in 1983 that Se-laden agricultural drain water was having serious effects on the reproductive success of waterfowl. A remedial measure involving permanent flooding with low-Se water, aimed at taking advantage of low Se solubility under reducing conditions, was proposed as a means of limiting Se movement into groundwater and biota. A field experiment was undertaken to evaluate the feasibility of the proposed remedial measure, its impact on the quality of shallow

groundwater and for quantifying Se immobilization and transport through a newly flooded pond bottom soil. Extensive soil water and groundwater sampling demonstrated that although initial soluble Se concentrations in the top 1.22 m (4 ft) of soil typically ranged from approximately 1000 to 3000 $\mu g\ L^{-1}$, Se concentrations declined dramatically after flooding and elevated concentrations below 1.22 m were observed at only one of five sampling sites. Analysis of the temporal and spatial changes in the distribution of dissolved Se and Cl indicated that 66 to 108% of the initial soluble Se present in the cop 1.22 m was immobilized shortly after flooding. These estimates were consistent with the low Se concentrations observed in shallow monitoring wells. The extent to which Se immobilization occurred correlated inversely with average pore water velocity. Data presented suggest that reducing conditions in the newly flooded soils lead to the microbially mediated transformation of selenate to less soluble or mobile forms.

Manlowe, D.J., and Radke, C.J., 1990. A pore-level investigation of foam/oil interactions in porous media. SPE Res. Eng., v. 5, no. 4, p. 495–502 (LBL-30040).

Direct visual studies of foam flow in etched-glass micromodels containing residual oil demonstrate that foam decays as a result of breakage of pseudoemulsion films. Foam films collapse whenever nearby thin aqueous films separating gas bubbles and oil rupture. Consequently, surfactant formulation for foam insensitivity to oil in porous media should be based on stabilizing pseudoemulsion films.

Martel, S.J., 1990. Formation of compound strike-slip fault zones, Mount Abbot quadrangle, California. J. Struct. Geol., v. 12, no. 7, p. 869–882 (LBL-28071).

Numerous strike-slip fault zones in granitic rocks of the Mount Abbot quadrangle, California, developed from steeply-dipping, subparallel joints. These joints generally were less than 50 m long and were spaced several centimeters to several meters apart. Some joints subsequently slipped and became small faults. *Simple fault zones* formed as oblique dilatant fractures (splay fractures) linked non-coplanar faults side-to-side and end-to-end. These simple fault zones are as much as 1 km long and accommodated displacements as great as 10 m. *Compound fault zones* formed as splay fractures linked small faults and simple fault zones. They are as much as several kilometers long and accommodated displacements as great as 100 m. These zones are distinctly different from 'Riedel shear zones' and the mechanics of their formation are unlikely to be described well by Mohr-Coulomb mechanisms. Simple and compound fault zones are composed of non-coplanar segments that join at steps or bends; splay fracture length determines step widths. The longest splay fractures occur along the longest fault zones, allowing step widths to increase as the length and displacement across the zones increase. These findings are consistent with the structure of some active seismogenic faults, and they provide a mechanically consistent, field-based conceptual model for fault zones that grow in basement rocks from a pre-existing set of joints.

Moreno, L., Tsang, Y.W., and Tsang, C.F., 1990. Some anomalous features of flow and solute transport arising from fracture aperture variability. Water Resour. Res., v. 26, no. 10, p. 2377–2391 (LBL-29167).

Model fractures with variable apertures are generated by a statistical method, and water flow and tracer transport in these fractures are calculated. Tracer injection and collection are simulated for parallel and convergent flow fields. The impact of the use of different injection flow rates and the different locations of injection and collection points are studied. The results show that the transport time, dispersion, and the so-called mass balance fracture aperture are very sensitive to the location of the injection point and the injection flow rate. These anomalous effects appear to be consistent with observations in several recent field experiments. The implications of the calculated results on the analysis of tracer tests are discussed. It is concluded that because of the stochastic nature of variable fracture apertures (and their permeabilities) a point tracer test in a fracture is not sufficient to characterize the properties of the fracture. Dispersivities and apertures calculated from different tracer tests in the same fracture may vary by orders of magnitude depending on the flow rate and the location of the injection. However, a line injection of tracer, averaged over a series of adjacent points, may avoid some of these problems.

Nitsche, H., Standifer, E.M., and Silva, R.J., 1990. Neptunium(V) complexation with carbonate. Lanthanide & Actinide Res., v. 3, no. 3, p. 203–212 (LBL-27349).

The formation constant for the reaction $NpO_2^+ + CO_3^{2-} = NpO_2CO_3^-$ was determined in 0.1 M $NaClO_4$ solution by absorption spectrophotometry. Addition of carbonate to neptunium(V) perchlorate solution led to an absorption band at 991 nm which increased with increasing carbonate concentration while the band for NpO_2^+ at 980 nm decreased. The absorption bands were fitted with a non-linear least-squares method. The resulting log β_{11} (0.1 M) = 4.34 ± 0.11 was extrapolated to infinite dilution. We used the specific-ion-interaction theory (S.I.T.) with literature data, because no activity coefficients for NpO_2^+ and $NpO_2CO_3^-$ or suitable model compounds exist at 0.1 M ionic strength. A non-weighted linear least-squares regression resulted in log β_{11}^0 = 4.69 ± 0.13.

Persoff, P., Pruess, K., Benson, S.M., Wu, Y.S., Radke, C.J., Witherspoon, P.A., and Shikari, Y.A., 1990. Aqueous foams for control of gas migration and water coning in aquifer gas storage. Energy Sources, v. 12, p. 479–497 (LBL-28862).

Two causes of poor recoverability are migration of stored gas far from the injection well and upward coning of water into withdrawal wells. The authors conducted laboratory and numerical simulation investigation of the use of aqueous foams to block the flow of gas or liquid to ameliorate these problems. Experiments in sandstone cores showed that foam reduces the permeability to gas and liquid by approximately three orders of magnitude. A numerical simulation study showed that water coning could be significantly delayed by placing a horizontal foam lens just above the gas-water interface. Also discussed are the conditions for forming foam in situ, the feasibility of emplacing a foam bank, and the durability of permeability reduction. Laboratory experiments and numerical simulation indicate potential for significantly improving the efficiency of aquifer gas storage with aqueous foams. A field trial of foam to prevent water coning is recommended.

Pruess, K., 1990. Modeling of geothermal reservoirs: Fundamental processes, computer simulation and field applications. Geothermics, v. 19, no. 1, p. 3–15 (LBL-28414).

This article attempts to critically evaluate the present state of the art of geothermal reservoir simulation. Methodological aspects of geothermal reservoir modeling are briefly reviewed, with special emphasis on flow in fractured media. We then examine some applications of numerical simulation to studies of reservoir dynamics, well test design and analysis, and modeling of specific fields. Tangible impacts of reservoir simulation technology on geothermal energy development are pointed out. We conclude with consideration on possible future developments in the mathematical modeling of geothermal fields.

Pruess, K., and Tsang, Y.W., 1990. On two-phase relative permeability and capillary pressure of rough-walled rock fractures. Water Resour. Res., v. 26, no. 9, p. 1915–1926 (LBL-27449).

This paper presents a conceptual and numerical model of multiphase flow in fractures. The void space of real rough-walled rock fractures is conceptualized as a two-dimensional heterogeneous porous medium, characterized by aperture as a function of position in the fracture plane.

Portions of a fracture are occupied by wetting and nonwetting phase, respectively, according to local capillary pressure and global accessibility criteria. Phase occupancy and permeability are derived by assuming a parallel-plate approximation for suitably small subregions in the fracture plane. For lognormal aperture distributions, a simple approximation to fracture capillary pressure is obtained in closed form; it is found to resemble the typical shape of Leverett's *j* function. Approximations to wetting and nonwetting phase relative permeabilities are calculated by numerically simulating single phase flows separately in the wetted and nonwetted pore spaces. Illustrative examples indicate that relative permeabilities depend sensitively on the nature and range of spatial correlation between apertures. It is also observed that interference between fluid phases flowing in a fracture tends to be strong, with the sum of wetting and nonwetting phase relative permeabilities being considerably less than 1 at intermediate saturations.

Pruess, K., Wang, J.S.Y., and Tsang, Y.W., 1990. On thermohydrologic conditions near high-level nuclear wastes emplaced in partially saturated fractured tuff. 1. Simulation studies with explicit consideration of fracture effects. Water Resour. Res., v. 26, no. 6, p. 1235–1248 (LBL-24563).

We have performed modeling studies on the simultaneous transport of heat, liquid water, vapor, and air in partially saturated, fractured porous rock. Formation parameters were chosen as representative of the potential nuclear waste repository site in the Topopah Spring unit of the Yucca Mountain tuffs. The presence of fractures makes the transport problem very complex, both in terms of flow geometry and physics. The numerical simulator used for our flow calculations takes into account most of the physical effects believed to be important in multiphase fluid and heat flow. It has provisions for handling the extreme nonlinearities that arise in phase transitions, component disappearances, and capillary discontinuities at fracture faces. We model a region around an infinite linear string of nuclear waste canisters, taking into account both the discrete fractures and the porous matrix. Thermohydrologic conditions in the vicinity of the waste packages are found to depend strongly on relative permeability and capillary pressure characteristics of the fractures, which are unknown at the present time. If liquid held on the rough walls of drained fractures is assumed to be mobile, strong heat pipe effects are predicted. Under these conditions the host rock will remain in two-phase conditions right up to the emplacement hole, and the formation temperatures will peak near 100°C. If it is assumed that liquid cannot move along drained fractures, the region surrounding the waste packages is predicted to dry up, and formation temperatures will rise beyond 200°C. A substantial fraction of waste heat can be removed if emplacement holes are left open and ventilated, as opposed to backfilled and sealed emplacement conditions. Comparing our model predictions with observations from in situ heater experiments reported by Zimmerman and coworkers, some intriguing similarities are noted. However, for a quantitative evaluation, additional carefully controlled laboratory and field experiments will be needed.

Pruess, K., Wang, J.S.Y., and Tsang, Y.W., 1990. On thermohydrological conditions near high-level nuclear wastes emplaced in partially saturated fractured tuff. 2. Effective continuum approximation. Water Resour. Res., v. 26, no. 6, p. 1249–1261 (LBL-24564).

This paper presents an effective continuum approximation for modeling of fluid and heat flow in fractured porous media. The approximation is based on the thermohydrologic behavior observed in detailed simulations with explicit consideration of fracture effects (see the companion paper, part 1). The crucial concept in the development of an effective continuum approximation is the notion of local thermodynamic equilibrium between rock matrix and fractures. Where applicable it provides a substantial simplification of the description of fluid and heat flow in fractured porous media. We derive formulas for effective continuum characteristic curves (relative permeabilities and capillary pressures) in terms of the properties of fracture and matrix continua, respectively. Numerical simulations demonstrate that under favorable conditions the effective continuum approximation closely matches predictions obtained from an explicit modeling of fracture effects. It is also demonstrated that the approximation breaks down under unfavorable conditions (very tight rock matrix). A simple criterion for the applicability of an effective continuum approximation is derived from consideration of diffusive processes. A quantitative evaluation shows the criterion to be consistent with results of our numerical simulations.

Pyrak-Nolte, L.J., Myer, L.R., and Cook, N.G.W., 1990. Transmission of seismic waves across single natural fractures. J. Geophys. Res., v. 95, no. B6, p. 8617–8638 (LBL-26616).

Fractures and other nonwelded contacts are important mechanical and hydrological features of rock masses. Their effects on seismic wave propagation can be modeled as a boundary condition in the seismic wave equation. Seismic stress is continuous across such a boundary, but seismic particle displacement and seismic particle velocity are not. The complete solutions for seismic wave reflection, conversion, and transmission across a displacement and velocity discontinuity between two half-spaces with different densities and elastic properties are derived for all angles of the incident wave. The ratio between the seismic stress across this boundary and the seismic particle displacement and velocity are described by a specific stiffness and a specific viscosity, respectively. A displacement discontinuity results in frequency-dependent reflection and transmission coefficients and a frequency-dependent group time delay. The velocity discontinuity results in frequency-independent coefficients and zero delay. Results of laboratory experiments on compressional and shear wave transmission across three different natural fractures in a quartz monzonite are described. Measurements were made at different effective stresses under dry and saturated conditions at room temperature. It is shown that the effect of these fractures on the spectral amplitudes for compressional and shear pulses transmitted across these fractures are described well by a displacement discontinuity for compressional pulses under dry and saturated conditions and by a combined displacement and velocity discontinuity for shear wave pulses under dry and saturated conditions. Values of specific stiffness and specific viscosity vary between fractures and increase with increasing effective stress, as does the static specific stiffness of these fractures. Changes in the spectral amplitudes of transmitted pulses are also analyzed in terms of attenuation using the seismic quality factor Q, which is found to be a function of frequency.

Pyrak-Nolte, L.J., Myer, L.R., and Cook, N.G.W., 1990. Anisotropy in seismic velocities and amplitudes from multiple parallel fractures. J. Geophys. Res., v. 95, no. B7, p. 11,345–11,358 (LBL-26851).

Many rock structures include multiple, near-parallel, planar discontinuities such as bedding planes or joints. The effects of these nonwelded interfaces on seismic wave propagation are often analyzed using effective moduli, in terms of which seismic wave propagation is independent of frequency and without loss, unless the moduli include imaginary terms. An alternative approach is to treat these interfaces as a boundary condition in the seismic wave equation, across which seismic stress is continuous, but seismic particle displacements are discontinuous. The ratio of the stress to displacement is called the specific stiffness of the interface and characterizes the elastic properties of a fracture. For a completely elastic system this results in frequency-dependent reflection and transmission coefficients for each interface as well as a frequency-dependent group time delay. Using multiple, parallel displacement discontinuities and ignoring converted and reflected waves, expressions derived for transmitted wave amplitudes and group velocities show that these depend on frequency, angle of incidence, and polarization in the case of shear waves. Measurements on a laminated steel block show that shear pulses propagating parallel to the laminations and polarized parallel and perpendicular to the place of the laminations both travel at the velocity for solid steel, although the spectra of these pulses differ considerably. However, the energy of the pulse polarized perpendicular to the laminations may propagate as an interface wave between each pair of laminations. Predictions of the displacement discontinuity model have features quite distinct from many crustal observations to date. We suggest that we are able to model dense populations of coplanar cracks that cannot be treated by effective moduli methods which require a dilute concentration of cracks.

Reiner, E.S., and Radke, C.J., 1990. Variational approach to the electrostatic free energy in charged colloidal suspensions: General theory for open systems. J. Chem. Soc. Faraday Trans., v. 86, no. 23, p. 3901–3912 (LBL-29169).

A general variational technique for calculating the electrostatic free energy of a system of interacting double layers is presented. A stationarity principle for a large class of electrical potential- and position-dependent ion distribution functions and boundary conditions is derived and shown to be unique. The functional satisfying this principle for an open system is identified with the corresponding grand canonical excess surface free energy Ω. The special case of a functional quadratic in the potential ψ (i.e. the Debye-Hückel approximation for the ion distributions together with generalized linear boundary conditions) is shown to permit reduction of the free energy calculation to the evaluation of surface integrals. Illustrations of the approach are presented in the Debye-Hückel approximation for two interacting planar double layers and in the non-linear Poisson-Boltzmann approximation for an isolated planar interface under both constant surface charge density and constant surface potential conditions.

The variational approach is straightforward to implement for a variety of double-layer geometries and surface charge conditions. Moreover, it directly and unambiguously identifies the appropriate electrostatic free energy. We believe the variational technique to be a powerful and versatile method for calculating interactions between colloidal particles.

Segall, P., McKee, E.H., Martel, S.J., and Turrin, B.D., 1990. Late Cretaceous age of fractures in the Sierra Nevada batholith, California. Geology, v. 18, p. 1248–1251 (LBL-30719).

Regional sets of steeply dipping joints and faults are common throughout the Sierra Nevada batholith, yet relatively little is known about how or when they formed. Within some east-northeast-striking, left-lateral fault zones in the Mount Abbot quadrangle of the central Sierra Nevada, the host granodiorite is hydrothermally altered to a lower greenschist assemblage that contains muscovite. The muscovite yields a mean K-Ar and $^{40}Ar/^{39}Ar$ age of 79 Ma, which provides a minimum age for the faulting. Field relations show that these faults developed from earlier formed, mineralized joints, so these ages also provide a minimum age for the jointing. Published ages of biotite, hornblende, and zircon from the host granodiorite of Lake Edison are 80 Ma (K-Ar), 85 Ma (K-Ar), and 90 Ma (U-Pb), respectively. The geochronology, field relations, and hydrothermal mineral assemblages together suggest that the mineralized joints and faults all formed between 85 and 79 Ma, soon after the host pluton was emplaced.

Staudigel, H., Hart, S.R., Schmincke, H.-U., and Smith, B.M., 1990. Reply to "Global CO_2 degassing and the carbon cycle": A comment by R.A. Berner. Geochim. Cosmochim. Acta, v. 54, p. 2891 (LBL-30805).

Stewart, B.W., and DePaolo, D.J., 1990. Isotopic studies of processes in mafic magma chambers: II. The Skaergaard intrusion, East Iceland. Contrib. Mineral. Petrol., v. 104, p. 125–141 (LBL-30804).

Isotopic ratios of Nd and Sr have been measured in a suite of samples spanning most of the exposed stratigraphy of the Skaergaard intrusion in order to detect and quantify input (such as assimilated wallrock and fresh magma) into the magma chamber during crystallization. Unlike $\delta^{18}O$ and δD, Nd and Sr isotope ratios do not appear to have been significantly affected by circulation of meteoric waters in the upper part of the intrusion. Variations in initial $^{87}Sr/^{86}Sr$ and ε_{Nd} suggest that the Skaergaard magma chamber was affected during its crystallization by a small amount (2%–4%) of assimilation of Precambrian gneiss wallrock (high $^{87}Sr/^{86}Sr$, low ε_{Nd}) and possibly recharge of uncontaminated magma. Decreases in ε_{Nd} and increases in $^{87}Sr/^{86}Sr$ during the early stages (0%–30%) of crystallization give way to approximately unchanging isotopic ratios through crystallization of the latest-deposited cumulates. Modelling of assimilation-fractional crystallization-recharge processes using these data as constraints shows that the assimilation rate must have been decreasing throughout crystallization. In addition, the isotope data allow replenishment by an amount of uncontaminated magma equal to 20%–30% of the total intrusion mass, occurring either continuously or in pulses over the first 75% of crystallization. Comparison of the recharge models with published $Mg/(Mg + Fe^{2+})$ data from Skaergaard cumulates shows that the modelled replenishment rates are not inconsistent with available major element data, although significant recharge during the final ~25% of crystallization can be ruled out. The isotope data show that the Skaergaard magma could have incorporated only a small amount of the gneiss that it displaced from the floor of the chamber; assimilation appears to have taken place primarily across a partially molten zone that formed at the roof from the wallrock that was dislodged during emplacement. In the latest stages of crystallization (>75% crystallized), the Skaergaard magma may have become stratified into two separately-convecting layers, effectively insulating Layered Series cumulates from further contamination.

Tsang, C.F., Hufschmied, P., and Hale, F.V., 1990. Determination of fracture inflow parameters with a borehole fluid conductivity logging method. Water Resour. Res., v. 26, no. 4, p. 561–578 (LBL-24752, NDC-1).

There is much current interest in determining the flow characteristics of fractures intersecting a well bore in order to provide data for use in estimating the hydrologic behavior of fractured rocks. Inflow rates from these fractures into the well bore are usually very low. Moreover, in most cases only a few percent of the fractures identified by core inspection and geophysical logging actually conduct water, the rest being closed, clogged, or isolated from the water flow system. A new procedure is proposed and a corresponding method of analysis developed to locate water-conducting fractures and obtain fracture inflow rates by means of a time sequence of electric conductivity logs of the borehole fluid. The physical basis of the analysis method is discussed, and the procedure is applied to an existing set of data, which shows initiation and growth of nine conductivity peaks in a 900-m section of a 1690-m borehole, corresponding to nine water-conducting fractures intersecting the borehole. By applying our analysis to these nine peaks, the flow rates and the salinity of the water from these fractures are determined. These results are used with other information to obtain transmissivities of the nine fractures, which are validated against independent hydraulic measurements by packer tests. The salinities measured in fluids from the fractures are also validated against salinity values obtained by chemical sampling of fluid from different depths of the borehole. The applicability of this technique is discussed in the context of a borehole-testing program.

Vasco, D.W., 1990. Moment tensor invariants: Searching for non-double-couple earthquakes. Bull. Seismol. Soc. Am., v. 80, no. 2, p. 354–371 (LBL-28510).

A method for assessing the presence of a non-double-couple component in seismic sources is presented. The equation for the principal values of the moment tensor is a cubic equation with coefficients which are polynomial combinations of the tensor components. These coefficients are invariants of the tensor that relate to its symmetry and do not depend on the coordinate system used to describe the source. Each coefficient has a physical interpretation: The constant coefficient is determined by how well one or two double-couples describe the source, and the quadratic coefficient is the volume change associated with the source. If volume change is assumed to be absent, the constant term represents a measure of the double-couple nature of the source. A seismic waveform inversion method is presented which exactly explores the range of values of these properties. The method of extremal models is used to determine minimum and maximum values of the invariants subject to the constraint that the data must be satisfied within prescribed errors. For the invariant associated with the source volume change, this constraint results in a linear programming problem and a global solution may be found. For the other invariants a nonlinear programming problem results which may

be solved by a reduced gradient algorithm. Two events were examined: A deep earthquake from the Bonin Islands and the Harzer nuclear explosion. A double-couple mechanism is essentially compatible with the Bonin Islands waveforms. Models with a positive volume change were required to fit the Harzer data. Some variation in the mechanism is possible due to gaps in the station distribution and possibly due to significant scattering from lateral heterogeneities. However, in spite of a range in the isotropic component, the event could not be fit with a double-couple mechanism.

Vasco, D.W., 1990. Seismic source representation in orthogonal functions. Geophys. J. Int., v. 102, p. 531–535 (LBL-28664).

The moment tensor density is expanded in a series of orthogonal basis functions. The expansion coefficients represent integrated averages of the moment tensor density, a symmetric tensor of rank 2. A wide range of sources may be represented in this manner, from variable slip over a curved fault surface to the conventional point source expansion in moments. With this general formulation it is simple to change basis functions and to derive expressions for waveform inversion. Higher order terms in the expansion may be determined by a stable numerical integration over the basis elements.

Weres, O., Bowman, H.R., Goldstein, A., Smith, E.C., Tsao, L., and Harnden, W., 1990. The effect of nitrate and organic matter upon mobility of selenium in groundwater and in a water treatment process. Water, Air, & Soil Pollution, v. 49, p. 251–272 (LBL-23499).

Kesterson Reservoir in Merced County, California was formerly used as a storage and evaporation facility for Se-contaminated agricultural drain water. Very little Se entered the shallow aquifer below the ponds with percolating pond water. With few localized exceptions, most of the Se was removed from the water and retained in the first decimeter of soil, which was rich in decaying organic matter. Where it was present in groundwater, Se was nearly always associated with nitrate. Nitrate induces mildly oxidizing conditions (Eh ≈ 350 mV) and inhibits microbial fixation of Se. In the absence of nitrate, relatively reducing conditions prevail in the groundwater (Eh ≈ −50 mV), and Se is quickly removed. Selenate follows oxygen and nitrate in the order that soil microbes utilize electron acceptors. The process of Se removal from water by soil was reproduced in the laboratory, and the effect of nitrate was confirmed. This natural process might be applied to water treatment for Se removal. The deep water ecosystem at Kesterson Reservoir was highly productive. Vegetation growing in water treatment ponds should supply enough organic matter to maintain anaerobic conditions in the sediment. This process, including algae culture, was operated in an outdoor 79 cm column for 100 days. At percolation rates of 15 and 30 m yr^{-1} Se removal averaged 94%, with an additional 2% converted to volatile compounds.

Weres, O., Jaouni, A.R., and Tsao, L., 1989. The distribution, speciation and geochemical cycling of selenium in a sedimentary environment at Kesterson Reservoir, California, U.S.A. Appl. Geochem., v. 4, p. 543–563 (LBL-26452).

The well-defined and intensively studied episode of Se contamination at Kesterson Reservoir (Merced County, California, U.S.A.) provided a unique opportunity to describe the distribution, speciation and geochemical transformations of Se in a variety of geochemical and ecological settings, ranging from permanent ponds to semi-arid grasslands and salt flats. Kesterson Reservoir comprises 500 ha of land contaminated with Se from agricultural drain water. In most places, Se was concentrated in surficial organic detritus and the surficial decimeter of mineral soil. At dry sites, selenate ion predominated below 20 cm depth. Elemental selenium (Se^0) also was prominent. The amount of zero-valent Se increased slowly with time. Although selenate is thermodynamically stable in the vadose zone in the presence of oxygen, Se^0 is an additional, metastable product of the mineralization of organic selenium. Thiols and inorganic sulfides dramatically increase the solubility of Se^0. Decreasing pH inhibits the reaction, explaining the observed decrease in solubility and biological availability of Se in soil and aquatic systems at low pH. Adding thiols or methionine to soil increases the emission of volatile Se compounds several-fold, suggesting that thiols play a major role in microbial cycling of Se in soil.

White, A.F., Peterson, M.L., Wollenberg, H., and Flexser, S., 1990. Sources and fractionation processes influencing the isotopic distribution of H, O and C in the Long Valley hydrothermal system, California, U.S.A. Applied Geochemistry, v. 5, p. 571–585 (LBL-30710).

The isotopic ratios of H, O and C in water within the Long Valley caldera, California reflect input from sources external to the hydrothermal reservoir. A decrease in δD in precipitation of 0.5‰ km^{-1}, from west to east across Long Valley, is caused by the introduction of less fractionated marine moisture through a low elevation embayment in the Sierra Nevada Mountain Range. Relative to seasonal fluctuations in precipitation (−158 to −35‰), δD ranges in hot and cold surface and groundwaters are much less variable (−135 to −105‰). Only winter and spring moisture, reflecting higher precipitation rates with lighter isotopic signatures, recharge the hydrological system. The hydrothermal fluids are mixtures of isotopically heavy recharge (δD = −115‰, $\delta^{18}O$ = −15‰) derived from the Mammoth embayment, and isotopically lighter cold water (δD = −135‰, $\delta^{18}O$ = −18‰). This cold water is not representative of current local recharge. The $\delta^{13}C$ values for dissolved carbon in hot water are significantly heavier (−7 to −3‰) than in cold water (−18 to −10‰) denoting a separate hydrothermal origin. These $\delta^{13}C$ values overlie the range generally attributed to magmatic degassing of CO_2. However, $\delta^{13}C$ values of metamorphosed Paleozoic basement carbonates surrounding Long Valley fall in a similar range, indicating that hydrothermal decarbonization reactions are a probable source of CO_2. The $\delta^{13}C$ and $\delta^{18}O$ values of secondary travertine and vein calcite indicate respective fractionation with CO_2 and H_2O at temperatures approximating current hydrothermal conditions.

Wollenberg, H.A., and Revzan, K.L., 1990. Radium regionalization in California. Geophys. Res. Lett., v. 17, no. 6, p. 805–808 (LBL-28317).

The amount of ^{222}Rn that enters a house depends to a large extent on the concentration of radon's parent, ^{226}Ra in the soil. With the assumption that radium is in radioactive equilibrium with its ultimate parent, ^{238}U, we used the National Aerial Radiometric Reconnaisance (NARR) data and a database covering the concentration and distribution of uranium in California rocks to estimate the regional distribution of radium. A north-to-south increase in radium occurs between 42° and 36°N, then radium decreases southward. This pattern is explained by the distribution of rock types. The overall mean radium concentrations estimated from the aeroradiometric and lithologic data are similar, but there is a significant discrepancy between aeroradiometric and lithologic-estimated radium in central California. Ground measurements suggest that the radium values from aeroradiometric measurements there are erroneously high, pointing out the necessity of verifying aeroradiometrically-determined data before they are used to help predict radon production.

Wollenberg, H.A., and Smith, A.R., 1990. A geochemical assessment of terrestrial γ-ray absorbed dose rates. Health Physics, v. 58, no. 2, 1990, p. 183–189 (LBL-27395).

A survey of the geochemical literature and unpublished data has resulted in the classification of the concentrations of the naturally occurring radioelements U, Th, and K by their associated rock types. A data base of over 2500 entries has been compiled, permitting calculation of terrestrial γ-ray absorbed dose rates. The general lithology of terrains may be distinguished by their radioelement ratios, relative abundances, and total γ radioactivities. The γ-ray absorbed dose rates in air above igneous rocks generally vary with their silica contents, and with the exception of shale, sedimentary rocks have lower K:U and K:Th ratios

than most igneous rocks. The appreciable difference between the overall mean terrestrial γ-ray dose rate for rock of the continental surface ($\sim 7 \times 10^{-8}$ Gy h^{-1}) and the mean dose rate from field measurements over soil ($\sim 5 \times 10^{-8}$ Gy h^{-1}) is explained by the substantial differences between radioelement concentrations of soil and rock, differences that may vary markedly with rock type.

Wu, Y.-S., and Pruess, K., 1990. An analytical solution for wellbore heat transmission in layered formations. SPE Res. Eng., v. 5, no. 4, p. 531–538 (LBL-30725).

This paper presents a new analytical solution for wellbore heat transmission. Previous treatments of the wellbore heat-transfer problem are improved in several aspects: (1) nonhomogeneous formations are approximated as layered formations with different physical properties; (2) closed-form analytical solutions are obtained in both real and Laplace space; and (3) a more accurate formula is provided for the transient heat-conduction function, $f(t_D)$.

Zimmerman, R.W., Bodvarsson, G.S., and Kwicklis, E.M., 1990. Absorption of water into porous blocks of various shapes and sizes. Water Resour. Res., v. 26, no. 11, p. 2797–2806 (LBL-27511).

Approximate solutions are presented for absorption of water into porous spherical, cylindrical, and slablike blocks whose characteristic curves are of the van Genuchten-Mualem type. The solutions are compared to numerical simulations of absorption into blocks of the Topopah Spring member (Paintbrush tuff) from the site of the proposed nuclear waste repository at Yucca Mountain, Nevada. Guided by these results, a scaling law, based on the ratio of surface area to volume, is then proposed for predicting the rate of absorption into irregularly shaped blocks. This scaling law is tested against a numerical simulation of absorption into an irregularly shaped, 2-dimensional polygonal block and is shown to be a good approximation.

APPENDIX B: OTHER PUBLICATIONS

TOPICAL REPORTS

LBL-24725
Jacobsen, J.S., and Carnahan, C.L., 1990. Coupled transport processes in semipermeable media: Analytical solutions of the linearized governing equations.

LBL-24910
Billaux, D., Long, J.C.S., and Peterson, J.E., Jr., 1990. CHANGE: A numerical model for three-dimensional modelling of channelized flow in rock. Theory and design.

LBL-24911
Billaux, D., and Peterson, J.E., Jr., 1990. CHANGE: A numerical model for three-dimensional modelling of channelized flow in rock. Users manual and listing.

LBL-25413 (NDC-5)
Pruess, K., 1990. Numerical modeling of gas migration at a proposed repository for low and intermediate level nuclear wastes at Oberbauenstock, Switzerland.

LBL-25618
Carnahan, C.L., and Jacobsen, J.S., 1990. Coupled transport processes in semipermeable media. Part I: Theoretical basis.

LBL-25619
Jacobsen, J.S., and Carnahan, C.L., 1990. Coupled transport processes in semipermeable media. Part II: Numerical method and results.

LBL-26612
Aunzo, Z., Bodvarsson, G.S., Laky, C., Lippmann, M.J., Steingrimsson, B., Truesdell, A.H., and Witherspoon, P.A., 1989. The Ahuachapán geothermal field, El Salvador—Reservoir analysis. Three volumes: I. Text and main figures. II. Appendices A through E. III. Appendices F through I.

LBL-27045
Pigford, T.H., Chambré, P.L., and Lee, W.W.-L., 1990. A review of near-field mass transfer in geologic disposal systems.

LBL-27182
Long, J.C.S., Karasaki, K., Davey, A., Peterson, J., Landsfeld, M., Kemeny, J., and Martel, S., 1990. Preliminary predictions of inflow into the D-holes at the Stripa mine.

LBL-27338
Ahn, J., Kim, C.-L., Chambré, P. ., Pigford, T.H., and Lee, W.W.-L., 1989. Intermediate field transport of contaminants: Areal sources in fractured rock and point sources in porous media.

LBL-27528 (NDC-11)
Karasaki, K., 1989. Prematurely terminated slug tests.

LBL-27863 (NDC-12)
Long, J.C.S., Majer, E.L., Martel, S.J., Karasaki, K., Peterson, J.E., Jr., Davey, A., and Hestir, K., 1990. Hydrologic characterization of fractured rocks—An interdisciplinary methodology.

LBL-27864 (NDC-15)
Davey, A., Karasaki, K., Long, J.C.S., Landsfeld, M., Mensch, A., and Martel, S.J., 1989. Analysis of hydraulic data from the MI fracture at the Grimsel Rock Laboratory, Switzerland.

LBL-27900
Earth Sciences Division, 1990. Earth Sciences Division Annual Report 1989.

LBL-27912 (NDC-16)
Martel, S.J., and Peterson, J.E., Jr., 1989. Use of integrated geologic and geophysical information for characterizing the structure of fracture systems at the US/BK site, Grimsel Laboratory, Switzerland.

LBL-27913 (NDC-14)
Majer, E.L., Myer, L.R., Peterson, J.E., Jr., Karasaki, K., Long, J.C.S., Martel, S.J., Blümling, P., and Vomvoris, S., 1989. Joint seismic, hydrogeologic, and geomechanical investigations of a fracture zone in the Grimsel Rock Laboratory, Switzerland.

LBL-27914 (NDC-6)
Karasaki, K., 1989. Analysis of well test data from selected intervals in Leuggern deep borehole—Verification and application of PTST method.

LBL-27993
Earth Sciences Division, 1989. Hydrological, geochemical, and ecological characterization of Kesterson Reservoir: Annual report, October 1, 1988 through September 30, 1989.

LBL-28171
Zhou, Q., 1989. Audio-frequency electromagnetic tomography for reservoir evaluation (Ph.D. thesis).

LBL-28207
Zawislanski, P.T., 1989. Bare soil evaporation at Kesterson Reservoir, Merced County, California: Estimation by physical and chemical methods (M.S. thesis).

LBL-28594
Witherspoon, P.A., S. Benson, P. Persoff, K. Pruess, C.J. Radke, and Y.-S. Wu, 1990. Feasibility analysis and development of foam-protected underground natural gas storage facilities. Final Report, January 1986–June 1989.

LBL-28612
Polek, J.M., 1990. Studies of the hydraulic behavior of hierarchically fractured rock geometries (M.S. thesis).

LBL-28618
Bodvarsson, G.S., Cox, B.L., Fuller, P., Ripperda, M., Tulinius, H., Witherspoon, P.A., Goldstein, N., Flexser, S., Pruess, K., and Truesdell, A., 1989. A database for The Geysers geothermal field. Three volumes: I. Text and main figures. II. Appendix A: Steam flowrates and cumulative mass flows. III. Appendix B: Wellhead pressures and

degree of superheat; Appendix C: Injection rates and cumulative injection.

LBL-28638
Chen, Z.-X., Zimmerman, R.W., Bobdvarsson, G.S., and Witherspoon, P.A., 1990. A new formulation for one-dimensional horizontal imbibition in unsaturated porous media.

LBL-28642
Wu, Y.-S., 1990. Theoretical studies of non-Newtonian and Newtonian fluid flow through porous media.

LBL-28712
Wu, Y.-S., 1988. A comparison of analytical approaches for wellbore heat transmission in layered formations (M.S. thesis).

LBL-28807 (NDC-4)
Majer, E.L., Peterson, J.E., Jr., Blümling, P., and Sattel, G., 1988. P-wave imaging of the FRI and BK zones at the Grimsel Rock Laboratory.

LBL-28808 (NDC-7)
Majer, E.L., Peterson, J.E., Jr., Blümling, P., and Sattel, G., 1988. Shear-wave components at the Grimsel Laboratory.

LBL-28809 (NDC-8)
Loew, S., Tsang, C.F., Hale, F.V., and Hufschmied, P., 1989. The application of moment methods to analysis of fluid electrical conductivity logs in boreholes.

LBL-28810 (NDC-13)
Finsterle, S., Schlueter, E., and Pruess, K., 1989. Exploratory simulations of multiphase effects in gas injection and ventilation tests in an underground rock laboratory.

LBL-28818
Schlueter, E., and Pruess, K., 1990. Sensitivity studies on parameters affecting gas release from an underground rock cavern.

LBL-28819
Tsang, Y.W., and Pruess, K., 1989. Preliminary studies of gas phase flow effects and moisture migration at Yucca Mountain, Nevada.

LBL-28937
Wu, Y.-S., Pruess, K., and Chen, Z.X., 1990. Buckley-Leverett flow in composite porous media.

LBL-28938
Wu, Y.S., Pruess, K., and Witherspoon, P.A., 1990. Integral solutions for transient fluid flow through deformable media.

LBL-28958
Tura, M.A.C., 1990. Acoustic and elastic diffraction tomography and its application for fracture detection (Ph.D. thesis).

LBL-29127
Tsang, Y.W., and Pruess, K., 1990. Further modeling studies of gas movement and moisture migration at Yucca Mountain, Nevada.

LBL-29128
McNab, W.W., Jr., 1990. First-order kinetics-controlled multiple species reactive transport of dissolved organic compounds in groundwater: Development and application of a numerical model (M.S. thesis).

LBL-29203
Chen, D.-W., 1990. Coupled stiffness-permeability analysis of a single rough surfaced fracture by the three-dimensional boundary element method (Ph.D. thesis).

LBL-29235
Shan, C., 1990. Characteristics of leaky faults (Ph.D. thesis).

BOOK CONTRIBUTIONS

Chambers, K.T., and Radke, C.J., 1990. Capillary phenomena in foam flow through porous media (Chapter 6). *In* N.R. Morrow (ed.), Interfacial Phenomena in Oil Recovery. Marcel Dekker, New York, p. 191–255 (LBL-29149).

Pabalan, R.T., and Pitzer, K.S., 1990. Models for aqueous electrolyte mixtures for systems extending from dilute solutions to fused salts (Chapter 4). *In* D.C. Melchior and R.L. Bassett (eds.), Chemical Modeling of Aqueous Systems II (ACS Symposium Series 416). American Chemical Society, Washington, D.C., p. 44–57 (LBL-26468).

Stump, E., Borg, S.G., and Sheridan, M.F., 1990. Sheridan Bluff. *In* W.E. LeMasurier and J.W. Thomson (eds.), Volcanoes of the Antarctic Plate and Southern Oceans. American Geophysical Union Antarctic Research Series (Vol. 48), p. 136–137 (LBL-30806).

Stump, E., Borg, S.G., and Sheridan, M.F., 1990. Mt. Early. *In* W.E. LeMasurier and J.W. Thomson (eds.), Volcanoes of the Antarctic Plate and Southern Oceans. American Geophysical Union Antarctic Research Series (Vol. 48), p. 138–139 (LBL-30807).

Walawender, M.J., Gastil, R.G., Clinkenbeard, J.P., McCormick, W.V., Eastman, B.G., Wernicke, R.S., Wardlaw, M.S., Gunn, S.H., and Smith, B.M., 1990. Origin and evolution of the zoned LaPosta-type plutons, eastern Peninsular Ranges batholith, southern and Baja California. *In* J.L. Anderson (ed.), Nature and Origin of Cordilleran Magmatism. Geological Society of America Memoir 174, p. 1–18, 1990 (LBL-30808).

CONFERENCE PAPERS

Ahn, J., Chambré, P.L., Pigford, T.H., and Lee, W.W.-L., 1989. Transient diffusion from a waste solid into water-saturated, porous rock. Presented at the International Symposium on the Safety Assessment of Radioactive Waste Repositories, Paris, France, October 9–13, 1989 (LBL-27401).

Benson, S.M., Delamore, M., and Hoffman, S., 1990. Kesterson crisis: Sorting out the facts. Presented at the National Conference on Irrigation and Drainage Engineering, Durango, Colorado, July 11–13, 1990 (LBL-30587).

Birkholzer, J., Rouve, G., Pruess, K., and Noorishad, J., 1990. An efficient semianalytical method for numerical modeling of flow and solute transport in fractured media. Presented at the International Conference on Methods in Water Resources, Venice, Italy, June 1990 (LBL-30753).

Bodvarsson, G.S., Gaulke, S., and Ripperda, M., 1989. Some considerations on resource evaluation of The Geysers.

Presented at the Geothermal Resources Council 1989 Annual Meeting, Santa Rosa, California, October 1–4, 1989 (LBL-27598).

Carnahan, C.L., 1989. Modeling of coupled geochemical and transport processes: An overview. Presented at the International Symposium on the Safety Assessment of Radioactive Waste Repositories, Paris, France, October 9–13, 1989 (LBL-28048).

Carnahan, C.L., 1990. Simulation of reactive chemical transport in a varying thermal field with reaction-flow coupling. Presented at the International High Level Radioactive Waste Management Conference, Las Vegas, Nevada, April 8–12, 1990 (LBL-28328).

Chen, Z., Bodvarsson, G.S., and Witherspoon, P.A., 1990. An integral equation formulation for two-phase flow and other nonlinear flow problems through porous media. Presented at the 1990 SPE Annual Technical Conference and Exhibition, New Orleans, Louisiana, September 23–26, 1990 (LBL-30718).

Cook, A.M., Myer, L.R., Cook, N.G.W., and Doyle, F.M., 1990. The effects of tortuosity on flow through a natural fracture. Presented at the 31st U.S. Rock Mechanics Symposium, Golden, Colorado, June 18–20, 1990 (LBL-28443).

Cook, N.G.W., and Tsang, C.F., 1990. Dynamic use of geoscience information to develop scientific understanding for a nuclear waste repository. Presented at the International High Level Radioactive Waste Management Conference, Las Vegas, Nevada, April 8–12, 1990 (LBL-28329).

Cox, B.L., Pruess, K., and Persoff, P., 1990. A casting and imaging technique for determining void geometry and relative permeability behavior of a single fracture specimen. Presented at the Fifteenth Workshop on Geothermal Reservoir Engineering, Stanford, California, January 23–25, 1990 (LBL-28485).

Ettinger, R.A., and Radke, C.J., 1989. The influence of texture on steady foam flow in Berea sandstone. Presented at the 1989 SPE Annual Technical Conference and Exhibition, San Antonio, Texas, October 8–11, 1989 (LBL-27729).

Feighner, M.A., and Goldstein, N.E., 1990. A gravity model for the Coso geothermal area, California. Presented at the 1990 International Symposium on Geothermal Energy, Kailua-Kona, Hawaii, August 20–24, 1990 (LBL-28878).

Gillis, J.V., and Radke, C.J., 1990. A dual-gas tracer technique for determining trapped gas saturation during steady foam flow in porous media. To be presented at the 1990 SPE Annual Technical Conference and Exhibition, New Orleans, Louisiana, September 23–26, 1990 (LBL-29222).

Hesler, G.J., III, Zheng, Z., and Myer, L.R., 1990. In-situ fracture stiffness determination. Presented at the 31st U.S. Rock Mechanics Symposium, Golden, Colorado, June 18–20, 1990 (LBL-28444).

Hwang, Y., Pigford, T.H., Chambré, P.L., and Lee, W.W.-L., 1989. Mass transport in bedded salt and salt interbeds. Presented at the International High Level Radioactive Waste Management Conference, Las Vegas, Nevada, April 8–12, 1990 (LBL-27735).

Hwang, Y., Pigford, T.H., Lee, W.W.-L., and Chambré, P.L., 1989. Analytic solution of pseudocolloid migration in fractured rock. Presented at the American Nuclear Society Winter Meeting, San Francisco, California, November 26–30, 1989. Trans. Am. Nucl. Soc., v. 60, p. 107–109 (LBL-27429).

Hwang, Y., Chambré, P.L., Pigford, T.H., and Lee, W.W.-L., 1989. Analytic studies of colloidal transport in fractured porous media. Presented at the Materials Research Society Fall Meeting, Boston, Massachusetts, November 27–30, 1989, Scientific Basis for Nuclear Waste Management XIII (LBL-27200).

Isayama, Y., Chambré, P.L., Pigford, T.H., and Lee, W.W.-L., 1989. Isotopic effects on solubility-limited mass transfer. Presented at the American Nuclear Society Winter Meeting, San Francisco, California, November 26–30, 1989. Trans. Am. Nucl. Soc., v. 60, p. 110–112 (LBL-27428).

Javandel, I., and Shan, C., 1990. Hydrologic characterization of faults and other potentially conductive features in the unsaturated zone. Presented at the International High Level Radioactive Waste Management Conference, Las Vegas, Nevada, April 8–12, 1990 (LBL-28330).

Karasaki, K., Landsfeld, M., and Grossenbacher, K., 1990. Building of a conceptual model at UE25-c hole complex. Presented at the International High Level Radioactive Waste Management Conference, Las Vegas, Nevada, April 8–12, 1990 (LBL-28331).

Kumar, S., Zimmerman, R.W., and Bodvarsson, G.S., 1990. Study of fractal aperture distribution and flow in fractures. Presented at the International High Level Radioactive Waste Management Conference, Las Vegas, Nevada, April 8–12, 1990 (LBL-28362).

Lee, K.H., Majer, E.L., McEvilly, T.V., and Morrison, H.F., 1990. Application of geophysical methods for fracture characterization. Presented at the International High Level Radioactive Waste Management Conference, Las Vegas, Nevada, April 8–12, 1990 (LBL-28332).

Light, W.B., Lee, W.W.-L., Chambré, P.L., and Pigford, T.H., 1990. Radioactive colloid advection in a sorbing porous medium: Analytical solution. Presented at the Annual Meeting of the American Nuclear Society, Nashville, Tennessee, June 11–14, 1990. Trans. Am. Nucl. Soc., v. 61, p. 81–83 (LBL-28426).

Light, W.B., Pigford, T.H., and Lee, W.W.-L., 1989. ^{14}C transport in a partially saturated, fractured, porous medium. Presented at the Materials Research Society Fall Meeting, Scientific Basis for Nuclear Waste Management XIII, Boston, Massachusetts, November 27–30, 1989 (LBL-27199).

Lippmann, M.J., and Bodvarsson, G.S., 1990. Reservoir technology research at LBL addressing Geysers issues. Presented at the DOE Geothermal Program Review VIII, San Francisco, California, April 18–20, 1990 (LBL-29045).

Lippmann, M.J., and Truesdell, A.H., 1990. Reservoir simulation and geochemical study of Cerro Prieto I wells. Presented at the Fifteenth Workshop on Geothermal Reservoir Engineering, Stanford, California, January 23–25, 1990 (LBL-28851).

Lippmann, M.J., and Truesdell, A.H., 1990. Beneficial effects of groundwater entry into liquid-dominated geothermal systems. Presented at the 1990 International Symposium on Geothermal Energy, Kailua-Kona, Hawaii, August 20–24, 1990 (LBL-28971).

Long, J.C.S., Hestir, K., Karasaki, K., Davey, A., Peterson, J., Kemeny, J., and Landsfeld, M., 1989. Fluid flow in fractured rock: Theory and application. Presented at the NATO Advanced Study Institute on Transport Processes in Porous Media, Pullman, Washington, July 9–18, 1989. *In* J. Bear and M.Y. Corapcioglu (eds.), Transport Processes in Porous Media, Kluwer Academic Publishers, The Netherlands (LBL-27879).

Majer, E.L., Peterson, J.E., McEvilly, T.V., and Tura, M.A., 1990. The application of vertical seismic profiling and cross-hole tomographic imaging for fracture characterization at Yucca Mountain. Presented at the International High Level Radioactive Waste Management Conference, Las Vegas, Nevada, April 8–12, 1990 (LBL-28316).

Mensch, A., and Benson, S.M., 1990. Application of an expert system for analysis of geothermal well tests. Presented at the Fifteenth Workshop on Geothermal Reservoir Engineering, Stanford, California, January 23–25, 1990 (LBL-29617).

Myer, L.R., Pyrak-Nolte, L.J., and Cook, N.G.W., 1990. Seismic characterization of fracture properties. Presented at the International High Level Radioactive Waste Management Conference, Las Vegas, Nevada, April 8–12, 1990 (LBL-28333).

Myer, L.R., Pyrak-Nolte, L.J., and Cook, N.G.W., 1990. Effect of single fractures on seismic wave propagation. *In* N. Barton and O. Stephansson (eds.), Rock Joints. Proceedings, International Symposium on Rock Joints, Loen, Norway, June 4–6, 1990, p. 467–473 (LBL-28442).

Narasimhan, T.N., and Apps, J.A., 1990. Reactive chemical transport in ground-water hydrology: Challenges to mathematical modeling. Presented at the First USA/USSR Joint Conference on Environmental Hydrology and Hydrogeology, Leningrad, USSR, June 18–21, 1990 (LBL-29492).

Nitsche, H., 1989. Solubility studies of transuranium elements for nuclear waste disposal: Principles and overview. Presented at the Second International Conference on Chemistry and Migration Behavior of Actinides and Fission Products in the Geosphere, Monterey, California, November 6–10, 1989 (LBL-27173).

Nitsche, H., and Becraft, K., 1990. The complexation behavior of neptunium and plutonium with nitrilotriacetic acid. Presented at the 200th ACS National Meeting, Washington, D.C., August 26–31, 1990 (LBL-28821).

Noorishad, J., and Tsang, C.F., 1990. Development and verification of a numerical technique for coupled hydromechanical phenomena in rocks. *In* N. Barton and O. Stephansson (eds.), Rock Joints. Proceedings, International Symposium on Rock Joints, Loen, Norway, June 4–6, 1990, p. 557–564 (LBL-30751).

Persoff, P., Pruess, K., Benson, S.M., Wu, Y.S., Radke, C.J., Witherspoon, P.A., and Shikari, Y.A., 1989. Aqueous foams for control of gas migration and water coning in aquifer gas storage. Presented at the 1989 International Gas Research Conference, Tokyo, Japan, November 6–9, 1989 (LBL-27274).

Peterson, J.E., Jr., Majer, E.L., Tura, A., and Davey, A., 1989. Practical aspects of crosswell tomographic surveys. Presented at the International Symposium on Borehole Geophysics for Petroleum, Hydrogeology, Mining and Engineering Applications, Tucson, Arizona, February 1–3, 1990 (LBL-28279).

Pigford, T.H., 1989. Analytical methods for predicting contaminant transport. Presented at the International Symposium on the Safety Assessment of Radioactive Waste Repositories, Paris, France, October 9–13, 1989 (LBL-27400).

Pigford, T.H., Chambré, P.L., and Lee, W.W.-L., 1989. Mass transfer and transport in salt repositories. Presented at the International Symposium on the Safety Assessment of Radioactive Waste Repositories, Paris, France, October 9–12, 1989 (LBL-26852).

Pruess, K., 1990. Overview of TOUGH2, a general purpose numerical simulator for multiphase nonisothermal flows. Presented at the TOUGH Workshop, Lawrence Berkeley Laboratory, Berkeley, California, September 13–14,1990 (LBL-29525).

Pruess, K. (editor), 1990. Proceedings of the TOUGH Workshop, Berkeley, California, September 13–14, 1990 (LBL-29710).

Pyrak-Nolte, L.J., Cook, N.G.W., and Myer, L.R., 1990. A stratified percolation model for saturated and unsaturated flow through natural fractures. Presented at the International High Level Radioactive Waste Management Conference, Las Vegas, Nevada, April 8–12, 1990 (LBL-28334).

Rutqvist, J., Noorishad, J., Ljunggern, C., Stephansson, O., and Tsang, C.F., 1990. Theoretical and field investigations of fracture hydromechanical response under fluid injection. *In* N. Barton and O. Stephansson (eds.), Rock Joints. Proceedings, International Symposium on Rock Joints, Loen, Norway, June 4–6, 1990, p. 557–564 (LBL-30752).

Sadeghi, M.M., Lee, W.W.-L., Pigford, T.H., and Chambré, P.L., 1990. Diffusive release rates of radionuclides into saturated and unsaturated tuff. Presented at the Annual Meeting of the American Nuclear Society, Nashville, Tennessee, June 11–14, 1990. Trans. Am. Nucl. Soc., v. 61, p. 70–72 (LBL-28428).

Sadeghi, M.M., Lee, W.W.-L., Pigford, T.H., and Chambré, P.L., 1990. The effective diffusion coefficient for porous rubble. Presented at the Annual Meeting of the American Nuclear Society, Nashville, Tennessee, June 11–14, 1990. Trans. Am. Nucl. Soc., v. 61, p. 67–68 (LBL-28429).

Sadeghi, M.M., Lee, W.W.-L., Pigford, T.H., and Chambré, P.L., 1990. Release rates of radionuclides into dripping groundwater. Presented at the Annual Meeting of the American Nuclear Society, Nashville, Tennessee, June 11–14, 1990. Trans. Am. Nucl. Soc., v. 61, p. 68–70 (LBL-28430).

Schiffman, P., Bettison, L.A., and Smith, B.M., 1990. Mineralogy and geochemistry of epidosites from the Solea graben, Troodos ophiolite, Cyprus. *In* Ophiolites: Oceanic Crustal Analogues. Proceedings of the Symposium "Troodos 1987." Ministry of Agriculture and Natural Resources, Nicosia, Cyprus, p. 673–683 (LBL-30809).

Truesdell, A.H., and Lippmann, M.J., 1990. Interaction of cold-water aquifers with exploited reservoirs of the Cerro Prieto geothermal field. Presented at the 1990 International Symposium on Geothermal Energy, Kailua-Kona, Hawaii, August 20–24, 1990 (LBL-29046).

Tsang, C.F., 1989. A broad view of model validation. Presented at the International Symposium on the Safety Assessment of Radioactive Repositories Paris, France, October 9–13, 1989 (LBL-28094).

Tsang, C.F., 1990. Coupled behavior of rock joints. *In* N. Barton and O. Stephansson (eds.), Rock Joints. Proceedings, International Symposium on Rock Joints, Loen, Norway, June 4–6, 1990, p. 505–518 (LBL-28600).

Tsang, Y.W., and Tsang, C.F., 1990. Permeability and dispersivity of variable-aperture fracture systems. Presented at the International High Level Radioactive Waste Management Conference, Las Vegas, Nevada, April 8–12, 1990 (LBL-28335).

Tsang, Y.W., and Tsang, C.F., 1990. Hydrological characterization of variable-aperture fractures. *In* N. Barton and O. Stephansson (eds.), Rock Joints. Proceedings, International Symposium on Rock Joints, Loen, Norway, June 4–6, 1990, p. 423–431 (LBL-28759).

Witherspoon, P.A. (ed.), 1991. Geological Problems in Radiactive Waste Isolation—A World Wide Review. Proceedings of Workshop 3B, 28th International Geological Congress, Washington, D.C., July 15–16, 1989 (LBL-29703).

Wollenberg, H.A., Flexser, S., and Myer, L.R., 1990. Drill-back studies to examine fractured, heated rock. Presented at the International High Level Radioactive Waste Management Conference, Las Vegas, Nevada, April 8–12, 1990 (LBL-28336).

Wu, Y.-S., Pruess, K., and Witherspoon, P.A., 1990. Flow and displacement of Bingham non-Newtonian fluids in porous media. Presented at the 1990 SPE California Regional Meeting, Ventura, California, April 4–6, 1990 (LBL-28340).

Zimmerman, R.W., and Bodvarsson, G.S., 1989. Semi-analytical solutions for flow problems in unsaturated porous media. *In* R.R. Eaton et al. (eds.), Multiphase Transport in Porous Media, Proceedings, Winter Annual Meeting of the American Society of Mechanical Engineers, San Francisco, California, December 10–15, 1989, p. 23–28 (LBL-27578).

Zimmerman, R.W., and Bodvarsson, G.S., 1990. Combined analytical/numerical approaches to solving fluid flow problems in the unsaturated zone at Yucca Mountair.. Presented at the International High Level Radioactive Waste Management Conference, Las Vegas, Nevada, April 8–12, 1990 (LBL-28358).

Zimmerman, R.W., Chen, D.W., Long, J.C.S., and Cook, N.G.W., 1990. Hydromechanical coupling between stress, stiffness, and hydraulic conductivity of rock joints and fractures. *In* N. Barton and O. Stephansson (eds.), Rock Joints. Proceedings, International Symposium on Rock Joints, Loen, Norway, June 4–6, 1990, p. 571–577 (LBL-28601).

Zwahlen, E.D., Pigford, T.H., Chambré, P.L., and Lee, W.W.-L., 1989. Gas flow in and out of a nuclear waste container. Presented at the American Nuclear Society Winter Meeting, San Francisco, California, Novmber 27–30, 1989. Trans. Am. Nucl. Soc., v..60, p. 109–110 (LBL-27225).

Zwahlen, E.D., Pigford, T.H., Chambré, P.L., and Lee, W.W.-L., 1990. A gas-flow source term for a nuclear waste container in an unsaturated medium. Presented at the International High Level Radioactive Waste Management Conference, Las Vegas, California, April 8–12, 1990 (LBL-27734).

END

DATE
FILMED
11/08/91